

DAMAGE RESISTANT DESIGN METHODOLOGY FOR MULTI-HAZARD RESILIENT BUILDINGS

AISC Milek Fellowship Final Report

Michael Pollino¹, Derek Slovenec², Laura Rendos³, Gwen Evans⁴

¹Associate Professor, Case Western Reserve University, mcp70@case.edu

²Graduate Research Assistant, PhD Candidate, Case Western Reserve University

³Engineer, Magnusson Klemencic Associates, Seattle, WA (Former MS Student, CWRU)

⁴Engineer, Kellermeyer Godfryt Hart, Chicago, IL (Former MS Student, CWRU)

January 2019

Table of Contents

1. Introduction and Research Objectives	1-1
2. Background and Literature Review	2-1
2.1. Overview of Façade Connections	2-1
2.2. Building Envelope Systems Practice	2-3
2.2.1. Typical Details for Masonry Cavity Wall Systems.....	2-4
2.2.2. Typical Details for Precast Concrete Wall Panels	2-5
2.2.3. Typical Details for EIFS Panel System.....	2-5
2.3. Blast Design and Testing of Building Facades	2-6
2.4. Overview of Energy Dissipating Devices.....	2-8
2.5. Overview of A500 Hollow Structural Steel Material Properties	2-11
3. Multi-hazard Façade System (MHFS) Loading and Performance Objectives	3-1
3.1. Background and Definitions	3-1
3.2. Façade System Loading and Performance Objectives.....	3-3
3.2.1. Thermal/Moisture Effects and Temperature/Shrinkage Panel Reinforcement .	3-5
3.2.2. Dead Load (D; Self-Weight)	3-7
3.2.3. Seismic ($E = E_i + E_d + E_c$).....	3-8

3.2.3.1.	Inertia Effects (E_i).....	3-9
3.2.3.2.	In-Plane Drift Accommodation (E_d).....	3-10
3.2.3.3.	Corner Panel Contact Accommodation (E_c).....	3-12
3.2.4.	Wind.....	3-13
3.2.4.1.	Basic Wind Speed Pressures (W).....	3-13
3.2.4.2.	Tornado Winds (T_w).....	3-13
3.2.4.3.	Tornado Suction due to Atmospheric Pressure Drop (P_T).....	3-14
3.2.5.	Impulsive Loading (I).....	3-14
3.2.5.1.	Air-Blast (I_b).....	3-16
3.2.5.2.	Impact (I_i).....	3-17
3.3.	Load Combinations.....	3-18
4.	Behavior and Mechanics of Components.....	4-1
4.1.	Façade Panel.....	4-2
4.2.	Plastic Mechanics of Round Hollow Structural Section (HSS) Tubes.....	4-3
4.2.1.	Radial Force-Deformation Relationship.....	4-4
4.2.1.1.	Elastic Behavior.....	4-4
4.2.1.2.	Crushing Behavior.....	4-5
4.2.1.3.	Pulling Behavior.....	4-6
4.2.2.	Longitudinal Shearing of HSS Tube.....	4-9

4.2.3.	Rolling Force-Deformation Relationship.....	4-12
4.2.3.1.	Elastic Rolling Behavior.....	4-12
4.2.3.2.	Large Rolling Deformations.....	4-14
4.3.	U-Shaped Flexural Plate (UFP) Connector Mechanics	4-15
4.3.1.	UFP Rolling Mechanics	4-16
4.3.2.	UFP Crushing Mechanics.....	4-18
4.3.3.	UFP Pulling Mechanics.....	4-19
4.4.	Simplified Dynamic Model for Impulsive Load Design	4-22
4.4.1.	Panel Shape Function and Equivalent Mass and Stiffness.....	4-22
4.4.2.	Panel Kinetic, Elastic Potential, and Plastic Work Energies.....	4-24
4.4.3.	MDC and UFP Elastic Potential and Plastic Work Energies	4-27
4.4.4.	Simplified Nonlinear Dynamic Response under Uniform Impulsive Pressure Loading	4-29
5.	Design of Components to Achieve Performance Objectives	5-1
5.1.	Selection of Cross Section Geometry	5-2
5.2.	U-Shaped Flexural Plates (UFPs)	5-4
5.2.1.	Total Width of UFPs along Panel Edge	5-5
5.2.2.	Maximum UFP Forces for Connection Detailing and MDC Capacity Design.	5-8
5.2.3.	Connection Detailing Considerations.....	5-10

5.2.3.1.	Design Force Eccentricities	5-12
5.2.3.2.	Bolted UFP-to-Plate Connections	5-13
5.2.3.3.	Welded UFP-to-Plate Connections.....	5-13
5.3.	Multi-Hazard Ductile Connectors (MDCs)	5-14
5.3.1.	Lateral in-Plane Load-Carrying MDC: MDC-L	5-15
5.3.2.	Vertical Load-Carrying MDCs: MDC-V	5-16
5.3.3.	Minimum Total MDC HSS Length for Non-Impulsive Demands.....	5-17
5.3.4.	Controlling MDC-L and Total HSS Length per Panel Edge for Non-Impulsive Demands	5-18
5.3.5.	Design for Impulsive OP Demands.....	5-19
5.3.5.1.	Air-Blast	5-20
5.3.5.2.	Impact	5-22
5.3.6.	OP Bearing-Only MDC: MDC-B	5-22
5.3.7.	Connection Detailing Considerations.....	5-23
5.3.7.1.	Design Force Eccentricity	5-24
5.3.7.2.	HSS-to-Plate Welds.....	5-26
5.3.7.3.	End Plate Dimensions and Bolted Connections	5-27
5.4.	Capacity Design of Façade Panels.....	5-28
5.5.	Building Frame Interaction	5-29

6.	Integrated Design Procedure	6-1
6.1.	Step-by-Step Design Guideline.....	6-1
6.2.	Example Design of Reinforced Concrete (RC) Façade Panel System	6-7
6.3.	Viability of Design Methodology for Alternate Façade Panel Systems	6-8
7.	Multi-hazard Design Connector (MDC) Experimental Testing	7-1
7.1.	Experimental Testing Phase I: MDC Pulling, Crushing, Shearing Tests	7-1
7.1.1.	MDC1 and MDC2 Experiments.....	7-3
7.1.1.1.	Testing Setup	7-3
7.1.1.2.	Loading Protocols.....	7-5
7.1.1.3.	Instrumentation.....	7-8
7.1.2.	MDC3 Experiment	7-11
7.1.2.1.	Test Setup	7-11
7.1.2.2.	Loading Protocol	7-12
7.1.2.3.	Instrumentation.....	7-12
7.1.3.	Experimental Test Results.....	7-14
7.1.3.1.	Material Coupon Tension Test Results	7-14
7.1.3.2.	MDC1 Specimen Test Results.....	7-16
7.1.3.3.	MDC2 Specimen Test Results.....	7-16
7.1.3.4.	MDC3 Specimen Test Results.....	7-18

7.1.4.	Summary of Phase I Tests	7-19
7.2.	Experimental Testing Phase II: MDC Rolling Tests (Seismic In-plane Drift Load Case) 7-20	
7.2.1.	Introduction	7-20
7.2.2.	Test Specimen	7-21
7.2.3.	Deformation Protocol	7-22
7.2.4.	Test Setup and Instrumentation.....	7-23
7.2.5.	Results	7-27
7.2.6.	Summary of Phase II Tests	7-30
8.	Development and Validation of MDC Finite Element Model	8-1
8.1.	Introduction.....	8-1
8.2.	Base Model	8-1
8.2.1.	Model Description.....	8-1
8.2.2.	Verification of Base Model Results	8-3
8.3.	MDC Models of Experimental Specimens	8-4
8.3.1.	Introduction	8-4
8.3.2.	MDC Material Models	8-5
8.3.3.	MDC Type 1 Model (MDC1)	8-6
8.3.3.1.	Model Descriptions.....	8-6

8.3.3.2.	Convergence Study.....	8-7
8.3.3.3.	Results	8-8
8.3.4.	MDC Type 2 Model (MDC2)	8-10
8.3.4.1.	Model Description	8-10
8.3.4.2.	Convergence Study.....	8-11
8.3.4.3.	Results	8-12
8.3.5.	MDC Type 3 Model (MDC3)	8-13
8.3.5.1.	Model Description	8-13
8.3.5.2.	Convergence Study.....	8-14
8.3.5.3.	Results	8-14
8.4.	Summary	8-15
9.	MHFS Component and Building System Confirmation Analyses	9-1
9.1.	Introduction.....	9-1
9.2.	Multi-hazard Façade System (MHFS) Connectors.....	9-1
9.2.1.	Multi-hazard Ductile Connectors (MDCs).....	9-3
9.2.1.1.	Radial Crushing	9-4
9.2.1.2.	Radial Pulling	9-7
9.2.1.3.	Longitudinal Shearing	9-8
9.2.1.4.	Rolling	9-11

9.2.2.	U-shaped Flexural Plates (UFPs)	9-12
9.2.2.1.	Rolling	9-13
9.2.2.2.	Radial Crushing	9-14
9.2.2.3.	Radial Pulling	9-17
9.3.	MHFS Air-Blast Impulse Dynamic Analysis	9-18
9.4.	Building with MHFS Dynamic Analysis	9-22
9.4.1.	Seismic Response	9-22
9.4.2.	Air-blast Impulse Response	9-31
10.	Summary, Conclusions, and Recommendations for Future Work	10-1
10.1.	Summary and Conclusions	10-1
10.2.	Recommendations for Future Work	10-5
11.	References	11-1

List of Tables

Table 2-1: Critical Façade System Dynamic Behavior Properties Extracted from Literature	2-13
Table 3-1: Structural Hazards and System Performance Objectives	3-20
Table 3-2: Design Parameters for Tornado Winds (Adapted from USNRC, 2007).....	3-20
Table 3-3: Design Façade Impulse Values	3-21
Table 3-4: MHFS Load Combinations	3-22
Table 4-1: MDC and UFP Load Demands and Design Criteria	4-33
Table 5-1: Total UFP Width Design with $t_{UFP} = 0.25$ in. for Reinforced Concrete Façade Panel (normal weight, 13'x30'x6") at Ground Elevation.....	5-31
Table 5-2: Total UFP Width Design with $t_{UFP} = 0.25$ in. for Reinforced Concrete Façade Panel (normal weight, 13'x30'x6") at Roof Elevation	5-32
Table 5-3: MDC-V HSS Length Design with $t_{HSS} = 0.25$ in. for Reinforced Concrete Façade Panel (normal weight, 13'x30'x6") at Ground Elevation.....	5-33
Table 5-4: MDC-V HSS Length Design with $t_{HSS} = 0.25$ in. for Reinforced Concrete Façade Panel (normal weight, 13'x30'x6") at Roof Elevation.....	5-34
Table 5-5: MDC-L HSS Length Design with $t_{HSS} = 0.25$ in. for Reinforced Concrete Façade Panel (normal weight, 13'x30'x6") at Ground Elevation.....	5-35
Table 5-6: MDC-L HSS Length Design with $t_{HSS} = 0.25$ in. for Reinforced Concrete Façade Panel (normal weight, 13'x30'x6") at Roof Elevation	5-36
Table 5-7: Total MDC-V+L HSS Length Design with $t_{HSS} = 0.25$ in. for Reinforced Concrete Façade Panel (normal weight, 13'x30'x6") at Ground Elevation	5-37

Table 5-8: Total MDC-V+L HSS Length Design with $t_{HSS} = 0.25$ in. for Reinforced Concrete Façade Panel (normal weight, 13'x30'x6") at Roof Elevation	5-38
Table 5-9: MDC-B HSS Length Design with $t_{HSS} = 0.25$ in. for Reinforced Concrete Façade Panel (normal weight, 13'x30'x6")	5-39
Table 5-10: Maximum Inter-Story Drift for Light, East-Coast Office Building Design Subjected to Air-Blast Events.....	5-40
Table 6-1: Example Reinforced Concrete Façade Panel System Design for Building in Los Angeles, CA (Story 1 of 3).....	6-11
Table 6-2: Example Reinforced Concrete Façade Panel System Design for Building in Los Angeles, CA (Story 2 of 3).....	6-12
Table 6-3: Example Reinforced Concrete Façade Panel System Design for Building in Los Angeles, CA (Story 3 of 3).....	6-13
Table 6-4: Example Designs for Alternative Façade Systems.....	6-14
Table 7-1: Nominal Dimensions of MDC Specimen Components	7-32
Table 7-2: Comparison of MDC experimental results to design values.....	7-32
Table 7-3: Seismic Qualification Testing Displacement Protocol.....	7-33
Table 7-4: Instrumentation Inventory	7-33
Table 8-1: Convergence study mesh sizes for each MDC component. Final mesh size for each MDC model is bold.	8-17
Table 8-2: Comparison of the FEA results to the desired design values for each MDC.....	8-17
Table 9-1: HSS Radial Plastic Mechanism Strength FEA Results.....	9-38
Table 9-2: HSS Radial Stiffness Calculation Comparison with FEA Results.....	9-38

Table 9-3: HSS Longitudinal Shear Mechanism Strength Calculation Comparison with FEA Results	9-38
Table 9-4: HSS Longitudinal Shear FEA Stiffness	9-38
Table 9-5: HSS Rolling Mechanism Strength Calculation Comparison with FEA Results	9-39
Table 9-6: HSS Rolling Stiffness Calculation Comparison with FEA Results	9-39
Table 9-7: Prototype MHFS Design with Reinforced Concrete Panels	9-39
Table 9-8: Prototype Braced Frame Seismic Analysis Model Dynamic Properties	9-40
Table 9-9: Prototype Moment Frame Seismic Analysis Model Dynamic Properties....	9-40
Table 9-10: Peak Drift Response of Prototype Braced Frame Building without MHFS...	9-41
Table 9-11: Peak Drift Response of Prototype Braced Frame Building with MHFS....	9-42
Table 9-12: Drift Ratios for Prototype Braced Frame Building with and without MHFS	9-43
Table 9-13: Peak Drift Response of Prototype Moment Frame Building without MHFS	9-44
Table 9-14: Peak Drift Response of Prototype Moment Frame Building with MHFS .	9-45
Table 9-15: Drift Ratios for Prototype Moment Frame Building with and without MHFS	9-46
Table 9-16: Peak MDC-V Demand-to-Capacity Ratio (D/C) of Prototype Braced Frame Building.....	9-47
Table 9-17: Peak MDC-V D/C of Prototype Moment Frame Building.....	9-48

Table 9-18: Peak MDC-L D/C of Prototype Braced Frame Building Subjected to MCE Suite	9-49
Table 9-19: Peak MDC-L D/C of Prototype Moment Frame Building Subjected to MCE Suite	9-50
Table 9-20: Peak UFP Deformation Ratio of Prototype Braced Frame Building Subjected to FrE Suite	9-50
Table 9-21: Peak UFP Deformation Ratio of Prototype Moment Frame Building Subjected to MCE Suite.....	9-51
Table 9-22: 3D Light-Mass Prototype Braced Frame Building Model Dynamic Properties	9-51
Table 9-23: Maximum Inter-Story Drifts for Prototype Building Subjected to Design Blast Scenario (DBS) Events	9-52
Table 9-24: Maximum MHFS Connector Crushing Deformations during DBS1 Simulation	9-52
Table 9-25: Maximum MHFS Panel Bending Moment Ratios during DBS1 Simulation	9-52
Table 9-26: Maximum MHFS Panel Hinge Rotation during DBS1 Simulation	9-52
Table 9-27: Maximum MHFS Connector Crushing Deformations during DBS2 Simulation	9-53
Table 9-28: Maximum MHFS Panel Bending Moment Ratios during DBS2 Simulation	9-53
Table 9-29: Maximum MHFS Connector Crushing Deformations during DBS3 Simulation	9-53

Table 9-30: Maximum MHFS Panel Bending Moment Ratios during DBS3 Simulation 9-

53

List of Figures

Fig. 2-1: Examples of eccentricity and connection type (Parker, 2008).....	2-14
Fig. 2-2: Typical masonry cavity wall system components and connections (adapted from Parker 2008).....	2-14
Fig. 2-3: Typical concrete panel column supported bearing connection (adapted from Parker 2008).....	2-15
Fig. 2-4: Typical EIFS cross-section geometry (adapted from Parker 2008).....	2-15
Fig. 2-5: Typical EIFS spandrel panel connection (adapted from Parker 2008).....	2-16
Fig. 2-6: Steel stud wall improved connections for blast loading (adapted from Salim et. al. 2005)	2-16
Fig. 2-7: Typical steel stud wall system with EIFS façade cross section geometry (adapted from Salim et. al. 2005)	2-17
Fig. 2-8: Typical “sandwich” concrete panel cross section geometry (adapted from Salim et. al. 2005)	2-17
Fig. 2-9: Typical precast concrete wall panel cross section geometry (adapted from Salim et. al. 2005)	2-17
Fig. 2-10: Typical insulated metal panel cross section geometry (adapted from Idriss et. al. 2016).....	2-18
Fig. 2-11: Deformation modes of different thicknesses of frusta (Mamalis, Johnson, & Viegelahn, 1984).....	2-18
Fig. 2-12: Force-deformation relationship for square aluminum extrusions filled with aluminum foam. (Hanssen et al., 2000)	2-19

Fig. 2-13: Force-deformation relationship for circular aluminum extrusions filled with aluminum foam (Hanssen et al., 2000)	2-19
Fig. 2-14: Two of five multi-cell cross sections tested in the study by Kim (Kim, 2002) 2-20	
Fig. 2-15: Force-displacement relationship for a square column and two multi-cell columns with the cross sections pictured in Fig. 2-13 (Kim, 2002).....	2-20
Fig. 2-16: Stable and unstable specimens plotted with geometric data. S is the spacing between stiffeners, t is the tube wall thickness, d is the stiffener thickness, and w is the height of one stiffener (Salehghaffari et al., 2011)	2-21
Fig. 2-17: Experimental force-displacement relationships a) HSS7x0.25 b) HSS10.75x0.25 c) HSS16x0.375 (Lavarney, 2013)	2-21
Fig. 2-18: Force-displacement relationships for four of seven specimens a) single cell section b) double cell section c) triple cell section d) triple cell section (Zhang & Zhang, 2014).....	2-22
Fig. 2-19: Force-displacement relationship for four of fourteen specimens; the “S” specimens represent straight tube and the “CD” tube represents corrugated specimens; S101 and CD10D have the same diameter, thickness, and length, as do S151 and CD15D (Eyvazian et al., 2014)	2-23
Fig. 2-20: Mean load for the study specimens (Alavi Nia & Parsapour, 2014)	2-23
Fig. 2-21: R_y and R_t values for standard steel sections and reinforcing (AISC 2010b) 2-24	
Fig. 2-22: Tensile coupon locations throughout the cross section of HSS10x6x1/4 (right) and HSS10x8x1/4 (left) (Fadden, 2013).....	2-24
Fig. 2-23: Tensile coupon results a) HSS10x6x1/4 b) HSS10x8x1/4 (Fadden, 2013)..	2-25

Fig. 3-1: Multi-Hazard Façade System (MHFS) Features	3-23
Fig. 3-2: MHFS Connector Layout and Functions	3-24
Fig. 3-3: Façade Panel Free Body Diagrams	3-25
Fig. 3-4: Seismic Building Drift Corner Panel Contact Accommodation Mechanism..	3-26
Fig. 3-5: Minimum Design Out-of-Plane Forces per 13'x30'x6" Reinforced Concrete Façade Panel for 9-Story Buildings Located in Boston, MA, and Los Angeles, CA....	3-27
Fig. 3-6: Design Tornado Wind Regions (Adapted from USNRC, 2007).....	3-27
Fig. 3-7: MHFS Out-of-Plane Performance Objectives and Progression of Inward Yielding	3-28
Fig. 3-8: Design Façade Impulse Values for 13'x30' Façade Panel.....	3-29
Fig. 4-1: Mechanics of Radially Deformed Round HSS (a) Initial Plastic Mechanism, (b) Crushing behavior, and (c) Pulling Behavior	4-34
Fig. 4-2: Normalized Geometric Relationships for Large HSS Tube Pulling Deformations	4-35
Fig. 4-3: Elastic Force Limit of Longitudinally Sheared Round HSS Considering (a) Tube Bending, (b) Wall Bending, and (c) Peak Resulting Combined Normal Stress	4-36
Fig. 4-4: Von Mises Stress Contour Plots for Longitudinally Sheared HSS Tube.....	4-37
Fig. 4-5: Mechanics of Rolling Round HSS (a) Initial Plastic Mechanism and (b) Elastic Stiffness.....	4-38
Fig. 4-6: HSS Tube Rolling Force-Deformation Model for Large Deformations	4-39
Fig. 4-7: UFP Mechanics during (a) Rolling, (b) Crushing, and (c) Pulling	4-40
Fig. 4-8: Normalized Geometric Relationships for Large UFP Pulling Deformations .	4-41

Fig. 5-1: Pseudo-Static Experimental Testing of MDCs Subjected to (a) Design Blast Loading and (b) Radial Pulling (Adapted from Rendos, 2018).....	5-41
Fig. 5-2: Total UFP Width per Panel Edge with $t_{UFP} = 0.25$ in. for Reinforced Concrete Panels at (a,b) Roof or (c,d) Ground Elevation, Primarily Considering (a,c) Wind or (b,d) Seismic Hazards.....	5-42
Fig. 5-3: MDC-V HSS Length with $t_{HSS} = 0.25$ in. for Reinforced Concrete Panels at (a,b) Roof or (c,d) Ground Elevation, Primarily Considering (a,c) Wind or (b,d) Seismic Hazards	5-43
Fig. 5-4: MDC-L HSS Length with $t_{HSS} = 0.25$ in. for Reinforced Concrete Panels at (a,b) Roof or (c,d) Ground Elevation, Primarily Considering (a,c) Wind or (b,d) Seismic Hazards	5-44
Fig. 5-5: Total MDC-V+L HSS Length with $t_{HSS} = 0.25$ in. for Reinforced Concrete Panels at (a,b) Roof or (c,d) Ground Elevation, Primarily Considering (a,c) Wind or (b,d) Seismic Hazards	5-45
Fig. 5-6: MDC-B HSS Length with $t_{HSS} = 0.25$ in. for Reinforced Concrete Panels	5-46
Fig. 5-7: MDC HSS Length per Panel Edge Design for Reinforced Concrete Panel Façade System Subjected to Impulsive Loading.....	5-47
Fig. 5-8: MDC HSS Length per Panel Edge Design for Brick Veneer with Steel Stud Wall Façade System Subjected to Impulsive Loading	5-48
Fig. 5-9: MDC HSS Length per Panel Edge Design for EIFS with Steel Stud Wall Façade System Subjected to Impulsive Loading.....	5-49
Fig. 5-10: MDC HSS Length per Panel Edge Design for Insulated Metal Panel Façade System Subjected to Impulsive Loading.....	5-50

Fig. 5-11: MDC (a) Plate Detail, (b) Design Eccentricity, and (c) Weld Detail	5-51
Fig. 5-12: MHFS Connector Layout and Functions for Alternative “Staggered” Panel Placement.....	5-52
Fig. 5-13: MDC-V Detail Illustration.....	5-53
Fig. 5-14: MDC-L Detail Illustration for (a) Centered or (b) Staggered Panel Placement with (c) Weak-Axis or (d,e) Strong-Axis Exterior Columns using (c,d) Bolted or (e) Welded Connections	5-54
Fig. 5-15: Detail Illustrations for (a) UFPs, and MDC-B with (b) Centered or Staggered Panel Placement with (c) Weak-Axis or (d) Strong-Axis Perimeter Columns.....	5-55
Fig. 7-1: MDC1 axes and details	7-34
Fig. 7-2: MDC2 axes and details	7-35
Fig. 7-3: MDC3 axes and details	7-36
Fig. 7-4: Experimental Setup a) Plan view of the laboratory with test equipment b) Elevation view of the laboratory with test equipment	7-37
Fig. 7-5: MDC1 experimental loading protocol a) 55-kip actuator, floor table, and wall table deformation protocol b) Resulting MDC translation and rotation.....	7-38
Fig. 7-6: MDC2 experimental loading protocol a) 55-kip actuator and floor table deformation protocol and wall table loading protocol b) Resulting MDC translation and rotation	7-39
Fig. 7-7: Instrumentation Layouts a) Instrumentation layout for the MDC1 experiment b) Instrumentation layout for MDC2 experiment	7-40
Fig. 7-8: MDC3 Experiment Setup a) Equipment and instrumentation in 220kip machine b) Vic 3-D DIC speck pattern on the HSS.....	7-41

Fig. 7-9: MDC1 plate stress-strain curves from two tensile coupons and the nominal yield strength and tensile strength for ASTM A36 steel.....	7-42
Fig. 7-10: HSS stress-strain curves from two tensile coupons and the nominal yield strength and tensile strength for ASTM A500 Grade C steel	7-43
Fig. 7-11: MDC1 Experiment Results a) Applied radial deformation $+x_L$ and rotation (about $+z_L$) b) Approximate deformations of the MDC components c) Force-Deformation curve d) Moment-Rotation curve e) Deformation of the MDC at various times.....	7-44
Fig. 7-12: MDC2 Experiment 1 Results a) Applied radial deformation $-x_L$ and applied rotation (about y_L) b) Applied gravity load $+z_L$ c) Force-Deformation curve d) Moment-Rotation curve e) Deformation of the MDC at times throughout the loading protocol f) Nut contact with the HSS at times throughout the loading protocol	7-45
Fig. 7-13: MDC 2 Experimental 1-4 Results a) Applied radial deformations $-x_L$ and applied rotations (about y_L) for four consecutive experiments b) Applied gravity loads $+z_L$ for four consecutive experiments c) Force-Deformation curves for four consecutive experiments d) Final fracture surfaces at the end of MDC2 Experiment 4 on panel plate (left) and frame plate (right).....	7-47
Fig. 7-14: MDC3 Experiment Results a) The shearing deformation imposed between the MDC plates in z_L b) Force-Deformation curve c) Deformation of the MDC d) Failure surface of MDC3 (left) and failure locations (right).....	7-49
Fig. 7-15: MDC3 Vic-3D DIC first principal strain results.....	7-51
Fig. 7-16: MDC Rolling Experimental Test Specimen Fabrication Drawings.....	7-53
Fig. 7-17: Test Setup Elevation View.....	7-54
Fig. 7-18: Test Setup Plan View.....	7-55

Fig. 7-19: Test Instrumentation.....	7-56
Fig. 7-20: Photograph of Test Setup.....	7-57
Fig. 7-21: Photograph of Test Setup Details.....	7-58
Fig. 7-22: Photographs of Specimen Details and Failure	7-59
Fig. 7-23: Actuator Displacements	7-60
Fig. 7-24: String Potentiometer Displacement Readings.....	7-61
Fig. 7-25: Specimen Displacement.....	7-62
Fig. 7-26: Actuator Load Cell Readings.....	7-63
Fig. 7-27: Strain Gauge Readings.....	7-64
Fig. 7-28: Specimen Rolling Force Calculations	7-65
Fig. 7-29: Specimen Force-Deformation Hysteresis and Comparison with FEA and Theoretical Response	7-66
Fig. 7-30: Specimen Force-Deformation Hysteresis Detail.....	7-67
Fig. 8-1: An example base model showing the coordinate system for all of the base and MDC models.....	8-18
Fig. 8-2: Stress-strain curves input into the base FEA models for HSS16x0.375 and HSS10.75x0.25. Based on tensile coupon data from Lavarney (2013) experiments.	8-18
Fig. 8-3: HSS10.75x0.25 Base Model FEA Results a) Force-deformation response including comparison between FEA and Lavarney (2013) experiment b) Deformed shapes of HSS10.75x0.25 c) Von-Mises stress of the HSS10x0.25 at $\delta_{HSS}=6''$. Stress in units of ksi. d) Plastic strain of the HSS10x0.25 at $\delta_{HSS}=6''$	8-19
Fig. 8-4: HSS16x0.375 Base Model FEA Results a) Force-deformation response including comparison between FEA and Lavarney (2013) experiment b) Deformed shapes of	

HSS16x0.375 c) Von-Mises stress of the HSS16x0.375 at $\delta_{HSS}=6''$. Stress in units of ksi.	
d) Plastic strain of the HSS16x0.375 at $\delta_{HSS}=6''$	8-21
Fig. 8-5: Stress-Strain data defining MDC material models for A36 plate and A500 Grade C HSS used in the FEA.....	8-23
Fig. 8-6: MDC1 Convergence study at design basis of 3.1in translation and 0.025 rads rotation a) Deformation (x-direction) and rotation (about z- axis) applied in the FEA b) Approximate point locations on MDC1 cross section analyzed for convergence study c) Model 1 and Model 2 boundary conditions d) Force-Deformation results e) Convergence results of P1 on HSS f) Convergence results of P2 on HSS g) Convergence results of P3 on frame plate h) Convergence results of P4 on panel plate.....	8-24
Fig. 8-7: FEA Results of MDC1 a) Force-deformation curves of the FEA and MDC1 experiment b) Force-deformation curves of the MDC components from the FEA and MDC1 experiment c) Deformed shapes throughout the FEA	8-28
Fig. 8-8: FEA MDC1 Stress and Strain Contours a) Model 1 Von-Mises stress (ksi) contours at the design deformation and rotation b) Model 2 Von-Mises stress (ksi) contours at the design deformation and rotation c) Model 1 Equivalent plastic strain contours at the design deformation and rotation d) Model 2 Equivalent plastic strain contours at the design deformation and rotation.....	8-30
Fig. 8-9: MDC2 Convergence Study a) Deformation (x-direction) and rotation (about y-axis) applied in the FEA b) Vertical gravity load (z-direction) applied in the FEA c) Applied boundary conditions d) Approximate point locations on MDC2 cross section analyzed for convergence study e) Force-Deformation results f) Convergence results of P1 on HSS g) Convergence results of P2 on HSS	8-34

Fig. 8-10: FEA Results of MDC2 a) Force-deformation curves of the FEA and MDC2 experiment b) Deformed shapes throughout the FEA c) Von-Mises stress (ksi) contours at the design deformation and rotation d) Equivalent plastic strain contours at the design deformation and rotation..... 8-37

Fig. 8-11: MDC3 Convergence Study a) Deformation (z-direction) applied in the FEA b) Approximate point locations on MDC3 cross section analyzed for convergence study c) Applied boundary conditions d) Force-Deformation results e) Convergence results of P1 on HSS f) Convergence results of P2 on HSS 8-39

Fig. 8-12: FEA Results of MDC3 a) Force-deformation curves of the FEA and MDC3 experiment b) Deformed shapes throughout the FEA c) Von-Mises stress (ksi) contours at the design deformation d) Von-Mises elastic strain contours at the design deformation e) Equivalent plastic strain contours at the design deformation 8-42

Fig. 9-1: ASTM A500 Gr. B Steel Material Stress-Strain Model for Round HSS Tubes . 9-54

Fig. 9-2: MDC with 12-inch HSS6 Tube Radial Crushing Force-Deformation Behavior 9-55

Fig. 9-3: Von Mises Stress Contours for Radially Crushed HSS Tube 9-56

Fig. 9-4: Equivalent Plastic Strain Contours for Radially Crushed HSS Tube 9-57

Fig. 9-5: MDC with 12-inch HSS6 Tube Radial Crushing FEA Maximum Plastic Strain 9-58

Fig. 9-6: MDC with 12-inch HSS6 Tube Radial Pulling Force-Deformation Behavior 9-59

Fig. 9-7: Von Mises Stress Contours for Radially Pulled HSS Tube 9-60

Fig. 9-8: Equivalent Plastic Strain Contours for Radially Pulled HSS Tube..... 9-61

Fig. 9-9: MDC with 12-inch HSS6 Tube Radial Pulling FEA Maximum Plastic Strain ..	9-62
Fig. 9-10: MDC with 12-inch HSS6 Tube Longitudinal Shearing Force-Deformation Behavior	9-63
Fig. 9-11: HSS Tube Longitudinal Shearing Elastic Stiffness	9-64
Fig. 9-12: Von Mises Stress Contours for Longitudinally Sheared HSS Tube	9-65
Fig. 9-13: Equivalent Plastic Strain Contours for Longitudinally Sheared HSS Tube..	9-66
Fig. 9-14: MDC with 12-inch HSS6 Tube Longitudinal Shearing FEA Maximum Plastic Strain.....	9-67
Fig. 9-15: MDC with 12-inch HSS6 Tube Rolling Force-Deformation Behavior	9-68
Fig. 9-16: Von Mises Stress Contours for Rolling HSS Tube.....	9-69
Fig. 9-17: Equivalent Plastic Strain Contours for Rolling HSS Tube	9-70
Fig. 9-18: MDC with 12-inch HSS6 Tube Rolling FEA Maximum Plastic Strain	9-71
Fig. 9-19: ASTM A36 Steel Material Stress-Strain Model for Flat Plates.....	9-71
Fig. 9-20: UFP with $d=6''$, $b=4''$, $t=0.25''$, and $l_{free}=4''$ Rolling Force-Deformation Behavior	9-71
Fig. 9-21: Von Mises Stress Contours for Rolling UFPs.....	9-72
Fig. 9-22: Equivalent Plastic Strain Contours for Rolling UFP	9-73
Fig. 9-23: UFP with $d=6''$, $b=4''$, $t=0.25''$, and $l_{free}=4''$ Maximum Plastic Strain	9-74
Fig. 9-24: UFP with $d=6''$, $b=4''$, $t=0.25''$, and $l_{free}=4''$ Radial Crushing Force-Deformation Behavior.....	9-74
Fig. 9-25: Von Mises Stress Contours for Radially Crushed UFPs.....	9-75
Fig. 9-26: Equivalent Plastic Strain Contours for Radially Crushed UFP.....	9-76

Fig. 9-27: UFP with $d=6''$, $b=4''$, $t=0.25''$, and $l_{free}=4''$ Radial Pulling Force-Deformation Behavior.....	9-77
Fig. 9-28: Von Mises Stress Contours for Radially Pulled UFPs.....	9-78
Fig. 9-29: Equivalent Plastic Strain Contours for Radially Pulled UFP.....	9-79
Fig. 9-30: MHFS Finite Element Analysis Model.....	9-80
Fig. 9-31: MHFS Finite Element Analysis Model Modal Periods and Shapes	9-81
Fig. 9-32: MHFS Air-Blast Response Time Histories.....	9-82
Fig. 9-33: Braced Frame Building Model.....	9-83
Fig. 9-34: Moment Frame Building Model	9-84
Fig. 9-35: MHFS Seismic Response Interaction Model.....	9-85
Fig. 9-36: Braced Frame Building with and without MHFS Seismic Inter-Story Drift Results.....	9-86
Fig. 9-37: Drift Ratios for Prototype Braced Frame Building with and without MHFS.....	9-87
Fig. 9-38: Moment Frame Building with and without MHFS Seismic Inter-Story Drift Results.....	9-88
Fig. 9-39: Drift Ratios for Prototype Moment Frame Building with and without MHFS.....	9-89
Fig. 9-40: 3D Braced Frame Building with MHFS Model for Air-Blast Response.....	9-90
Fig. 9-41: 3D Braced Frame Building with MHFS Design Blast Scenario 1 (DBS1) Response Time History.....	9-91

Abstract:

The design of critical buildings must consider extreme load effects from earthquakes, wind and tornado, blast and impact, among others. Many hazardous loads—such as wind pressures, blast impulses, and projectile impacts—originate at the façade system and are transferred via connections to the main structural system and, ultimately, to the foundation; resilient design for such extreme loads requires controlling damage along this load path. This research proposes a multi-hazard façade system (MHFS) design methodology capable of achieving multiple performance objectives for all credible hazards while focusing damage to easily replaceable connectors, thereby reducing operational downtime and repair costs following an extreme event. This methodology is supported by fundamental mechanics and dynamics, advanced nonlinear transient analyses at the component, system, and building levels, and quasi-static experimental testing of multi-hazard ductile connectors (MDCs). Façade-frame interaction during blast scenario analyses suggest adequate performance of typical building frames with MHFS, while seismic analyses suggest interaction that is not necessarily detrimental to performance but should likely be considered during lateral force resisting system (LFRS) design. The proposed MHFS is believed to be a practical and effective approach for improving building performance considering extreme events.

1. Introduction and Research Objectives

Buildings provide controlled interior spaces in which recreational, commercial, and domicile activities can safely be conducted. While the primary function of a building is to keep its inhabitants safe, modern building design has advanced this goal towards reducing potential repair costs, operational downtime, and environmental impacts over the building's lifetime. These consequences are largely driven by rare, high-intensity events such as earthquakes and extreme wind scenarios (tornados, hurricanes, etc.), among others. Design for hazardous events generally focuses on the building's primary lateral force resisting system (LFRS), which transfers these extreme loads through the building and, ultimately, to the foundation along a load path which concentrates ductile demands (i.e. damage) to designated members. Often neglected in this approach is the role of the façade system, which serves as the gateway for all hazardous loads, which are incident upon the building's exterior envelope. Additionally, interaction between façade and building frame systems during seismic events have caused premature failure and detachment of façade panels, exposing the interior space to environmental hazards (water infiltration, inhospitable temperatures, etc.) and rendering it unusable until the enclosure can be repaired or replaced. Building envelopes also serve as the primary means of defense against potential targeted attacks, emphasizing their importance particularly for critical infrastructure (e.g. hospitals).

This project seeks to provide a performance-based design methodology for façade systems and their interaction with the building frame to minimize damage and hasten the recovery of buildings back to (essentially) full functionality following any credible extreme loading event. Façade panel and connection details are often prescriptive and intended to

provide the minimum required mechanical strength while focusing on practical concerns including on-site installation and adjustability to within specified tolerances. The proposed multi-hazard façade system (MHFS) design methodology must include these features while also introducing controlled ductility and capacity-proportioned strength of the façade panel and its connection to the structural frame to provide adequate performance during extreme loading events and concentrate damage to replaceable components. These replaceable components include multi-hazard ductile connectors (MDCs) developed in this research, as well as U-shaped flexural plates (UFPs) which have been employed in past research. Atypical hazardous loading scenarios which are unique to façade systems—including air-blast effects due to accidental or deliberate explosions, tornado effects including high wind and suction phenomena, and the impact of blown debris borne by such events—are evaluated alongside more traditional hazardous loads to expand upon and promote façade system functionality as an integral facet of the overall building structure.

The primary objectives of this research include: (1) develop a multi-hazard, damage-resistant structural system which includes the building envelope, its connection to the LFRS, and interaction between the two systems, (2) provide practical design aids, equations, and procedural guidelines with illustrative examples for the newly-proposed MHFS, and (3) evaluate the performance of the proposed system subjected to a variety of hazardous loading scenarios to ensure adequate performance at the component, system, and building levels, including any effects—beneficial or detrimental—resulting from interaction between building frame and envelope systems. Research methods include principles of elastic and plastic mechanics including large-deformation effects, design for dynamic loads, multi-degree-of-freedom experimental testing of proposed connector

components, and nonlinear static and dynamic finite element analysis (FEA) at the component, system, and building levels including coupled MHFS and LFRS models subjected to seismic ground motion and simulated air-blast events.

This report begins with a review of key background literature and materials utilized in this research, followed by a detailed description of all service-level and hazardous loading scenarios, their implications for design, and MHFS performance objectives for each. Critical mechanics and behaviors of the proposed MHFS connector components are then developed and combined with the loading scenarios and performance objectives in an integrated design procedure. Experimental testing performed as part of this research is described, compared to the proposed theoretical behaviors, and verified through FEA using detailed shell element models. The proposed design procedure is then verified through a series of confirmation analyses performed using prototype MHFS and building designs subjected to hazardous loading scenarios. Finally, some conclusions and recommendations for future research on the topics examined in this study are discussed.

2. Background and Literature Review

2.1. Overview of Façade Connections

The building envelope (or façade) is a critical component that must resist various types of hazardous loading which may be applied as pressures, often on the exterior of the façade, or contact resulting from inter-story building deformations. The façade encloses the interior building spaces from the outside environment and its failure can result in further building performance issues (moisture penetration, thermal, etc.). The connection between the building façade to the building frame must transfer forces (façade dead load, wind forces, seismic inertia forces), accommodate differential movement of the structure under serviceability conditions (temperature and moisture expansion and contraction), allow for construction tolerances, and also accommodate the seismic drift in the plane of the panel such that lateral force is not resisted by the façade. Furthermore, for defense critical structures or those near high-energy sources, air-blast and projectile impact loading on the façade might also be considered in the façade design. All of these connection functions must be accomplished in a space only a few inches wide between the LFRS and the structural frame. The design of such connectors requires large elastic load carrying capacity in some directions and nonlinear force-deformation behavior in other directions to achieve acceptable performance under all conditions. The type of façade and utilization of the floor slab overhanging the spandrel beam tend to control the connection design rather than the discussed connection functions (Parker, 2008).

When façade connections are designed, the type of façade is a controlling component of the design. Some of the most common types of facades include brick veneer,

precast concrete panels, and aluminum curtain walls. All of these façade types require different quantities, thicknesses, and tolerances of membranes, backup walls, and other components between the building frame and the façade. Additionally, the façade type can control or limit the connection hinge location (Fig. 2-1). If the façade connection can be embedded into the façade, the connection can directly bear on the floor slab. This type of façade connection may be applicable to a precast concrete panel that allows the connection to be cast into the concrete. However, this type of connection may not be feasible for all facades, such as curtain walls. Facades connections may need to be attached to the back of the façade, which creates eccentric forces on the connection. The type of connections required for a type of façade will cause the loading and eccentricity to vary, which affects the size and shape of the connection (Parker, 2008).

Just as the façade type is crucial to the connection design, the floor slabs also play a role in façade connection design. The location the facade relative to the steel frame, the amount of slab overhanging the spandrel beam, the strength of the slab, and the degree that the slab edge is similar throughout the structural frame all affect the façade connection design. The façade connection design normally occurs after these aspects of the structure have been designed, so the slab design must anticipate necessary accommodations required for the façade connection design. The connection can apply the façade load directly to the slab overhanging the spandrel beam, or it can transmit load through a steel assembly to the slab. Transmitting the load directly to the slab is the most economical approach to connection design, but transmitting it through a steel assembly creates a connection more adaptable to the slab design. Although both the type of façade and the slab design affect

the façade connection, connection designs are at the discretion of the structural engineer and can vary widely across structures (Parker, 2008).

2.2. Building Envelope Systems Practice

The terms “envelope”, “façade”, and “cladding” are sometimes used interchangeably, but the building envelope system and the building façade system are different systems. The building envelope serves several purposes, namely to minimize water and air penetration into a building, control heat gain or loss into or out of the building, and provide a barrier between the building and the outdoors. The building envelope is comprised of the exterior walls, roof, fenestration, and doors. The façade is the exterior wall system and is a lateral component of the building envelope. The façade itself is composed of several components, including the cladding (i.e. brick masonry, EIFS (external insulation and finishing system), metal panels, etc.), the back-up structure (if separate from the cladding), water and air barriers, joints, and insulation. The facade may be selected for functionality or appearance and be able to accommodate loading from its self-weight, as well as external loads applied to it (including wind, seismic, and blast loads). The façade system is also designed to accommodate a level of differential movements, between the components of the building envelope and between the building envelope and the structure.

All of these design criteria are considered when designing the attachment from the building facade to the structure. Facade attachments must have sufficient strength, ductility, and redundancy to support the facade and to resist applied loads. Attachment of the facade to the building frame typically includes gravity load supporting connections in only two locations per panel, primarily for ease of design and constructability. However, there may be more than two lateral supports per façade panel. The façade connections

typically connect to the building structure at the building frame, but, if properly designed, the façade connections can be placed at the deck slab. The façade connections are detailed differently for different façade systems. Typical façade connections for several façade types are discussed in more detail below.

2.2.1. Typical Details for Masonry Cavity Wall Systems

Masonry cavity wall systems consist of several components, as displayed in Fig. 2-2. The exterior is a brick veneer cladding, laid in a bond pattern, typically around 4 inches thick. There is a cavity (typically about 2 inches wide) left between the brick masonry and the backup. The backup consists of sheathing, a water barrier, insulation, and a steel stud wall backup. The brick veneer is supported on a steel shelf angle, typically occurring at each story (at 10 feet). This shelf angle carries the vertical load of the brick masonry. There are also steel anchors provided at approximately every 4 square feet of brick masonry, which tie the masonry to the backup. These steel anchors provide lateral, out-of-plane support to the masonry.

In order to allow for differential movement (due to the variety of materials employed in a masonry cavity wall system), movement joints are a necessary component of a masonry cavity wall system. Horizontal movement joints are typically placed below each shelf angle, both to allow for differential movement and to ensure loads are not transferred from one story to the brick veneer below the shelf angle. Vertical control joints are installed to accommodate differential movement and volume change. Vertical control joints are typically placed every 20 feet, on center (Parker 2008).

2.2.2. Typical Details for Precast Concrete Wall Panels

Precast concrete wall panels are either solid, reinforced concrete or concrete “sandwich” panels, consisting of two layers of concrete with a layer of rigid insulation “sandwiched” between, with all layers tied together. These panels are supported by no more than two load bearing connections in order to properly determine the force distribution to the connections. These connections either are direct bearing connections or are eccentric connections, depending on the panel layout and structure design. There is a small gap between the structure slab edge and the concrete panel for tolerance during erection and fire-safing material. Additionally, tieback connections are installed to provide lateral restraint. Adequate joints must be installed in the precast concrete wall panel system in order to accommodate differential movement and volume change. The simplest and most efficient connection is a column-supported bearing connection; this is shown in Fig. 2-3. However, multiple variations of panel connections can be designed based on the conditions and constraints of the building.

There is a wide variety in the size and shape of precast concrete panels, and design choices for aesthetics, economy, and ease of erection can influence the design of the precast panels. Panels can be fabricated in nearly any size, as long as it can be transported to the site and erected (Parker 2008). A typical panel is around 20 feet wide, although panels have been manufactured up to 50 feet wide.

2.2.3. Typical Details for EIFS Panel System

EIFS (exterior insulation and finish system) is a relatively new type of façade system, developed in the 1950s. This lightweight system is made of the EIFS cladding connected

to a steel stud backup, as shown in Fig. 2-4. The EIFS cladding is made up of a rigid expanded polystyrene insulation board. The interior side has sheathing, attached with adhesive. The exterior side of the insulation board is covered in a polymer-modified cement base coat, glass-fiber fabric, and an acrylic-based, textured finish. EIFS panels are very lightweight; they are not load bearing and are not designed to resist large lateral loads.

The connections from EIFS panels to the primary building structure vary depending on the structural conditions. The EIFS panel system is hung from the structure, and only two bearing connections are used per panel. Panels can either be attached at the floor slabs or spandrel panels (as shown in Fig. 2-5). There is a small gap between the floor slab and the EIFS Panel system, in order to account for fire-safing material and to accommodate constriction tolerances. The EIFS panels can come in a variety of sizes and are designed to meet aesthetic desires, movement and adjustability requirements, and durability. As with other systems, joints are required to accommodate differential movement and volume changes in the panels (Parker 2008).

2.3. Blast Design and Testing of Building Facades

Several studies on the behavior, analysis, and testing of different facade systems subjected to blast loading have been performed. This section reviews various typical facade systems and discusses the critical dynamic and nonlinear force-deformation characteristics obtained or quantified from the reviewed reports.

Salim et. al. (2005) performed multiple static and dynamic tests of steel stud walls with a brick façade with various connection details (one of which is shown in Fig. 2-6). These tests confirm that improvements in the connections can improve the performance of a steel stud wall system under blast loading. The changes included adding additional

screws per stud and installing the stud wall with a rigid slip track. These changes were shown through blast load testing to improve the ductility of the system and thus improving its capacity to absorb blast energy. The type of sheathing used can also increase the stability of the system.

Naito, et. al. (2011) also tested the blast loading performance of steel stud walls with an exterior insulation and finishing system (EIFS) facade and a “sandwich” precast concrete panel (exterior concrete panels with insulating material in between), as well as a precast concrete panel, and as shown in Fig. 2-7, Fig. 2-8, and Fig. 2-9, respectively. The study determined the effectiveness of using precast concrete panels and “sandwich” concrete panels as a retrofit method of blast protection to an existing building. The effectiveness of these concrete panels stems from their large mass, providing a large inertial resistance. Naito et al. confirmed that the precast wall system provides significant protection, but their study of EIFS facades show that this system can also perform quite well under blast loading. Models predicted and testing proved that maintaining a larger cavity between the panel and structure could prevent damage to the structure under blast loading.

Idriss, et. al. (2016) performed analysis of insulated metal panels, made up of thin gage metal on the exterior and interior face, with insulation between, shown in Fig. 2-10. These systems are light but have a higher moment of inertia, due to the space in between panels. However, the thin panels are also prone to buckling prior to flexural yielding of the panel. This test was performed with bladders taking up the confined space in the testing apparatus, allowing a uniform static pressure to be applied to the metal

panels. Idriss et al. also proved that traditional analysis might under-predict response, as opposed to testing.

The critical structural and dynamic properties of various façade systems were extracted from the literature and noted in Table 2-1.

2.4. Overview of Energy Dissipating Devices

Within current structural engineering design, many types of loads (wind, seismic, ice, etc.) and loading scenarios must be considered during the building design process. However, seismic loading, extreme wind loading, and blast loading are unique loading scenarios that are special design considerations. These loading scenarios require a structure to absorb the kinetic energy associated with the loading. This energy absorption can be accomplished with an energy-absorbing device that plastically deforms to absorb the loading energy (Alghamdi, 2001). A variety of devices that vary in shape, size, and material properties were studied in this review for their energy dissipating properties. Yet, no energy-dissipating device has undergone a multi-hazard assessment to determine its ability to satisfy design objectives for two or more extreme-loading events. This review will examine previous studies of metallic energy dissipating connectors in order to determine which dissipaters are most suitable for acting as a façade connection that experiences a multi-hazard loading assessment.

Within the metallic energy absorbing devices, there are a variety of metals, shapes, and sizes used. Metallic energy absorbing devices are commonly studied for both structural engineering purposes and crashworthiness for vehicles. This review focused on steel, aluminum, and brass energy dissipaters. The review focuses on circular tubes, square tubes, corrugated tubes, stiffened tubes, multicellular tubes, and frusta.

In the mid-1980s, Mamalis, Johnson, and Viegelaahn (1984) studied the plastic deformation of thin-walled, steel frusta under axial loading. One experimental study found that the thickness of the steel frusta dictated the mode with which the frusta collapsed under axial compression (Fig. 2-11). When the wall frusta wall thickness increased, the peak and post-buckling load increased. The researchers also found that increasing the semi-apical angle of the frusta increases the peak and post-buckling load (Mamalis, Johnson, & Viegelaahn, 1984). A second experimental study in 1986 concluded that the wall thickness/diameter ratio played a key role in the deformation mode of aluminum and steel frusta. The narrow ends of frusta with a large thickness/diameter ratio deformed in circumferential rings, while the larger ends with a smaller thickness/diameter ratio deformed as lobes (Mamalis, Manolakos, Saigal, Viegelaahn, & Johnson, 1986).

In 2000, Hanssen, Langseth, and Hopperstad studied the static and dynamic crushing of square and circular aluminum extrusions filled with aluminum foam. The square extrusion experiments focused on the effects of wall thickness and the density of the aluminum foam for energy absorption. The researchers found that foam-filled extrusions deformed less and were capable of withstanding higher loads than the same aluminum extrusions without foam. The force capacity of the foam-filled extrusion also increased as the foam density increased (Hanssen, Langseth, & Hopperstad, 2000). Similar results were determined from the circular extrusion experiments. Additionally, both sets of experiments found that the force capacity of the foam filled extrusions were higher than the combined force capacity of the separate extrusion and foam (Fig. 2-12 and Fig. 2-13). An interaction between the extrusion and foam contributes to the higher load capacity (Hanssen et al., 2000).

Afterwards, in 2002, Kim investigated the properties of multi-cell aluminum extrusions under axial crushing using finite element modeling. The study modeled a variety of square extrusions that contained smaller cell extrusions within the square. It also investigated a square extrusion with circular cell extrusions inside the corners (Fig. 2-14, Fig. 2-15). The multi-cell extrusions were found to have higher energy absorption and weight efficiency than a single cell aluminum square extrusion. This increased energy absorption is due to the more complex mode of deformation for the multi-cell extrusions (Kim, 2002).

After the 2002 study by Kim, Saleghaffari, Rais-Rohani, and Najafi studied the axial crushing of externally stiffened tubes in 2011. The geometric properties of the stiffeners located on the outside of the tube determined the crushing stability, energy absorption, and peak crushing force for the tube. The stiffener spacing/tube thickness ratio determined if the crushing was unstable or stable (Fig. 2-16). The stiffened tubes were deemed more efficient than circular tubes at energy absorption (Salehghaffari, Rais-Rohani, & Najafi, 2011).

Lavarnway (2013) tested the radial energy absorbing capacity of steel tubes under building blast conditions. The tubes were welded radially between two plates, which simulated the façade and the structural frame of a building. The tubes were expected to act as a typical connection between the façade and frame before dissipating energy from the blast. During experiments in which the tubes were loaded radially, the tubes successfully dissipated high blast forces with large deformations (Fig. 2-17). It was determined that the use of a tube shaped section as a façade connection would significantly improve the blast resistance of a structure by absorbing the energy of the blast (Lavarnway, 2013).

During 2014, research projects occurred that tested the energy absorption of a variety of shapes. Zhang performed one such project, which tested the absorption capacity of multi-cell circular extrusions made of aluminum. Single, double, triple, and quadruple cell circular tubes were investigated. The multi-cell extrusions had a higher energy absorption capacity than the single cell extrusions (Fig. 2-18). The double cell tube also had a different deformation mode than the triple or quadruple cell (Zhang & Zhang, 2014).

Additionally, Evyazian, Habibi, Hamouda, and Hedayati (2014) tested the crushing and energy absorption of corrugated tubes. The corrugations in the tube caused the tube to plastically deform at predetermined locations. Some tubes that were tested had the corrugations parallel to the force, while others had corrugations that were perpendicular to the force. The study found that the mean load of the corrugated tubes was less than that of a straight walled tube (Fig. 2-19), but that the corrugated tube has a load uniformity during deformation (Evyazian, K. Habibi, Hamouda, & Hedayati, 2014).

Alavi Nia and Parsapour (2014) studied the energy absorption of many different triangular, square, hexagonal, and octagonal thin-walled, aluminum sections. Each type of specimen has a simple, single cell section tested for that shape. Two multi-cell modifications of each shape were also tested. The multi-cell modifications had a higher mean load than the single cell of each shape (Fig. 2-20). The modifications also had a higher energy absorption than their single cell counterparts (Alavi Nia & Parsapour, 2014).

2.5. Overview of A500 Hollow Structural Steel Material Properties

The Seismic Provisions for Structural Steel Buildings (AISC 341-10) include guidance to evaluate the expected material yield and tensile strengths of common structural grade steels in order to better estimate the true strength of materials. The provisions use factors that

can be applied to the minimum nominal yield and tensile strengths to estimate the expected yield and tensile strengths of a section (Fig. 2-21). The yield strength is multiplied by the R_y factor and the tensile strength is multiplied by the R_t factor (AISC 2010b).

Fadden (2013) studied hollow structural steel (HSS) sections to determine if the sections could improve seismic moment resisting frames. An intensive study into the material properties of A500 Grade B HSS was conducted as part of this research. Fadden tested 114 tensile coupons from locations throughout the cross sections of 11 different rectangular HSS (Fig. 2-22). Many of the coupons were from the side-walls of the rectangular HSS, but coupons were also taken from the rounded corners and the welded seam of the sections. Coupons were tested from many areas of the HSS cross section to evaluate the variation of material properties across the cross section. The rolling process and welding used to create HSS shapes leaves residual stresses in the sections, which affects its material properties. Fadden determined that while material properties of the HSS sidewalls were not affected by the rolling process, the material properties of the rounded corners and welded seams had significantly different stress-strain characteristics as seen in Fig. 2-23. The rounded corners and welded seams were less ductile and had slightly lower R_y and R_t ratios than recommended in the Seismic Provisions for Structural Steel Buildings. The changes in the material properties were localized to the corner and weld locations (Fadden, 2013).

The combination of test data from Fadden (2013) and the AISC Seismic Provisions (2010b) are used in finite element modeling to help establish the material models used in the analysis.

Table 2-1: Critical Façade System Dynamic Behavior Properties Extracted from Literature

System Type	Dead Loads [B]	Section Details	Width	Height	Unsupported Width	Modulus of Elasticity	Moment of Inertia (per foot width)	(E)I _{eff} (per foot width)	Natural Period	Yield Deflection at Midspan	Max Deflection at Midspan	Load at Yield (per foot width)	Maximum Load (per foot width)	Maximum Rotation at Support	Yield Strength	Maximum Shear Force	Maximum Bending Moment
Insulated Metal Panel [C]	15 psf	2.75" thick panel with two outer steel skins and interior insulation layer	Not Given	60 inches	58 inches	29,000 ksi	0.852 in ⁴	24650 kip*in ²	30 ms	0.8 inches	6.6 inches	93.6 lb/in	158.4 lb/in	12.82°	36 ksi	4.59 kips	39.36 kip-inches
Steel Stud Wall System with Brick Cladding [D]	50 psf	227 MPa (33 ksi) Clark 600S162-43 studs spaced at 406 mm (16 in.) with an external brick veneer cladding.	144 inches	144 inches	144 inches	29,000 ksi	12.073 in ⁴	350100 kip*in ²	140 ms	0.98 inches	6.3 inches	61.282 lb/in	396 lb/in	5.00°	36 ksi	28.5 kips	1026.4 kip-inches
Steel Stud Wall System with EIFS Cladding [D]	10 psf	227 MPa (33 ksi) Clark 600S162-43 studs spaced at 406 mm (16 in.) with an external EIFS cladding	144 inches	144 inches	144 inches	29,000 ksi	12.073 in ⁴	350100 kip*in ²	63 ms	1.96 inches	13.97 inches	122.57 lb/in	396 lb/in	10.98°	36 ksi	28.5 kips	1026.4 kip-inches
Steel Stud Wall System with EIFS Cladding [E]	10 psf	228 Mpa (33 ksi) 800162-33 studs spaced at 406 mm (16 in.) with an external EIFS cladding	88 inches	133.35 inches	133.35 inches	29,000 ksi	1.345 in ⁴	390000 kip*in ²	155 ms	0.59 inches	5.89 inches	6.425 lb/in	134 lb/in	5.05°	36 ksi	8.93 kips	297.9 kip-inches
Steel Stud Wall System with Sandwich Precast Concrete Panel [E]	105 psf	8" thick panel with two outer concrete layers and interior insulation layer	81.89 inches	136.5 inches	136.5 inches	Concrete = 3,000 ksi Steel = 29,000 ksi	517.987 in ⁴	1162000 kip*in ²	84 ms	0.16 inches	1.25 inches	43.56 lb/in	134 lb/in	1.05°	3 ksi	9.14 kips	312.1 kip-inches
Solid Precast Concrete Panel [E]	80 psf	6" thick reinforced concrete panel	81.89 inches	136.5 inches	136.5 inches	3,000 ksi	216 in ⁴	324000 kip*in ²	114 ms	0.33 inches	2.94 inches	38.28 lb/in	317.8 lb/in	2.47°	3 ksi	21.7 kips	740.2 kip-inches

Notes: [C]=Idriss et. al. (2016), [D]=Salim et. al. (2005), [E]=Naito et. al. (2011)

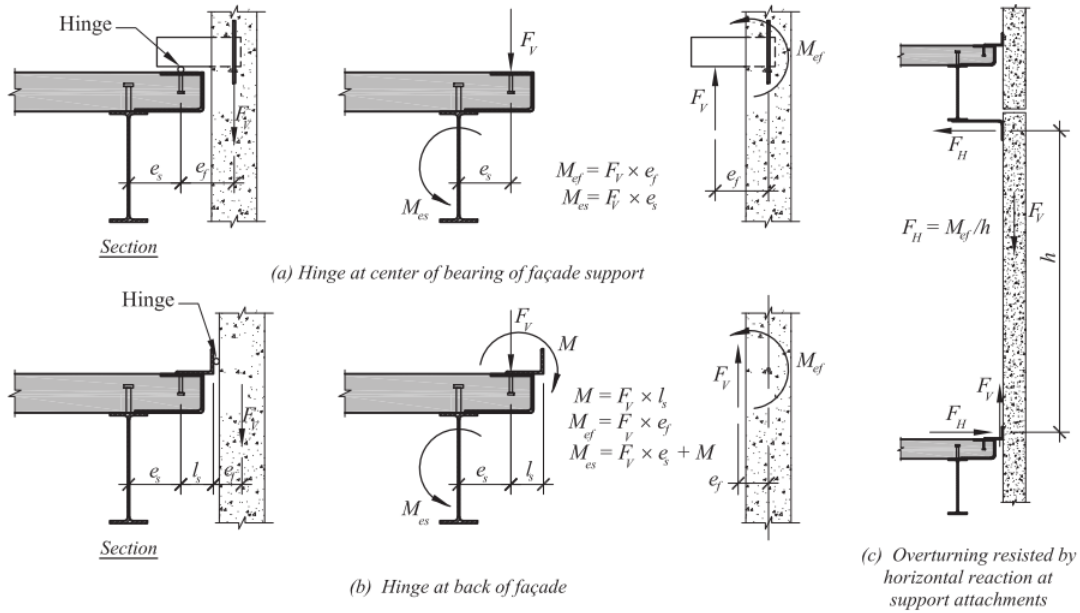


Fig. 2-1: Examples of eccentricity and connection type (Parker, 2008)

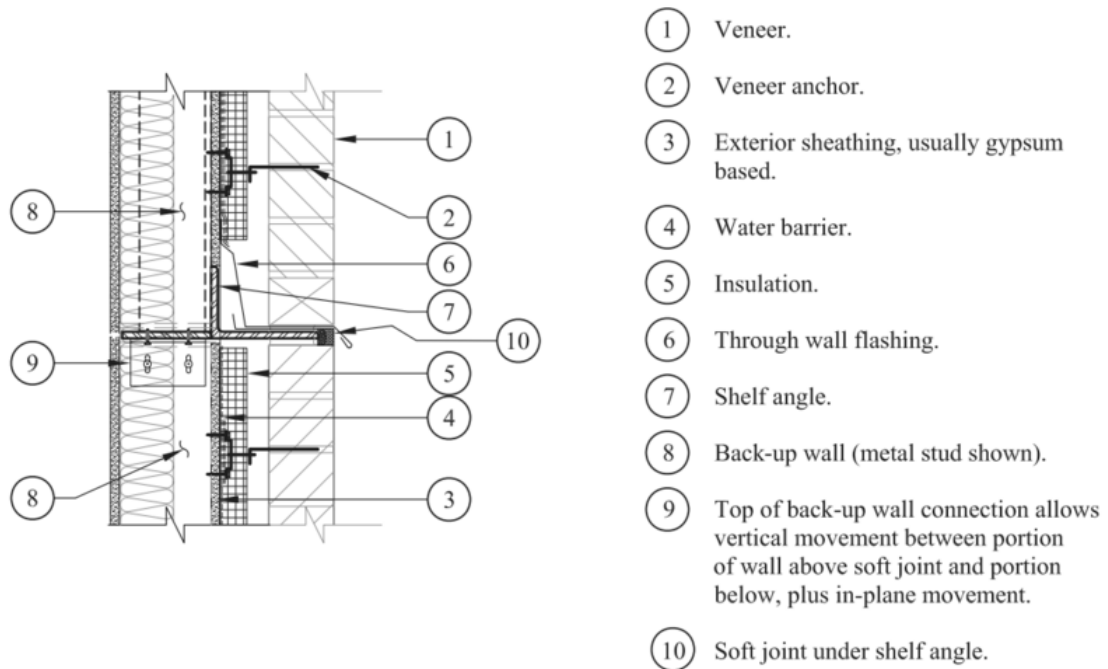
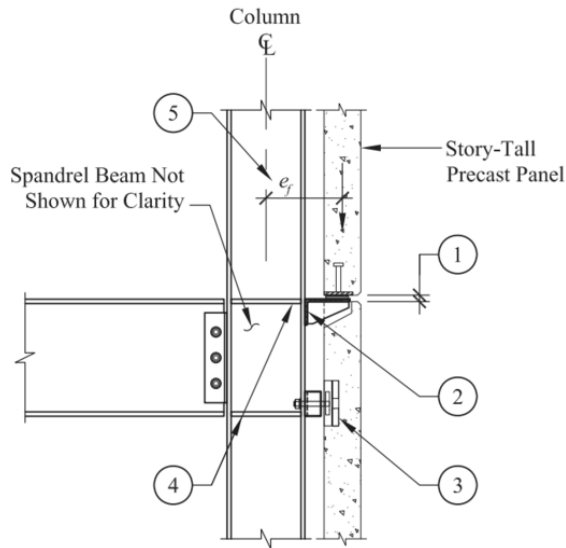


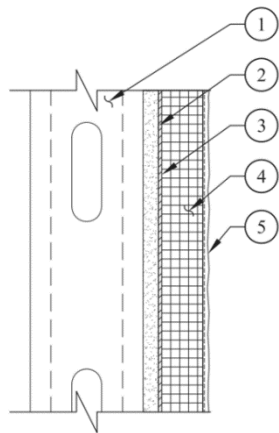
Fig. 2-2: Typical masonry cavity wall system components and connections (adapted from Parker 2008)



NOTES:

- ① Joint to allow differential vertical movement. Shim stack (or leveling bolt) bearing support at panel joint.
- ② Steel bracket bearing connection. Typically designed by the SSE.
- ③ Tie-back connection at top of lower panel to allow vertical and horizontal relative movement.
- ④ Stiffeners if required. Consider impact of stiffeners on the out-of-plane spandrel beam connection.
- ⑤ Maximum allowable eccentricity, e_r , specified by the Structural Engineer of Record.

Fig. 2-3: Typical concrete panel column supported bearing connection (adapted from Parker 2008)



NOTES:

- ① Metal stud backup panel frame.
- ② Sheathing.
- ③ Adhesive.
- ④ Rigid expanded polystyrene insulation board (EPS) insulation.
- ⑤ Polymer-modified cement base coat, glass-fiber fabric, and acrylic-based, textured finish.

(a) Conventional EIFS

Fig. 2-4: Typical EIFS cross-section geometry (adapted from Parker 2008)

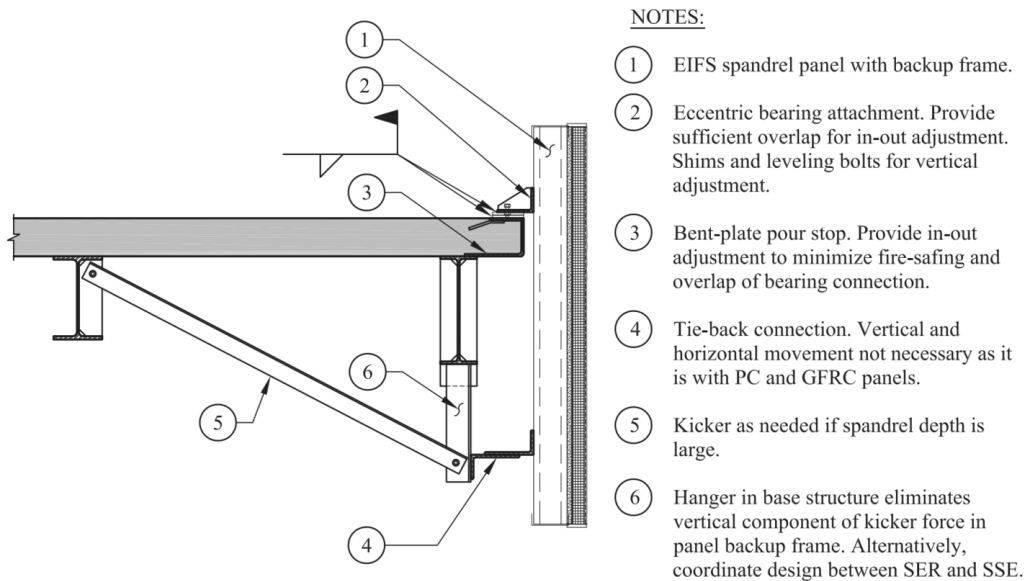


Fig. 2-5: Typical EIFS spandrel panel connection (adapted from Parker 2008)

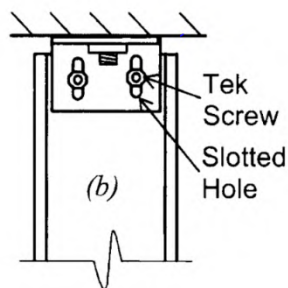


Fig. 2-6: Steel stud wall improved connections for blast loading (adapted from Salim et. al. 2005)

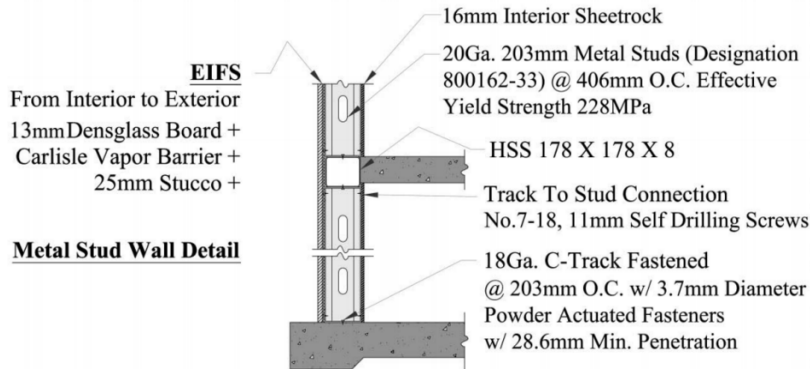


Fig. 2-7: Typical steel stud wall system with EIFS façade cross section geometry (adapted from Salim et. al. 2005)

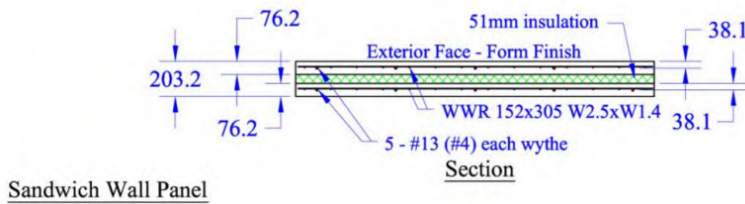


Fig. 2-8: Typical "sandwich" concrete panel cross section geometry (adapted from Salim et. al. 2005)

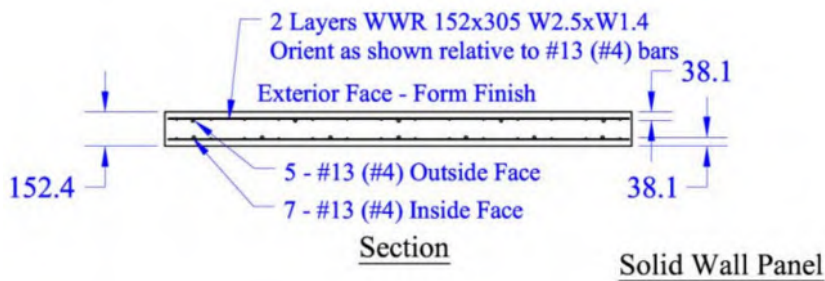


Fig. 2-9: Typical precast concrete wall panel cross section geometry (adapted from Salim et. al. 2005)

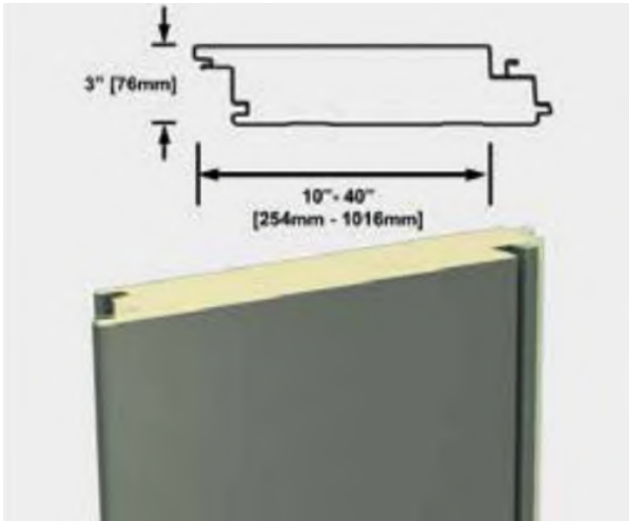


Fig. 2-10: Typical insulated metal panel cross section geometry (adapted from Idriss et. al. 2016)

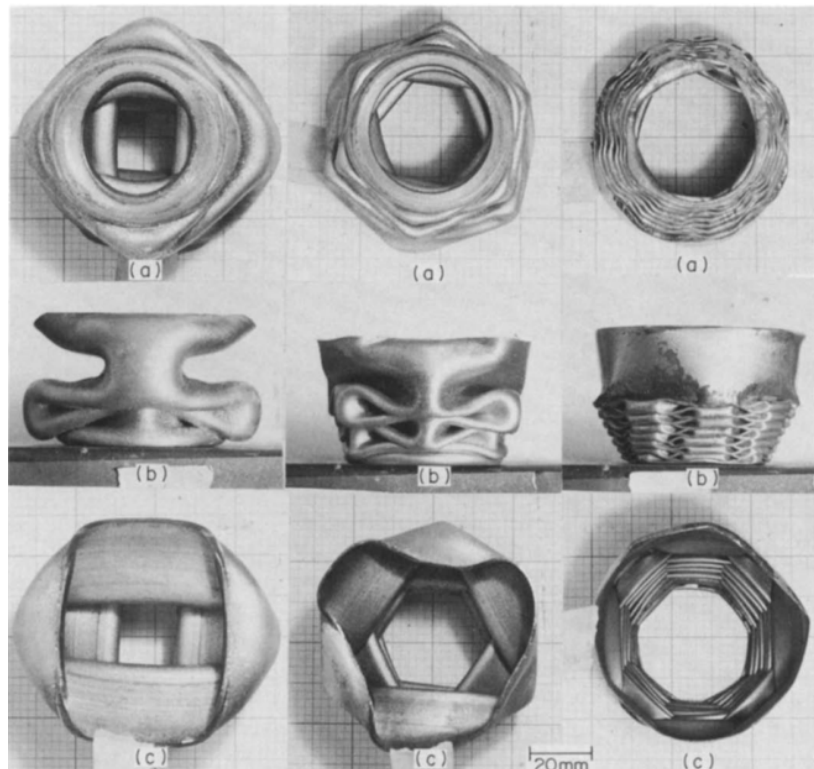


Fig. 2-11: Deformation modes of different thicknesses of frusta (Mamalis, Johnson, & Viegeln, 1984)

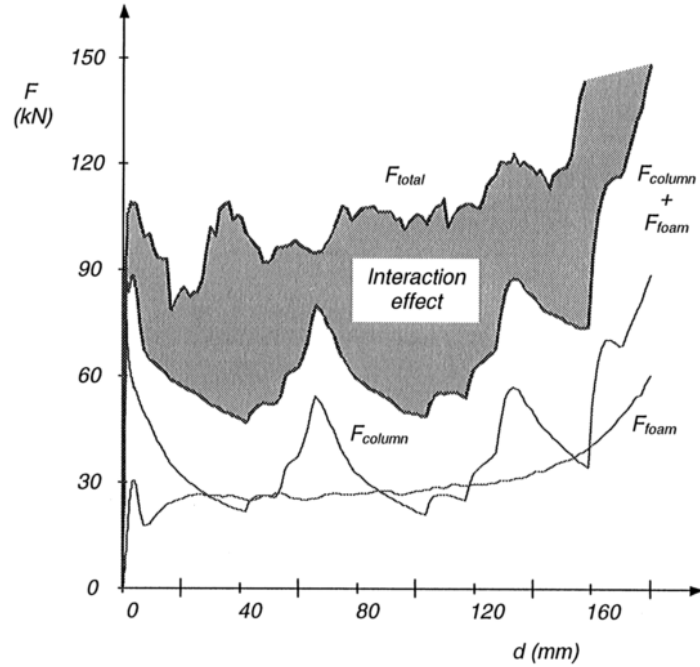


Fig. 2-12: Force-deformation relationship for square aluminum extrusions filled with aluminum foam. (Hanssen et al., 2000)

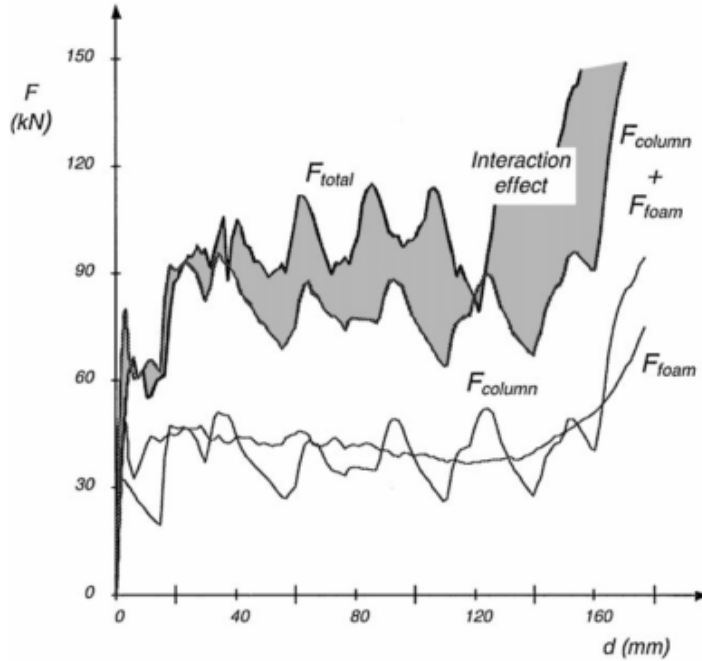


Fig. 2-13: Force-deformation relationship for circular aluminum extrusions filled with aluminum foam (Hanssen et al., 2000)

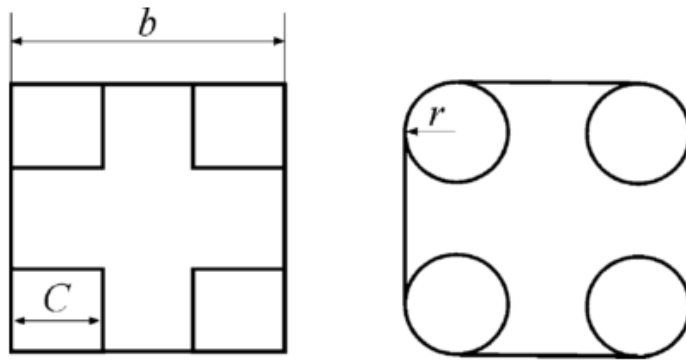


Fig. 2-14: Two of five multi-cell cross sections tested in the study by Kim (Kim, 2002)

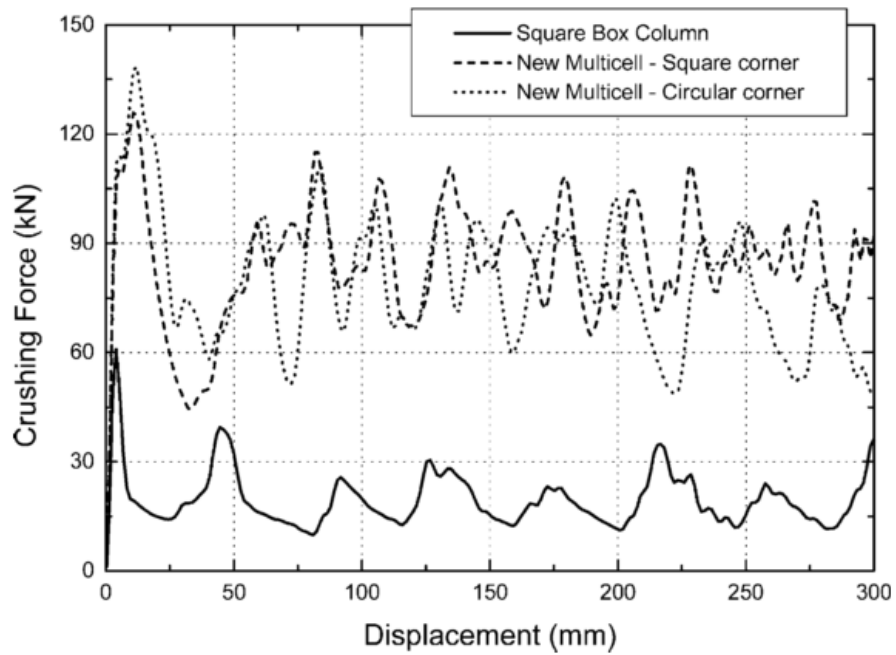


Fig. 2-15: Force-displacement relationship for a square column and two multi-cell columns with the cross sections pictured in Fig. 2-13 (Kim, 2002)

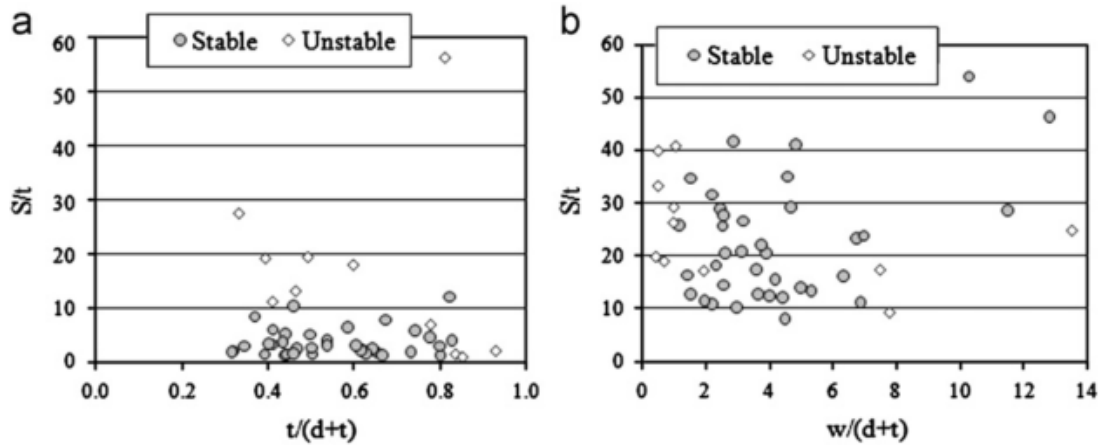


Fig. 2-16: Stable and unstable specimens plotted with geometric data. S is the spacing between stiffeners, t is the tube wall thickness, d is the stiffener thickness, and w is the height of one stiffener (Salehghaffari et al., 2011)

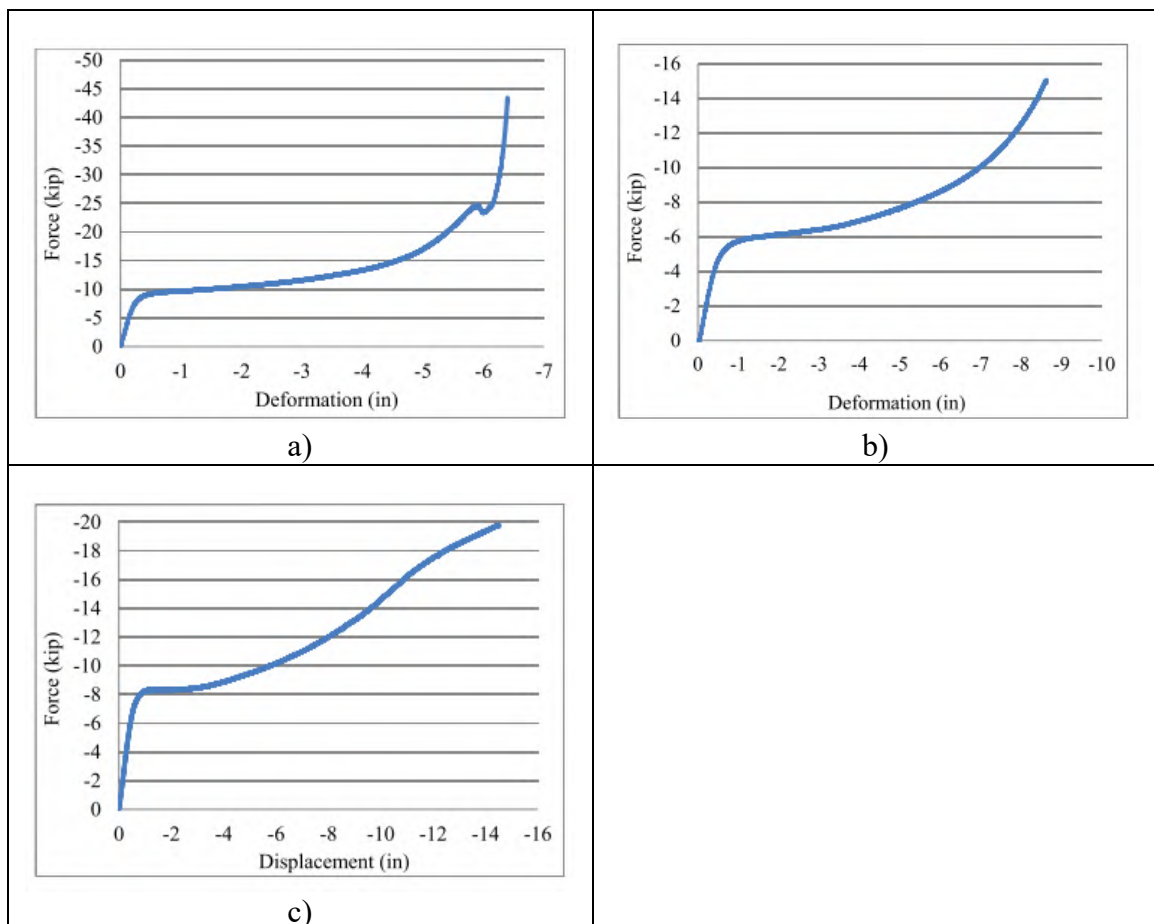


Fig. 2-17: Experimental force-displacement relationships a) HSS7x0.25 b) HSS10.75x0.25 c) HSS16x0.375 (Lavarney, 2013)

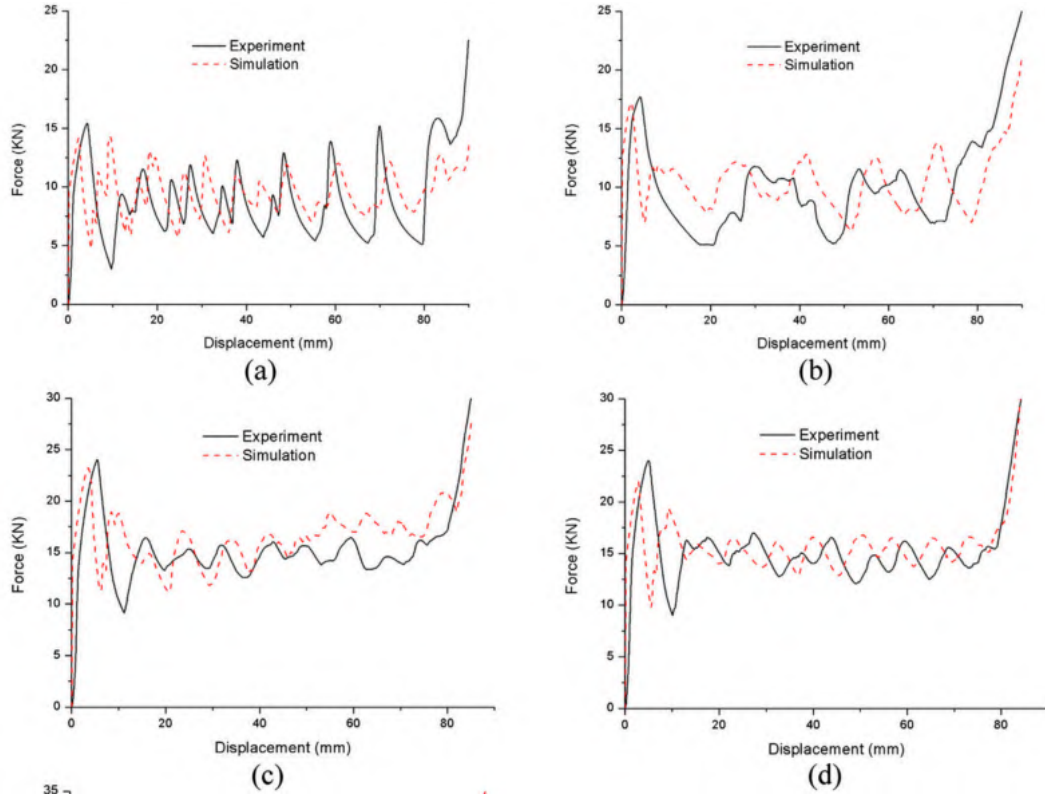


Fig. 2-18: Force-displacement relationships for four of seven specimens a) single cell section b) double cell section c) triple cell section d) triple cell section (Zhang & Zhang, 2014)

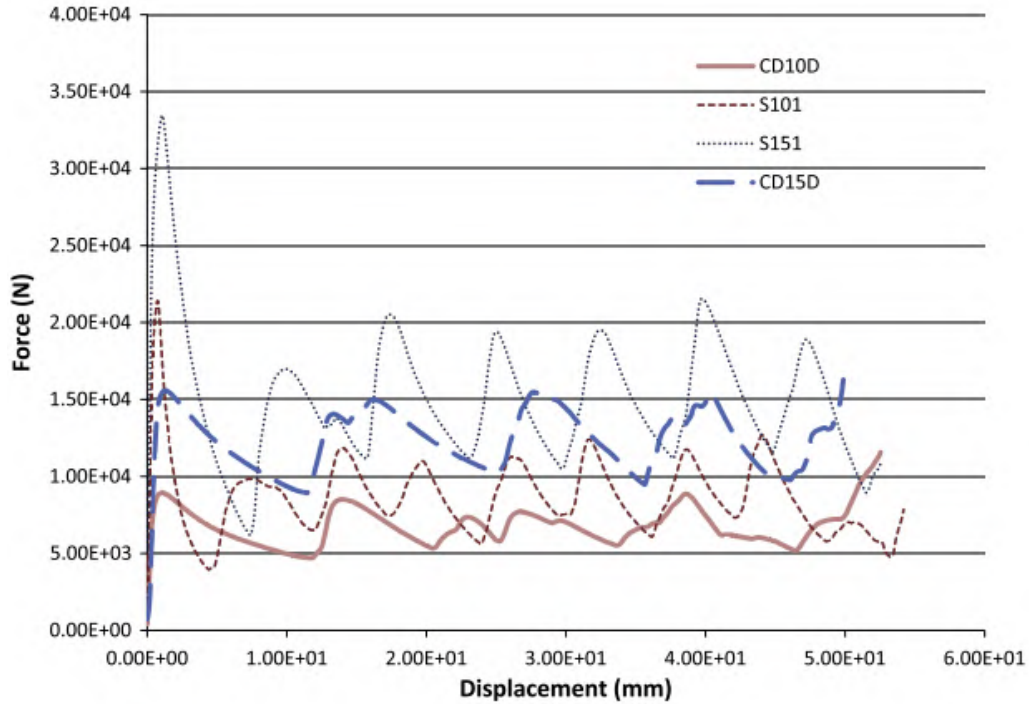


Fig. 2-19: Force-displacement relationship for four of fourteen specimens; the “S” specimens represent straight tube and the “CD” tube represents corrugated specimens; S101 and CD10D have the same diameter, thickness, and length, as do S151 and CD15D (Eyvazian et al., 2014)

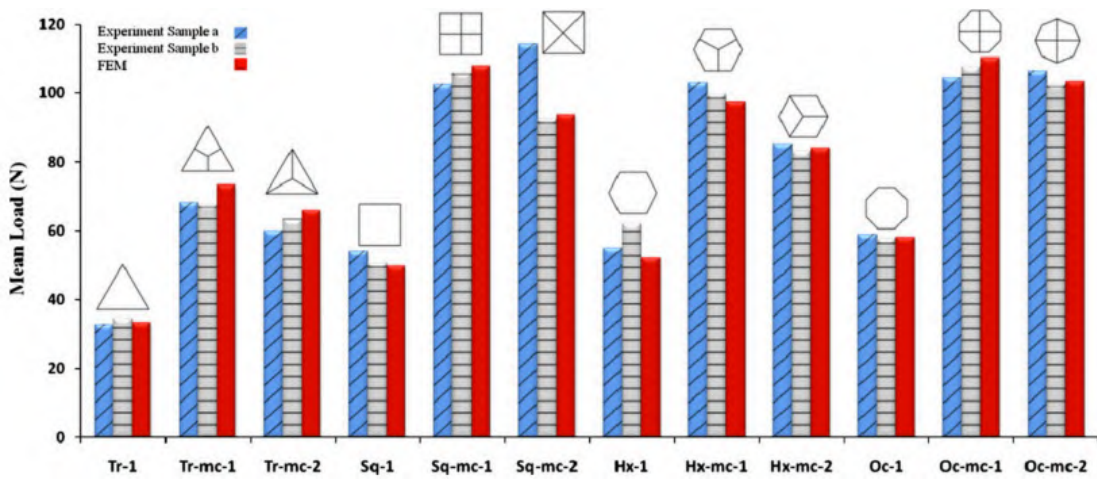


Fig. 2-20: Mean load for the study specimens (Alavi Nia & Parsapour, 2014)

TABLE A3.1 <i>R_y</i> and <i>R_t</i> Values for Steel and Steel Reinforcement Materials		
Application	<i>R_y</i>	<i>R_t</i>
Hot-rolled structural shapes and bars:		
• ASTM A36/A36M	1.5	1.2
• ASTM A1043/1043M Gr. 36 (250)	1.3	1.1
• ASTM A572/572M Gr. 50 (345) or 55 (380), ASTM A913/A913M Gr. 50 (345), 60 (415), or 65 (450), ASTM A588/A588M, ASTM A992/A992M	1.1	1.1
• ASTM A1043/A1043M Gr. 50 (345)	1.2	1.1
• ASTM A529 Gr. 50 (345)	1.2	1.2
• ASTM A529 Gr. 55 (380)	1.1	1.2
Hollow structural sections (HSS):		
• ASTM A500/A500M (Gr. B or C), ASTM A501	1.4	1.3
Pipe:		
• ASTM A53/A53M	1.6	1.2
Plates, Strips and Sheets:		
• ASTM A36/A36M	1.3	1.2
• ASTM A1043/1043M Gr. 36 (250)	1.3	1.1
• A1011/A1011M HSLAS Gr. 55 (380)	1.1	1.1
• ASTM A572/A572M Gr. 42 (290)	1.3	1.0
• ASTM A572/A572M Gr. 50 (345), Gr. 55 (380), ASTM A588/A588M	1.1	1.2
• ASTM 1043/1043M Gr. 50 (345)	1.2	1.1
Steel Reinforcement:		
• ASTM A615, ASTM A706	1.25	1.25

Fig. 2-21: *R_y* and *R_t* values for standard steel sections and reinforcing (AISC 2010b)

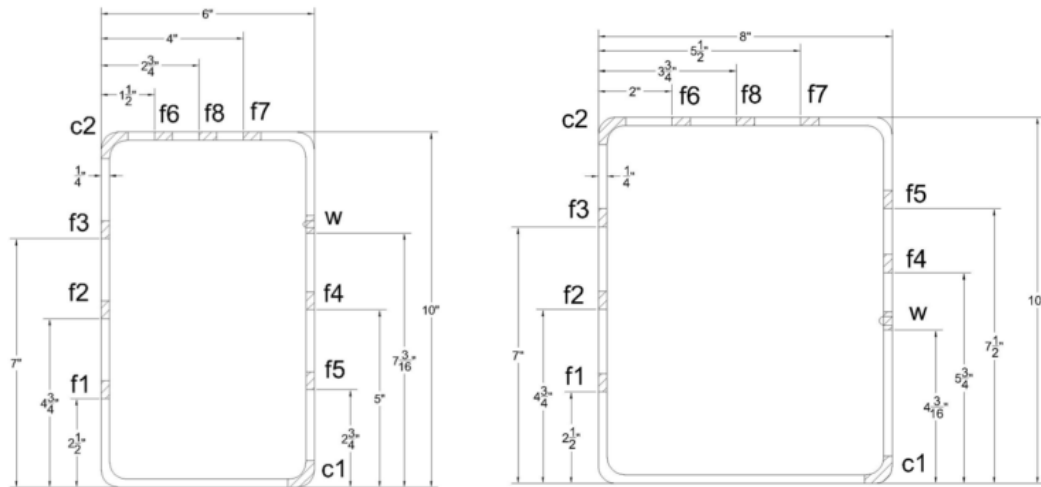


Fig. 2-22: Tensile coupon locations throughout the cross section of HSS10x6x1/4 (right) and HSS10x8x1/4 (left) (Fadden, 2013)

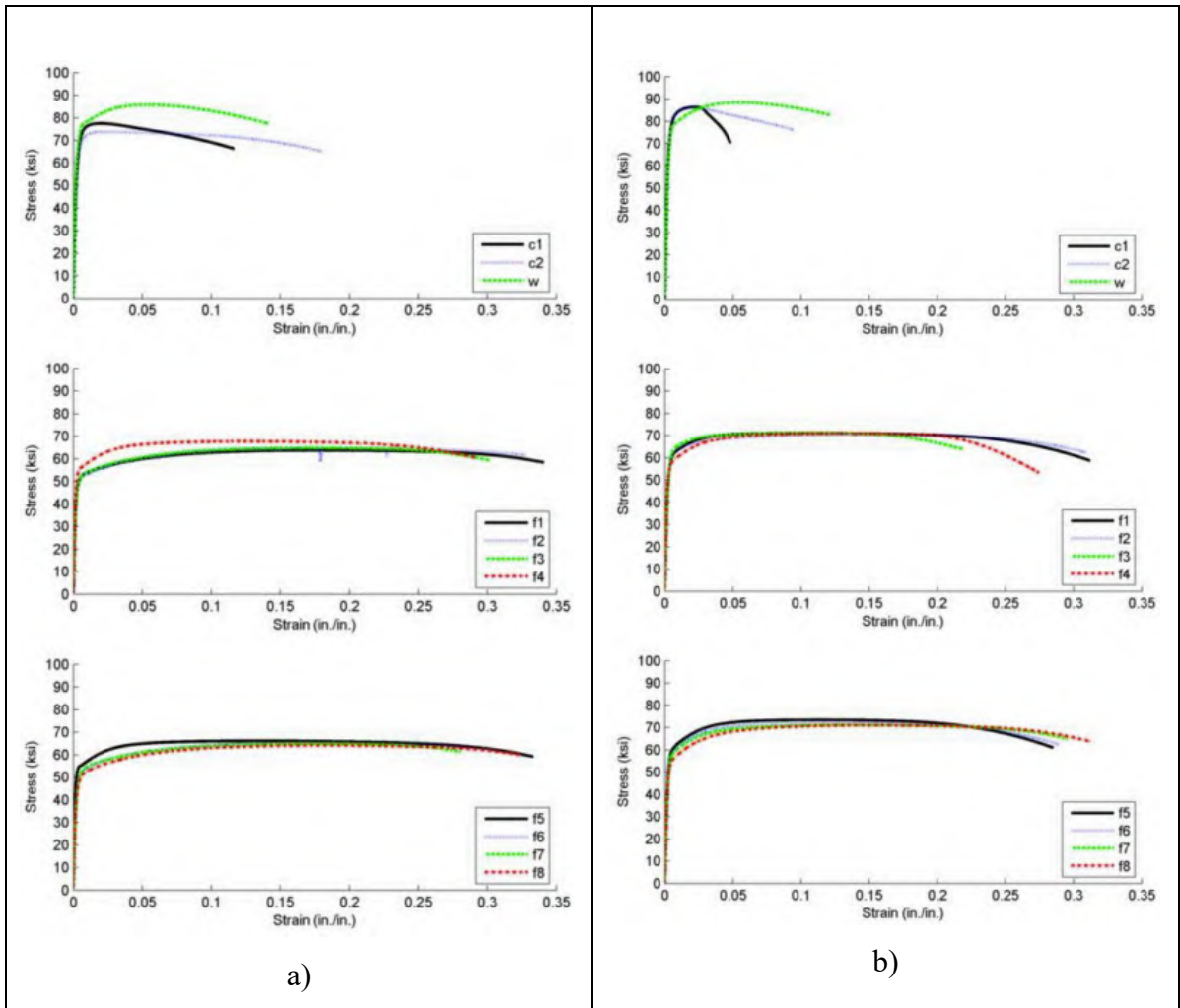


Fig. 2-23: Tensile coupon results a) HSS10x6x1/4 b) HSS10x8x1/4 (Fadden, 2013)

3. Multi-hazard Façade System (MHFS) Loading and Performance Objectives

3.1. Background and Definitions

The use of multi-hazard ductile connectors (MDCs) and U-shaped flexural plates (UFPs) for façade panel-to-structural frame connections in low- to mid-rise steel buildings is investigated in an effort to improve the performance of such structures subjected to any credible hazard. A design procedure has been developed which details the proposed multi-hazard façade system (MHFS) considering wind, seismic, blast, and impact hazards with varying performance objectives. The following directions/degrees-of-freedom are defined relative to the façade panel as-installed on a building (Fig. 3-1):

- Out-of-plane (OP): defined by a vector normal to the outer surface of the panel.
- Vertical (V): defined as the direction along the height of the panel/building.
- Lateral in-plane (LIP or IP): horizontal direction along the width of the panel/building; mutually perpendicular to the OP and V directions.

U-shaped flexural plate (UFP) connectors have been incorporated into the proposed design methodology to accommodate story drifts with in-plane shear forces less than the panel's capacity to avoid damaging the panel. Each UFP consists of a steel plate bent into an elongated U-shape and connected to the panel and structural frame on either side via either welded or bolted connections to flat plates (Fig. 3-1). At least two UFPs are required along whichever panel edge (top or bottom) is to be “released” relative to in-plane floor motion. Various configurations of the connectors are possible (see Appendix B) and have various advantages and disadvantages. Configuration 3 of that appendix is discussed here.

A critical element of the MDCs is a length of round HSS tube, which is welded between two diametrically opposed flat plates. The following HSS tube actions/degrees-of-freedom are utilized to provide the desired response considering each panel demand:

- Radial: inward “crushing” or outward “pulling” of the circular cross section.
- Rolling: shearing of the tube in-plane with the circular cross section.
- Longitudinal: shearing parallel to the tube’s longitudinal axis.

These actions/degrees-of-freedom are also referenced in discussion of the UFPs, however the MDC and UFP mechanics differ in critical ways, which will be detailed in Section 4.

Three main MDC types have been developed to resist demands in each panel degree-of-freedom:

- MDC-V: MDCs with the HSS tubes’ longitudinal axes aligned with the panel’s vertical (V) degree-of-freedom. Two MDC-1s should be included along one panel edge (top or bottom), preferably near the corners; exactly two MDC-Vs are preferred for installation (as described later). These MDCs are designed to elastically resist all vertical façade loads (self-weight, seismic inertia, etc.).
- MDC-L: MDC with HSS longitudinal axis in the LIP direction. This MDC is designed to elastically resist all LIP forces due to seismic inertia and (if the panel is located at a building corner) contact with other façade panels during building drift. Exactly one MDC-L is included along the panel edge (top or bottom) which also contains the MDC-Vs, preferably near the middle (centered left-to-right). If the total HSS length along this panel edge is not sufficient to achieve all desired

performance objectives for OP loading, additional tube length can be added to the MDC-L to increase the overall strength of this panel edge.

- MDC-B: MDC with HSS longitudinal axis in the LIP direction. This MDC is not connected to the frame-side plate (bearing only), therefore it only acts during inward OP loading (radial crushing as tube bears against plate). The MDC-B is located along the panel edge with containing the UFPs and is designed to supplement their inward OP strength to equal that of the opposite panel edge.

3.2. Façade System Loading and Performance Objectives

Façade systems enclose interior building spaces while providing protection, insulation, and aesthetic appeal from the exterior. Failure of a building envelope prohibits the intended usage of the interior space resulting in economic losses due to both operational downtime and the required repair cost; furthermore, exposure to moisture or extreme temperatures may allow mold to develop, water pipes to freeze, etc. resulting in additional losses. During seismic events, façade panel damage and detachment has been observed due to deformation incompatibility between the façade panels and attached floor slabs as the building stories undergo lateral drifts (Hutchinson *et al.*, 2014). Additionally, buildings subjected to extreme external lateral pressures, such as large explosive or strong wind/tornado/hurricane events, have a reduced chance of progressive collapse when the façade system remains intact (NIST, 2007). Therefore, it is in the interest of both public safety and reducing probable economic losses that the design and detailing of robust, practical façade systems is developed herein.

A building's façade system serves as the barrier separating the interior and exterior environments. Differences between these environments must be resolved by the façade system to maintain the integrity of the enclosure. Changes in temperature and moisture content can create volumetric strains within the façade panels depending on material properties. The change in panel dimensions due to these volumetric strains must be accommodated by the façade connectors, in addition to fabrication, installation, and on-site adjustment tolerances (PCI, 2000). These requirements are traditionally dealt with using slotted or oversized bolt holes and leveling bolt connections. A statically determinate connection scheme is preferable to allow for easier on-site adjustment of each panel to an acceptable final position. Details of the arrangement and features of MDCs and UFPs which accommodate these deformations are included in Fig. 3-2.

ASCE 7-10 (2013) details minimum requirements for façade system design, including thermal/moisture effects and loads due to self-weight (dead load), seismic inertia, and wind. These minimum design loads must be resisted elastically by the façade system by providing an adequate load path for all out-of-plane (OP; direction normal to the exterior building surface), vertical (V; direction along the panel/building height), and lateral in-plane (LIP or IP; direction along the panel/building width, mutually perpendicular to the OP and V directions) loads. Wind and lateral seismic panel inertia are the minimum design OP demands. Lateral seismic panel inertia must also be considered in the LIP direction. Vertical demands include dead weight and vertical seismic panel inertia. The factored load combinations specified in ASCE 7 must be considered when determining controlling design demands for both the façade panel and connections to the structural frame in each

degree-of-freedom. Free body diagrams of a façade panel supported as shown in Fig. 3-1 subjected to various types of loading are shown in Fig. 3-3.

In addition to these minimum loads, the façade system may be subjected to impulsive loads resulting from explosive blasts or impact debris due to blast or extreme wind events. These rare but potentially high-damage hazards must also be considered in design to protect essential facilities. A list of credible hazards and desired performance objectives for a low- to mid-rise steel building frame with reinforced concrete panel multi-hazard façade system (MHFS) is provided in Table 3-1. The proposed MDC design approach achieves these performance objectives through capacity design principles and consideration of the interaction between building frame and façade panels. Characterization of the nature and magnitude of façade panel demands is the first step in the proposed MDC design methodology.

3.2.1. Thermal/Moisture Effects and Temperature/Shrinkage Panel Reinforcement

The volumetric expansion and contraction due to changes in temperature and moisture content must be accounted for when designing reinforced concrete or brick and mortar cladding façade systems. These deformations are typically accommodated locally (within the façade system itself) using joints (gaps) between panels and degree-of-freedom releases in the façade panel-to-structural frame connections. Joints also ease the installation process, and allow for some differential seismic displacement of the floors attached to a given façade panel prior to panels coming into contact. ASCE 7-10 Chapter 13.5.3 specifies a minimum panel joint size of $\frac{1}{2}$ " , however a typical 13' by 30' reinforced concrete panel requires $\frac{3}{4}$ " LIP and $\frac{1}{2}$ " V joints to allow for the expansion due to a design

temperature fluctuation of +/- 50 degrees Fahrenheit (100 degrees total). The material coefficients of thermal and moisture expansion can be used to estimate the maximum (relative to nominal) panel dimensions, and joints can then be sized to allow for this expansion without contact occurring between panels:

$$\Delta_{\text{exp}} = k_t S_e \Delta_T + k_e S_e = W_j e_j \quad (3-1)$$

where Δ_{exp} is the expected maximum change in dimension, k_t is the material coefficient of thermal expansion ($6 \times 10^{-6}/^\circ\text{F}$ for concrete, $4 \times 10^{-6}/^\circ\text{F}$ for masonry), S_e is the nominal dimension of the material in the direction of expansion, Δ_T is the expected change in temperature, k_e is the material coefficient of moisture expansion (2×10^{-4} for concrete, 5×10^{-4} for masonry), W_j is the required joint width, and e_j is the maximum strain of the joint material (possibly 50%, or 0.5). Without adequate joints, expanding panels can come into contact and rapidly develop large forces resulting in cracks and potential fracture of façade-to-frame connections.

The façade panel-to-structural frame connections must be able to accommodate both panel contraction and expansion due to thermal and moisture effects to avoid distortion and potential fracture as the panel deforms in-plane. This is typically achieved by including slotted bolt holes in the façade-to-frame connectors, and arranging these connections to allow for in-plane panel deformations while also providing reactions in each degree-of-freedom as shown in Fig. 3-2. The connection arrangement and slotted/oversized bolt hole details shown in Fig. 3-1 satisfy these criteria; all connectors provide OP reactions while the frame is free to deform relative to the panel in the LIP direction from the MDC-L, and in the vertical direction from the MDC-V panel edge. This connection configuration also provides a statically determinate condition considering all

panel degrees-of-freedom. The long-term reliability of functioning (sliding) bolt slots is questionable; however, the MDCs and UFPs themselves are capable of accommodating panel expansion/contraction through deformation of the HSS tubes (MDCs) and bent steel plates (UFPs) if the bolted connections “lock up”. The fatigue life of these HSS tubes subjected to this cyclic loading has been evaluated in Appendix A.

For reinforced concrete panels, thermal and moisture effects require a minimum amount of reinforcement—with a reinforcement ratio of 0.18%—to minimize cracking (ACI, 2011). This minimum reinforcement ratio can be used to determine the minimum flexural strength of the panel when subjected to (say, uniformly distributed) loading in the OP direction. For other cladding types, code requirements should be checked to ensure similar serviceability.

3.2.2. Dead Load (D; Self-Weight)

The façade-to-frame connections must have adequate strength to support the panel’s weight (dead load) in the vertical direction. The total weight of a reinforced concrete (or similar) panel can be calculated using the volumetric weight of the material and the nominal panel dimensions:

$$W_p = \gamma_p hbt \quad (3-2)$$

where γ_p is the volumetric material weight, and h, b, and t are the nominal height, width, and thickness of the panel, respectively. This total weight should then be divided by the number of vertical load-bearing connections for design; two vertical supports are ideal to maintain static determinacy. For the MDC configuration shown in Fig. 3-1, the MDC-V connectors along the panel’s top edge will carry all vertical loads. This dead load should

be factored and considered in combination with vertical seismic load effects for design according to ASCE 7-10.

All vertical loads should be assumed to act at mid-thickness of the panel. This line-of-action is eccentric relative to the connectors, and the resulting moment demand on these connectors must be included in their design criteria to prevent failure under design loading. Accounting for this eccentricity will be discussed in further detail in the context of MDC design (Section 5.3.7.1). Vertical deflections and creep (for reinforced concrete frames only) in the connecting spandrel beam should also be considered if such deformations would impart a differential vertical displacement between vertical load-bearing panel connection points, however this should not be an issue if these connections are laid out symmetrically on the panel (with respect to the V axis) and anchored near a beam-column joint where vertical beam deflections are negligible.

3.2.3. Seismic ($E = E_i + E_d + E_c$)

Seismic events create façade system demands in the OP, LIP, and V directions. The inertia of the panel's mass in motion must be resisted in each of these degrees-of-freedom (Fig. 3-3). Additionally, deformation compatibility between the drifting building frame and rigid in-plane panels must be accommodated to avoid distortion of the panels and ultimately failure of the connections. The proposed MDC and UFP configuration (Fig. 3-1) relies on the MDC-Vs to resist all vertical seismic forces, and the lone MDC-L for all LIP forces. Vertical seismic forces should be considered in combination with the dead load, and the controlling combination should be used for design (1.4 times dead load, or 1.2 times dead load plus seismic loads). Large building drifts in-plane with a given panel

are accommodated through ductile deformation of all UFPs in the rolling direction, while out-of-plane drifts are accommodated through rotation of the HSS tubes and UFPs about the panel's LIP axis (which is easily accommodated based on test results in Rendos (2018)). Contact between adjacent panels during large building drifts is expected (as described in Section 3.2.3.3) however all deformations will be accommodated by the UFPs to prevent panel damage or failure of the connections.

3.2.3.1. Inertia Effects (E_i)

ASCE 7-10 Chapter 13 gives a procedure for calculating design seismic inertia loads for non-structural components, which includes façade panels and their connections. The design vertical seismic inertia force can be taken as the product of $2/3^{\text{rds}}$ of the design short-period spectral acceleration and the panel mass. Table 13.5-1 in ASCE 7-10 gives coefficients, a_p and R_p , which act as dynamic amplification and response modification factors, respectively, for design lateral (OP and LIP) seismic inertia forces. These factors can significantly change the magnitude of each design-basis force, and care must be taken to ensure appropriate factors are used for all elements along each load path. All forces used to design fasteners (bolts and welds) within the MDCs should use $a_p = 1.25$ and $R_p = 1.0$ as “fasteners of the connecting system” under “exterior nonstructural wall elements and connections”. The MDCs and UFPs are different from traditional exterior wall connectors; therefore, the factors given under the general category of “other rigid components” should be consulted. For OP loading, the all connectors are loaded in their radial direction and are considered “high deformability elements and attachments” with $a_p = 1.0$ and $R_p = 3.5$. In the LIP direction, the MDC-L HSS tube is subjected to longitudinal shearing, which is the

stiffest and least ductile deformation mode therefore it can conservatively be treated the same as the bolts and welds ($a_p = 1.25$ and $R_p = 1.0$). These characterizations are validated through examination of HSS tube and UFP mechanics considering these actions (Section 4). Note that the equation for nonstructural component lateral seismic inertia given by ASCE 7-10 Chapter 13 is generally controlled by the expression which includes a term calculated as the elevation of the component's attachment to the structure as a fraction of the total building height (z/h); all references to "minimum" or "ground elevation" seismic force/design herein assigns a zero value to this term, whereas "maximum" or "roof-elevation" refers to this term taking a value of one. The UFPs do not carry any LIP seismic inertia forces because they are meant to yield to accommodate drift as described in the following subsection.

3.2.3.2. In-Plane Drift Accommodation (E_d)

In modern steel buildings, ductile design of the lateral force resisting system (LFRS) is used to economically resist large lateral forces during seismic events. Yield of the LFRS results in inelastic story drifts. Panels are anchored to the floor systems at the top and bottom of each panel and differential motion of the floors in the OP and LIP directions must be accommodated by the façade system to avoid developing large forces due to in-plane distortion of the panels, which generally have large in-plane stiffness. This is traditionally done through detailing of the façade-to-frame connections, similar to the approach taken for thermal/moisture effects; however, slotted bolt connections may not be reliable for accommodating building drifts if corrosion or large frictional forces prevent the desired sliding action. Therefore, the proposed design methodology incorporates U-

shaped flexural plate (UFP) connectors along one of the panel edges to accommodate all seismic drift effects. UFPs have been successfully implemented in both commercial and research applications for drift compatibility and seismic energy dissipation through plastic “rolling” of the section (Baird, 2014), however their inclusion in this application relies upon their “pulling” and “crushing” capacities as well.

Considering a panel with the connector layout shown in Fig. 3-1 subjected to a large building drift in the LIP direction, the panel moves laterally with the upper floor because the MDC-L connecting the panel and spandrel beam is very stiff and designed to remain elastic (essentially no deformation across the MDC undergoing longitudinal shear). On the opposite panel edge, the differential LIP displacement between the spandrel beam and panel is accommodated by the UFPs through highly ductile plastic rolling of their semicircular sections. A maximum expected rolling deformation equal to (plus/minus) the design maximum story drift (possibly considered as the code drift limit of 2.5% of the story height, or $C_d\delta_e$ where C_d is the deflection amplification factor for the chosen LFRS and δ_e is the elastic story displacement under the elastic (reduced) design seismic inter-story shear) should be determined to inform aspects of the UFP geometry which largely govern their behavior in the design-critical degrees-of-freedom (discussed in mechanics and design sections). The LIP force driving the UFP rolling deformations is provided by the MDC-L, which is capacity-designed to resist the UFPs maximum expected rolling forces in addition to the LIP seismic inertia of the panel. These opposing LIP forces are applied at different elevations along the panel’s height, resulting in a net moment about the panel’s OP axis. This moment is resisted via a force-couple formed by the MDC-Vs as shown in Fig. 3-3. Building drift in the OP direction can be accommodated through bending of the

connectors about the panel's LIP axis. Vertical differential displacement between floors is typically much smaller than lateral drift and can essentially be ignored if proper accommodation of thermal/moisture expansion and contraction is included via vertical slotted bolt holes and an appropriate connection configuration as previously discussed.

3.2.3.3. Corner Panel Contact Accommodation (E_c)

As a given story undergoes drift primarily in one direction, the panels located at the building's corners may experience deformation incompatibility due to differences in the anchorage of adjacent corner panels as shown in Fig. 3-4. The OP panel—relative to the direction of the larger story drift—rotates as discussed in the previous paragraph while remaining anchored to both adjacent floors, while the LIP panel is effectively a rigid body which is anchored to one floor via the MDC-L and released from the other by UFP rolling. Contact between these panels will occur due to this difference in panel anchorage when story drift results in LIP panel displacement exceeds the gap between panels. This contact can be avoided if a large, undesirable gap (equal to the design maximum story drift) is included between the panels. Alternatively, a standard gap can be used with connections that are detailed to act as a “fuse” along the load path to limit the force, which develops as the corner panels come into contact, thereby accommodating seismic building drift through yielding of the connectors. An approach using yielding connections to accommodate corner panel contact was considered by Hutchinson *et al.* (2014). The approach taken in this design methodology is to utilize the weak outward pulling strength of the OP panel's UFPs as the force-limiting “fuse” during corner panel contact with the MDCs designed to

elastically resist the resulting expected forces as shown in Fig. 3-4. The mechanics of this action will be developed in detail in a later section.

3.2.4. Wind

3.2.4.1. Basic Wind Speed Pressures (W)

The design-level wind pressure on a given façade panel can be calculated from the procedures in ASCE 7-10 Chapters 26 and 30. The design wind event for façade panels can be treated as a sustained, static load. A variety of factors—including building dimensions, location, and site exposure—are used to formulate a design pressure profile incident upon each building face. This pressure profile can then be integrated over the area of the panel of interest to determine a total OP design force. For simplicity, this design force can be treated as a uniformly distributed load over the surface area of each panel by dividing the total OP wind force by the panel's height and width. This approximation allows for simple calculation of the peak flexural demand (uniformly distributed load on the one-way panel) to determine if the system requires additional reinforcement beyond its minimum flexural strength. The MDCs and UFPs should be designed to resist all design-basis wind loads in the OP direction (inward and outward). A comparison of design OP wind and seismic inertia forces is provided in Fig. 3-5 for buildings located in Los Angeles, CA and Boston, MA.

3.2.4.2. Tornado Winds (Tw)

For extreme wind events, such as tornadoes, the design wind pressure profile can be amplified by the square of the ratio of reference wind speeds—the sustained three-second

gust at ten meters above-grade associated with an event of known annual probability of exceedance—to determine a “maximum considered” OP wind load. Reference wind speeds for tornados in various regions of the contiguous United States is shown in Fig. 3-6 (USNRC, 2007).

3.2.4.3. Tornado Suction due to Atmospheric Pressure Drop (P_T)

Tornado events include an additional hazard in the form of a significant, rapid drop in atmospheric pressure. This phenomenon is non-concurrent with the high velocity winds. The difference between interior (unchanged) air pressure and reduced exterior air pressure results in an outward, pseudo-static, uniformly distributed “suction” force acting on the façade system in the OP direction. If consideration of tornado events is included in the design, this pressure drop should be included as well for the design of all elements in the façade systems (panels and connectors). Pressure drop values and reference tornado gust velocities are given in Table 3-2.

3.2.5. Impulsive Loading (I)

Impulsive loading on a building façade generally has the effect of imparting an initial velocity to the panel mass based on the principle of momentum conservation. This type of response can result from a force (or pressure) acting over a duration of time which is much shorter (typically $1/5^{\text{th}}$ or less) than the fundamental period of vibration response of the structural system (Chopra, 2011). This is generally an appropriate characterization of an air-blast effect when designing protective structures (DOD, 2008). Impulsive loading can also result from a collision between a mass-containing body and structure, where momentum (or kinetic energy) is conserved. This can occur when debris due to a blast or

high-wind event impacts the building's exterior. In either case, the integrity of the load path from façade panels, to connections, and through the main structural frame is critical for protecting the building's inhabitants, preventing infiltration of the blast or impact missile into the building (which can significantly increase economic losses), and minimizing the potential for progressive collapse due to damage of the primary structural system (NIST, 2007). A protective façade system design for these extreme hazards can be achieved through appropriate proportioning of the MHFS components' strengths.

For a given façade panel, the controlling impulsive loading scenario is a function of both the magnitude of the design impulse, as well as the performance objective for the façade system subjected to that event (Table 3-1). Large impulsive loading events are rare and the precise design scenario(s) will likely never occur, however a resilient protective design can be achieved through consideration of a spectrum of loading scenarios and performance objectives. This is accomplished using capacity design principles to induce a desired progression of component damage with increasing demand along the load path where each behavioral transition is benchmarked by the controlling load type with the performance objective to remain within that particular damage state. This concept is illustrated in Fig. 3-7 for the OP loading conditions and performance objectives detailed herein. The design resulting from this approach will ultimately be more robust when subjected to any load type than a design strictly considering the maximum magnitude event. The mechanics and design of each component will be developed in subsequent sections to formulate a methodology capable of achieving all desired objectives and improving façade system performance.

3.2.5.1. Air-Blast (I_b)

When an explosion occurs, a high-velocity overpressure wave propagates radially in all directions from the source of the blast. When this wave encounters a boundary plane, such as the side of a building, it reflects off of the surface, exerting a brief inward (positive) pressure. The duration of this pressure is typically on the order of a few to tens of milliseconds, which is much shorter than the fundamental period of vibration response of any typical façade system in the OP direction (typically on the order of tenths of one second). The integral of positive reflected blast pressure over time yields the impulse value for protective design of the façade system. This value is a function of the charge weight (W ; typically presented in terms of equivalent pounds of TNT), straight-line distance between the charge and boundary surface, and the angle of incidence between the straight-line distance ray and boundary surface normal (DOD, 2008). A more general “standoff distance” term (denoted by the variable R), defined as the minimum along-ground distance between the blast source and building surface, is typically used along with W to characterize a blast event for structural design. These parameters are commonly combined into a single “scaled distance” value, Z , equal to R divided by the cubed root of W .

In traditional protective design, a threat-based assessment is performed to determine a credible blast scenario to consider for design. Example design blast impulse values are provided in Table 3-3 for three ground-level design blast scenarios (DBS): DBS1, with a standoff distance, R , of 30 feet and a charge weight, W , of 500 lbsTNT ($Z = 3.78$); DBS2, with $R = 100$ feet and $W = 300$ lbsTNT ($Z = 14.9$); and DBS3, with $R = 200$ feet and $W = 100$ lbsTNT ($Z = 43.1$). These values were obtained by integrating the positive pressure values over time calculated by the numerical procedure developed by

Appelbaum (2013) and based on Department of Defense 3-340-02 (DOD, 2008) for each blast scenario over a 30-foot wide by 13-foot high area (typical bay width and story height dimensions; considered the nominal area of each façade panel). This also considers each panel centered on a wide, tall building surface (to eliminate edge clearing effects). These design blast scenarios represent low- (DBS3), moderate- (DBS2), and high- (DBS1) intensity blast events, which represent a range of threats suggested by FEMA 427 (2003). All air-blast events considered in this study are assumed to be caused by a ground-level, spherical charge detonation. Performance objectives for each MHFS component subjected to these air-blast intensity events are noted in Table 3-1.

3.2.5.2. Impact (Ii)

Table 3-3 includes design impact missile impulse values, which are adapted from the United States Nuclear Regulatory Commission (USNRC, 2007) for the protection of nuclear facilities against tornado effects. The design missile for “global” (non-penetrative) failure is a car with mass and impact velocity determined by the mapped tornado wind regions shown in Fig. 3-6. This impact missile can strike at any elevation up to thirty feet above grade. Although the USNRC guidelines state that plastic deformation (energy dissipation) of the car can be considered during this collision, this can be conservatively ignored to obtain a larger design impact missile impulse value. The design impulse values in Table 3-3 are compared in Fig. 3-8, however these values are not directly comparable for design because the load type drastically changes the response of the panel and connectors when comparing blast and impact scenarios of apparently equivalent impulse. An impact missile can be characterized as a point or partially distributed (based on the

impact missile's dimensions) load acting on the panel with the missile's mass added to the panel at the point or area of contact (assuming plastic collision). While in reality an impact load's duration may not be brief relative to the façade system's first mode dynamic response period, the transfer of momentum during the collision imparts an initial kinetic energy state, which is analogous to the effect of air-blast overpressure described in the previous section.

3.3. Load Combinations

Each façade connector must be designed considering the maximum combined demands to ensure the panel remains supported in all degrees-of-freedom even during extreme hazardous loading events. The demands described in the preceding subsections include force, deformation, and hysteretic work requirements to satisfy the desired performance objectives. Free body diagrams of the basic load cases are shown in Fig. 3-3. The MDC-Vs must consider all loads in combination with the panel dead load increased by a factor of 1.2 per most ASCE-7 load combinations. Seismic inertia effects must be combined with forces resulting from deformation compatibility, including in-plane plastic yielding of the UFPs for all panels and OP panel contact for corner panels (free body diagram of this load case shown in Fig. 3-4). All relevant load combinations are provided in Table 3-4. These

combinations are derived from those given in ASCE 7-10 (2013). These factored load combinations are summarized as follows:

1. Dead load (V)
2. Dead load (V) plus design-basis wind (OP)
 - a. Inward OP wind
 - b. Outward OP wind
3. Dead load (V) plus earthquake load effects (100-30-30 directionality considered)
 - a. Primary ground motion action in panel's LIP direction
 - b. Primary ground motion action in panel's OP direction (inward or outward)
 - c. Primary ground motion action in panel's vertical direction (downward)
4. Dead load (V) plus tornado wind (OP)
 - a. Inward OP tornado wind
 - b. Outward OP tornado wind
5. Dead load (V) plus impulsive loading (OP)
 - a. Air-blast impulsive loading
 - b. Missile impact impulsive loading

Table 3-1: Structural Hazards and System Performance Objectives

Hazard	Intensity	Return Period (years) ^a	Building Component Performance		
			LFRS	Connectors	Façade Panels
Seismic	Low	75-350	Elastic or limited plasticity	Elastic	Elastic
	Design-basis	475	Plastic with acceptable max drift	(vertical), drift	
	Maximum-considered	2475	Plastic with acceptable max drift	accommodation	
	Collapse-level	5000+	Highly plastic, potential failure	(lateral)	
Wind	Low	10-75	Elastic	Elastic	Elastic
	Design-basis	300-1700		Elastic	
	Tornado	100,000-10,000,000		Plastic	
Blast	Low	Maximum 125,000.	Elastic	Elastic	Elastic
	Moderate	Reduced significantly		Plastic	Elastic
	High	for essential structures ^b		Plastic	Plastic
Impact	Design-basis	Linked to blast/tornado ^c	Elastic	Plastic	Plastic

Notes:

- a. Return periods given as ranges have exact values determined by building occupancy/usage.
- b. Maximum estimated from current U.S. building population and annual bombing incident data (USBDC 2016).
- c. Impact determined from tornado region with probability conditional on the occurrence of blast or tornado events.

Table 3-2: Design Parameters for Tornado Winds (Adapted from USNRC, 2007)

Tornado Region	Reference Wind Gust Velocity (mph)	Design Pressure Drop (psi)
1	230	1.2
2	200	0.9
3	160	0.6

Table 3-3: Design Façade Impulse Values

Type:	Design Blast Scenario (DBS)						Impact Missile (Tornado Region, TR) ^a					
Scenario:	DBS1		DBS2		DBS3		TR1		TR2		TR3	
Parameter ^b :	R (ft)	W (lbsTNT)	R (ft)	W (lbsTNT)	R (ft)	W (lbsTNT)	M (lbs)	V (ft/s)	M (lbs)	V (ft/s)	M (lbs)	V (ft/s)
Value	30	500	100	300	200	100	4000	135	4000	112	2595	79
Story	Design Impulse (kip-s)											
10	2.556		1.854		0.691		0		0		0	
9	2.891		2.161		0.765		0		0		0	
8	3.271		2.376		0.793		0		0		0	
7	3.781		2.608		0.820		0		0		0	
6	4.575		2.836		0.844		0		0		0	
5	5.641		3.079		0.866		0		0		0	
4	7.334		3.336		0.884		0		0		0	
3	10.042		3.574		0.898		16.784		13.924		6.372	
2	14.554		3.768		0.908		16.784		13.924		6.372	
1	19.097		3.866		0.914		16.784		13.924		6.372	

Notes: a. Adapted from USNRC, 2007. Design impact missile (car) treated as non-deforming body. Applicable up to 30 ft. above grade.
b. R = Standoff distance, W = charge weight; M = missile mass, V = missile velocity.

Table 3-4: MHFS Load Combinations

[1]	$1.4D$
[2a]	$1.2D + 1.0W$
[2b]	$1.2D + 1.0(-W)$
[3a]	$1.2D + 1.0(1.0E_{i,LIP} + 0.3E_{i,OP} + 0.3E_{i,V}) + E_d$
[3b]	$1.2D + 1.0(0.3E_{i,LIP} + 1.0E_{i,OP} + 0.3E_{i,V}) + E_d$
[3c]	$1.2D + 1.0(0.3E_{i,LIP} + 0.3E_{i,OP} + 1.0E_{i,V}) + E_d$
[4a]	$1.2D + 1.0T_W$
[4b]	$1.2D + 1.0(-T_W)$
[4c]	$1.2D + 1.0P_T$
[5a]	$1.2D + I_b$
[5b]	$1.2D + I_i$

OP	Out-of-plane lateral panel degree-of-freedom
LIP	Lateral in-plane panel degree-of-freedom
V	Vertical panel degree-of-freedom
D	Dead load (tributary panel self-weight)
W	Design wind load
E	Earthquake load effects
E_d	Earthquake in-plane deformation compatibility
E_i	Earthquake inertia
T_W	Tornado wind load
P_T	Tornado pressure drop suction force
I_b	Impulsive blast loading
I_i	Impulsive impact loading

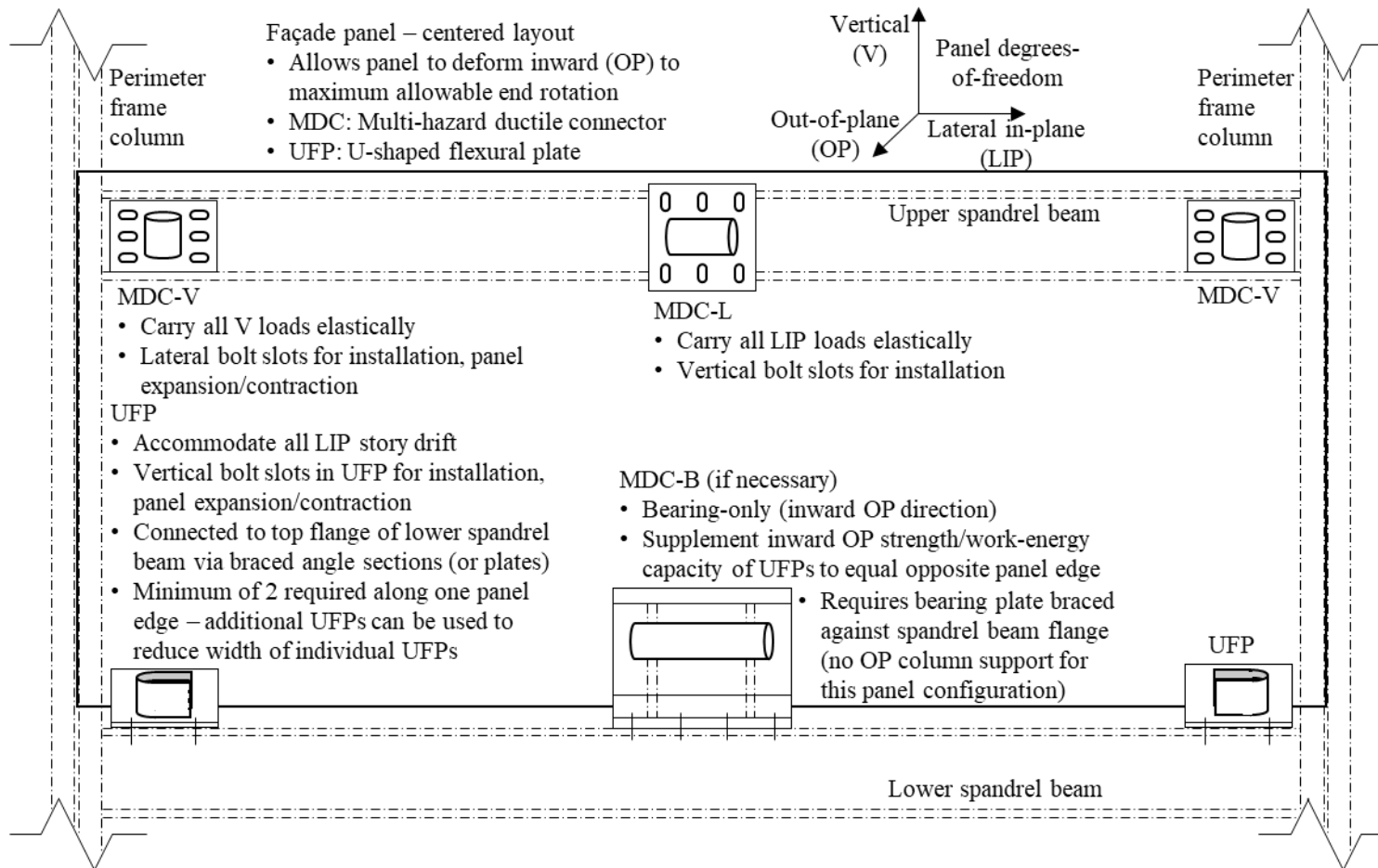


Fig. 3-2: MHFS Connector Layout and Functions

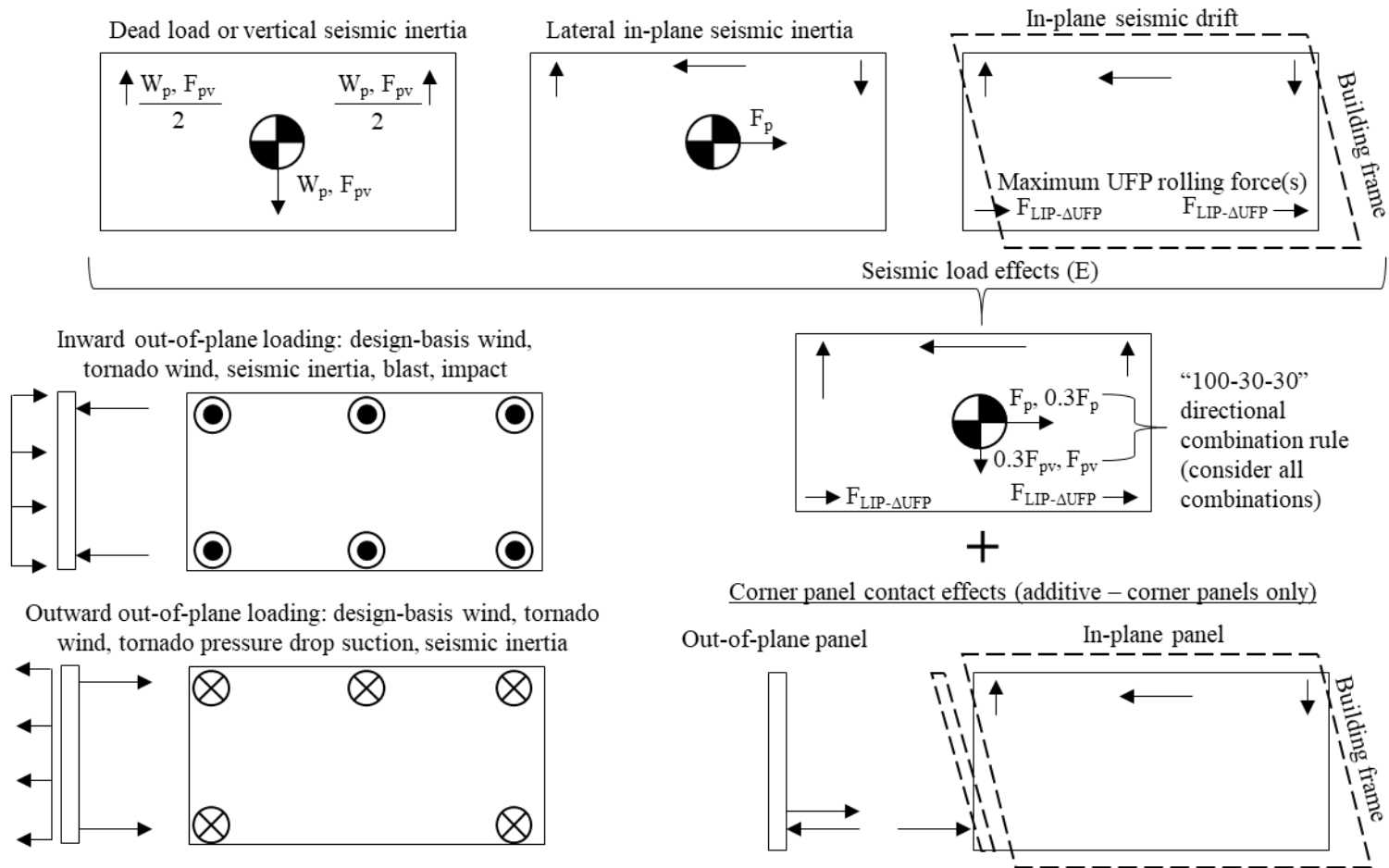


Fig. 3-3: Façade Panel Free Body Diagrams

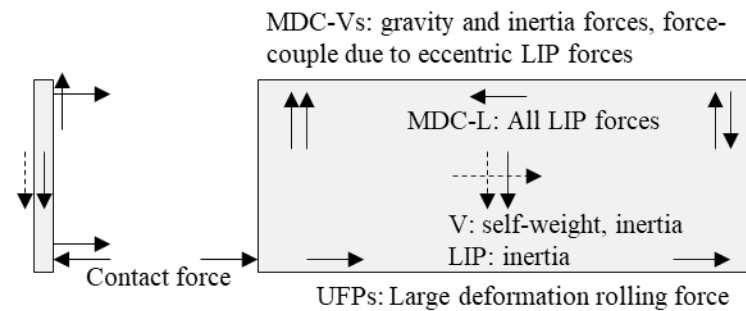
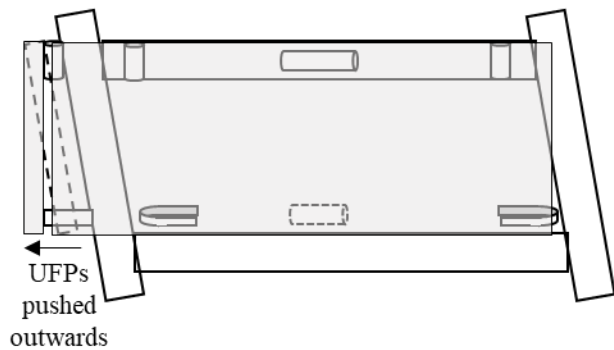
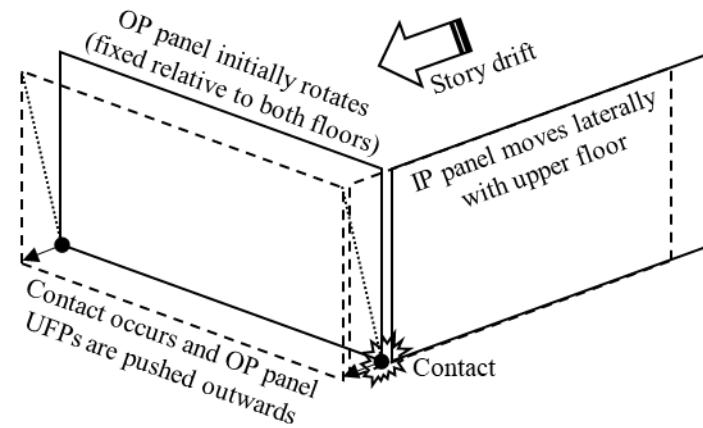
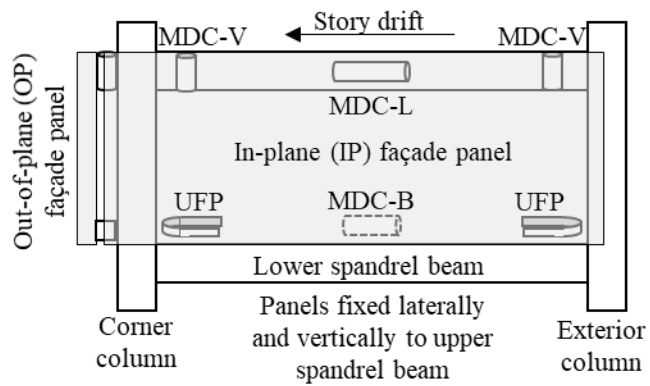


Fig. 3-4: Seismic Building Drift Corner Panel Contact Accommodation Mechanism

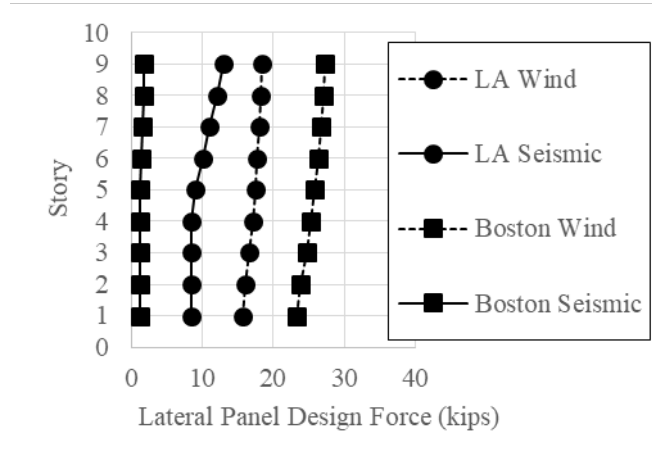


Fig. 3-5: Minimum Design Out-of-Plane Forces per 13'x30'x6" Reinforced Concrete Façade Panel for 9-Story Buildings Located in Boston, MA, and Los Angeles, CA

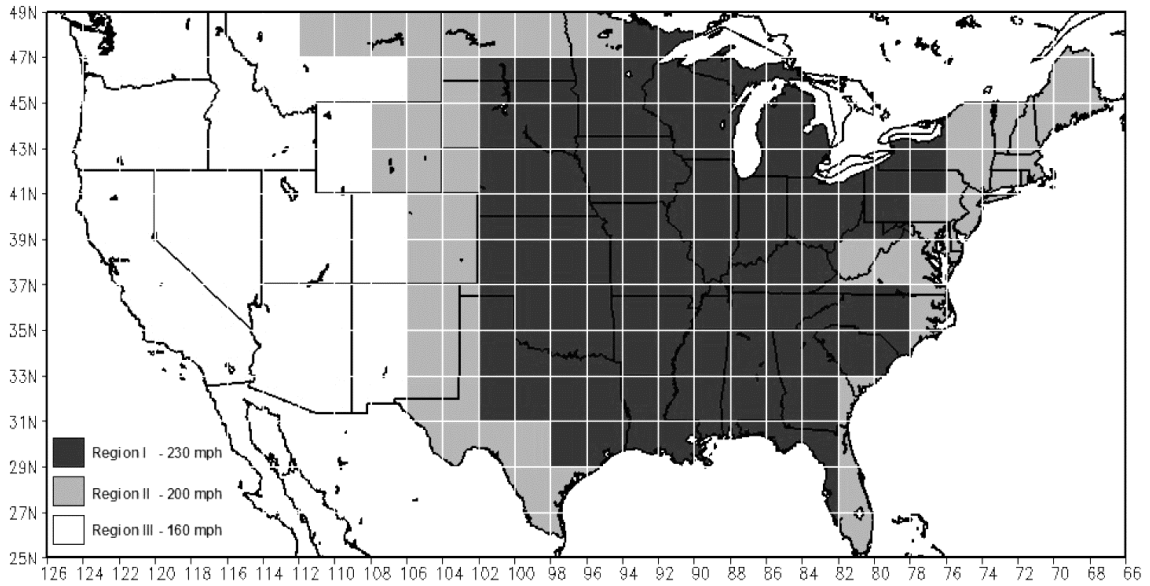


Fig. 3-6: Design Tornado Wind Regions (Adapted from USNRC, 2007)

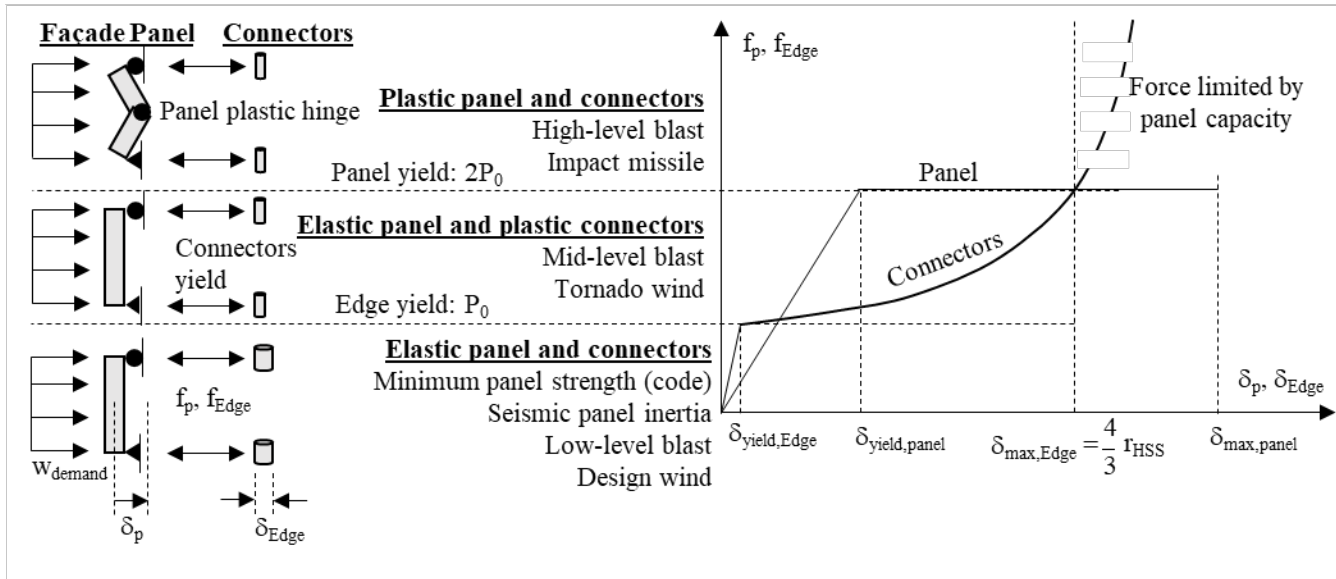


Fig. 3-7: MHFS Out-of-Plane Performance Objectives and Progression of Inward Yielding

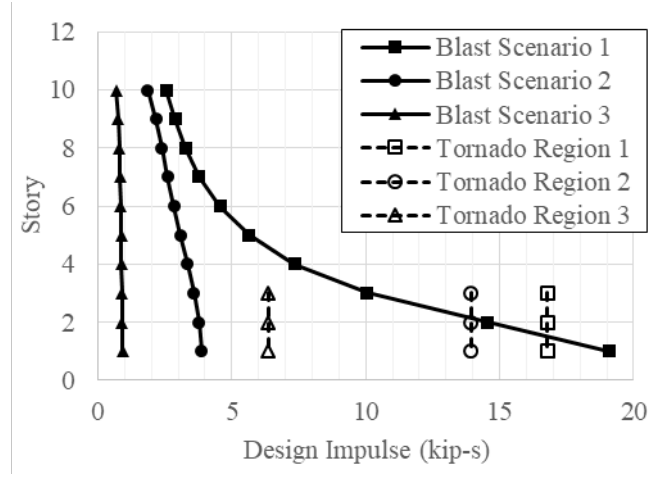


Fig. 3-8: Design Façade Impulse Values for 13'x30' Façade Panel

4. Behavior and Mechanics of Components

The structural behavior and mechanics of each component along the façade-to-frame load path must be understood to develop a design methodology for multi-hazard ductile connectors (MDCs) and U-shaped flexural plates (UFPs) capable of achieving all previously discussed performance objectives. The MDCs and UFPs are critical as they link the façade panels to the primary structural frame and thus govern the interaction between these systems. A potential MDC design which utilizes round hollow structural section (HSS) tubes as key force- and deformation-compliant elements along this load path has been investigated previously for air-blast effects only (Lavarney, 2013) and is believed to effectively achieve all multi-hazard design requirements in this study. This MDC design relies on highly plastic behavior and atypical section demands for an HSS tube application; the tubes are oriented such that OP demands on the façade panel exert a radial force on the circular tube walls. The tube wall section is subjected to eccentric longitudinal forces when supporting the panel in the vertical and LIP directions, which requires shear and flexural resistance from the tube wall section. Large UFP “rolling” deformations are required to accommodate seismic building drifts in the LIP direction. While this behavior is fairly well understood (Baird, 2014), these members will also be relied upon for highly inelastic response in both the inward “crushing” and outward “pulling” degrees-of-freedom in the proposed design methodology. These behaviors will be developed in the following subsections, beginning with the mechanics of façade panels and the ensuing demands imparted onto the MDCs and UFPs.

4.1. Façade Panel

Common façade panel (or veneer) types include precast reinforced concrete, brick masonry, insulated metal panels, and exterior insulation and finish systems (EIFS). A façade system's mass—and, therefore, dead load, seismic inertial forces, and impulse-momentum—is generally concentrated in the veneer elements. Typical brick masonry and EIFS applications include a backup wall consisting of cold-formed steel channel sections spaced at one- to two-foot intervals (on-center); these systems rely primarily on the flexural resistance of this backup wall to resist large OP loads. For reinforced concrete and insulated metal panel systems, both the mass and flexural resistance are integral to the veneer itself. Brick masonry systems are somewhat unique in that the veneer is considered as sacrificial (contains mass but has negligible flexural resistance after cracking) when subjected to blast loading (Salim *et al.*, 2005); these systems require regular anchorage (on, say, an 18- or 24-inch square grid) to the stud wall to provide (approximately) continuous support of the fragile veneer against OP loading. Note that this discussion refers generally to the façade “panel” as an integrated mass-and-resistance element (such as a precast reinforced concrete panel) for simplicity, however some façade systems have decoupled mass and resistance elements which conjointly form an effective “panel”; when considering such systems, the properties of the primary mass and resistance elements should be ascribed to the “panel” as described below.

A façade panel supported as shown in Fig. 3-1 can be idealized as a simply supported beam where the primary flexural element(s) provide the material and section properties required to characterize the system's response to OP loading. The required panel strength for the controlling minimum OP design load (wind, seismic inertia) can be

calculated assuming these demands approximate a uniformly distributed load. Some panel types might have requirements, which provide strength exceeding these design loads (i.e. temperature and shrinkage reinforcement in reinforced concrete panels). The performance objective for these loads is for the panel to remain essentially elastic (with cracking on the tension side expected), therefore the maximum moment due to a distributed load on a simply supported beam—equal to $wh^2/8$, where w is the load per unit length, and h is the panel height—must remain within acceptable limits.

The reaction forces at each edge of the panel “beam” are provided by the combined OP action of the connectors along each edge. For a uniformly distributed load, the reaction force per edge, P , is equal to $wh/2$. A relationship between maximum panel moment under a uniformly distributed load and the edge reaction force is given by:

$$M = \frac{Ph}{4} = \frac{wh^2}{8} = \frac{(pb)h^2}{8} \quad (4-1)$$

where M is the maximum panel moment, P is the edge reaction force, p is pressure on the panel surface, w is the distributed load caused by p over the panel’s height (product of p and b), and all other terms have been previously defined. This relationship is critical for capacity design of the panel and connectors to achieve the desired damage progression during extreme OP loading, where the connectors yield prior to the panel thereby limiting the maximum moment in the panel and protecting the cladding from damage or failure.

4.2. Plastic Mechanics of Round Hollow Structural Section (HSS) Tubes

The proposed MDC design approach includes round hollow structural section (HSS) tubes oriented such that OP panel demands apply a radial load to the circular tube walls (Fig. 3-1). For this type of load, the elastic stiffness, initial plastic mechanism strength, and post-

yield hardening behaviors are of interest considering both crushing (radial deformation towards the section's center) and pulling (away from center) deformations. An elastic force limit for HSS tubes subjected to longitudinal shear is required to proportion their length to resist vertical (MDC-V) and LIP (MDC-L) panel demands. The eccentricity (relative to the tube's central longitudinal axis) of these forces must also be included to ensure the tubes remain elastic when desired under combined loading. Although HSS "rolling" deformations are not relied upon in the proposed MDC design methodology (except possibly small deformations due to thermal/moisture panel expansion/contraction if the slotted bolt holes lock up), the elastic and plastic behaviors of this behavior are also developed in case this action is of interest in a future application of this type of connector.

4.2.1. Radial Force-Deformation Relationship

The elastic stiffness and initial plastic mechanism strength are identical in the radial crushing and pulling directions, however the post-yield behaviors differ due to the difference in boundary conditions resulting from the large deformation mechanics that develop: when crushed, the circular section is flattened along the (assumed rigid) plates on either side, while the pulling direction straightens the circular cross section without rigid boundary constraints until it acts essentially as a tension member. These behaviors are illustrated in Fig. 4-1.

4.2.1.1. Elastic Behavior

The initial plastic mechanism strength is the most critical mechanical property as it must be large enough to resist the panel edge reaction force for OP demands with an elastic MDC performance objective, and also determines the magnitude of post-yield forces in either

(inward or outward) loading direction. The plastic mechanism strength, P_0 , can be calculated by the principle of virtual work considering the formation of four flexural plastic hinges (see Fig. 4-1a):

$$P_0 = \frac{t_{HSS}^2 R_y \sigma_y l_{HSS}}{r_{HSS}} \quad (4-2)$$

where t_{HSS} is the HSS section wall thickness, R_y is the expected material tensile yield overstrength factor relative to the specified minimum material yield stress, σ_y , l_{HSS} is the (longitudinal) length of the HSS section, and r_{HSS} is the outer radius of the HSS section. The material overstrength factor (R_y) should be omitted when calculating elastic connector strength to resist traditional (i.e. given by ASCE 7) OP façade loads for consistency with the load and resistance factor design (LRFD) methodology which assumes minimum (as opposed to expected) material yield stress. The (linear) elastic stiffness, k_{HSS} , of a radially-deformed round HSS section (both crushing and pulling) is given by Young & Budynas (2002) as:

$$k_{HSS} = \left(\frac{\pi}{4} - \frac{2}{\pi} \right)^{-1} \left(\frac{E l_{HSS} t_{HSS}^3}{12 r_{HSS}^3} (1 - \nu^2) \right) = \frac{(14779.3 \text{ ksi}) t_{HSS}^3 l_{HSS}}{r_{HSS}^3} \quad (4-3)$$

where E is the material modulus of elasticity (29000 ksi for steel), ν is the Poisson's ratio of the material (0.3 for steel), and all other terms have been previously defined.

4.2.1.2. Crushing Behavior

The post-yield HSS crushing behavior is critical for sizing the HSS for large design impulse scenarios, where a conservation of energy approach is used to determine the required MDC hysteretic work to ensure a desirable progression of damage in the connectors and façade panel. Both geometric effects and material stress-strain nonlinearity must be accounted for

when formulating a force-deformation relationship for radial crushing of a thin-walled circular section. A suitably accurate model was formulated by Reid and Reddy (1978) which includes elliptically-deformed “plastica” hinge regions which spread along each side tube wall allowing for slope continuity (geometric effects), and a bilinear material stress-strain model (material nonlinearity). The resulting (normalized) force-deformation model is included in Fig. 4-1 as the “True P- δ curve”. This model has shown strong agreement with both experimental and analytical results (Reid & Reddy, 1978; Lavarney, 2013), albeit without an elastic loading region. For design purposes, the post-yield crushing model is approximated by a linear function, which reaches twice the initial plastic mechanism strength ($2P_0$, where P_0 is given by Equation (4-2)) at a radial deformation equal to $2/3$ the original tube diameter. This model simplifies the MDC blast design calculations while providing a nearly identical hysteretic work term to the conservation of energy expressions used to size the HSS tube for large blast scenarios.

4.2.1.3. Pulling Behavior

HSS pulling behavior is relevant for all outward OP panel demands. The assumed geometry of a radially pulled HSS includes rigid rotation of the HSS section about the plate-adjacent plastic hinges, and straightened “free” hinge regions spanning the points of tangency perpendicular to the plate surfaces (Fig. 4-1). The following relationship between pulling deformation, δ_{pull} , and the straightened length of the HSS section, l_p , can be derived simply based on the assumed deformed geometry as:

$$\delta_{\text{pull}} = 2r_{\text{HSS}} \left(\sin \left(\frac{\pi r_{\text{HSS}} - l_p}{2r_{\text{HSS}}} \right) - 1 \right) + l_p \quad (4-4)$$

where all terms have been previously defined. This changing geometry with increased pulling deformation reduces the effective radius, r_{eff} , between the plate-adjacent and “free” plastic hinges, which increases the plastic mechanism strength according to Equation (4-2) replacing r_{HSS} with r_{eff} . With the assumption that the total length around the deformed HSS section remains equal to its original circumference, the effective radius, r_{eff} , can be calculated as a function of the straightened length of HSS section by the following equation:

$$r_{\text{eff}} = r_{\text{HSS}} \left(1 - \cos \left(\frac{\pi r_{\text{HSS}} - l_p}{2r_{\text{HSS}}} \right) \right) \quad (4-5)$$

where all terms have been previously defined. For a given pulling deformation, Equation (4-4) can be solved numerically for l_p , which can then be used to solve for r_{eff} using Equation (4-5). This solution is plotted in Fig. 4-2 along with a second-order polynomial fit function:

$$\frac{r_{\text{eff}}}{r_{\text{HSS}}} \approx -0.4688 \left(\frac{\delta_{\text{pull}}}{r_{\text{HSS}}} \right)^2 - 0.2924 \left(\frac{\delta_{\text{pull}}}{r_{\text{HSS}}} \right) + 1 \quad (4-6)$$

where r_{eff} is the effective radius (Equation (4-5)) and all other terms have been previously defined. This approximate solution is suitable for calculating the deformation factors associated with large HSS pulling deformations.

In addition to changing geometry, material hardening must also be considered to calculate an accurate large deformation pulling force. An expression for estimating this material hardening (P/P_0) as a function of the deformed geometry is given by:

$$f_H = \frac{\delta_{\text{pull}} - \delta_{\text{limit}}}{2 \left(\delta_{\text{limit}} - \frac{P_0}{k_{\text{HSS}}} \right)} + \frac{3}{2} \quad (4-7)$$

where δ_{limit} is the maximum outward deformation which can be achieved via rigid rotation of the circular section quadrants about the plastic hinges (Equation (4-9)) and all other terms have been previously defined. This expression varies linearly from a value of one at the yield deformation to 1.5 at δ_{limit} . These benchmarked values were chosen to match finite element analysis (FEA) results discussed in Section 8. The effective radius, r_{eff} , replaces the r_{HSS} term in Equation (4-2), giving the following expression for the post-yield HSS pulling force, P_P :

$$P_P = \frac{P_0 r_{\text{HSS}}}{r_{\text{eff}}} f_H \leq 2l_{\text{HSS}} t_{\text{HSS}} R_y \sigma_y \quad (4-8)$$

where P_0 is the initial plastic mechanism strength (Equation (4-2)), f_H is the material hardening factor (Equation (4-7)), and all other terms have been previously defined. The overall hardening is a product of material (f_H) and geometry ($r_{\text{HSS}}/r_{\text{eff}}$) effects. The terms to the right of the inequality limit the pulling force to the expected yield force of the tube walls in pure tension.

The normalized HSS pulling force-deformation curve in Fig. 4-1 indicates a rapid stiffness increase as the section approaches the pure tension force limit. It is advantageous to limit the HSS pulling deformation to a maximum value preceding this rapid hardening to limit the force, which develops during outward OP panel loading. A suitable HSS deformation limit was found by simply rotating the HSS section quadrants rigidly about four discrete plastic hinges. The maximum pulling deformation, δ_{limit} , which can be achieved by this method, is given by:

$$\delta_{\text{limit}} = 2r_{\text{HSS}}(\sqrt{2}-1) \quad (4-9)$$

where all terms have been previously defined. This value corresponds to rapid hardening behavior observed in the HSS pulling force-deformation model, as well as finite element

analysis (FEA) simulation results. For design purposes, a bilinear force-deformation model defined by the linear elastic region up to yield with post-yield hardening up to about 3.5 times (Fig. 4-1) the initial plastic mechanism strength, P_0 (Equation (4-2)) at δ_{limit} is assumed.

4.2.2. Longitudinal Shearing of HSS Tube

The proposed MDC arrangement (Fig. 3-1) relies on longitudinally sheared HSS tubes to carry all vertical (MDC-V) and LIP (MDC-L) force demands. The MDCs are expected to resist all vertical loads elastically; therefore, the only mechanical property of interest for longitudinal shearing is the HSS tube yield strength. The derivation of an equation to predict this yield force is shown in Fig. 4-3. The approach taken here is to combine the so-called “tube” and “wall” normal stresses due to bending, find the location of maximum combined normal stress, set this stress equal to yield, and solve for the corresponding longitudinal shear force. The applied shear force requires bending moments (in the plane parallel to end plates at the HSS-to-end plate interface) equal to the product of applied shear and HSS outer radius to maintain equilibrium. The “tube” stress is calculated by dividing the internal bending moment—which varies linearly between the end plates—by the elastic section modulus of the longitudinally-oriented tube walls as shown in Fig. 4-3a. This term alone does not adequately describe the tube’s state of stress because it neglects the circular aspect of the shape, which introduces an eccentricity to the internal forces resisting the bending moment.

The internal bending moment can be converted into a distributed, linearly-varying force applied to the tube section. Resultant forces can be calculated considering the top and bottom halves of the tube, and these forces separated by a distance of $(2/3)l_{\text{HSS}}$ equal

the internal bending moment. Considering an arc length portion of the circular section, these resultant forces act radially with an eccentricity governed by the equation of the circle as shown in Fig. 4-3b. This eccentric force requires a bending moment about the “wall” section, and a corresponding normal stress can be calculated using the elastic modulus of this section. Note that the section modulus is calculated considering the full tube length despite the fact that the radial resultant forces are calculated for the top and bottom halves of the tube (i.e. assumes the entire tube is bending however the resultant radial force considering the entire tube length is zero). This questionable aspect of the assumed mechanics is recognized as somewhat imprecise, however it greatly simplifies the solution allowing for ease of use in design, and the resulting solution is consistently conservative compared to FEA results, which capture a more complex bending behavior, observed in the tube walls. The total normal stress is taken as the sum of “tube” and “wall” bending stresses. These stress terms vary by location; zero normal stress is calculated at the midway point between end plates because the internal tube bending moment is zero, which in turn means zero half-tube resultant radial force to cause wall bending. At either end plate, the tube bending is maximum however; there is zero eccentricity—and, therefore, zero wall bending moment—for the radial half-tube resultant forces.

The location of maximum combined normal stress due to tube and wall bending can be determined as shown in Fig. 4-3c by taking partial derivatives with respect to the tube axes, setting the expression equal to zero, and solving for the remaining spatial variable. The equation, which describes the circular section effectively, eliminates one spatial variable since it can be calculated directly from another. Performing this calculation yields the location(s) of maximum combined normal stress as the “quarter points” around

the circle (45-degree angle within each quadrant) at either end of the tube (top or bottom relative to the tube's longitudinal axis). This value can then be substituted into the combined stress equation, which is set equal to the (nominal) material yield stress. Solving the resulting expression for the applied longitudinal shear gives:

$$V_0 = \frac{8I_{HSS}^2 t_{HSS}^2 \sigma_y}{9r_{HSS}^2 + 12\sqrt{2}t_{HSS}r_{HSS}} \quad (4-10)$$

where V_0 is an estimate of the elastic force carrying capacity of an HSS tube subjected to longitudinal shear and all other terms have been previously described. This solution neglects shear stresses resulting from the applied force for simplicity. Shear stress can be included using, say, a von Mises yield criterion however this adds significant complexity to the derived expression and only changes the resulting value by about 5%.

The result of Equation (4-10) is compared to FEA results in Table 9-3 for various HSS6 sections. This comparison indicates that the derived expression gives a consistently conservative value, which is appropriate for use in design. The FEA results indicate that the longitudinal shear response is the stiffest action examined for the HSS tube; however, a suitable expression for this stiffness could not be derived. While a significant post-yield hardening region (beyond twice the initial yield strength) was observed in the FEA results, this HSS deformation mode is expected (and was observed via experimental testing) to be the least ductile among those investigated in this research. Thus, MDCs are configured on the panel such that only elastic performance is expected in the longitudinal shearing direction. Von Mises stress contour plots of a longitudinally sheared MDC FEA model are shown in Fig. 4-4. These plots indicate that the locations of maximum stress are consistent with what the proposed mechanics predict (maximum stresses at the circular section's quarter points, which increase moving towards the tube ends).

4.2.3. Rolling Force-Deformation Relationship

The application of diametrically opposed tangential shear forces to the HSS cross section results in so-called “rolling” response of the tube (Fig. 4-5). The elastic stiffness, plastic mechanism strength, and post-yield force-deformation behavior considering this action are not directly utilized in the proposed MDC design methodology, however these behaviors are relevant for assessing potential fatigue issues considering expansion/contraction of the panel, as well as possibly supplementing the resistance against progressive collapse using the façade system. This behavior may also be of interest in future applications of MDC-type connectors.

4.2.3.1. Elastic Rolling Behavior

The elastic stiffness for a thin-walled, hollow cylindrical tube was calculated using superposition of elementary load cases developed by Young and Budynas (2002). Considering one-half of the tube section as a circular arch with fixed-free boundary conditions, virtual loads were separately applied to the free end in the (1) radial direction, (2) tangential direction, and (3) in-plane rotational (moment) direction. The radial, tangential, and rotational displacements of the free end considering each of these loads was calculated and superposed (via addition of their respective deformation terms), and boundary conditions were applied to consider a unit tangential (rolling) deformation with the other degrees-of-freedom restrained. This approach is illustrated in Fig. 4-5. Solving the resulting expressions for the applied tangential force divided by the rolling deformation gives the following expression for the elastic stiffness of the rolling HSS tube, k_R :

$$k_R = \frac{E I_{HSS} t_{HSS}^3}{3 \pi r_{HSS}^3 (1 - \nu^2)} \quad (4-11)$$

where all terms have been previously defined. This expression is compared with rolling stiffness values taken from FEA results in Table 9-6 for various HSS6 sections. These results show that Equation (4-11) underestimates k_R but the calculated values are generally no more than 10% different from analysis results. These differences can be attributed at least in part to hoop and shear stress factors, which are neglected in the formulation of Equation (4-11). Additionally, Equation (4-11) assumes each half-tube is semicircular however in reality the free span of each “arch” is slightly less than a semicircle due to the non-zero distance between weld points on the same plate-side (included in the FEA model by constraining a set of nodes near the HSS-to-end plate as described in Section 8).

The plastic mechanism, which forms during tube rolling, is illustrated in Fig. 4-5. Note the similarities to the radial loading plastic mechanism discussed previously; in each case, the tube wall section forms a plastic hinge at the locations of maximum moment, however the maximum distance between these hinges is twice as great considering the rolling mechanism. As with the radial loading case, the principle of virtual work is applied to determine the rolling plastic mechanism strength, R_0 :

$$R_0 = \frac{t_{HSS}^2 R_y \sigma_y l_{HSS}}{2 r_{HSS}} = \frac{P_0}{2} \quad (4-12)$$

where all terms have been previously defined. The force required to form the rolling plastic mechanism is exactly half the force required to form the radial mechanism due to the increased distance between yield points (by a factor of two). As with the radial yield mechanism (Equation (4-2)), the R_y term included here should be omitted when considering typical LRFD load combinations (ASCE, 2013), however no such design loads

(or desired performance objectives) of rolling HSS tubes are included in the connector configuration shown in Fig. 3-1. This equation is compared to FEA results in Table 9-5 for various HSS6 sections. Similar to the elastic stiffness calculation, Equation (4-12) gives results within about 10% of those observed in FEA results.

4.2.3.2. Large Rolling Deformations

An HSS tube rolling post-yield force-deformation model has been developed and is shown in Fig. 4-6. For a given rolling deformation, the distance between two diametrically opposed points must increase if radial deformations are prevented (believed to be the case for MDCs installed on a panel). This elongation can be treated as a radial pulling deformation, and a corresponding force acting along a line defined by the two points can be calculated using Equation (4-8). This force can be resolved into radial and tangential (rolling) components using the deformed geometry. While the rolling component of this force should provide an estimate of the post-yield rolling force, comparison with FEA results (detailed in Section 9.2.1.4) indicates that this component alone significantly underestimates the observed rolling force. This is possibly due to neglect of the interaction between the rigid plates and deforming tube, as well as the boundary conditions of the bending tube wall sections as shown in Fig. 4-6. A modified solution has been proposed which takes the average of tangential (rolling) and radial components of the calculated pulling force as the rolling force for a given deformation:

$$R_R = P_P \left(\sqrt{\delta_R^2 + 4r_{HSS}^2} - 2r_{HSS} \right) \frac{\delta_R (2r_{HSS} + \delta_R)}{2(4r_{HSS}^2 + \delta_R^2)} \sqrt{\frac{4r_{HSS}^2}{\delta_R^2} + 1} \geq R_0 \quad (4-13)$$

where P_P is the pulling force (Equation (4-8)) at the deformation calculated within the parenthesis which follow this term, δ_R is the rolling deformation, R_0 is the rolling plastic

mechanism force (Equation (4-12)), and all other terms have been previously defined. This solution has been found to match force-deformation results obtained via FEA within about 5% in the deformation range of about two and four inches for HSS6 sections. The lower bound value of R_0 generally controls for deformations near yield.

Experimental testing was performed to examine this rolling behavior in more detail and determine if large deformations could be achieved in the hopes of using MDCs to accommodate in-plane seismic drift (Section 7.2). An HSS6x0.375 section was capable of achieving a rolling deformation of about 2.25 inches (3/8 of the tube diameter) prior to failure. This failure was caused by a concentration of strain just outside of the welded region, which cannot be reduced in full circular sections such as an HSS tube. This shortcoming of the HSS tube MDC design lead to the proposed inclusion of UFPs to accommodate in-plane seismic building drifts. UFPs are mechanically similar to the proposed MDCs with a few critical geometric alterations, which make them particularly well-suited to achieve the large rolling deformations required to accommodate in-plane seismic building drift.

4.3. U-Shaped Flexural Plate (UFP) Connector Mechanics

UFPs have been successfully implemented in both commercial and research applications (Baird, 2014). The force-limited, large deformation response of these members subjected to rolling deformations makes them ideal for accommodating in-plane seismic building drifts at the façade-building frame interface while limiting the shear forces imparted onto façade panels. These connectors are created by bending a flat plate around a 180-degree arc to form an elongated U-shape as shown in Fig. 3-1. The mechanics of UFPs are controlled by four geometric variables: plate thickness, t_{UFP} ; (outer) bend radius (or

diameter), r_{UFP} (d_{UFP}); strip width (length of member normal to the plane of curvature), b_{UFP} ; and “free” length of straight, unrestrained plate between the curved and connected (via bolts or welds) regions of the UFP, l_{free} . UFP thickness and radius are chosen to match the MDC HSS tubes, while l_{free} is determined by the maximum expected lateral in-plane story drift. This leaves the total UFP width along the panel edge, B_{UFP} , as the only unknown geometric variable. With known force and deformation demands from the panel, and UFP material properties and mechanics, B_{UFP} can be calculated to provide the required strength and ductility to achieve all performance objectives.

In typical UFP applications, the bent plate is only relied upon to undergo rolling deformations, and a more traditional alternate OP load path is provided, such as a UFP housing or supplemental connection system in-parallel with the UFP itself. In this application, both the elastic strength and ultimate deformation capacity of the UFPs are relied upon for demands in the OP panel direction including wind, seismic inertia and corner panel contact, and impulsive (blast or impact) loading. The plastic mechanics of interest for UFPs in this application are illustrated in Fig. 4-7 and detailed in the following subsections.

4.3.1. UFP Rolling Mechanics

The mechanics of UFPs undergoing large rolling deformations are well established (Baird, 2014). The elastic stiffness of this action is given by Baird (2014) as:

$$k_{R,UFP} = \frac{16Eb_{UFP}}{27\pi} \left(\frac{t_{UFP}}{d_{UFP}} \right)^3 \quad (4-14)$$

where b_{UFP} is the width of UFP normal to the plane of curvature, t_{UFP} is the UFP’s thickness, d_{UFP} is the (outer) diameter of the circular portion of the UFP, and all other terms have been

previously defined. Plastic hinges form at either end of the curved arc as shown in Fig. 4-7a when a sufficient rolling shear force is applied. The maximum achievable plastic rolling force is given by:

$$R_{0,UFP} = \frac{b_{UFP} t_{UFP}^2 R_t \sigma_u}{2d_{UFP}} \quad (4-15)$$

where R_t is the expected material overstrength relative to the material's nominal minimum ultimate stress, σ_u , and all other terms have been previously defined. Note that the nominal UFP rolling plastic mechanism strength can be determined by omitting the R_t term and replacing σ_u with σ_y in this expression; there are no minimum force design requirements for the UFPs in this application, and Equation (4-15) is meant to determine the maximum rolling force (at large deformations) for capacity design of the MDCs as discussed in Section 5.2.2. A unique aspect of this mechanism is that the peak plastic strain remains constant for any rolling deformation less than l_{free} because the plastic hinges are able to “travel” rather than remain stationary and accumulate additional strain. The member is essentially flattening out an initially curved section on one side while curving an initially flat section on the other, meaning that the peak plastic strain, ϵ_{UFP} , is constant and can be calculated from the curvature of the semicircle as:

$$\epsilon_{UFP} = \frac{t_{UFP}}{d_{UFP} - t_{UFP}} \quad (4-16)$$

where all terms have been previously defined.

The mechanism behavior changes when a hinge travels to the end of the “free” region (rolling deformation greater than or equal to l_{free}), at which point the plastic strains accumulate as the plate bends at this fixed boundary. This more concentrated bending is analogous to the behavior observed in rolling HSS tubes, which do not have a free region,

which allows the plastic hinges to travel. While additional rolling deformations can be achieved beyond l_{free} , failure is expected after about $3/8^{th}$ d_{UFP} of additional deformation beyond the chosen free length based on experimental testing of rolling HSS tubes, as well as FEA of both MDCs and UFPs.

4.3.2. UFP Crushing Mechanics

The mechanics of UFP crushing are very similar to those discussed in Section 4.2.1.2 for HSS tubes. This mechanism is illustrated in Fig. 4-7b. Note that this mechanism is essentially identical to the mechanism for radially-loaded HSS tubes shown in Fig. 4-1a, albeit with only half of the circular section. As such, the plastic mechanism is half as strong as the full tube mechanism strength with all other geometric and material properties being equal:

$$P_{0,UFP} = \frac{b_{UFP} t_{UFP}^2 R_y \sigma_y}{d_{UFP}} \quad (4-17)$$

where all terms have been previously defined. Note that HSS tubes and UFPs will typically be fabricated using different grades of steel, with UFPs being made from flat plate stock (typically A36 steel). Care must be taken to ensure the relevant material properties are not used interchangeably when, for example, the MDCs are being capacity designed for an expected UFP force. As with the MDC radial mechanism strength (Equation (4-2)), the R_y term should be omitted when considering elastic response of UFPs subjected to LRFD load combinations. For non-impulsive inward OP design forces with yielding connectors as the performance objective (typically only tornado/extreme wind), a hardened crushing strength equal to twice the initial mechanism strength given by Equation (4-17) can be used for simplicity. Additionally, the elastic stiffness of a radial crushed UFP is given by:

$$k_{0,UFP} = \frac{k_{HSS}}{2} \quad (4-18)$$

where k_{HSS} is the elastic stiffness of a radially crushed HSS tube (Equation (4-3)).

4.3.3. UFP Pulling Mechanics

UFPs subjected to radial pulling demands form the plastic mechanism illustrated in Fig. 4-7c. This action is critical in the design of UFPs as it controls the total required UFP width per panel (B_{UFP}). For the connector layout illustrated in Fig. 3-1, the bottom panel edge is supported in the outward OP direction by the UFPs, which must have sufficient strength to elastically resist all design-basis seismic and wind loads. The UFP radial pulling plastic mechanism strength is given by:

$$P_{P,UFP} = \frac{b_{UFP} t_{UFP}^2 \sigma_y}{2(r_{UFP} + l_{free})} \quad (4-19)$$

where l_{free} is the straight plate length between the circular curved and connected regions of the UFP, and all other terms have been previously defined. The material overstrength factor is omitted from this expression to ensure a conservative pulling capacity is obtained for design. Comparing Equation (4-19) to Equation (4-17) shows that the pulling mechanism strength is always less than the crushing mechanism strength for a nonzero free length.

To accommodate corner panel contact, the UFPs must be capable of outward deformation equal to the maximum expected story drift. An estimation of the maximum pulling force at large deformations is needed to determine the capacity design forces for the MDCs. The large deformation geometry shown in Fig. 4-7c is used to calculate the effective moment arm, r_{eff} , between plastic hinges which can then be substituted into

Equation (4-19) (along with material hardening and overstrength factors) to determine the pulling force at a given deformation. Considering one half of a UFP (split at the apex of the semicircle), the free length is assumed to rotate about the plastic hinge adjacent to the connection region. The curved portion of the tube is assumed to remain circular with unchanged arc length, increased radius, and decreased angle swept. Slope continuity is assumed at the boundary between the straight and curved regions, while the other end of the curved region has a vertical tangent. The total “width” of this deformed shape is the moment arm between hinges, r_{eff} , given by:

$$r_{\text{eff}} = l_{\text{free}} \cos(\theta) + \frac{\pi r_{\text{UFP}}}{\frac{\pi}{2} - \theta} (1 - \sin(\theta)) \quad (4-20)$$

where θ is the angle of rotation at the plastic hinge at the end of the free (straight) length region of the UFP, and all other terms have been previously defined. This expression can be solved for θ values ranging from zero (undeformed) up to $\pi/2$ (UFP is pulled completely straight).

While Equations (4-19) and (4-20) can be combined to form an expression for pulling force as a function of hinge rotation, θ , a relationship between pulling force and pulling deformation is more meaningful and practical for design. The pulling deformation, δ_{pull} , for the deformed shape shown in Fig. 4-7c and described in the previous paragraph can be calculated from the vertical “height” of the entire shape:

$$\delta_{\text{pull}} = 2l_{\text{free}} \sin(\theta) + \frac{\pi r_{\text{UFP}}}{\frac{\pi}{2} - \theta} \cos(\theta) - 2r_{\text{UFP}} \quad (4-21)$$

where all terms have been previously defined. This expression gives the pulling deformation for the entire UFP (not just the half shown in the illustration) and can be solved

for θ ranging from zero up to $\pi/2$ similar to Equation (4-20). A closed-form solution for r_{eff} as a function of δ_{pull} cannot be obtained mathematically because the assumed geometry results in expressions which include the product of trigonometric functions of an angle and the angle itself which cannot be simplified via trigonometric identities, substitutions, or otherwise.

An r_{eff} value at the pulling deformation of interest can be obtained by solving both Equations (4-25) and (4-21) for an discretized set of θ values between zero and $\pi/2$ and choosing the r_{eff} value corresponding to the θ value which yields the δ_{pull} value of interest. A plot of r_{eff} and δ_{pull} normalized by $r_{\text{UFP}} + l_{\text{free}}$ is shown in Fig. 4-8. The dotted line is a third-order polynomial fit function given by:

$$\frac{r_{\text{eff}}}{r_{\text{UFP}}+l_{\text{free}}} \approx -0.368 \left(\frac{\delta_{\text{pull}}}{r_{\text{UFP}}+l_{\text{free}}} \right)^3 + 0.472 \left(\frac{\delta_{\text{pull}}}{r_{\text{UFP}}+l_{\text{free}}} \right)^2 - \frac{0.334\delta_{\text{pull}}}{r_{\text{UFP}}+l_{\text{free}}} + 1 \quad (4-22)$$

where all terms have been previously defined. This plot and fit function were calculated for r_{UFP} and l_{free} of three and four inches, respectively, and are not valid for different proportions of these two variables. The pulling force at the deformation of interest can be calculated as:

$$P_{T,\text{UFP}} = \frac{b_{\text{UFP}} t_{\text{UFP}}^2 R_t \sigma_u}{2r_{\text{eff}}} \quad (4-23)$$

where r_{eff} is the effective moment arm between plastic hinges in the deformed shape (Equation (4-20)), and all other terms have been previously defined. For r_{UFP} and l_{free} of three and four inches, respectively, at δ_{pull} of four inches, this expression can be taken as twice the initial pulling mechanism strength given by Equation (4-19). The geometric model gives a pulling force-deformation relationship which compares favorably to FEA results, however a different model may be required if significantly different r_{UFP} , l_{free} , or

maximum δ_{pull} values are considered. Although they share some similarities, the large pulling deformation model discussed in this section and that discussed in Section 4.2.1.3 for HSS tubes give significantly different solutions, with the HSS tubes hardening more rapidly than the UFPs as a function of pulling deformation (beneficial behavior in this application).

4.4. Simplified Dynamic Model for Impulsive Load Design

Design for impulsive OP loading can be performed using a generalized single degree-of-freedom dynamic representation of the façade panel and connectors system. Here, the (maximum) panel deflection at panel mid-height is chosen as the generalized displacement, and convolution integrals are performed using the section properties and deflected shape function over the panel's height to determine the dynamically-equivalent SDoF mass and elastic stiffness.

4.4.1. Panel Shape Function and Equivalent Mass and Stiffness

For low-intensity impulsive loads for which connectors and panels are expected to remain elastic, the shape function, $\psi(x)$, is considered as the first elastic mode shape (with unit magnitude) for a simply supported beam with a constant cross section and is given by:

$$\psi(x) = \sin\left(\frac{\pi x}{h}\right) \quad (4-24)$$

where x is the dimension along the panel height, h . The equivalent SDoF elastic stiffness, k^* , is given by:

$$k^* = EI_x \int_0^h \frac{d^2 \psi(x)}{dx^2} dx = \frac{\pi^4 EI_x}{2h^3} \quad (4-25)$$

where E is the material's modulus of elasticity, and I_x is the cross section's moment of inertia. Note that I_x should be taken as the cracked section moment of inertia for reinforced concrete façade panels (can be estimated as, say, one half of the gross section moment of inertia). The generalized SDoF mass, m^* , is required for calculation of the panel's initial velocity and kinetic energy when subjected to an impulsive load, and is given by:

$$m^* = m \int_0^h (\psi(x))^2 dx = \frac{mh}{2} \quad (4-26)$$

where m is the panel mass per unit length (along the panel's height). The generalized SDoF mass term given by Equation (4-26) is equal to one half the total panel mass assuming a constant cross section. This generalized “half mass” term is only valid if the panel supports—provided by the connectors along each panel edge—remain elastic thereby providing the necessary boundary conditions for first mode elastic dynamic response (assumed shape function; Equation (4-24)) of the panels.

For larger impulsive loads (moderate- to high-intensity), plastic response of the connectors may be chosen as the performance objective (Table 3-1) to limit the edge force (and bending moment; Equation (4-1)) imparted onto the panel (Fig. 3-7). In these cases, the panel mass effectively translates in the OP direction as a rigid body with a unit shape function. Substituting a unit shape function into Equation (4-24) results in a generalized SDoF mass, m^* , equal to the total mass of the panel. In summary, when considering uniformly distributed impulsive OP loads where the connectors are designed to act as plastic force-limiting elements (plastic MDC/UFP performance objective), the generalized SDoF mass should be taken as the full mass of the panel; otherwise (elastic MDC/UFP performance objective), the generalized mass should be taken as one half the total panel

mass. Note that use of plastically deforming connectors doubles the effective mass to resist impulsive loading compared to a traditional “fixed” panel connector.

4.4.2. Panel Kinetic, Elastic Potential, and Plastic Work Energies

The response of a façade system subjected to an impulsive load can be characterized using the generalized SDoF dynamic system developed in the previous section and peak response obtained through energy conservation. Based on momentum conservation, the applied impulse divided by m^* gives the initial velocity of the generalized SDoF system, v_i^* . The initial kinetic energy of the (generalized) system, KE_p , is equal to the product of one half m^* and the initial velocity squared, which can be expressed as:

$$KE_p = \frac{I_D^2}{2m^*} \quad (4-27)$$

where I_D is the design impulse value, and m^* is the generalized SDoF system mass (Equation (4-26)). The inversely proportional relationship between initial kinetic energy and mass means that, from a design perspective, a more massive façade system (such as reinforced concrete panel or brick masonry systems) benefits from less kinetic energy which must be conserved through elastic storage or plastic work for a given impulse magnitude.

Equation (4-27) represents the initial state of the system subjected to an impulsive load. The system will eventually come to rest, at which time the panel will be at its point of maximum deformation. The transition between these two energy states can be represented as:

$$KE_p = PE_p + W_p \quad (4-28)$$

where PE_P is the elastic potential energy stored in the deformed panel, and W_P is the plastic work performed during any permanent deformation of the panel. Equation (4-28) is an expression of energy conservation between the initial and deformed system states. The right-hand terms in this equation can be calculated from areas under the force-deformation (or moment-rotation) curve for each component. Deriving these terms requires an understanding of the panel's and connectors' force-deformation response from the elastic region to the point of failure.

The moment-rotation relationship of a flat, simply supported (along 2 edges) plate subjected to uniform impulsive loading can be approximated as linear-elastic perfectly-plastic with maximum moment taken as the average of the elastic ($S_x R_y \sigma_y$, where R_y is the expected material over-strength relative to the minimum nominal yield strength, σ_y) and plastic ($Z_x R_y \sigma_y$) section capacities (DOD, 2008). Substituting this maximum moment into Equation (4-1) and rearranging terms gives an expression for the panel edge reaction force, P , at (dynamic, elasto-plastic) flexural yield. This yield force can be divided by the equivalent OP stiffness at mid-height of the panel, k^* , to obtain the maximum elastic panel deflection, δ_y , calculated as:

$$\delta_y = \frac{2}{hk^*} (S_x + Z_x) R_y \sigma_y \quad (4-29)$$

where all terms have been previously defined. This stiffness and maximum deformation can be used to calculate the elastic potential energy of the deformed panel, PE_P , as:

$$PE_P = \frac{1}{2} k^* \delta_y^2 = \frac{5\pi^4 P \delta_y}{768} \quad (4-30)$$

where all terms have been previously defined. The right-most form of this equation is useful for the design of connectors as it puts the panel's elastic potential energy in terms of the OP reaction force per edge.

The yield deflection given by Equation (4-29) can be converted to a hinge rotation at yield, θ_y , considering small angle approximations and disregarding elastic deformations:

$$\theta_y = \frac{4\delta_y}{h} \quad (4-31)$$

where all terms have been previously defined. This conversion is useful when considering the panel's plastic work capacity; UFC 3-340-02 provides moment-rotation relationships with damage states correlated to plastic hinge rotations up to the point of failure (DOD, 2008). For a flat steel plate, twelve degrees of hinge rotation (six degrees at each end) corresponds to failure of the panel. This same rotation limit can be justified for under-reinforced concrete slabs by examining the section mechanics of a typical six-inch thick reinforced concrete façade panel (section curvature at maximum allowable material strain). These rotation limits, along with Equation (4-1), can be used to calculate the plastic work capacity of an (assumed) elasto-plastic façade panel:

$$W_P = \frac{Ph}{4} (\theta_{\max} - \theta_y) \quad (4-32)$$

where θ_{\max} is the maximum plastic hinge rotation given by UFC 3-340-02 (or otherwise derived), and all other terms have been previously defined. This expression is put in terms of the OP reaction force per panel edge, P , similar to Equation (4-30). The value, which this panel edge reaction term takes, is governed by the force-deformation relationship of the MDCs and UFPs, which act as critical force-compliant elements in the OP load path.

4.4.3. MDC and UFP Elastic Potential and Plastic Work Energies

The elastic potential and maximum plastic work energies, which the connectors can achieve when subjected to crushing deformations, are needed to characterize the simplified nonlinear dynamic response of the façade system subjected to uniform impulsive loading in the OP direction. The connectors act in series with the equivalent SDoF mass and resistance function derived in the previous subsection, and, as such, they can be designed to limit the force and deformation required of the panel itself.

Equations (4-2) and (4-3) can be used to calculate the elastic potential energy of these radially-deforming HSS tubes, PE_{HSS} , given by:

$$PE_{HSS} = \frac{P_0^2}{2k_{HSS}} \quad (4-33)$$

where all terms have been previously defined. A deformation of 2/3 the original tube diameter is considered as the maximum crushing deformation for design because complete crushing of the tube is impossible due to the thickness of the tube walls, as well as the expected failure and splitting of the tube due to extreme strains at the outer fibers in the plastic regions. Additionally, the rapid strength increase observed beyond 2/3 the original tube diameter would require proportional strengthening of the façade and building frame and is thus avoided. With these approximations, the plastic work capacity of a radially crushed HSS tube, W_{HSS} , is given by:

$$W_{HSS} = P_0 \left(2r_{HSS} - \frac{3P_0}{2k_{HSS}} \right) \quad (4-34)$$

where all terms have been previously defined. Note that this work term represents the area under the idealized force-deformation curve shown in Fig. 4-1 (Equation (4-34) subtracts out elastic strain energy).

The elastic potential energy capacity of UFPs can be calculated using Equation (4-33) by replacing the plastic mechanism strength and radial crushing stiffness with the relevant terms derived for the UFPs (given by Equations (4-17) and (4-18)). The maximum UFP crushing force (at $(2/3)d_{UFP}$) can be calculated as:

$$P_{W,UFP} = 2P_{0,UFP} \left(\frac{R_t \sigma_u}{R_y \sigma_y} \right) \quad (4-35)$$

where $P_{0,UFP}$ is the initial UFP crushing mechanism strength given by Equation (4-17), and all other terms have been previously defined. Similar to the HSS tubes, the UFPs are assumed to have a bilinear force-deformation relationship defined by the elastic stiffness, $k_{0,UFP}$ (Equation (4-18)), initial plastic mechanism strength, $P_{0,UFP}$ (Equation (4-17)), and strength at maximum crushing deformation, $P_{W,UFP}$ (Equation (4-35)). Using these terms to calculate the area under the nonlinear force-deformation curve yields an expression for plastic work capacity of the UFPs:

$$W_{UFP} = \frac{(P_{W,UFP} + P_{0,UFP})}{2} \left(\frac{2}{3} d_{UFP} - \frac{P_{0,UFP}}{k_{0,UFP}} \right) \quad (4-36)$$

where all terms have been previously defined. Note that Equation (4-35) essentially substitutes the material's expected maximum stress for the expected yield stress, which was not included in the derivation of force terms to calculate work-energy capacity of the crushed MDC HSS tubes. This modification for UFPs is necessary due to observed differences in the force-deformation response of UFPs and HSS tubes subjected to crushing deformations.

FEA results indicate that the actual behavior of UFPs crushed to $(2/3)d_{UFP}$ (chosen as the crushing deformation limit for HSS tubes) involves more hardening than that observed in HSS tubes. This is due to increased concentration of plastic strain (and the

resulting material hardening) at the “side” hinge (between the end plates). Increasing plastic strain demands at the plate-adjacent hinges can spread into the free length region thereby reducing the concentration of rotation at the straight-to-curved section transition, whereas the side hinge outer fibers cannot redistribute these demands due to equal and opposite bending moments applied at either side of the plastic region. When considering the case of the full circular HSS section, the plate-adjacent plastic regions have similar boundary conditions as the side hinges, with equal and opposite moments on either side requiring rotation across the hinge. The full tube shares the plasticity demands more equally amongst its plastic hinges, so the material hardening is less significant as a function of crushing deformation compared to the UFP’s semicircular section. There is potential for fracture at the side hinges due to large plastic strains, particularly for UFPs due to the aforementioned strain concentration. Experimental testing of an HSS6x0.25 tube to a crushing deformation of $(2/3)d_{HSS}$ indicates that, despite FEA indicating peak strains in excess of the material’s minimum ultimate strain (about 21% plastic strain for ASTM A500 Grade B steel), HSS sections are capable of undergoing large crushing deformations while still maintaining longitudinal load-carrying capacity (in this case, the tributary dead load of a reinforced concrete façade panel). Additional analytical and perhaps experimental work is needed to determine if the UFPs are capable of similar large crushing deformations.

4.4.4. Simplified Nonlinear Dynamic Response under Uniform Impulsive Pressure Loading

The final design of the panel and connectors is intended to provide the same support conditions in the inward OP direction at both (top and bottom) panel edges in terms of elastic strength, plastic strength, and work-energy capacity to satisfy all performance

objectives and ensure the desired progression of yielding for the various load types as shown in Fig. 3-7. With the connector layout shown in Fig. 3-1, providing identical support conditions for all response types is not possible because of the differences in MDC and UFP post-yield crushing mechanics discussed in Sections 4.2.1.2, 4.3.2, and 4.4.3; if, say, the same initial crushing plastic mechanism strength is provided along both edges, the plastic work-energies will differ because the HSS tubes and UFPs reach different strengths as a function of this initial yield strength at the desired maximum crushing deformation (Equations (4-34) and (4-36)). The purpose of the MDC-B along the UFP edge is to provide as close to equal inward OP support conditions as possible given this inherent inequality. The approach taken herein is to calculate the MDC-B length to match the initial crushing strength, P_0 (Equation (4-2)), of the opposite edge when acting in parallel with the UFPs. Although this approach results in slightly different work-energy capacities along the two edges, the initial mechanism strength is thought to be the more critical parameter as design-basis, elastic performance objective loads are more common than high-intensity impulsive loads, and any potential impulsive loading will not be perfectly uniform or exactly equal in magnitude to the assumed design case(s) which would require a perfectly balanced design to reach the exact chosen peak response. With this concession, the panel and connector system can be assumed to have identical support conditions along both edges with responses given by the MDC mechanics terms developed in Sections 4.2.1.2 and 4.4.3. This assumption simplifies the resulting work-energy expressions used for impulsive design by eliminating the need to account for the differences in HSS and UFP mechanics by treating both edges as MDC-supported, with the understanding that the addition of the MDC-B along the UFP panel edge will largely eliminate the discrepancy.

Design of connectors for the impulsive OP loading scenarios and performance objectives given in Table 3-1 relies on the conservation of energy expression given by Equation (4-28), with the addition of the HSS energy terms from Section 4.4.3 to the right-hand side, and substitution of the HSS crushing strength (Equation (4-2), Fig. 4-1). Considering the generalized SDoF system upon which Equation (4-28) is based, the OP force-deformation action provided by the top and bottom sets of connectors can be readily added into this system as OP translation at these connection points translates directly to translation at panel mid-height, which is the generalized displacement coordinate. To ensure capacity protection of the panel up to the maximum crushing deformation of the connectors (Fig. 3-7), the panel edge reaction force term, P , in Equations (4-1), (4-30), and (4-32) should be replaced by the maximum HSS tube crushing strength, $2P_0$ (two times Equation (4-2)). With these modifications to Equation (4-28), the impulsive loading design equation is given by:

$$KE_P = 2PE_{HSS} + PE_P(2P_0) + 2W_{HSS} + W_P(2P_0) \quad (4-37)$$

where KE_P is the initial kinetic energy of the façade panel subjected to a known impulse (Equation (4-28)), PE_{HSS} is the elastic potential energy of the radially-crushed HSS tube length per panel edge (Equation (4-33)), $PE_P(2P_0)$ is the elastic potential energy of the façade panel (Equation (4-30)) with the maximum crushing strength, $(2P_0$, where P_0 is given by Equation (4-2)) of the HSS tube length per panel edge substituted for the panel edge reaction force, P , W_{HSS} is the plastic work capacity of the HSS tube lengths per panel edge (Equation (4-34)), and $W_P(2P_0)$ is the plastic work capacity of the façade panel with $2P_0$ replacing P in Equation (4-32). Note that the plastic work terms take values of zero whenever the performance objective for that component subjected to a given design

impulse scenario is to remain elastic (Table 3-1). Substituting the known work-energy expressions into Equation (4-37) yields the following (equivalent) expression:

$$\frac{I_D^2}{2m^*} = \frac{P_0^2}{k_{HSS}} + P_0 \delta_y + P_0 \left(4r_{HSS} - \frac{3P_0}{k_{HSS}} \right) + \frac{P_0 h}{2} (\theta_{\max} - \theta_y) \quad (4-38)$$

where all terms have been previously defined. This expression can be solved for P_0 for a given design impulse value. For a chosen HSS section, P_0 can then be solved for l_{HSS} per panel edge.

Table 4-1: MDC and UFP Load Demands and Design Criteria

Connector	Panel DOF	Component DOF	Load Combination	Design Limit State Behavior	Design Performance Criteria
MDC-V	V	Shearing	[1], [3a], [3c]	C	$V_0 > V_u$
	OP (in)	Crushing	[2a], [3b]	C	$P_0 > P_u$
			[4a]	M	$2P_0 > P_u$
			[5a], [5b]	U	Equation (39)
	OP (out)	Pulling	[2b], [3b]	C	$P_0 > P_u$
			[4b], [4c]	M	$2P_0 > P_u$
MDC-L	LIP	Shearing	[3a]	C	$V_0 > V_u$
	OP (in)	Crushing	[2a], [3b]	C	$P_0 > P_u$
			[4a]	M	$2P_0 > P_u$
			[5a], [5b]	U	Equation (39)
	OP (out)	Pulling	[2b], [3b]	C	$P_0 > P_u$
			[4b], [4c]	M	$2P_0 > P_u$
UFP	LIP	Rolling	[3]	Δ	$d_{UFP} \geq \Delta_{LIP,max}$
	OP (in)	Crushing	[2a], [3b]	C	$P_{0,UFP} > P_u$
			[4a]	M	$2P_{0,UFP} > P_u$
			[5a], [5b]	U	Equation (39)
	OP (out)	Pulling	[2b], [3b]	C	$P_{P,UFP} > P_u$
			[3b] + E_c	Δ	$P_{T,UFP} > P_u$
[4b], [4c]			M	$P_{T,UFP} > P_u$	
MDC-B	OP (in)	Crushing	[5a], [5b]	U	Equation (49)

- DOF Degree-of-freedom
- OP Out-of-plane lateral panel DOF
- LIP Lateral in-plane panel DOF
- V Vertical panel DOF
- MDC Multi-hazard ductile connector
- UFP U-shaped flexural plate
- C Strength capacity (elastic)
- M Hardened plastic capacity
- U Work-energy capacity
- Δ Ultimate deformation capacity
- E_c Earthquake panel contact accommodation (corner panels only)
- V_u Design MDC longitudinal shearing demand
- V_0 Design MDC longitudinal shearing capacity
- P_u Design OP reaction force per panel edge
- P_0 Design connector radial mechanism strength (crushing, pulling) per edge
- $P_{P,UFP}$ UFP radial pulling plastic mechanism strength
- $P_{T,UFP}$ UFP radial pulling hardened plastic capacity
- d_{UFP} (Outer) diameter of UFPs

Notes: See previous table for load combinations
 See mechanics, design equations for design performance criteria variables

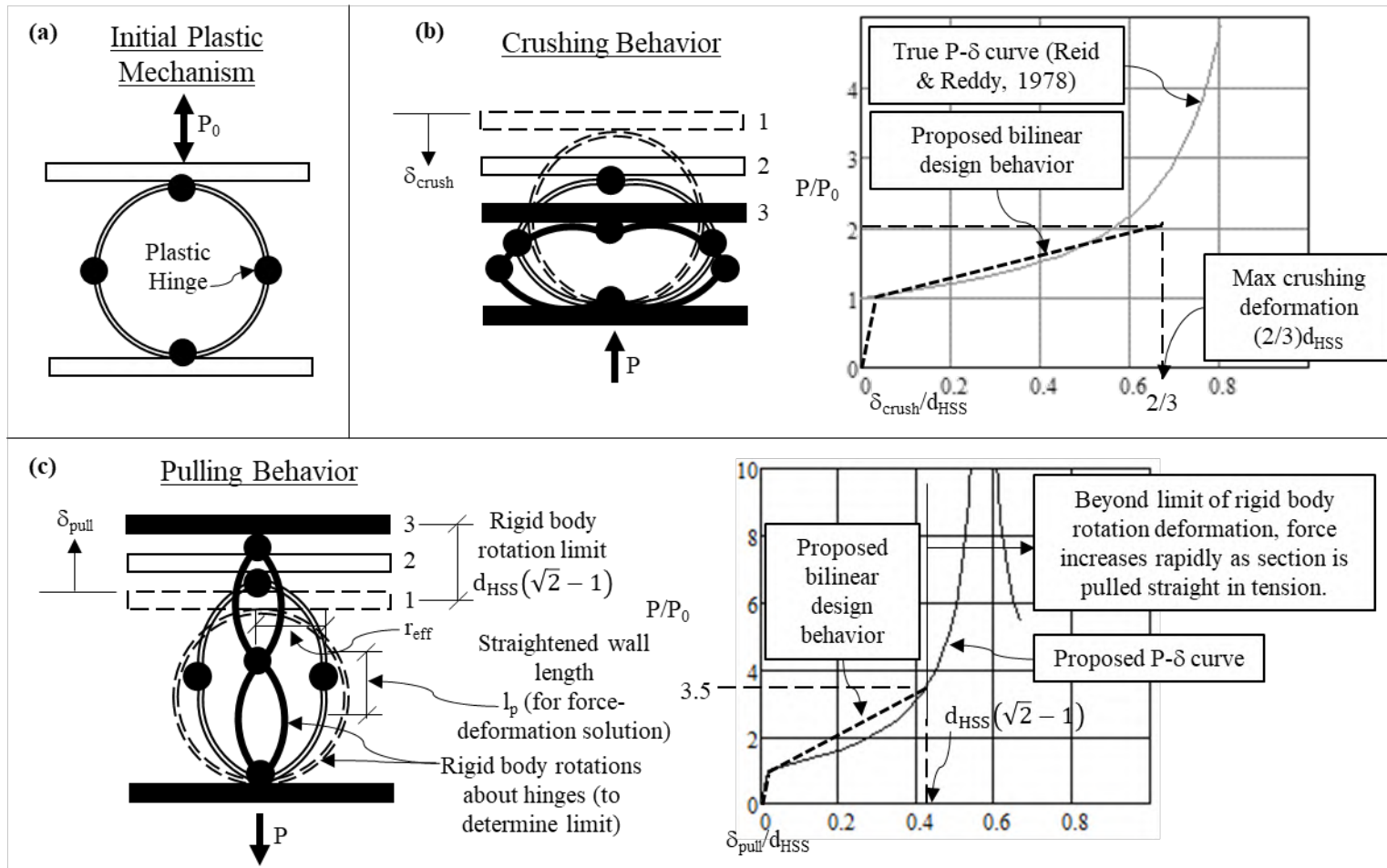


Fig. 4-1: Mechanics of Radially Deformed Round HSS (a) Initial Plastic Mechanism, (b) Crushing behavior, and (c) Pulling Behavior

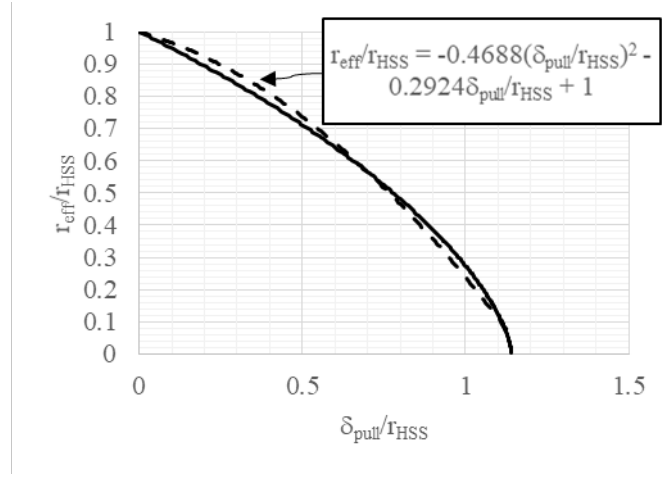


Fig. 4-2: Normalized Geometric Relationships for Large HSS Tube Pulling Deformations

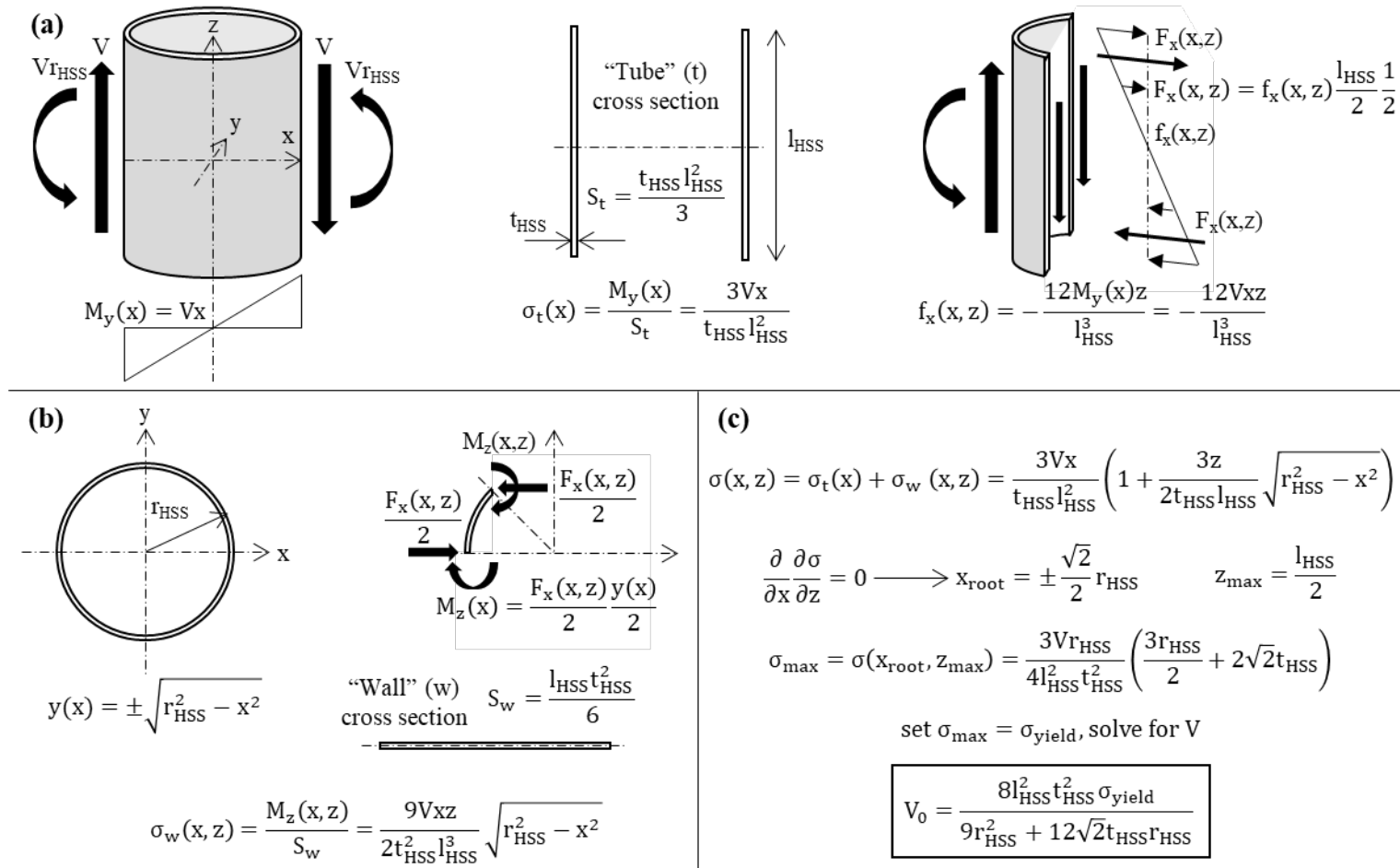


Fig. 4-3: Elastic Force Limit of Longitudinally Sheared Round HSS Considering (a) Tube Bending, (b) Wall Bending, and (c) Peak Resulting Combined Normal Stress

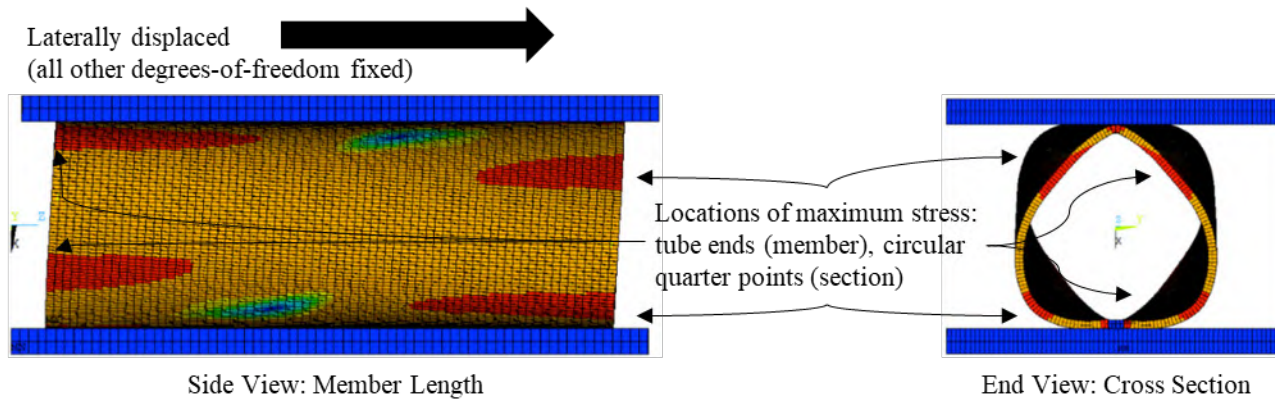
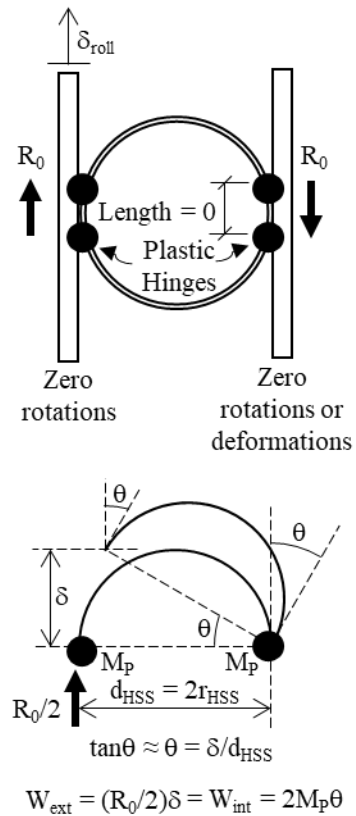
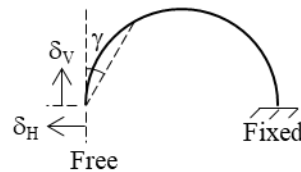


Fig. 4-4: Von Mises Stress Contour Plots for Longitudinally Sheared HSS Tube

(a) Rolling Plastic Mechanism

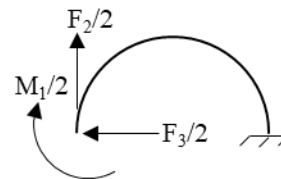


(b) Primary Structure
Circular Arch, 1/2 HSS Tube



Load Cases - Superposition

1. Moment at free end
2. Tangential force at free end
3. Radial force at free end



Note: 1/2 factors for load cases due to each half carrying 1/2 total applied demand while undergoing full deformation (δ_{roll}). The total stiffness of these two "arches" acting in parallel is twice the stiffness of each half tube.

Boundary Conditions
 $\gamma = 0, \delta_v = \delta_{roll} (\delta_H = \text{unknown})$

Note: All δ_H terms cancel when combining these load cases, i.e. $\delta_H = 0$ for elastic response.

Solution

Solve for F_2/δ_v considering superposition of load cases and prescribed boundary conditions.

$$k_{roll} = R/\delta_{roll}$$

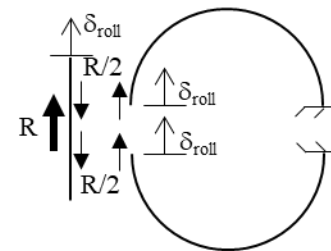


Fig. 4-5: Mechanics of Rolling Round HSS (a) Initial Plastic Mechanism and (b) Elastic Stiffness

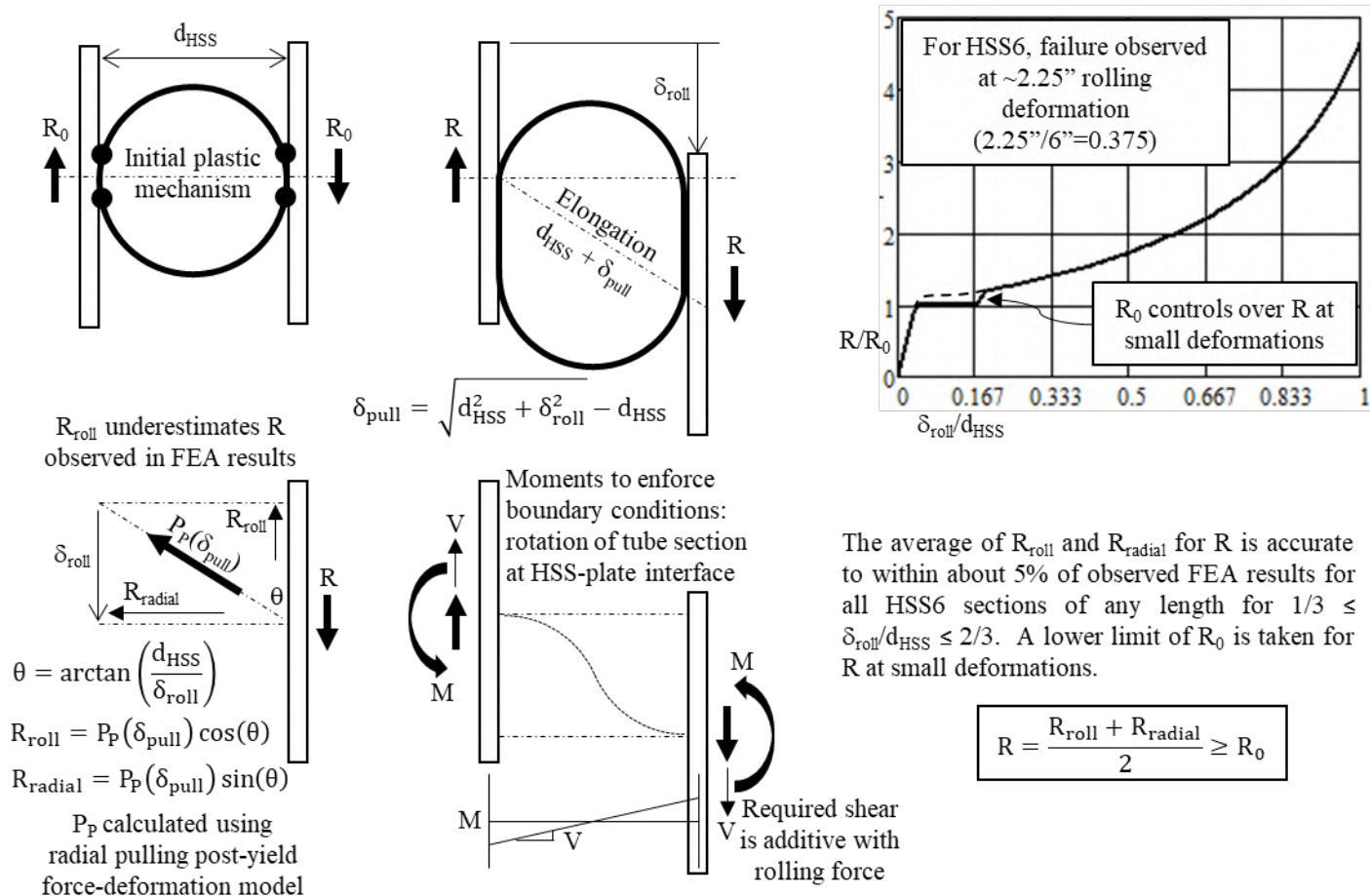


Fig. 4-6: HSS Tube Rolling Force-Deformation Model for Large Deformations

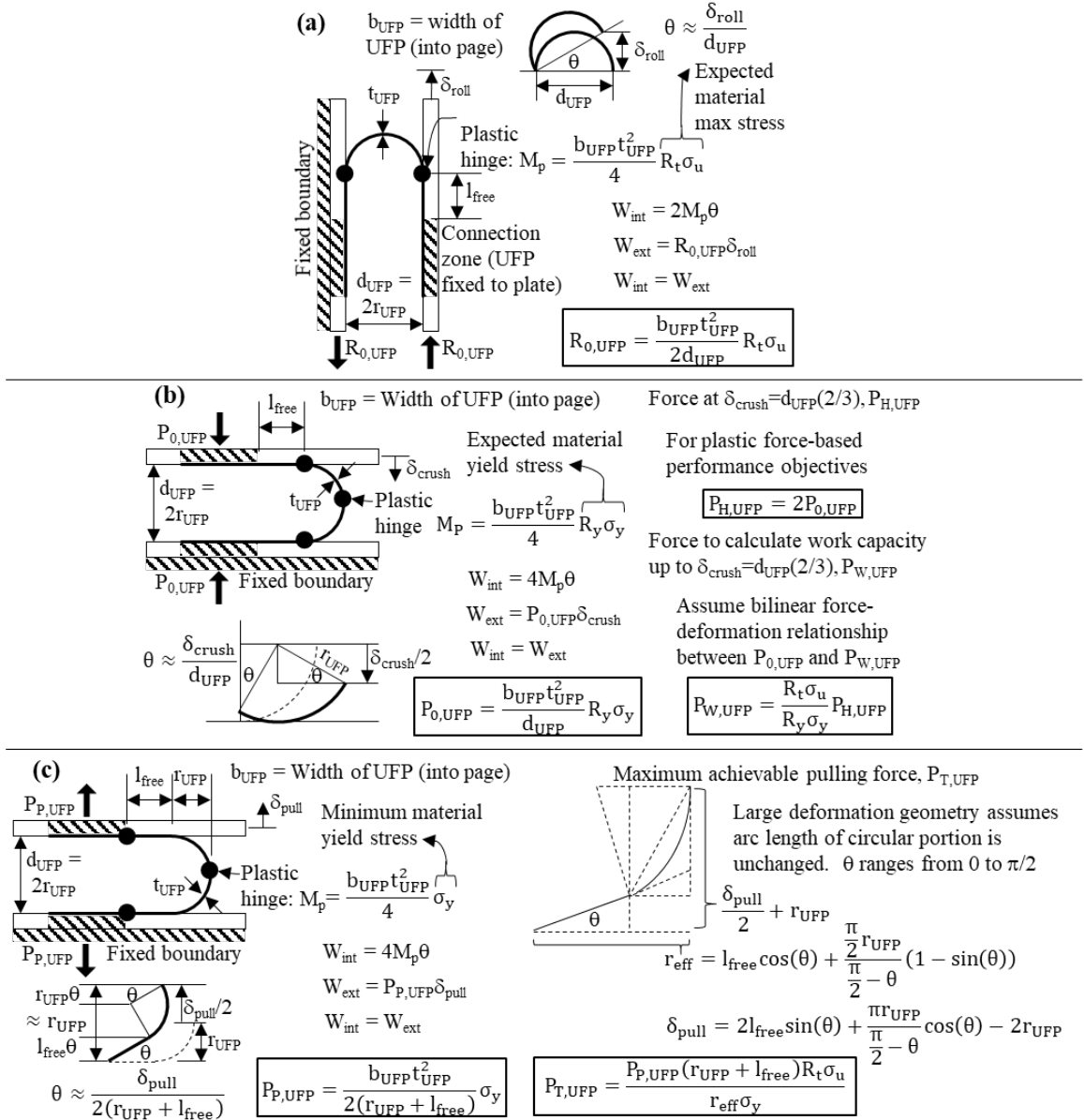


Fig. 4-7: UFP Mechanics during (a) Rolling, (b) Crushing, and (c) Pulling

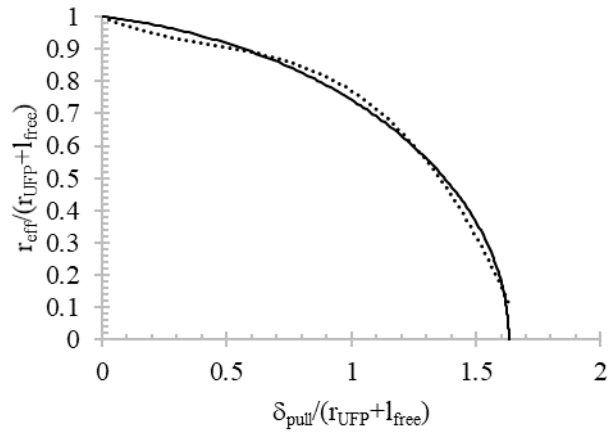


Fig. 4-8: Normalized Geometric Relationships for Large UFP Pulling Deformations

5. Design of Components to Achieve Performance Objectives

The mechanics developed in Section 4 and façade system demands established in Section 3 can be used to design the UFPs, MDCs, and façade panels to achieve all desired performance objectives in each degree-of-freedom. The design steps presented in the following subsections are summarized as follows:

1. Choose cross section geometry for MDCs and UFPs (Section 5.1)
2. Determine the total required UFP width along one panel edge (Section 5.2.1)
3. Calculate capacity design forces from large UFP deformations for use in MDC design (Section 5.2.2)
4. Determine minimum MDC-L (Section 5.3.1) and MDC-V (Section 5.3.2) HSS tube lengths
5. Determine minimum combined MDC-V and MDC-L HSS tube length required to satisfy all OP performance objectives (including impulsive demands, if considered; Sections 5.3.3 through 5.3.5). Add HSS tube length to MDC-L (and/or MDC-Vs, space-permitting) if needed for OP performance
6. Calculate the required MDC-B HSS tube length from the MDC-V, MDC-L, and UFP details to supplement UFPs in the inward OP direction and thus provide (approximately) equal panel edge support conditions (Section 5.3.6)
7. Calculate the required façade panel flexural plastic moment capacity to achieve the desired progression of damage to MHFS components (Section 5.4)

These steps can be followed in-order to produce a design with little to no iteration, provided the initial geometric assumptions for connector cross sections (MDC and UFP diameter

and thickness) are capable of achieving the required large plastic deformations. Relevant load combinations and associated connector performance criteria are given in Table 3-4 and Table 4-1, respectively.

5.1. Selection of Cross Section Geometry

Aspects of the MDC HSS tubes' and UFP's cross sections must be chosen at the outset of design. The (outer) diameter and wall thickness of HSS tubes are limited by the available sections (AISC, 2010b). UFP diameter is likely limited by the equipment available to steel fabricators to create accurate circular bends from flat plate, while thickness is limited to A36 steel plate stock (1/16" increments up to 3/8" then 1/8" increments up to 1"; AISC, 2010b). The UFP outer bend diameter and thickness should be chosen to match the HSS section as closely as possible given these limitations. The diameter of the HSS and UFPs must be approximately equal to allow each panel edge to crush the connectors inwards to the same deformation, which is the assumption in the design for impulsive loading as detailed in Section 4.4.4. Choosing a UFP thickness which is approximately equal to the HSS tube thickness helps minimize the inherent differences in post-yield hardening behavior during radial crushing (Section 4.4.3, Equations (4-34), (4-35), and (4-36)), as well as issues related to peak plastic strain which are common to both members.

Large diameter sections can undergo more plastic crushing deformation during impulsive loading, however the larger diameter also increases the eccentricity of vertical and LIP loads assumed to act at mid-thickness of the panel veneer, which can result in excessive required HSS tube lengths. Increasing the section thickness increases the strength of all plastic mechanisms and, therefore, elastic potential and plastic work-energies, resulting in less total required HSS tube length and UFP width. Although this

may appear advantageous for design, the wall thickness-to-diameter ratio controls the maximum plastic strain at the outer fibers of the MDC and UFP plastic hinges, which can result in fracture prior to reaching the maximum crushing deformation, potentially negating any increase in plastic work-energy capacity. Additionally, shorter HSS tubes require thicker welds for a given MDC longitudinal shearing force, which can necessitate thicker MDC end plates, further increasing the eccentricity of the design-basis forces relative to the welds (i.e. thicker welds require thicker plates which increases the demand on the welds). The ideal section geometry strikes a balance between these conflicting effects.

For a thirteen-foot (high) by thirty-foot (wide) six-inch thick normal weight reinforced concrete panel (the prototype panel for much of the following discussion), six-inch diameter HSS sections (HSS6) have been found to be effective for MDC design; the HSS6x0.25 section in particular is an effective choice for most panel types considered in this research. This section is also useful in this application because the (nominal) wall thickness matches a common A36 steel plate thickness, which can be chosen for the UFPs. Experimental tests have been performed on MDCs using this cross section, details of which are provided in Section 7. Pictures from two of these tests are provided in Fig. 5-1. Fig. 5-1a shows a test which simulated blast response of an MDC-V connector by applying inward crushing deformation to the target maximum followed by rotation (to simulate the panel's inward deflection) and then rebound back to the original position, all while supporting the tributary dead load from the prototype reinforced concrete panel via longitudinal shearing of the HSS tube. Successful completion of this testing protocol indicates that the HSS6x0.25 is capable of undergoing large inward plastic crushing deformations while maintaining vertical load-carrying capacity. Fig. 5-1b shows a radial

pulling test performed on a similar HSS6x0.25 design, which showed significant ductility and strength, as well as confirmation of both theoretical and analytical modeling of this deformation mode. Note that the yield deformation of the plates apparent in these pictures was by design as part of an earlier MHFS configuration and MDC design approach, which accommodated corner panel contact through combined MDC pulling, and plate yield deformations (see Appendix B, configuration 1).

The final aspect of the cross sectional geometry which must be chosen at the onset of design is the so-called “free” length, l_{free} , of the UFP section which indicates the length of flat plate between the bent and connected regions as shown in Fig. 4-7 and discussed in Section 4.3.1. It is recommended to choose a free length equal to the maximum (nominal) inter-story drift expected under design-basis earthquake (DBE) loading, and ensuring the UFP diameter is large enough to allow for additional rolling deformations for larger drifts under maximum-considered earthquake (MCE) loading. For a 13-foot story height building with maximum DBE drift of 2.5% and 6” diameter UFPs (and HSS tubes), a free length of 4” will adequately accommodate both DBE $((156'')(0.025) = 3.9'')$ and MCE $((1.5)(3.9'') = 5.85'' < 4'' + (3/8)(6''))$ story drifts. It is not recommended to significantly oversize the free length because doing so reduces the radial pulling mechanism strength, which generally controls the total UFP width along one panel edge, B_{UFP} , in design.

5.2. U-Shaped Flexural Plates (UFPs)

U-shaped flexural plates (UFPs) are included in the proposed design methodology for the primary purpose of accommodating in-plane seismic drifts through ductile, force-limited deformations in these connectors. The efficacy of these components for this type of application is well established (Baird, 2014), however their utility has traditionally been

limited to single-axis rolling deformations while supplementary load paths handle demands in all other degrees-of-freedom. This application seeks to expand the functionality of UFPs to include both elastic and plastic radial crushing and pulling behaviors which provide force, deformation, and work-energy capabilities that enhance the resilience of traditional façade systems while also remaining practical for installation purposes (Table 4-1). UFPs can be designed to provide OP support similar to traditional façade connectors and the proposed MDCs through radial loading of the cross section (Fig. 4-7), while the connections to the structural frame and/or façade panel can include slotted or oversized bolt holes to allow for thermal/moisture panel expansion/contraction, erection tolerances, and on-site adjustment during installation.

5.2.1. Total Width of UFPs along Panel Edge

The mechanics of UFPs in the relevant degrees-of-freedom which were developed in Section 4.3 are used to determine the total required width of UFPs along one panel edge, B_{UFP} , as shown in Fig. 3-1. There are no minimum strength requirements for UFPs in the rolling degree-of-freedom (panel's LIP degree-of-freedom). As discussed in Section 4.3.3, the radial pulling plastic mechanism is always weaker than the crushing mechanism for a nonzero l_{free} (Equations (4-17) and (4-19)), therefore the pulling mechanism strength is used to determine the B_{UFP} based on the reaction force per panel edge, P , and desired connector performance under the various non-impulsive OP panel demands. These demands and performance objectives—organized in Table 4-1—include elastic resistance of seismic panel inertia and design-basis wind demands, and plastic response during tornado wind and suction. The wind/tornado/suction demands can be calculated as an equivalent uniformly distributed pressure as described in Section 3.2.4 (p term in Equation

(4-1)), while the reaction force per panel edge (P term in Equation (4-1)) for panel seismic inertia can be calculated as described in Section 3.2.3 knowing the building's design short-period spectral acceleration (S_{DS}), the weight of the façade panel (Equation (3-2)), the connector dynamic amplification and response modification factors (a_p , R_p), and the elevation of the panel relative to the total building height (z/h).

The required UFP width along one panel edge for all non-impulsive OP demands with an elastic connector performance objective can be calculated by rearranging the terms in Equation (4-17) to solve for B_{UFP} :

$$B_{UFP-E} = \frac{pbh(r_{UFP} + l_{free})}{\sigma_y t_{UFP}^2} = \frac{wh(r_{UFP} + l_{free})}{\sigma_y t_{UFP}^2} = \frac{2P(r_{UFP} + l_{free})}{\sigma_y t_{UFP}^2} \quad (5-1)$$

where all terms have been previously defined. The three forms of this expression shown here can be used interchangeably depending on preference; the pressure and distributed load forms are generally more useful for wind/tornado/suction calculations, while the edge reaction force is more useful for the design seismic inertia force. Non-impulsive OP demands with a plastic connector performance objective can be calculated by modifying Equation (5-1) to account for the post-yield hardening behavior during radial UFP pulling:

$$B_{UFP-P} = \frac{pbh r_{eff}}{R_t \sigma_u t_{UFP}^2} = \frac{wh r_{eff}}{R_t \sigma_u t_{UFP}^2} = \frac{2Pr_{eff}}{R_t \sigma_u t_{UFP}^2} \quad (5-2)$$

where r_{eff} is the post-yield UFP pulling moment arm between plastic hinges (Equation (4-20)) and all other terms have been previously defined. Note that r_{eff} is dependent on pulling deformation, δ_{pull} , as described in Section 4.3.3 (Equations (4-20) through (4-22)). An assumption for δ_{pull} can be made when solving Equation (5-2) however this value should be no greater than, say, $\delta_{pull} = 0.175l_{free}$ (limits hinge rotation, θ , to about ten degrees; Fig. 4-7c) to avoid relying on a maximum pulling force which cannot realistically be achieved.

Although the ultimate material stress and expected overstrength (relative to minimum) factor are not typically used to determine minimum strength values for design, they are perhaps appropriate in this context to account for the expected material hardening at large deformations which has been observed in FEA results (Section 8). The minimum nominal yield stress can instead be used to achieve a more conservative design considering this action.

Considering the prototype reinforced concrete façade panel described in Section 5.1 and A36 steel UFPs with $t_{UFP} = 0.25''$ and $l_{free} = 4''$, the variables involved in determining B_{UFP} can be reduced to (1) uniform wind/tornado/suction pressures acting on the panel (with associated performance objectives), (2) building design short-period spectral acceleration, S_{DS} (with elastic performance objective), and (3) elevation of the panel as a fraction of total building height. This reduction of unknowns allows solutions for B_{UFP} (Equations (5-1) and (5-2)) to be depicted graphically in a manner which provides some insight into how the remaining variables affect the UFP design; a set of plots for determining B_{UFP} as a function of the remaining unknowns is provided in Fig. 5-2. In this figure, the top plots (a, b) are for a panel located at the top of a building (affects seismic inertia forces), while the bottom plots (c, d) are for a panel at ground elevation. B_{UFP} values can be linearly interpolated for panels located at any fractional height (z/h) using values taken for ground- ($z/h = 0$) and roof-elevation ($z/h = 1$) panels. The right-side plots (b, d) have S_{DS} as the independent variable (x-axis) with different curves representing a uniform panel pressure (for wind/tornado/suction), while the left-side plots (a, c) reverse these variables to show the uniform panel pressure on the x-axis with curves plotted for various S_{DS} values. Note that the left- and right-side plots for the same elevation depict the same

solutions for B_{UFP} depicted from different perspectives (seismic or wind demands along the x-axis). This plot format is also used to examine various MDC HSS tube design lengths in a similar fashion.

The B_{UFP} solutions shown in Fig. 5-2 are tabulated in Table 5-1 and Table 5-2 for ground- and roof-elevation panels, respectively. These tables also indicate where seismic and uniform pressure demands control B_{UFP} . Note that the UFP designs for different uniform pressure performance objectives—elastic response for design-basis wind, plastic response for tornado wind and suction—can be accounted for in these tables and figure by dividing the calculated uniform pressure by the ratio of large-deformation pulling force to initial mechanism strength. For the prototype UFPs ($d_{UFP} = 6''$, $t_{UFP} = 0.25''$, $l_{free} = 4''$), this ratio can be taken as equal to two based on the post-yield pulling force-deformation model developed in Section 4.3.3 (Equations (4-19) and (4-23)). With this hardening ratio, a tornado suction force calculated as, say, 160 psf of uniform pressure can be looked up in the design aid plots and tables as 80 psf with the understanding that the UFP will develop its maximum pulling force with the full 160 psf of suction applied to the panel.

5.2.2. Maximum UFP Forces for Connection Detailing and MDC Capacity Design

Once the total UFP width has been determined, the maximum expected rolling and radial pulling forces must be calculated to provide capacity-design forces for the MDCs. The maximum rolling force occurs during peak in-plane seismic story drift. This force—given by Equation (4-15)—acts in the LIP direction along the panel edge which contains UFPs; a free body diagram of this load state is shown in Fig. 3-3. For UFPs located along the bottom edge of a panel (recommended for reasons yet to be detailed in this text), the rolling force they apply on the panel opposes the direction of story drift, while UFPs along the top

panel edge apply a rolling force to the panel in the same direction as story drift. The relative LIP displacement between the panel and spandrel beam along the UFP edge is what causes contact with the adjacent out-of-plane panel (for corner panels only) as discussed in Section 3.2.3.3 and illustrated in Fig. 3-4.

Corner panel contact will always initiate along the UFP edge, and adjacent corner panels must have UFPs located along the same panel edge to allow for accommodation of this contact through plastic deformation of the UFPs. The contact force is a compression-only force acting on the panel as shown in the panel contact free body diagrams in Fig. 3-3 (contact force acting alone) and Fig. 3-4 (contact force in combination with all other relevant forces). The magnitude of the contact force can be calculated from the UFP pulling force-deformation model developed in Section 4.3.3 (Equation (4-23)) with δ_{pull} given by the maximum expected inter-story drift for a DBE event. Any drifts larger than this maximum amount will likely engage the MDC-Vs and MDC-L in radial pulling and possibly fracture of the UFPs, however with UFPs on the bottom panel edge the panel's eccentric self-weight causes a moment which rotates the panel inwards towards the building such that the bottom edge will bear on the fractured UFPs and MDC-B thereby preventing detachment from the building. The contact force acting in the LIP direction on the in-plane panel (relative to the predominant direction of story drift) is always additive with the UFP rolling force regardless of which panel edge contains the UFPs. This same contact force must be considered for the out-of-plane panel in that panel's (outward) OP direction. Both panels at a given building corner should be designed considering (2) separate contact scenario load cases where each panel assumes the role of in-plane and out-of-plane panel relative to the predominant direction of story drift.

The entirety of the maximum UFP rolling force and LIP contact force (for corner panels) is resisted by the MDC-L located along the opposite panel edge, and the moment arm between these forces requires an opposing force-couple from the MDC-Vs as shown in the free body diagrams in Fig. 3-3 and Fig. 3-4. The design LIP force on the panel due to large plastic deformations of the UFPs is given by:

$$F_{LIP-\Delta UFP} = R_{0,UFP} + P_{T,UFP} \quad (5-3)$$

where $R_{0,UFP}$ is the maximum expected rolling force considering the total width of UFPs along one panel edge, B_{UFP} , given by Equation (4-15), and $P_{T,UFP}$ is the large-deformation UFP radial pulling force with δ_{pull} equal to the maximum expected story drift under a DBE event (Equations (4-20) through (4-23)). The $P_{T,UFP}$ term in Equation (5-3) can be taken as zero for panels, which are not located at a building corner. The design vertical force per MDC-V due to the UFPs is given by:

$$F_{V-\Delta UFP} = \frac{h}{b} F_{LIP-\Delta UFP} \quad (5-4)$$

where $F_{LIP-\Delta UFP}$ is the lateral in-plane force on the panel due to large plastic deformations of the UFPs (Equation (5-3)), and all other terms have been previously defined. This expression assumes moment arms for the LIP and V forces in the contact mechanism panel free body diagram (Fig. 3-3) have moment arms equal to the entire panel height (h) and width (b), respectively, which can be modified based on the final geometry of the connectors if a more precise force is desired for a final design check.

5.2.3. Connection Detailing Considerations

Connecting UFPs to the structural frame and façade panel can be accomplished in a number of ways provided the load path has sufficient strength to transfer the maximum forces and

moments expected during large UFP deformations. The total UFP width (B_{UFP}) determined in Section 5.2.1 must be evenly divided amongst at least two UFPs and spaced equally along the width of the chosen UFP panel edge (Fig. 3-1). More than two UFPs can be used if B_{UFP} is large. Both bolted and welded UFP-to-boundary plate connections have been used in past applications (Baird, 2014). Boundary plates must extend beyond the UFPs “free” length by at least an additional l_{free} distance to provide the contact conditions necessary to maintain the desired large deformation rolling behavior (traveling plastic hinges as described in Section 4.3.1) up to the design maximum story drift. All other boundary plate dimensions are controlled by the UFP dimensions and connection strength requirements. It is highly recommended to use bolted connections somewhere along the load path (most likely for the connection to the structural frame) so that slotted or oversized bolt holes can be included which allow for panel expansion/contraction, building erection tolerances, and on-site adjustment. Any connection allowance for vertical and LIP movements are permitted as the UFPs do not have any minimum force capacity design requirements in these degrees of freedom, however these releases must not lessen the strength of the connection in the OP direction.

An illustration of a potential UFP connection detail is shown in Fig. 5-15a for UFPs located along the bottom edge of the façade panel. As shown in Fig. 3-2, the panel edge with UFPs will generally not overlap vertically with the adjacent spandrel beam, therefore an angled connection to the top flange of this beam is recommended. This angled member can be a hot rolled angle section if the width of individual UFPs, b_{UFP} , is small enough to fit within the available angle sizes, or an assembly of welded plates can be used to create an angle of any size. For fabrication and installation purposes considering reinforced

concrete façade panels, it may be convenient to use a welded connection to attach the UFP to a plate embedded within the panel, which can then be bolted to the angle connector installed on the spandrel beam. Stiffener plates are recommended as shown in Fig. 5-15a to prevent excessive bending of the angle and potential failure of the connection during OP loading. The critical locations for these stiffeners are around (and possibly within, space permitting) the UFP-to-angle connection region and the free-to-curved boundary of the UFP section because this is the point of bearing during OP (radial UFP crushing) loading of the panel (Fig. 4-7b).

5.2.3.1. Design Force Eccentricities

The UFP-to-boundary plate connections must be designed for the eccentricity of the applied design forces in addition to their magnitudes. There are two critical cases to consider separately: (1) radial pulling of the UFP, and (2) UFP rolling. The eccentricities of these forces can be determined from the UFP cross section as shown in Fig. 4-7. During radial pulling, the maximum force, $P_{T,UFP}$ (Equation (4-23)), can be conservatively assumed to act at a perpendicular distance equal to $l_{free} + r_{UFP}$ relative to the connection zone (assumes maximum pulling force occurs with zero deformation of the section which reduces this moment arm. The full moment arm can preliminarily be assumed to equal, say, $l_{free} + d_{UFP}$ to include an approximation of the distance between the start of the connection zone and its center of resistance. For UFP rolling, the maximum force, $R_{0,UFP}$ (Equation (4-15) considering only the width of individual UFPs, b_{UFP}) acts at a perpendicular distance equal to the outer diameter of the UFP bend, d_{UFP} , therefore this is taken as the design eccentricity of this force.

5.2.3.2. Bolted UFP-to-Plate Connections

Using bolts to connect a UFP to a boundary plate generally results in a smaller connection region overall compared to welds. Bolted connections can also be used to release one or more degrees of freedom via the use of large oversized or slotted holes. A minimum of two bolts are recommended to allow for the formation of a force-couple in the UFP cross section plane to resist the eccentric pulling force described in the previous subsection. UFPs in past applications have generally been smaller in terms of b_{UFP} than those proposed for this application due to the addition of minimum strength requirements in the radial pulling direction. These wider UFPs (with b_{UFP} greater than, say, six inches) should use two rows of bolts, which span along the width of the member and include a minimum of two bolts each (minimum of four bolts total in a rectangular pattern). Design of these bolts for strength should include combined shear and tension stresses, with additional tension due to the eccentric radial pulling force and bolt prying action. Bolts should be placed such that the holes are completely outside of the free length region, while also adhering to all bolt hole center-to-center and center-to-edge spacing requirements (AISC, 2010b).

5.2.3.3. Welded UFP-to-Plate Connections

A fillet welded UFP-to-plate connection consists of three weld lengths: one length along the UFP width (b_{UFP}) at the end of the connection zone, and two parallel lengths in the cross sectional plane at either end of the UFP, which terminate at the start of the free length region. All relevant load cases should be checked to determine the controlling weld thickness and lengths, however the maximum radial pulling force has been found to control UFP weld designs in part because of the bending stress due to the eccentricity of the force.

The elastic method is recommended to determine adequate weld lengths and thicknesses, which can adequately carry the required loads (AISC, 2010b). For a given weld thickness and known b_{UFP} , the centroid of this weld group can be calculated as a function of the in-plane weld length. The peak weld stress due to bending can be calculated using the design force and eccentricity (detailed in Section 5.2.3.1), the maximum distance from the weld group's centroid, and the weld group's moment of inertia, all of which can also be calculated as a function of the in-plane weld length. This peak stress is additive with the (uniform) stress caused by the pulling force. The required in-plane weld length can be determined by setting the resulting maximum stress expression equal to the (factored) allowable weld material stress and solving for the unknown length.

5.3. Multi-Hazard Ductile Connectors (MDCs)

Three MDC subtypes are distinguished by their primary functions (Fig. 3-2); one MDC-L and two MDC-Vs are designed to elastically carry all LIP and vertical panel demands, respectively, via longitudinal shearing of their HSS tubes, and the MDC-B is designed to supplement the inward OP yield mechanism force of the UFPs along the panel edge opposite the MDC-Vs and MDC-L without engaging in any other degree-of-freedom response. The MDC-Vs and MDC-L must be located along the same panel edge (top or bottom) because these connectors fix the panel to the adjacent spandrel beam in-plane, and maintaining support reactions while also accommodating differential displacements between panel edge and spandrel beam would require a more complex connector scheme than that proposed herein. This arrangement provides a statically determinate support condition considering all panel directions, which allows for kinematic adjustment during installation to ensure the final position is within prescribed tolerances (PCI, 2000).

Each MDC includes different frame-side bolted connection details as illustrated in Fig. 3-1, which allow for erection/fabrication/adjustment tolerances, panel expansion/contraction, and release from engagement in degrees-of-freedom, which are primarily handled by other connectors (e.g. vertical release for MDC-L and LIP release for MDC-Vs). The MDC-B is not connected to the frame-side plate, therefore it only engages in inward OP resistance by bearing on this plate in the tube's radial crushing direction. The required bolt hole slot/oversize dimensions can be determined using Equation (3-1) (disregarding the joint material strain term); for a reinforced concrete panel with nominal dimensions of 13-by-30 feet, the slotted/oversized hole dimensions should be the bolt diameter $\pm 3/8^{\text{th}}$ of an inch. With an understanding of the connector arrangement and detailing requirements, completed UFP designs (Section 5.2), and a chosen MDC HSS cross section (Section 5.1), the length of HSS tube for each MDC type can be determined to provide the required strength in all panel degrees-of-freedom.

5.3.1. Lateral in-Plane Load-Carrying MDC: MDC-L

The LIP capacity-design forces from UFPs determined in Section 5.2.2 (Equation (5-3)) are additive with the design LIP seismic panel inertia force, F_{LIP-S} , detailed in Section 3.2.3 ($a_p = 1.25$, $R_p = 1.0$) to determine the total longitudinal shear design force, F_{LIP} . These demands are illustrated in the free body diagrams in Fig. 3-3 (all panels) and Fig. 3-4 (corner panel contact; corner panels only). The minimum required MDC-L HSS tube length to elastically resist these demands can then be determined by rearranging Equation (4-10):

$$l_{\text{HSS-L,min}} = \sqrt{\frac{F_{\text{LIP}}(9r_{\text{HSS}}^2 + 12\sqrt{2}t_{\text{HSS}}r_{\text{HSS}})}{8\phi_y t_{\text{HSS}}^2 \sigma_y}} \quad (5-5)$$

where F_{LIP} is the controlling LIP load combination for the entire panel, and all other terms have been previously defined. This design length may need to be increased to provide additional OP strength or work-energy capacity along this panel edge to achieve all performance objectives (Table 4-1).

5.3.2. Vertical Load-Carrying MDCs: MDC-V

The MDC-Vs resist all vertical demands. These demands—as detailed in Section 3.3 include factored combinations of the panel’s self-weight (dead load), and all vertical forces due to seismic effects including inertia of the panel and the (additive) vertical force-couples which resist the LIP force couples as described in Sections 5.2.2 and 5.3.1 and shown in Fig. 3-3 (all panels) and Fig. 3-4 (corner panel contact; corner panels only). The controlling vertical force for design of the MDC-Vs is given by:

$$F_{\text{MDC-V}} = \max \left(\frac{1.4W_P}{2}, \frac{1.2W_P}{2} + F_{V-\Delta\text{UFP}} + \max \left(0.3 \frac{2W_P S_{\text{DS}}}{(3)(2)g} + \frac{\frac{h}{2} F_{\text{LIP-S}}}{b}, \frac{2W_P S_{\text{DS}}}{(3)(2)g} + 0.3 \frac{\frac{h}{2} F_{\text{LIP-S}}}{b} \right) \right) \quad (5-6)$$

where W_P is the total façade panel weight (Equation (3-2)), g is the acceleration due to gravity, $F_{V-\Delta\text{UFP}}$ is the vertical force required to resist the maximum expected UFP forces (Equation (5-4)), $F_{\text{LIP-S}}$ is the design-basis LIP seismic inertia force for the entire panel, and all other terms have been previously defined. The elastic longitudinal shearing force-carrying capacity given by Equation (4-10) can be rearranged to solve for the required MDC-V HSS tube length to carry all vertical force demands:

$$l_{\text{HSS-V}} = \sqrt{\frac{F_{\text{MDC-V}}(9r_{\text{HSS}}^2 + 12\sqrt{2}t_{\text{HSS}}r_{\text{HSS}})}{8\phi_y t_{\text{HSS}}^2 \sigma_y}} \quad (5-7)$$

where $F_{\text{MDC-V}}$ is the controlling vertical load combination per MDC-V (Equation (5-6)) and all other terms have been previously defined.

Results of Equation (5-7) are shown in Fig. 5-3 and tabulated in Table 5-3 (ground elevation) and Table 5-4 (roof elevation) for the HSS6x0.25 cross section considering a reinforced concrete panel. Note that $l_{\text{HSS-V}}$ is still a function of uniform pressure demands (wind/tornado/suction) despite these acting only in the OP direction because these demands can control B_{UFP} , which in turn affects $F_{\text{V-}\Delta\text{UFP}}$. Factored self-weight (load factor of 1.4) alone only controls the vertical design force (Equation (5-6)) for negligible S_{DS} and design uniform pressure values, while the combined self-weight (load factor of 1.2) and vertical seismic forces control for essentially all realistic hazard combinations. Indication of hazard combinations where seismic demands control in these tables refers to B_{UFP} controlled by OP seismic inertia (Section 5.2.1), which then contributes to the controlling term in $F_{\text{MDC-V}}$. Uniform pressure demands control B_{UFP} for all other cases.

5.3.3. Minimum Total MDC HSS Length for Non-Impulsive Demands

Out-of-plane loads impart radial demands on the MDCs. The design-basis (per ASCE 7-10) wind and OP seismic loads discussed in Section 3 can be combined with the reaction force per panel edge (Equation (4-1)) and radial HSS mechanics described in Section 4.2.1 to determine the total required HSS tube length per panel edge to elastically resist these demands:

$$l_{\text{Edge-E}} = \frac{pbhr_{\text{HSS}}}{2\sigma_y t_{\text{HSS}}^2} = \frac{whr_{\text{HSS}}}{2\sigma_y t_{\text{HSS}}^2} = \frac{Pr_{\text{HSS}}}{\sigma_y t_{\text{HSS}}^2} \quad (5-8)$$

where all terms have been previously defined. The total HSS tube length between the two MDC-Vs and one MDC-L must at least equal the value given by Equation (5-8) to satisfy the elastic connector performance objectives for non-impulsive OP loading (Table 4-1). This equation can be modified to determine the required total HSS tube length per panel edge for non-impulsive OP demands with plastic connector performance objectives:

$$l_{\text{Edge-P}} = \frac{p_y bhr_{\text{HSS}}}{4\sigma_y t_{\text{HSS}}^2} = \frac{w_y hr_{\text{HSS}}}{4\sigma_y t_{\text{HSS}}^2} = \frac{P_y r_{\text{HSS}}}{2\sigma_y t_{\text{HSS}}^2} \quad (5-9)$$

Where p_y , w_y , and P_y are a uniform pressure, distributed (along the panel's height) load, and panel edge reaction force, respectively, with yielding connectors as the performance objective, and all terms have been previously defined. This expression is identical to the previous one with an additional factor of two in the denominator which is taken as the maximum desired post-yield strength hardening factor (relative to the initial mechanism strength, P_0 , given by Equation (4-2)). This hardening factor can be achieved considering all HSS sections considering either radial crushing (inward OP panel loading) or pulling (outward OP panel loading) action as described in Section 4.2.1.

5.3.4. Controlling MDC-L and Total HSS Length per Panel Edge for Non-Impulsive Demands

If the total MDC HSS tube length per panel edge—determined as the maximum of Equations (5-8) and (5-9) for elastic and plastic connector performance objectives for OP loading, respectively—exceeds two times the (individual) MDC-V HSS tube length (Equation (5-7)) plus the minimum MDC-L HSS tube length (Equation (5-5)), the

difference can be added to the MDC-L to ensure all performance objectives for non-impulsive demands can be achieved. This solution for l_{MDC-L} considering the prototype reinforced concrete façade panel, UFPs, and HSS sections is plotted in Fig. 5-4 with numerical values for ground- and roof-elevation panels given in Table 5-5 and Table 5-6, respectively. These solutions indicate that l_{MDC-L} only needs to be increased to satisfy non-impulsive OP performance objectives for extreme uniform pressures (100 psf for elastic performance or 200 psf for plastic). With these solutions for l_{MDC-V} and l_{MDC-L} , the total HSS tube length per panel edge, which satisfies all non-impulsive performance objectives for the prototype system, can be determined. A plot of this solution is provided in Fig. 5-5 with numerical values given in Table 5-7 and Table 5-8. These solutions are simply the addition of those presented in Fig. 5-3 (multiplied by two since there are two MDC-Vs) and Fig. 5-4 (and their corresponding tabular values). This HSS tube per panel edge is compared to that calculated to satisfy impulsive OP demand performance objectives, and any additional required HSS length can be added to the MDC-L.

5.3.5. Design for Impulsive OP Demands

Impulsive demands impart an initial velocity to the panel mass, and the kinetic energy of this dynamic system is resolved through a combination of elastic potential and plastic work energies from the deformation of both panel and connector elements as described in Section 4.4. Equating the initial kinetic energy of the dynamic system to the energy stored (elastic potential energy) and work performed (plastic work-energy) at the maximum deformation state (with zero kinetic energy) implies that the total system energy is conserved. With this assumption and the component mechanics developed in Section 4, a solution for the required strengths and relative proportions thereof for the panel and its connectors can be

determined to achieve a specified maximum deformation state for a known impulsive demand. Credible impulsive demands considered in this research include overpressure due to air-blast events (deliberate or accidental blast/explosion) and blown debris missile impact due during blast or extreme wind events. Protective design for these events can be reduced to determining the total HSS tube length required along the MDC-V and MDC-L panel edge using the mechanics developed in Section 4. Once the total HSS tube length per panel edge is finalized by comparing the controlling designs for non-impulsive and impulsive demands, the required MDC-B HSS tube length and panel flexural strength to ensure the desired progression of yielding can be determined.

5.3.5.1. Air-Blast

Design for air-blast events requires a target threat assessment to determine what credible threat(s) might exist for the building in question. These methods are detailed in publicly available United States Department of Defense (DoD) Unified Facilities Criteria (UFC) documents. Specific design charge weights and standoff distances are classified, however the discussion of these design-critical parameters in general terms provided by DoD are valuable for classifying and estimating reasonable scenarios for design. Charge weights—measured in equivalent pounds of TNT (lbsTNT)—generally fall into three categories: hand-deliverable charges are on the order of tens of lbsTNT, car-delivered charges are on the order of hundreds of lbsTNT, and truck-delivered charges can exceed 1000 lbsTNT (e.g. the truck-delivered charge used in the 1995 Oklahoma City bombing was estimated to contain about 5000 lbsTNT equivalent). The potential standoff distances change based on the delivery method as vehicle-delivered charges are generally confined to the nearest street, while hand-delivered charges can potentially be placed very close to the target

building. For a given charge weight, reducing the standoff distance focuses panel damage near the explosion with less damage distributed over the entire blast-facing building front. This tendency coupled with the chosen performance objectives for various credible blast scenarios may result in different blast scenarios controlling the design of panels at different locations (vertical and lateral) on the blast-facing building front. The controlling blast scenario for a given panel can be determined by calculating the total impulse imparted onto the panel (as described in Section 3.2.5) and calculating the required panel edge strength based on the simplified dynamic system detailed in Section 4.4 with terms in Equation (4-38) included based on the chosen performance objective.

The solution of Equation (4-38) for various HSS6 sections and façade panel types are provided in Fig. 5-7 through Fig. 5-10. The properties of the façade panel systems, other than the reinforced concrete panel, are adapted from Salim *et al.* (2005) and Idriss *et al.* (2016). These solutions provide designs for various performance objectives as a function of the design impulse value. Equation (4-38) includes work-energy terms for both MDCs and the façade panel; however, these terms are omitted when an elastic performance objective is specified for that component. Various OP wind and seismic (elastic performance) design values are provided on these plots for comparison. For any design where the total required HSS length per panel edge to satisfy impulsive performance objectives is greater than that determined for non-impulsive demands (Section 5.3.4), the MDC-L HSS tube length can be increased (and MDC-B HSS tube length along the UFP edge), otherwise the HSS length per panel edge for non-impulsive demands controls, and sufficient protection against impulsive loading is inherited from this design.

5.3.5.2. Impact

During impact, the impulse is only applied to a portion of the system mass (which is weighted towards the impact location with the addition of the missile's mass) which induces large localized demands on the panel, often before significant deformations at the connectors can develop thereby precluding their ability to protect the panel from damage through capacity design for a desired progression of member yielding. Preliminary study of the impact missile problem suggests that, while the ductility afforded by the MDC and UFP connectors at the panel edges does help reduce panel demands after first mode dynamic response becomes the predominant system behavior, the peak panel demands occur prior to this stage and are generally controlled by the panel characteristics (mass and moment capacity). The behavior of the system during this initial phase is complex and can change significantly as a function of the panel's mass, stiffness, and strength, as well as the missile mass, initial velocity, and impact area. Therefore, it is recommended to examine impact response via finite element analysis (FEA) after an MDC, UFP, and panel design, which satisfies all other desired criteria, is proposed. If this design performs inadequately when subjected to impact, the panel's flexural strength can be increased (to an extent) without detrimental effects on the system's performance considering other hazards until the desired impact performance is achieved.

5.3.6. OP Bearing-Only MDC: MDC-B

The MDC-B is located along the same panel edge as the UFPs with its HSS tube's longitudinal axis aligned with the panel's LIP axis (Fig. 3-1). As described in Section 4.4, the MDC-B HSS tube length is calculated to supplement the UFPs during inward OP

loading of the panel to ensure simultaneous yielding of the connectors along both (top and bottom) panel edges. The radial crushing mechanics for UFPs and MDCs developed in Section 4 indicate that the initial plastic mechanism strengths for these connectors differ due to the differences in cross section geometry and material properties. The required MDC-B HSS tube length, l_{MDC-B} , can be determined using the controlling UFP, MDC-V, and MDC-L designs and comparing the initial collapse mechanism strength for all connectors along each edge. Solving this expression for l_{MDC-B} gives:

$$l_{MDC-B} = \left(\frac{R_{yHSS} \sigma_{yHSS} t_{HSS}^2}{r_{HSS}} (2l_{MDC-V} + l_{MDC-L}) - \frac{R_{yP} \sigma_{yP} t_{UFP}^2 B_{UFP}}{d_{UFP}} \right) \frac{r_{HSS}}{R_{yHSS} \sigma_{yHSS} t_{HSS}^2} \quad (5-10)$$

where R_y is the expected material overstrength factor relative to the specified minimum, σ_y , for HSS tubes (HSS) or plates (P), l_{MDC-V} and l_{MDC-L} are the lengths of HSS tube for each MDC-V and MDC-L, respectively, and all other terms have been previously defined. The solution to Equation (5-10) for various MDC-V+L HSS lengths and total UFP widths are plotted in Fig. 5-6, with numerical values given in Table 5-9. Note that the negative values in this table do not have any physical meaning and would never arise from an actual design due to the relative plastic mechanism strengths and capacity-proportioned design of the MDC-Vs and MDC-L for maximum expected UFP forces; these values are included in the table for linear interpolation of intermediate values.

5.3.7. Connection Detailing Considerations

Detailing of the MDC welds, bolts, and plates requires some assumptions and iterations to ensure a reliable connection for the myriad of load scenarios to which these connectors are

subjected. Design forces for MDC connections can be determined using the maximum achievable forces of the HSS tube in each degree-of-freedom (rolling, radial pulling, longitudinal shearing). The following guidelines pertain primarily to the MDC-Vs and MDC-L, as the MDC-B has essentially no force-based design requirements and can, therefore, be treated as simply mechanical connections with minimum specified weld and bolt dimensions. The MDC-B's interface with the frame-side plate through radial bearing during inward OP panel loading (Fig. 3-1) and should not include any HSS-to-plate welds on this side. An illustration of MDC connection details is provided in Fig. 5-11. Illustrations of potential MDC connections to the structural frame are provided in Fig. 5-13 (MDC-V), Fig. 5-14 (MDC-L), and Fig. 5-15b (MDC-B). The “staggered” panel placement referred to in these figures are for a possible panel configuration where the panels span over exterior frame columns, which may have advantages for both detailing of the MDC-L and MDC-B, as well as providing an alternative load path through the façade system for progressive collapse scenarios.

5.3.7.1. Design Force Eccentricity

The controlling V and LIP load cases must include the eccentricity of these loads. Moment demands can be calculated by multiplying the controlling force values by a conservative design eccentricity. For simplicity, the façade panel (at mid-thickness) and structural frame (at the MDC plate-to-structural frame boundary) are assumed to have equal flexural stiffness; this implies that an inflection point (point of zero moment) in the deformed shape of the frame-MDC-panel system exists halfway between the “boundaries” (panel mid-thickness and MDC plate-to-frame boundary). The design eccentricity—illustrated in Fig. 5-11—is taken as the distance between this inflection point and the MDC plate-to-frame

boundary. A conservative assumption that the MDC plates are one-inch thick can be used, and the design eccentricity, e_{des} , can be calculated as:

$$e_{des} = \frac{t}{4} + r_{HSS} + t_p \quad (5-11)$$

where t_p is the thickness of each MDC plate (preliminary assumption of one inch) and all other terms have been previously defined. The controlling vertical and LIP design forces should be multiplied by Equation (5-11) to determine the design moments for the MDCs. All combinations of the vertical/LIP, moment, and (elastic) OP demands must be considered for detailing calculations for the MDC-to-plate welds and bolted connection designs.

The proposed MDC-B detail illustrated in Fig. 5-15b applies an eccentric lateral force at mid-span of the spandrel beam during MDC-B crushing. This eccentric force applies torsion to the spandrel beam, which may exceed capacity, especially for gravity frame members with simple beam end connections (less torsional restraint). This demand may require bracing of the spandrel beam against, say, the floor slab, however this force may locally crush or otherwise damage the floor slab if the MDC-B HSS tube is particularly strong. A potential option, which would mitigate the torsional demand, would be to split the MDC-B HSS tube length in half and move both halves away from the panel center towards the UFPs at the panel corners (possibly even moving the MDC-Bs to the corners and the UFPs inwards). Moving the applied torsion away from mid-span reduces the demand on the beam, and could possibly provide a more desirable load path for torsional bracing via the out-of-plane beam framing into the adjacent column.

5.3.7.2. HSS-to-Plate Welds

The HSS-to-plate welds consist of two legs spanning the full HSS tube length which connect the outer surface of the tube to a weld bar, and two full-length weld legs connecting the weld bar (on the back-side bar surface parallel to the HSS surface tangent) to the MDC plate through its thickness. The weld size can be specified by using the elastic vector analysis method (AISC, 2010b) to calculate the required weld strength per thickness for each source of stress (load and moment), and then combining these “stresses” using a vector sum of the normal and shear components for all load cases. Once the maximum weld “stress” is determined, the weld size can be specified per AISC 360 (2010b). Note that the bar-to-plate thickness welds will have a slightly reduced effective throat due to the oversize of the MDC plate slot (similar to a standard bolt hole; slot width 1/16-inch greater than weld bar width), therefore the thickness of each weld leg should be increased by 1/16-inch to ensure adequate strength considering the minimum plane area through the weld. The required weld thickness determines the minimum dimensions of the weld bar and MDC plate thickness; as shown in Fig. 5-11, the weld bar must have a width (tangent to HSS surface) equal to at least two weld thicknesses and a depth (into the plate thickness) of at least one weld thickness, while the MDC plate thickness is at least two weld thicknesses.

The weld bar width should be increased above the minimum if a larger cross sectional area (length—equal to the full length of the HSS tube—by width) is required to develop the full strength of the welds. For ease of construction, all MDC plates should have the same thickness; therefore, the minimum MDC plate thickness is twice the maximum required MDC weld thickness. The MDC plate thickness should be no greater

than one inch (or whatever value was assumed for the design eccentricity) based on Equation (5-11). The depth (into the MDC plate thickness) of the weld bars for each MDC should be the largest nominal bar dimension increment for which the bar-to-MDC plate welds remain within the thickness of the MDC plate; this allows for easier access to the weld location during fabrication of the MDCs while maintaining a flat surface on the backside of each MDC plate. Note that a bevel along the inside edge of the MDC plate weld bar slot (Fig. 5-11) is necessary for the HSS tube to sit flush against the MDC plates, which is consistent with the boundary conditions in the round HSS crushing model (Fig. 4-1). This slot in the MDC plates should have a standard oversized width (1/16-inch greater than the weld bar width), and circular ends to allow for expansion of the weld filler material under stress and to eliminate stress concentrations in the plate due to geometric discontinuity. From the center of these circular slot-ends, the minimum bolt hole center-to-plate edge distance (AISC, 2010b) can be added to the length of the HSS tube per MDC to determine the minimum MDC plate dimension in the direction along the tube's longitudinal axis.

5.3.7.3. End Plate Dimensions and Bolted Connections

The MDC plate dimensions and bolted connection design are highly interdependent. Example illustrations of the bolts and slotted bolt holes for each MDC type and plate side are shown in Fig. 3-1. Thermal expansion/contraction slotted holes are included on the frame-side MDC-V and MDC-L plates. The oversized dimension of these holes should have a length equal to the expected expansion/contraction of the panel (+/- 3/8-inch for reinforced concrete panels) plus the bolt diameter. All bolt hole centers—including at the extreme ends of slotted/oversized holes—should be at least one tube diameter away from

the centerline of the HSS-to-plate connections to allow for access to the bolts/nuts during installation, and to prevent premature contact between the bolts/nuts and HSS tube wall during crushing as the tube flattens against the plates. The number of bolts along the longitudinal axes of HSS tubes should be determined considering the minimum bolt hole center-to-center spacing (2-2/3 to 3 times the nominal bolt diameter) and available length of MDC plate in this direction, as well as the (outward) bending capacity of the trial plate.

For plates on the panel side, the required prying stress from the bolt hole to the plate edge should also be calculated and limited (by extending the bolt-to-edge distance, if necessary) to less than the maximum compressive stress of the panel material. Regardless of which side the plate is on, the required prying force from each bolt line should be calculated to include in the bolt strength design procedure. For MDC-1s, this prying force plus the maximum OP force on the MDC should be used to size the bolts on either side of the HSS tube along with shear interaction from the controlling vertical and LIP demands, respectively. If the required bolt diameters differ from those assumed to obtain a trial plate size, the process must be repeated to ensure all plate strength and bolt spacing and strength requirements are satisfied. Finally, the bolted connections and plate should be checked for bolt bearing/tear-out, block shear, net section fracture, and gross section yield limit states to prevent premature failure along each MDC load path.

5.4. Capacity Design of Façade Panels

The required flexural strength of the façade panel is a function of the controlling support strength provided by the connectors along each panel edge in the inward OP direction (MDC HSS tube and UFP radial crushing). The target behavior of the system is for the panel to reach its maximum moment capacity when the connectors reach their maximum

crushing deformation corresponding to a force equal to twice the MDCs initial plastic mechanism strength, P_0 (Equation (4-2)). Assuming the demands on the panel approximate a uniformly distributed load, the design panel moment capacity, M_p , is given by:

$$M_p = \frac{P_0 h}{2} \quad (5-12)$$

where P_0 is the MDC strength per panel edge (Equation (4-2)) and all other terms have been previously defined. Proportioning the of the façade panel and MDCs strengths in this manner regardless of the controlling OP hazard and performance objective follows the capacity design philosophy to achieve a desired progression of damage along the load path. This approach provides a guarantee of some force-limited protection of the panel's integrity regardless of the loading type or magnitude.

5.5. Building Frame Interaction

Proportional strengthening of the façade system for high hazard events ultimately allows larger forces to propagate into the main building frame during such events. An early question raised in this research was whether this reinforcement would require proportional strengthening of the building's LFRS relative to traditional design lateral loads due to wind and seismic inertia. The resulting inter-story shear forces considering static application of, say, all connectors at their initial radial crushing mechanism strengths (Equations (4-2) and (4-17)) is on the order of—and in some cases exceeds—traditional LFRS design demands. A summary of preliminary analysis results of a light-mass braced frame office building located in Boston, MA with reinforced concrete façade panels, MDCs, and UFPs subjected to blast scenarios is provided in Table 5-10. These results suggest that, although several façade panels may develop their ultimate capacities, the spatial and temporal distribution

of these forces acting on the main structural framing results in peak story drifts, which are generally much smaller than what might be predicted considering static application of the total potential force transfer from façade-to-frame. The analysis models used in this investigation included connectors which frame directly into the main building floor mass (with rigid diaphragm constraints), and the inertia of this mass may be adequate to effectively “absorb” the brief, large forces the façade exerts on the main building frame (impulsive loading relative to the main building systems; see Equation (4-27) with large mass term).

Table 5-1: Total UFP Width Design with $t_{UFP} = 0.25$ in. for Reinforced Concrete Façade Panel (normal weight, 13'x30'x6") at Ground
Elevation

BUFP (in) w_{wind} (psf)	Design Short Period Spectral Acceleration, S_{Ds} (g)															
	0	0.1	0.2	0.3	0.4	0.5	0.6	0.7	0.8	0.9	1	1.1	1.2	1.3	1.4	1.5
0	0	2.64	5.28	7.92	10.56	13.20	15.83	18.47	21.11	23.75	26.39	29.03	31.67	34.31	36.95	39.59
10	12.13	12.13	12.13	12.13	12.13	13.20	15.83	18.47	21.11	23.75	26.39	29.03	31.67	34.31	36.95	39.59
20	24.27	24.27	24.27	24.27	24.27	24.27	24.27	24.27	24.27	24.27	26.39	29.03	31.67	34.31	36.95	39.59
30	36.40	36.40	36.40	36.40	36.40	36.40	36.40	36.40	36.40	36.40	36.40	36.40	36.40	36.40	36.95	39.59
40	48.53	48.53	48.53	48.53	48.53	48.53	48.53	48.53	48.53	48.53	48.53	48.53	48.53	48.53	48.53	48.53
50	60.67	60.67	60.67	60.67	60.67	60.67	60.67	60.67	60.67	60.67	60.67	60.67	60.67	60.67	60.67	60.67
60	72.80	72.80	72.80	72.80	72.80	72.80	72.80	72.80	72.80	72.80	72.80	72.80	72.80	72.80	72.80	72.80
70	84.93	84.93	84.93	84.93	84.93	84.93	84.93	84.93	84.93	84.93	84.93	84.93	84.93	84.93	84.93	84.93
80	97.07	97.07	97.07	97.07	97.07	97.07	97.07	97.07	97.07	97.07	97.07	97.07	97.07	97.07	97.07	97.07
90	109.20	109.20	109.20	109.20	109.20	109.20	109.20	109.20	109.20	109.20	109.20	109.20	109.20	109.20	109.20	109.20
100	121.33	121.33	121.33	121.33	121.33	121.33	121.33	121.33	121.33	121.33	121.33	121.33	121.33	121.33	121.33	121.33

Notes: Divide extreme wind demands with plastic connector performance objective by 2 (200 psf = 100 psf shown here).
Gray boxes indicate seismic demands control.

Table 5-2: Total UFP Width Design with $t_{UFP} = 0.25$ in. for Reinforced Concrete Façade Panel (normal weight, 13'x30'x6") at Roof
Elevation

BUFP (in) w_{wind} (psf)	Design Short Period Spectral Acceleration, S_{DS} (g)															
	0	0.1	0.2	0.3	0.4	0.5	0.6	0.7	0.8	0.9	1	1.1	1.2	1.3	1.4	1.5
0	0	3.02	6.03	9.05	12.07	15.09	18.10	21.12	24.14	27.16	30.17	33.19	36.21	39.22	42.24	45.26
10	12.13	12.13	12.13	12.13	12.13	15.09	18.10	21.12	24.14	27.16	30.17	33.19	36.21	39.22	42.24	45.26
20	24.27	24.27	24.27	24.27	24.27	24.27	24.27	24.27	24.27	27.16	30.17	33.19	36.21	39.22	42.24	45.26
30	36.40	36.40	36.40	36.40	36.40	36.40	36.40	36.40	36.40	36.40	36.40	36.40	36.40	39.22	42.24	45.26
40	48.53	48.53	48.53	48.53	48.53	48.53	48.53	48.53	48.53	48.53	48.53	48.53	48.53	48.53	48.53	48.53
50	60.67	60.67	60.67	60.67	60.67	60.67	60.67	60.67	60.67	60.67	60.67	60.67	60.67	60.67	60.67	60.67
60	72.80	72.80	72.80	72.80	72.80	72.80	72.80	72.80	72.80	72.80	72.80	72.80	72.80	72.80	72.80	72.80
70	84.93	84.93	84.93	84.93	84.93	84.93	84.93	84.93	84.93	84.93	84.93	84.93	84.93	84.93	84.93	84.93
80	97.07	97.07	97.07	97.07	97.07	97.07	97.07	97.07	97.07	97.07	97.07	97.07	97.07	97.07	97.07	97.07
90	109.20	109.20	109.20	109.20	109.20	109.20	109.20	109.20	109.20	109.20	109.20	109.20	109.20	109.20	109.20	109.20
100	121.33	121.33	121.33	121.33	121.33	121.33	121.33	121.33	121.33	121.33	121.33	121.33	121.33	121.33	121.33	121.33

Notes: Divide extreme wind demands with plastic connector performance objective by 2 (200 psf = 100 psf shown here).
Gray boxes indicate seismic demands control.

Table 5-3: MDC-V HSS Length Design with $t_{HSS} = 0.25$ in. for Reinforced Concrete Façade Panel (normal weight, 13'x30'x6") at
Ground Elevation

LMDC-V (in) w_{wind} (psf)	Design Short Period Spectral Acceleration, S_{Ds} (g)															
	0	0.1	0.2	0.3	0.4	0.5	0.6	0.7	0.8	0.9	1	1.1	1.2	1.3	1.4	1.5
0	8.98	8.98	9.31	9.76	10.20	10.62	11.02	11.41	11.79	12.15	12.51	12.85	13.18	13.51	13.83	14.14
10	9.27	9.54	9.80	10.06	10.31	10.62	11.02	11.41	11.79	12.15	12.51	12.85	13.18	13.51	13.83	14.14
20	10.13	10.38	10.62	10.86	11.09	11.31	11.54	11.76	11.97	12.18	12.51	12.85	13.18	13.51	13.83	14.14
30	10.92	11.15	11.38	11.60	11.82	12.03	12.24	12.45	12.65	12.85	13.05	13.24	13.43	13.62	13.83	14.14
40	11.66	11.88	12.09	12.30	12.50	12.71	12.91	13.10	13.29	13.48	13.67	13.86	14.04	14.22	14.40	14.57
50	12.36	12.56	12.76	12.96	13.16	13.35	13.54	13.72	13.91	14.09	14.27	14.45	14.62	14.80	14.97	15.14
60	13.02	13.21	13.40	13.59	13.78	13.96	14.14	14.32	14.50	14.67	14.84	15.01	15.18	15.35	15.51	15.68
70	13.64	13.83	14.01	14.19	14.37	14.55	14.72	14.89	15.06	15.23	15.40	15.56	15.72	15.89	16.04	16.20
80	14.24	14.42	14.60	14.77	14.94	15.11	15.28	15.44	15.61	15.77	15.93	16.09	16.25	16.40	16.56	16.71
90	14.82	14.99	15.16	15.33	15.49	15.65	15.82	15.98	16.13	16.29	16.45	16.60	16.75	16.90	17.05	17.20
100	15.37	15.54	15.70	15.86	16.02	16.18	16.34	16.49	16.64	16.80	16.95	17.10	17.25	17.39	17.54	17.68

Notes: Divide extreme wind demands with plastic connector performance objective by 2 (200 psf = 100 psf shown here).
 Gray boxes indicate seismic demands control.
 Bold values indicate dead load (self-weight) demands control.

Table 5-4: MDC-V HSS Length Design with $t_{HSS} = 0.25$ in. for Reinforced Concrete Façade Panel (normal weight, 13'x30'x6") at
Roof Elevation

LMDC-V (in) w_{wind} (psf)	Design Short Period Spectral Acceleration, S_{Ds} (g)															
	0	0.1	0.2	0.3	0.4	0.5	0.6	0.7	0.8	0.9	1	1.1	1.2	1.3	1.4	1.5
0	8.98	8.99	9.62	10.22	10.78	11.31	11.82	12.30	12.77	13.22	13.66	14.08	14.49	14.89	15.28	15.66
10	9.27	9.67	10.05	10.42	10.78	11.31	11.82	12.30	12.77	13.22	13.66	14.08	14.49	14.89	15.28	15.66
20	10.13	10.50	10.85	11.20	11.53	11.85	12.17	12.48	12.78	13.22	13.66	14.08	14.49	14.89	15.28	15.66
30	10.92	11.26	11.60	11.92	12.23	12.54	12.84	13.13	13.42	13.70	13.97	14.24	14.50	14.89	15.28	15.66
40	11.66	11.98	12.30	12.60	12.90	13.19	13.47	13.75	14.03	14.29	14.56	14.81	15.07	15.32	15.56	15.81
50	12.36	12.66	12.96	13.25	13.53	13.81	14.08	14.35	14.61	14.87	15.12	15.37	15.61	15.85	16.09	16.33
60	13.02	13.31	13.59	13.86	14.14	14.40	14.66	14.92	15.17	15.42	15.66	15.90	16.14	16.37	16.60	16.83
70	13.64	13.92	14.19	14.45	14.71	14.97	15.22	15.47	15.71	15.95	16.19	16.42	16.65	16.88	17.10	17.32
80	14.24	14.51	14.77	15.02	15.27	15.52	15.76	16.00	16.24	16.47	16.70	16.92	17.14	17.36	17.58	17.80
90	14.82	15.07	15.32	15.57	15.81	16.05	16.28	16.51	16.74	16.97	17.19	17.41	17.63	17.84	18.05	18.26
100	15.37	15.62	15.86	16.10	16.33	16.56	16.79	17.01	17.23	17.45	17.67	17.88	18.09	18.30	18.51	18.71

Notes: Divide extreme wind demands with plastic connector performance objective by 2 (200 psf = 100 psf shown here).
Gray boxes indicate seismic demands control.
Bold values indicate dead load (self-weight) demands control.

Table 5-5: MDC-L HSS Length Design with $t_{HSS} = 0.25$ in. for Reinforced Concrete Façade Panel (normal weight, 13'x30'x6") at
Ground Elevation

LMDC-L (in) w_{wind} (psf)	Design Short Period Spectral Acceleration, S_{Ds} (g)															
	0	0.1	0.2	0.3	0.4	0.5	0.6	0.7	0.8	0.9	1	1.1	1.2	1.3	1.4	1.5
0	0	3.76	5.32	6.52	7.52	8.41	9.22	9.95	10.64	11.29	11.90	12.48	13.03	13.56	14.08	14.57
10	6.21	6.66	7.08	7.47	7.85	8.41	9.22	9.95	10.64	11.29	11.90	12.48	13.03	13.56	14.08	14.57
20	8.78	9.11	9.42	9.72	10.01	10.29	10.57	10.84	11.10	11.36	11.90	12.48	13.03	13.56	14.08	14.57
30	10.76	11.02	11.28	11.53	11.78	12.02	12.26	12.49	12.72	12.95	13.17	13.38	13.60	13.81	14.08	14.57
40	12.42	12.65	12.88	13.10	13.32	13.53	13.74	13.95	14.16	14.36	14.56	14.76	14.95	15.14	15.33	15.52
50	13.89	14.10	14.30	14.50	14.70	14.89	15.08	15.27	15.46	15.65	15.83	16.01	16.19	16.37	16.54	16.71
60	15.22	15.40	15.59	15.77	15.95	16.13	16.31	16.49	16.66	16.83	17.00	17.17	17.34	17.50	17.67	17.83
70	16.43	16.61	16.78	16.95	17.12	17.29	17.45	17.62	17.78	17.94	18.10	18.26	18.42	18.57	18.73	18.88
80	17.57	17.73	17.89	18.05	18.21	18.37	18.53	18.68	18.84	18.99	19.14	19.29	19.44	19.59	19.73	19.88
90	18.64	18.79	18.94	19.09	19.24	19.39	19.54	19.69	19.83	19.98	20.12	20.26	20.41	20.55	20.69	20.83
100	22.16	22.27	22.39	22.51	22.63	22.76	22.89	23.02	23.16	23.29	23.43	23.58	23.72	23.87	24.02	24.18

Notes: Divide extreme wind demands with plastic connector performance objective by 2 (200 psf = 100 psf shown here).
Gray boxes indicate out-of-plane (OP) demands control.

Table 5-6: MDC-L HSS Length Design with $t_{HSS} = 0.25$ in. for Reinforced Concrete Façade Panel (normal weight, 13'x30'x6") at
Roof Elevation

LMDC-L (in) w_{wind} (psf)	Design Short Period Spectral Acceleration, S_{Ds} (g)															
	0	0.1	0.2	0.3	0.4	0.5	0.6	0.7	0.8	0.9	1	1.1	1.2	1.3	1.4	1.5
0	0	5.18	7.33	8.98	10.37	11.59	12.70	13.72	14.66	15.55	16.39	17.19	17.96	18.69	19.40	20.08
10	6.21	7.47	8.55	9.51	10.38	11.59	12.70	13.72	14.66	15.55	16.39	17.19	17.96	18.69	19.40	20.08
20	8.78	9.72	10.57	11.36	12.10	12.79	13.45	14.08	14.68	15.55	16.39	17.19	17.96	18.69	19.40	20.08
30	10.76	11.53	12.26	12.95	13.60	14.22	14.81	15.39	15.94	16.47	16.99	17.49	17.98	18.69	19.40	20.08
40	12.42	13.10	13.74	14.36	14.95	15.52	16.06	16.59	17.11	17.60	18.09	18.56	19.02	19.47	19.91	20.34
50	13.89	14.50	15.08	15.65	16.19	16.71	17.22	17.72	18.20	18.67	19.12	19.57	20.01	20.44	20.85	21.26
60	15.22	15.77	16.31	16.83	17.34	17.83	18.31	18.77	19.23	19.67	20.11	20.53	20.95	21.36	21.76	22.15
70	16.43	16.95	17.45	17.94	18.42	18.88	19.33	19.78	20.21	20.63	21.05	21.45	21.85	22.24	22.63	23.01
80	17.57	18.05	18.53	18.99	19.44	19.88	20.31	20.73	21.14	21.55	21.94	22.33	22.72	23.09	23.47	23.83
90	18.64	19.09	19.54	19.98	20.41	20.83	21.24	21.64	22.03	22.42	22.81	23.18	23.55	23.92	24.27	24.63
100	22.16	22.17	22.20	22.23	22.27	22.31	22.36	22.51	22.89	23.27	23.64	24.00	24.36	24.71	25.06	25.40

Notes: Divide extreme wind demands with plastic connector performance objective by 2 (200 psf = 100 psf shown here).
Gray boxes indicate out-of-plane (OP) demands control.

Table 5-7: Total MDC-V+L HSS Length Design with $t_{HSS} = 0.25$ in. for Reinforced Concrete Façade Panel (normal weight, 13'x30'x6") at Ground Elevation

LMDC-Edge (in) w_{wind} (psf)	Design Short Period Spectral Acceleration, S_{DS} (g)															
	0	0.1	0.2	0.3	0.4	0.5	0.6	0.7	0.8	0.9	1	1.1	1.2	1.3	1.4	1.5
0	17.96	21.72	23.93	26.04	27.92	29.65	31.26	32.78	34.22	35.59	36.91	38.18	39.40	40.59	41.74	42.86
10	24.74	25.73	26.68	27.59	28.46	29.65	31.26	32.78	34.22	35.59	36.91	38.18	39.40	40.59	41.74	42.86
20	29.04	29.86	30.65	31.43	32.19	32.92	33.65	34.35	35.04	35.72	36.91	38.18	39.40	40.59	41.74	42.86
30	32.60	33.33	34.04	34.73	35.42	36.09	36.74	37.39	38.02	38.64	39.26	39.86	40.46	41.04	41.74	42.86
40	35.75	36.41	37.06	37.70	38.33	38.95	39.56	40.15	40.75	41.33	41.90	42.47	43.03	43.58	44.12	44.66
50	38.61	39.22	39.83	40.42	41.01	41.59	42.16	42.72	43.28	43.83	44.37	44.90	45.43	45.96	46.47	46.98
60	41.25	41.83	42.40	42.96	43.51	44.06	44.60	45.13	45.66	46.18	46.69	47.20	47.71	48.20	48.70	49.19
70	43.72	44.27	44.81	45.34	45.86	46.38	46.90	47.40	47.91	48.40	48.90	49.38	49.87	50.34	50.82	51.29
80	46.06	46.58	47.09	47.60	48.10	48.59	49.08	49.57	50.05	50.53	51.00	51.47	51.93	52.39	52.85	53.30
90	48.27	48.77	49.26	49.75	50.23	50.70	51.17	51.64	52.10	52.56	53.02	53.47	53.91	54.36	54.80	55.23
100	52.90	53.35	53.79	54.23	54.67	55.12	55.56	56.00	56.44	56.89	57.33	57.77	58.22	58.66	59.10	59.54

Notes: Divide extreme wind demands with plastic connector performance objective by 2 (200 psf = 100 psf shown here).

Table 5-8: Total MDC-V+L HSS Length Design with $t_{HSS} = 0.25$ in. for Reinforced Concrete Façade Panel (normal weight, 13'x30'x6") at Roof Elevation

LMDC-Edge (in) w_{wind} (psf)	Design Short Period Spectral Acceleration, S_{DS} (g)															
	0	0.1	0.2	0.3	0.4	0.5	0.6	0.7	0.8	0.9	1	1.1	1.2	1.3	1.4	1.5
0	17.96	23.17	26.58	29.41	31.92	34.21	36.33	38.32	40.20	42.00	43.71	45.36	46.95	48.48	49.96	51.40
10	24.74	26.81	28.66	30.35	31.94	34.21	36.33	38.32	40.20	42.00	43.71	45.36	46.95	48.48	49.96	51.40
20	29.04	30.71	32.27	33.75	35.15	36.50	37.79	39.03	40.23	42.00	43.71	45.36	46.95	48.48	49.96	51.40
30	32.60	34.06	35.45	36.78	38.06	39.30	40.49	41.65	42.77	43.86	44.93	45.97	46.98	48.48	49.96	51.40
40	35.75	37.07	38.34	39.56	40.75	41.89	43.01	44.10	45.16	46.19	47.20	48.19	49.16	50.10	51.03	51.95
50	38.61	39.82	41.00	42.14	43.25	44.33	45.38	46.41	47.42	48.40	49.36	50.31	51.23	52.14	53.04	53.92
60	41.25	42.38	43.49	44.56	45.61	46.63	47.63	48.61	49.57	50.51	51.43	52.34	53.23	54.10	54.97	55.81
70	43.72	44.79	45.83	46.85	47.85	48.82	49.78	50.71	51.63	52.53	53.42	54.29	55.15	56.00	56.83	57.65
80	46.06	47.07	48.06	49.03	49.98	50.91	51.83	52.73	53.61	54.48	55.34	56.18	57.01	57.82	58.63	59.42
90	48.27	49.24	50.19	51.11	52.03	52.92	53.80	54.67	55.52	56.36	57.18	58.00	58.80	59.59	60.38	61.15
100	52.90	53.41	53.92	54.42	54.93	55.43	55.94	56.54	57.36	58.17	58.97	59.76	60.54	61.31	62.07	62.82

Notes: Divide extreme wind demands with plastic connector performance objective by 2 (200 psf = 100 psf shown here).

Table 5-9: MDC-B HSS Length Design with $t_{HSS} = 0.25$ in. for Reinforced Concrete Façade Panel (normal weight, 13'x30'x6")

LMDC-B (in) BUFP (in)	Total MDC-V and MDC-L HSS Tube Length, LMDC-Edge (in)												
	0	10	20	30	40	50	60	70	80	90	100	110	120
0	0	10.00	20.00	30.00	40.00	50.00	60.00	70.00	80.00	90.00	100.00	110.00	120.00
10	-3.63	6.37	16.37	26.37	36.37	46.37	56.37	66.37	76.37	86.37	96.37	106.37	116.37
20	-7.27	2.73	12.73	22.73	32.73	42.73	52.73	62.73	72.73	82.73	92.73	102.73	112.73
30	-10.90	-0.90	9.10	19.10	29.10	39.10	49.10	59.10	69.10	79.10	89.10	99.10	109.10
40	-	-4.53	5.47	15.47	25.47	35.47	45.47	55.47	65.47	75.47	85.47	95.47	105.47
50	-	-8.17	1.83	11.83	21.83	31.83	41.83	51.83	61.83	71.83	81.83	91.83	101.83
60	-	-11.80	-1.80	8.20	18.20	28.20	38.20	48.20	58.20	68.20	78.20	88.20	98.20
70	-	-	-5.43	4.57	14.57	24.57	34.57	44.57	54.57	64.57	74.57	84.57	94.57
80	-	-	-9.07	0.93	10.93	20.93	30.93	40.93	50.93	60.93	70.93	80.93	90.93
90	-	-	-12.70	-2.70	7.30	17.30	27.30	37.30	47.30	57.30	67.30	77.30	87.30
100	-	-	-	-6.34	3.66	13.66	23.66	33.66	43.66	53.66	63.66	73.66	83.66
110	-	-	-	-9.97	0.03	10.03	20.03	30.03	40.03	50.03	60.03	70.03	80.03
120	-	-	-	-13.60	-3.60	6.40	16.40	26.40	36.40	46.40	56.40	66.40	76.40

Notes: Negative values included for interpolation purposes. Minimum LMDC-B = 0 in.

Table 5-10: Maximum Inter-Story Drift for Light, East-Coast Office Building Design

Subjected to Air-Blast Events

W (lbsTNT):	500	300	100
R (ft)	30	100	200
Story	Maximum Inter-Story Drift (%)		
3	0.29	0.19	0.06
2	0.16	0.08	0.02
1	0.24	0.08	0.03
Note:	Air-blast analyses performed on 3-story steel braced frame office building designed for Boston, MA hazards with floor mass equivalent to uniform 60psf load per floor (light mass).		

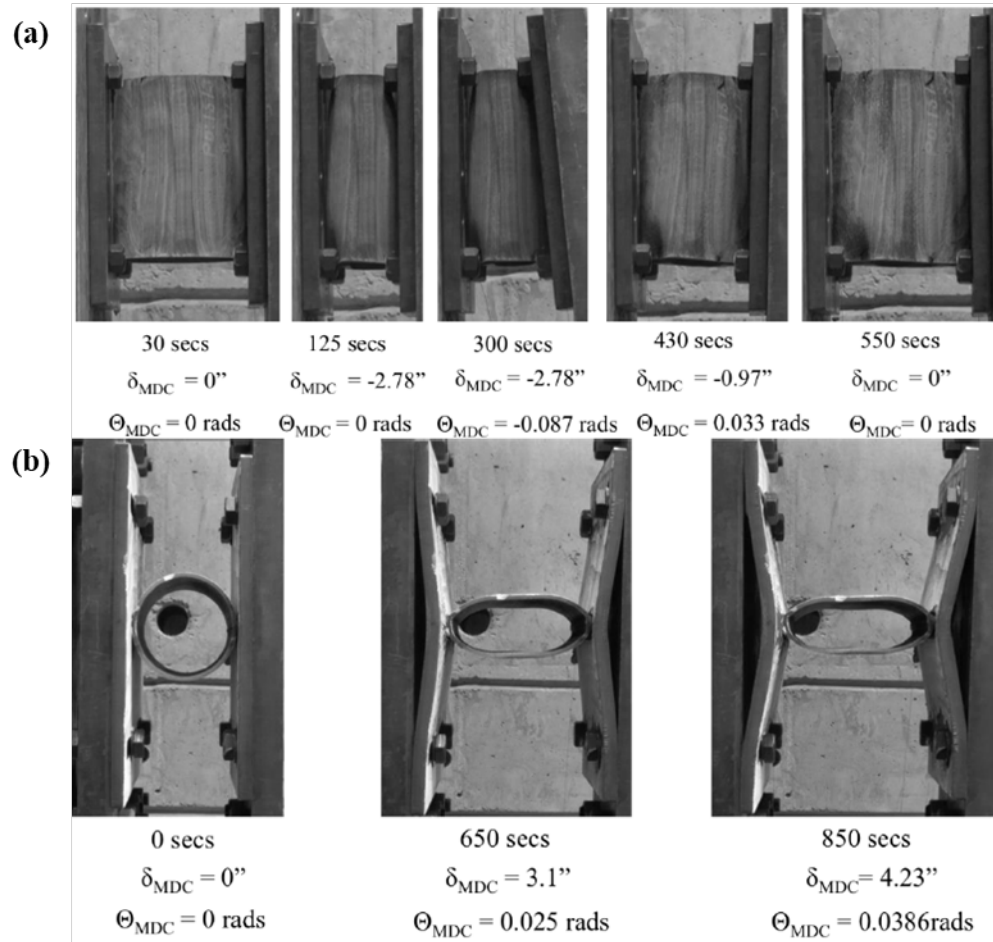


Fig. 5-1: Pseudo-Static Experimental Testing of MDCs Subjected to (a) Design Blast Loading and (b) Radial Pulling (Adapted from Rendos, 2018)

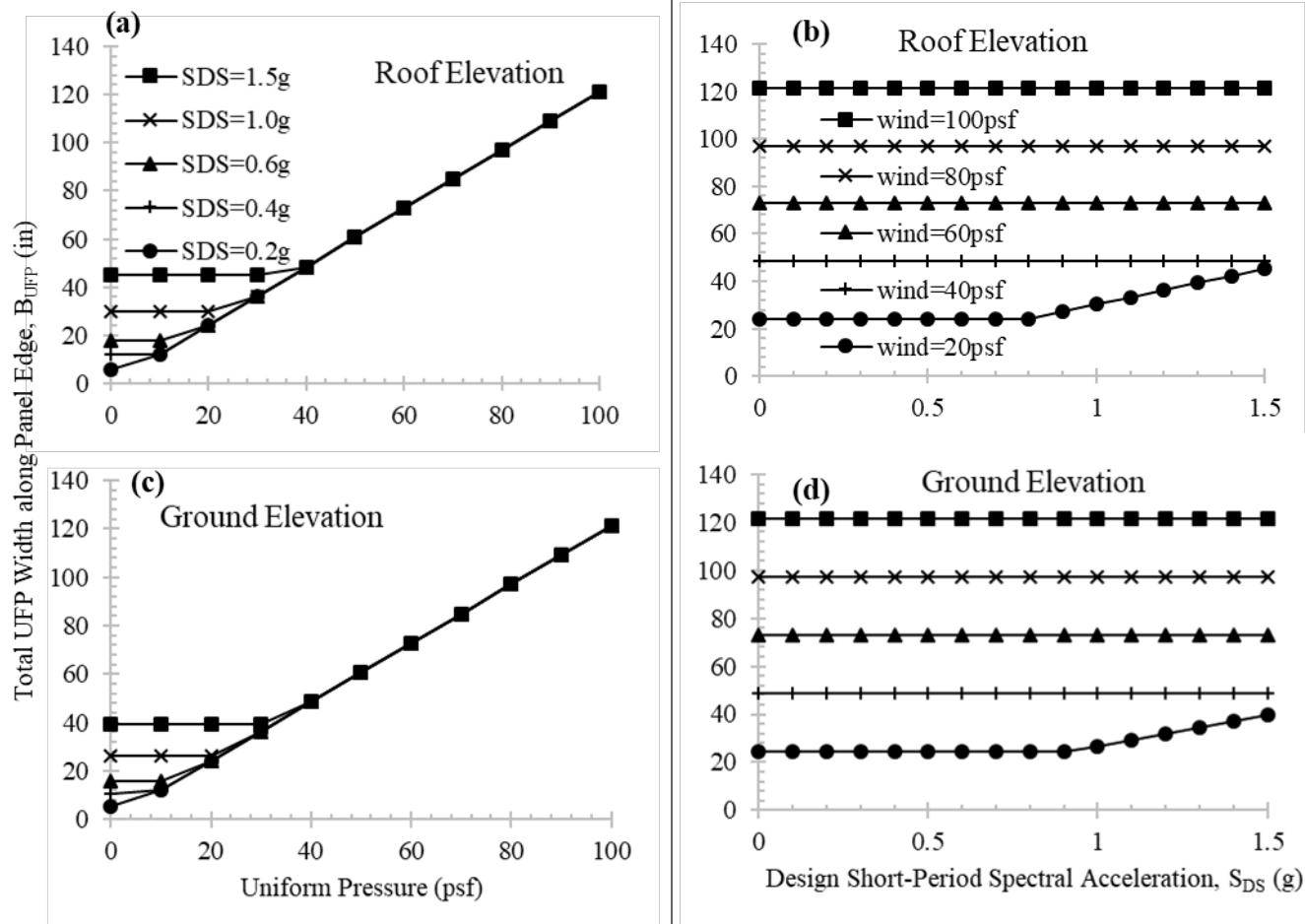


Fig. 5-2: Total UFP Width per Panel Edge with $t_{UFP} = 0.25$ in. for Reinforced Concrete Panels at (a,b) Roof or (c,d) Ground Elevation, Primarily considering (a,c) Wind or (b,d) Seismic Hazards

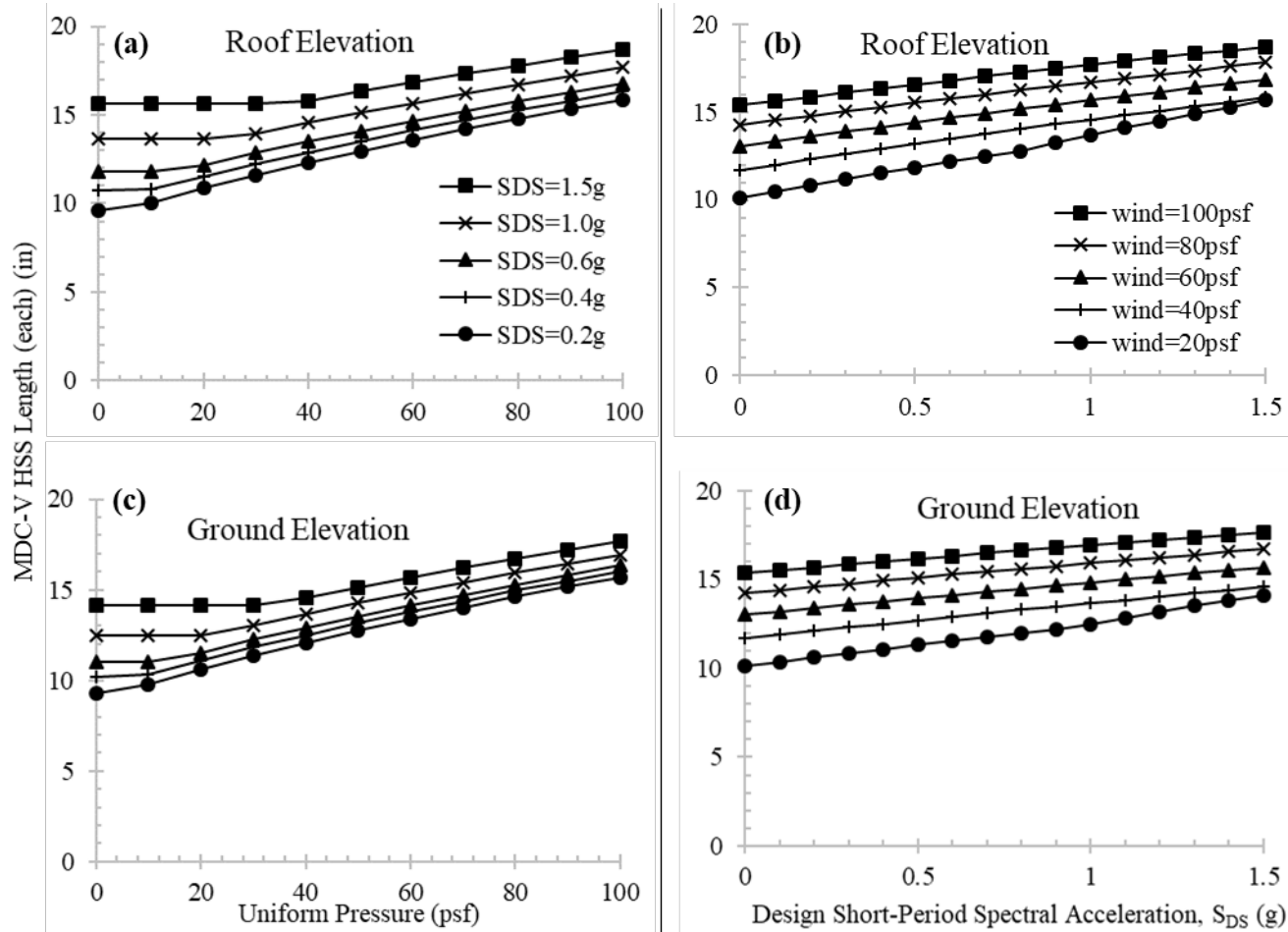


Fig. 5-3: MDC-V HSS Length with $t_{HSS} = 0.25$ in. for Reinforced Concrete Panels at (a,b) Roof or (c,d) Ground Elevation, Primarily considering (a,c) Wind or (b,d) Seismic Hazards

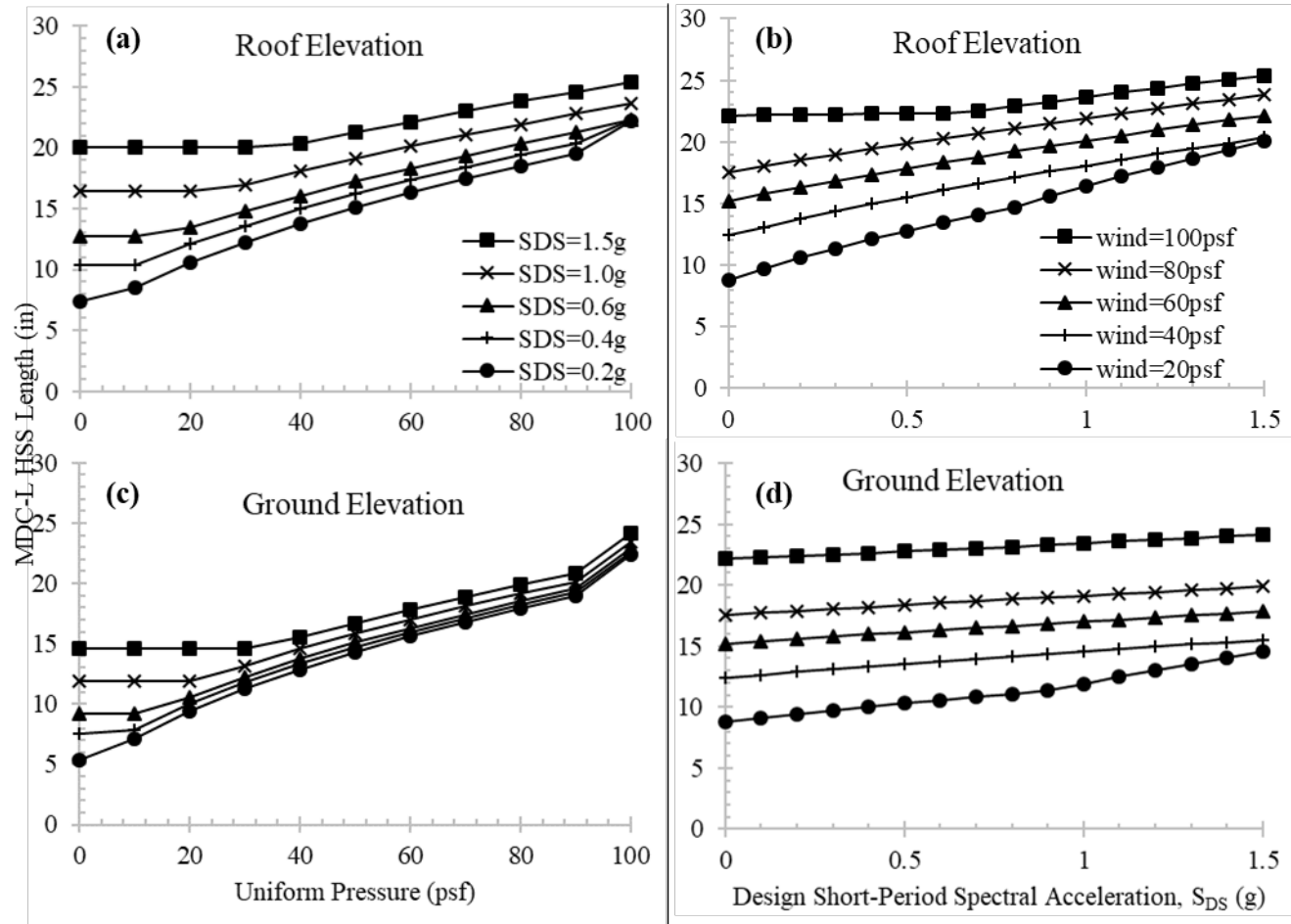


Fig. 5-4: MDC-L HSS Length with $t_{HSS} = 0.25$ in. for Reinforced Concrete Panels at (a,b) Roof or (c,d) Ground Elevation, Primarily considering (a,c) Wind or (b,d) Seismic Hazards

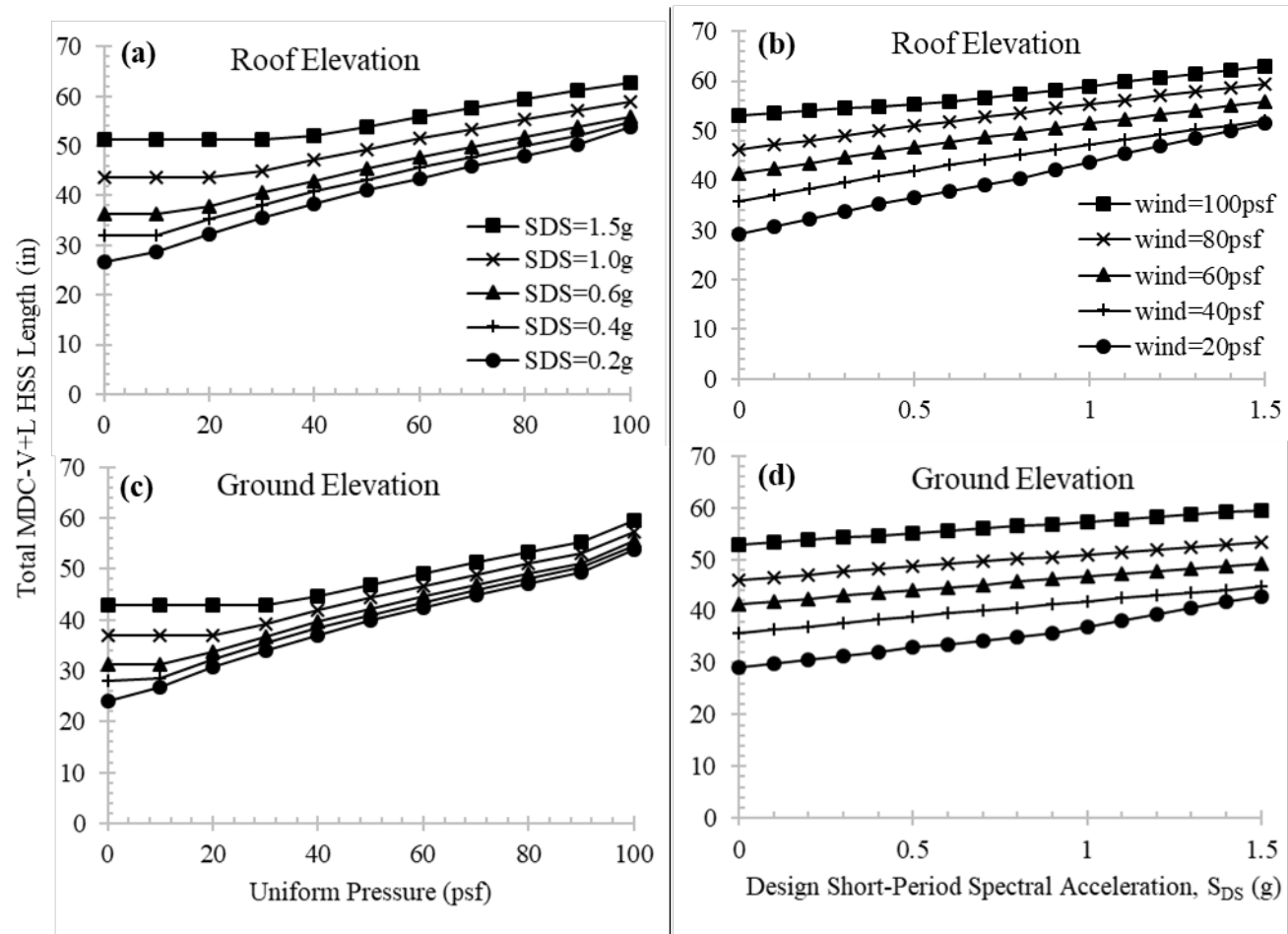


Fig. 5-5: Total MDC-V+L HSS Length with $t_{HSS} = 0.25$ in. for Reinforced Concrete Panels at (a,b) Roof or (c,d) Ground Elevation, Primarily considering (a,c) Wind or (b,d) Seismic Hazards

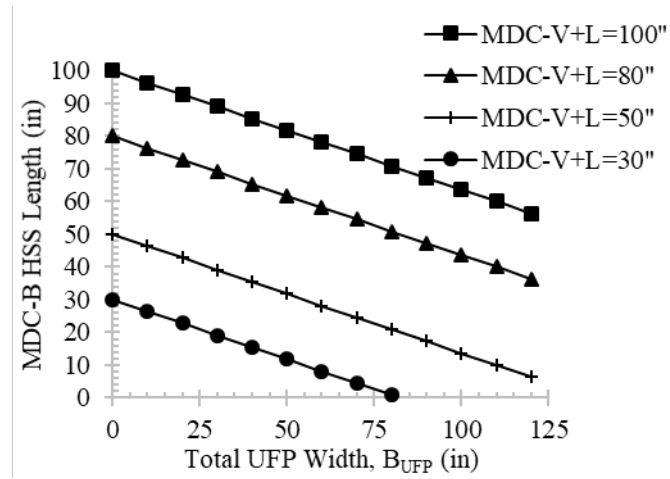


Fig. 5-6: MDC-B HSS Length with $t_{HSS} = 0.25$ in. for Reinforced Concrete Panels

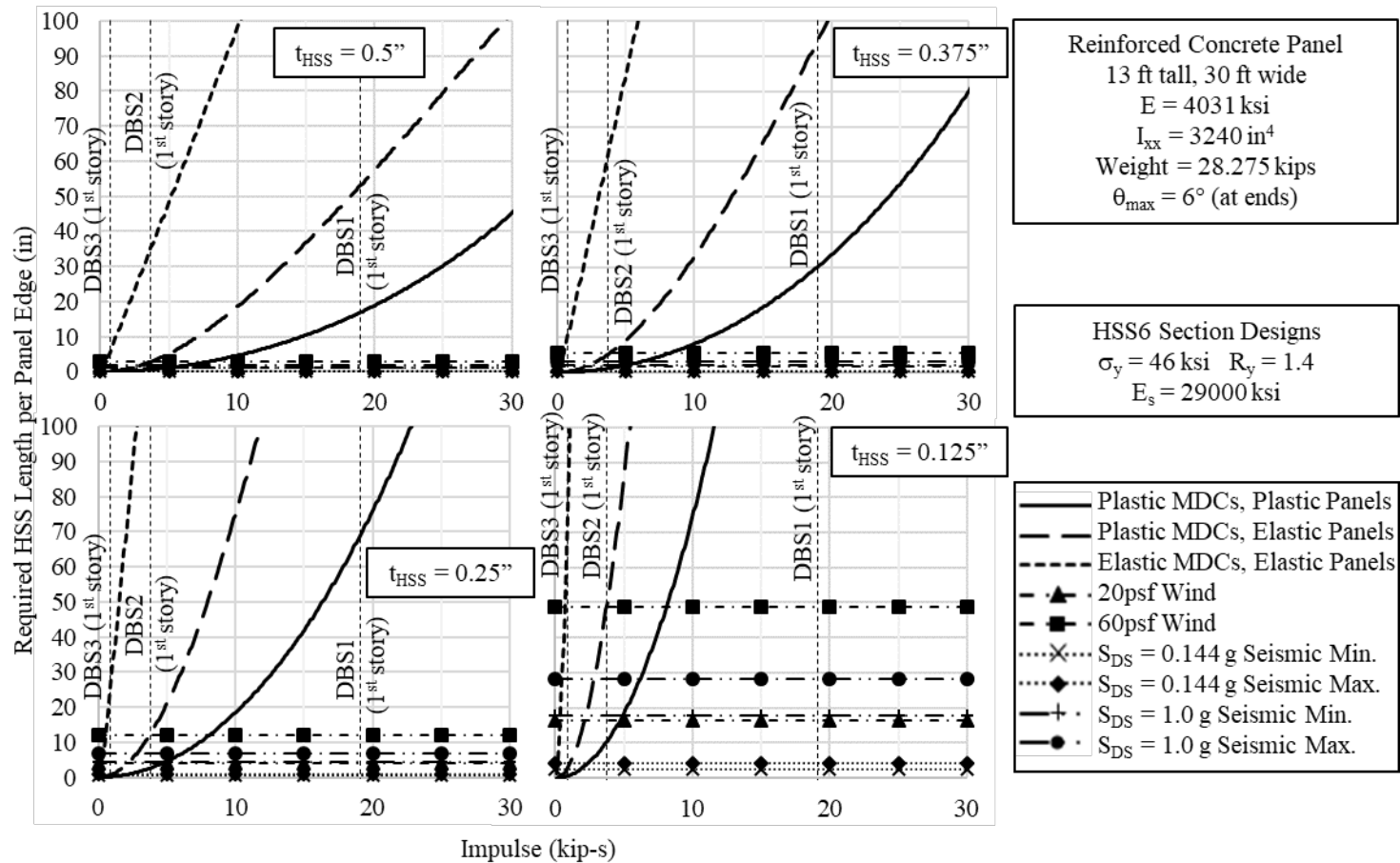


Fig. 5-7: MDC HSS Length per Panel Edge Design for Reinforced Concrete Panel Façade System Subjected to Impulsive Loading

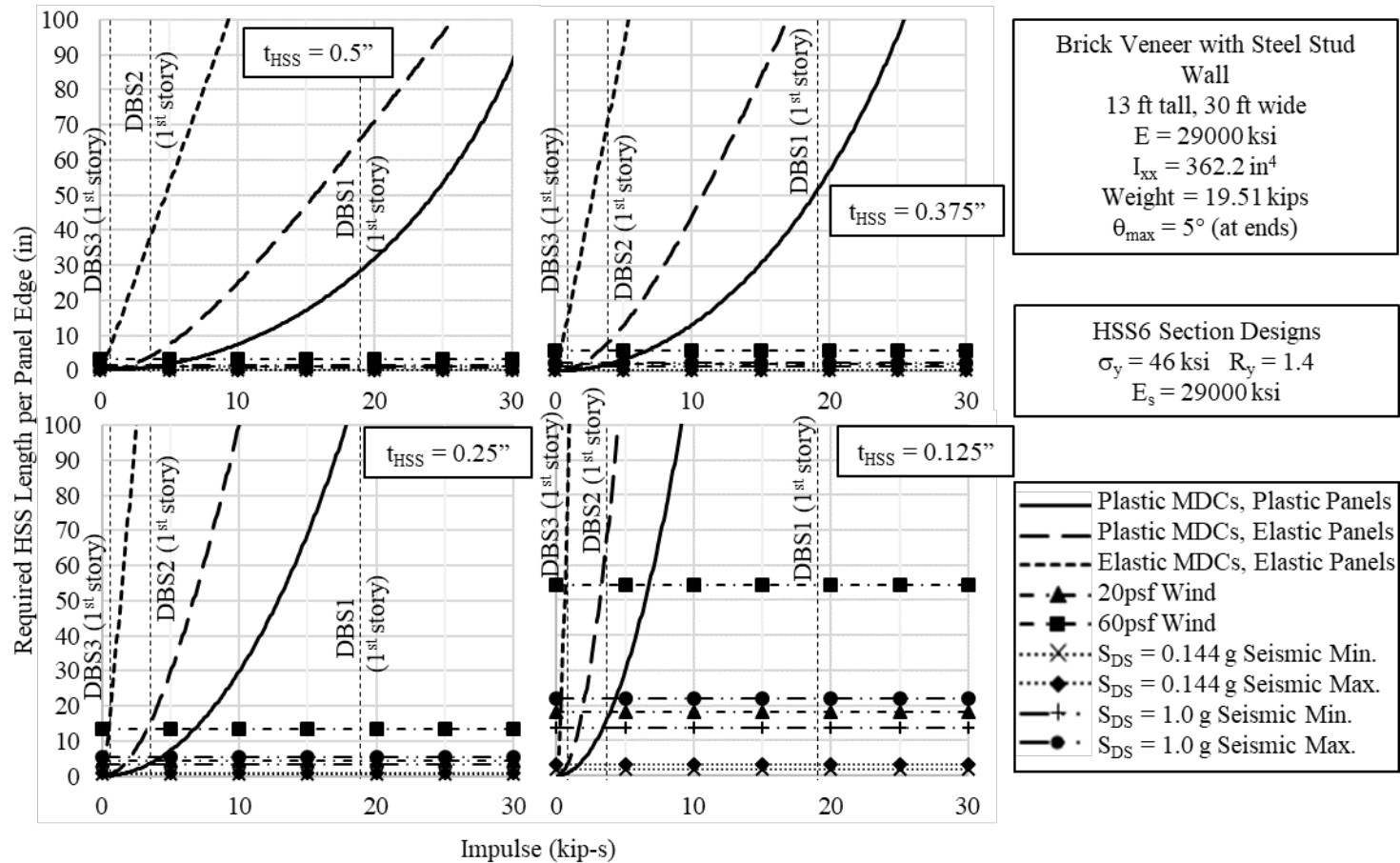


Fig. 5-8: MDC HSS Length per Panel Edge Design for Brick Veneer with Steel Stud Wall Façade System Subjected to Impulsive Loading

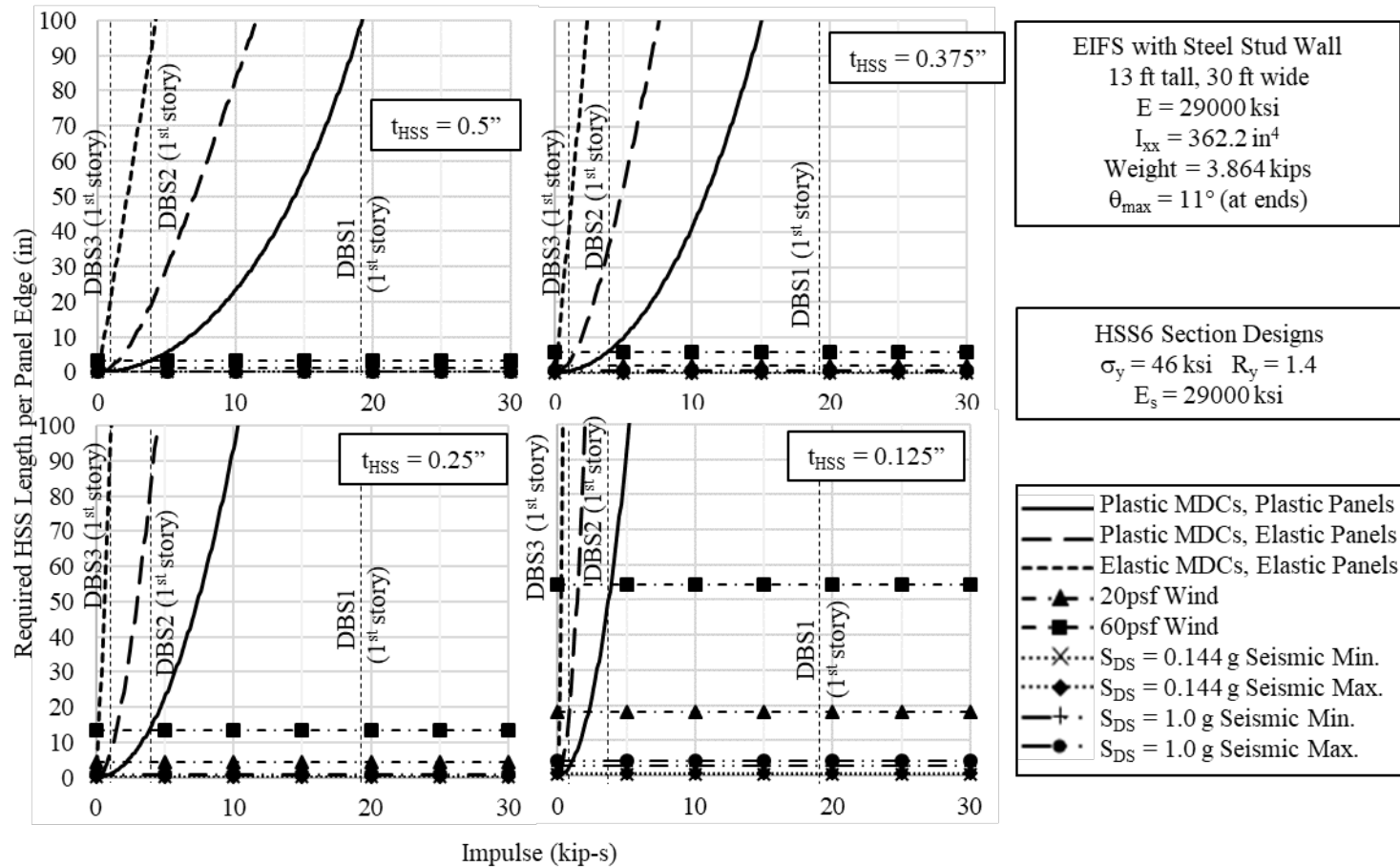


Fig. 5-9: MDC HSS Length per Panel Edge Design for EIFS with Steel Stud Wall Façade System Subjected to Impulsive Loading

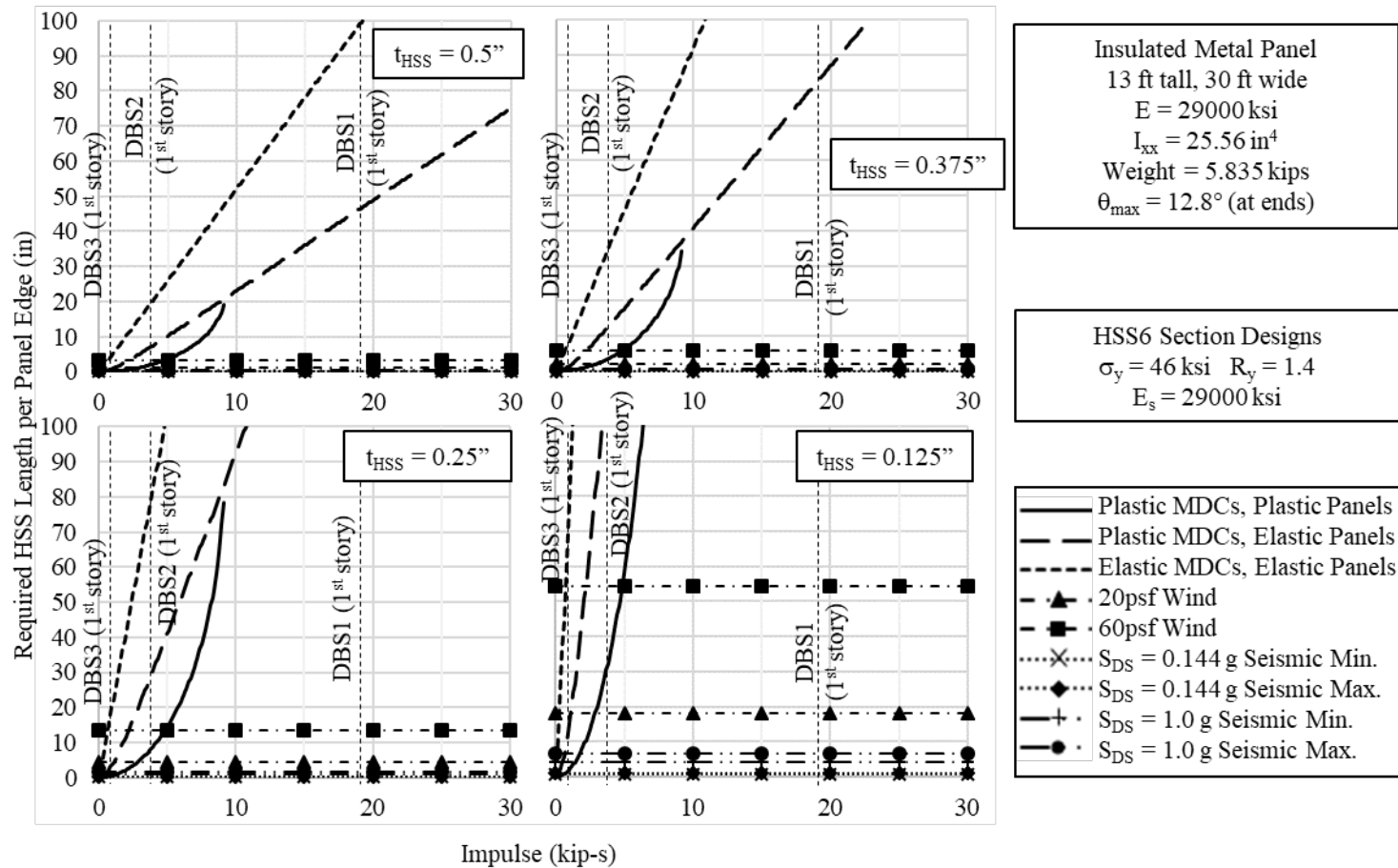


Fig. 5-10: MDC HSS Length per Panel Edge Design for Insulated Metal Panel Façade System Subjected to Impulsive Loading

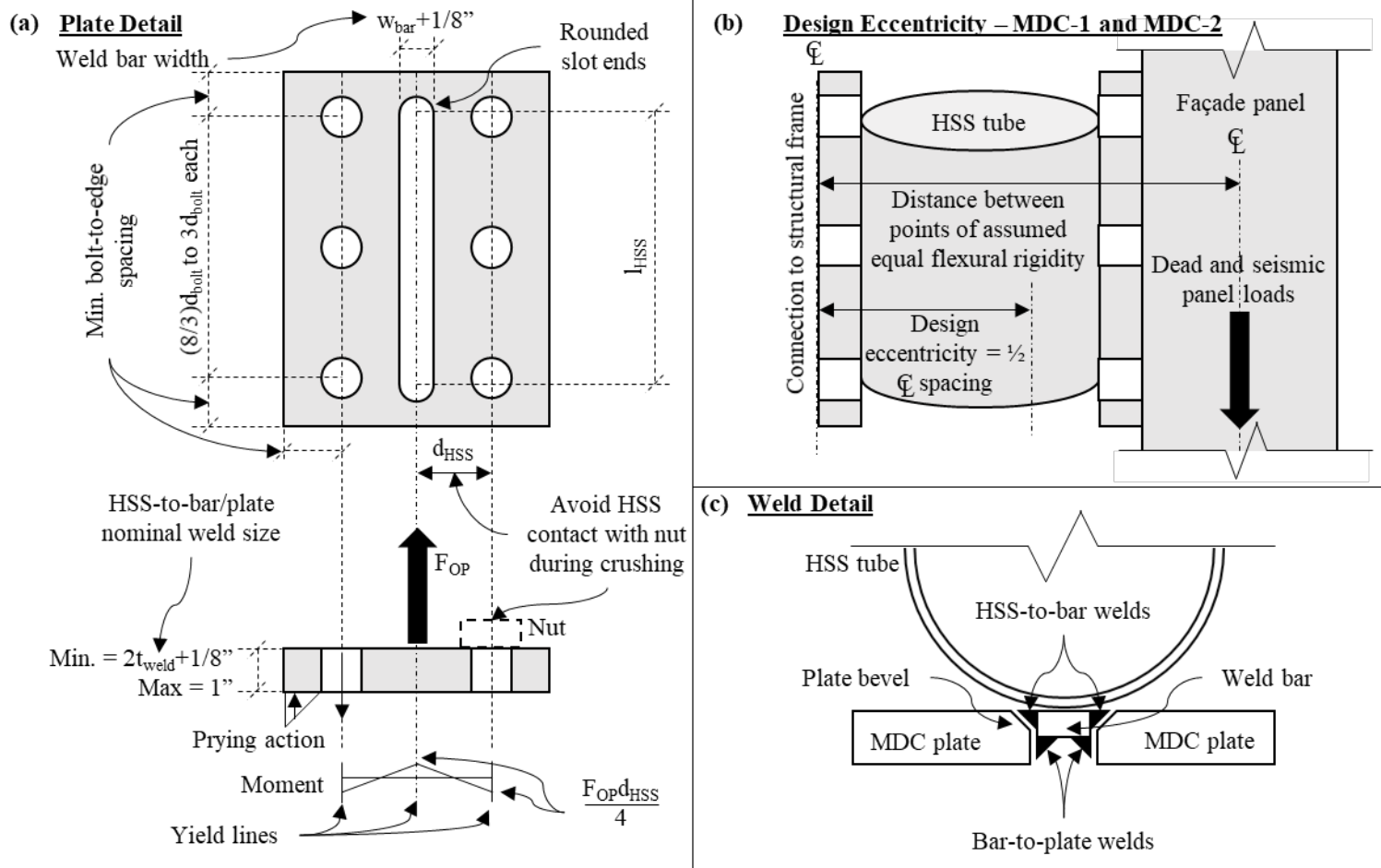


Fig. 5-11: MDC (a) Plate Detail, (b) Design Eccentricity, and (c) Weld Detail

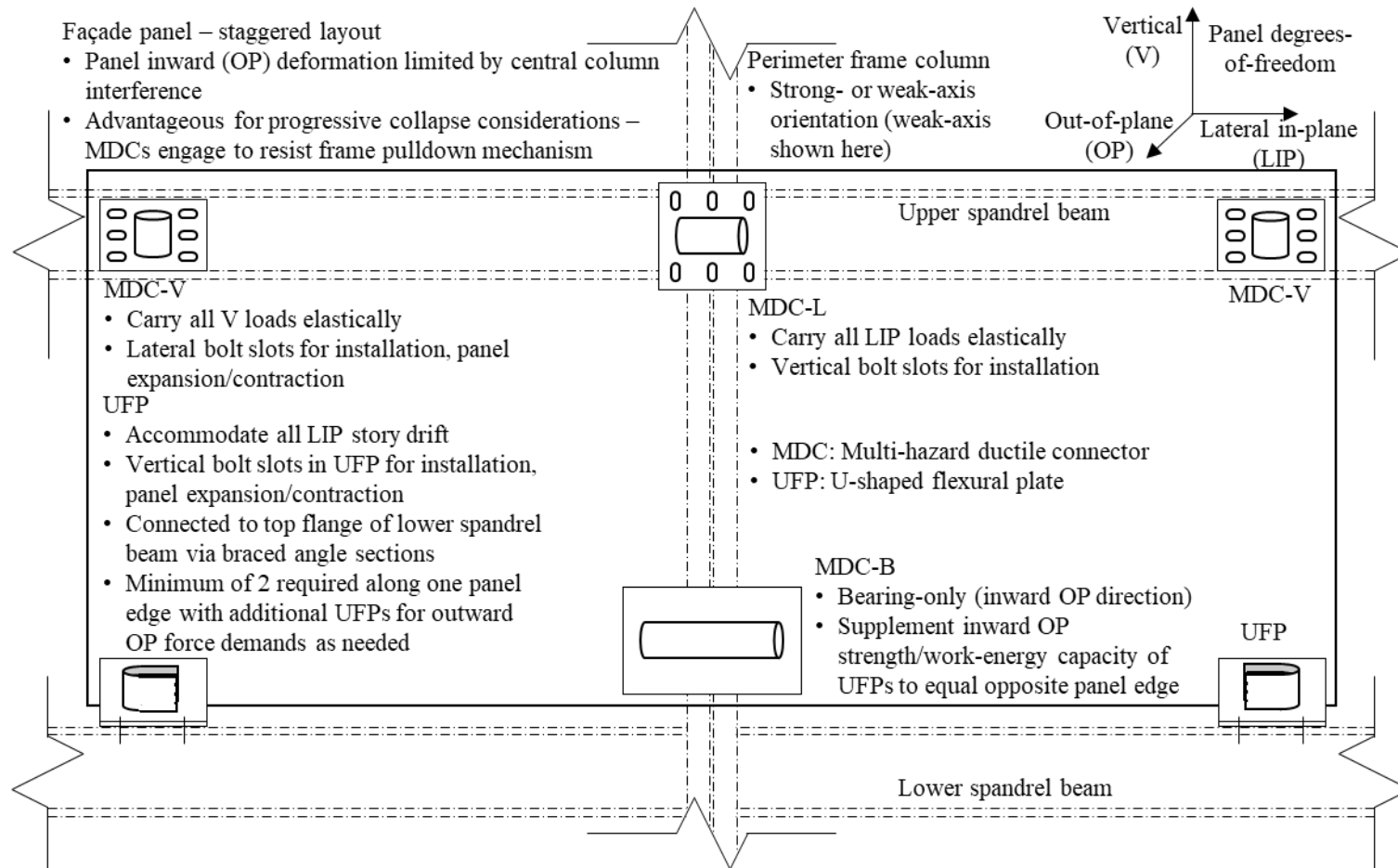


Fig. 5-12: MHFS Connector Layout and Functions for Alternative “Staggered” Panel Placement

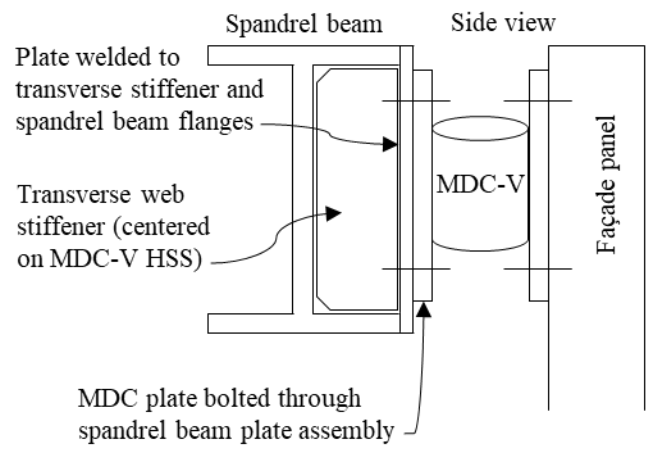


Fig. 5-13: MDC-V Detail Illustration

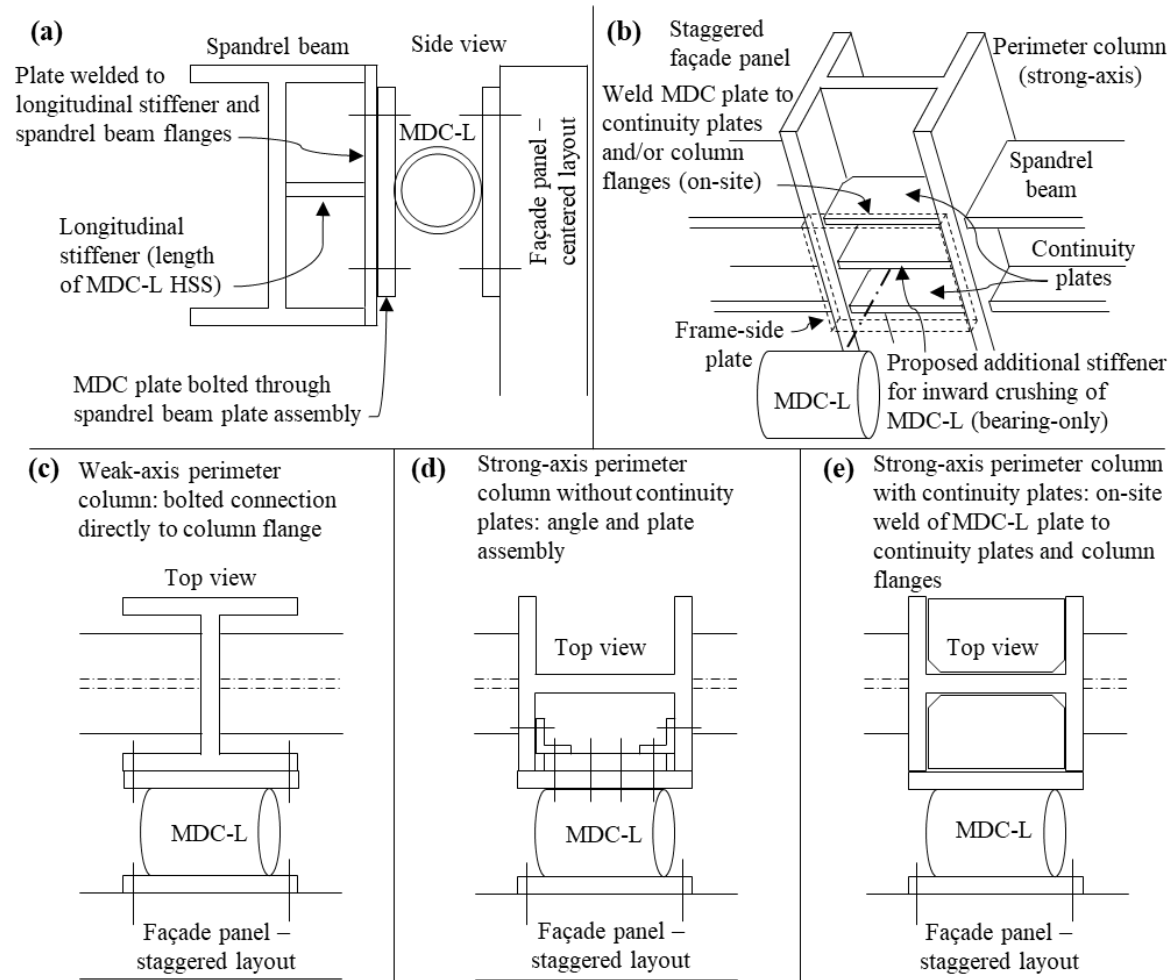


Fig. 5-14: MDC-L Detail Illustration for (a) Centered or (b) Staggered Panel Placement with (c) Weak-Axis or (d,e) Strong-Axis

Exterior Columns using (c,d) Bolted or (e) Welded Connections

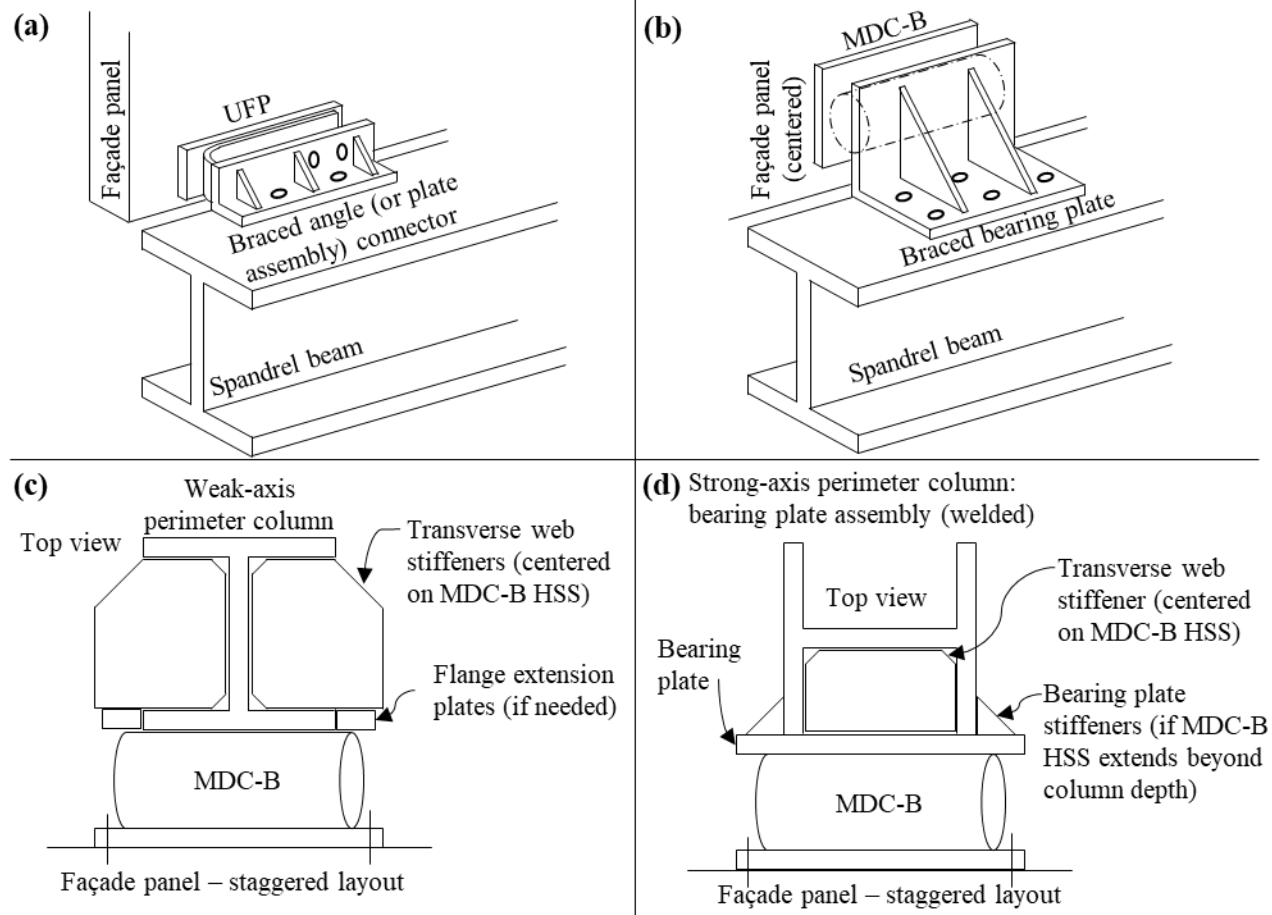


Fig. 5-15: Detail Illustrations for (a) UFPs, and MDC-B with (b) Centered or Staggered Panel Placement with (c) Weak-Axis or (d)

Strong-Axis Perimeter Columns

6. Integrated Design Procedure

The detailed procedures from the previous sections will be summarized in this section with a step-by-step guideline to the proposed MDC and UFP design procedure. An example design of a reinforced concrete façade panel system with MDCs and UFPs will be presented, as well as a discussion of the viability of the proposed approach for other common façade types.

6.1. Step-by-Step Design Guideline

1. A few known values and assumptions should be established going into the design procedure, such as:
 - a. Gross building dimensions (BxDxH), façade panel dimensions and properties (material weight/mass, flexural strength and stiffness, deformation capacity).
 - b. Performance objectives for panel and connectors subjected to various hazards (Table 3-1).
 - c. Configuration/location of MDC types (Sections 3, Fig. 3-1 and Fig. 3-2).
 - d. Round HSS section diameter, d_{HSS} (recommended six inches), and wall thickness, t_{HSS} (recommended 1/4"), for all MDCs (Section 5.1)
 - e. Plate bend diameter, d_{UFP} , and thickness, t_{UFP} , for UFPs, which match MDC cross sectional properties as closely as possible, based on availability (Section 5.1).

- f. Length of unconnected, straight plate included in UFP cross section, l_{free} , at least equal to the maximum expected inter-story drift under design-basis earthquake (DBE) loading (Section 5.1).
2. Calculate the required UFP length per panel edge, B_{UFP} , to satisfy all non-impulsive outward OP demands (Section 5.2).
 - a. Obtain design reference wind speed and seismic spectral acceleration values. Follow the procedures in ASCE 7-10 to calculate the design components and cladding load for the façade panel of interest (Section 3). Also, determine any minimum panel strengths (such as that considering temperature and shrinkage reinforcement ratio for reinforced concrete panels of 0.18%) which might provide a lower-bound limit on the connector and panel strengths.
 - b. Determine controlling total UFP width per panel edge considering elastic (Equation (5-1)) and plastic (Equation (5-2)) performance considering outward OP (radial pulling of UFP section) loads (Fig. 5-2, Table 5-1, and Table 5-2).
 - c. Calculate the maximum in-plane UFP rolling force and (for corner panels only) corner panel contact force (Section 5.2.2; and Equation (5-3)). From this force, calculate the vertical force per MDC-V required forming a couple which resists the moment caused by the eccentric UFP LIP force (Equation (5-4)).

3. Calculate the required HSS tube length for (two) MDC-Vs, $l_{\text{MDC-V}}$, and the (single) MDC-L, $l_{\text{MDC-L,min}}$, to elastically resist all vertical and LIP forces, respectively, via longitudinal shearing of the HSS tubes.
 - a. Determine $l_{\text{MDC-L,min}}$ (Section 5.3.1; Equation (5-5), Fig. 5-4, Table 5-5, and Table 5-6).
 - b. Determine $l_{\text{MDC-V}}$ (Section 5.3.2; Equations (5-6) and (5-7), Fig. 5-3, Table 5-3, and Table 5-4).
4. Calculate the required HSS tube length per panel edge, $l_{\text{MDC-Edge}}$, for all non-impulsive OP panel demands (Section 5.3.3)
 - a. Determine HSS tube length per edge for non-impulsive OP loads with elastic performance objective (Equation (5-8), Fig. 5-5, Table 5-7, and Table 5-8).
 - b. Determine HSS tube length per edge for non-impulsive OP loads with plastic performance objective (Equation (5-9), Fig. 5-5, Table 5-7, and Table 5-8).
 - c. Compare $l_{\text{MDC-Edge}}$ to $2l_{\text{MDC-V}}$ plus $l_{\text{MDC-L,min}}$ and add any additional HSS tube length per panel edge required for non-impulsive OP demands to the MDC-L HSS tube length (Section 5.3.4).
5. Calculate the required HSS tube length per panel edge for design blast loading (if considered).
 - a. Determine appropriate design-basis blast scenarios and performance objectives (Sections 3.2.5 and 5.3.5; Table 3-1).

- b. Determine the required HSS tube length per panel edge to satisfy all performance objectives for the design-basis scenario(s) (Section 5.3.5; Equation (4-38), Fig. 5-7 through Fig. 5-10).
 - c. Compare the total HSS tube length per panel edge for blast and non-impulsive demands and add any additional length required for blast demands to the MDC-L HSS tube length.
6. Calculate the required inward OP bearing-only MDC-B HSS tube length, l_{MDC-B} , based on the total MDC-V plus MDC-L HSS tube length and the total UFP width (Section 5.3.6; Equation (5-10)).
7. Capacity design the façade panel flexural yield capacity, M_p , for the desired progression of damage during extreme OP loading based on the controlling total HSS tube length per panel edge (Section 5.4; Equation (5-12)).
8. Evaluate the design for impact loading (optional; Sections 3.2.5.2 and 5.3.5.2).
 - a. Develop an FEA model, which captures the OP response of the façade panel and connectors based on the established mechanics (Section 4).
 - b. Determine design basis impact missile(s) and calculate applied impulse (momentum transferred) from the object's mass and impact velocity.
 - c. Define critical impact point or area where loading is applied to panel. Add object mass to panel in this impact zone. Optionally, loading and panel mass can be applied to the panel through an in-series elasto-plastic spring element with properties, which approximate the expected energy dissipation due to plastic deformation of the impact missile.

- d. Define loading time history and magnitude to achieve the design-basis momentum transfer (impulse).
 - e. Perform analysis and evaluate peak response. Strengthen panel M_p as needed until satisfactory performance is observed. If such a design cannot be achieved, increased connector strength per panel edge may help however, care should be taken to avoid interfering with the system performance considering other load types (recheck hazards and associated performance objectives for all load combinations). If a satisfactory design still cannot be achieved, choosing a different façade panel type and restarting the design procedure may be necessary.
9. Perform detailing calculations for the final UFP (Section 5.2.3) and MDC (Section 5.3.7) designs.
- a. Determine required vertical and lateral bolt slot dimensions based on expected thermal/moisture panel expansion/contraction (Section 3.2.1; Equation (3-1)).
 - b. Assume end plate thickness of one inch for all connectors and calculate the design force eccentricities and corresponding moment values for all relevant connector degrees-of-freedom (Sections 5.2.3.1 and 5.3.7.1; Equation (5-11)).
 - c. Design MDC connection details (Section 5.3.7).
 - i. Set minimum MDC plate thickness equal to twice the maximum specified weld thickness among all MDCs (Section 5.3.7.2).

- ii. Assume trial bolt size and configuration and plate dimensions (Section 5.3.7.3).
 - iii. Calculate plate bending strength and adjust dimensions (or iterate HSS section choice) as necessary to provide adequate strength. Ensure plate thickness does not exceed what was assumed when calculating the design eccentricity (maximum plate thickness of one-inch is recommended; Equation (5-11)).
 - iv. Calculate required number and size of bolts per MDC plate considering shear-axial force interaction and prying action due to plate bending.
 - v. Check bolted connection limit states: bolt bearing/tear-out, block shear, net section fracture, and gross section yielding.
- d. Design UFP connection details (Section 5.2.3)
- i. Determine number of UFPs located along panel edge (at least two required) and split B_{UFP} evenly amongst these connectors.
 - ii. Take end plate thickness equal to the final MDC end plate thickness.
 - iii. Calculate the required number and size of bolts to attach UFPs to end/boundary plates (if bolted connections are used; Section 5.2.3.2).
 - iv. Calculate the required weld thickness and leg lengths (if welded connections are used; Section 5.2.3.3).
 - v. Perform limit state checks on the connection detail and adjust design as needed.

6.2. Example Design of Reinforced Concrete (RC) Façade Panel System

Details of a reinforced concrete panel façade system with MDCs and UFPs are provided in Table 6-1 through Table 6-3 for a three-story office building located in Los Angeles, CA (high seismic, low wind/tornado hazards). The façade panels are six-inch thick normal weight reinforced concrete assumed to span the entire thirteen-foot high, thirty-foot wide story and bay dimensions. These panels are located at the corner of the building (includes corner panel contact and increased wind design force). The façade panel strength factors shown in this table are relative to the strength of a panel with the code-prescribed minimum reinforcement ratio per ACI (2011); this minimum strength is calculated to be about 1148 kip-in for a 6-inch thick 30-foot wide panel with 5 ksi compressive strength concrete and reinforcing steel yield stress of 60 ksi. All MDCs use HSS6x0.25 sections, while UFPs have $d_{UFP} = 6''$ and $t_{UFP} = 1/4''$ to match. The UFP cross section “free” length, l_{free} , is taken as 4” assuming a maximum inter-story drift of 2.5% ($(13') (0.025) = 3.9''$).

On the first story (Table 6-1), the total MDC-V plus MDC-L HSS tube length—and, consequently, the panel moment capacity—is controlled by design blast scenario 1 (500lbsTNT at 30 ft with plastic panel and connector performance objectives). The increase in panel flexural strength can be achieved with a reinforcement ratio of about 1.2%, which does not result in an over-reinforced section. Panels and MDCs on the upper stories (Table 6-2 and Table 6-3) are controlled by the minimum required HSS lengths to resist vertical and LIP demands. The UFPs are controlled by the design-basis wind, which is identical for all stories in this low-rise prototype building. The 56” total UFP width is assumed to be split into four separate connectors (14” each) along the bottom edge of the panel with all connections using four bolts on either side of the UFP section. The L_{UFP}

term included in this table refers to the distance between the UFP section curve apex to the far end of the section including the connection zone (bolts with minimum hole center-to-edge spacing provided). Connection details (welds, bolts, plate dimensions) included for MDCs and UFPs were designed following the guidelines provided in this document. The maximum expected crushing force for MDC-Bs is also included to assist in detailing the connection/bracing scheme at the spandrel beam.

6.3. Viability of Design Methodology for Alternate Façade Panel Systems

The MDC and UFP design methodology detailed herein was largely developed considering precast reinforced concrete façade panels. This common façade type benefits from the inherent flexural strength considering even minimum reinforcement and cracked panel section moduli; the OP strength considering the minimum reinforcement ratio for temperature and shrinkage is often greater than the requirements for design wind and seismic forces. This panel type is also desirable for blast and impact protection due to its high mass, which reduces the panel's initial kinetic energy and requires less plastic work/elastic energy storage to achieve a given performance objective (Equation (4-38)). Preliminary work has been done to determine the viability of the proposed MDC design approach for other common façade systems, including brick veneer with steel stud backing, exterior insulation and finish systems (EIFSs) with steel stud backing, and insulated metal panels (IMPs) (Fig. 5-8 through Fig. 5-10). Typical as-built properties relevant to blast design were taken from Salim *et al.* (2005) and Idriss *et al.* (2016). Relative to the high-mass reinforced concrete system, the brick veneer system is characterized as “intermediate” mass, while both EIFSs and IMPs have low mass. IMPs have approximately the same flexural moment capacity as reinforced concrete panels

considering typical as-built details. The steel stud-backed systems (brick veneer and EIFS) rely primarily on cold-formed steel channels, which comprise the backing wall during OP loading. The flexural strength of the brittle brick wall is disregarded for blast design as it is expected to fracture, however the stud wall alone provides almost five times the flexural strength of a minimally reinforced concrete panel. EIFSs benefit from the strength of the stud wall plus the flexural strength of the veneer panel resulting in a composite section, which is roughly an order of magnitude stronger than a minimally reinforced concrete panel. Example MDC and UFP system designs for these façade types are summarized in Table 6-4. These designs consider the same prototype Los Angeles, CA office building used to design the example MDC and UFP system for reinforced concrete panels. Design for impact loading was disregarded for these façade types. The panel flexural strength factors shown in this table are relative to typical as-built details described by Salim *et al.* (2005) and Idriss *et al.* (2016). The insulated metal panel façade type requires the most strengthening due to its low mass and elastic stiffness, making it a poor choice for blast-protected structures. However, the steel stud wall-backed systems are likely viable for blast protection using MDCs and/or UFPs. Significant reinforcement of the steel stud wall systems can be achieved through use of thicker cold-formed steel stud sections and/or decreased center-to-center spacing of studs, while insulated metal panels can likely only be reinforced through the use of thicker gauge metal which has a limited effect due to the lack of section depth (bending stresses have a relatively small moment arm).

Steel stud walls can achieve fairly large ductile rotations during blast loading (Salim *et al.*, 2005), however incorporation of the MDCs and/or UFPs within the connection load path(s) may not be possible without significant alteration of typical design

practice, which normally has the stud walls standing outside of the building floor slabs' footprint. Additionally, brick veneer systems require anchorage to the stud wall on a regular grid (say, 18- or 24-inches square) to provide pseudo-continuous OP support of the relatively brittle brick wall, likely making any veneer-to-stud wall MDC/UFP placement unrealistic. MDCs with HSS tubes oriented with their longitudinal axes in the façade's LIP direction could be included at each floor elevation; however, this would require the stud wall to be pushed even further outside the building footprint to make room for the MDCs. Another possible option is to move the stud wall within the building footprint such that each story contains a single slab-to-slab wall span. The round HSS sections could be attached to the top- and bottom-end cap channels (and anchored to the slabs) such that OP loading engages the tubes in their rolling direction. The MDCs in either of these arrangements would have more space available for HSS tube length (up to the entire width of the "panel"), as well as a greater selection of HSS section diameters. Additional work is needed to determine if either of these approaches are realistic for steel stud wall-backed façade systems.

Table 6-1: Example Reinforced Concrete Façade Panel System Design for Building in Los Angeles, CA (Story 1 of 3)

Building Layout	Story Location Placement	1 of 3 Edge panel Centered on frame					
MDCs (1) MDC-L + (2) MDC-Vs on one edge, (1) MDC-B on opposite edge	HSS section	HSS6x0.25		MDC-V plates			
	L_{HSS} / edge (in)	74.75	d_{bolts} (in)	Count	h_{plate} (in)	b_{plate} (in)	
	P_0 / edge (kips)	100	0.5	12	16.25	16	
	W_{MDC} / edge (kip-in)	578	MDC-L plates				
	L_{MDC-V} (in)	14.25	d_{bolts} (in)	Count	h_{plate} (in)	b_{plate} (in)	
	L_{MDC-L} (in)	46.25	0.625	32	48.25	16	
	L_{MDC-B} (in)	54.5	Weld details (in)				
	$2P_0$ MDC-B (kips)	146	W_{weld}	W_{gap}	W_{bar}	t_{bar}	
	t_{plates} (in)	0.75	5/16	0.75	0.625	0.25	
	UFPs (4) on edge with MDC-B	d_{UFP} (in)	6	UFP details			
t_{UFP} (in)		0.25	L_{UFP} (in)	l_{free} (in)	d_{bolts} (in)	Count	
B_{UFP} / edge (in)		56	10	4	0.625	4	
Façade panel	Panel type	Reinforced concrete					
	M_p min. (kip-in)	1148					
	M_p (kip-in)	7823					
	Factor increase	6.81 ($\rho_L = 6.81 \times 0.0018 = 1.22\%$)					
Controlling Design Considerations							
B_{UFP} / edge	OP strength (outward)	Elastic	Design wind				
			Seismic inertia				
		Plastic	Tornado suction				
Tornado wind							
Length of MDC-L + MDC-Vs (for LIP, V loads)							
L_{HSS} / edge	Non-impulsive demands	OP strength	Elastic	Design wind			
				Seismic (+contact)			
			Plastic	Tornado suction			
	Tornado wind						
	Impulsive demands	Blast	DBS1: $W = 500\text{lbsTNT}$, $R = 30\text{ft}$ Plastic panel and MDCs				
			DBS2: $W = 300\text{lbsTNT}$, $R = 100\text{ft}$ Elastic panel, plastic MDCs				
DBS3: $W = 100\text{lbsTNT}$, $R = 200\text{ft}$ Elastic panel and MDCs							
Impact	Impact	TR3: $W_M = 2595\text{lbs}$, $V_M = 79\text{ft/s}$ Plastic panel and MDCs					

Table 6-2: Example Reinforced Concrete Façade Panel System Design for Building in Los Angeles, CA (Story 2 of 3)

Building Layout	Story Location	2 of 3		Edge panel		
	Placement	Centered on frame				
MDCs (1) MDC-L + (2) MDC-Vs on one edge, (1) MDC-B on opposite edge	HSS section	HSS6x0.25		MDC-V plates		
	L_{HSS} / edge (in)	46.25	d_{bolts} (in)	Count	h_{plate} (in)	b_{plate} (in)
	P_0 / edge (kips)	62	0.625	12	16.5	16
	W_{MDC} / edge (kip-in)	358	MDC-L plates			
	L_{MDC-V} (in)	14.5	d_{bolts} (in)	Count	h_{plate} (in)	b_{plate} (in)
	L_{MDC-L} (in)	17.25	0.625	14	19.25	16
	L_{MDC-B} (in)	26	Weld details (in)			
	$2P_0$ MDC-B (kips)	70	w_{weld}	w_{gap}	w_{bar}	t_{bar}
t_{plates} (in)	0.75	5/16	0.75	0.625	0.25	
UFPs (4) on edge with MDC-B	d_{UFP} (in)	6	UFP details			
	t_{UFP} (in)	0.25	L_{UFP} (in)	l_{free} (in)	d_{bolts} (in)	Count
	B_{UFP} / edge (in)	56	10	4	0.625	4
Façade panel	Panel type	Reinforced concrete				
	M_p min. (kip-in)	1148				
	M_p (kip-in)	4840				
	Factor increase	4.22				
Controlling Design Considerations						
B_{UFP} / edge	OP strength (outward)	Elastic	Design wind			
			Seismic inertia			
		Plastic	Tornado suction			
			Tornado wind			
L_{HSS} / edge	Non-impulsive demands	Length of MDC-L + MDC-Vs (for LIP, V loads)				
		OP strength	Elastic	Design wind		
				Seismic (+contact)		
			Plastic	Tornado suction		
	Impulsive demands	Blast	DBS1: $W = 500\text{lbsTNT}$, $R = 30\text{ft}$			
			Plastic panel and MDCs			
		Impact	DBS2: $W = 300\text{lbsTNT}$, $R = 100\text{ft}$			
			Elastic panel, plastic MDCs			
		DBS3: $W = 100\text{lbsTNT}$, $R = 200\text{ft}$				
		Elastic panel and MDCs				
		TR3: $W_M = 2595\text{lbs}$, $V_M = 79\text{ft/s}$				
		Plastic panel and MDCs				

Table 6-3: Example Reinforced Concrete Façade Panel System Design for Building in
Los Angeles, CA (Story 3 of 3)

Building Layout	Story Location	3 of 3		Edge panel		
	Placement	Centered on frame				
MDCs (1) MDC-L + (2) MDC-Vs on one edge, (1) MDC-B on opposite edge	HSS section	HSS6x0.25		MDC-V plates		
	L_{HSS} / edge (in)	48.25	d_{bolts} (in)	Count	h_{plate} (in)	b_{plate} (in)
	P_0 / edge (kips)	65	0.625	12	17	16
	W_{MDC} / edge (kip-in)	373	MDC-L plates			
	L_{MDC-V} (in)	15	d_{bolts} (in)	Count	h_{plate} (in)	b_{plate} (in)
	L_{MDC-L} (in)	18.25	0.625	14	20.25	16
	L_{MDC-B} (in)	28	Weld details (in)			
	$2P_0$ MDC-B (kips)	75	w_{weld}	w_{gap}	w_{bar}	t_{bar}
t_{plates} (in)	0.75	5/16	0.75	0.625	0.25	
UFPs (4) on edge with MDC-B	d_{UFP} (in)	6	UFP details			
	t_{UFP} (in)	0.25	L_{UFP} (in)	l_{free} (in)	d_{bolts} (in)	Count
	B_{UFP} / edge (in)	56	10	4	0.625	4
Façade panel	Panel type	Reinforced concrete				
	M_p min. (kip-in)	1148				
	M_p (kip-in)	5049				
	Factor increase	4.40				
Controlling Design Considerations						
B_{UFP} / edge	OP strength (outward)	Elastic	Design wind			
			Seismic inertia			
		Plastic	Tornado suction			
			Tornado wind			
L_{HSS} / edge	Non-impulsive demands	Length of MDC-L + MDC-Vs (for LIP, V loads)				
		OP strength	Elastic	Design wind		
				Seismic (+contact)		
			Plastic	Tornado suction		
	Impulsive demands	Blast	DBS1: $W = 500\text{lbsTNT}$, $R = 30\text{ft}$			
			Plastic panel and MDCs			
		Impact	DBS2: $W = 300\text{lbsTNT}$, $R = 100\text{ft}$			
			Elastic panel, plastic MDCs			
		DBS3: $W = 100\text{lbsTNT}$, $R = 200\text{ft}$				
		Elastic panel and MDCs				
		TR3: $W_M = 2595\text{lbs}$, $V_M = 79\text{ft/s}$				
		Plastic panel and MDCs				

Table 6-4: Example Designs for Alternative Façade Systems

Brick Veneer with Steel Stud Backing Wall						
Story	L _{MDC-V} (in)	L _{MDC-L} (in)	L _{MDC-B} (in)	B _{UFP} (in)	M _p (kip-in)	Factor
3	8.75	28.25	25.5	56	4788	1
2	8.75	55.5	52.75	56	7639	1.6
1	8.75	138.5	135.75	56	16330	3.41
EIFS with Steel Stud Backing Wall						
Story	L _{MDC-V} (in)	L _{MDC-L} (in)	L _{MDC-B} (in)	B _{UFP} (in)	M _p (kip-in)	Factor
3	10	89.5	89.25	56	11460	1
2	10	274.25	274	56	30790	2.69
1	8.75	291.75	291	56	32570	2.85
Insulated Metal Panel						
Story	L _{MDC-V} (in)	L _{MDC-L} (in)	L _{MDC-B} (in)	B _{UFP} (in)	M _p (kip-in)	Factor
3	10.5	27	27.75	56	5023	4.28
2	10.25	74.25	74.5	56	9916	8.45
1	10.25	127.75	128	56	15510	13.22

Notes: All designs use HSS6x0.25 for MDCs, $d_{UFP} = 6"$, $t_{UFP} = 1/4"$
 All panels 13'x30' surface area (nominal)
 Seismic and wind demands for Los Angeles, CA
 Corner panel designs, but contact force ignored for brick veneer
 Design for impact disregarded for these façade types
 Factor increases in M_p are relative to typical as-built details

7. Multi-hazard Design Connector (MDC) Experimental Testing

7.1. Experimental Testing Phase I: MDC Pulling, Crushing, Shearing Tests

The first phase of experimental testing was conducted during Summer/Fall 2017 at the Case Western Reserve University Vanderhoof Research and Education Facility (a.k.a Case Structural Engineering Laboratory, CSEL) to evaluate the quasi-static behavior of multi-hazard ductile connectors (MDCs). A total of (3) specimens were tested during this testing phase. The multi-hazard ductile connector (MDC) designs were tested quasi-statically in a setup that was capable of applying the critical façade panel gravity loads, deformations, and rotations to various MDC specimens. The testing was intended to physically evaluate the designs and provide critical data for the calibration and validation of the MDC finite element analysis models. The tested specimens represented MDCs connected at different locations on the prototype building panel as described below:

- “MDC1” Pulling Test (Seismic Corner Panel Contact Load Case)
 - The MDC specimen shown in Fig. 7-1 was tested for outward seismic drift compatibility expected for corner façade panels, which includes outward (tensile) translation and rotation about horizontal.

- “MDC2” Crushing with Gravity Load Test (Air-blast Impulse Load Case)
 - The MDC specimen shown in Fig. 7-2 was tested with constant façade panel gravity loading and quasi-static blast deformation history including inward (compressive) translation, outward (tensile) translation, and rotation (about horizontal). The deformation protocol was determined based on the design air-blast scenarios and analyses described in previous sections.

- “MDC3” Longitudinal Shearing Test (Panel In-plane Shear Load Case)
 - The MDC specimen shown in Fig. 7-3 was tested to determine maximum load carrying capacity along the MDC longitudinal axis.

Critical dimensions of the first three MDC designs (MDC1, MDC2, MDC3) are provided in Table 7-1 while fabrication drawings for are provided in Appendix C. Note that the end plate bolt hole details are significantly different for each MDC type. Each type needs to accommodate moisture, thermal, or seismic drift deformations in different directions.

Note: At the time of this testing phase, connector Configuration 1 (see Appendix B) was utilized for design. These designs included end plates, which are intended to accommodate seismic in-plane and corner-contact drift compatibility through slotted holes and end plate bending. Later designs included UFPs to accommodate seismic drift compatibility (not utilizing the potentially unreliable long bolt hole slots).

Drawings of each MDC design are provided in Appendix C and annotated pictures of each MDC specimen are shown in Fig. 7-1, Fig. 7-2, and Fig. 7-3. The steel grade of the HSS was ASTM A500 grade C and the MDC end plates were fabricated from ASTM A36 steel.

Tensile test coupons were taken from the same section of HSS tube used for all MDC types and the end plates for MDC1. The HSS coupon specimens possessed the tube curvature across its width. The MDC1 end plate coupon specimens were machined from the 3/4” thick plates into 3/8” thick plates to fit the end grips available within the Case Western Reserve University’s Structural Engineering Laboratory (CSEL) test setup. The coupon dimensions and tension test procedure were based on ASTM standard A370-12

(ASTM 2012). These coupons were used to determine the stress-strain behavior of the steel used to fabricate the MDCs.

7.1.1. MDC1 and MDC2 Experiments

7.1.1.1. Testing Setup

An illustration of the test setup arranged in the laboratory is shown in Fig. 7-4. The key components of the facility used for the experiments include the strong floor, L-shaped strong wall, a 55-kip actuator with 6 inch total stroke (+-3”), and (2) uni-directional shake tables (run quasi-statically in these experiments). Each shake table had a 22-kip force capacity and 10 inch total stroke (+-5”) and was attached to the strong floor or strong wall W1 in the positions shown in Fig. 7-4.

A reaction frame was designed and installed in the laboratory to resist loading from the 55-kip actuator. The reaction frame consisted of a vertical column (Reaction Frame, RF Column) to which the actuator was attached, a foundation beam (attached to the laboratory strong floor), and a diagonal brace between the RF column and foundation beam. The RF column and foundation beam were used in prior experiments in the lab and had adequate capacity for the MDC tests. Minor fabrication was performed on the RF column and foundation beam at connection points. The frame diagonal and lateral bracing were designed as part of this test setup. Due to errors in the diagonal brace fabrication, it did not completely bear on the foundation beam. A mortar pad was made to allow the base of the diagonal brace to fully bear on the foundation beam. The mortar pad was 1” thick at its highest location.

The specimen was installed between the vertical table (attached to strong wall W1) and a vertical column. The vertical column (Rocker Bearing, RB column) was supported at its base on a rocker bearing attached to the floor table. The top of the RB column was attached to the 55-kip actuator. The movements of the 55-kip actuator and the floor table allowed both translation and rotation of the RB column, which was then imposed on one end plate of the MDC specimen. In the MDC1 test, the 55-kip actuator was directly attached to the RB column using high-strength threaded rods with some “spacing” nuts. However, in the MDC2 experiment, there was a steel spacer section between the RB column and the actuator.

The entire setup was designed to the force limits of the equipment rather than the expected force demands from the specimens. Early MDC designs suggested that (2) 55-kip actuators would be necessary to supply appropriate force to deform and rotate the MDC specimens. All connections and the reaction frame were designed to remain within the elastic range under the application of a maximum lateral force of 132 kips ($2 \times 55 \text{ kip} + 22 \text{ kip}$) and a maximum vertical force of 22 kips to the MDC specimen. Final MDC specimen designs only required (1) 55kip actuator. The setup used in the experiments could apply a maximum lateral force of 77 kips ($55 \text{ kip} + 22 \text{ kip}$) and a maximum vertical force of 22 kips.

The floor table and actuator were capable of imposing translation and/or rotation to the RB column to apply an inward panel (-X, -x_L) translation, outward panel (+X, +x_L) translation, and/or rotation on one end plate of the MDC1 and MDC2 specimens. The differential movement between the floor table and the actuator created the rotation of the MDC specimen. The vertical table attached to the W1 strong wall provided a constant

gravity load (panel vertical in-plane, -Y) for the MDC2 test and held a constant position (Y) for the MDC1 test.

Lateral bracing was provided to both the RB column, which translated and rotated significantly during the tests, and to the RF column, which remained essentially stationary during the tests. The RB column had a lateral bracing system consisting of two anchors attached to the strong wall W2 and HSS sections spanning between the two anchors. The RB column was installed between the HSS sections, and a low-friction plastic was placed between the RB column and HSS sections to reduce the friction between the two components during test movements. This lateral bracing system allowed the RB column to move and rotate in the direction of the MDC specimen deformations, but stopped out-of-plane movement. The RF column also had a lateral bracing system that directly attached to the strong wall W2. It consisted of two plates, two threaded rods, and two Dwydag bars cantilevered from the strong wall and attached to the RF column. This bracing system ensured that the RF column did not move out of plane during the testing. The lateral bracing systems were designed based on the requirements of the AISC Specifications (AISC 2010b) Appendix 6.

A four channel MTS Flextest 60 controller, with a model number of 494.06, was used during all experiments. This controller utilized the MTS software model 793.10 MultiPurpose TestWare Version 5.6 to run all of the equipment and record all experimental data.

7.1.1.2. Loading Protocols

The experimental program was established for what is believed to be the most critical loading conditions for each MDC type. For instance, MDC1 participates in the blast

resistance of the panel but is also critical for the seismic drift compatibility scenario for corner panels. The MDC1 specimen was tested to simulate the seismic drift compatibility requirements for a façade corner panel where contact between panels from two perpendicular sides of the building is expected to occur. The load protocol requires application of a radially outward (tensile) deformation of the HSS tube of 3.1 inches (+ x_L direction) while simultaneously applying a rotation (about the horizontal) of 0.025 radians (about z_L axis). These deformations are based on basic deformation compatibility requirements of this connector when the building is at an inter-story drift of 2.5%. However, the test was run to deformations and rotations exceeding these design-basis deformations and to the stroke limits of the testing equipment. The deformation protocol for each of the controlled experimental channels and the intended resulting MDC1 deformations and rotations are illustrated in Fig. 7-5.

The MDC2 specimen test simulated the tributary façade panel gravity load to the MDC and the deformations and rotations resulting from the critical blast loading scenario. The wall shake table represented the building frame side and the RB column was the façade panel side of the MDC. This configuration allowed the maximum MDC deformations and rotations to be applied to the specimen. It fully utilized the stroke of the floor table while maintaining the gravity loading and rotation consistent with the loading and movement of the façade panel during the critical blast load scenario. The vertical shake table applied the tributary gravity load to a single MDC2 which was equal to 15.08 kips in z_L direction of MDC2. The gravity load was held constant on the single MDC2 over the entire test. This loading was applied vertically upward by the wall table, which represented the vertical support reaction provided on the building frame side. The design blast deformation

required applying a radially inward (compressive) deformation on the HSS of -4 inches (x_L direction) followed by a rotation (about the horizontal) of 0.105 radians (about y_L axis). The actual rotation of the specimen was limited to a slightly smaller value of 0.097 rad due to the stroke limits of the 55-kip actuator and floor table. The max translation applied in the experiment was reduced to -3 inches due to contact between the HSS and plate nuts. The translation was reduced to limit the influence of contact between the HSS and plate nuts in the experiment. Contact with the nuts is not considered in the design and was a design oversight. The HSS/nut contact could have been avoided by moving the connection hardware further from the HSS on the end plates. The -3 inch translation and 0.097 radians of rotation was followed by reversing the deformations to a radial translation of -0.945 inches (x_L direction) and rotation of +0.037 radians (about y_L axis) relative to the undeformed MDC shape. The simulated blast deformation history is based on nonlinear dynamic blast analyses (Section 9.3). The loading protocol for each of the controlled experimental channels and the intended resulting MDC2 deformations are illustrated in Fig. 7-6.

The MTS controller separately operated each piece of equipment in either a force or deformation-controlled mode. During the MDC2 experiment, the shake table on strong wall W1 was operated in force control mode to simulate the tributary façade panel gravity loading to MCD2. The wall shake table was run in displacement-controlled mode with a zero relative displacement during the MDC1 experiment because MDC1 does not support any of the façade panel gravity load. Both the floor shake table and 55kip actuator operated in deformation control in the MDC1 and MDC2 experiments. The deformation control

mode of these pieces of equipment simulated the translation and rotation imposed on the MDCs by the façade panel under the relevant loading scenario.

7.1.1.3. Instrumentation

The instrumentation layout for the MDC1 and MDC 2 experiments is shown in Fig. 7-7.

The following instruments were used to collect the raw experimental results:

- Strain gauges (SG1, SG2, SG3, SG4): Four Micro-Measurement EA-06-250BG-120/L strain gauges were attached to the RB column below the MDC. Two strain gauges were attached to each flange of the RB column, which is a W12x58 section. The readings from these gauges were used to determine the internal shear force and bending moment in the RB column. These RB column forces were then used to calculate lateral force and moment acting on the MDC.
- String potentiometers (SPot1, SPot2, SPot3, SPot4): Four Unimeasure HX-PB-10 string potentiometers were used to record the movement of the MDC during the test. Each string potentiometer had a 10 inch (+/-5") total range. SPot1 and SPot2 were set up to record the radial (x_L) movement of the MDC to obtain the MDC translation and rotation. The other two sting potentiometers were placed to record vertical MDC movement and differential movement between the MDC plates.
- Actuator Load Cells (F_{Act} , F_{HT} , F_{VT}) of the 55-kip Actuator, Horizontal (Floor) and Vertical (Wall) Shake Tables: All of the actuator and table load cell data was recorded during the experiments. The 55-kip actuator uses an MTS 661.22C-01 load cell. The 22-kip actuators in the horizontal

and vertical tables utilize MTS 661.20E-03 load cells. The actuator and the vertical wall table load cell data were used to calculate MDC loads. Although the horizontal floor table load cell data was recorded, it was not used in the MDC calculations.

- Actuator LVDTs (δ_{Act} , δ_{HT} , δ_{VT}): The movement of the 55-kip actuator and tables were recorded using the standard LVDTs for the MTS 244.22 and 244.31 actuators. This data was not used in the MDC deformation calculations because these LVDT measurements included elastic deformations of the test setup components and any slippage within connections of the experimental setup.
- Camera (δ_{HSS_1} , δ_{PP_1} , δ_{FP_1}): Both MDC1 and MDC2 experiments were recorded with a Panasonic HC-V700 video camera. Still shots of the video were used to estimate the relative deformations of the MDC1 HSS, panel plate, and frame plate at critical states during the tests.

Measuring the strains, displacements, and forces allowed for calculation of the following desired quantities: lateral force applied to MDC (F_{MDC_Lat}), vertical force applied to MDC (F_{MDC_Vert}), moment applied to MDC (M_{MDC}), total centerline displacement of MDC (δ_{MDC}), rotation of MDC (θ_{MDC}), and the local deformations across MDC1 (δ_{HSS_1} , δ_{PP_1} , δ_{FP_1}). All of these desired quantities are calculated from the measured instrument quantities except the local deformations across MDC1, which were estimated using video recordings of the test for each component of the MDC (end plates and HSS). The relevant dimensions between the strain gauges, string potentiometers, MDC, and equipment relevant to the MDC calculations are shown in Fig. 7-4 and Fig. 7-7. The lateral force

applied to the MDC (F_{MDC_Lat}) is equal to the sum of the 55-kip actuator load cell measurement (F_{Act}) and shear force in the RB column (obtained from the strain gauges):

$$F_{MDC_Lat} = F_{Act} + \frac{\frac{E_{steel} \cdot I_{x,RBC}}{d_{RBC}} \cdot (\varepsilon_{SG1} - \varepsilon_{SG2})}{H_{SG1}} \quad (7-1)$$

The vertical force on the MDC (F_{MDC_Vert}) was determined from the vertical wall table load cell:

$$F_{MDC_Vert} = F_{VT} \quad (7-2)$$

The moment applied to the MDC (M_{MDC}) is determined from the 55 kip actuator load cell and moment in the RB column (obtained from the strain gauges) and can be determined using the equation:

$$M_{MDC} = \frac{E_{steel} \cdot I_{x,RBC}}{d_{RBC}} \cdot (\varepsilon_{SG1} - \varepsilon_{SG2}) - F_{Act} \cdot (H_{Act} - H_{MDC}) - F_{MDC_Vert} \cdot e_{RBC} \quad (7-3)$$

The deformation applied to the MDC (δ_{MDC}) is determined from the string pots lateral movement measurement and calculated from the following:

$$\delta_{MDC} = \delta_{SPot2} + \frac{D_{MDC}}{D_{SPot}} \cdot (\delta_{SPot1} - \delta_{SPot2}) \quad (7-4)$$

The rotation applied to the MDC (θ_{MDC}) is also determined from the string pots lateral movement measurement and can be calculated using the following equation:

$$\theta_{MDC} = \tan^{-1}\left(\frac{(\delta_{SPot1} - \delta_{SPot2})}{D_{SPot}}\right) \quad (7-5)$$

7.1.2. MDC3 Experiment

7.1.2.1. Test Setup

While MDC1 and MDC2 required a specially designed and constructed experimental setup to simulate the critical hazardous loading scenarios, MDC3 utilized a self-reacting MTS 220-kip compression machine in the CSEL. The MTS 220-kip compression machine has a total stroke of 5.8 inches (+/-2.9"). A critical design loading scenario for MDC3 occurs during seismic loading and requires this MDC to carry the entire lateral seismic inertia force and the lateral force imposed during contact of the building corner panels. This MDC is intended to remain elastic under this loading scenario. The test's primary objective was to evaluate the maximum load carrying capacity of this MDC design. Therefore, this MDC is subjected to a large lateral shear force in the longitudinal HSS direction (z_L direction). Because the MDC3 end plates experienced fixed end conditions imposed by the building façade panel and connection to the perimeter frame, the MDC experiences equal and opposite end moments in addition to the applied shear. In the experiment, MDC3 was attached to loading arms and placed inside the compression machine load frame (Fig. 7-8). The loading arms allowed a compression force to be applied by the machine concentrically through the HSS centerline, which resulted in a shear force and equal and opposite moments on the two plates of the MDC. A cylindrical steel member was placed between the bottom load arm and the bottom of the loading frame to act as a roller bearing. At the top loading arm, the springhead of the actuator also acted as a bearing. These bearings ensured that only a concentric compressive force was applied to the loading arms during the experiment.

7.1.2.2. Loading Protocol

The controller applied a slowly ramped deformation history to the MDC3 specimen until it ran out of actuator stroke or the operator stopped the test. Translation was applied to the MDC at a rate of 0.00235 in/sec.

7.1.2.3. Instrumentation

The MTS 220kip compression machine was run using the same MTS 494.06 Flextest controller and 793.10 MultiPurpose TestWare Version 5.6 software as in the previously described MDC1 and MCD2 experimental setup.

The instrumentation used in this test is shown in Fig. 7-8. The following instruments were used to collect the raw experimental results:

- String potentiometers (SPot1_3 and SPot2_3): Two Unimeasure HX-PB-10 string potentiometers were used to record the movement of the MDC during the test. Each string potentiometer had a 10 in (+/-5") total range. One string pot was attached to each of the two MDC plates to record the vertical movement of each plate separately.
- Actuator LVDT (δ_{Act_3}): The deformation of the 220-kip actuator was recorded using the standard LVDT for the MTS 244.51 actuator. Although this data was recorded, it was not used to calculate relevant MDC3 data.
- Actuator Load Cell (F_{Act_3}): The 220-kip actuator in the compression frame uses a 661.31A-02 load cell to record the force it applies. The load cell force is equal to the applied longitudinal shear force on MDC3.

- Camera: The MDC3 experiment was recorded with a Panasonic HC-V700 video camera.
- Vic-3D V7 Digital Image Correlation (DIC) System (ϵ_{HSS} contours): Two cameras and software for the Vic-3D V7 system from Correlated Solutions were used to map the MDC HSS strain contours over the test. A white background with a black speckle pattern was painted onto one side of the MDC HSS. The dots in the speckle pattern were tracked by the DIC system throughout the test. The software analyzed the speckle pattern movement, which created strain contours on the HSS over the experiment length.

Measuring the displacements and forces allowed for calculation of the following desired quantities: shear force applied to MDC (F_{MDC_Shear}) and total differential displacement of MDC plates (δ_{MDC}). The vertical force that was applied to the MDC was determined using the actuator load cell:

$$F_{MDC_Shear} = F_{Act_3} \quad (7-6)$$

The differential movement between the MDC plates was calculated using the data from the string potentiometers. The actuator LVDT was not used because it recorded both the deformations in the MDC specimen and the deformations in the entire setup (loading arms, rocker bearings, bolted connections, etc.). The differential shearing movement between the MDC3 end plates is:

$$\delta_{MDC_3} = \delta_{SPot1_3} - \delta_{SPot2_3} \quad (7-7)$$

7.1.3. Experimental Test Results

7.1.3.1. Material Coupon Tension Test Results

A total of four tensile coupons were tested to examine the material properties of the MDC components. Two coupons were tested for both the MDC1 end plate material (specified as ASTM A36) and the HSS material (specified as ASTM A500 Gr. C). The results from these tests were intended to develop material stress-strain curves for the FEA models of the MDCs (Section 8).

The resulting stress-strain curves for the MDC1 end plate coupons are provided in Fig. 7-9. The yield stress of the MDC1 plate coupons was approximately 50 ksi. The measured plate yield stress met the criteria of A36 steel (36 ksi minimum). MDC1 was designed assuming that the plates would have a yield stress of $1.3 \cdot F_y$ (46.8 ksi), which is the expected yield stress ($R_y F_y$) for A36 steel based on the AISC Seismic Provisions (AISC 2010a). During the hardening phase, the MDC1 plate strain hardened from 50 ksi to approximately 70 ksi. The expected tensile stress ($R_t F_u$) from AISC (2010a) is equal to $1.2 \cdot 58$ ksi (69.6 ksi) and is consistent with the observed measurements. Overall, the MDC1 plate material behaved as expected. The coupon stress-strain data for the MDC1 end plates was used in the finite element models in the following section (Section 8).

The HSS expected yield stress ($R_y F_y$) and expected tensile stress ($R_t F_u$) were also determined using the AISC Seismic Provisions (AISC 2010a). The yield strength of the two HSS tensile coupons varied greatly. Coupon 1 had a yield stress of 52 ksi and coupon 2 had a yield stress of 36 ksi, which are significantly lower than the expected yield stress ($R_y F_y$) of 64 ksi (Fig. 7-10). Additionally, the coupons also had a tensile stress ($R_t F_u$) that

was lower than the expected value of 80.6ksi. These discrepancies may be due to the machining of the coupon and subsequent modifications required to adjust the coupon.

The HSS coupons were cut out of the HSS tube section that was used in the MDC fabrication such that the long side of the coupon was cut from the longitudinal dimension of the tube. The coupons possessed the HSS curvature across its width. Extracting these coupons from the tube is a more difficult and involved process than machining a coupon from plate. As a result, the dimensions of HSS coupons were more variable than those of the plate coupons. In order to allow the grips of the testing machine to sufficiently grip an appropriate area of the coupon ends, the curvature of the coupon ends needed to be reduced. The coupon ends were placed between two pieces of wood and flattened with an actuator applying a force of approximately 30 kips to the coupon ends. However, even after this flattening process, the coupon ends were too curved and slipped in the machine grips. The coupon ends were then ground down to a flatter surface using a surface grinder. This created a flattened surface on the coupon ends that could be appropriately gripped by the machine for tensile testing. Although the grip ends of the coupon were flattened before the tensile tests, the reduced section of both the coupons maintained the HSS tube curvature. During the tensile tests, the curvature of the reduced sections also flattened. This flattening visibly occurred very early in the coupon 2 test, but was not observed in the coupon 1 test until near the end of the test. Ultimately, the HSS coupon test results were deemed unreliable and are not used as the basis for the material model of the finite element analysis of Section 8.

7.1.3.2. MDC1 Specimen Test Results

During this experiment, MDC1 was deformed to +4.53 inches in the tensile direction ($+x_L$) while simultaneously rotated (about z_L axis) +0.0357 radians. This deformation and rotation was beyond the design-basis deformations of +3.1 inches and +0.025 rad. These deformations were limited by the equipment stroke limits. Fig. 7-11a shows the deformation and rotation of the MDC throughout the experiment. MDC1 was designed to allow yielding of both the HSS and its end plates in order to accommodate the seismic drift compatibility requirements. Forcing all of the deformation onto the HSS alone would have resulted in an increase in force due to the large deformation stiffening of the HSS. The MDC component contributions to the total deformation are shown in Fig. 7-11b. The MDC plates began deforming approximately at +0.2 inches and a rotation of +0.0025 radians. At +3.1 inches of translation and +0.025 radians of rotation, the HSS deformed approximately +1.8 inches, the panel plate deformed about +0.6 inches, and the frame plate also deformed about +0.7 inches. At the maximum MDC displacement of +4.53 inches, the HSS deformed +2.2 inches, the panel plate approximately deformed +1.3 inches, and the frame plate deformed +1.0 inch. The MDC experienced a maximum force of 59 kips of tension and a maximum moment of 58 kip-ft, which both occurred at a +4.23 inches of deformation (Fig. 7-11c-d).

7.1.3.3. MDC2 Specimen Test Results

Initially, a gravity load of 15.08 kips was applied to MDC2, which was held constant throughout the experiment (Fig. 7-12b). Then, a deformation of -2.75 inches (compression) was applied to the MDC. That deformation was maintained while a rotation

of -0.087 radians was applied. Then, a compressive deformation of -0.96 inches and a rotation of $+0.031$ radians (both relative to the original MDC position) were applied to the MDC. All of the deformations and rotations throughout the experiment are available in Fig. 7-12a. As with MDC1, the prescribed movement of the tables and actuators were intended to create the desired MDC deformation and rotations described above. However, the experimental setup components between the actuators and the MDC also deformed, reduced the deformation and rotation applied at the MDC location. MDC 2 experienced a maximum force of 23.3 kips of compression and a maximum moment of 43 kip-ft. Both of these maximum values occurred when the MDC was deformed to -2.75 inches and rotated to -0.087 radians. The nuts that attached at the MDC2 end plates to attach to the test equipment contacted the HSS at about -0.75 inches of compression ($-x_L$) and any further compression. The resulting HSS deformation at a nut location is pictured in Fig. 7-12f. MDC2 absorbed approximately 43 kip-inches of energy throughout the entire experiment. The design energy absorption was 42.4 kip-in. This energy absorption was determined using the trapezoidal rule for the area under the force-deformation curve in Fig. 7-12c from the undeformed position at 0 inches to the maximum displacement of -2.78 inches:

$$energy = area = \Delta x \cdot \left(\frac{y_0}{2} + y_1 + y_2 + \dots + \frac{y_n}{2} \right) \quad (7-8)$$

After the initial experiment, MDC2 was deformed in three further experiments. Experiment 2 applied nearly the same deformations and rotations as experiment 1. Experiment 3 and 4 applied -4.0 inches of compression ($-x_L$) to MDC2 and did not apply any rotation (Fig. 7-13a). All four of the experiments applied the 15.08 kip tributary gravity load to MDC2 (z_L direction) (Fig. 7-13b). Over the course of the experiments, the

maximum force on MCD2 increased (Fig. 7-13c). Ultimately, at the end of Experiment 4, MDC2 failed. The HSS fractured outside the plate weld locations on both the frame and panel plate. The HSS entirely separated from the frame plate and partially separated from the panel plate (Fig. 7-13d).

7.1.3.4. MDC3 Specimen Test Results

The resulting force-deformation plot for the MDC3 specimen is shown in Fig. 7-14b. The data recorded by the instrumentation had a noticeable variance throughout the experiment. The data was modified by finding a linear approximation from 0 inches to 0.075 inches and 0.75 inches to 0.22 inches of MDC translation. This linear modification created a smoother force-deformation curve. The specimen behaved linear-elastically to a loading of approximately 140 kips, which was the design elastic strength. At its limit, MDC3 experienced approximately 0.27 inches of differential movement between the MDC plates and a maximum force of 172 kips. After about 0.27 inches of deformation, the loading arms began to rotate out-of-plane and the force applied to the MDC began to decrease. Tearing of the HSS just outside the weld bar (connected into the end plate) was observed as seen in Fig. 7-14d and is believed to have triggered an asymmetric failure mode resulting in torsion and twisting of the specimen. The test was stopped due to the out-of-plane rotation of the loading arms. In Fig. 7-14c, a clear yield line is visible on the HSS in the picture at the ultimate displacement. This yield line began developing about half way through the experiment and continued to propagate until the full yield line appeared.

The Vic-3D DIC software and cameras recorded the HSS speckle pattern movement throughout the experiment. The first principal strain contours at points throughout the experiment, including the design loading of 135 kips, are available in Fig. 7-15. The

cameras and software did not recognize small areas within the speckle pattern, so there are small areas on the HSS that do not have principal strain data available. The DIC recorded principal strain contours that were roughly symmetric about the center (z-direction) of the HSS.

7.1.4. Summary of Phase I Tests

All of the MDC designs and tensile coupons were experimentally tested in the CSEL. Four tensile coupons were tested for the MDC materials, including two plate coupons and two HSS coupons. The plate coupons produced results close to the expected stress-strain curves for A36 steel. However, the HSS coupon results were drastically different from the expected stress-strain curves for A500 grade C steel. This discrepancy may be due to the machining and flattening of the coupon. The plate coupon data was used in the following finite element models, but the HSS coupon data was not utilized for the models.

The MDC1 and MDC2 designs were tested in a custom experimental setup designed to apply gravity loads, lateral translations, and rotations. MDC3 was tested in an MTS 220-kip compression frame that applied a shear deformation to the MDC. Each MDC was tested using a loading protocol based on its controlling hazardous loading condition. All raw strains, deformations, and forces were recorded from the equipment and through additional instrumentation as applicable for each experiment. This raw data was used to create force-deformation curves for each MDC, which confirmed each MDC design and will be used to validate the finite element models described in Section 8. A comparison of the design objectives and the recorded experimental values are available in Table 7-2. The MDC1 experimental results showed that the maximum tensile force was within about 11%

of the design maximum tensile force. In the experiment, the MDC1 HSS translated more than expected from the design while the MDC1 plates translated less than expected. MDC2 dissipated 1.5% more energy than anticipated in the design. MDC2 had a higher maximum compressive force than the design maximum compressive force. MDC3 remained elastic up to the 140 kips design elastic strength. It experienced an ultimate strength of 172 kips.

7.2. Experimental Testing Phase II: MDC Rolling Tests (Seismic In-plane Drift Load Case)

7.2.1. Introduction

A series of experimental tests were performed in the summer of 2018 at the Case Western Reserve University Vanderhoof Research and Education Facility to examine the response of multi-hazard ductile connectors (MDCs) considering “rolling” action of the round HSS tubes, which provide strength and ductility to foster improved performance of façade systems subjected to various hazardous load effects. During a previous iteration of the proposed multi-hazard façade system (MHFS) design methodology (Configuration 1), all MDCs had HSS tubes with their longitudinal axes oriented vertically. While this configuration appeared satisfactory considering all potential hazards and performance objectives, some questions remained regarding the connectors’ capacity to accommodate large inter-story drifts due to seismic events via rolling action of the HSS tubes along the top and bottom panel edges. Although finite element analyses (FEA) of this behavior suggested peak plastic strains which exceed failure prior to reaching the target deformation, a previous MDC experimental test where an HSS tube was radially crushed while maintaining a longitudinal shear load suggested that the analytically-predicted failure was

perhaps premature. This uncertainty in the predicted rolling deformation capacity prompted the performance of the experimental tests described in the following sections.

7.2.2. Test Specimen

A prototype MHFS was designed for an office building located in Los Angeles, CA with three stories measuring thirteen feet each and thirty-foot bay widths. The façade system was chosen as a normal-weight (145 pcf) reinforced concrete panel type with nominal dimensions of 13'x30'x6" (height by width by thickness). The panel was assumed to be on the top story of the building to maximize design seismic and wind forces; the panel type was also chosen to maximize mass and, therefore, seismic inertia forces. The final MDC design for this prototype building and panel used two HSS6x0.375 lengths at the top and bottom edges of the panel (four MDCs total), with nine inches per top-edge MDC and 4.5 inches per bottom-edge MDC. The 4.5-inch long tubes were chosen for testing because all rolling mechanics are—aside from some minor anticlastic bending effects—a linear function of tube length, and the predicted force required to reach the maximum desired deformation (barring failure) of this shorter tube could be achieved with available laboratory equipment. Fabrication drawings of the design are shown in Fig. 7-16. Bolt slots or oversized (greater than standard) bolt holes were not specified for the test specimen despite their inclusion in this MHFS connector configuration because the intent of these tests was to evaluate the HSS tube itself, not necessarily the MDC connector's function (including bolt slots) as a whole. The size and location of bolt holes (and, consequently, the plate dimensions) were chosen to conform with existing adapter plates, which were fabricated for prior MDC tests. Three identical specimens were ordered for fabrication by

the same local steel fabricator that was used for the previous tests due to the quality of those specimens and for consistency.

7.2.3. Deformation Protocol

The intent of these tests was to evaluate the performance of the proposed MDC configuration during seismic (in-plane) story drifts. Preliminary analytical nonlinear dynamic analysis of the proposed MDC configuration suggested that peak MDC rolling deformations were generally equal to or slightly greater than peak inter-story drifts. The seismic prequalification testing protocol for beam-to-column moment connections in AISC 341-10 (AISC, 2010a) Chapter K was chosen to formulate an appropriate specimen deformation time history because it is a function of story drift (as opposed to, say, member hinge rotation specified for other seismic prequalification deformation protocols). This protocol consists of incrementally larger sets of story drift cycles (plus/minus excursions of a given amplitude) to perform until failure. The story drift and corresponding deformation protocol chosen for testing are provided in Table 7-3. Note that this protocol does not end at the last set of two cycles at ± 0.04 radians, but continues until failure with sets of two cycles with drifts increasing by 0.01 radians after each set however; failure of the specimen was expected prior to this stage. Successful completion of the protocol is defined as the completion of all cycles up to and including the maximum expected inter-story drift without failure. A target inter-story drift of 2.5% (3.9 inches for a 13-foot story height) was chosen for the MDCs as this is the limit for newly constructed buildings.

The deformation protocol given in Table 7-3 was turned into a pseudo-static, saw-tooth deformation time history with several-second pauses between cycle sets and at all deformation peaks. A similar low-amplitude test protocol was also formulated consisting

of two cycles within the specimen's elastic deformation range to check instrumentation output and correct for any difference between displacement commands and deformation readings due to bolt slippage. A dynamic test was proposed which would prescribe a story drift time history from a prototype moment frame building with peak drift at 2.5% when subjected to a scaled ground motion record across the specimen; however, this test was not performed due to the results of the cyclic, pseudo-static testing. A high-cycle fatigue testing protocol based on temperature fluctuation effects on the reinforced concrete panel was also investigated, however the decision was made to abandon this test as it would potentially damage laboratory equipment (e.g. shake table bearings). For all tests, specimen deformation protocols had to be appropriately split between actuator signals in the proposed test setup to ultimately achieve the desired deformation across the specimen.

7.2.4. Test Setup and Instrumentation

Testing the specimen to the desired deformation presented a challenge due to the lack of a single hydraulic actuator with adequate force capacity and stroke to perform the test to failure, assuming the specimen was able to achieve larger rolling deformations than predicted via FEA (as was the case for HSS tube crushing experimental tests). The Vanderhoof laboratory includes four unidirectional shake tables, each powered by a 22-kip hydraulic actuator with a stroke of +/- 5.25 inches. A 55-kip capacity, +/- 3.25" stroke actuator was also available. If the specimen were to survive to a rolling deformation of, say, five inches, FEA results indicated that a force of about 25 kips would be required, with a sharp increase in force after this point (about 60 kips required at six inches). This force cannot be achieved by the longer stroke (22-kip) actuators, and the target deformation (at least 3.9 inches) cannot be achieved by the stronger (55-kip) actuator.

The solution to this issue—illustrated in Fig. 7-17 and Fig. 7-18—was to: (1) utilize two shake tables, each powered by two actuators – one “internal” 22-kip actuator installed within the table, and one “external” actuator attached to the tabletop; (2) distribute the specimen deformation protocol amplitude between the two tables (both internal and external actuators) and run these protocols in opposite directions; and (3) link the specimen to both tables via a loading beam, resulting in a total deformation across the specimen equal to the full amplitude protocol. With this setup, the force capacity of each table is increased due to multiple actuators running in parallel, and the deformation capacity across the specimen increases by applying displacements on both sides of the specimen. A 22-kip actuator was used as the external Table 1 actuator and installed on the strong wall and tabletop (via an adapter fabricated in-house). The 55-kip actuator was used as the Table 2 external actuator because the last remaining 22-kip actuator was installed on a shake table mounted to the strong wall which could not be removed without significant effort; additionally, this test setup allowed the test to be performed without the need for the extra stroke afforded by using a 22-kip external actuator as opposed to the 55-kip actuator. The 55-kip actuator was installed on a reaction column attached to a foundation beam, which was tensioned to the laboratory strong floor. With this setup, a maximum force capacity of 44 kips—limited by the two 22-kip actuators powering Table 1—and maximum stroke of +/- 8.5”—5.25” from Table 1 plus 3.25” from Table 2 (limited by 55-kip actuator)—could be achieved. These limits were believed to be likely adequate to perform the desired tests.

The loading beam was adapted from previous MDC tests where it served as the pseudo-façade panel for quasi-static blast and seismic corner panel contact testing. The

rocker bearing attaching the loading beam to Table 1 has a single large pin, which effectively provides an idealized “pinned” boundary condition with zero moment resistance. This boundary condition was desired to allow the beam to rotate with the specimen, approximating the “free” other degree-of-freedom constraint as discussed in Section 8. Note that this is not an exact recreation of the “free” condition because the rocker bearing is essentially fixed to the tabletop, preventing the beam from dropping vertically as the specimen deforms radially. In reality, the boundary condition is likely somewhere between the “free” and “fixed” conditions; therefore, this configuration was believed to be reasonably realistic. The specimen is attached to fastener plates on either side, and the adapter plates connect to the loading beam and tabletop via threaded rod as shown in Fig. 7-17. These Adapter plates were fabricated for the previous MDC tests to account for misalignments between the shake table(s) and rocker bearing and load beam assembly. Spacer plates and extra nuts and washers were added along the free span of threaded rods to increase the cross section to resist bending demands during loading (checked and confirmed to be less than the bending capacity of the bars). The shearing action performed in these tests necessitated calibrated torquing of all slip-critical connections to minimize slippage.

Lateral bracing was devised and constructed to prevent lateral instabilities during testing due to eccentric loading and/or buckling of the loading beam. This scheme consisted of two towers installed on each shake tabletop, with one tower on either side of the loading beam. A rectangular HSS tube sections coated with a polymer material (to reduce friction) extended to contact the beam flanges, thereby bracing it against any lateral motion. The two towers on the Table 2 (where the specimen was installed) were connected

at the top via a welded length of steel angle section to increase the torsional stiffness of the bracing near the specimen.

An instrumentation plan was developed to capture all measured quantities of interest during testing. The primary quantities of interest were the force and deformation applied across the specimen. The instrumentation inventory and illustration of the plan are provided in Table 7-4 and Fig. 7-19, respectively. All actuators include a built-in load cell for measuring force, and linear variable displacement transducer (LVDT) for measuring displacement. These measurements could be used to determine force and deformation across the specimen; however, a more direct measure of these quantities was desired due to the multitude of slip-critical connections in-series between the actuators and specimen. A group of four strain gauges was installed on a clear span on the loading beam between the rocker bearing and specimen as shown in Fig. 7-19 to calculate applied force using another method. The average strain of strains of top and bottom of a given cross section can be used to calculate axial force in the beam, which should equal the rolling force applied to the specimen. This strain gauge array can also be used to calculate bending moment and shear force diagrams of the loading beam throughout the test. String potentiometers (string pots) were installed on the top and bottom specimen adapter plates to calculate rolling deformation closer to the specimen. Another string pot was installed on top of the upper adapter plate to monitor radial deformations of the specimen; the housing of this string pot was placed on the overhead crane near the ceiling in the lab to minimize the angle of the measurement line with respect to vertical as the measurement point displaces laterally. A final string pot was planned to measure out-of-plane

deformations of the specimen however; this instrument was not included in the final test setup.

A set of photographs of the finished test setup are provided in Fig. 7-20 through Fig. 7-22. Fig. 7-20 shows the elevation view (as illustrated in Fig. 7-17), with a closer angle and additional details shown in Fig. 7-21. The lateral bracing can clearly be seen in Fig. 7-21, as well as the external actuator connection to Table 2 and the location of string pots to measure specimen displacement. The housing of these string pots were attached to the reaction column (where the 55-kip external Table 2 actuator was attached) rather than somewhere between the two tables as shown in Fig. 7-19. Detailed photos of the specimen installed within the setup before and after testing, as well as the failure surface of the section, are shown in Fig. 7-22.

7.2.5. Results

Some diagnostic tests were performed prior to installation of the test specimen, after which any deformations prescribed to any actuators would impose deformations across the specimen. The full-amplitude cyclic loading protocol was performed with all actuators running simultaneously to ensure the correct orientation was assigned to their respective displacement inputs. The external actuators were then attached to the tabletops and the test was repeated to monitor any potential feedback issues with multiple actuators driving one table. Time histories of actuator displacement signals (input) and readings (output) are shown in Fig. 7-23, with no discernable difference between the signals and readings. This test indicated that there were no problems running multiple actuators in-parallel, with only a small amount of force feedback observed in the 55-kip (Table 2 external) actuator. This is to be expected due to all other actuators being the same model, however the 55-kip

actuator has excess force capacity for the setup (limited to 44-kips by the combined Table 1 actuators) therefore this force feedback was not considered an issue. With the actuators working properly, the specimen was then installed. Small small-amplitude tests were performed with peak deformations within the specimen elastic range to check instrumentation output and attempt to identify and correct for any slippage in the setup. Some differences were observed in the prescribed and measured displacements; therefore, some adjustments were made to the deformation protocol to achieve the target displacement in each cycle. After making this correction, the full-scale cyclic test was performed.

String pot readings for the full-scale cyclic test are shown in Fig. 7-24. The summation of the two specimen string pot readings was used to calculate deformation across the specimen. This displacement is compared to the target (Table 7-3) and corrected deformation protocols in Fig. 7-25. The adjustments for slippage made to the target deformation protocol were successful in achieving the desired deformation, with errors on the order of hundredths of an inch. Some vertical displacement (radial specimen deformation) was observed, specifically at higher rolling deformation cycles. Note that this vertical deformation is all in one direction—positive indicating extension of the string pot corresponding to inward (crushing) radial deformation of the specimen, which is expected, based on the mechanics and observed FEA behavior.

Actuator load cell readings are shown in Fig. 7-26. The distribution of forces between internal and external actuators is different in the two tables; Table 1 is primarily drive by the external actuator, while Table 2 is mostly driven by the internal actuator. This is likely due to Table 1 having two identical actuators installed, and the external actuator

having perhaps a more direct load path to the loading beam than the internal actuator, while the response time (rate of hydraulic fluid flow) in the larger 55-kip actuator may allow it to simply lag slightly behind the internal 22-kip actuator, which responds quicker and, therefore, carries most of the force. Strain gauge readings are shown in Fig. 7-27, which indicate fairly stable (non-noisy) readings despite operating in a very small strain range. The rolling force across the specimen calculated from load cells and strain gauges are shown in Fig. 7-28. These calculated rolling forces seem to indicate that more force was required to impose deformations in one direction, which is likely a function of the test setup. Because the source of this behavior was unknown but consistent between both the strain gauge- and load cell-calculated rolling force, the strain gauge forces were believed to be more reliable as there are fewer connections between their locations and the specimen. Additionally, the axial force—which can be calculated from just two strain gauges—must be constant over the clear span, therefore having two pairs of gauge readings available lends some redundancy to the rolling force calculated using these instruments. The average of the applied rolling force calculated from the two pairs of strain gauges was taken as the most accurate measure of rolling force applied during the test.

The specimen rolling force-deformation hysteresis from the static cyclic test to failure is shown in Fig. 7-29 (entire curve) and Fig. 7-30 (detailed view). Results from FEA models and the theoretical HSS tube rolling force-deformation relationship are compared to these results. The experimental specimen elastic stiffness appears to be slightly higher than either the FEA or theoretical results, which match very closely. The FEA models match the transition from elastic to plastic behavior, with the theoretical (design) curve precisely predicting the onset of yield. At larger deformations, the test

specimen follows the “free” FEA model results fairly well, with some degradation of strength, which is not captured by the analytical models.

Failure of the specimen occurred during the 2.34” target displacement cycles due to fracture of the HSS tube wall right outside of the weld location as identified in Fig. 7-22. This failure location matches the FEA results, where the maximum equivalent plastic strains occurred in this region. The maximum deformation at failure matched the prediction as well (Section 9.2.1.4). Two specimens performed this full-amplitude test, with both failing during the same cycle; the results of the second specimen test are shown here as additional corrections were made to the displacement signals based on feedback from the first specimen’s full-amplitude test. The first specimen also failed along the HSS tube’s weld seam, which happened to be located right outside the HSS-to-plate weld location with maximum expected plastic strain. The decision was made to rerun the same test with a second specimen, whose HSS weld seam was not located near the plastic hinge region, however the same failure mode was observed at the same deformation amplitude.

7.2.6. Summary of Phase II Tests

Experimental tests were performed to evaluate the rolling deformation capacity of round HSS tubes to potentially accommodate inter-story drifts in an MDC application. A deformation protocol based on AISC 341-10, Chapter K for prequalified seismic beam-to-column moment connections was developed for testing, and a setup was devised and constructed in the CSEL. The tests were performed successfully, with the desired deformation protocol matching the measured specimen deformation almost exactly across all cycle amplitudes. Two specimens were subjected to the same deformation protocol, both of which failed during the +/- 2.34” deformation cycles. Failure of the specimens

well below the target minimum deformation of 3.9" (2.5% inter-story drift) prompted the abandonment of additional (seismic dynamic) planned testing, as well as this MDC layout/configuration.

Table 7-1: Nominal Dimensions of MDC Specimen Components

Specimen Design	HSS Diameter	HSS Wall Thickness	HSS Length	MDC End (Panel/Frame) Plate Thickness
MDC1	6.0in	0.25in	8.0in	0.75in
MDC2	6.0in	0.25in	13.5in	0.75in
MDC3	6.0in	0.25in	16.5in	1.0in

Table 7-2: Comparison of MDC experimental results to design values

MDC 1	Maximum Tensile Force (kips)		Maximum HSS Translation (in)	
	Design	Exp.	Design	Exp.
	45.9	50.7	1.6	1.95
	Maximum Panel Plate Translation (in)		Maximum Frame Plate Translation (in)	
	Design	Exp.	Design	Exp.
	0.75	0.58	0.75	0.58

MDC2	Energy Dissipation (kip-in)		Maximum Compressive Force (kips)	
	Design	Exp.	Design	Exp.
	42.4	43.0	19.1	23.3

MDC3	Elastic Strength (kips)		Ultimate Strength (kips)	
	Design	Exp.	Design	Exp.
	135	140	N/A	172.2

Table 7-3: Seismic Qualification Testing Displacement Protocol

Cycles	Story Drift (rad)	Displacement (in)
6	0.00375	0.585
6	0.005	0.78
6	0.0075	1.17
4	0.01	1.56
2	0.015	2.34
2	0.02	3.12
2	0.03	4.68
2	0.04	6.24

Notes: Protocol per ANSI/AISC 341-10.
Displacements for 13' story height.

Table 7-4: Instrumentation Inventory

Channel	Name	Type	Location	Units
1	D1i	LVDT	Internal Table 1 (w/rocker bearing) 22-kip actuator	inches
2	F1i	Load Cell	Internal Table 1 (w/rocker bearing) 22-kip actuator	kips
3	D1e	LVDT	External Table 1 (w/rocker bearing) 22-kip actuator	inches
4	F1e	Load Cell	External Table 1 (w/rocker bearing) 22-kip actuator	kips
5	D2i	LVDT	Internal Table 2 (w/specimen) 22-kip actuator	inches
6	F2i	Load Cell	Internal Table 2 (w/specimen) 22-kip actuator	kips
7	D2e	LVDT	External Table 2 (w/specimen) 55-kip actuator	inches
8	F2e	Load Cell	External Table 2 (w/specimen) 55-kip actuator	kips
9	SG1	Strain Gauge	Loading beam top flange closer to strong wall	μ strain
10	SG2	Strain Gauge	Loading beam bottom flange closer to strong wall	μ strain
11	SG3	Strain Gauge	Loading beam top flange closer to foundation beam	μ strain
12	SG4	Strain Gauge	Loading beam bottom flange closer to foundation beam	μ strain
13	SP1	String Pot	Specimen top adapter plate (lateral)	inches
14	SP2	String Pot	Specimen bottom adapter plate (lateral)	inches
15	SP3	String Pot	Loading beam flange at specimen location (vertical)	inches
16	SP4	String Pot	Specimen top adapter plate (out-of-plane)	inches

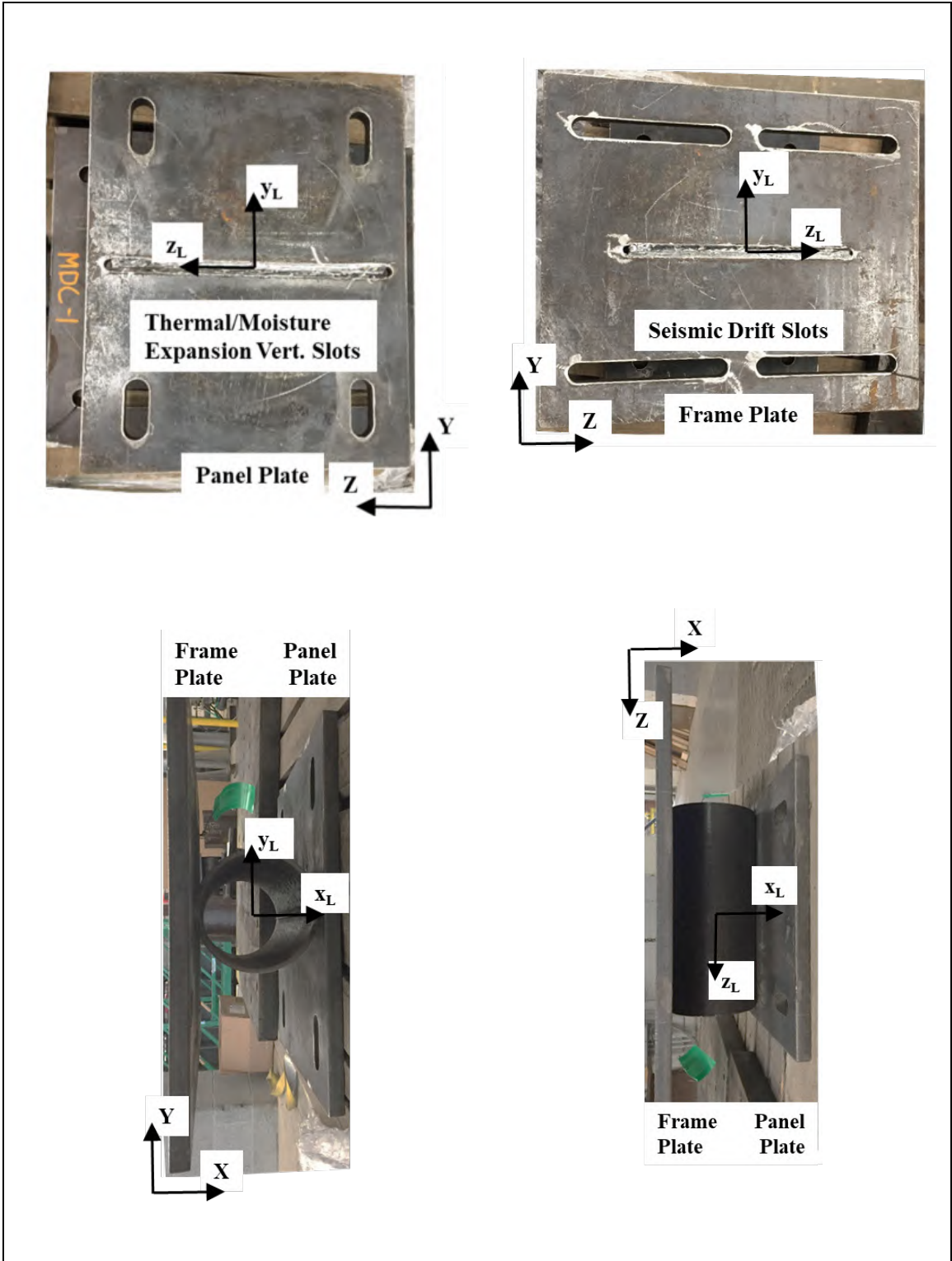


Fig. 7-1: MDC1 axes and details

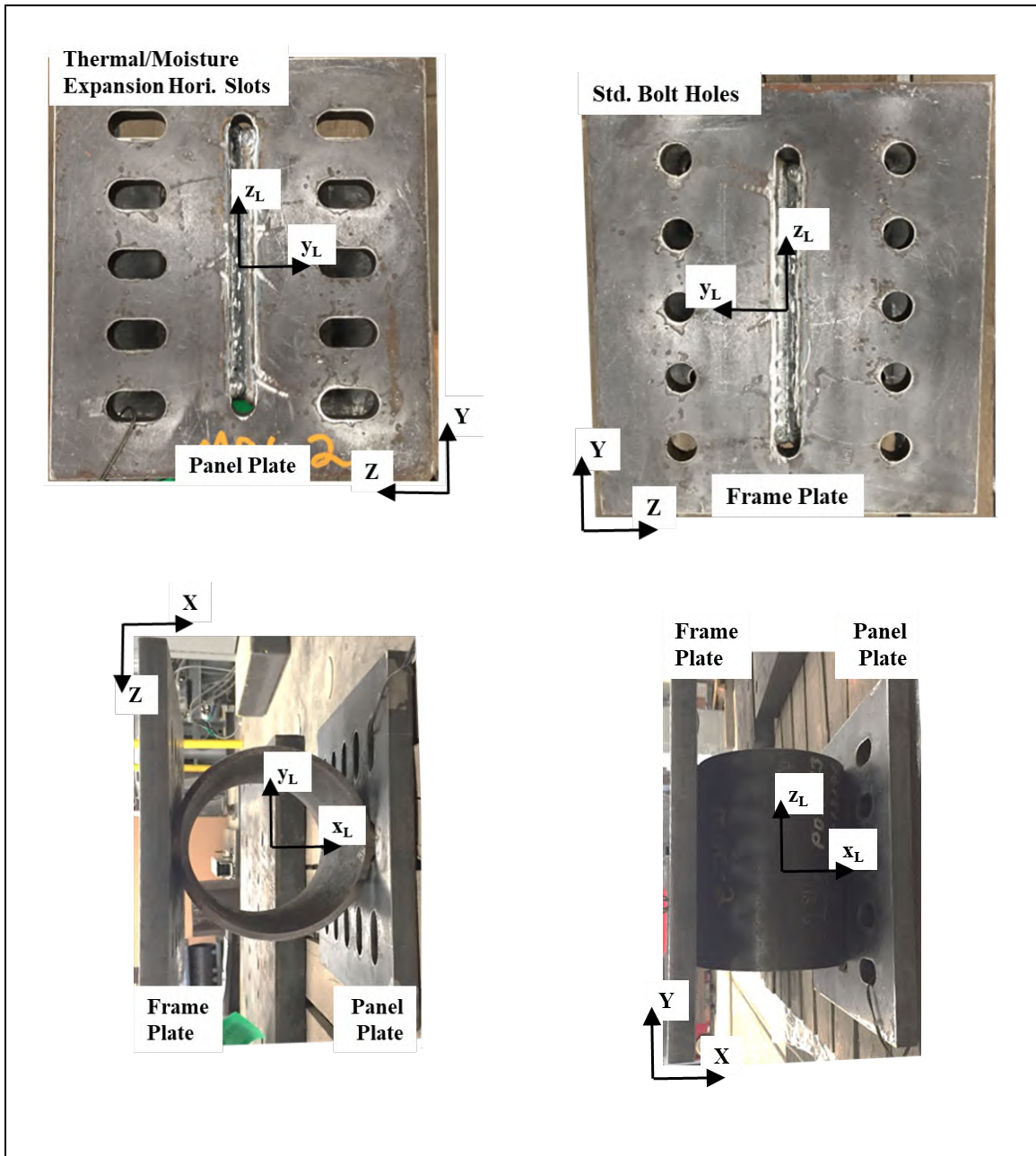


Fig. 7-2: MDC2 axes and details

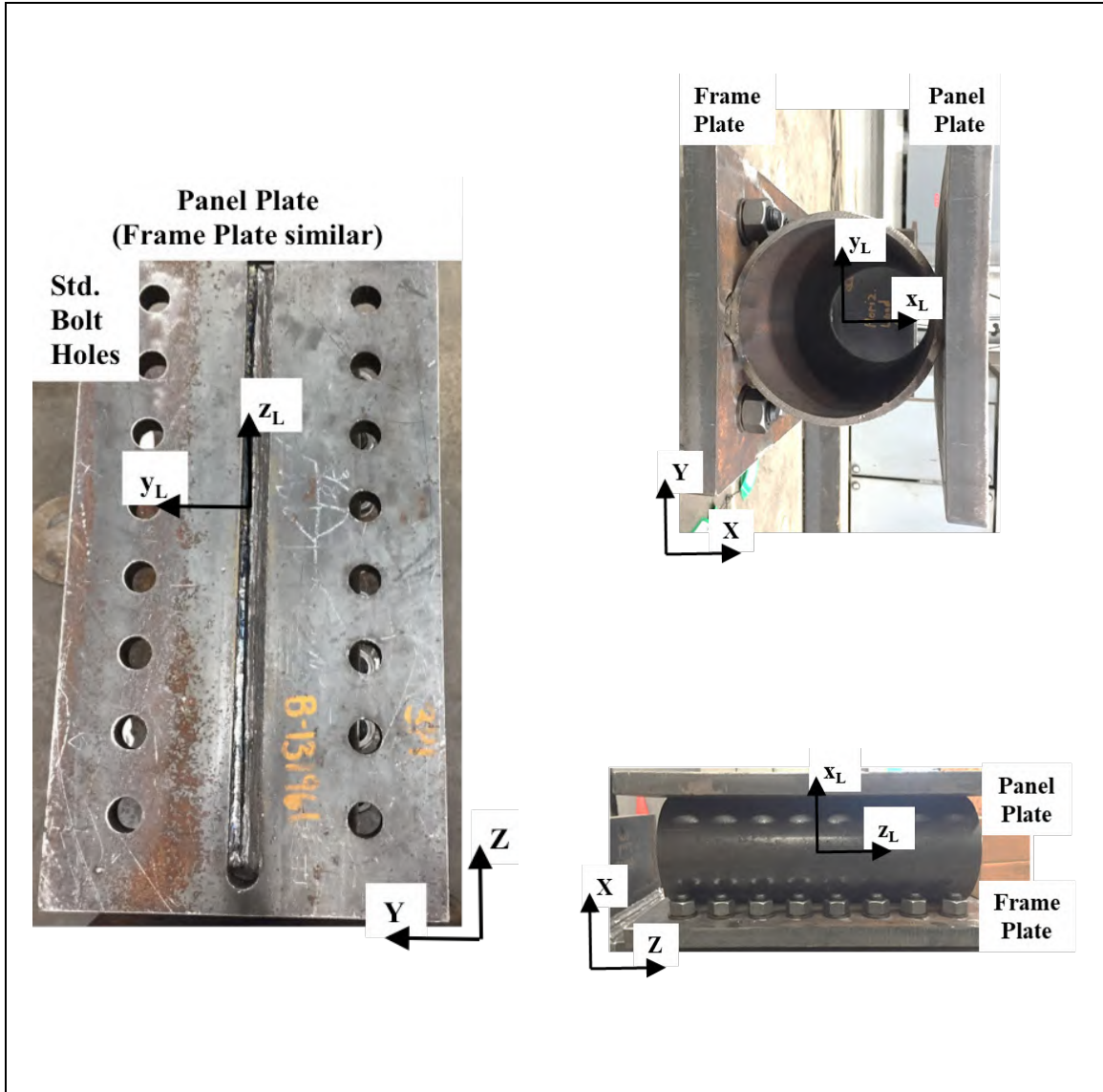


Fig. 7-3: MDC3 axes and details

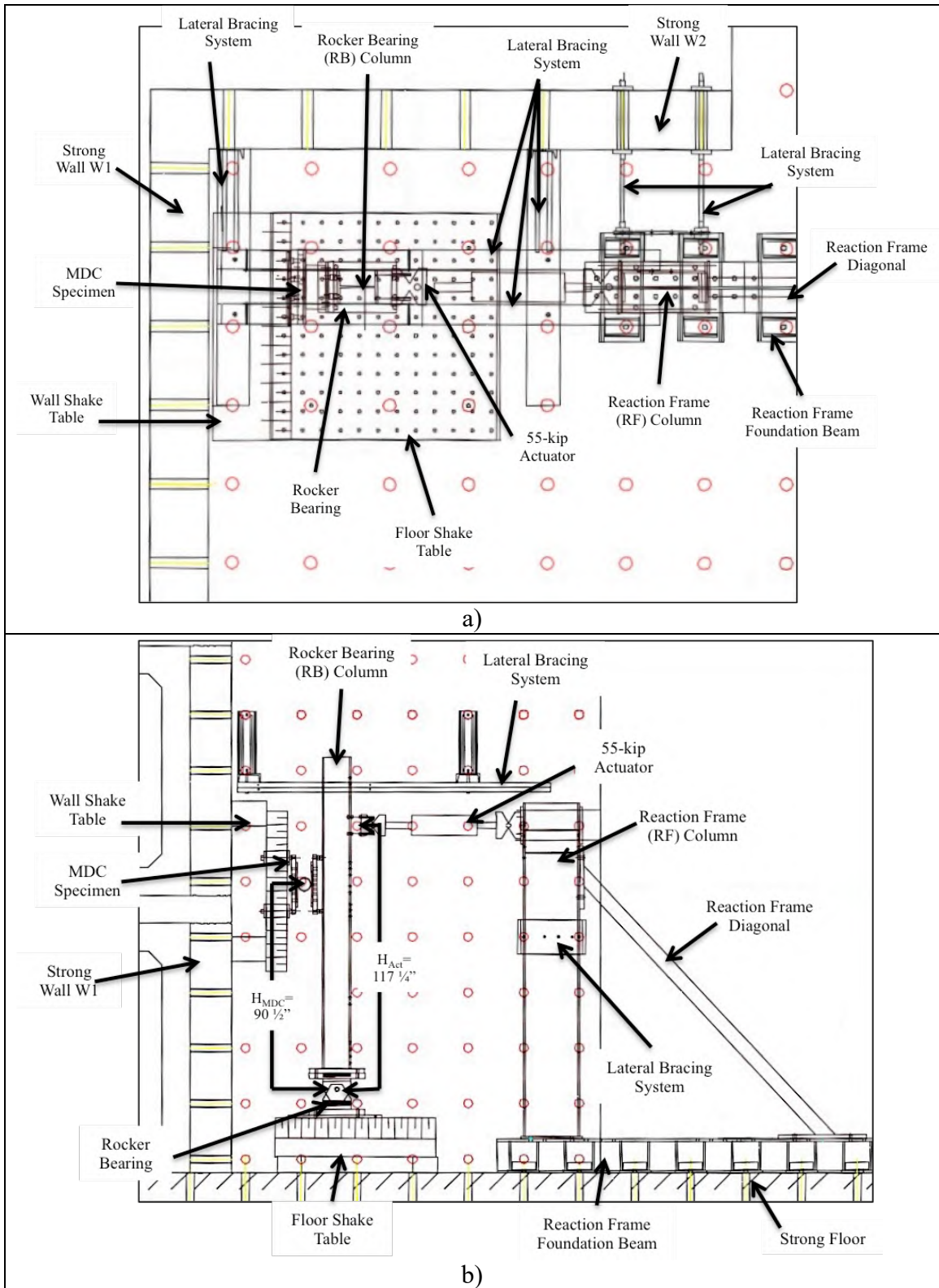


Fig. 7-4: Experimental Setup a) Plan view of the laboratory with test equipment b) Elevation view of the laboratory with test equipment

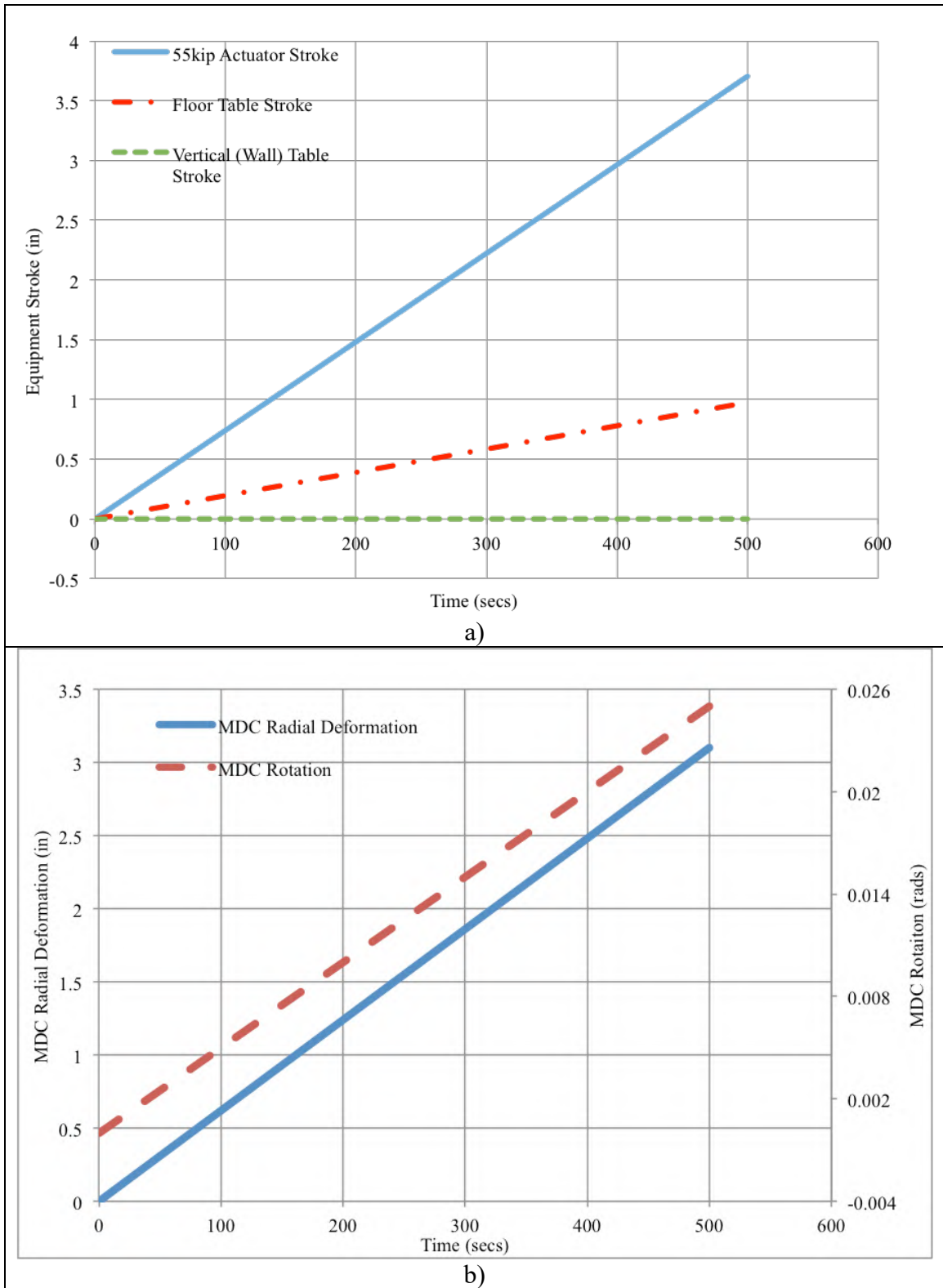
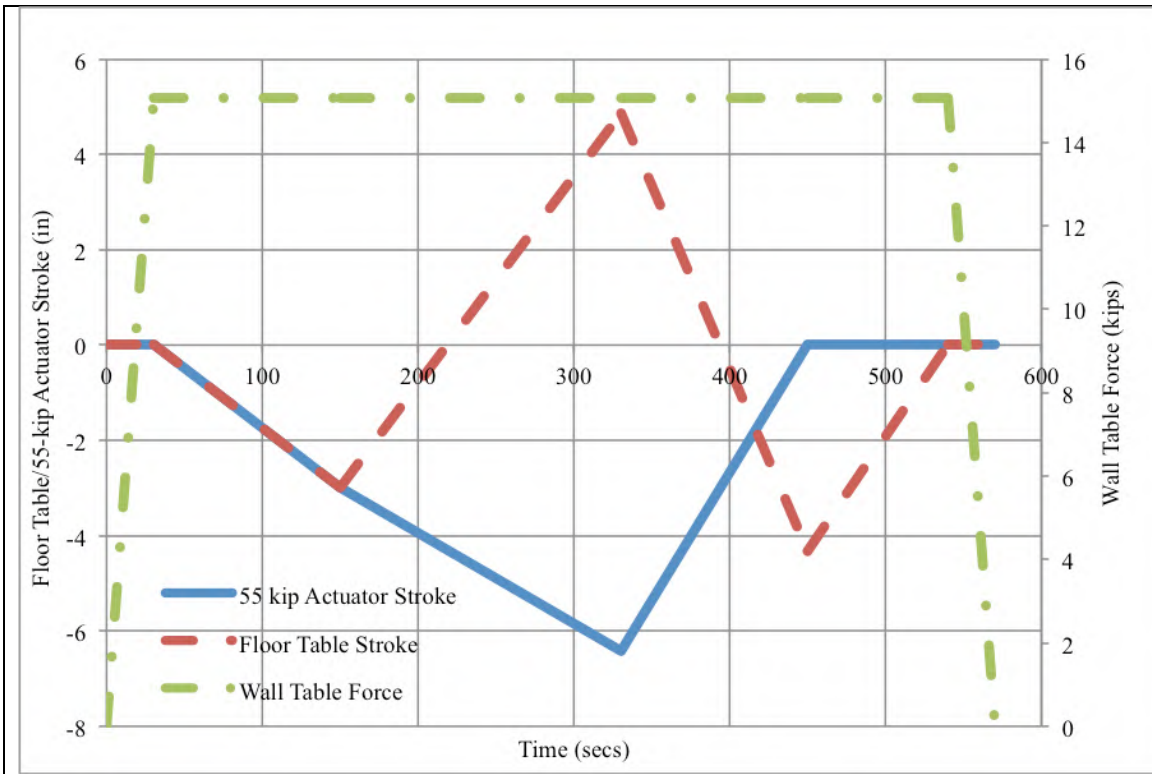
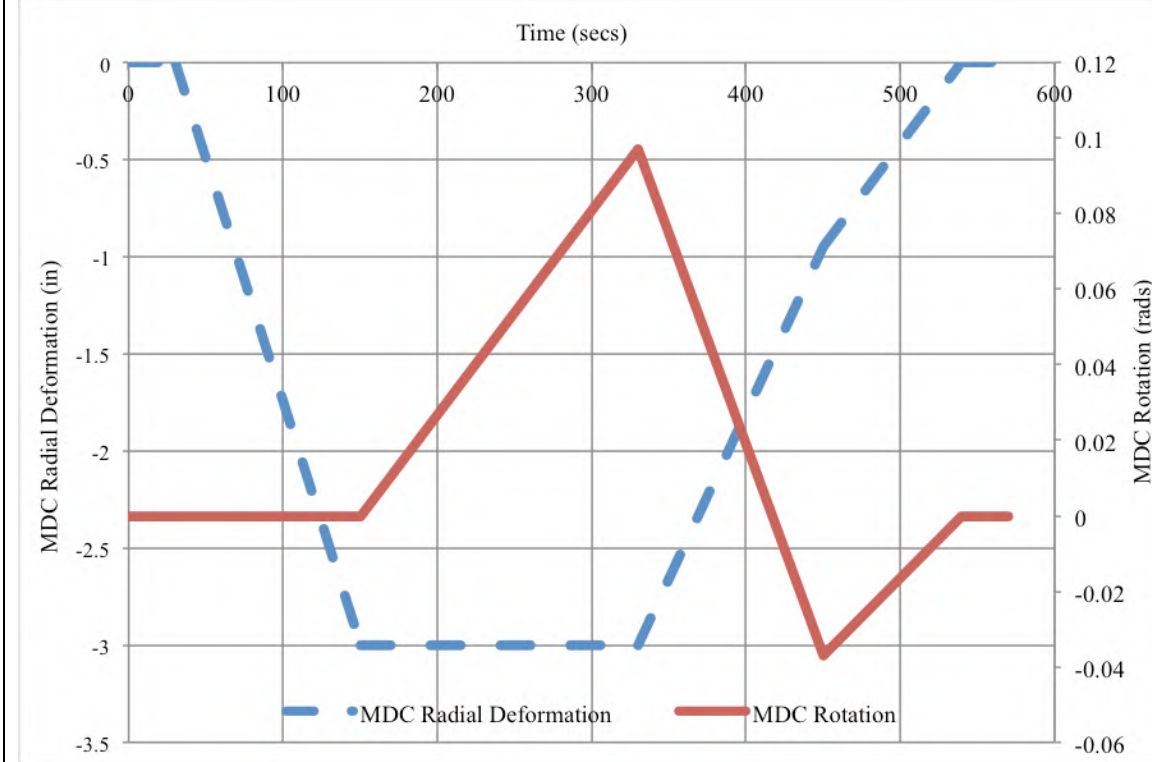


Fig. 7-5: MDC1 experimental loading protocol a) 55-kip actuator, floor table, and wall table deformation protocol b) Resulting MDC translation and rotation



a)



b)

Fig. 7-6: MDC2 experimental loading protocol a) 55-kip actuator and floor table deformation protocol and wall table loading protocol b) Resulting MDC translation and rotation

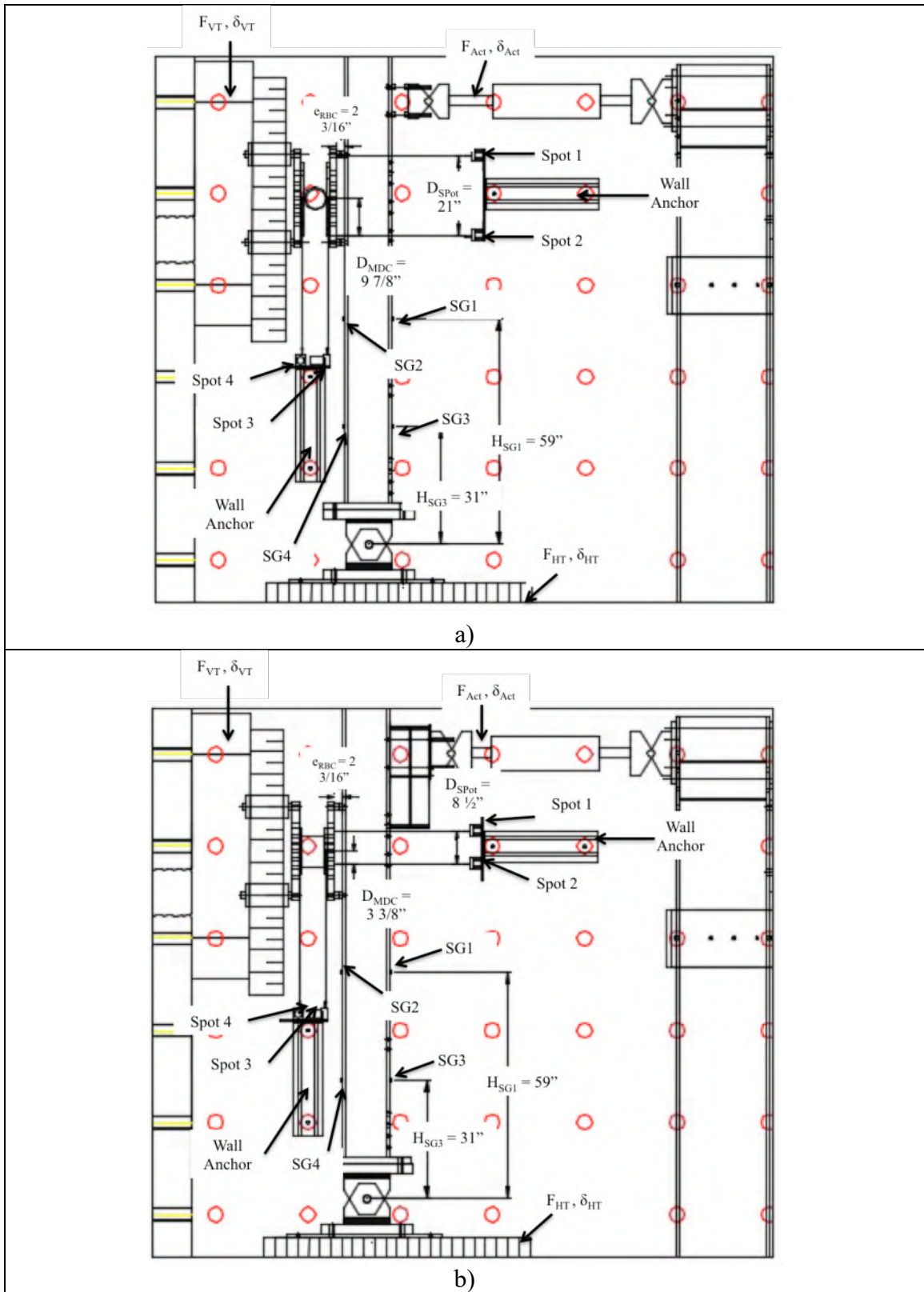


Fig. 7-7: Instrumentation Layouts a) Instrumentation layout for the MDC1 experiment b) Instrumentation layout for MDC2 experiment

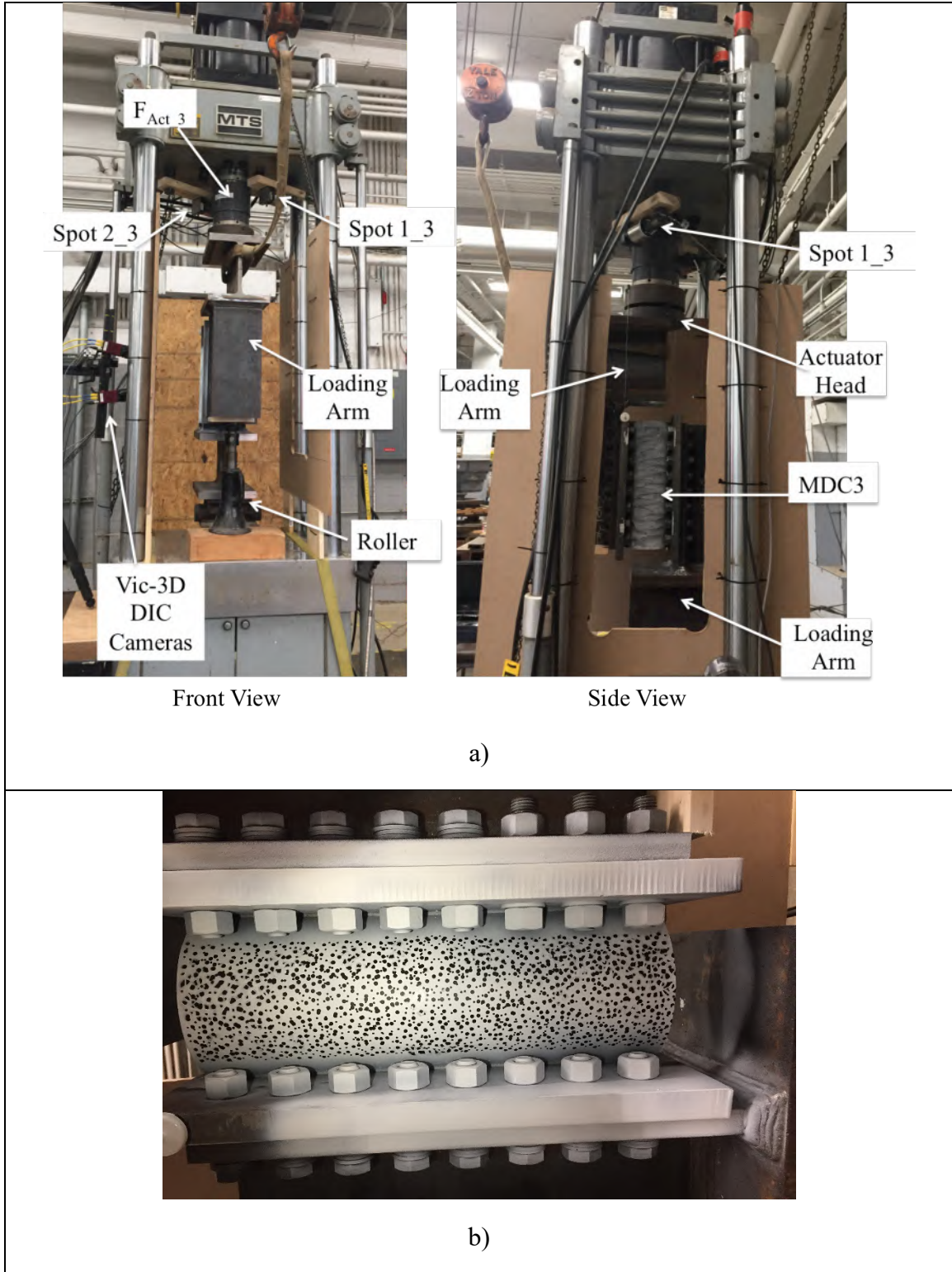


Fig. 7-8: MDC3 Experiment Setup a) Equipment and instrumentation in 220kip machine
 b) Vic 3-D DIC speck pattern on the HSS

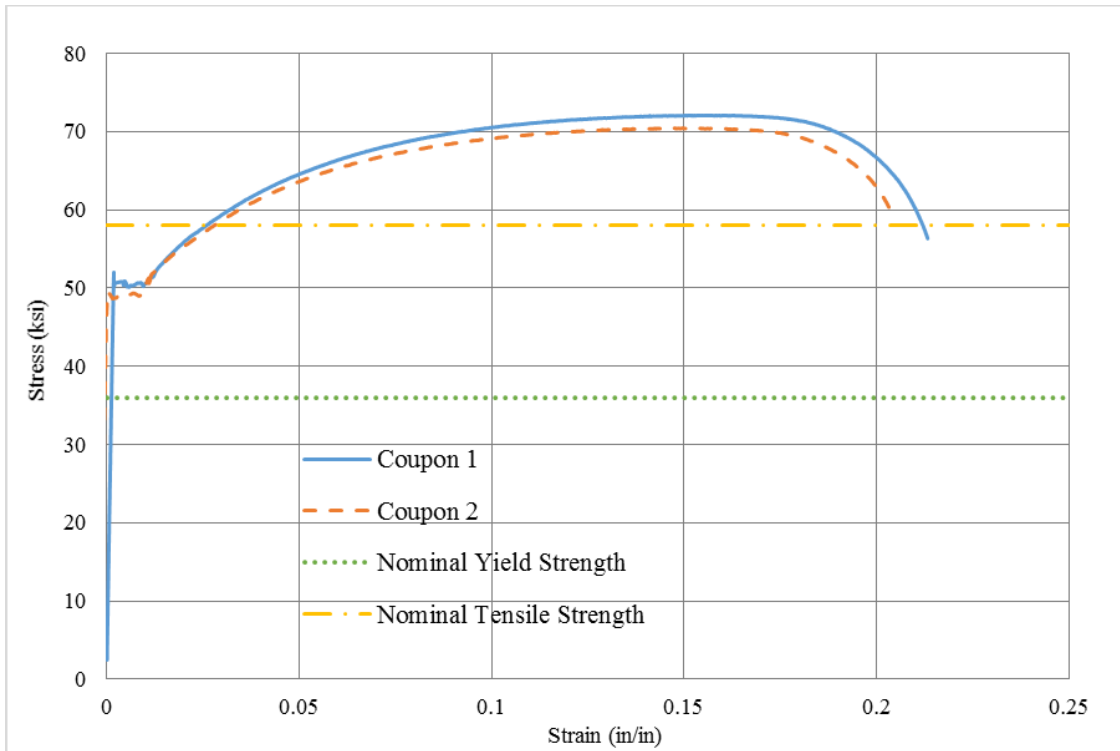


Fig. 7-9: MDC1 plate stress-strain curves from two tensile coupons and the nominal yield strength and tensile strength for ASTM A36 steel

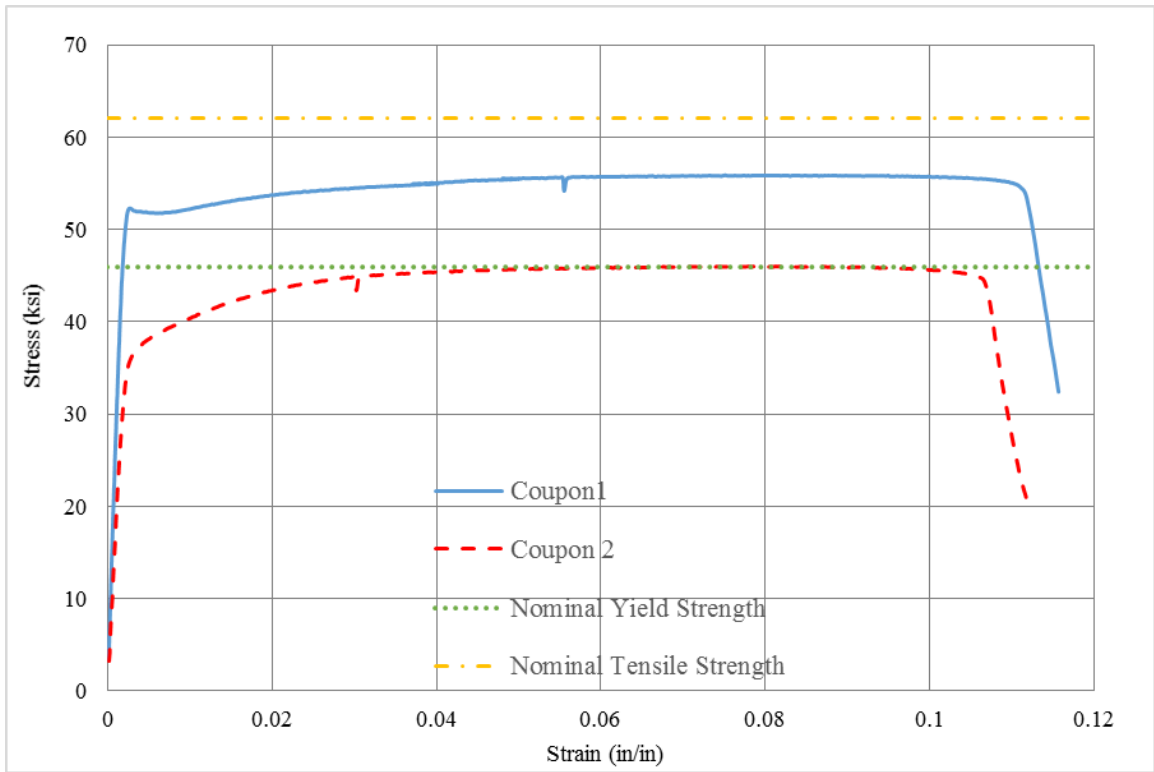


Fig. 7-10: HSS stress-strain curves from two tensile coupons and the nominal yield strength and tensile strength for ASTM A500 Grade C steel

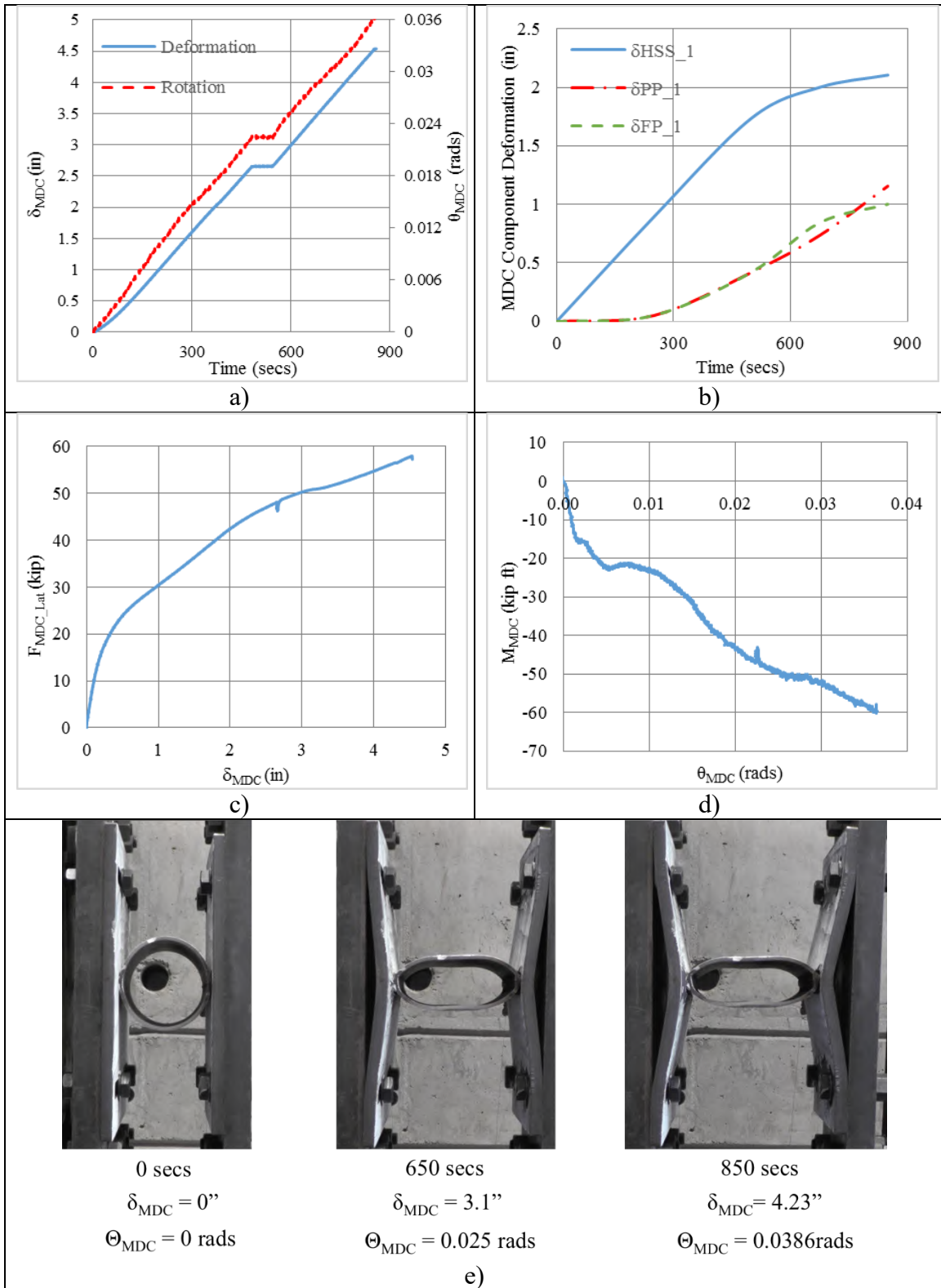
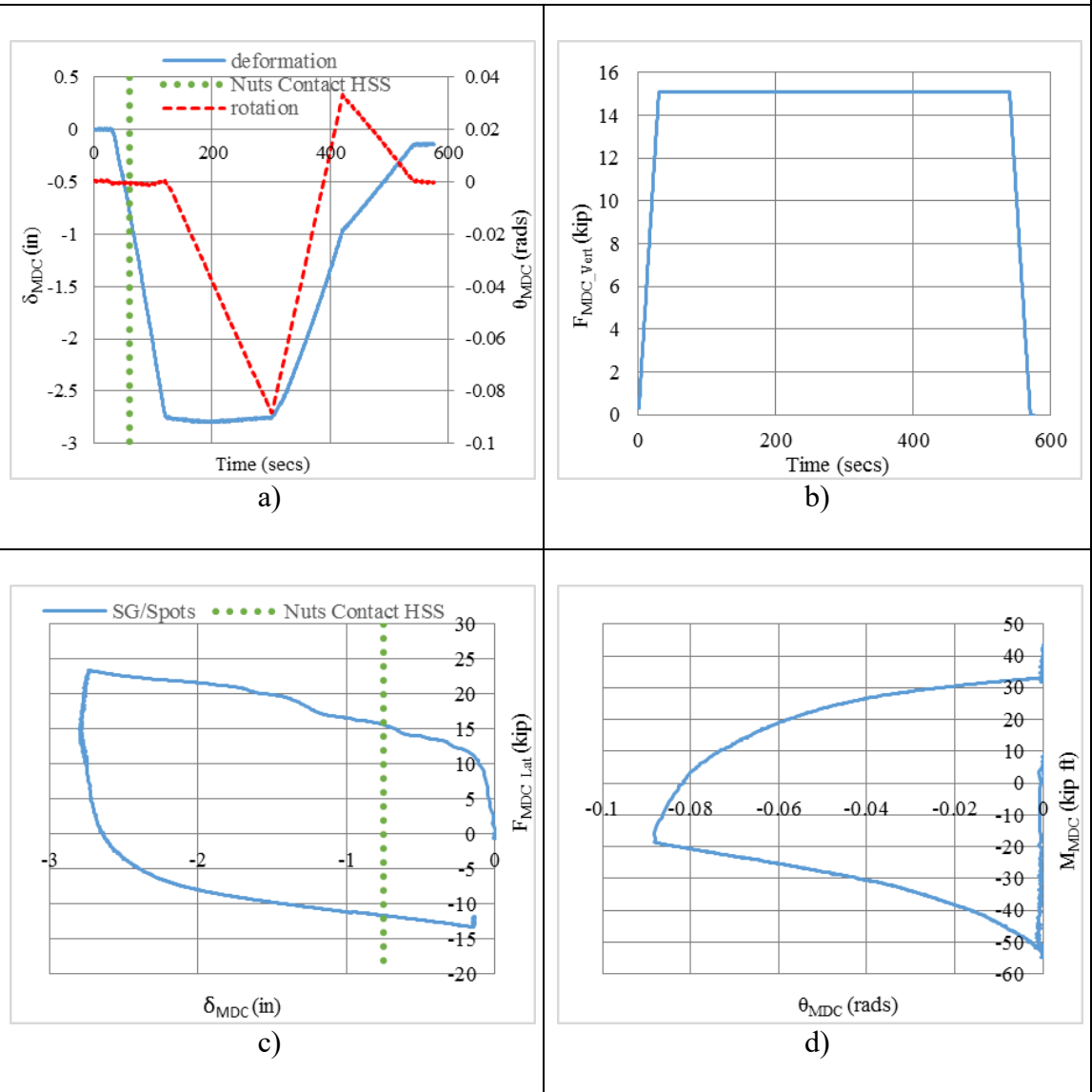


Fig. 7-11: MDC1 Experiment Results a) Applied radial deformation + x_L and rotation (about + z_L) b) Approximate deformations of the MDC components c) Force-Deformation curve d) Moment-Rotation curve e) Deformation of the MDC at various times

Fig. 7-12: MDC2 Experiment 1 Results a) Applied radial deformation $-x_L$ and applied rotation (about y_L) b) Applied gravity load $+z_L$ c) Force-Deformation curve d) Moment-Rotation curve e) Deformation of the MDC at times throughout the loading protocol f) Nut contact with the HSS at times throughout the loading protocol



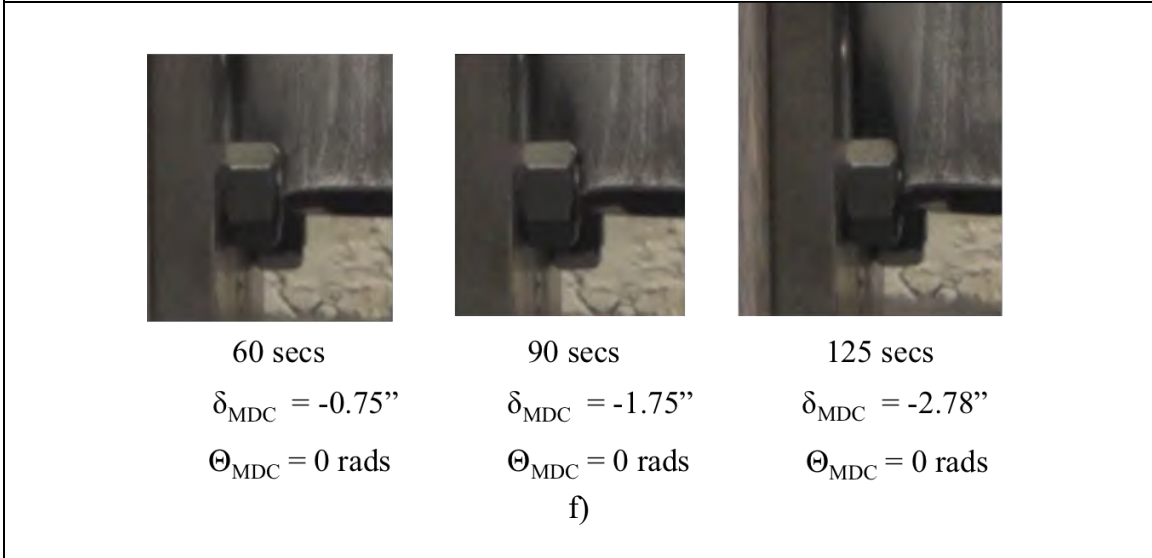
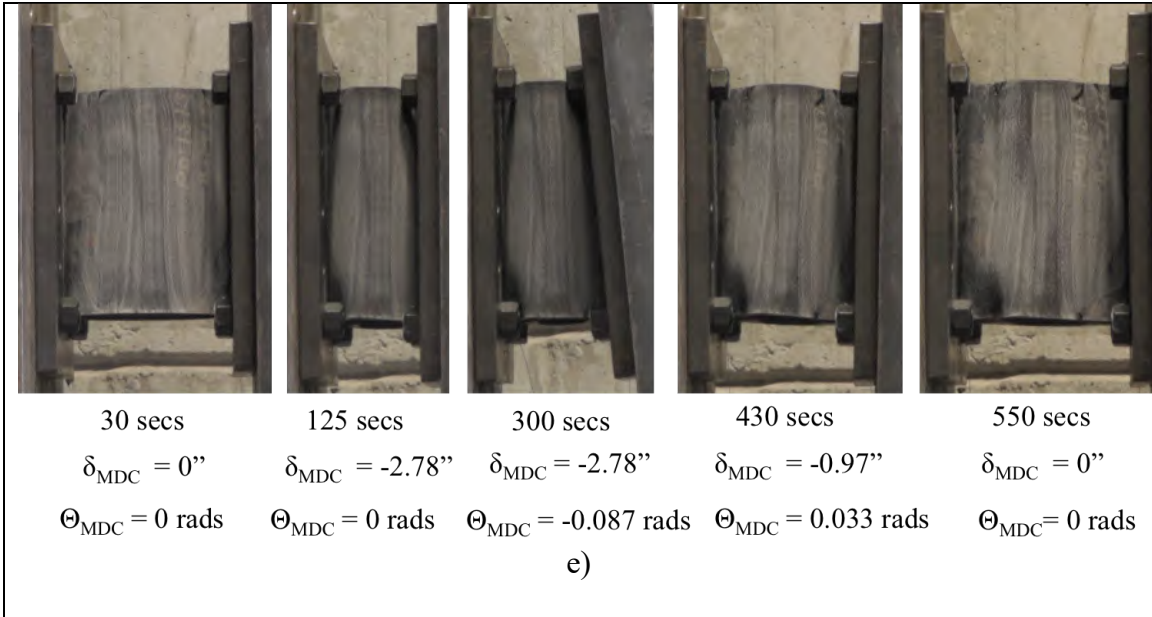
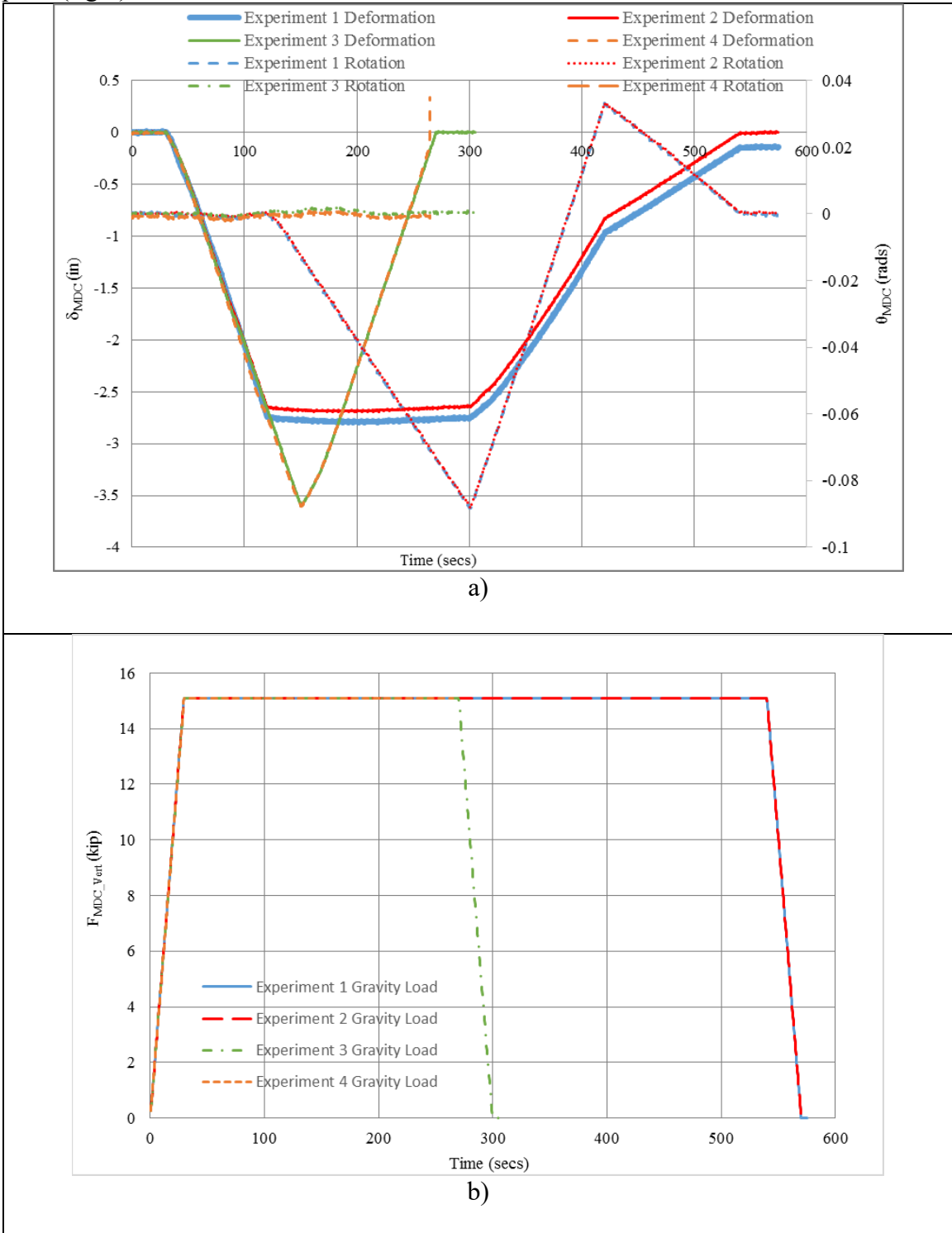
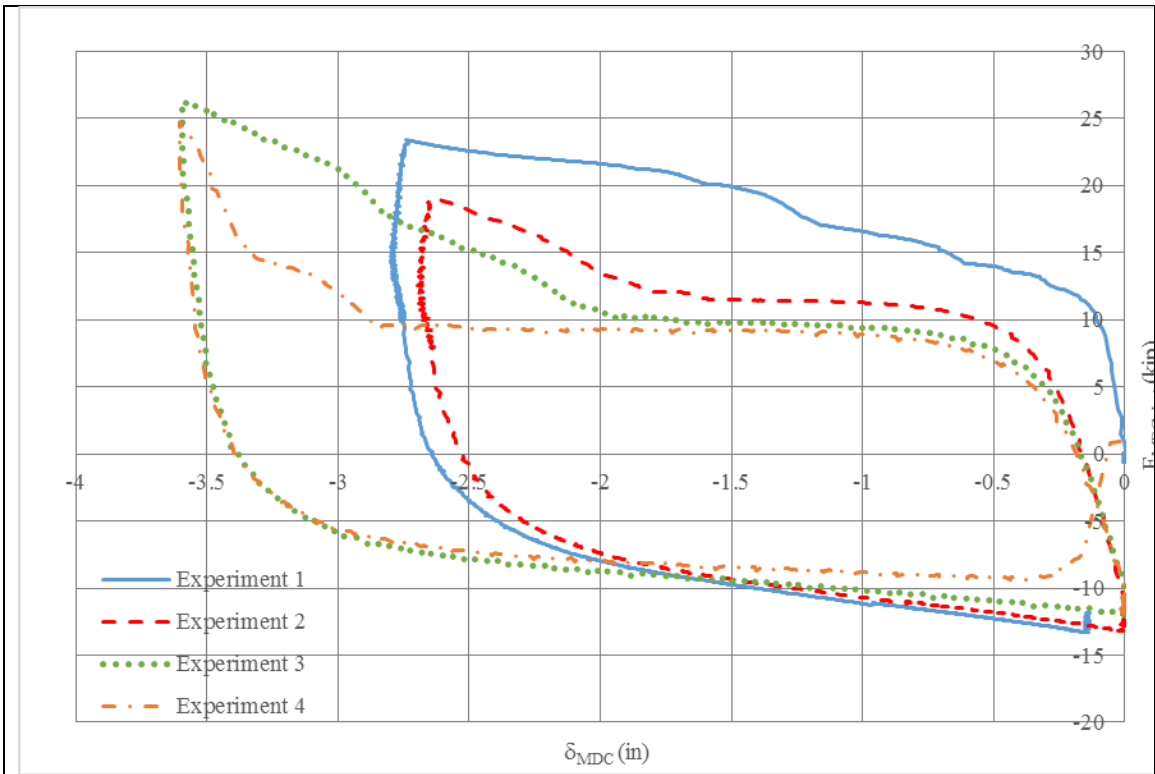
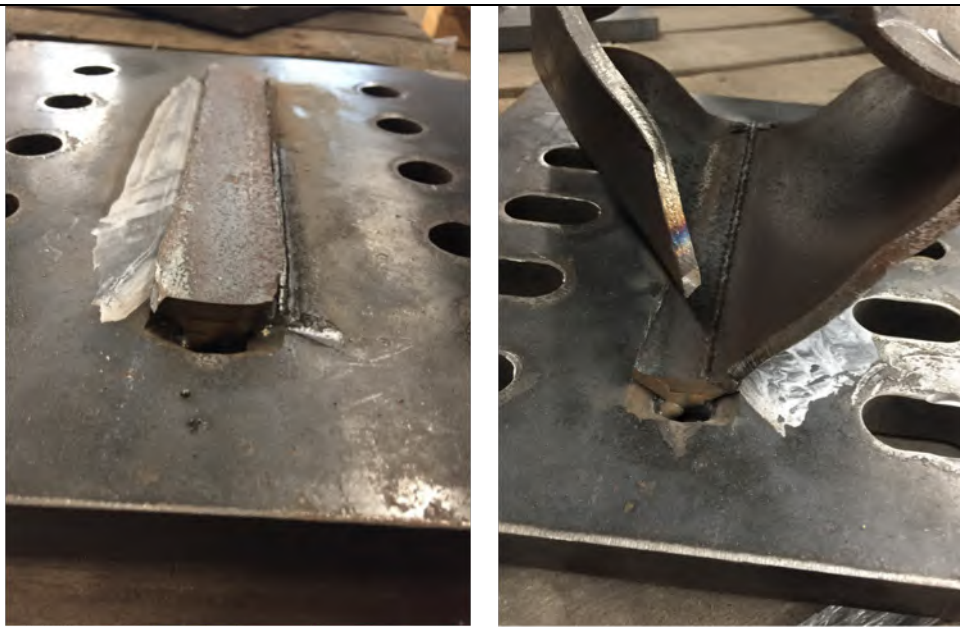


Fig. 7-13: MDC 2 Experimental 1-4 Results a) Applied radial deformations $-x_L$ and applied rotations (about y_L) for four consecutive experiments b) Applied gravity loads $+z_L$ for four consecutive experiments c) Force-Deformation curves for four consecutive experiments d) Final fracture surfaces at the end of MDC2 Experiment 4 on panel plate (left) and frame plate (right)



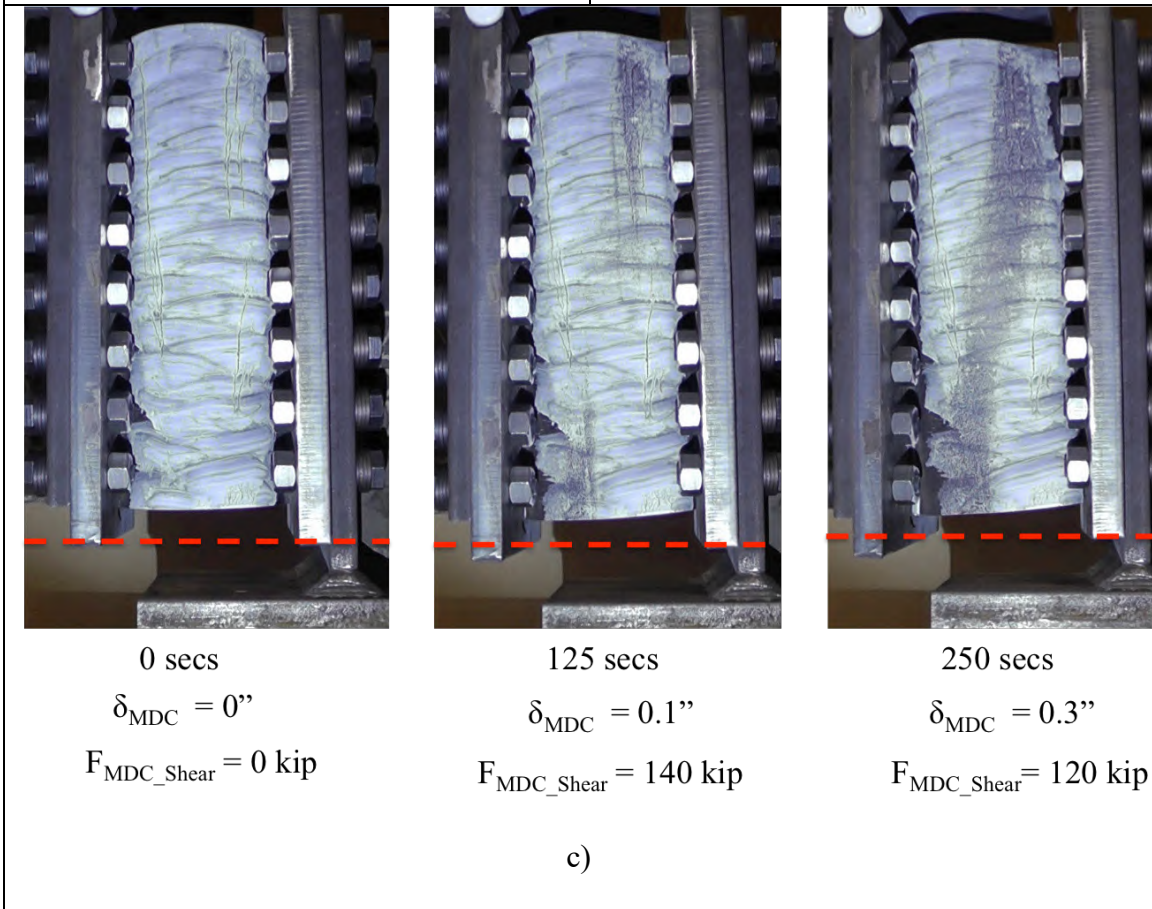
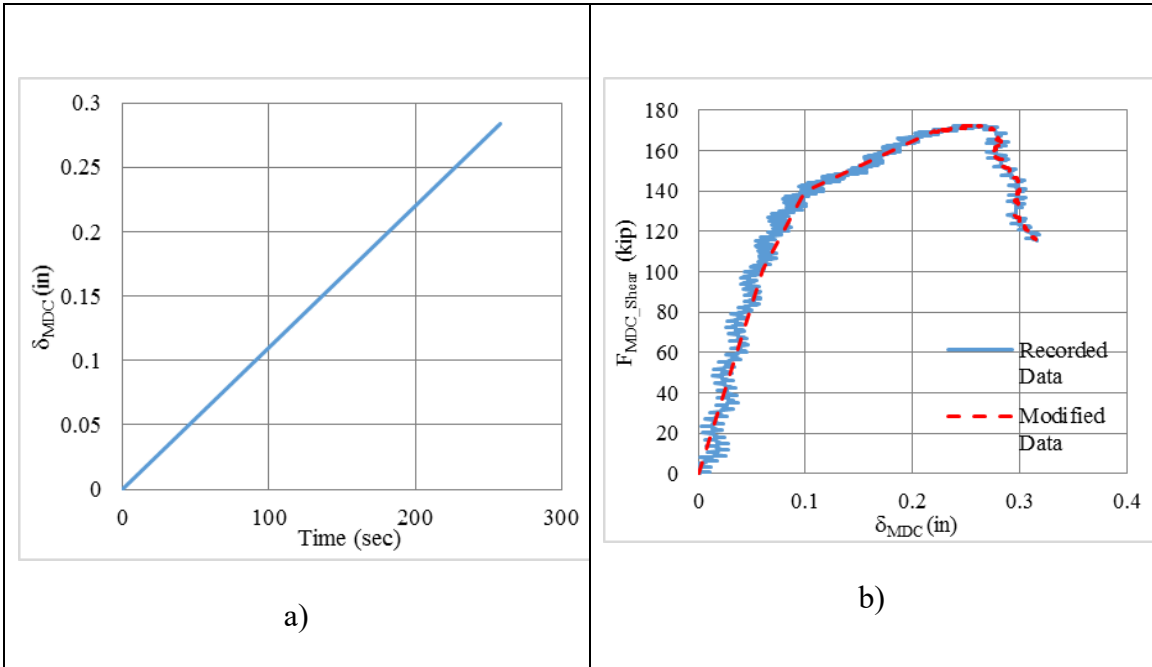


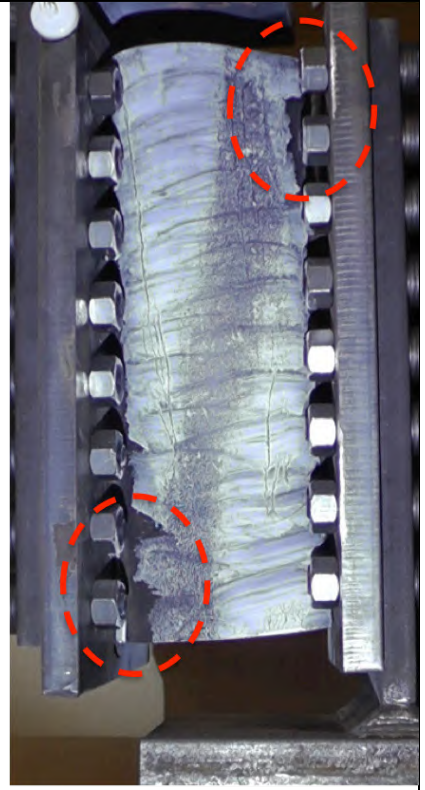
c)



d)

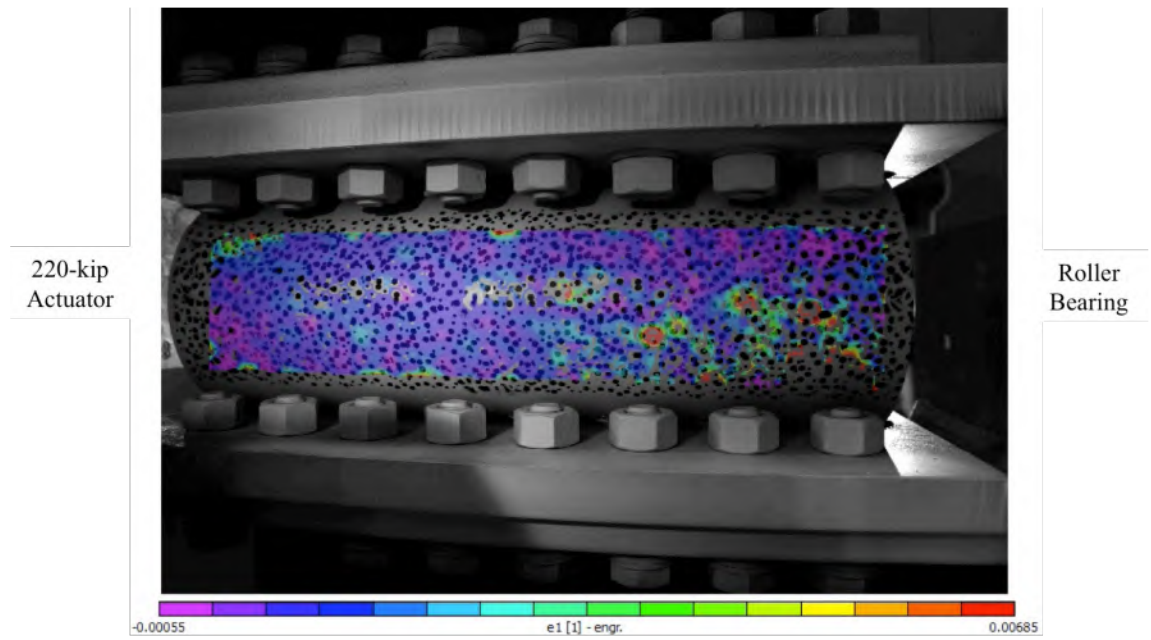
Fig. 7-14: MDC3 Experiment Results a) The shearing deformation imposed between the MDC plates in z_L b) Force-Deformation curve c) Deformation of the MDC d) Failure surface of MDC3 (left) and failure locations (right)



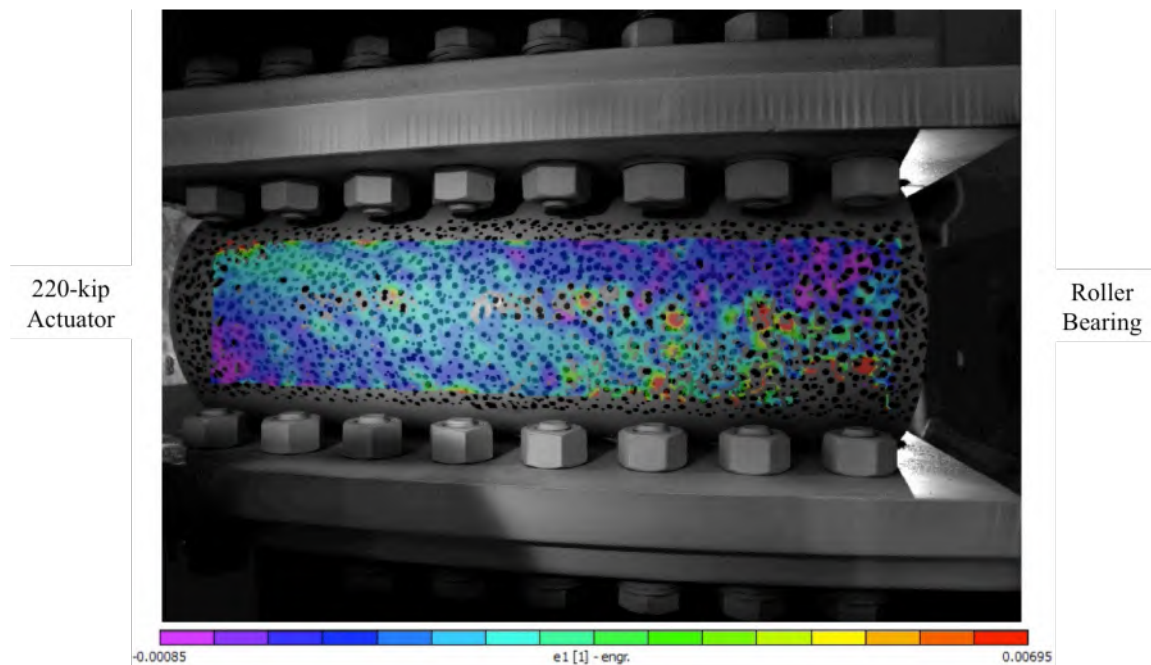


d)

Fig. 7-15: MDC3 Vic-3D DIC first principal strain results



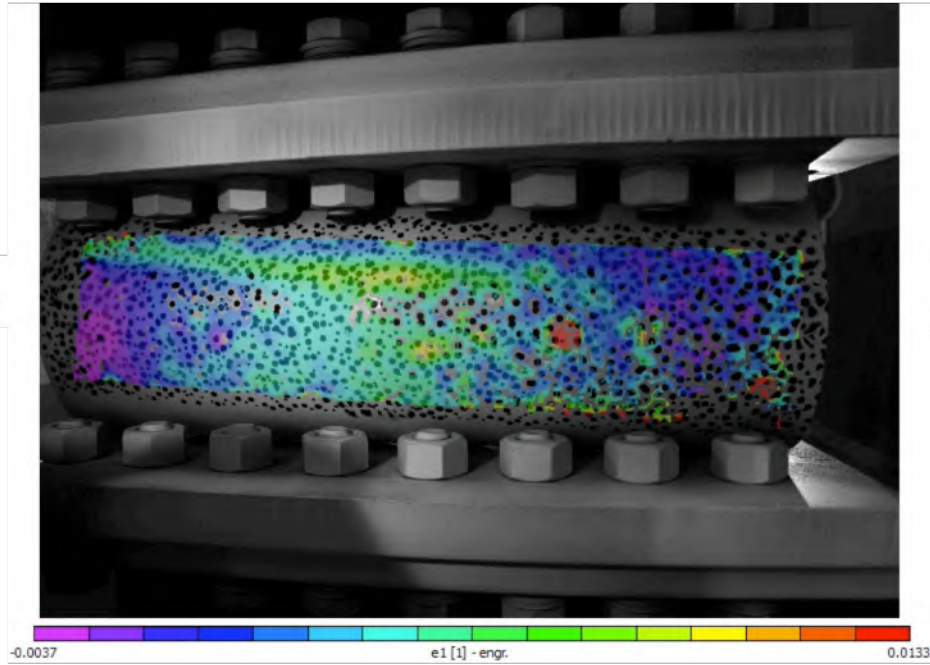
45 secs $\delta_{MDC} = 0.043''$ $F_{MDC_Shear} = 70.4$ kips



90 secs $\delta_{MDC} = 0.072''$ $F_{MDC_Shear} = 135$ kips

220-kip
Actuator

Roller
Bearing



260 secs

$\delta_{MDC} = 0.315''$

$F_{MDC_Shear} = 116$ kips

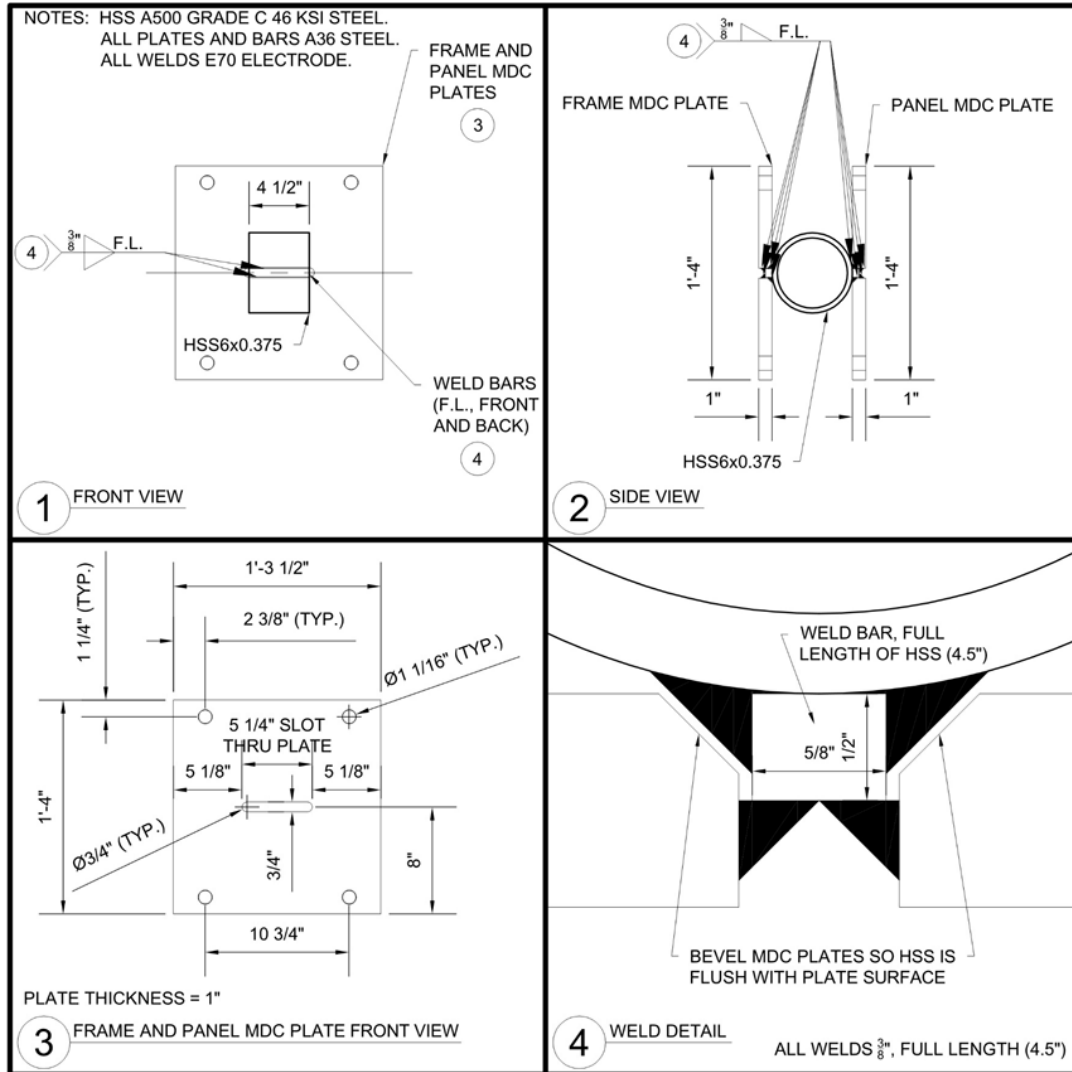


Fig. 7-16: MDC Rolling Experimental Test Specimen Fabrication Drawings

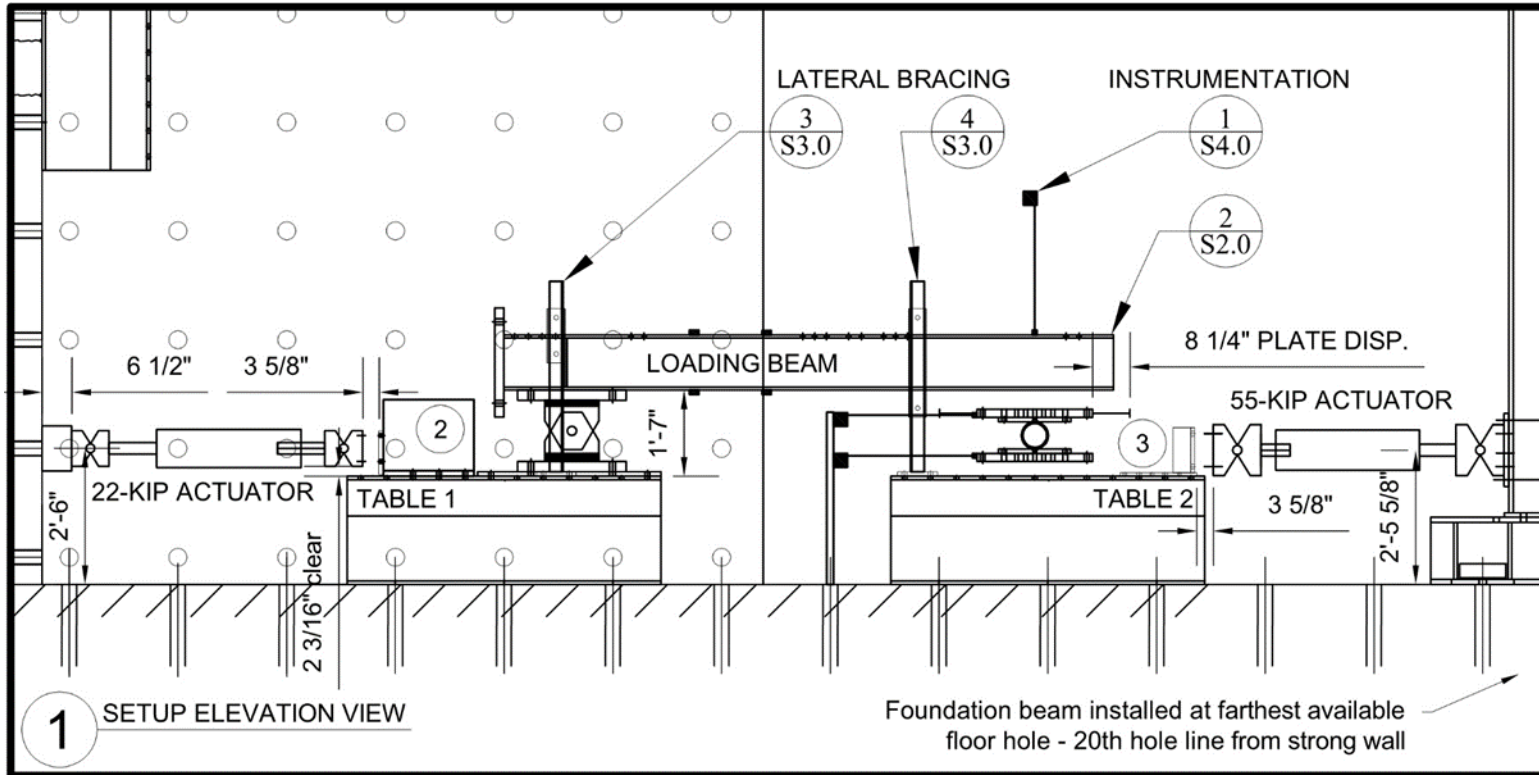


Fig. 7-17: Test Setup Elevation View

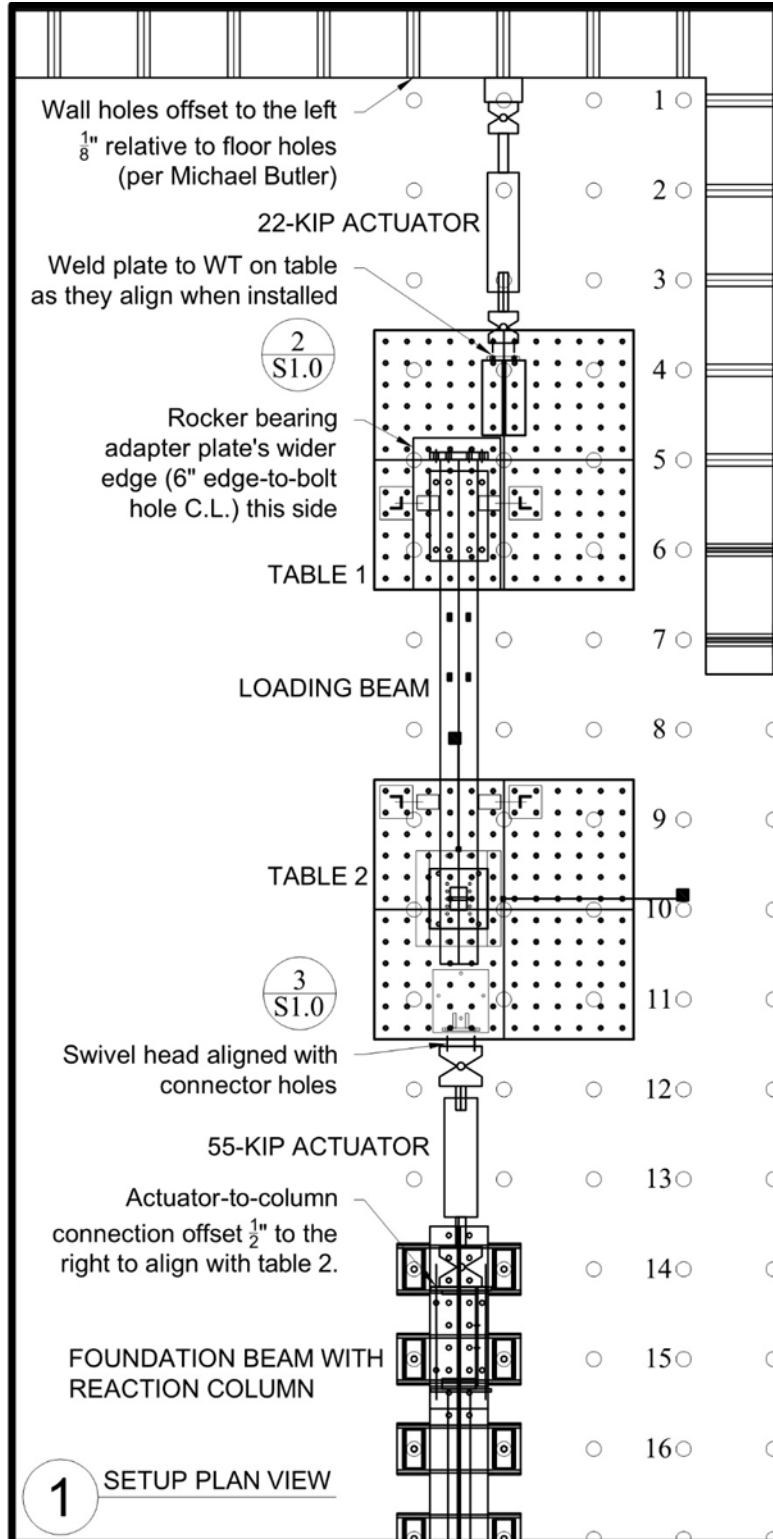


Fig. 7-18: Test Setup Plan View

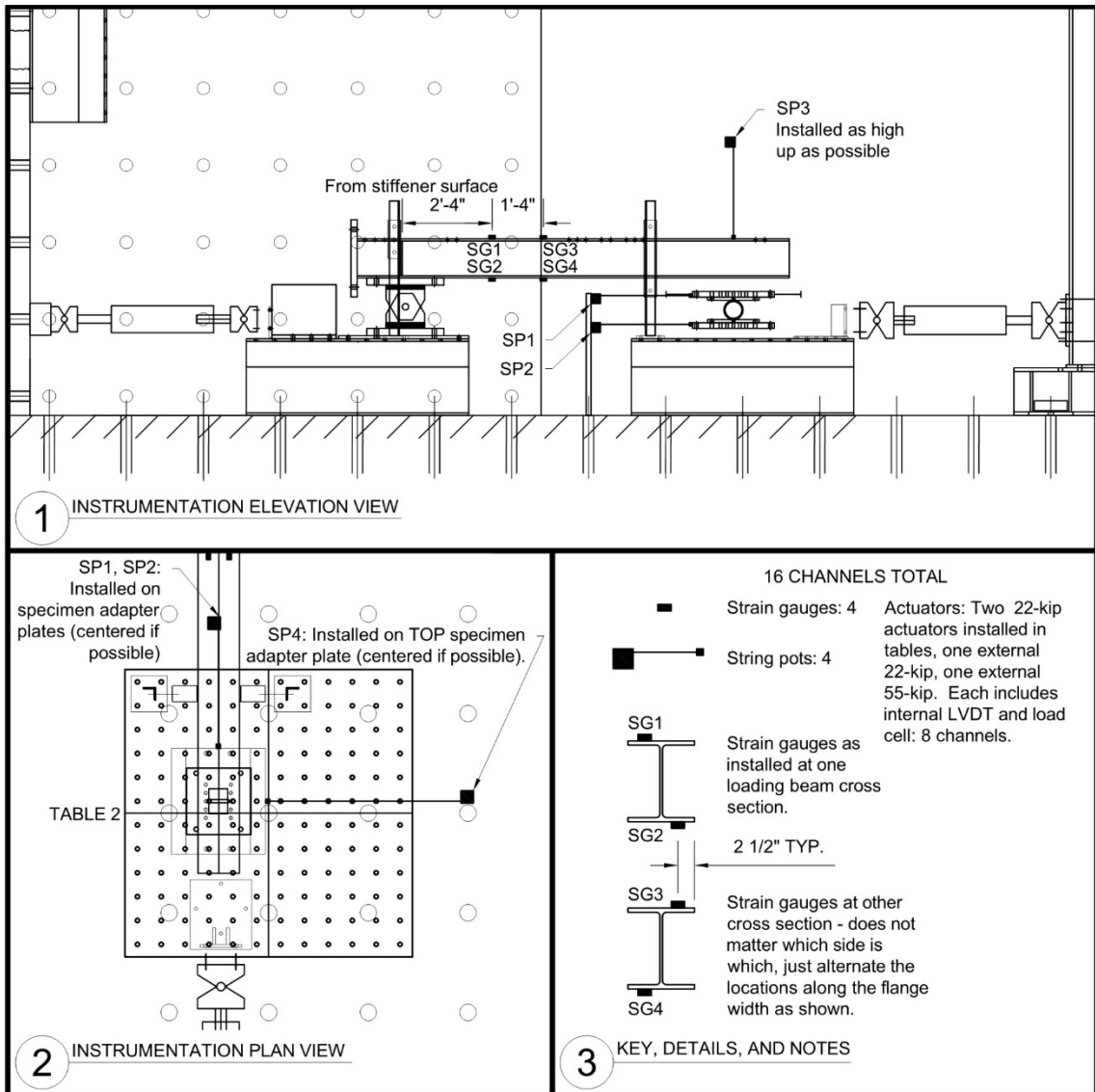


Fig. 7-19: Test Instrumentation

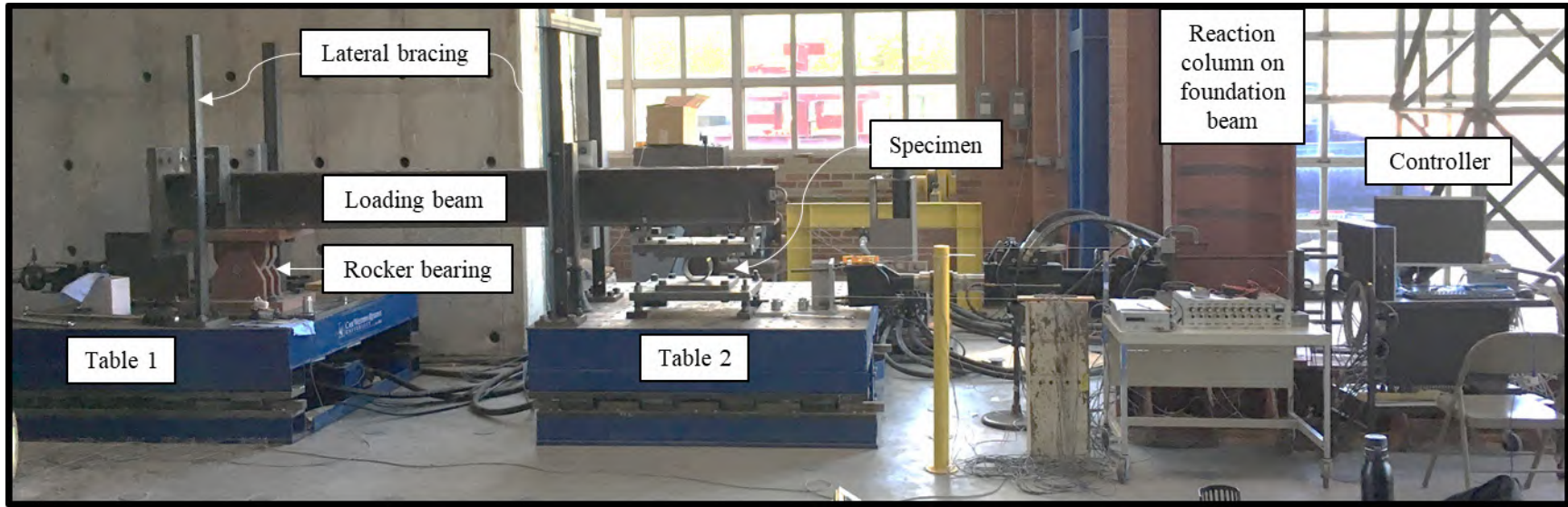


Fig. 7-20: Photograph of Test Setup

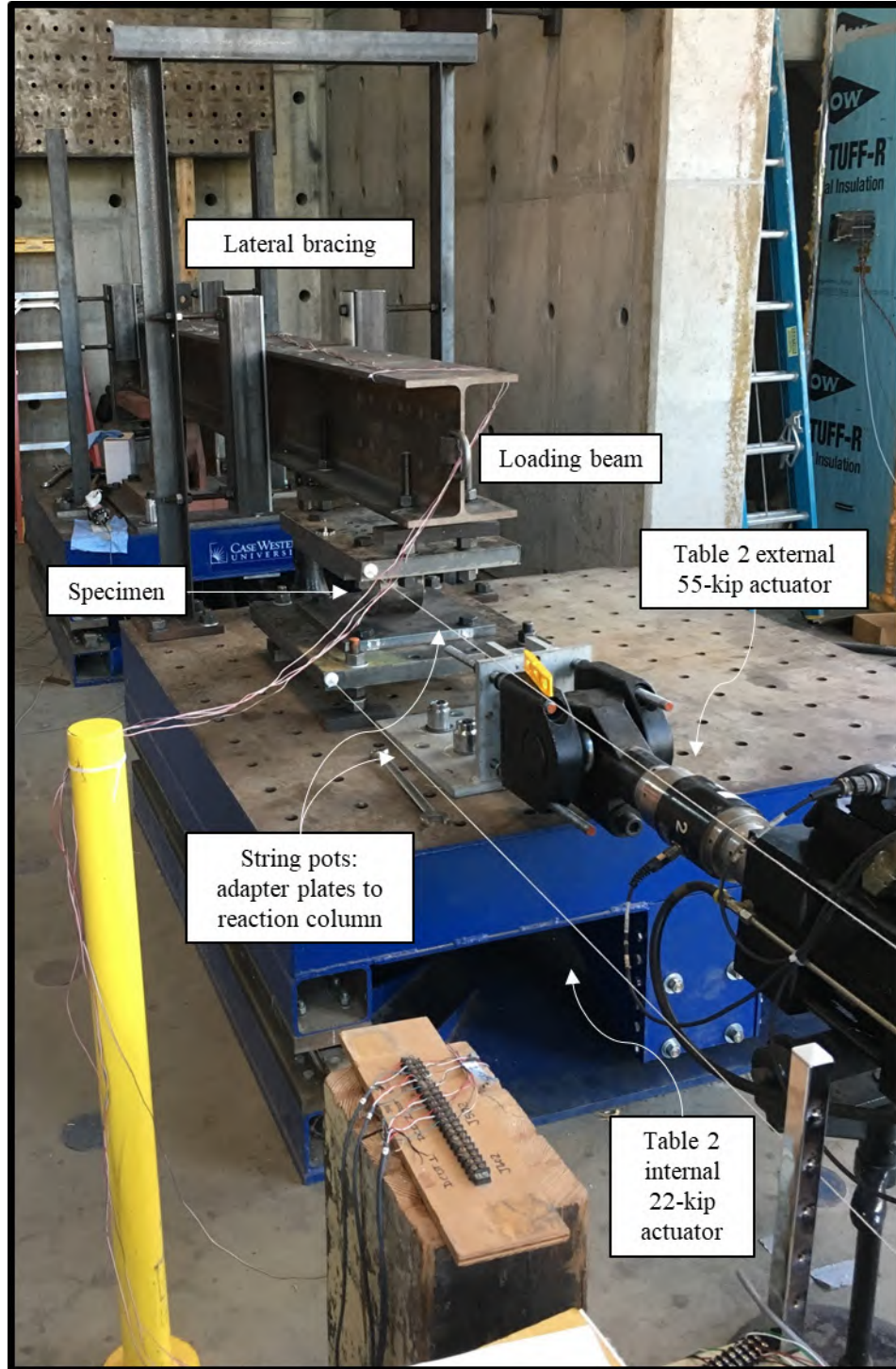


Fig. 7-21: Photograph of Test Setup Details

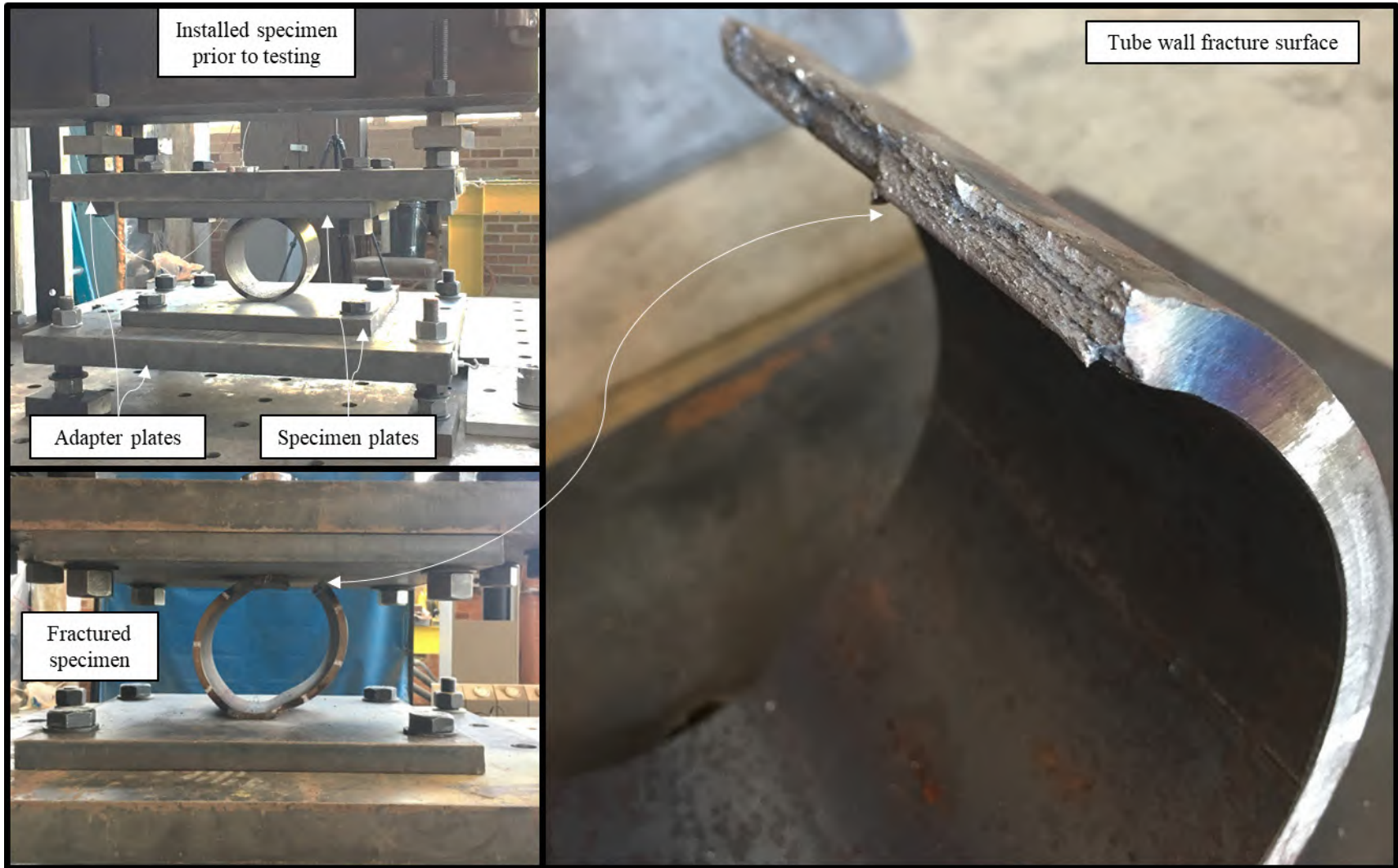


Fig. 7-22: Photographs of Specimen Details and Failure

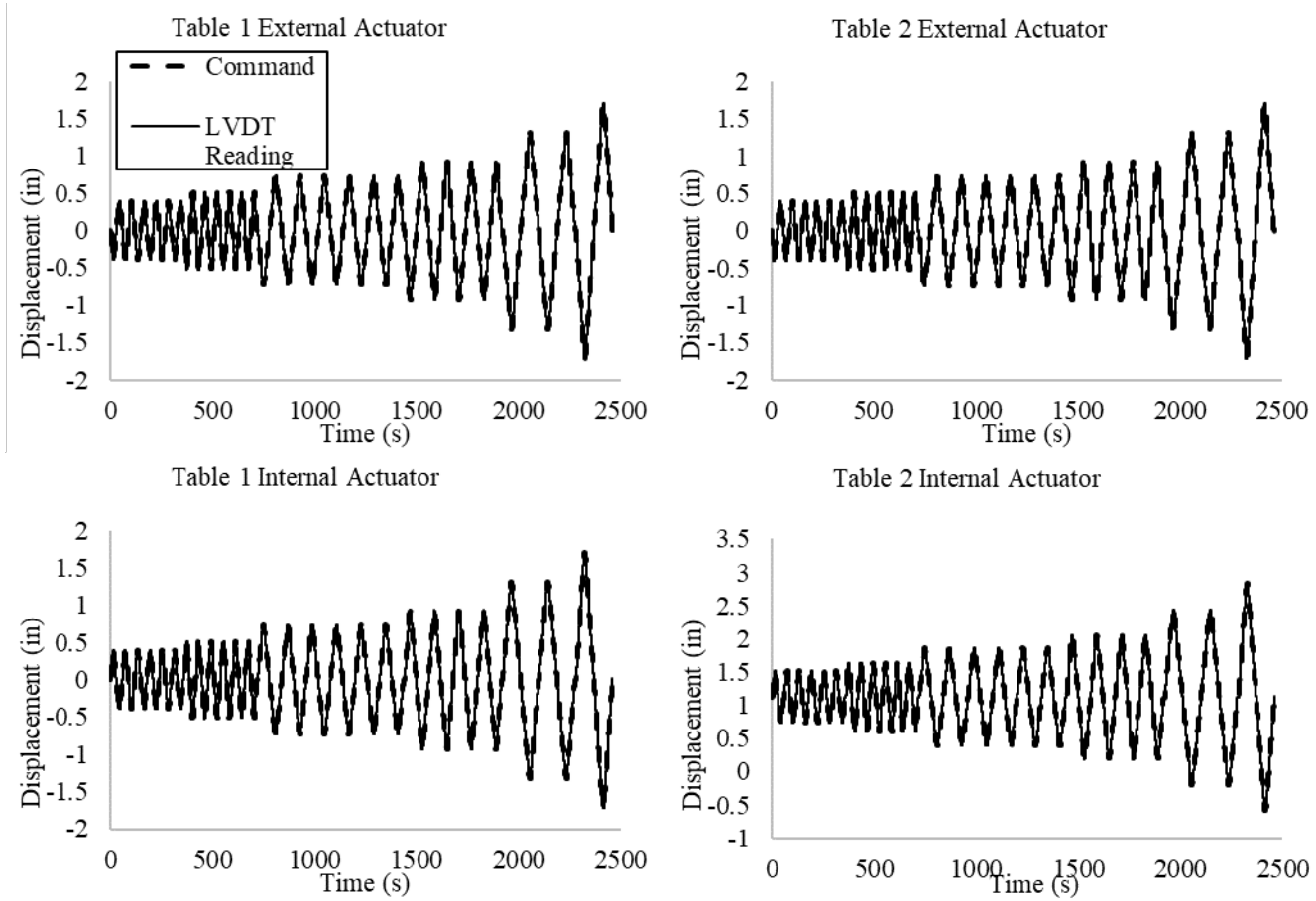


Fig. 7-23: Actuator Displacements

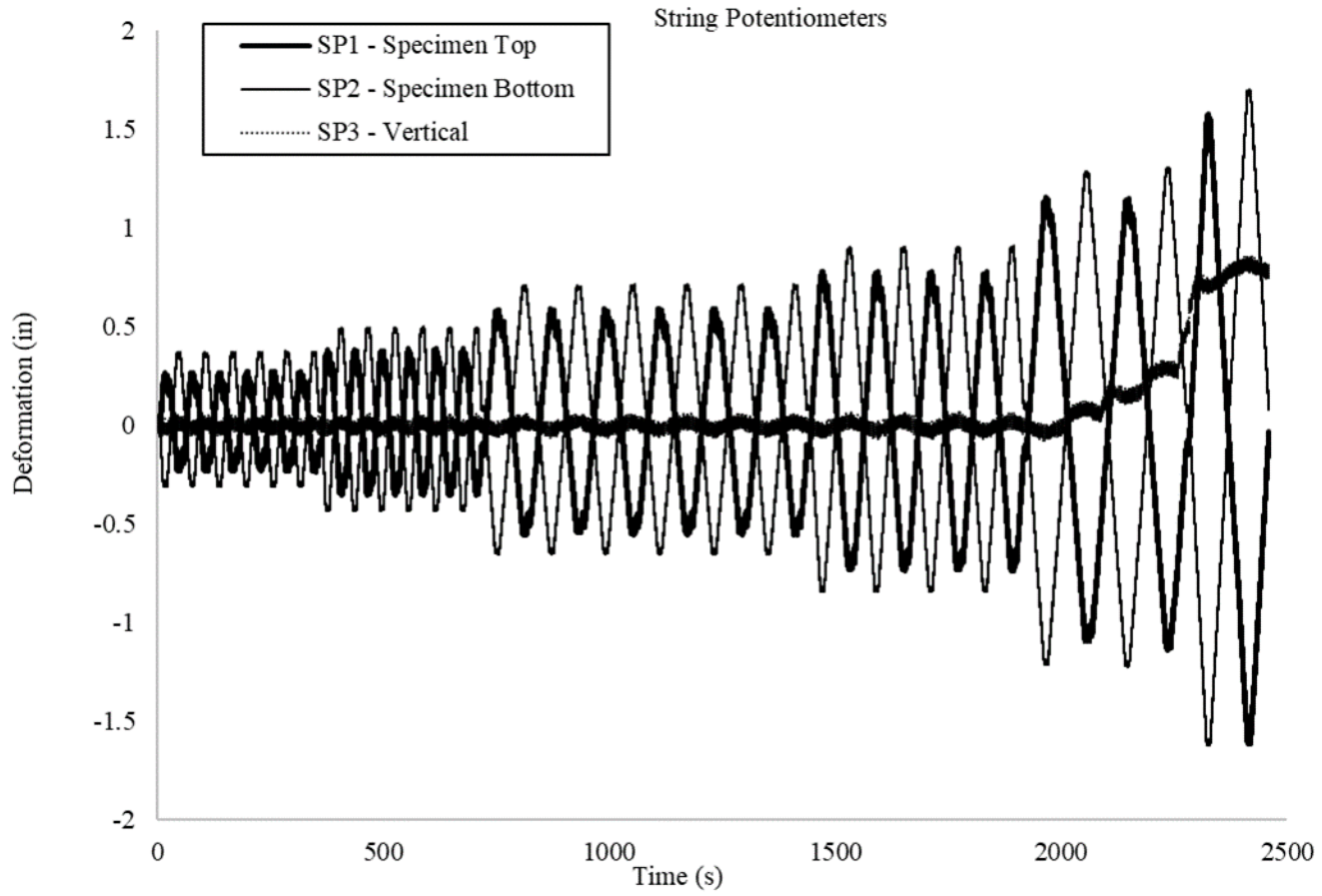


Fig. 7-24: String Potentiometer Displacement Readings

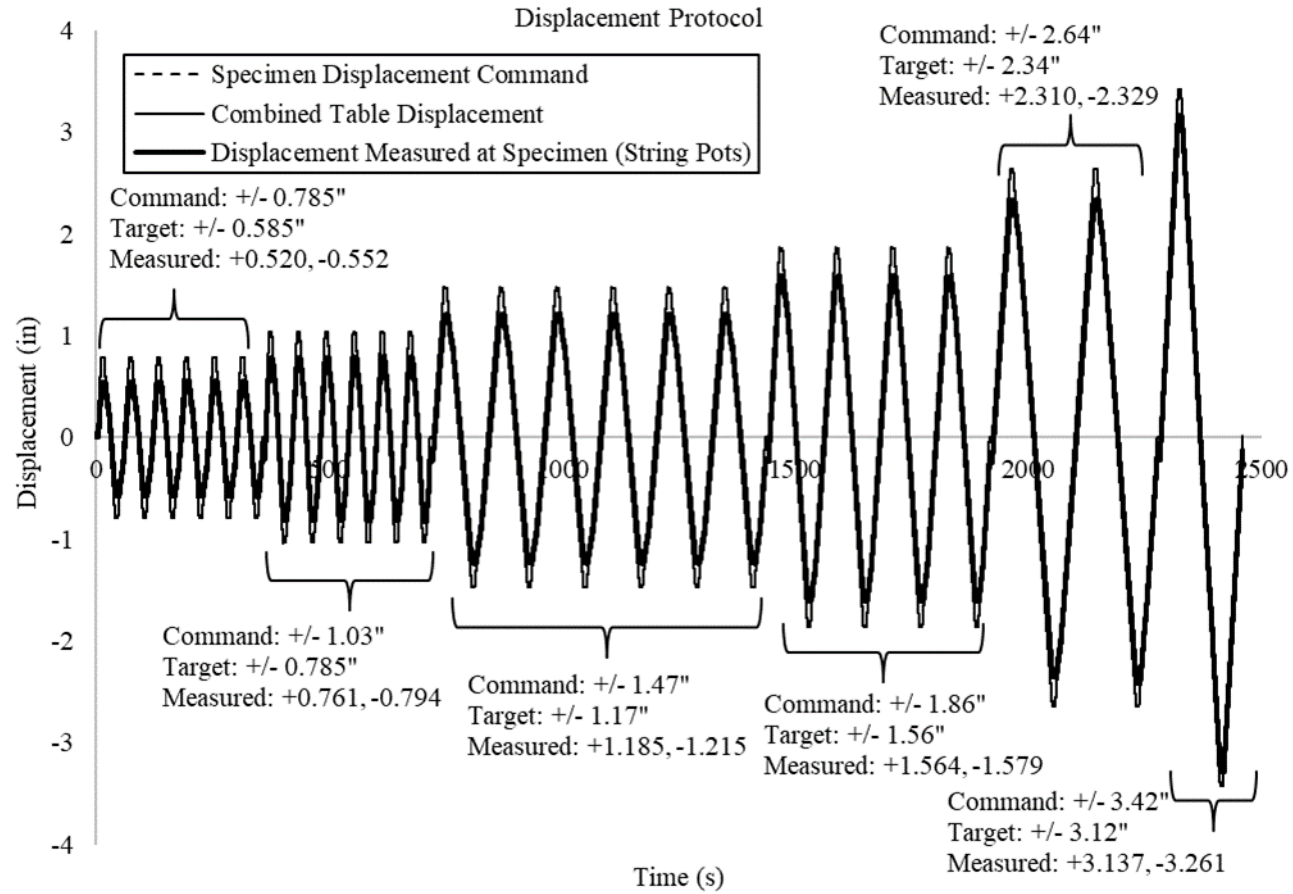


Fig. 7-25: Specimen Displacement

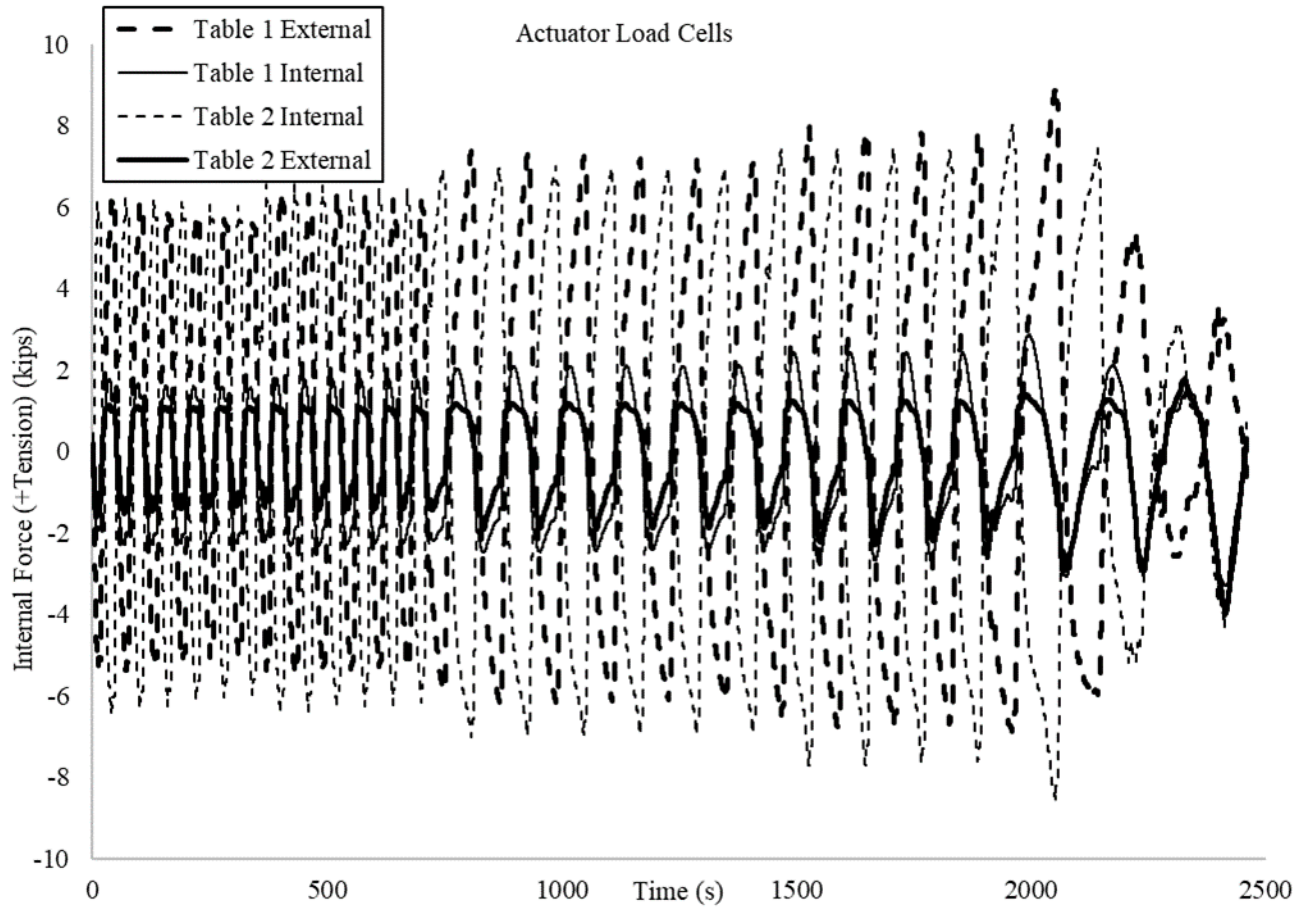


Fig. 7-26: Actuator Load Cell Readings

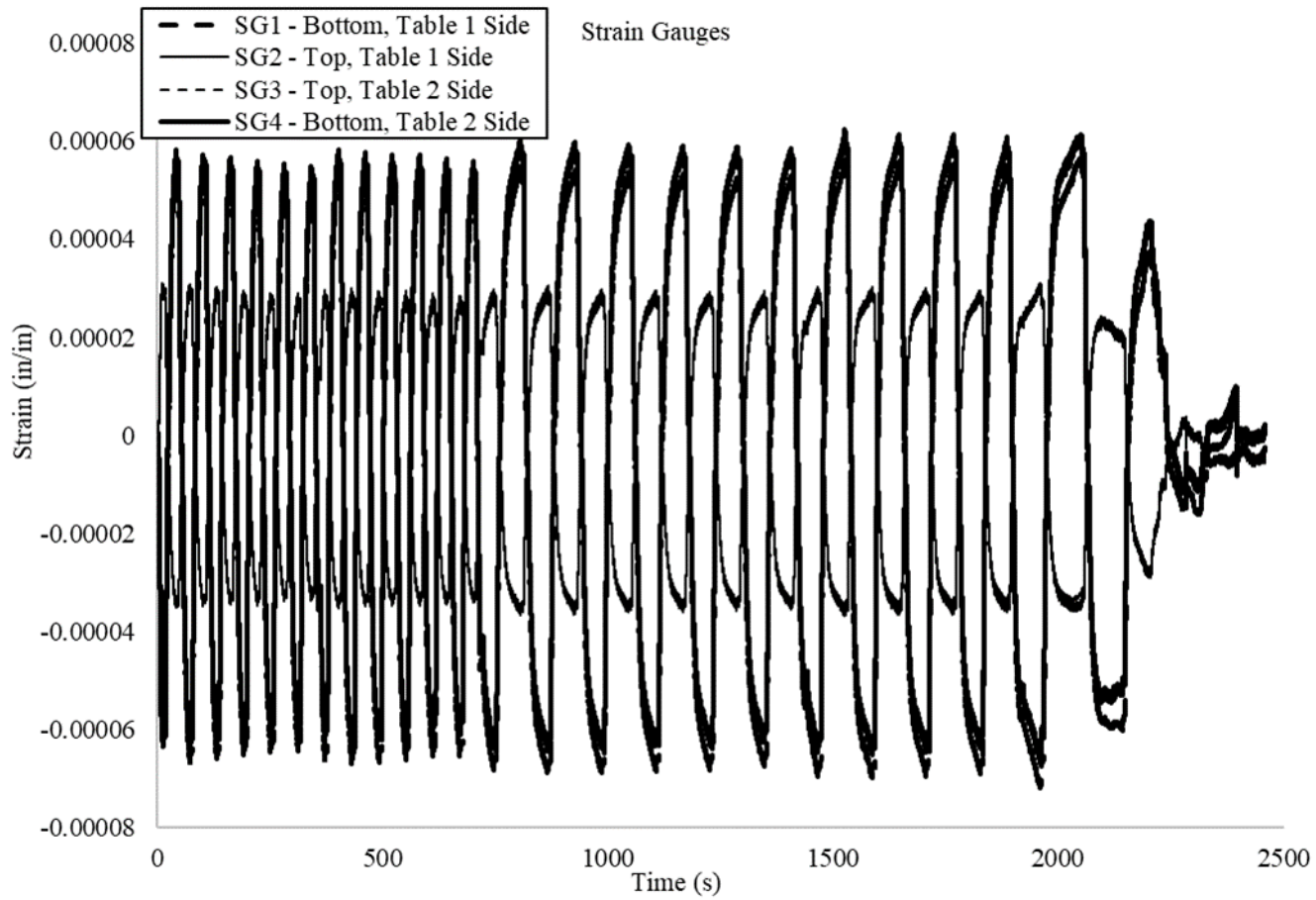


Fig. 7-27: Strain Gauge Readings

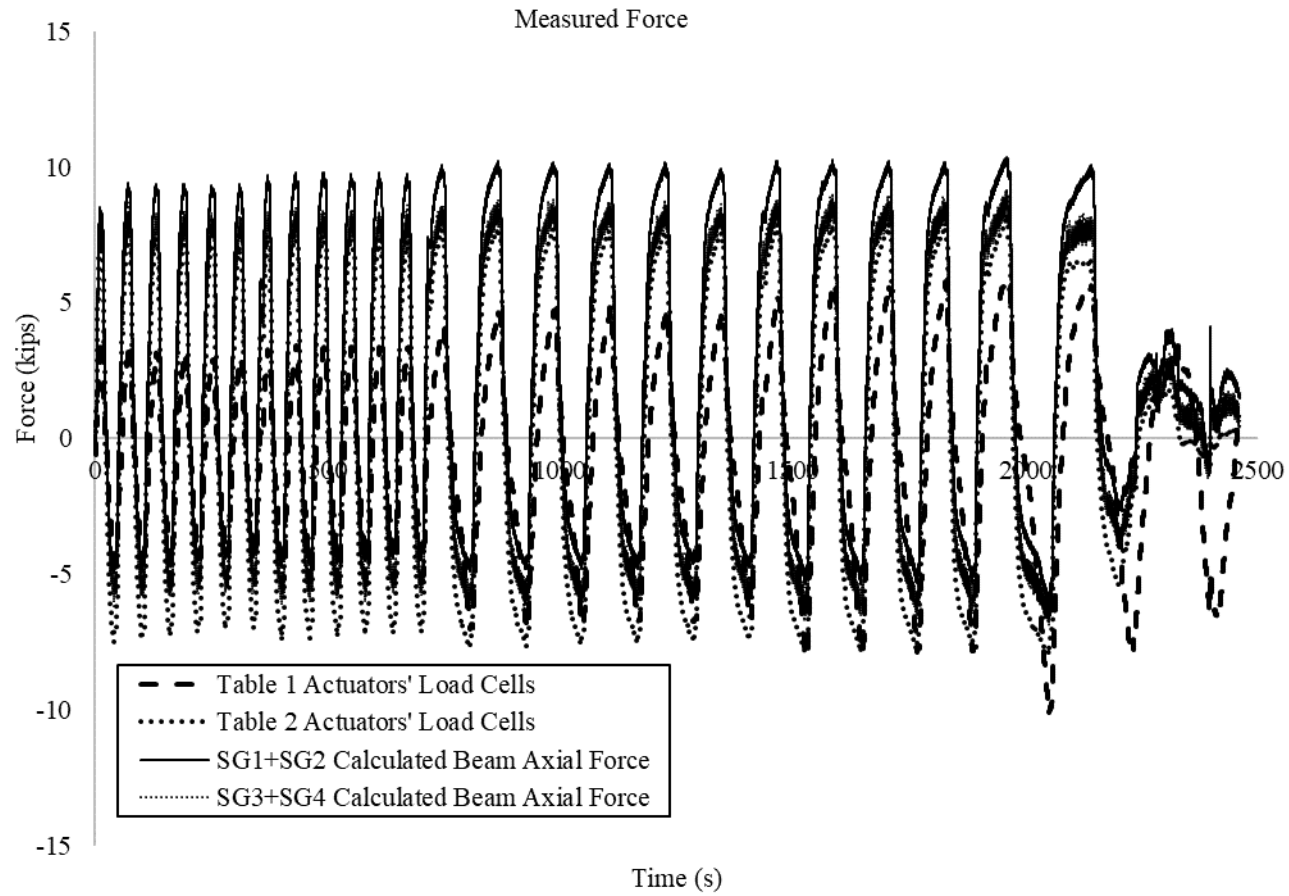


Fig. 7-28: Specimen Rolling Force Calculations

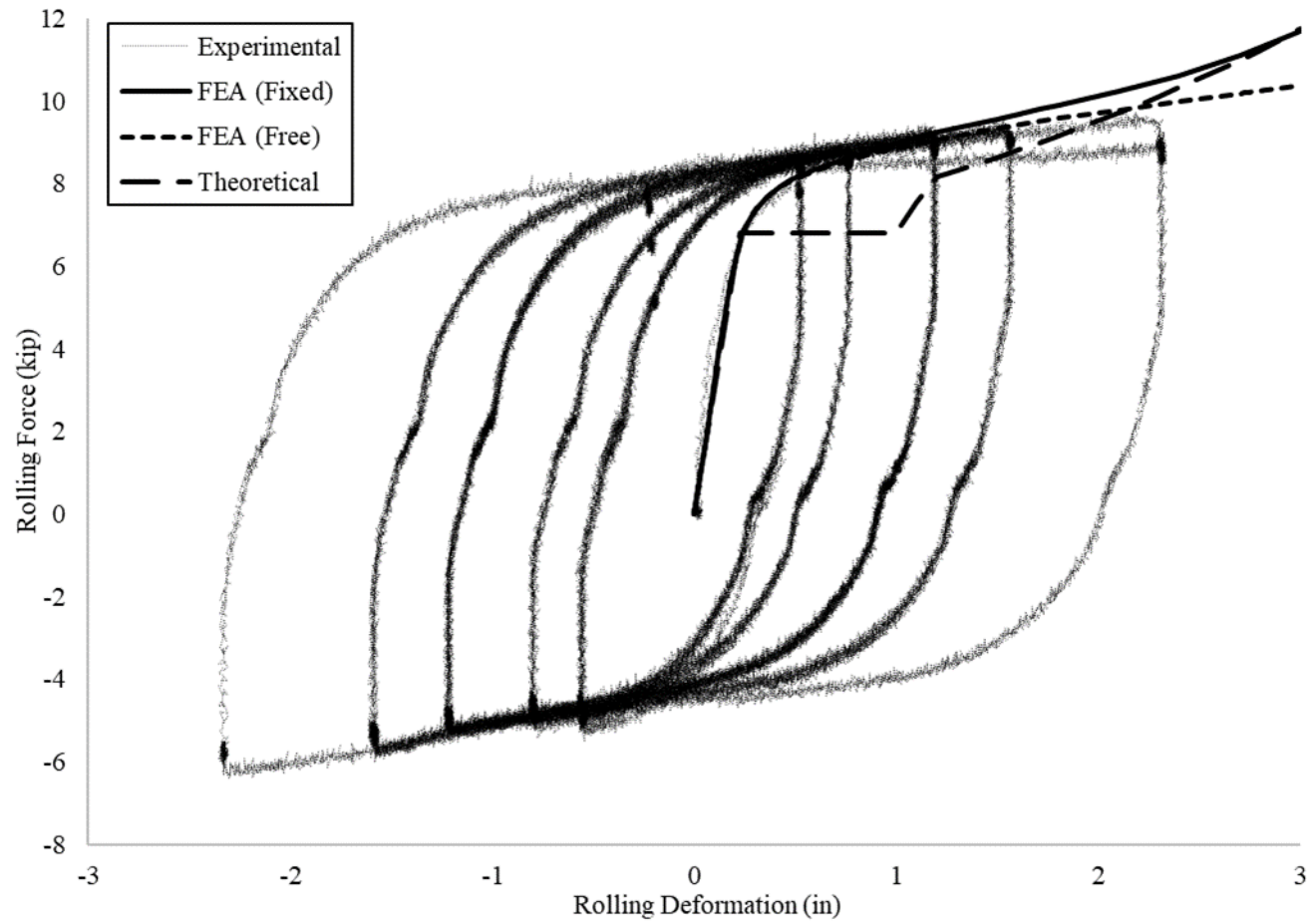


Fig. 7-29: Specimen Force-Deformation Hysteresis and Comparison with FEA and Theoretical Response

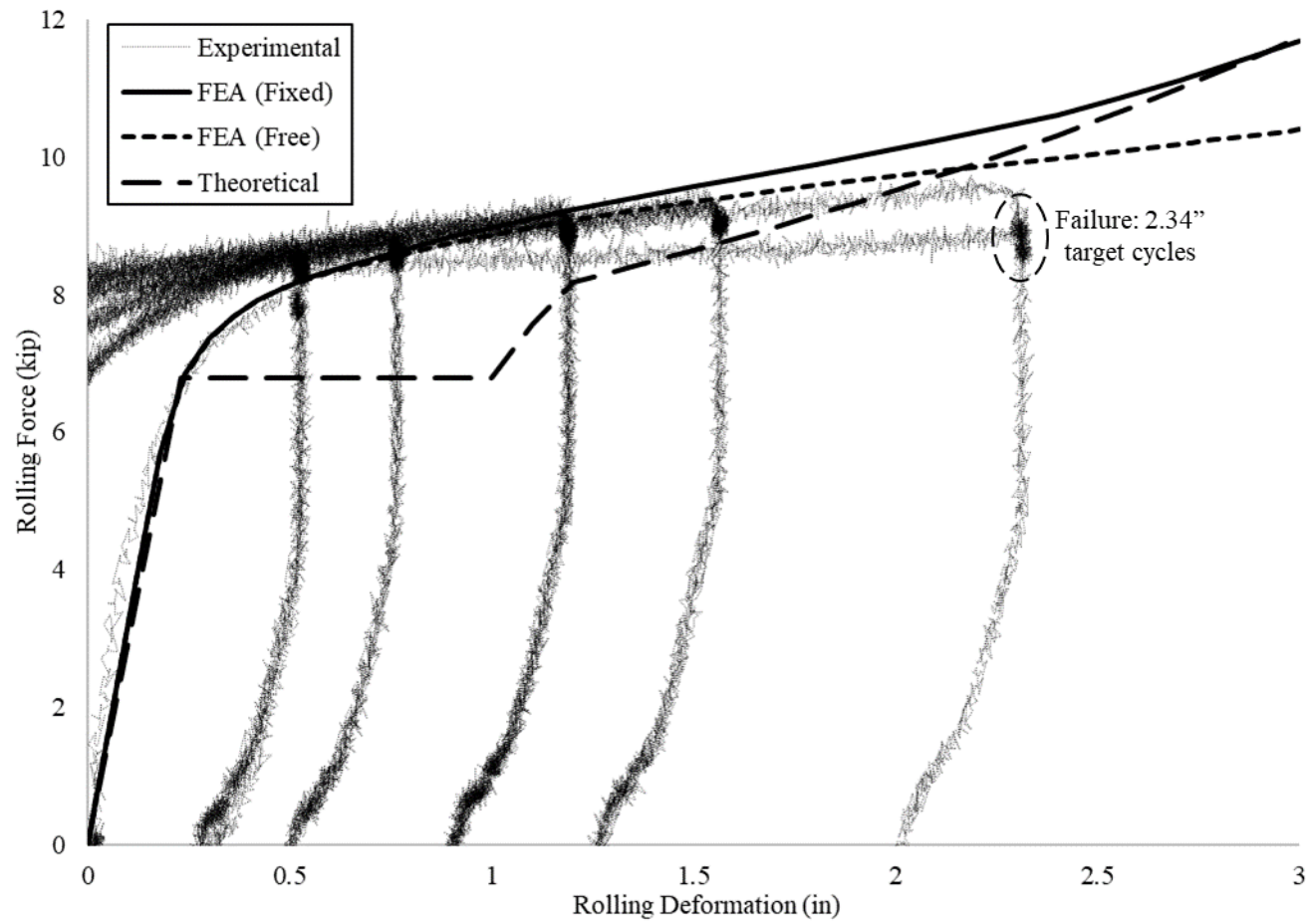


Fig. 7-30: Specimen Force-Deformation Hysteresis Detail

8. Development and Validation of MDC Finite Element Model

8.1. Introduction

Computational models of the experimentally tested multi-hazard ductile connector (MDC) designs were developed using finite element analysis (FEA) to simulate the static, nonlinear behavior of the MDC under various forms of loading expected from each hazard. The particular MDC considered was that proposed by Lavarney (2013), which consisted of a circular, steel hollow structural shape (HSS) connected between two flat steel plates. Initial baseline MDC models were analyzed and its results were compared with the experimental test results from Lavarney (2013). This study was chosen as the baseline analysis due to the simpler loading protocol compared to that of this project. These analyses will be referred to as “baseline” or “base” models. Once the base model reasonably matched the Lavarney (2013) results, the MDC model was adapted to the three current MDC designs and analyzed for the loading scenarios that occurred in the experiments as described in Section 7.1. This section provides a description and validation of the base model, development of a more comprehensive MDC model, and comparison of the FEA model results with design criteria.

8.2. Base Model

8.2.1. Model Description

All finite element analysis was performed using ANSYS Mechanical, Academic Research Version 17.2 (ANSYS Inc., 2016). The MDC considered by Lavarney consists of three

components, an HSS circular tube between two flat steel plates. A local coordinate system was used for all the FEA models as shown in Fig. 8-1. The end plates are connected to either the façade panel or the building frame and are assumed parallel to one another. The MDC was modeled using shell elements (ANSYS Shell 181), which are four-noded elements with six degrees of freedom per node (ANSYS Inc., 2016). The structural behavior of both the HSS and end plate components of the model are defined by the shell elements. The HSS and plate shell elements are assigned a plasticity material model that includes kinematic and isotropic hardening with a Von-Mises yield criterion (ANSYS Multi-linear Isotropic Hardening Model), and is defined by a series of stress-strain points. The stress-strain data for the baseline models and the MDC models are presented in their respective sections.

Contact between the HSS and end plates was simulated because the MDC is expected to undergo large deformations during high hazard loading events such as blast and impact loading. Large radial deformations to the HSS will cause it to contact the plates. Contact elements (ANSYS Conta 173) were used around the centerline of the HSS with a mesh matching the shell element mesh. These elements sit on the centerline of shell elements and are part of a pair of elements used to represent contact between 3D surfaces. Target elements (ANSYS Targe 170) are applied to the end plates. The target element mesh matches the shell element mesh of the flat plates. The contact and target elements identify the potential contact surfaces that may occur due to the HSS deformation during the analysis. However, these elements do not contribute to the modeled structural behavior, such as stiffness and strength.

The nodes in each flat plate are coupled together to behave as a rigid plane (ANSYS Cerig) to simulate the relatively rigid bodies to which the MDC end plates are attached. One plate represents the building frame and acts as a fixed connection that will not allow movement. The fixed plate is constrained in all directions. The opposite plate is then assigned the translational and/or rotational displacements of the façade panel during the high hazard loading event.

8.2.2. Verification of Base Model Results

Two baseline MDCs, consisting of HSS16x0.375 and HSS10.75x0.25, were modeled and verified with the results from the Lavarney (2013) experiments. An HSS7x0.25 MDC was also tested in the Lavarney (2013) experiments, but that size HSS was not considered for this verification. Since tensile coupon data was not available for this size HSS, its material properties were unknown. The stress-strain values considered in the FEA base model for the HSS16x0.375 and HSS10.75x0.25 are available in Fig. 8-2. These curves were developed from the tensile coupon tests performed as part of the Lavarney (2013) experiments. Both the HSS16x0.375 and HSS10.75x0.25 models were compressed 6 inches radially inward (x-direction). These deformations were performed to match the Lavarney (2013) experiment deformations.

Both the HSS16x0.375 and HSS10x0.25 FEA results closely matched with the Lavarney (2013) experimental results as seen in Fig. 8-3 and Fig. 8-4. HSS10.75x0.25 FEA yield strength is about 5.8 kips and the FEA strength at 6 inches of deformation (x-direction) is 8.6 kips. Both of these strengths closely match the Lavarney (2013) experimental strengths in Fig. 8-3a. Some difference was observed in the initial elastic strength, but the post-elastic strength and material strain hardening was well captured. In

Fig. 8-4a, the FEA yield strength of the HSS16x0.375 is 7.8 kips and FEA strength at 6 inches (x-direction) is 10.9 kips. The Lavarway (2013) experimental yield strength is 8.2 kips and the strength at 6 inches of deformation is 10.1 kips (Fig. 8-4a). The HSS16x0.375 FEA model experienced slightly more strain hardening than the experiment, but there was not a significant difference between the FEA Lavarway (2013) experimental results in the hardened region. Despite the small differences between the FEA and Lavarway (2013) experimental results, both of the force-deformation curves produced by the FEA models were deemed acceptably close to those of the experimental results. Reasonable deformed shapes were created in the FEA base model throughout the loading procedure (Fig. 8-3b and Fig. 8-4b). The equivalent plastic strain diagrams for both of the FEA models show plastic hinge yield lines are developing (Fig. 8-3d and Fig. 8-4d). The plastic hinges occurred in expected areas of the HSS where large changes in the HSS curvature are occurring. The maximum plastic strain in these diagrams show both models are experiencing likely acceptable levels of plastic strain. The Von-Mises stress diagrams in Fig. 8-3c and Fig. 8-4c show areas of high stress where the plastic hinges are forming corresponding to the strain levels and specified material model. Again, the maximum stress values available on these contour diagrams show reasonable values.

8.3. MDC Models of Experimental Specimens

8.3.1. Introduction

Once the base model results were verified against the Lavarway (2013) experimental data, the model was adapted to the designs of the different types of MDCs considered in this research (MDC1, MDC2, and MDC3). The three MDC designs still consisted of a circular

HSS attached between two parallel plates. The plates were ASTM A36 steel and the HSS were ASTM 500 Gr. C steel. All of the HSS tubes in the MDC designs were various lengths HSS6x0.25. The MDC plates included standard, short-slotted, or long-slotted bolt holes for attaching to the facade panel or building frame. Although the MDC design models were constructed from the base model, the geometries, material properties, contact surfaces, supports, and loading of the three designs varied from the base model. The FEA axis directions remained consistent with those of the base model as seen in Fig. 8-1.

8.3.2. MDC Material Models

The multi-linear plasticity material models for the HSS and plates with stress-strain properties for each MDC component are shown in Fig. 8-5. The material model of the A36 plates was developed from the tensile coupon data presented in Section 7.1.3.1. Due to the issues testing the HSS coupons discussed in Section 7.1.3.1, the HSS material model was developed from a combination of the expected stresses from AISC 341-10 Seismic Provisions for Structural Steel Buildings (AISC, 2010a) and the material tests in Fadden (2013). The HSS material model yield stress was specified as $R_y * F_y$ and the tensile stress as $R_t * F_u$. A value of 1.3 was used for R_y and a value of 1.2 was used for R_t per AISC 341-10. The model between the yield stress and tensile stress was developed based on the tests from Fadden (2013). The model was developed using the Fadden (2013) data from side-wall coupon tests from 0.25 inch thick HSS, the same HSS thickness used in this study. The coupons from the HSS corners were not used because the corner curvature is too large to be representative of the circular HSS. The corner areas experience significantly more strain hardening during the HSS fabrication process compared to the rest of the cross

section. The weld seam coupon data was also not used because it is not representative of the average material properties over the HSS cross-section.

8.3.3. MDC Type 1 Model (MDC1)

8.3.3.1. Model Descriptions

The drawings of MDC1 are available in Appendix C. The long bolt slots on the frame plate allow relative lateral movement to accommodate seismic drift and those on the panel plate allow relative vertical movement between the façade panel and connector for thermal expansion. The MDC type 1 (MDC1) was designed to simultaneously undergo 3.1 inches of outward radial translation (x-direction) and 0.025rads of rotation about the lateral in-plane panel axis (z-axis) (Fig. 8-6a). These deformations were determined from the critical loading scenario of out-of-plane seismic forces acting on a façade edge panel.

Two MDC1 models were considered, which are referred to as Model 1 and Model 2. Each model had different boundary conditions to simulate bounds of potential initial bolt-hole bearing contact (Fig. 8-6c). Neither of the MDC1 models utilized any contact/target planes because the deformed HSS will not contact the plates during tensile MDC deformation. Like the base model, the structure of the HSS and plates consisted of shell181 elements in both MDC1 models. The MDC welded connection at the end plate was modeled by coupling nodes at the weld slots between the plates and HSS using the ANSYS Cerig constraint equation.

Boundary conditions were the only difference between the two MDC1 models. Model 1 applied boundary conditions only to areas of the plates that would experience bearing on the façade panel or building frame. These areas were on the top and bottom of

both plates (y-direction) from the center of the bolt slot to the outside of the plate where plate prying will occur. These areas on each plate in Model 1 were coupled together using the “cerig” command. The top and bottom edges (y-direction) of the plates act as a rigid body while the centers of the plates allowed deformation. For both plates in Model 1, the boundary conditions were applied assuming that the bolt was in the center of the bolt slot. The panel plate was a fixed boundary while the frame plate experienced the translations (x-axis) and rotation (about z-axis) imposed on the MDC. Model 2 had these same plate boundary conditions on the panel plate plus additional boundary conditions on the frame plate. The moving frame plate changed slightly in Model 2 to account for the bolts on the panel plate. On this frame plate, the nodes around the bolt locations were assumed stationary and could not move in the z or y directions. They were free to move in the x direction with the prescribed movement of the rest of the plate. For both Model 1 and Model 2, the HSS and the plates in MDC1 are designed to yield to provide the necessary behavior and create boundary conditions consistent with the connection details. To determine the appropriate plate thicknesses for MDC1, analyses were performed for various plate thicknesses including 1in, 0.75in, and 0.50in. Ultimately, a plate thickness of 0.75in was chosen for MDC1 and used in the experiment. The same plate thicknesses were applied to MDC2 and MDC3 to maintain the same MDC thickness.

8.3.3.2. Convergence Study

Convergence studies were performed on Model 1 to determine appropriate mesh size for both MDC1 models. The same final mesh size was applied to both models because these models are fundamentally the same and differ only in their boundary conditions. Force-deformation, Von-Mises stress, Von-Mises elastic strain, and equivalent plastic strain were

studied for convergence at four points (P1, P2, P3, P4) on the MDC cross section (Fig. 8-6b). All of the points were studied near the center of the MDC length (z-direction). Once the change in the force-deformation, stress, and strain was below 3% between each mesh size, these criteria were considered adequately converged. The average mesh size for each MDC component used in the convergence study is available in Table 8-1. The force-deformation curve for MDC1 (Fig. 8-6d) converged before most of the stress and strain at localized points. The force-deformation data was converged by mesh size 3. The stress and strain generally converged at the same mesh size at each point. For P1 located on an HSS hinge area, the Von-Mises stress and equivalent plastic strain converged at mesh size 4 (Fig. 8-6e). The stress and strain at point P2, located between the HSS hinge locations, was near convergence (10%) by mesh size 6. However, the values did not reach below the 3% convergence threshold (Fig. 8-6f). The Von-Mises stress and elastic strain on frame plate point P3 converged by mesh size 5 (Fig. 8-6g). The Von-Mises stress and elastic strain on panel plate point P4 both achieved convergence at mesh 3 (Fig. 8-6h). After the convergence study was performed, mesh size 6 was used in Model 1 and Model 2 to accurately obtain force, stress, and strain data.

8.3.3.3. Results

The force-deformation curves of MDC1 Model 1 and Model 2 are shown in Fig. 8-7a with the MDC1 experimental curve. Model 1 matches the experimental curve better than Model 2 at low deformations. However, the Model 2 force-deformation curve matches the experimental results better at high deformations. Due to these force-deformation curves, it can be determined that the boundary conditions in the MDC1 experiment were a combination of the Model 1 and Model 2 boundary conditions. During the experiment, the

frame plate bolts engaged at higher deformations, which stopped the frame plate from moving in the y-direction at the bolt locations. The force-deformation plots for each MDC component in Model 1, Model 2, and the MDC1 experiment is available in Fig. 8-7b. Overall, both models underestimated the deformation of the HSS while overestimating the deformations of the panel and frame plates. Noticeable differences between the Model 1 and Model 2 deformed shapes occurred at the design deformations of 3.1in of translation (x-direction) and design rotation of 0.025 rads (about z-axis) (Fig. 8-7c). In Model 1, both the panel and frame plates show similar amounts of deformation at the MDC design deformation and rotation. However, in Model 2, the frame plate clearly shows more deformation than the panel plate. These differences in deformed shape were due to the different boundary conditions applied in the models. The true deformed shape at the design deformation and rotation is closer to that of Model 2 because this model better represents MDC1 at higher deformations. Although the deformed shapes of Model 1 and Model 2 vary slightly, there were no significant differences in the Von-Mises stress and equivalent plastic strain plots at the design deformation and rotation (Fig. 8-8a-d). In Fig. 8-8c-d, there are areas of significantly high plastic strains (40%-50%) in localized areas near the HSS weld connection to the plates. Such high plastic strains are not realistic and are due to the highly restrained mesh in these areas. The mesh refinement may also be locally inadequate in this area of the model. The average strains within the plastic hinge regions are on the order of 5-10% strain at the design deformation.

8.3.4. MDC Type 2 Model (MDC2)

8.3.4.1. Model Description

The MDC type 2 (MDC2) must withstand the tributary gravity load imposed on it by the façade panel in addition to the high hazard loading. The MDC2 drawings are available in Appendix C. The controlling out-of-plane loading for this connector is due to air-blast effects on the prototype system considered. The gravity load applied to each MDC2 on the considered panel connection configuration is 15.08kips (Fig. 8-9b). After the gravity load is applied, MDC2 was compressed by -2.78 in of translation (x-direction) then rotated by 0.087 rads about the horizontal in-plane façade panel axis (about y-axis). After this compression and rotation, a rebound phase occurs that creates an inward translation to -0.96 in (x-direction) and the rotation of -0.031 rads (about y-axis) relative to the original position (Fig. 8-9a). Lastly, MDC2 is brought back to its zero position (Fig. 8-9a).

Both the HSS and plates utilized the shell181 elements from the base model. When the MDC was compressed, the walls of the HSS contact the plates as the HSS deforms. Therefore, the model needed the contact/target elements from the base model. The ANSYS “target” elements were copied from the shell plate mesh to ensure they exactly overlapped. The plate shell nodes, plate target nodes, and the HSS nodes near the plate weld line were coupled together using the ANSYS “cerig” command to simulate the welded connection between the HSS and plates. The boundary conditions were then applied to each of these rigid areas using a master node. The standard holes on the frame plate and the short slotted holes on the panel plate were not modeled due to the plates behaving rigidly and not contributing to the MDC deformation. The frame plate was held fixed in all directions

while the panel plate experienced the translation (x-direction) and rotation (about the y-axis) imposed by the hazard loading as well as the gravity load (z-direction) (Fig. 8-9c). The panel plate was also constrained from rotating about the z-axis. The plates for MDC2 were made into rigid components because the plates do not deform or yield to absorb any of the loading energy. Only the circular HSS deforms to absorb the blast loading that MDC2 experiences.

8.3.4.2. Convergence Study

Convergence studies were conducted to determine an appropriate mesh size for the model force-deformation, stress, and strain data. The average mesh sizes of the MDC2 components are available in Table 8-1. Convergence studies were conducted at two points on the HSS cross section and no points on the rigid plates (Fig. 8-9d). Both of these HSS cross section points were analyzed at approximately the center of the HSS (z-direction). Point P1 is at a hinge location on the HSS and point P2 is between the HSS hinge locations. The convergence studies were conducted at the two design-level translations and rotations. The first design-level deformations occurred at load step 20 has -2.78 in of translation (x-direction) and 0.087 radians of rotation (about y-axis) and the second design-level deformations occurred at load step 29 has -0.96 in of translation (x-direction) and -0.031 radians of deformation (about y-axis). The mesh size was reduced until the changes of force-deformation, stress, and strain change by 3% or less between the mesh sizes. The force-deformation curve converged by mesh size 3 (Fig. 8-9e), which was before most of the Von-Mises stress, Von-Mises elastic strain, or equivalent plastic strain converged. At P1, the Von-Mises stress converged at mesh size 4 during step 20 and 29. The P1 equivalent plastic strain converged at mesh size 5 during step 20 and mesh size 4 during

step 29 (Fig. 8-9f). The Von-Mises stress and elastic strain at P2 converged with mesh size 2 at step 29 and mesh size 5 at step 20 (Fig. 8-9g). Point P1 required a finer mesh to converge because there is a large stress and strain gradient at the HSS hinge. Mesh size 5 was the required mesh size for the convergence of all relevant FEA data and was used in the final MDC2 model.

8.3.4.3. Results

The MDC2 force-deformation FEA results reasonably represent experimental results until approximately -0.75 inches of inward radial translation (x-direction) (Fig. 8-10a). The nuts holding the frame and panel plates to the experimental setup begin contacting the MDC HSS around this deformation, which is not represented in the model. The experimental results from -0.75 inches to -2.87 inches of compressed translation (x-direction) show a larger increase in force than during 0 inches to -0.75 inches of translation. This is expected because in the experiment the HSS had to deform around the nuts after contacting them. As the MDC is pulled back out (x-direction) to its original position, less force is also required to overcome the additional strain hardening caused by the nut contact. The energy that the MDC absorbed during the FEA was determined by numerical integration of the area under the resulting force-deformation curve. From 0 inches to -2.78 inches of translation (x-direction), MDC2 absorbed approximately 35.7 kip-in of energy. The FEA reasonably approximated the energy absorption, which was 43 kip-in in the MDC2 experiment. The FEA produced deformed shapes, Von-Mises stress contour plots, and equivalent plastic strain contour plots (Fig. 8-10b-c). The maximum plastic strains (Fig. 8-10d) were very high (25%-50%) in a few elements near the weld of the HSS to the plates. The maximum plastic strain outside these weld areas were 20-25%. The plates did not

experience stress, strain, or deformation during the FEA loading because they were assumed rigid during the analysis.

8.3.5. MDC Type 3 Model (MDC3)

8.3.5.1. Model Description

The MDC drawings are available in Appendix C. The MDC type 3 (MDC3) must withstand all of the lateral in-plane forces applied to the façade panels and is designed to have elastic behavior throughout its loading. The analysis applied a 0.315 inch translation (z-direction) on the MDC3 to determine its elastic strength and ultimate strength (Fig. 8-11a). Seismic loading controls the critical forces for design of MDC3.

Both the HSS and plates utilized the shell181 elements from the base model. When the deformation is applied to MDC3, the walls of the HSS contact the plates as the HSS deforms. Therefore, this model also required the contact/target elements from the base model. MDC3 also has weld slots and standard bolt holes on the plates. Each plate has a total of sixteen bolt holes, with eight holes above and eight below (y-direction) the weld slot. It is assumed that no relative movement can occur within these bolt holes. The contact planes, and end plate constraints were created similar to previous MDC models. Both the HSS contact elements and target plate elements had the same mesh as the respective shell elements. Both of the plates were made rigid using the “cerig” command and each had a master node to control plate movement. The deformation was applied by holding one plate fixed in all directions while the other was translated laterally in-plane (z-direction) (Fig. 8-11c). This moving plate was also constrained from moving out of plane in the x and y directions.

8.3.5.2. Convergence Study

A convergence study was conducted to evaluate an appropriate mesh size for MDC3. Average mesh sizes for each MDC component used in the study are available in Table 8-1. The force-deformation, Von-Mises stress, Von-Mises elastic strain, and equivalent plastic strain were evaluated for convergence. Convergence occurred when the difference between force-deformation, stress, and strain values were less than 3% between mesh sizes. Two points on the HSS cross-section were studied for convergence, both of which were located near the center of the HSS (z-direction) (Fig. 8-11b). The force-deformation curve converged at mesh size 3 (Fig. 8-11d). The Von-Mises stress and equivalent plastic strain at P1 also converged at mesh size 3 (Fig. 8-11e). At the location of P2, the Von-Mises stress and elastic strain converged at mesh size 4 (Fig. 8-11f). Because most of the desired quantities had converged by or before mesh size 5, this mesh size was used in the final MDC3 model.

8.3.5.3. Results

The MDC3 model force-deformation curve is compared with the experimental force-deformation data in Fig. 8-12a. Beyond 0.2 inches of translation, the experiment specimen began moving out-of-plane. This out-of-plane accounts movement is believed to cause the large difference between the curves at 0.2-0.315 inches of deformation. It is observed that the FEA slightly overestimates the MDC elastic stiffness and strength while the model underestimates its material hardening. The FEA created deformed shapes and Von-Mises stress contours (Fig. 8-12b-c). In the plastic strain contours in Fig. 8-12d, small areas of extremely high strain are found at the HSS connection to the plates. The high plastic strains

(50%-60%) in these regions are unreasonable and are likely due to the way the HSS was rigidly connected to the plates within the model. It may also be due to inadequate mesh refinement in these localized areas. The plate/HSS connection likely caused only a few elements to experience high strains, while the other element plastic strains are reasonable (1%-5%).

8.4. Summary

An FEA model was created and first validated against the experimental data from Lavarnway (2013). Following this validation, the model was adapted to three current MDC designs subjected to more complex loading protocols consistent with the hazardous loading considered. The MDC models also included more realistic fabrication details.

All three of the MDC designs deformed as expected in the analyses. Under radial compression (x), the circular HSS of MDC2 initially created four plastic yield lines and then six yield lines as contact between the HSS and end plates occurred. Under radial tension, the HSS in MDC1 formed four plastic hinges. The 0.75in thick end plates of the MDC1 was also designed to yield and form a plastic mechanism to accommodate the large radially outward deformations and absorb a portion of the energy from the loading scenario. The design intent of MDC3 was to resist the prescribed loads in an elastic manner however; the analysis performed determined the ultimate force deformation behavior of the MDC in addition to confirming the intended elastic strength. Overall, the analysis of the three MDC designs provided force-deformation behavior, deformed shapes, stress, and plastic strains consistent with the MDCs design intent. Some of the models experienced very large plastic strains. However, these high strains occurred on very few elements in

the models in regions where the mesh refinement was likely inadequate to capture the large strain gradient.

When compared to the design calculations, the FEA models performed as expected in terms of critical force, deformation, or energy absorption criteria for each MDC type (Table 8-2). The maximum tensile force of MDC1 FEA model was 51 kips, which is near the expected max force of 45.9 kips from the design calculations. However, the individual components of MDC1 behaved differently in the FEA model than in the design. The HSS was responsible for less than its design deformation, while the maximum plate deformation varied from their design deformation. Both plates were anticipated to deform the same about, and they did do so in MDC1 Model 1. However, the frame plate deformed more than the panel plate in MDC1 Model 2. MDC2 absorbed 35.7 kip-in of energy, which is 15% lower the design energy absorption. MDC2 also experienced approximately the same compressive force in the FEA as expected in the design (19 kips). Lastly, the MDC3 model showed the MDC remains elastic up to the design elastic load of 120 kips. MDC3 had an ultimate strength of 151 kips in the model. The calculations assumed that the shear capacity of the MDC3 tube was dependent on the center cross section of the HSS. The failure of the HSS in MCD3 may move from outside the center to the center, which would cause a lower maximum force.

MDC1	MDC Component	Mesh 1	Mesh 2	Mesh 3	Mesh 4	Mesh 5	Mesh 6
	HSS	1.89 in	0.94 in	0.63 in	0.47 in	0.31 in	0.24 in
	Frame Plate	0.70 in	0.53 in	0.42 in	0.35 in	0.26 in	0.21 in
	Panel Plate	1.16 in	0.70 in	0.50 in	0.39 in	0.27 in	0.20 in

MDC2	MDC Component	Mesh 1	Mesh 2	Mesh 3	Mesh 4	Mesh 5
	HSS	1.35 in	0.79 in	0.41 in	0.29 in	0.25 in
	Frame Plate	1.04 in	0.72 in	0.38 in	0.28 in	0.24 in
	Panel Plate	1.04 in	0.72 in	0.38 in	0.28 in	0.24 in

MDC3	MDC Component	Mesh 1	Mesh 2	Mesh 3	Mesh 4	Mesh 5
	HSS	1.57 in	0.67 in	0.41 in	0.30 in	0.24 in
	Frame Plate	1.58 in	0.70 in	0.42 in	0.32 in	0.24 in
	Panel Plate	1.91 in	0.84 in	0.51 in	0.38 in	0.30 in

Table 8-1: Convergence study mesh sizes for each MDC component. Final mesh size for each MDC model is bold.

MDC1	Maximum Tensile Force (kips)			Maximum HSS Translation (in)		
	Design	FEA Model 1	FEA Model 2	Design	FEA Model 1	FEA Model 2
	45.9	47.5	50.9	1.6	1.44	1.55
	Maximum Panel Plate Translation (in)			Maximum Frame Plate Translation (in)		
	Design	FEA Model 1	FEA Model 2	Design	FEA Model 1	FEA Model 2
	0.75	0.86	1.17	0.75	0.80	0.38

MDC2	Energy Dissipation (kip-in)		Maximum Compressive Force (kips)	
	Design	FEA	Design	FEA
	30.9	35.7	36.2	19.0

MDC3	Elastic Strength (kips)		Ultimate Strength (kips)	
	Design	FEA	Design	FEA
	135	120	N/A	151.4

Table 8-2: Comparison of the FEA results to the desired design values for each MDC

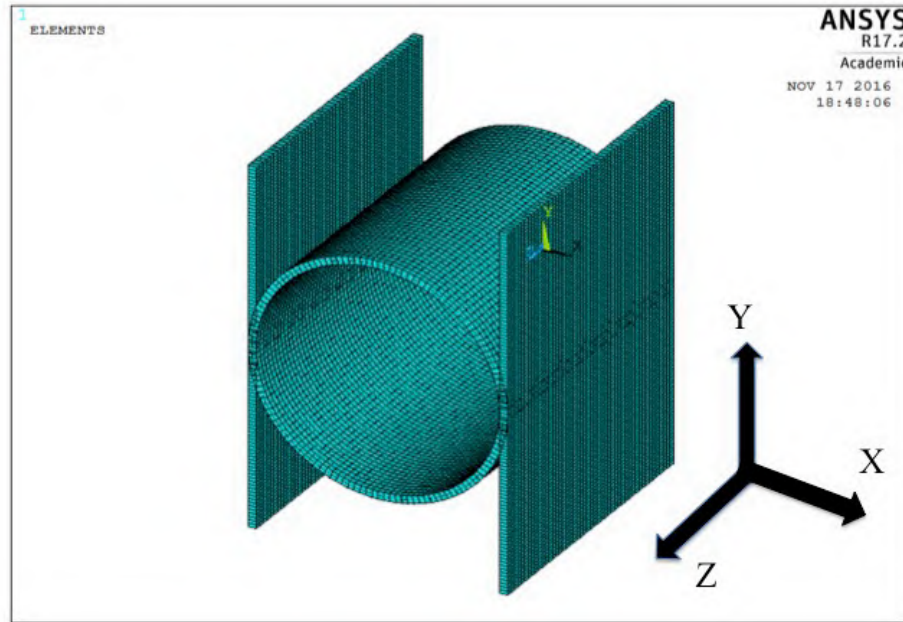


Fig. 8-1: An example base model showing the coordinate system for all of the base and MDC models

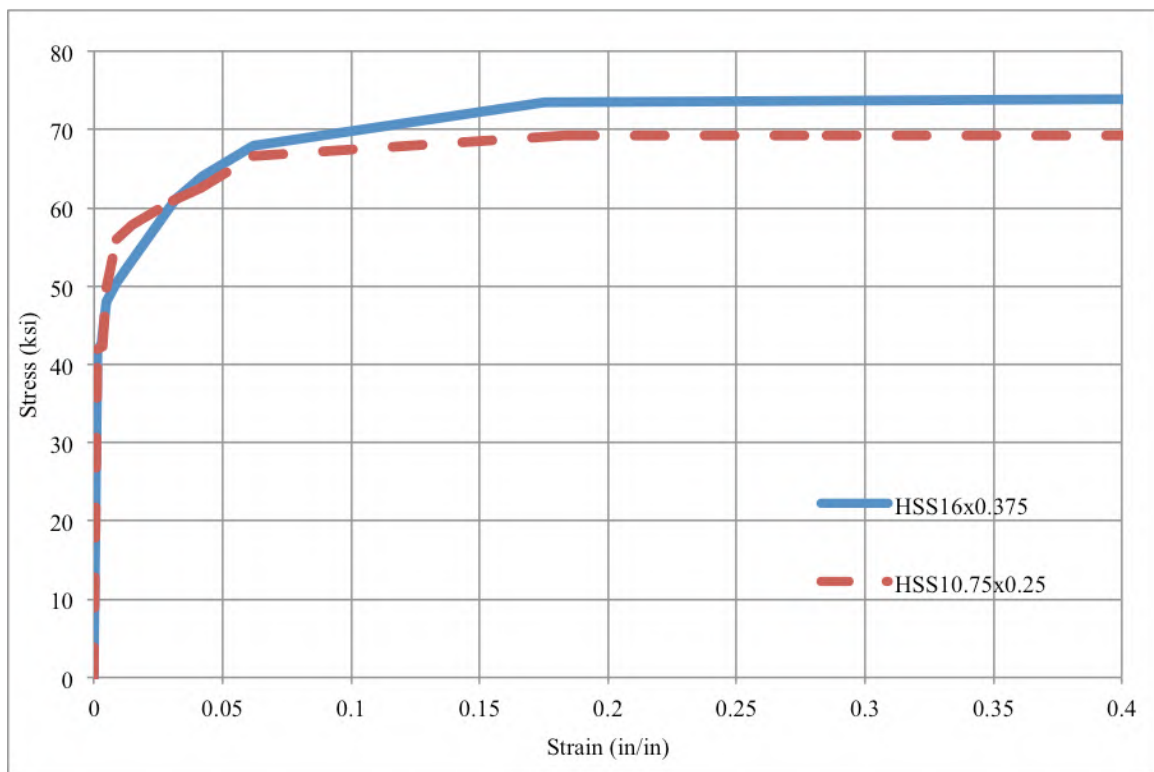
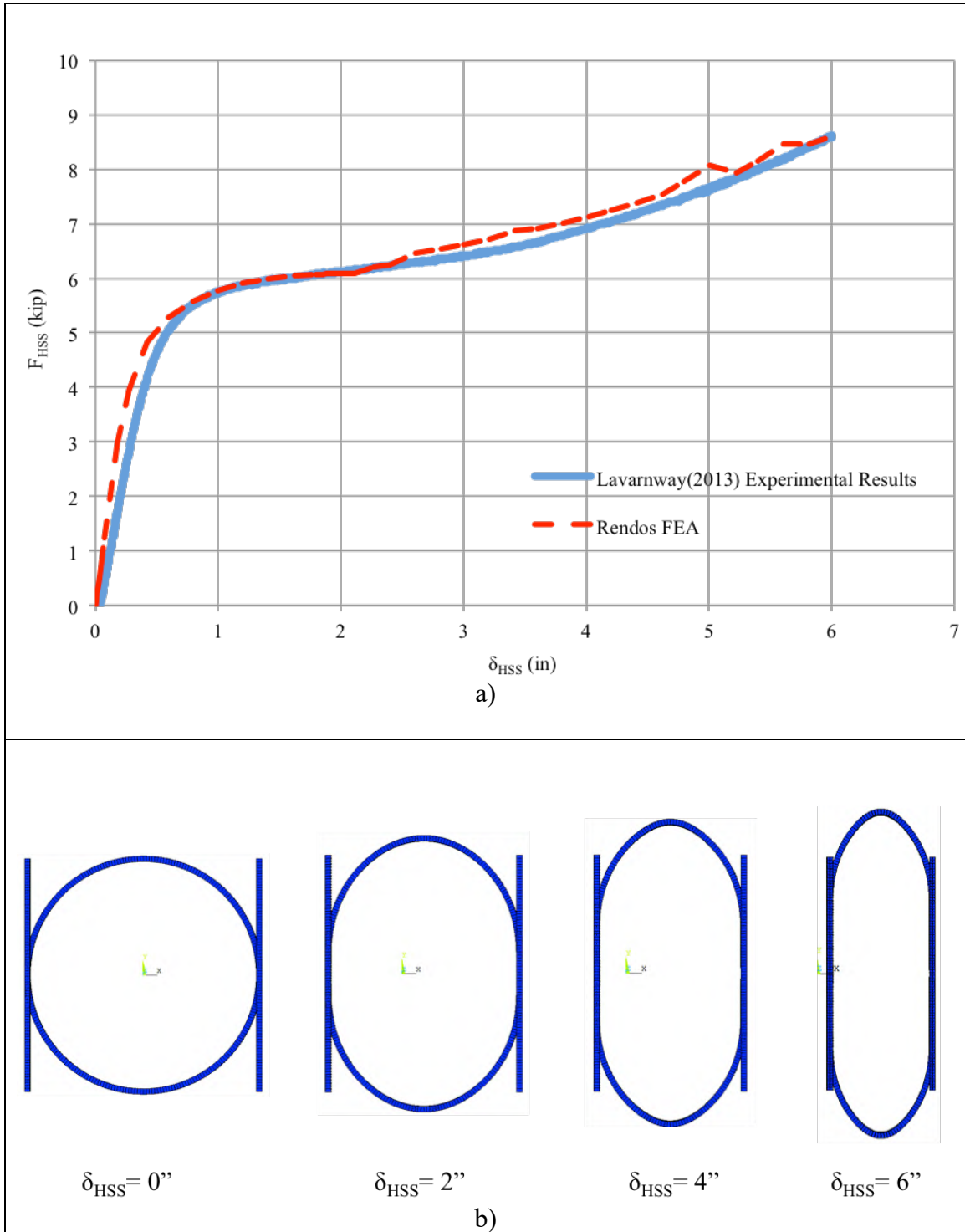


Fig. 8-2: Stress-strain curves input into the base FEA models for HSS16x0.375 and HSS10.75x0.25. Based on tensile coupon data from Lavarney (2013) experiments

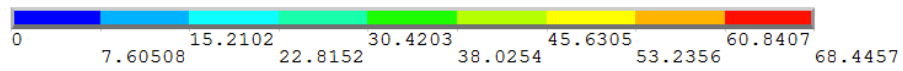
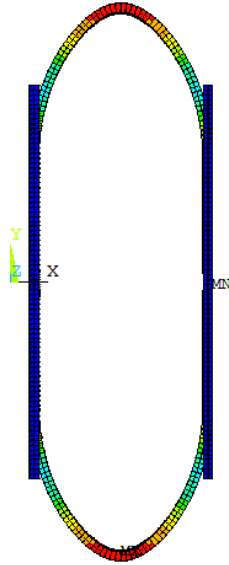
Fig. 8-3: HSS10.75x0.25 Base Model FEA Results a) Force-deformation response including comparison between FEA and Lavarney (2013) experiment b) Deformed shapes of HSS10.75x0.25 c) Von-Mises stress of the HSS10x0.25 at $\delta_{HSS}=6''$. Stress in units of ksi. d) Plastic strain of the HSS10x0.25 at $\delta_{HSS}=6''$



1
NODAL SOLUTION
STEP=12
SUB =3
TIME=12
SEQV (AVG)
DMX =6.00036
SMX =68.4457

ANSYS
R17.2
Academic

NOV 7 2017
12:28:24

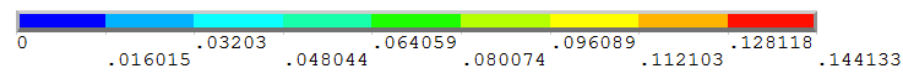
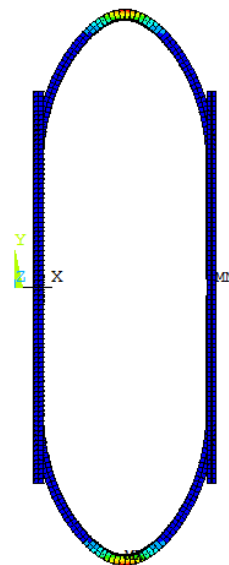


c)

1
NODAL SOLUTION
STEP=12
SUB =3
TIME=12
NLEPEQ (AVG)
RSYS=0
DMX =6.00036
SMX =.144133

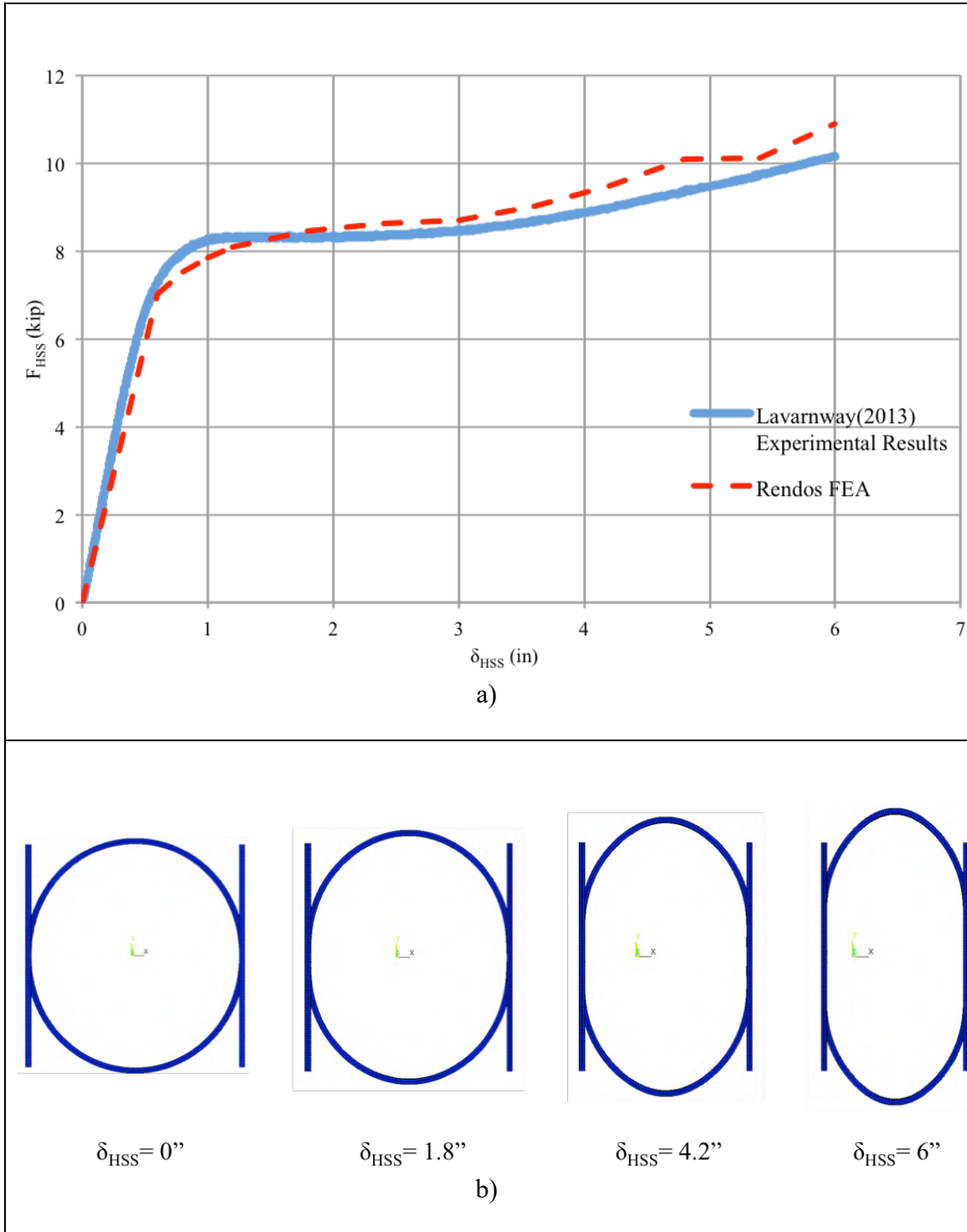
ANSYS
R17.2
Academic

NOV 7 2017
12:29:04



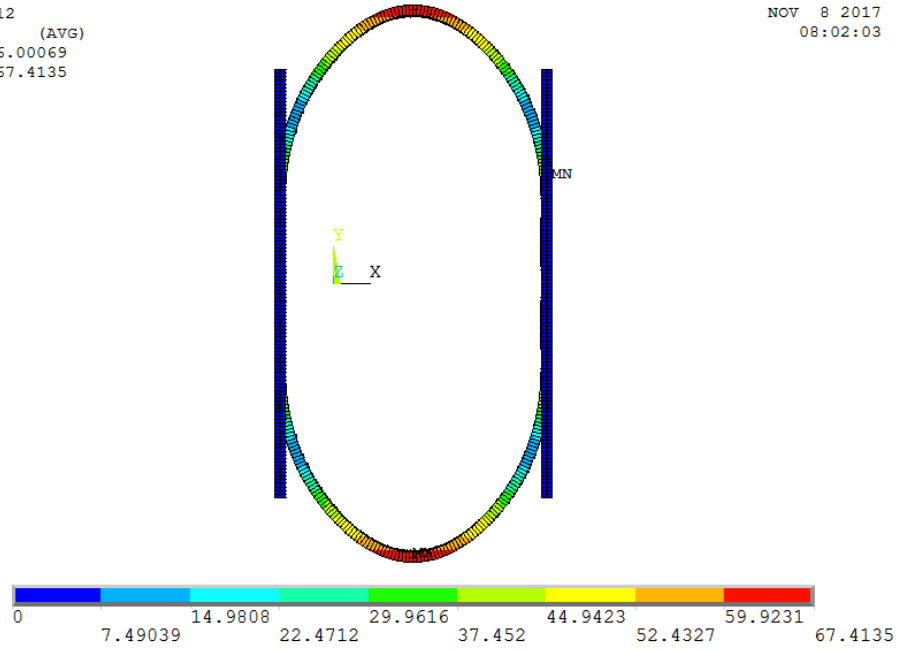
d)

Fig. 8-4: HSS16x0.375 Base Model FEA Results a) Force-deformation response including comparison between FEA and Lavarnway (2013) experiment b) Deformed shapes of HSS16x0.375 c) Von-Mises stress of the HSS16x0.375 at $\delta_{HSS}=6''$. Stress in units of ksi. d) Plastic strain of the HSS16x0.375 at $\delta_{HSS}=6''$



1
NODAL SOLUTION
STEP=12
SUB =1
TIME=12
SEQV (AVG)
DMX =6.00069
SMX =67.4135

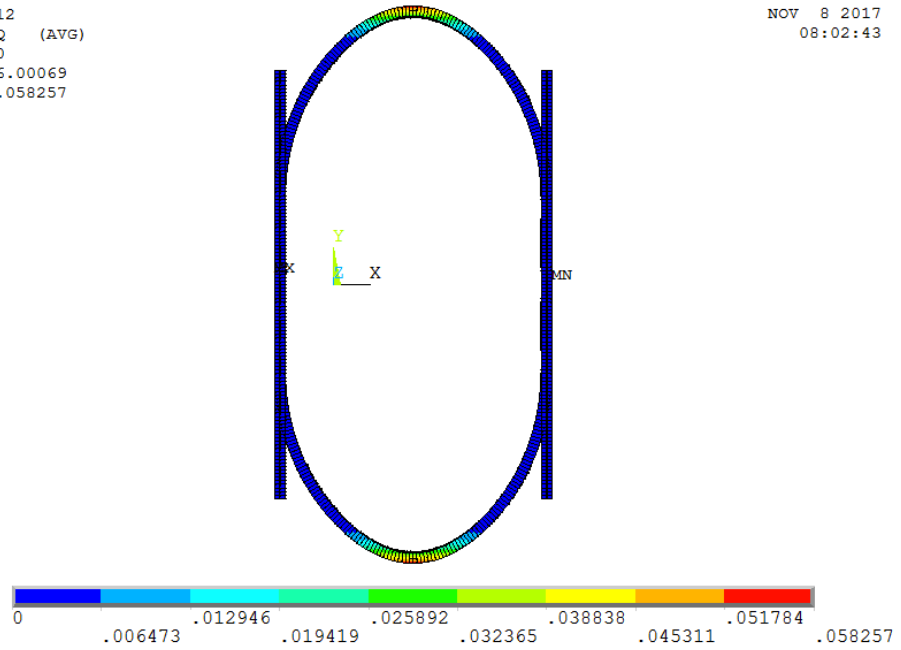
ANSYS
R17.2
Academic
NOV 8 2017
08:02:03



c)

1
NODAL SOLUTION
STEP=12
SUB =1
TIME=12
NLEPEQ (AVG)
RSYS=0
DMX =6.00069
SMX =.058257

ANSYS
R17.2
Academic
NOV 8 2017
08:02:43



d)

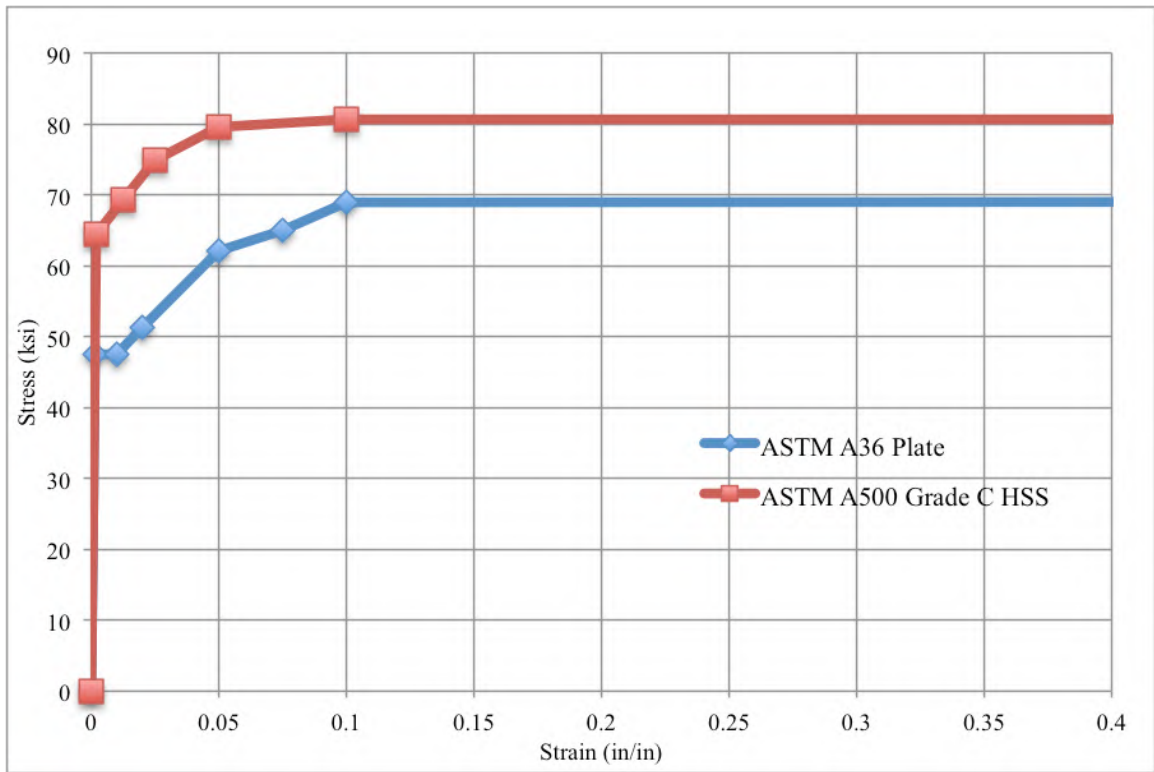
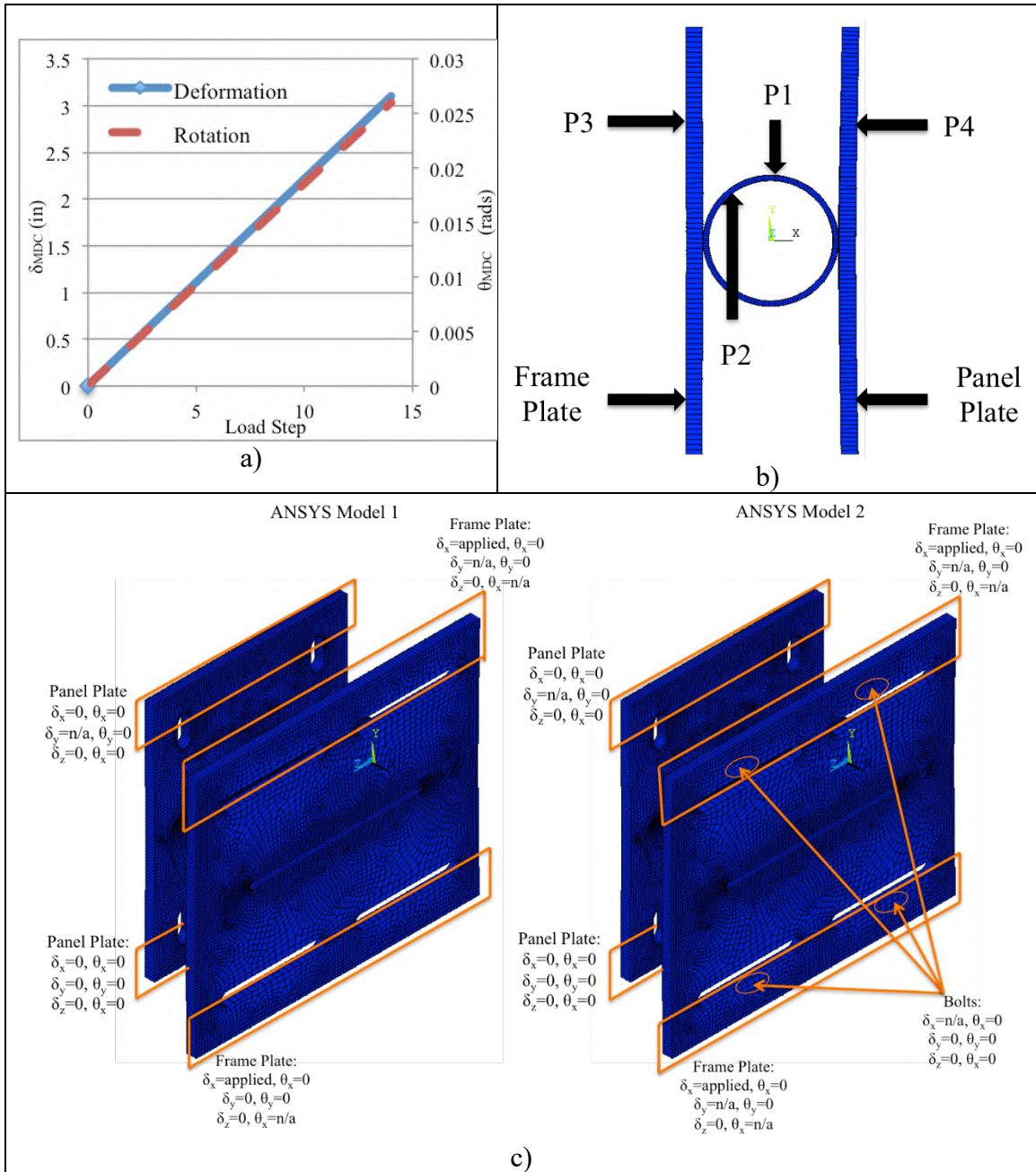
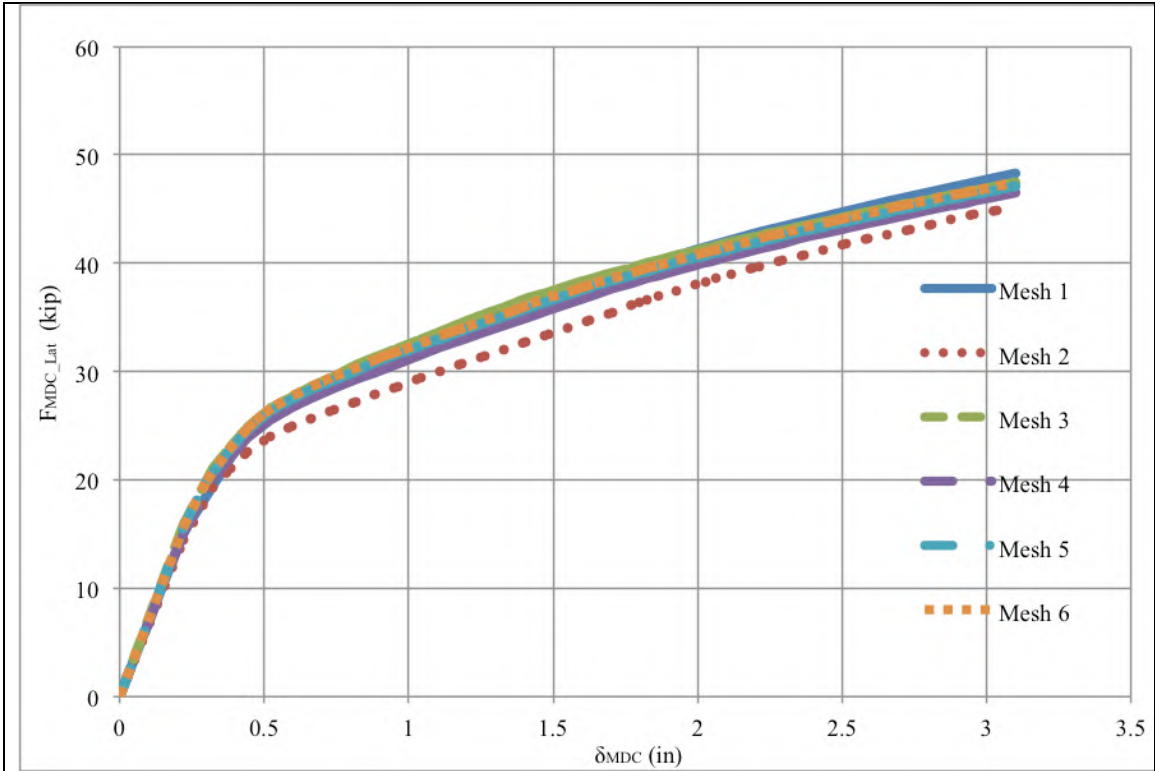


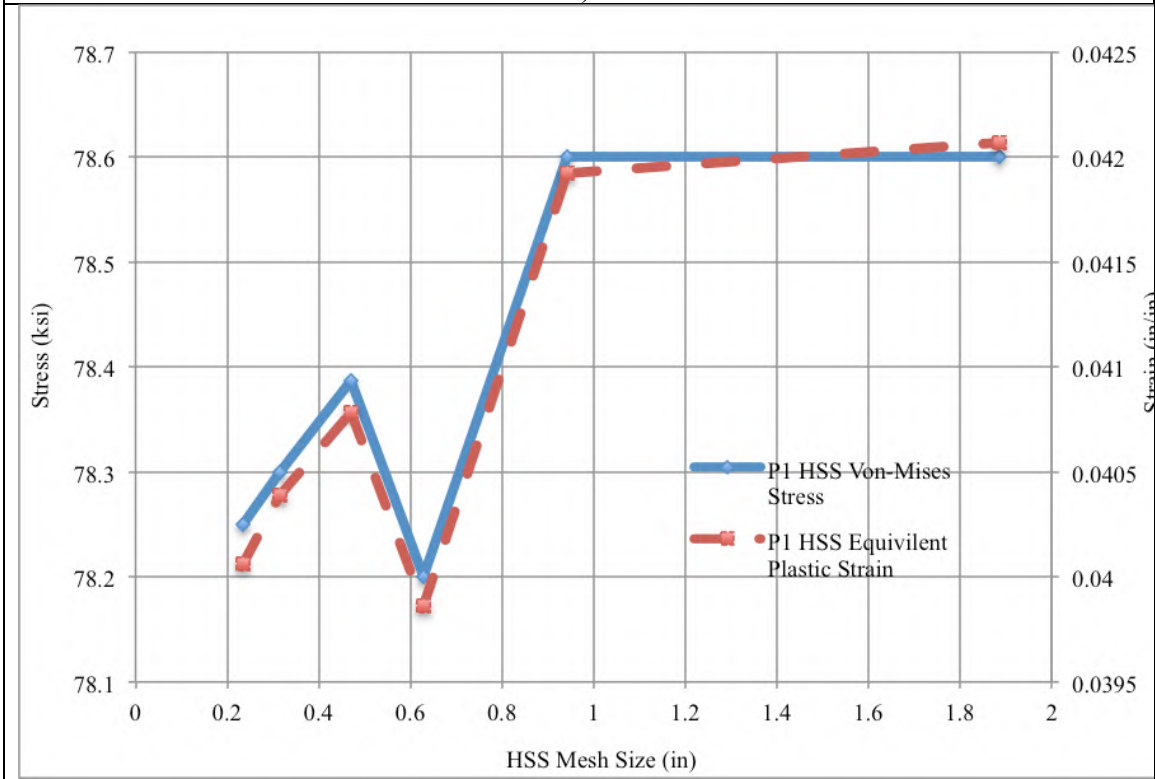
Fig. 8-5: Stress-Strain data defining MDC material models for A36 plate and A500 Grade C HSS used in the FEA

Fig. 8-6: MDC1 Convergence study at design basis of 3.1in translation and 0.025 rads rotation a) Deformation (x-direction) and rotation (about z- axis) applied in the FEA, b) Approximate point locations on MDC1 cross section analyzed for convergence study, c) Model 1 and Model 2 boundary conditions, d) Force-Deformation results, e) Convergence results of P1 on HSS, f) Convergence results of P2 on HSS,, g) Convergence results of P3 on frame plate, h) Convergence results of P4 on panel plate

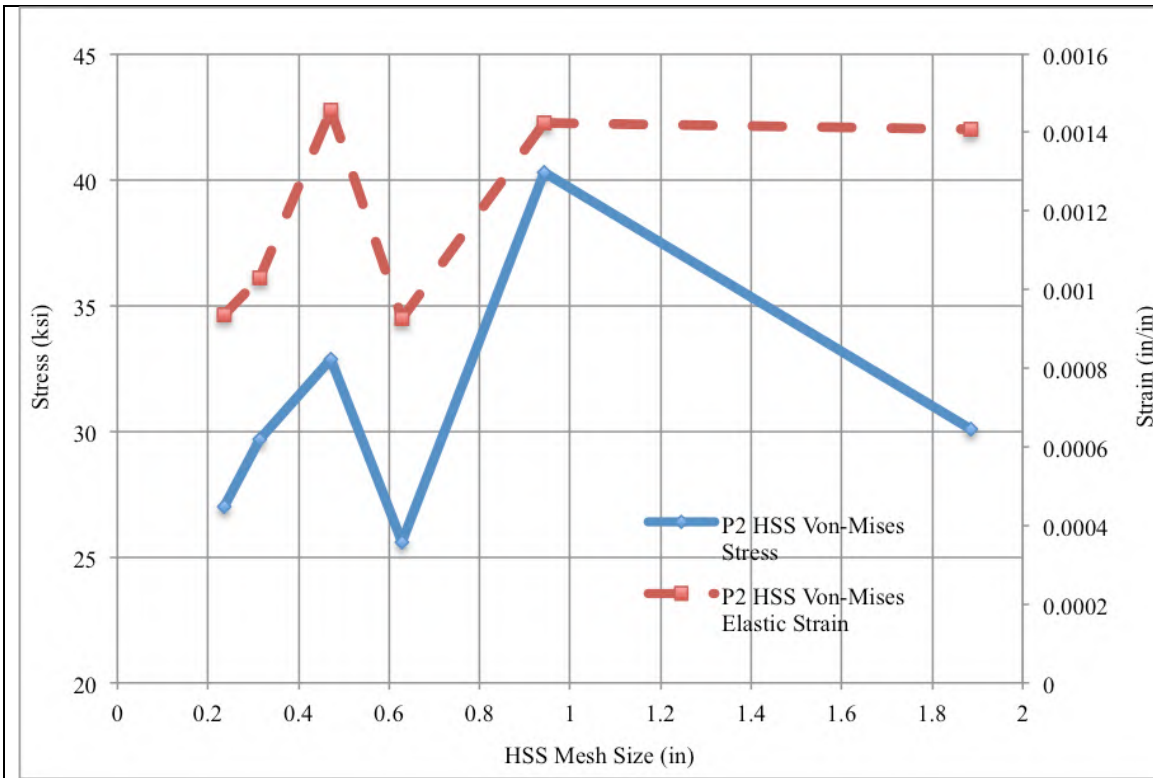




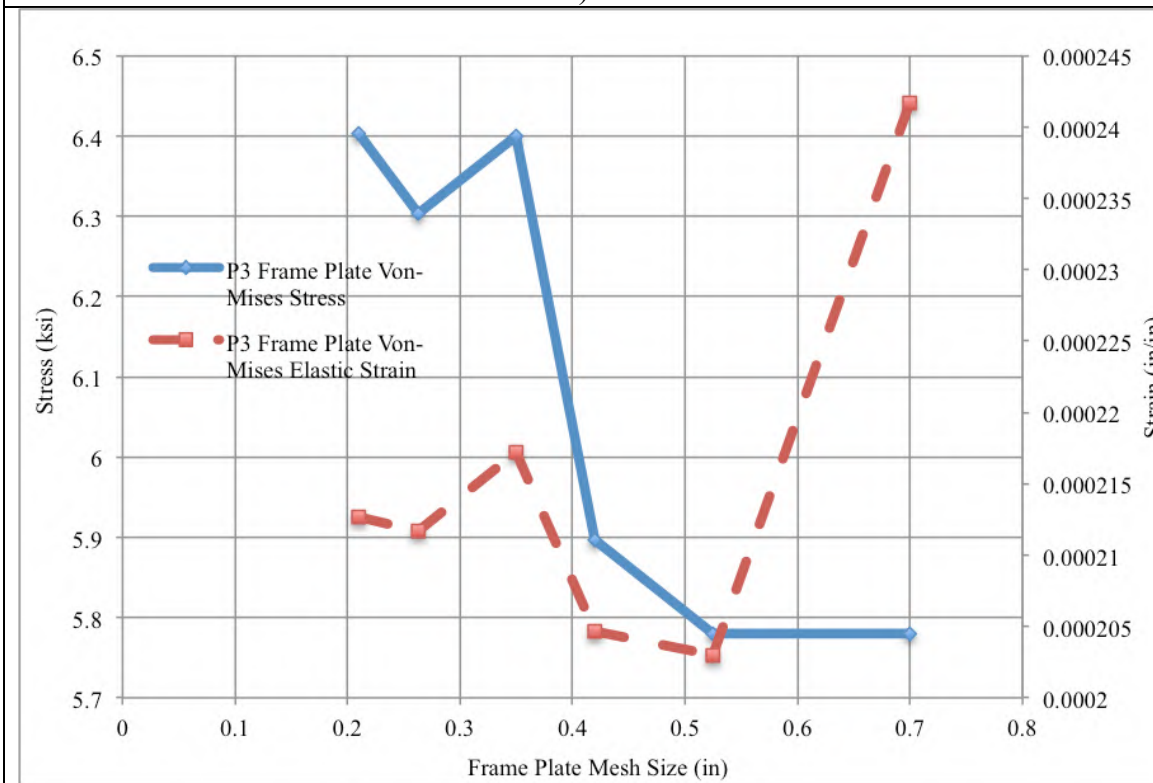
d)



e)



f)



g)

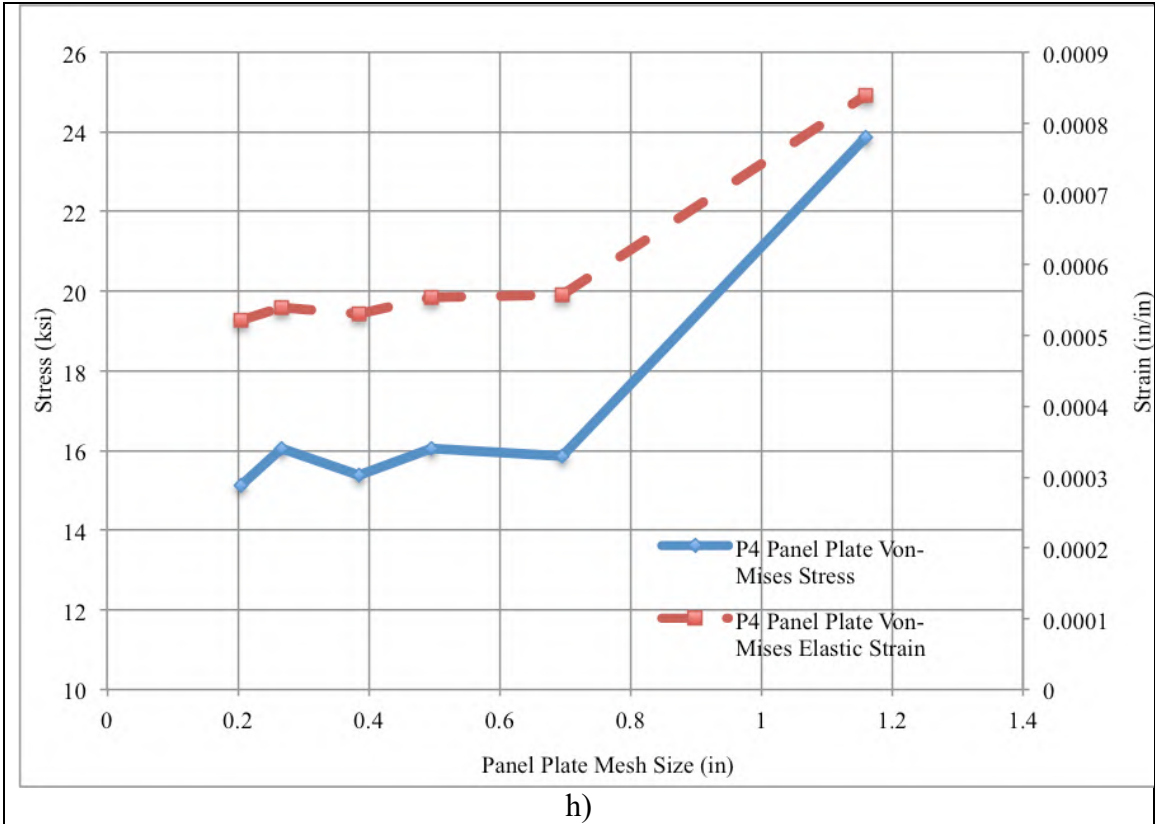
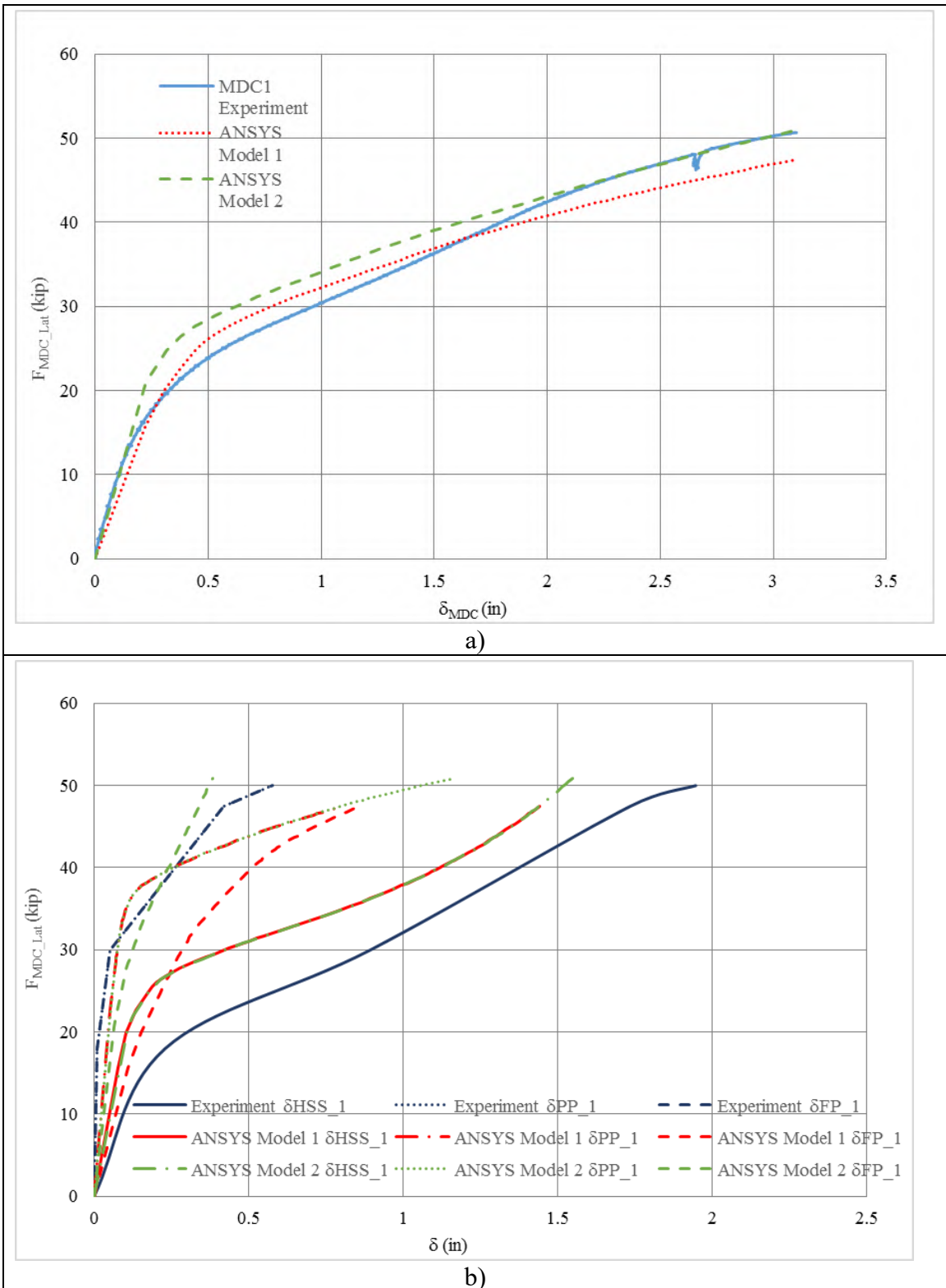


Fig. 8-7: FEA Results of MDC1 a) Force-deformation curves of the FEA and MDC1 experiment, b) Force-deformation curves of the MDC components from the FEA and MDC1 experiment, c) Deformed shapes throughout the FEA



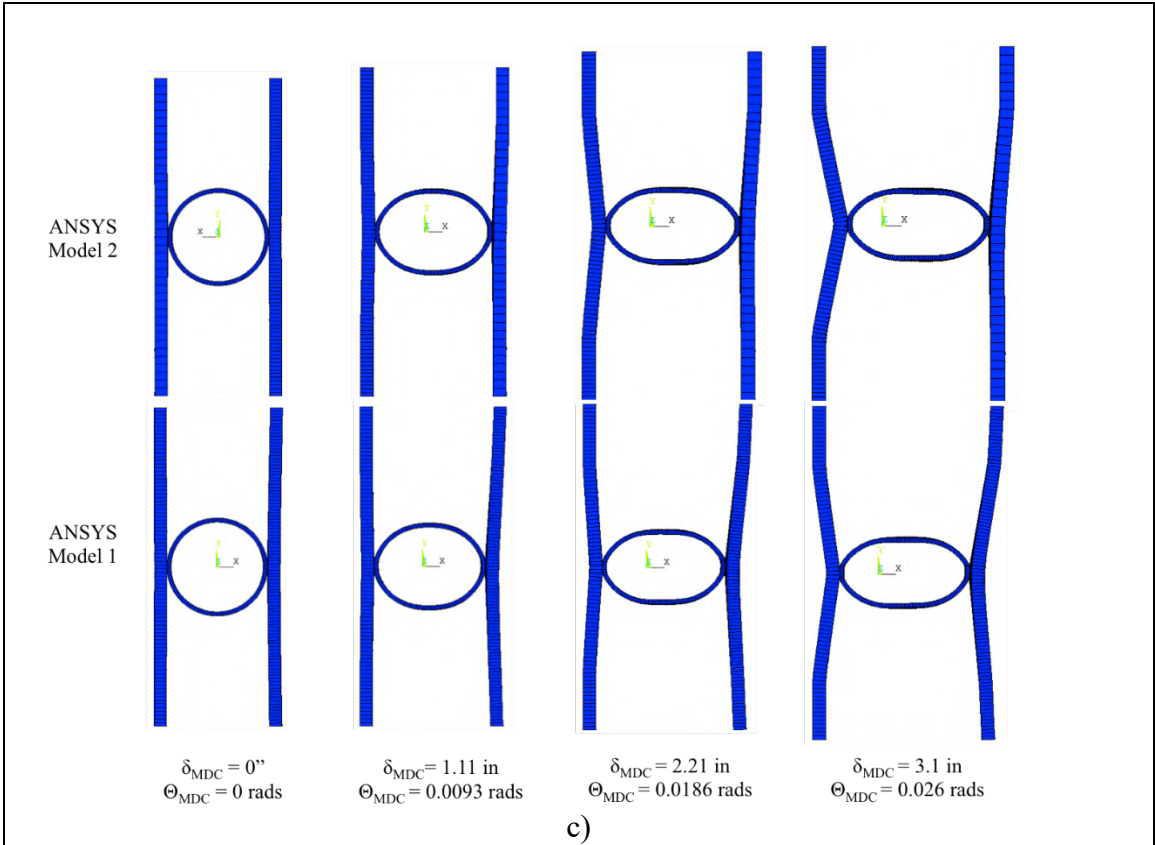
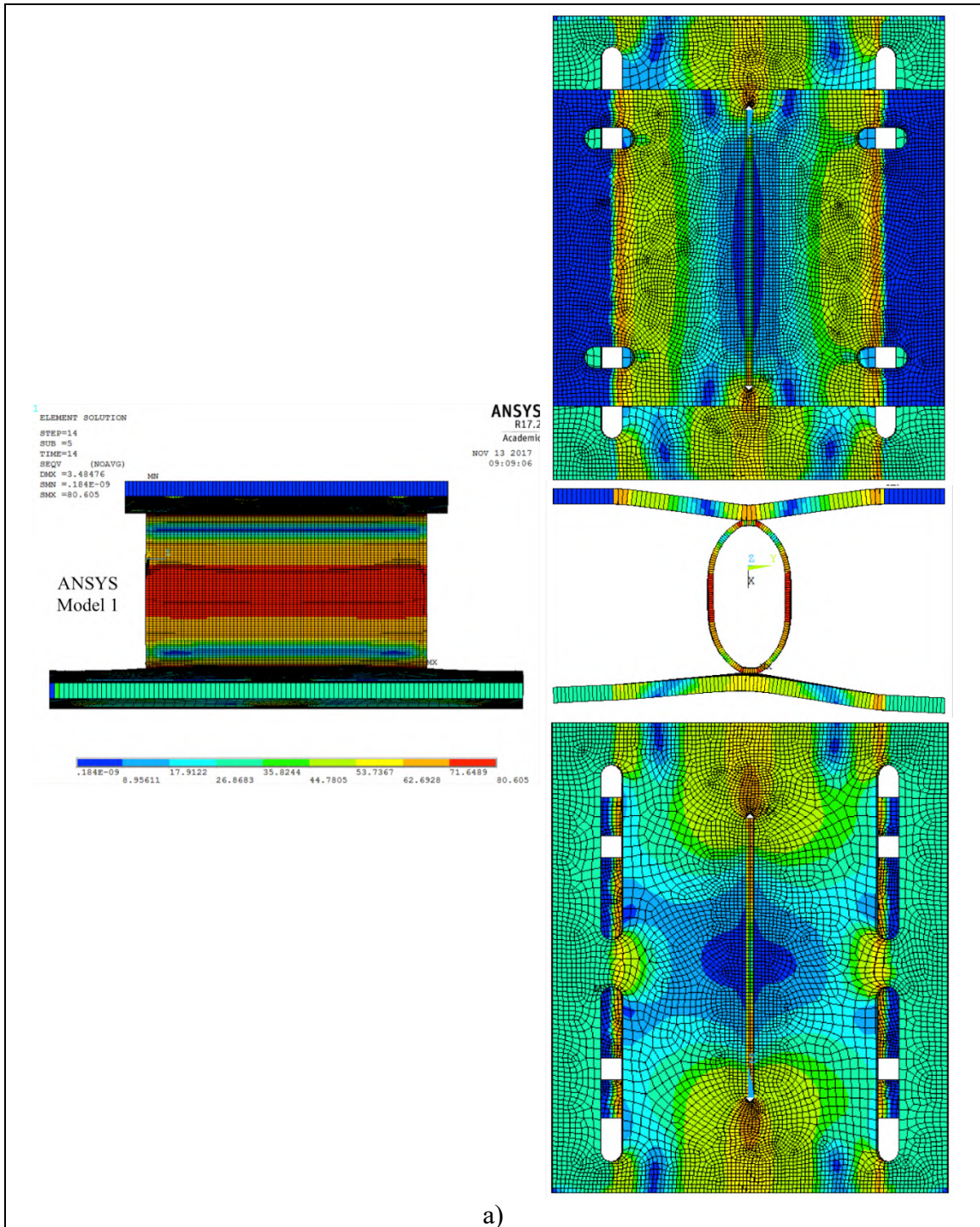


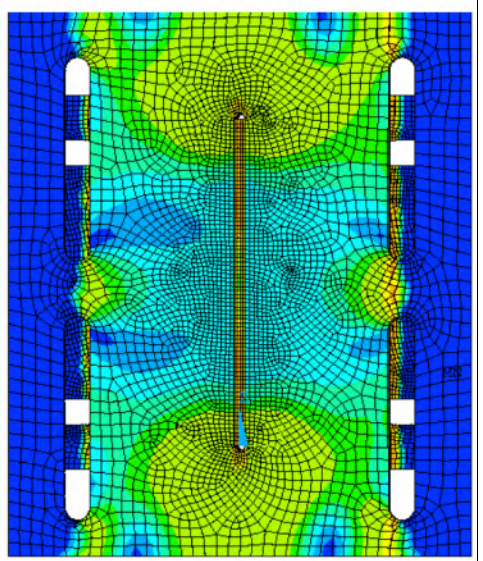
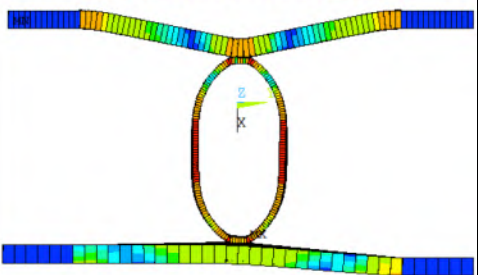
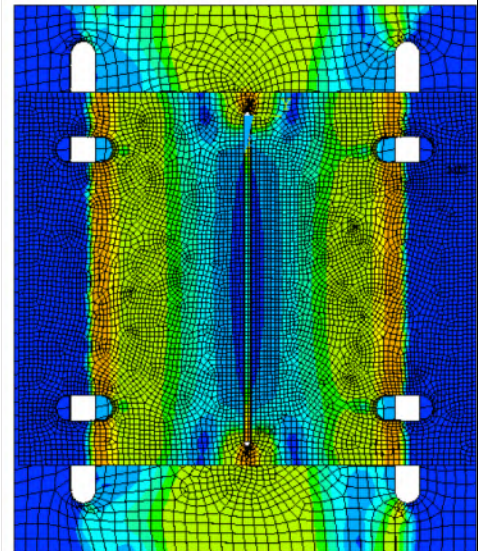
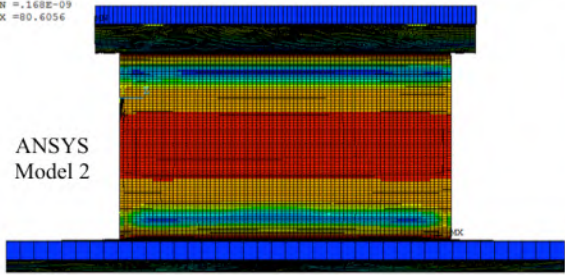
Fig. 8-8: FEA MDC1 Stress and Strain Contours a) Model 1 Von-Mises stress (ksi) contours at the design deformation and rotation b) Model 2 Von-Mises stress (ksi) contours at the design deformation and rotation c) Model 1 Equivalent plastic strain contours at the design deformation and rotation d) Model 2 Equivalent plastic strain contours at the design deformation and rotation



ELEMENT SOLUTION
STEP=14
SUB =5
TIME=14
SEQV (NOAVG)
DMX =3.37048
SMX =.168E-09
SMX =80.6056

ANSYS
R17.2
Academic
NOV 14 2017
10:29:03

ANSYS
Model 2

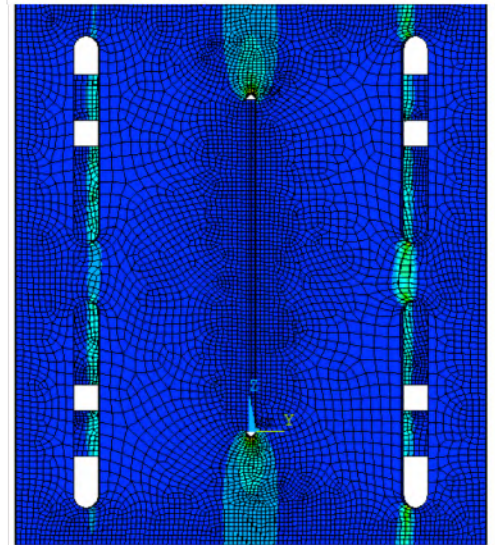
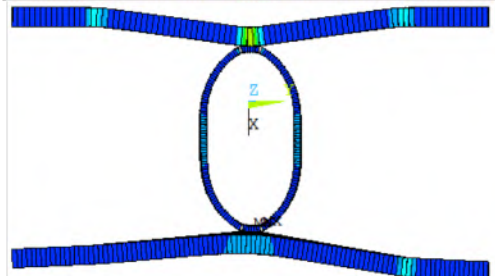
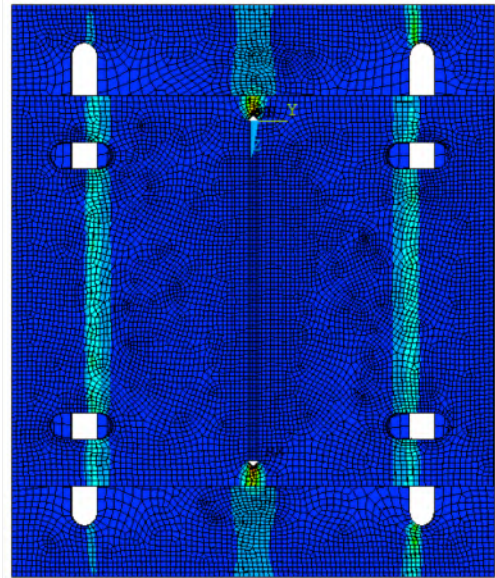
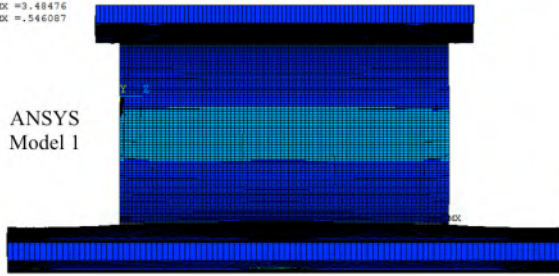


b)

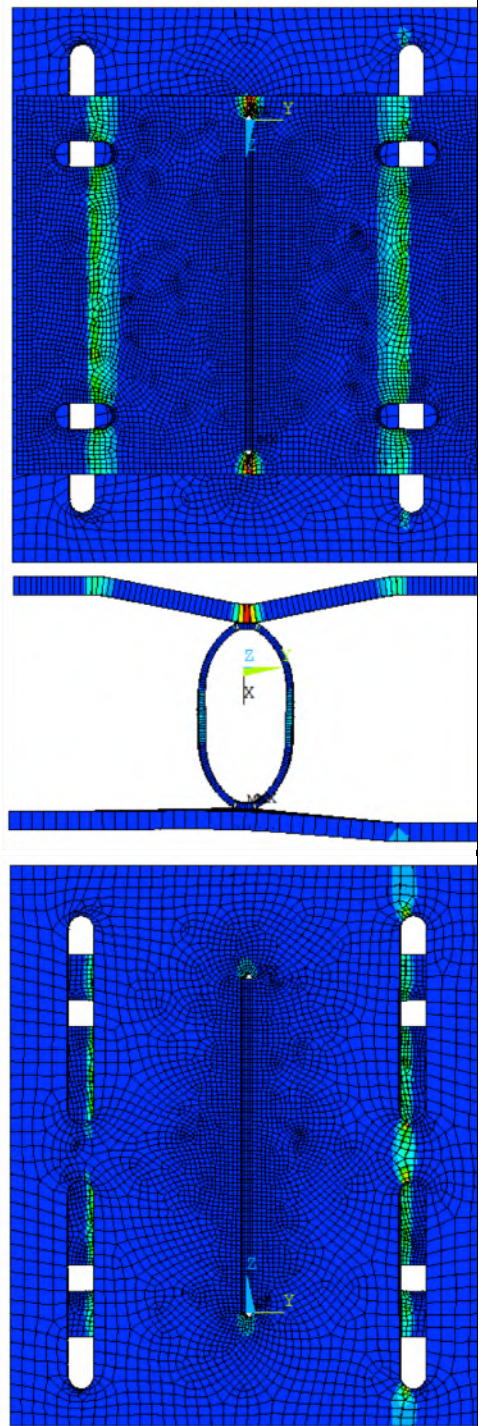
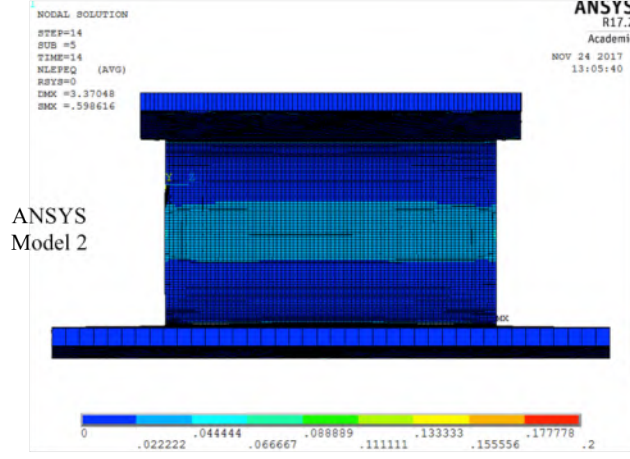
NODAL SOLUTION
STEP=14
SUB =5
TIME=14
NLESEQ (AVG)
RSYS=0
DMX =3.48476
SMX =.546087

ANSYS
R17.2
Academic
NOV 24 2017
14:24:56

ANSYS
Model 1

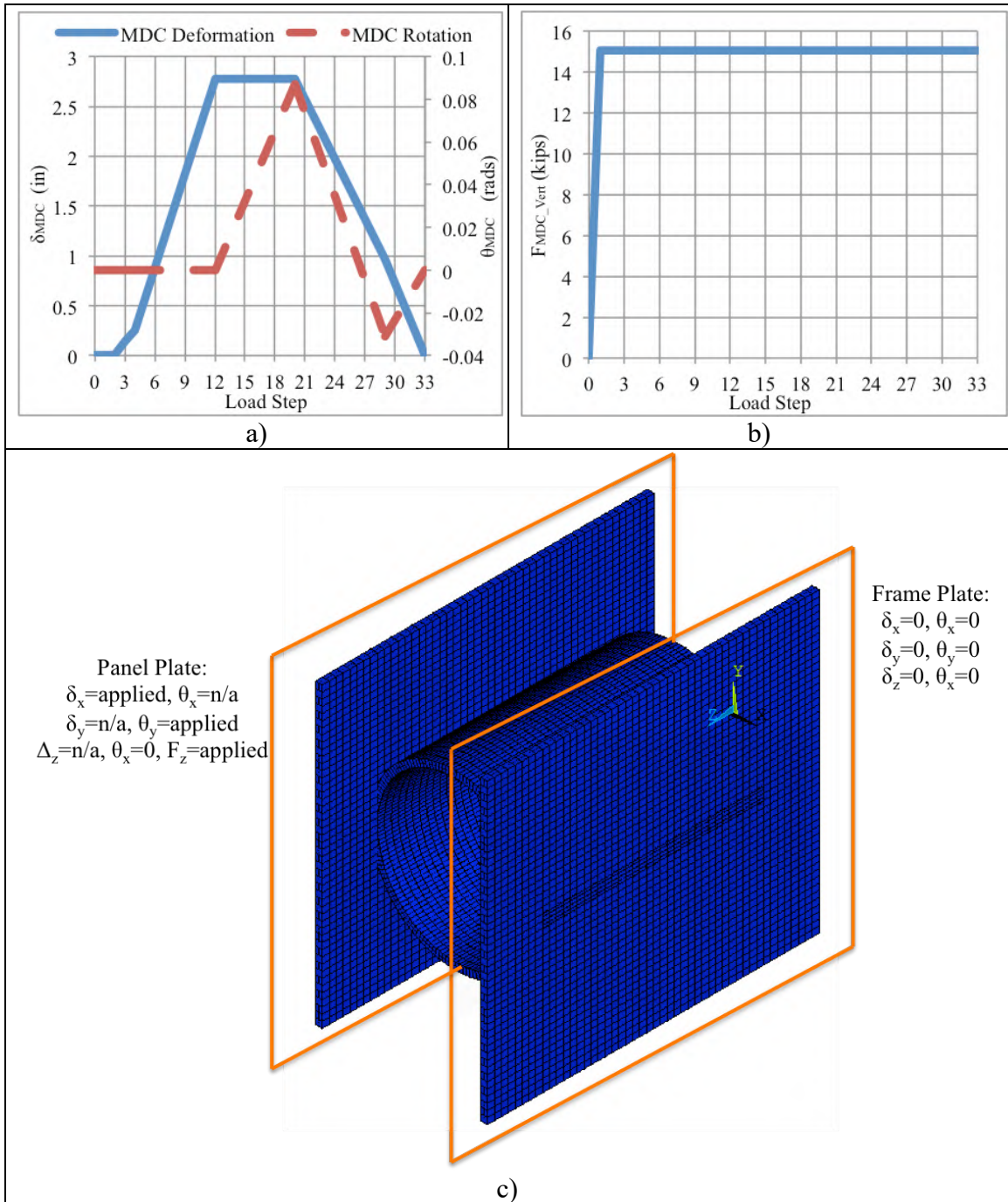


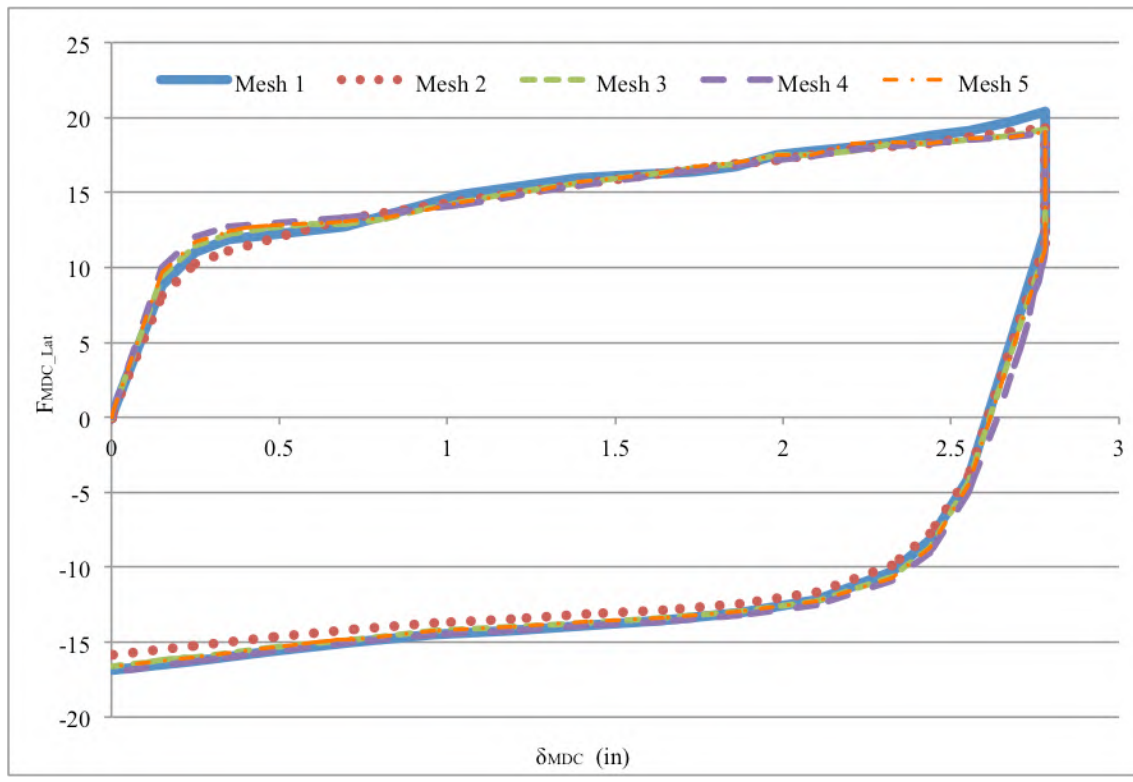
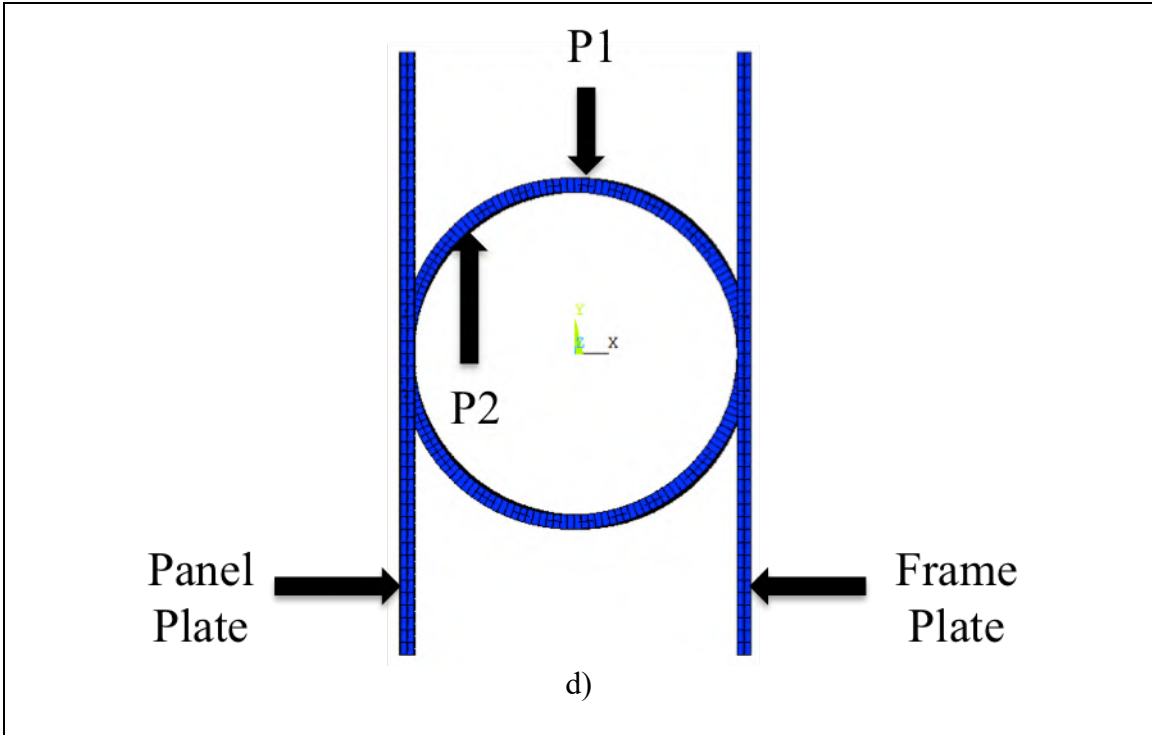
c)

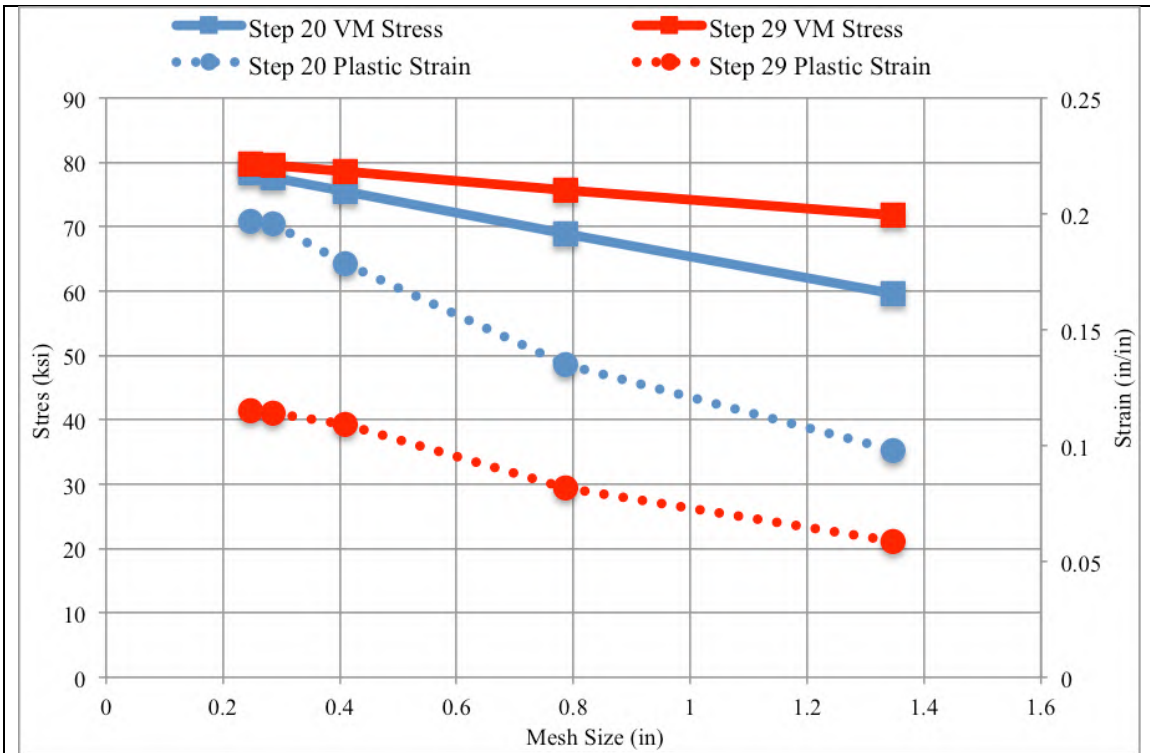


d)

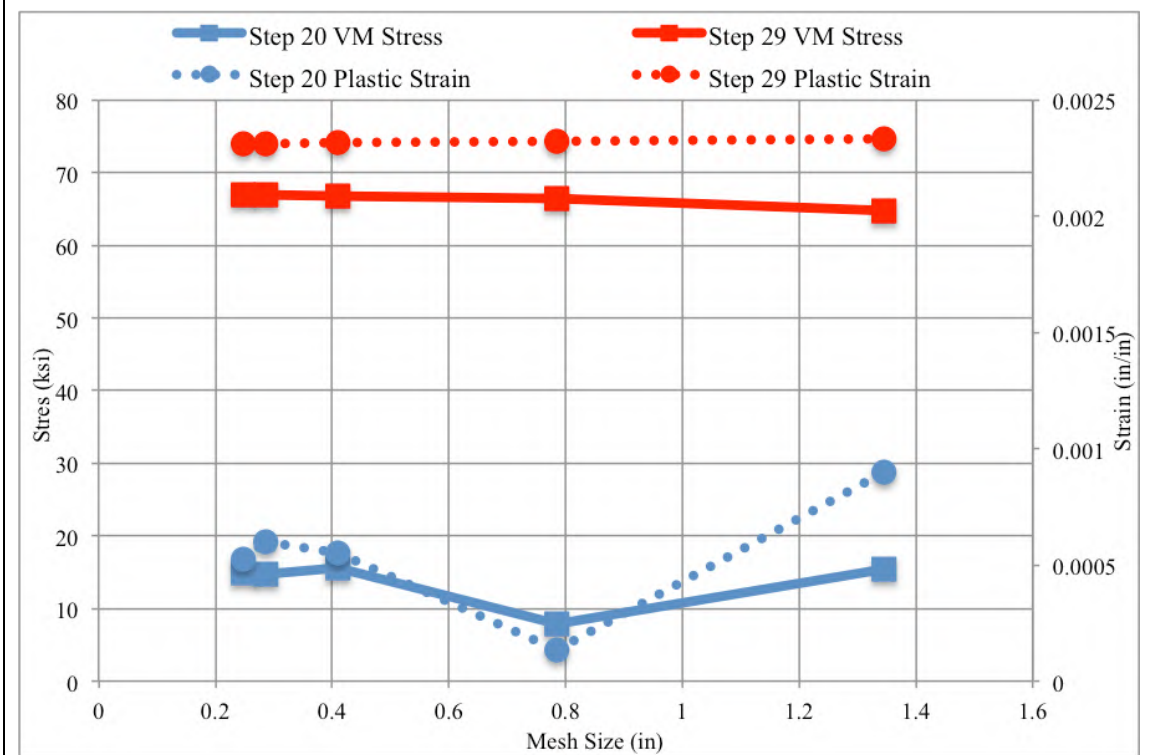
Fig. 8-9: MDC2 Convergence Study a) Deformation (x-direction) and rotation (about y-axis) applied in the FEA b) Vertical gravity load (z-direction) applied in the FEA c) Applied boundary conditions d) Approximate point locations on MDC2 cross section analyzed for convergence study e) Force-Deformation results f) Convergence results of P1 on HSS g) Convergence results of P2 on HSS





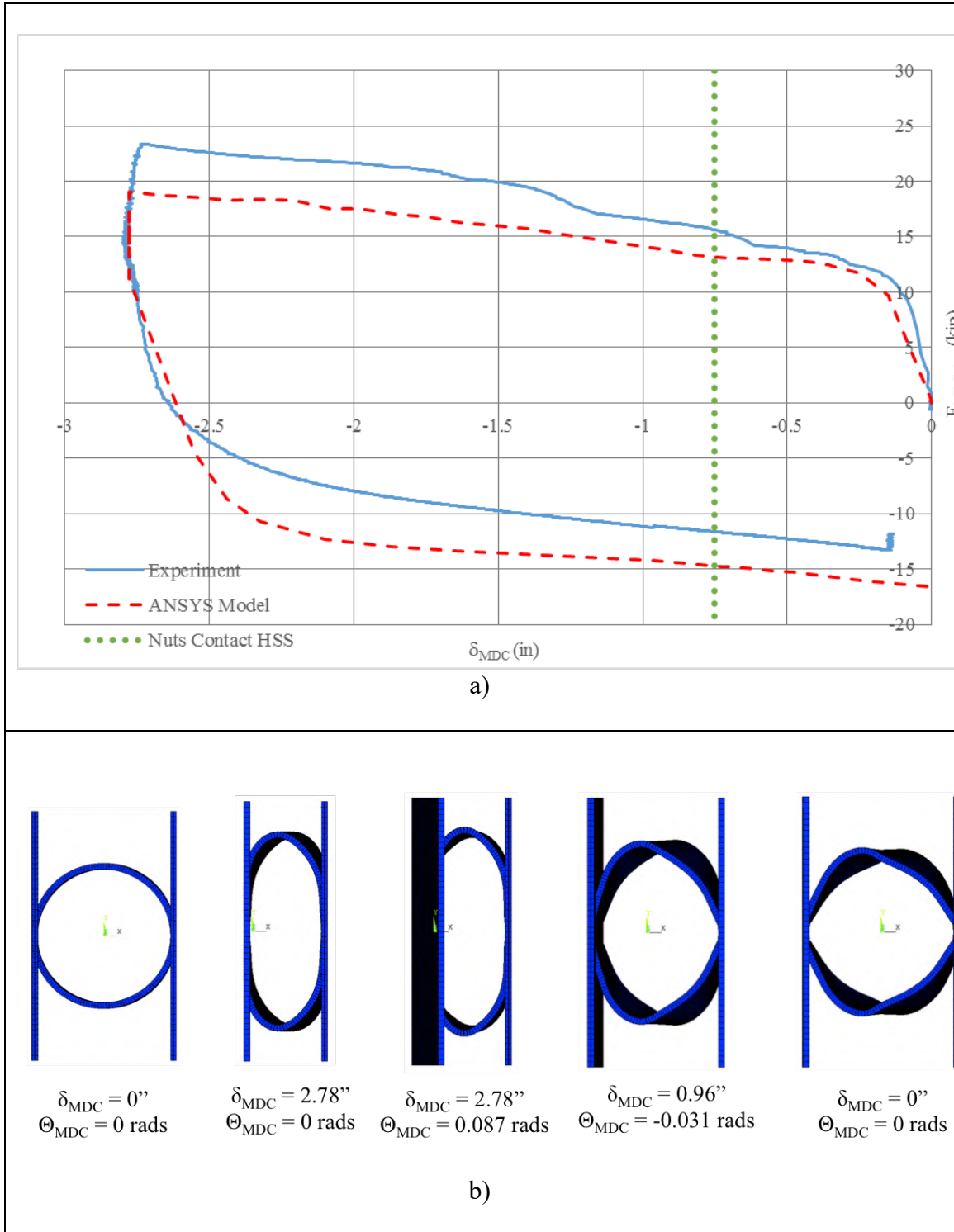


f)



g)

Fig. 8-10: FEA Results of MDC2 a) Force-deformation curves of the FEA and MDC2 experiment b) Deformed shapes throughout the FEA c) Von-Mises stress (ksi) contours at the design deformation and rotation d) Equivalent plastic strain contours at the design deformation and rotation



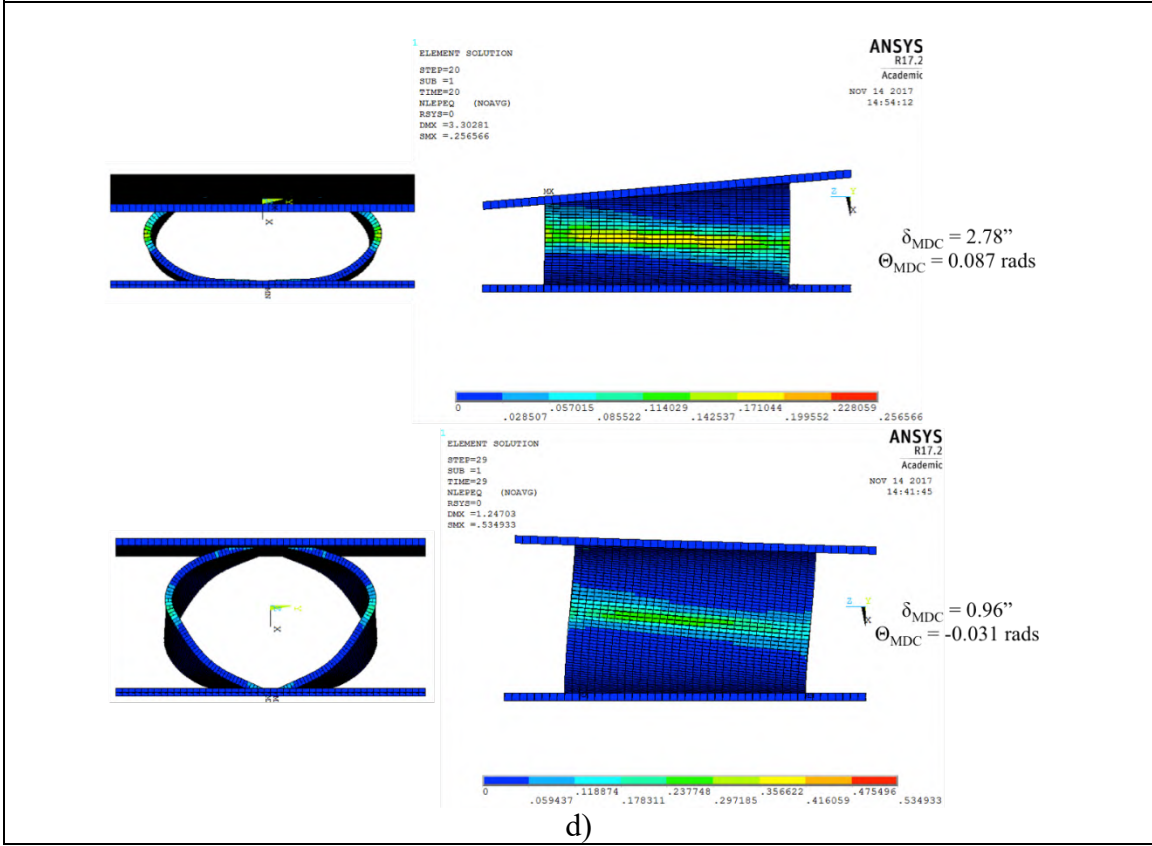
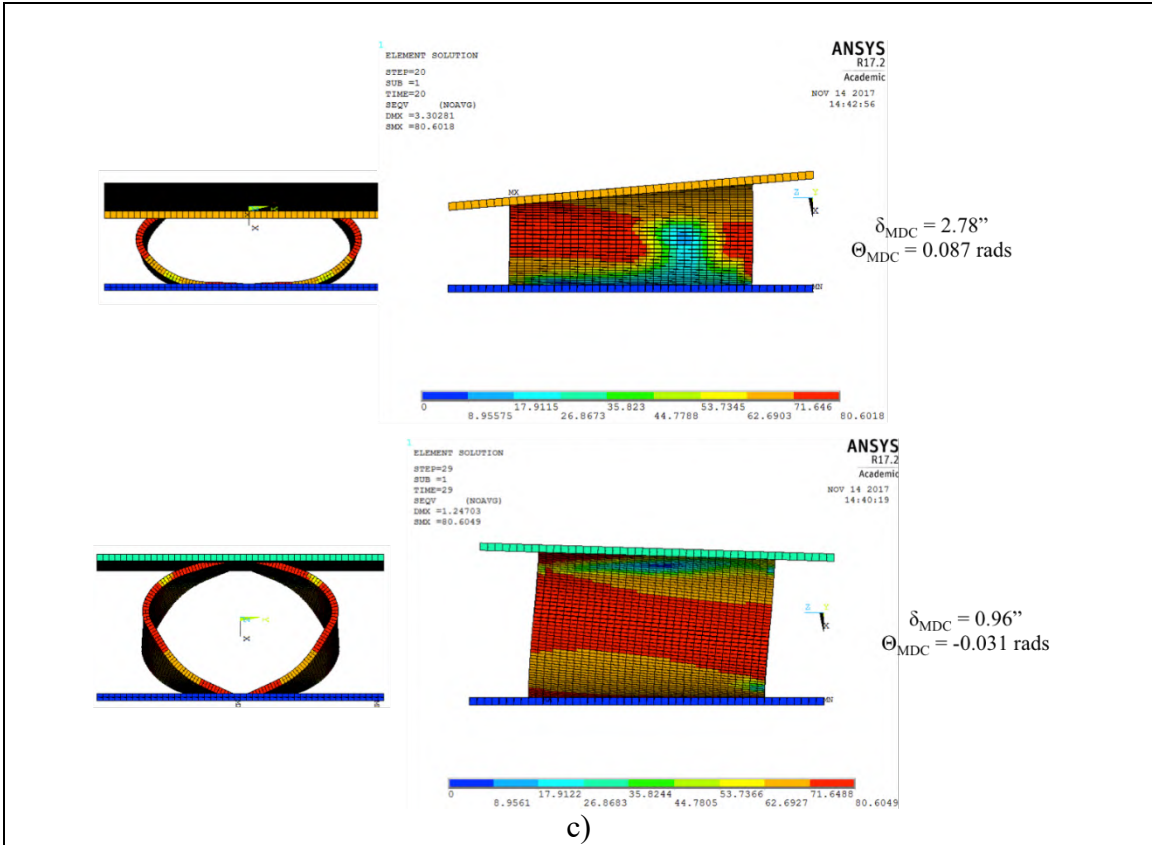
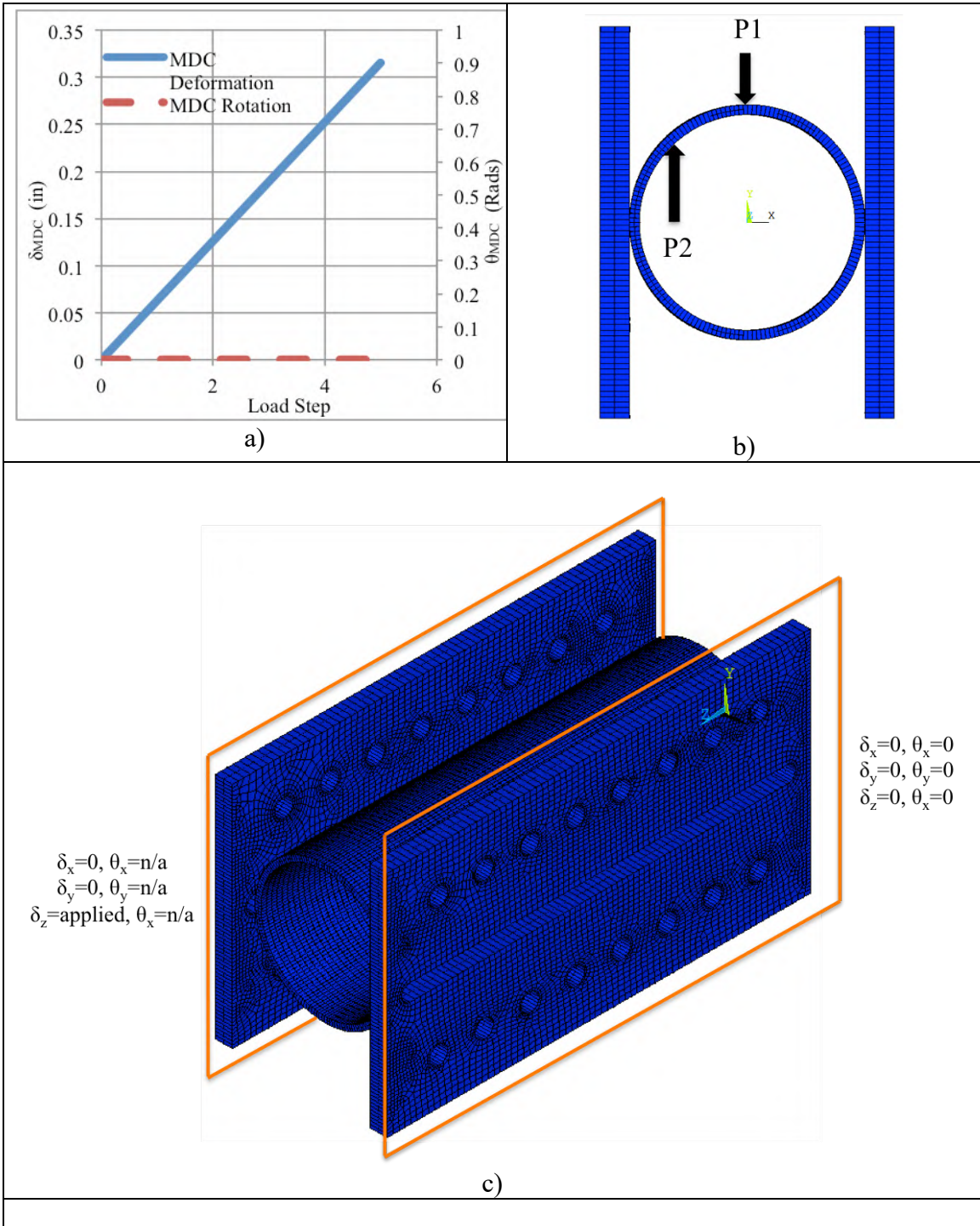
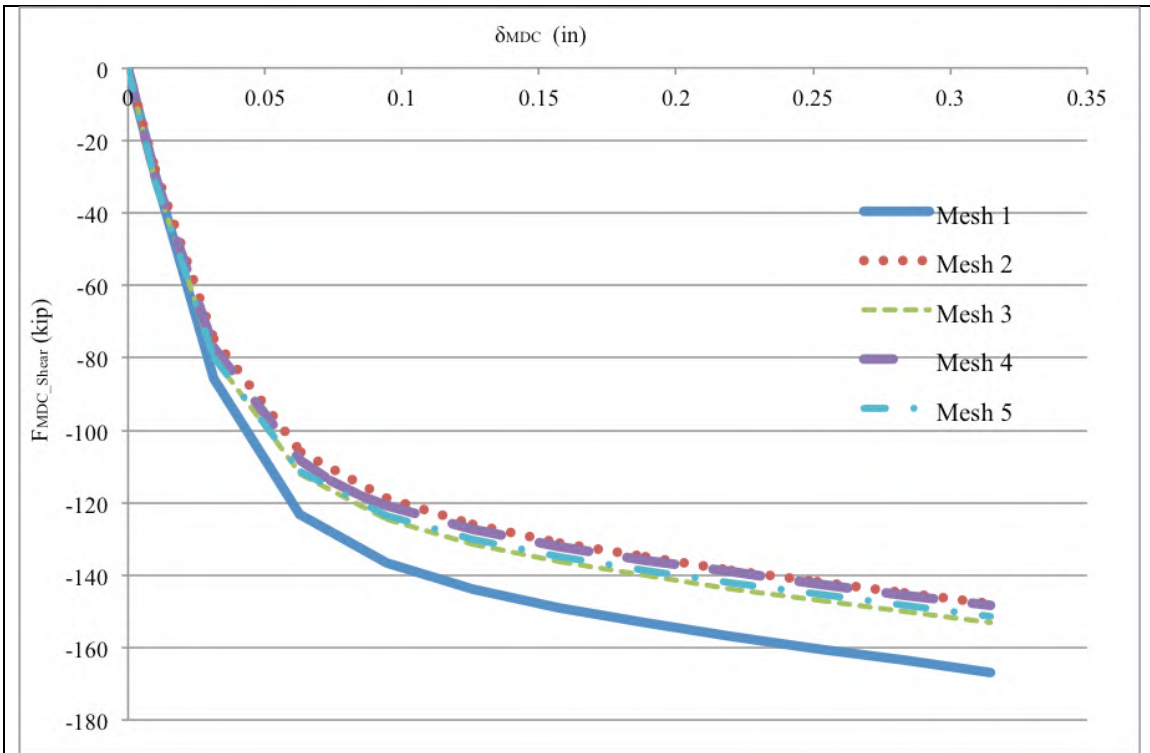
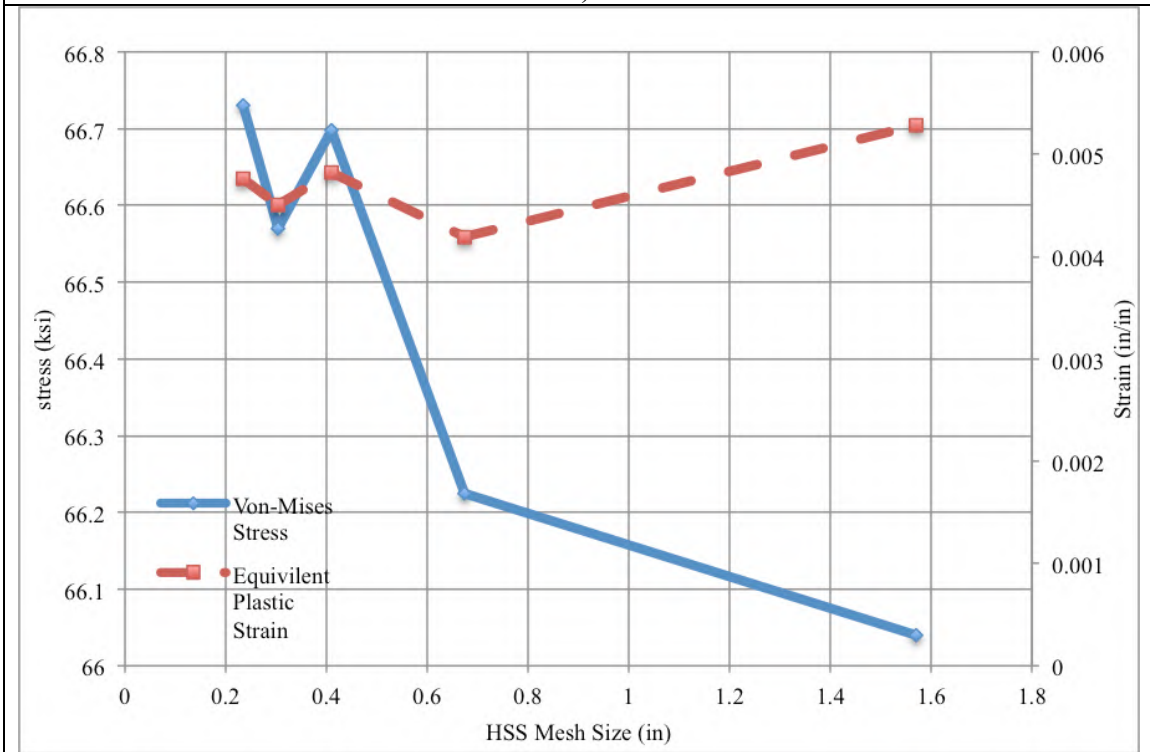


Fig. 8-11: MDC3 Convergence Study a) Deformation (z-direction) applied in the FEA b) Approximate point locations on MDC3 cross section analyzed for convergence study c) Applied boundary conditions d) Force-Deformation results e) Convergence results of P1 on HSS f) Convergence results of P2 on HSS





d)



e)

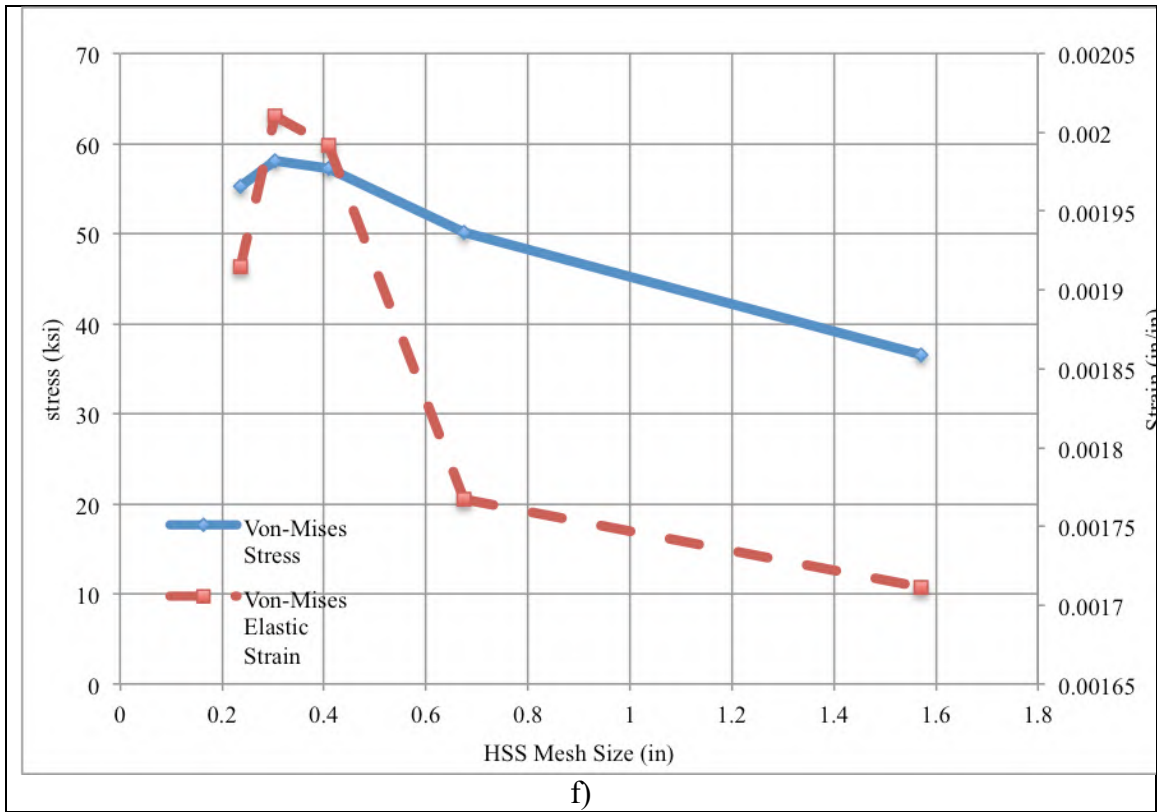
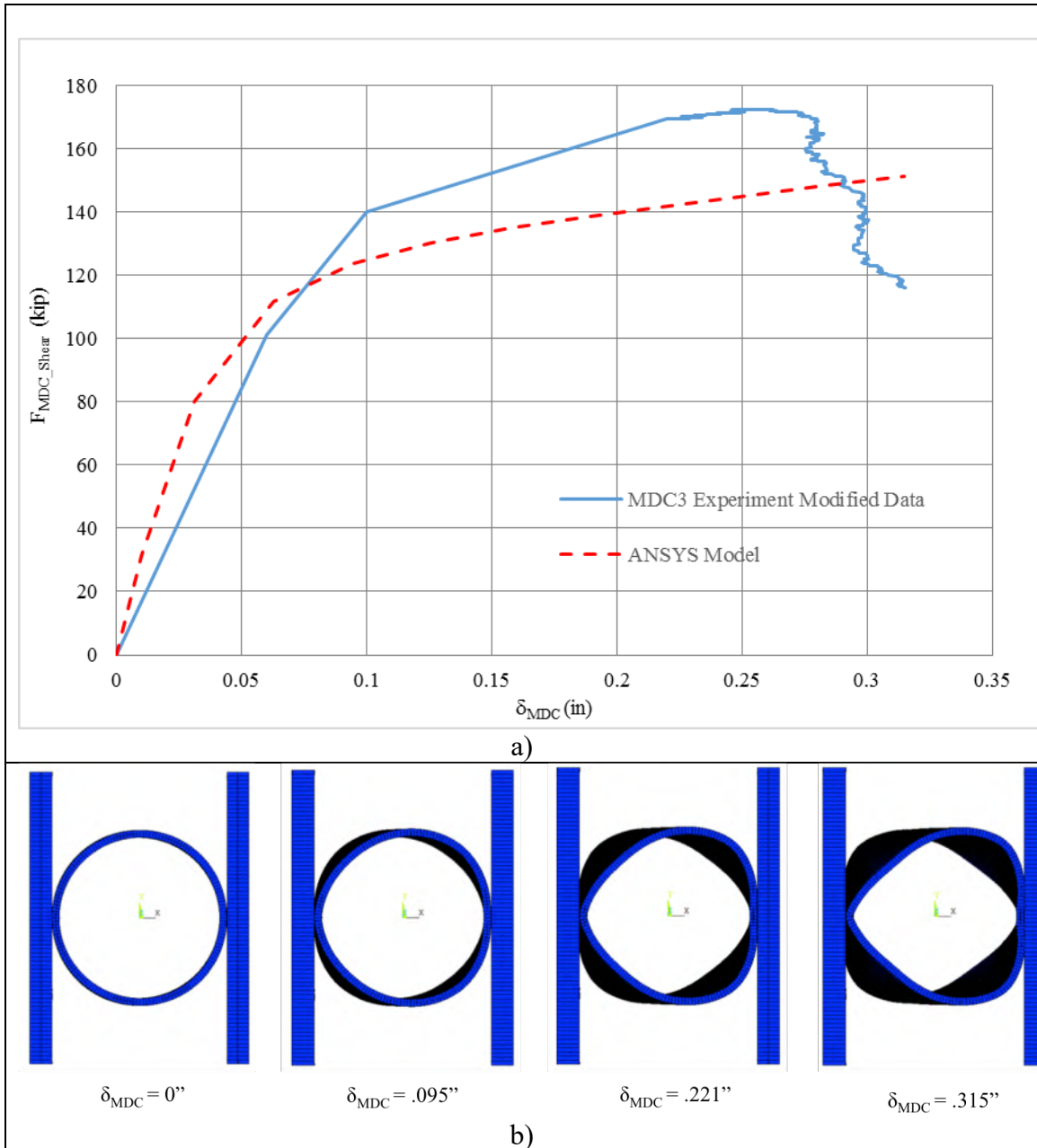
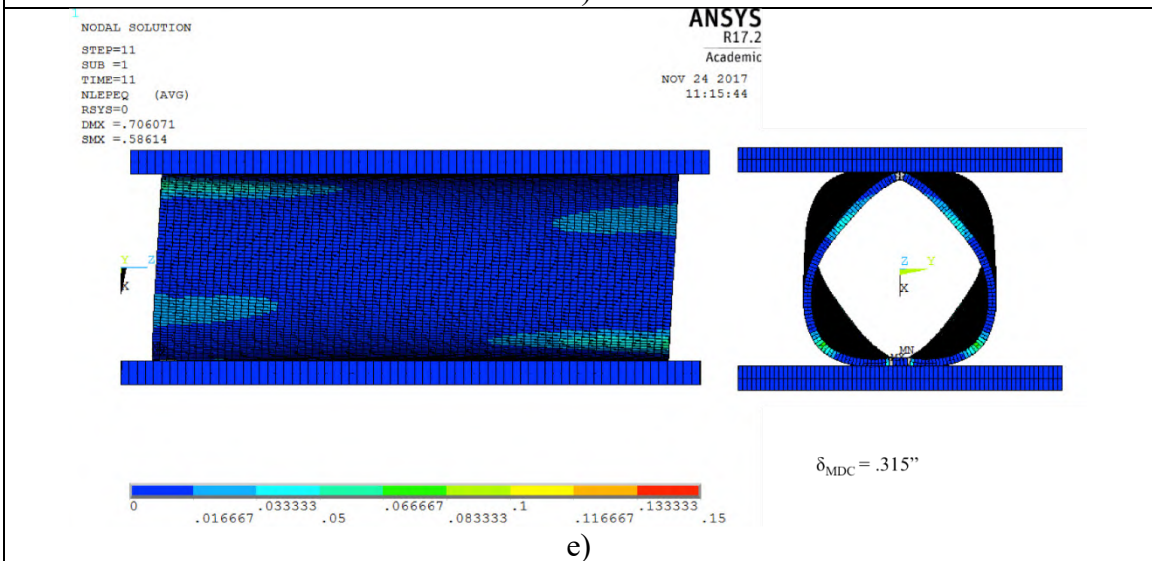
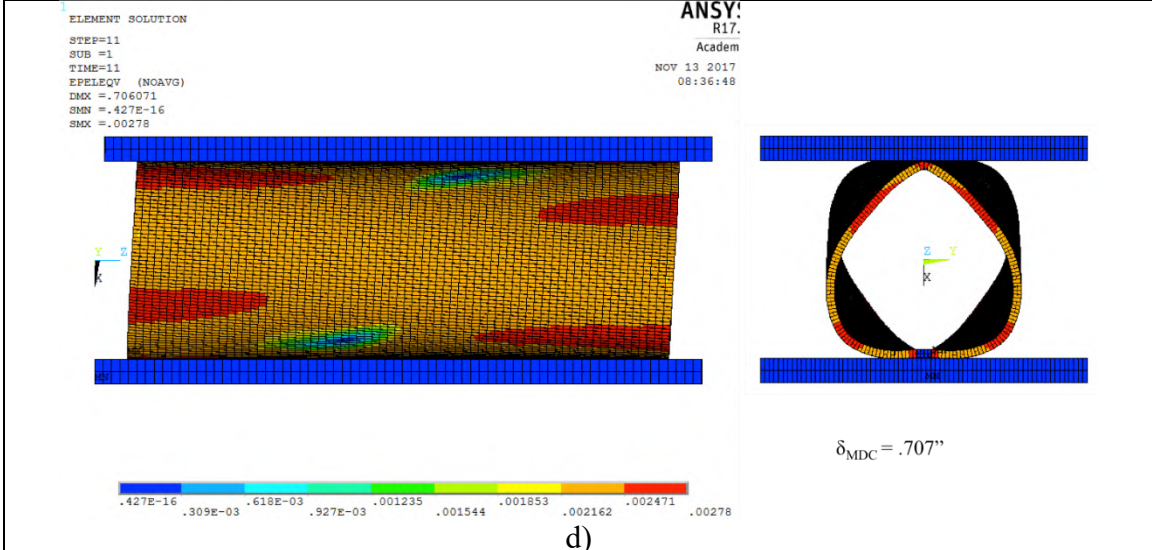
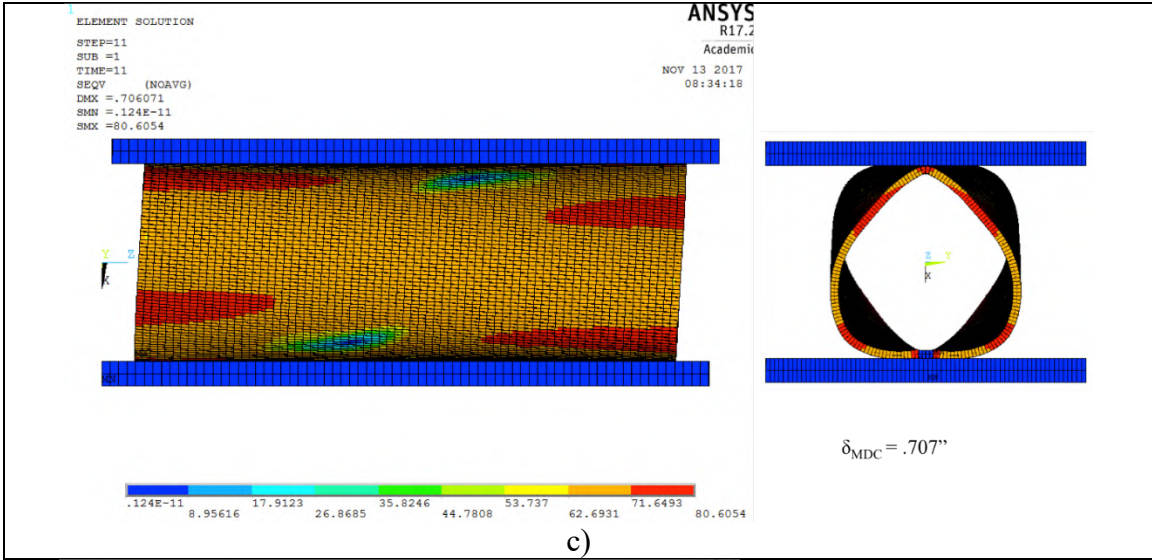


Fig. 8-12: FEA Results of MDC3 a) Force-deformation curves of the FEA and MDC3 experiment b) Deformed shapes throughout the FEA c) Von-Mises stress (ksi) contours at the design deformation d) Von-Mises elastic strain contours at the design deformation e) Equivalent plastic strain contours at the design deformation





9. MHFS Component and Building System Confirmation Analyses

9.1. Introduction

The proposed multi-hazard façade system (MHFS) design methodology relies on component and system behaviors ranging from elastic resistance of static loads, to large-deformation plastic response under dynamic or impulsive demands. While most design-critical prototype connector theoretical behaviors have been verified experimentally in this and past research (Baird, 2014; Rendos, 2018), the development of reliable finite element analysis (FEA) models allows for the expansion of the parameters of tested components, as well as the incorporation of component behaviors into larger system models which would otherwise be impractical to study via experimental testing. To this end, FEA models of (1) detailed models of the multi-hazard ductile connectors (MDCs) and U-shaped flexural plates (UFPs) were developed to confirm component-level behaviors, which were then incorporated into (2) single façade panel with connectors MHFS models, and finally (3) idealized building models including interaction between the lateral force resisting system (LFRS) and MHFS subjected to hazardous loading events. The development and analysis of component-, system-, and building-level models are detailed in this section.

9.2. Multi-hazard Façade System (MHFS) Connectors

FEA models were developed to confirm the mechanics and experimental testing results of both MDCs and UFPs considering all design-critical degrees-of-freedom for their respective applications within the proposed MHFS design methodology. All analyses were performed using ANSYS Mechanical ADPL Version 17.2 (ANSYS Inc., 2016). Each

model consisted of the connector's primary deformable body—the HSS tube for MDCs and U-shaped plate for UFPs—constrained to rigid, parallel planar boundary surfaces at the location of connections in the proposed design. A multi-linear material stress-strain model with kinematic and isotropic hardening and a von Mises yield criterion was assigned to all HSS and UFP elements; details of the stress-strain data for each connector type are included in their respective subsections. All deformable bodies used the SHELL181 element type in ANSYS, which is a four-node element with six degrees-of-freedom per node. All default options were specified with the exception of including full integration with incompatible modes, and nine integration points per element.

Each element spans the entire thickness of the cross section. For both MDCs and UFPs, each quarter arc of circular section is divided into 38 segments, and 32 divisions are used along the length of each element. SHELL181 elements are suitable for moderately-thick shell structures undergoing large nonlinear strains and rotations, and the proposed mesh resolution has been verified through a convergence study (Section 8). The parallel “plate” boundaries (as well as the flat “free” lengths of the UFP cross section) are meshed with (effectively) the same resolution. Potential contact between the deformable body and boundary plate(s) is included by adding “contact” and “target” surface elements to this mesh. These elements ensure that the target (boundary plates) and contact (centerline thickness of deformable body) surfaces cannot move freely through one another. Each boundary plate is constrained to remain planar using the CERIG command with a single, centrally-located master node for each plate. Analyses are performed by assigning zero deformation in all degrees-of-freedom at one boundary plate's master node, and incrementing deformations in the desired degree-of-freedom at the other master node. The

remaining degrees-of-freedom at the displacing master node are either prescribed as zero—referred to as the “fixed” models—or left unconstrained (“free” models). In MHFS applications, the effective connector boundary conditions are somewhere between these idealized “fixed” and “free” conditions, therefore both cases are examined for the applicable degrees-of-freedom to consider the extremes.

9.2.1. Multi-hazard Ductile Connectors (MDCs)

All MDC models used HSS6 cross sections, and wall thicknesses of 1/8”, 1/4”, and 1/2” were chosen to examine the full range of commercially-available HSS6 sections. Tube lengths of three, six, nine, twelve, and sixteen inches were considered for each tube length for a total of fifteen MDC models. The six-inch diameter of these sections refers to the outer diameter, which is reflected in the model geometry. Only HSS6 sections were considered because they have been the most effective sections for the prototype MHFS applications considered thus far. All MDC models have connection regions at the HSS-to-boundary plate intersections, which constrain a 1/2" wide strip along the entire HSS tube length to the adjacent (rigid) boundary plate nodes. This dimension was chosen to approximate the proposed MDC design detailing and experimental testing specimens which feature a bar welded to the HSS tube’s outer surface and slot in the boundary plate. The radial crushing and pulling, longitudinal shearing, and rolling degrees-of-freedom were examined to the maximum expected deformations, or at least until the expected onset of material failure due to large plastic strains. The length of the HSS tube only has a significant effect on longitudinal shearing behavior; the behavior considering other degrees-of-freedom of interest (crushing, pulling, rolling) is—aside from minor anticlastic curvature and boundary effects—a linear function of tube length. “Fixed” and “free”

boundary condition cases are only relevant for the rolling behavior where the tubes tend to deform radially (inward; crushing) at large deformations. Stress-strain points defining the HSS material model (ASTM A500 Gr. B steel assumed) are shown in Fig. 9-1. The first point on this curve is defined by the expected material yield strength ($R_y f_y = (1.4)(46 \text{ ksi}) = 64.4 \text{ ksi}$) and steel elastic modulus of 29,000 ksi, while the remaining points were taken from experimental testing data (Fadden, 2013).

9.2.1.1. Radial Crushing

Simulations of radial crushing of HSS tubes were performed up to a deformation of four inches, which was chosen as the maximum crushing deformation for air-blast design. One-foot long HSS6 sections were used for all simulations as the behavior in this deformation mode is (essentially) a linear function of tube length; wall thicknesses of 0.125", 0.25", and 0.5" were used. Force-deformation plots from these simulations are provided in Fig. 9-2, along with the proposed theoretical force-deformation behavior and bilinear idealization used in design. These plots show reasonable agreement between FEA and theoretical results over the elastic region and transitioning into the plastic region, with some apparent over-strength in the FEA models relative to the theoretical curves. The theoretical curves tend to underestimate strength at smaller deformations and overestimate strength at the target deformation of four inches, however the idealized bilinear approximation appears to capture the same area under the force-deformation curve (work-energy capacity) as the FEA results, which is critical for air-blast design.

Comparisons between FEA and theoretical plastic mechanism strengths and elastic stiffnesses are given in Table 9-1 and Table 9-2, respectively. Note that the theoretical expressions always underestimate both quantities by greater than 20% at times, however

this error can largely be accounted for by differences in the geometry used in the FEA model and theoretical expressions. The theoretical expressions use the nominal outer diameter (six inches), whereas in reality this diameter—which provides the moment arm for the crushing force resulting in bending of the tube walls—should be calculated from the tube wall cross section’s neutral axis (mid-thickness); this realistic geometry is included in the FEA model, resulting in a smaller moment arm and, therefore, less bending demand at tube wall hinges per unit crushing force. The dimensions of the connection region are also included in the FEA model but neglected in the theoretical expressions, further reducing the moment arm of the FEA model. This region should be neglected in design calculations because, in reality, the flexibility of the welds likely reduces the effects of this region on mechanism strength and elastic stiffness. Accounting for (all or some combination of) these geometric differences in the theoretical expressions reduces the error relative to FEA results to within 10%, which is typical of an FEA verification of mechanics. Contour plots of the von Mises stress and equivalent plastic strain of the 1/4" thick tube model are provided in Fig. 9-3 and Fig. 9-4, respectively. The maximum stress and strain at this crushing deformation is at the “side wall” hinges (midway between the boundary plates) at mid-length of the tube. The tube length and boundary effects at either tube end are visible in both plots.

Plastic strains can be used as a predictor for material failure, with 23% plastic strain as the specified minimum for A500 Grade B steel. The maximum equivalent plastic strain in the HSS tube was extracted from the analyses at each load step in an attempt to predict the onset of failure in this deformation mode. Maximum equivalent plastic strain is plotted as a function of crushing deformation in Fig. 9-5. These strain values exclude elements

which are at the “welded” connection boundaries as these zones tend to have the highest stress and strain at lower crushing deformations until contact between the HSS tube and boundary plates develops, however this is not likely realistic given the flexibility of the actual weld. Plastic strains develop more rapidly with larger tube wall thickness, and all tubes are expected to hit 23% plastic strain prior to reaching the four-inch target crushing deformation. The expected points of failure are also identified in Fig. 9-2. Note that the 1/2" tube thickness model could not run to the full four-inch target crushing deformation, even with reduced load steps and increased mesh resolution; this tube may require a different element type more suited to thick shells, however the simulations were able to run at least up to the predicted onset of failure.

Premature material failure may prevent MDCs (and UFPs) from reaching the target crushing deformation, which could necessitate changes to the design methodology. The pseudo-static air-blast experimental test successfully applied 2.78" of crushing deformation—the approximate onset point of material failure—plus rotation and load reversal all while supporting a tributary reinforced concrete panel gravity load (via longitudinal shearing of the HSS tube), so the predicted points of failure shown here are perhaps conservative, however this issue may require additional study to confirm the HSS tube’s ultimate radial deformation capacity. A small (but perhaps significant in this context) point to note is that the wall thicknesses used in these simulations are the nominal dimensions of real HSS6 sections, however the actual thicknesses are less than the nominal values, resulting in a reduction of the expected maximum plastic strains at any deformation as shown in Fig. 9-4. The failure strain of 23% is also a specified minimum, however the actual expected failure strain is not known.

9.2.1.2. Radial Pulling

Radial pulling simulations were performed using the same set of one-foot long HSS6 sections (wall thicknesses of 1/8", 1/4", and 1/2") to a maximum deformation of three inches. While the preferred MHFS connector layout (Configuration 3; Appendix B) does not include large radial pulling deformations of the MDCs as a performance objective for any hazard, there is interest in verifying the proposed mechanics and nonlinear behavior of this deformation mode for other potential applications and to assess the reserve capacity of these members for outward OP panel demands. Force-deformation response plots are provided in Fig. 9-6, along with the theoretical and idealized bilinear behaviors. Agreement between FEA and theoretical response is similar to the radial crushing deformation mode, with greater strength and stiffness in the FEA model. Plastic mechanism strength and elastic stiffness values are provided in Table 9-1 and Table 9-2; note that these quantities are theoretically the same considering radial crushing or pulling based on the established mechanics, and very small differences (less than 2%) were observed between crushing and pulling FEA results. The same geometric considerations discussed in the previous section apply here to account for a significant portion of the observed error. The shape of the theoretical force-deformation curves matches the FEA results particularly well up to a deformation of about 1.75", indicating that the proposed mechanics capture the observed response, albeit with the aforementioned over-strength in the FEA models.

Von Mises stress and equivalent plastic strain contour plots for the 1/4" thick tube wall model are shown in Fig. 9-7 and Fig. 9-8, respectively, at three inches of pulling deformation. At this point, the tube is effectively two flat plates in tension and—based on

the maximum equivalent plastic strain—would almost certainly have failed prior to this point. The location of maximum plastic strain is highly concentrated at the welded boundary region throughout these simulations, and failure at this location was observed during experimental testing. The maximum plastic strains for each wall thickness as a function of pulling deformation are provided in Fig. 9-9. As with the crushing case, these values neglected elements with constrained nodes (where the highest plastic strains were observed) to acknowledge the flexibility of the weld. Plastic strains accumulate more rapidly as a function of deformation during radial pulling than crushing. The predicted onset of material failure for each tube wall thickness is identified in both Fig. 9-9 and Fig. 9-6, with thicker walls failing sooner due to their increased rate of plastic strain accumulation.

9.2.1.3. Longitudinal Shearing

Analyses of longitudinally sheared HSS6 tubes were performed for all fifteen combinations of prototype dimensions: tube wall thicknesses of 1/8", 1/4", and 1/2", and tube lengths of three, six, nine, twelve, and sixteen inches. Examining different tube lengths is crucial for this degree-of-freedom as the proposed theoretical (and observed FEA); force-deformation response is not linearly related to tube length. The force-deformation response of each tube is given in Fig. 9-10. Longitudinal shearing response lacks a clear plastic mechanism formation point, with the onset of plastic stress and strains occurring at very small (less than 0.1") deformations in most cases and a gradual transition to a linear post-yield force-deformation relationship. Strength and stiffness are observed to increase with increased tube length and wall thickness, while increased thickness for a given tube length also tends to increase the acuteness of the transition between pre- and post-yield responses. The

plastic mechanism strength can be estimated using the intersection of trace lines included in the plots in Fig. 9-10, which are tangent to the initial elastic stiffness and post-yield regions. Plastic mechanism strengths obtained via this method are compared with the design longitudinal shearing capacity in Table 9-3. The large discrepancy between these values is partly because the design equation seeks to estimate the onset of significant nonlinear force-deformation response, which always preempts the tangent intersection taken as the plastic mechanism strength, garnered from FEA. The design equation is, therefore, predictably conservative, however it provides a good estimation for the point where the force-deformation response begins to deviate from the initial elastic tangent in any appreciable way.

Elastic stiffness values for this set of prototype HSS6 tubes are provided in Table 9-4 and plotted in Fig. 9-11. The top and bottom plots shown here are the same data set with different x-axes; the top plot is a function of tube length with curves for different thickness values, while the bottom plot is a function of thickness with different curves for tube lengths. These results indicate that this deformation mode is by far the stiffest of those examined in this study. The stiffness plots also include second-order polynomial regression equations with force zero-intercepts for each set of points, each of which has an R^2 value of at least 0.99 indicating an excellent fit. While no theoretical expression was developed for the longitudinal shearing elastic stiffness, these expressions can be used to estimate the stiffness based on the critical parameters. A similar regression equation was generated for this data set considering both tube length and wall thickness to be independent variables, however the fit was not nearly as good ($R^2 \sim 0.9$) and negative stiffness values were calculated by the fit equation within the domain of positive length

and thickness values. This, coupled with the extremely good fits obtained considering one independent variable at a time, indicates the true stiffness includes one or more terms which are a function of, perhaps, a non-integer exponential (e.g. square root, or raised to the power of $3/2$) of length and/or thickness, or a non-multiplicative operation (e.g. trigonometric ratio, logarithm, etc.) involving these (or other) variables.

The complexity of the longitudinal shearing behavior is apparent in the von Mises stress contour plots provided in Fig. 9-12. The HSS6 tube in this figure has a wall thickness of $1/4$ " and a one-foot length at one-inch of shearing deformation with all other degrees-of-freedom fixed. At this large (for this degree-of-freedom) deformation, the initially circular cross section forms mirrored teardrop-like shapes at either end with some tube-to-boundary plate contact at the wide side of each teardrop. At smaller deformations, the locations of maximum stress occur near both ends of the tube along the quarter points of the cross section as predicted in Section 4.2.2. These maximum stress locations never extend to the point where they span the full length of the tube. Shearing deformations are apparently accommodated through radial warping of the cross section, which varies along the tube length, and uniform (with respect to tube length) rotation of the cross section about the y-axis as shown in Fig. 9-12. Contour plots of equivalent plastic strains at this state of stress are shown in Fig. 9-13. The strain contours are comparatively simple, with the maximums occurring at the "weld" locations at the tube ends. This location of maximum strain is consistent with the failure observed during experimental testing of this deformation mode, where the tube was torn at these locations. Maximum plastic strains as a function of shearing deformation are provided in Fig. 9-14 for both the "free" and "fixed" other degree-of-freedom conditions. Here, the expected failure is at a much smaller

deformation than for other modes, therefore longitudinal shearing should not be relied upon for any large ductile deformations. The expected failure points are also identified in the force-deformation plots in Fig. 9-10, where applicable.

9.2.1.4. Rolling

Analyses of one-foot long HSS6 tubes with wall thicknesses of 1/8", 1/4", and 1/2" undergoing so-called "rolling" deformations were performed to verify the proposed elastic and large-deformation plastic mechanics. As with the radial crushing and pulling degrees-of-freedom, rolling response is (essentially) a linear function of tube length. Rolling force-deformation plots are provided in Fig. 9-15 along with the proposed theoretical relationships. Both the "fixed" and "free" non-rolling degree-of-freedom conditions as discussed in the introduction to this section. As expected, the increased constraints of the fixed case results in larger forces than the free case at a given deformation, however these differences do not become significant until about two inches of rolling deformation. The theoretical mechanism strength and stiffness appear to match very well with the observed results, with comparisons provided in Table 9-5 (mechanism strength) and Table 9-6 (elastic stiffness). The geometric issues which contributed to errors considering radial deformations are significantly reduced for the rolling degree-of-freedom because the applied force—and, therefore, moment arm in question—are perpendicular to those for radial deformations, rendering the reduction of moment arm due to the width of the constrained "welded" region negligible. The effects of tube wall thickness are still present, which may account in part for the remaining errors in stiffness and mechanism strength. The theoretical force-deformation relationship appears to approximate the fixed FEA

results between about two and four inches of rolling deformation, however the thicker tubes are expected to fail prior to reaching this deformation regardless of boundary conditions.

Von Mises stress and equivalent plastic strain contour plots are provided in Fig. 9-16 and Fig. 9-17, respectively, for the 1/4" thick, one-foot long HSS6 tube at a rolling deformation of five inches (fixed other degrees-of-freedom condition). Maximum stress and strain are concentrated at the welds, which is consistent with the failure location observed during experimental testing. Maximum plastic strains are plotted as a function of rolling deformation in Fig. 9-18 for both fixed and free cases. As previously mentioned, the rolling degree-of-freedom is the one most significantly affected by the fixed vs. free non-rolling degree-of-freedom distinction. Similar to the force-deformation response, the fixed case sees a more rapid accumulation of plastic strains with increasing rolling deformations than the free case. The expected onset of failure is also identified in Fig. 9-15 for both fixed and free cases. The failure observed during experimental testing is consistent with the onset of failure predicted here.

9.2.2. U-shaped Flexural Plates (UFPs)

A single prototype UFP design was used for all FEA analyses. This design has a six-inch (outer) diameter, 1/4" thickness, six-inch width, and four-inch "free" straight plate length between the curved and connected regions of the cross section. These dimensions were chosen to match the prototype UFP designs (diameter, free length and thickness; all behaviors of interest are a linear function of section width). Rolling and radial crushing and pulling were the degrees-of-freedom of interest for this connector. Only the "fixed" other degree-of-freedom condition was examined for the rolling case because the MDC-B (located along the same façade panel edge as the UFPs) provides significant strength and

stiffness relative to UFPs in the radial crushing direction, preventing any large out-of-plane panel deformations during in-plane building drifts (which result in UFP rolling deformations). Connection of the UFP to the boundary plates was achieved by constraining all nodes beyond the “free” section length to the adjacent boundary plate nodes. Stress-strain points for the UFP material model (A36 steel) are provided in Fig. 9-19; this data was obtained from tension coupon tests performed as part of this research (Rendos, 2018).

9.2.2.1. Rolling

The most critical function of UFPs is to provide force-limited, large-deformation rolling behavior to accommodate in-plane seismic drifts along one façade panel edge. This behavior has been examined in previous research (Baird, 2014); however, the UFPs used in this research differ somewhat from past applications in that they lack any “housing” for the UFP and feature an extended “free” length section between the circular and connected portions of the member cross section. The force-deformation relationship for the prototype UFP model is shown in Fig. 9-20 along with the theoretical relationship based on the elastic stiffness and maximum rolling force equations. The theoretical elastic stiffness—given by Baird (2014)—is low relative to the FEA model; however, this quantity is not critical for design. Conversely, the theoretical maximum force is conservative relative to the FEA response, which is desirable because this force is used solely for capacity design of the MDCs (there are no minimum force design requirements for rolling UFPs). The FEA force-deformation curve is relatively flat over a large deformation range, which indicates that this type of UFP functions similar to past applications by providing large deformation capacity with limited force.

Contour plots of von Mises stress and equivalent plastic strain for the prototype UFP at six inches of rolling deformation are shown in Fig. 9-21 and Fig. 9-22, respectively. The phenomena discussed in the context of UFP rolling mechanics (Section 4.3.1) can be seen in these plots, with the free length on one side rolling into the circular section corresponding with the location of maximum stress and strain, while an initially circular portion of the section is “unrolled” to join the straight, free length section at the other plate boundary. Maximum plastic strains are plotted as a function of rolling deformation in Fig. 9-23, which indicates a nearly constant maximum plastic strain after the formation of the rolling plastic mechanism consistent with Equation (4-16). There is a slight increase apparent near six inches of rolling deformation likely because this exceeds the initial free length of four inches, which halts the “traveling” plastic hinge behavior that prevents accumulation of plastic strains greater than those given by Equation (4-16). However, even at a rolling deformation, which is 50% greater than the initial free length, the maximum plastic strain is well below the expected failure strain of 23%, indicating that the prototype UFPs are expected to function reliably at story drifts which exceed the expected design maximum. This may justify reducing the free length used in design, which would reduce the total required UFP width per panel edge by strengthening the radial pulling mechanism which always controls this parameter.

9.2.2.2. Radial Crushing

UFPs are expected to undergo radial crushing deformations in parallel to the MDCs during extreme OP panel loading to mitigate damage to the façade panel itself. Ideally, the radial crushing force-deformation relationship of UFPs would precisely match that of MDCs, albeit with half the strength due to the semicircular portion of the UFP section as opposed

to the full-circle HSS used in MDCs. This is almost certainly not the case in reality, however, due to three primary reasons: (1) the preferred materials for UFPs (A36 steel) and HSS (A500 Grade B steel) are different, (2) the UFPs have a different boundary condition at the circular curve-to-boundary plate interface, and (3) thickness of the members will always be different based on the true (non-nominal) HSS thickness and standard available plate sizes for UFPs (e.g. in 1/8" increments).

An analysis of the prototype UFP model crushed radially to four inches was performed to examine the force-deformation response and identify any differences in behavior, which might have implications for the proposed MHFS design methodology. The force-deformation relationship obtained from this analysis is shown in Fig. 9-24, along with the idealized bilinear force-deformation relationship used in design. In contrast to the MDC crushing analyses, the theoretical elastic stiffness for UFPs is greater than the observed FEA stiffness, likely due to the design equation's neglect of the effects of the free length; this free length reduces some of the constraints, which are intrinsic to the design strength and stiffness equations. While the FEA model still shows greater plastic mechanism strength than predicted—likely due to the use of the outer diameter in design (neglects wall thickness)—the difference is less than that observed in the crushed MDC analyses. After formation of the plastic mechanism, the UFP force-deformation curve seems to increase in strength at a more constant rate than the MDCs, however this may simply be an artifact of these particular models rather than a genuine behavioral difference. In general, the idealized curve matches the UFP crushing force-deformation behavior well—perhaps better than the MDCs—and any differences between the UFP and MDC crushing responses are likely insignificant relative to the uncertainties of (and design

idealizations made for) the OP hazard façade loadings which might prompt radial crushing of the connectors.

Von Mises stress and equivalent plastic strain contour plots are shown in Fig. 9-25 and Fig. 9-26, respectively, for the UFP crushing analysis. These contours illustrate some of the similarities and differences in UFP and MDC (Fig. 9-3 and Fig. 9-4) crushing behaviors. In both cases, the maximum plastic strain is located at the “side” hinge at mid-length/width of the circular arc(s), however the UFP hinge is longer (along the arc length) resulting in less strain concentration and, therefore, smaller maximum plastic strain at the target crushing deformation of four inches. This is perhaps due, at least in part, to the differences in material models; the UFP material model (Fig. 9-19) features a more gradual transition up to its ultimate stress, whereas the MDC model (Fig. 9-1) hardens much more abruptly after yield. This rapid hardening of the material may promote increased concentration of strain because internal work is initially minimized by straining a local group of material fibers to reach this hardened strength, thereby generating the necessary internal forces (and resulting bending moments) to achieve equilibrium; after this point, additional crushing deformations can continue straining this local group of fibers to achieve the necessary hinge rotation for deformation compatibility without incurring a significant increase in stress (again, minimizing internal work). By contrast, the UFP material model promotes the spread of plastic strains to fibers surrounding the initial hinge as continued local strain accumulation results in a more significant increase in stress than in the HSS tube hinges.

In addition to these material model differences, the free length in UFPs clearly shows a distribution of plasticity in Fig. 9-25 and Fig. 9-26, which is not available to the

MDCs, further reducing the concentration of plastic strains. Maximum plastic strains as a function of crushing deformation are plotted in Fig. 9-23, with the onset of failure expected at about 3.5” of deformation, compared to about 2.75” for the 1/4" thick HSS MDC crushing analysis. While failure of UFPs prior to achieving the target crushing deformation of four inches is detrimental to MHFS performance during extreme OP loading (e.g. air-blast events), it is less consequential than failure of the MDCs because the UFPs do not support the weight of the panel and can hopefully be replaced before any design-level outward OP loading occurs which might pull the panel off of the building.

9.2.2.3. Radial Pulling

UFPs are relied upon to accommodate contact between adjacent corner panels during seismic building drifts via radial pulling. Analysis of this deformation mode was performed using the prototype UFP model to confirm the mechanics developed for design. The force-deformation results from this analysis are shown in Fig. 9-27, along with the idealized theoretical force-deformation model. An expression for theoretical elastic stiffness was not developed in this research, therefore the starting point of the idealized force-deformation curve was chosen as the FEA model deformation where its strength reached the theoretical plastic mechanism strength, which is a good match for the FEA model mechanism strength although the model is slightly stronger than predicted (consistent with all models developed in this research). This slight under-prediction of the plastic mechanism strength is conservative for design. After yield, the idealized force-deformation curve is a good match for the FEA results up to the maximum deformation of six inches, indicating that this model is appropriate for determining capacity design forces for the MDCs considering the seismic corner panel contact scenario.

Von Mises stress and equivalent plastic strain contour plots are provided in Fig. 9-28 and Fig. 9-29, respectively. These plots indicate that the maximum stress and strain occurs at the boundary between the constrained (connected) and free regions of the straight UFP sections. As such, this maximum strain is largely a function of the free length. The maximum strain as a function of UFP pulling deformation is shown in Fig. 9-23, which indicates that failure is not likely to occur during UFP pulling with these cross sectional dimensions.

9.3.MHFS Air-Blast Impulse Dynamic Analysis

A simplified model of a single façade panel and connectors was developed in OpenSees (McKenna & Fenves, 2004) to confirm the assumptions made in the proposed MHFS design methodology for uniformly-distributed out-of-plane (OP) impulsive loading, such as an air-blast event. This model—illustrated in Fig. 9-30—discretizes the façade panel into one-foot segments along its height with nonlinear fiber section beam-column elements (three integration points each) spanning between the mass-containing nodes. The model assumes a 13-foot high by 30-foot wide six-inch thick normal weight (145 pcf) reinforced concrete panel with a total weight of 28.275 kips which is distributed equally to the 14 nodes along the panel's height ($28.275 \text{ kips} / 386.4 \text{ in/s}^2 / 14 \text{ nodes} = 0.00523 \text{ kip-s}^2/\text{in}/\text{node}$). The nonlinear fiber cross section assigned to each panel element is six-inches deep (panel thickness) and 15-foot wide (half of the panel's width) with fibers which are one-inch (deep) by one-foot (wide). Only half of the panel's width is assigned to the section to capture the cracked section moment of inertia, which is assumed half of the gross section's moment of inertia. The panel material model is essentially elasto-plastic, with slight rounding near the yield point and very small post-yield stiffness (for convergence

purposes). The stiffness and yield strength are assigned to achieve the design plastic moment capacity at the calculated yield deformation when the section is fully plastic.

At the top and bottom panel nodes, a zero-length spring element with an idealized force-deformation behavior based on the MDC mechanics connects the panel to a rigid boundary. The top and bottom connector springs are identical, despite some differences in the post-yield crushing force-deformation behavior along these edges (UFPs vs. MDCs), and their force-deformation model is symmetric in the positive (tension) and negative (compression) directions based on idealized MDC crushing mechanics. The trilinear force-deformation behavior is defined by the elastic stiffness and plastic mechanism strength. The linear-elastic region ends at a deformation equal to the mechanism strength divided by the elastic stiffness. The force then varies linearly from the yield point to a value of twice the mechanism strength at a deformation of four inches ($2/3$ of the nominal HSS6 diameter). After four inches, the elastic stiffness is assigned with a large yield force to approximate the steep hardening observed at large crushing deformations. These simplifications are consistent with those made in design and are thus preserved in this model to confirm the nonlinear dynamic behavior of the system.

The prototype panel used in this model is taken from the first-story (interior) reinforced concrete MHFS design given in Table 9-7. The OP connector (and panel) strengths for this panel were controlled by the chosen performance objective of fully crushed connectors and maximum panel end rotation when subjected to design blast scenario (DBS) 1, which is a 500 lbsTNT charge at a standoff distance of 30 ft centered along the panel's width. Inherent in this design is the satisfaction all other DBS scenario performance objectives, namely crushed connectors and elastic panel response when

subjected to DBS2 (300 lbsTNT at 100 ft), and elastic connector and panel response for DBS3 (100 lbsTNT at 200 ft). The design impulse values for a first-story panel subjected to these events are 19.1 kip-s, 3.87 kip-s, and 0.914 kip-s for DBS1, 2, and 3, respectively, as described in Section 3.2. These impulsive loads were applied to the model using identical point loads applied at each mass-containing panel node as shown in Fig. 9-30. These loads have a triangular force time-history with very short duration (0.1 milliseconds), and the summation of the integral of all applied loads over time equals the desired impulse value for the DBS of interest. A load duration of 0.1 milliseconds was found to be sufficiently brief relative the panel's modal periods to render the loading essentially impulsive. The panel's first three modal periods and shapes are shown in Fig. 9-31; note that only odd-numbered (symmetric) modes participate in the response of this idealized model due to the symmetry of the model and loading. These mode shapes are consistent with those of a simply-supported beam with uniformly distributed mass, albeit with the inclusion of elastic springs in-series at each end (non-zero modal displacements at the ends). Simulations were performed with a time step of 0.01 milliseconds (i.e. loading takes place over 10 steps) with a duration of 0.2 seconds.

Time history responses of critical model deformations when subjected to the three DBS impulses are shown in Fig. 9-32. These plots show the deformation of connectors, the midpoint of the panel, and the difference between the two, which is the OP deformation of the panel itself from end(s) to midpoint. Positive deformation on these plots corresponds to inward (in the direction of loading) deformation, which in-turn corresponds to radial crushing of the connectors. When subjected to DBS1, the initial velocity (at the conclusion of the applied loading) is about 260 in/s, which is equal to the applied impulse divided by

the total panel mass, indicating that the panel is effectively displacing as a rigid body with negligible difference between OP displacements at the ends and midpoint. This observation is consistent with the design assumption that any performance objective, which includes crushed connectors, should use the full panel mass to determine the initial panel kinetic energy. The connectors reach their target crushing deformation of four inches, at which point the combination of connector hardening at this deformation and the capacity designed strength of the panel forestalls additional connector crushing deformations in exchange for increased rotation of the panel's plastic hinge (at midpoint). The maximum rotation of the panel hinge is about 8.8 degrees (6 inches of deformation between the panel ends and midpoint), which is less than the target maximum of 12 degrees. Given the fact that this model was designed to essentially replicate the MHFS design assumptions as closely as possible, this discrepancy in maximum rotation is not insignificant. One potential reason for the difference is the neglect of higher modes in design, which should be expected to participate due to the nature of impulsive loading as a "white" function (i.e. composed of all frequencies and, therefore, excites all modes).

The model's response to DBS2 and DBS3 impulse values are also shown in Fig. 9-32. The initial panel velocity for DBS2 is 52.2 in/s, which is approximately equal to the applied impulse divided by the entire panel mass as was the case for DBS1. The connectors do yield in this case (yield deformation is about 0.16 inches); however they do not reach the maximum crushing deformation. Nevertheless, the design assumption regarding the effective panel mass for yielding connectors still holds true. When subjected to DBS3, the connectors do not yield, resulting in an initial panel velocity of 12.4 in/s, which is again equal to the impulse divided by the entire panel velocity, however this is not consistent

with the assumption made in design. The belief was that since the connectors are stiff relative to the panel's effective OP stiffness (in a single degree-of-freedom idealization) and yield at such a small deformation (again, relative to the panel), they could be treated as effectively rigid boundaries, resulting in first mode dynamic response akin to that of a simply supported beam with uniformly distributed mass. The shape of this mode is a half-sine wave, and the effective mass of a single degree-of-freedom idealization is exactly one-half of the total mass. Hence, the assumption made in design was that if the connectors are to remain elastic, the initial panel kinetic energy should be calculated using half of the total panel mass, rather than the full mass used for crushed connector designs. This discrepancy simply makes the design aids for DBS3 conservative, since they effectively achieve the desired performance objectives while relying on half of the mass, which actually participates in the response. In these analyses, the performance objectives for both DBS2 and 3 are satisfied.

9.4. Building with MHFS Dynamic Analysis

9.4.1. Seismic Response

A set of prototype building frame and MHFS finite element models were constructed to perform nonlinear dynamic seismic analyses of varying intensity to assess the performance of MHFS components and to evaluate the effects of this system on peak building drift response. A prototype 3-story special concentrically braced frame (SCBF) office building in Los Angeles, CA was designed by Sabelli (2001) as an analog to the prototype special moment frame buildings developed by the SAC steel project (FEMA, 2000). These two versions (braced and moment frame) of the prototype building were chosen for this study

because they are representative of post-Northridge design practices and have fairly well-established dynamic properties and seismic performance (FEMA, 2000; Sabelli, 2001). Both buildings consist of three thirteen-foot stories and a four-by-six layout of thirty-foot bays with all lateral force-resisting systems (LFRSs) located along exterior column lines. Details of the prototype MHFS design used for both buildings are given in Table 9-7. Models of each type of LFRS, a leaning gravity column (to include P- Δ load effects), and the MHFS were constructed in OpenSees (McKenna & Fenves, 2004).

An Illustration of the prototype SCBF versions of the prototype building is given in Fig. 9-33. One half of the building is tributary to each exterior building face (with MHFS), therefore the model must consider at least half of all gravity framing and floor mass and two braced frames (per the prototype building design with four braced frames in each principal building direction) to adequately assess façade-building interaction. The leaning gravity column consists of a lumped floor mass, which serves as the master node for rigid diaphragm constraints applied to all other nodes at the same elevation, along with a (vertical) P- Δ load corresponding to the total floor mass applied at this node. Cross sectional area (A), moment of inertia (I), and plastic section modulus (Z) were calculated as the summation of the average of strong- and weak-axis (for I and Z) properties for all tributary gravity frame columns. The gravity column model is identical for either LFRS. The braced frame model includes details, which capture limit-state behaviors, and is suitable for analysis up to the point of collapse. This model has been used extensively in past research (Slovenec, 2016), and its nonlinear seismic response compares favorably with experimental testing results. Key features of the braced frame model illustrated in Fig. 9-33 include:

- Nonlinear fiber section brace elements discretized into 13 segments, which include initial out-of-straightness to simulate buckling response.
- Low-cycle fatigue material failure model for brace section fibers based on experimental testing of HSS braces. The model can simulate complete fracture of brace sections and continue to the point of frame collapse with the aid of elastic, low-stiffness “ghost truss” brace elements, which run parallel to each brace member (aid in convergence).
- Zero-length, nonlinear fiber gusset plate elements at each brace end to simulate “folding” of gusset plates along “ $2t$ ” (or elliptical) brace end clearance line.
- Rigid elastic zones at all member intersections to account for beam/column member section depths and large in-plane stiffness of brace gusset plates. Gusset plate/brace joint offsets based on the real dimensions of gusset plates designed for this prototype frame.
- Nonlinear fiber section beam and column elements (three integration points over each span).
- Zero-length nonlinear fiber section elements at beam shear tab locations to include moment resistance due to engagement of beam webs at these connections ostensibly designed as moment releases.

The moment frame version of the prototype building model is illustrated in Fig. 9-34. As with the braced frame version, this model is constrained to the (identical) gravity column at each floor level. Note that the rightmost column in the moment frame uses a smaller section than the others because this column is located at a building corner resulting in less tributary floor area and, therefore, less axial demand. Rigid offsets are included at

all beam-column joints with dimensions based on member cross sectional depths. Beam and column plasticity is concentrated at zero-length nonlinear rotational spring elements at the end of each clear span with plastic moment capacity and rotational stiffness determined by the section and member dimensions. The “Steel02” material model in OpenSees is assigned to these elements with the recommended hysteretic and isotropic hardening parameters based on example code on the OpenSees website. Elastic beam-column elements span between the concentrated plasticity springs to ensure all nonlinear behavior is relegated to the members’ ends. Although this model is not as robust as the braced frame version and likely not suitable for collapse-level analyses (e.g. degradation of strength and stiffness at flexural hinges is neglected), the intent in this study is to examine the behavior of the MHFS at design-level drifts and to compare the response with and without MHFS interaction; the prototype moment frame model is believed to be adequate for these purposes.

The prototype MHFS design (Table 9-7) model is illustrated in Fig. 9-35. When included, this model is simply added in parallel to the LFRS and gravity column by constraining each floor node to the corresponding lumped mass gravity column nodes. Each panel has its own lumped mass and applied vertical load at a central node. The sum of all panel masses in a given story are subtracted from the above floor mass node to effectively maintain the same mass matrix for analyses with or without the MHFS. In addition to the central mass-containing node, each panel has six additional nodes at the points of connection to the adjacent floors; panels are supported vertically along the top edge via MDC-Vs located at the corners, and laterally along this same edge by a single MDC-L in the center. The bottom corners of the panel are connected to the adjacent floor

nodes by “rolling” UFPs, and the center of the bottom panel edge has an out-of-plane bearing-only connector (MDC-B) which is not included in this model, as it does not participate in in-plane panel response. Each connector consists of a zero-length, single degree-of-freedom spring element with a bilinear (Steel02) material model based on the idealized force-deformation behavior of each prototype connector design. The panel connector and mass nodes are tied together with (essentially rigid) elastic beam-column elements to effectively enforce equal translation (vertically and laterally) of each individual panel’s nodes while still allowing for differential displacements between adjacent in-plane panels. These differential displacements must be allowed to capture the expected contact between panels, starting with the edge panel contacting the adjacent out-of-plane panel and potentially propagating in-plane if the differential displacement between any of these panels exceeds the initial gap spacing (0.75”). Corner panel contact is modeled using a zero-length “gap” bilinear spring element at the building corner-adjacent bottom node of all edge panels to apply the expected contact force to these panels based on the UFP pulling force-deformation model and prototype designs. These springs include a “damage” option where all plastic deformations are added to the initial gap to simulate the out-of-plane panel’s UFP edge being pushed outwards as designed. In plane panel contact uses similar gap spring elements between adjacent panel nodes without this damage option and with an essentially rigid elastic force-deformation material model.

Dynamic properties of the braced and moment frame models with and without MHFS are given in Table 9-8 and Table 9-9, respectively. The modal periods and shapes are consistent with the established dynamics of these prototype building models (FEMA, 2000; Sabelli, 2001; Slovenec, 2016). With the addition of the MHFS, all modal periods

are reduced due to an increase in lateral stiffness from the panel connectors. This added stiffness comes from the inclusion of UFPs along the bottom panel edges, without which the static imposition of floor displacements (i.e. the procedure by which a stiffness matrix is formed by hand) would not incite reaction forces from the MHFS as they would be attached to only one floor (above). As discussed during design (and confirmed in forthcoming analysis results), essentially all inter-story drift is accommodated in-plane by rolling deformation of the UFPs, hence the increase in stiffness due to the MHFS can be determined by considering the summation of UFP stiffness for all panels in a given story added (in parallel) to the primary LFRS stiffness. Based on the change in first mode period, the addition of the MHFS increases the stiffness of the prototype braced frame by a factor of about 1.1, while the moment frame stiffness is increased by about 1.8. This difference is expected as braced frames are generally always stiffer than moment frames and the same MHFS designs are used in both cases. Considering a design spectral acceleration curve (ASCE, 2013), the shift in periods for the braced frame building is less significant as it occupies the constant acceleration “plateau” of the curve with or without MHFS. For the moment frame building, the shift in periods brings the building to a higher design spectral acceleration value, which increases the seismic design forces for the LFRS. The design of the prototype moment frame was not altered to reflect this shift; however, this effect should not be neglected for any potential new building or retrofit applications of the MHFS.

The braced and moment frame prototype building models with and without MHFS (four configurations total) were subjected to three suites of ten scaled ground motion records each. The chosen ground motion suites come from the SAC steel project (FEMA, 2000) and represent frequent (FrE; 50% probability of exceedance in 50 years), design-

basis (DBE; 10% in 50 years), and maximum-considered (MCE; 2% in 50 years) earthquake hazard levels for Los Angeles, CA (location of the prototype building). All ground motion records used in this study are the fault-normal components of far-field recordings. Peak drift response in each story for the prototype braced frame building both with and without MHFS are given in Fig. 9-36, Table 9-10 (no MHFS), and Table 9-11 (with MHFS). While the drift results for the building without MHFS are simply presented as a “baseline” case for comparison, it should be noted that both the mean and median drift response to the DBE ground motion suite are below the code-prescribed maximum of 2.5% for new construction, indicating that this design performs adequately (at least with respect to drift) considering the seismic hazard. As is typical of braced frame buildings, drift is generally concentrated on one story—the first story, in this case—with peak drifts generally well below 2.5% in the other (upper) stories during even MCE events.

The ratio of peak drifts with to without MHFS (i.e. values greater than 1.0 indicate an increase in drift with the inclusion of MHFS) are given in Fig. 9-37 and Table 9-12 for comparison purposes. Peak drifts are smaller for the upper stories for all FrE, DBE, and MCE ground motions with the inclusion of the MHFS, with one exception (second story LA11 DBE motion). In the first story, where peak drifts are generally greatest, inclusion of the MHFS slightly increases the average peak drift for both the FrE and DBE suites with essentially no change to the MCE average peak response. These increased average drifts are still within acceptable limits, however there are a few notable outlier ground motions, the largest of which (LA13, DBE) is increased by a factor of 2.7. The median drift, which is not affected by these outliers, is less for all stories and ground motion suites with the inclusion of the MHFS. Reduction of peak drift is likely due to the added inter-story shear

capacity and load path provided by the MHFS, where the UFPs undergoing plastic deformations in response to story drift are additive with the primary LFRS. Increases in story drift are possibly due to the shift in modal periods, which may place the building in a higher intensity region of the spectrum for certain motions.

Peak drift results for the moment frame model are given in Fig. 9-38, Table 9-13 (without MHFS), and Table 9-14 (with MHFS). Peak drifts are generally more uniform over the building height for this model compared with the braced frame version, likely due at least in part to the lack of any strength degradation in the moment frame hinge elements. Moment frame peak drifts are also generally greater than the braced frame, which is typical due to the more flexible nature of moment frames. Even so, peak moment frame drifts are acceptable considering the DBE hazard level, with a mean slightly greater and median slightly less than the maximum of 2.5%. The drift ratio comparison for the moment frame model with and without MHFS is given in Fig. 9-39 and Table 9-15. This comparison indicates reduced peak drifts for the second and third stories for all ground motions. The mean and median peak first story drifts were not increased with the addition of the MHFS; however, the MCE first story peak drifts were increased for almost all ground motions. As with the braced frame, some of this can likely be attributed to the shift in periods into a higher intensity region of the spectral acceleration curve, particularly when considering the peak response of a single ground motion, however in general the moment frame has less variation in the change to peak drift response with the addition of the MHFS (peak increase is by a factor of 2.08).

In addition to studying the effects of MHFS interaction on overall building performance, confirming the response of individual MHFS connectors during seismic

events was a primary goal of these analyses. The MDC-Vs are likely the most critical connectors as they support the panel vertically. The maximum peak MDC-V force recorded in edge and interior panels during each ground motion was collected and compared to the design capacity. The ratio of these values (demand-to-capacity, or D/C) are shown in Table 9-16 for the braced frame model, and Table 9-17 for the moment frame model. Recall from the mechanics, design, and analysis of the longitudinally-sheared HSS tubes that the estimated elastic force limit is fairly conservative, therefore a D/C value greater than 1.0 likely does not constitute failure of the connector as significant hardening beyond the design force is expected. Nevertheless, nearly all analyses for both LFRS types had peak D/C ratios less than one, with only a few exceptions at the MCE level. It should be noted that these analyses did not include vertical ground accelerations—and, by extension, vertical panel inertia forces which are resisted by the MDC-Vs—however the maximum vertical seismic inertia force used in design is only about 0.2 D/C for the prototype MHFS designs and is not expected to coincide with the maximum lateral seismic effects (i.e. the full 0.2 D/C is not additive with the tabulated values). This omission is due to the lack of vertical ground acceleration records in the SAC ground motion suites; however, these ground motions were still deemed the most appropriate records for these analyses due to their extensive use in past studies and original development specifically for assessing the performance of the chosen prototype building.

D/C ratios for MDC-Ls are given for braced and moment frame analyses in Table 9-18 and Table 9-19, respectively. These values are generally well below 1.0, largely because the MDC-L HSS tube lengths for all stories are controlled by blast hazards, rather than the seismic hazards examined here. Additionally, the panel inertia, UFP rolling, and corner

panel contact forces were all assumed to be additive, which may not be the case (however, they should still be considered as additive for design). The final MHFS connector response of interest is the peak ratio of UFP deformation to story drift, results of which are given in Table 9-20 for the braced frame subjected to the FrE suite, and Table 9-21 for the moment frame subjected to the MCE suite. In both of these tables, all values are approximately equal to 1.0, indicating that for any case—braced or moment frame, small or collapse-level drift—all inter-story deformation is accommodated by the UFPs as intended.

9.4.2. Air-blast Impulse Response

A 3D prototype building model was developed to examine the behavior of an entire building with MHFS subjected to air-blast events. An illustration of this model is provided in Fig. 9-40. The prototype building is a light-mass (60 psf uniform floor loading assumed), ordinary concentrically braced frame (OCBF) 3-story office building designed for seismic and wind hazards in Boston, MA per ASCE 7-10 (2013). Each story is thirteen-feet high and all frame bays are thirty-feet wide, with a 4-by-6 bay plan layout. A light floor mass was chosen for this building to (1) increase the initial kinetic energy of the building stories resulting from impulsive load transfer from the MHFS to floor diaphragms, and (2) reduce seismic inter-story shear capacity forces for design, resulting in a building which is as vulnerable to blast damage (aside from the protective measures in the MHFS) as one can reasonably expect in a realistic building design.

The lateral force resisting system in this model is idealized using zero-length spring elements at mid-story height at each building corner (in both orthogonal lateral directions; 4 “frames” total in each direction) with bilinear force-deformation behaviors based on the inter-story strength and stiffness of square HSS sections (in a chevron configuration)

chosen to provide the required design inter-story shear capacity and post-yield stiffness of 20% of the elastic stiffness. The design and idealization of this prototype building model was based on the braced frames design by Sabelli (2001) as alternatives to the prototype moment frame designs developed in the SAC steel project (FEMA, 2000), as well as analytical work with more detailed FEA models of similar CBF designs by Slovenec (2016). Although a full model of each braced frame (such as those described in the previous section) would provide more accurate and realistic response of the building, this simplified model is believed to be adequate because the LFRS was found to undergo very limited yielding (to be discussed shortly), thus the behavior of either system (simple or detailed) is likely very similar, therefore it is not worth the computational effort to precisely model each braced frame.

Gravity frame column properties (cross sectional area, moment of inertia, plastic section modulus, and torsional moment of inertia) were summed and assigned to one member per story at the center of the building layout, and all floor mass and corresponding P- Δ loads were assigned to the central gravity column node at each floor elevation. A rigid diaphragm constraint links the four corner nodes to this central floor “master” node to ensure uniform translation of each floor. Extremely stiff elastic beam-column elements span the bays around the exterior of the building to provide points of connectivity for the façade panels while effectively maintaining the rigid diaphragm action without assigning constraints to the panel connector nodes, which caused computational problems in initial versions of the model.

The façade panel and connectors spanning each bay are modeled identically to the model detailed in Section 9.3, with the exception of the boundary nodes which connect to

the adjacent floors rather than applying fixed boundary conditions. Critical details of the prototype MHFS design used in this model are given in Table 9-7. Modal properties of the full model are provided in Table 9-22. The first three translational modes are essentially identical considering either principal lateral building direction (modal properties along the direction of loading are shown in this table). The panel mode is consistent with the first mode of the single panel model discussed in Section 9.3. The uniform torsional mode was included to comment briefly on torsional building response; torsional resistance comes from both the distance between parallel LFRS frames, as well as the torsional resistance assigned to the gravity column elements. These properties are needed for simulations considering off-center charge locations, however the all simulations discussed herein consider the charge to be centered along the longer (180-foot wide) building side. Off-center charge locations were examined during the course of this research, however they do not appear to cause significantly greater demands relative to an equivalent centered charge considering this (torsionally-regular) prototype building.

The loads applied to each panel node differ from the idealized single panel model; blast event force time-histories for each node (spaced at one-foot increments along each panel height) were generated using the procedure developed by Appelbaum (2013) in Matlab and assigned to model nodes on the blast-facing and rear building sides. Although this procedure is still ultimately an idealization of blast pressure load time-histories, it includes the effects of several known phenomena associated with air-blast events, including: negative phase loading, building edge clearing effects, angle-of-incidence effects, rear-wall blast loading, and staggered load arrival times based on the actual

distance (as opposed to nominal standoff distance, measured perpendicularly along the ground) from the charge. This model was subjected to DBS1, 2, and 3.

Inter-story drift time history response for the prototype building subjected to DBS1 is shown in Fig. 9-41. Positive drift on this plot indicates drift back towards the charge location, while negative drift is in the direction of blast wave propagation. At the onset of loading, the first story moves in the direction of blast loading while the upper stories move together in the opposite direction. This is because the first story panels at and near the center of the building side (where the charge is centered) are closest to the charge, therefore the forces are largest and arrive here first. As the panels respond, edge reactions apply forces to the floor slab with rigid diaphragm constraint. This excites the first floor's mass, setting it in motion in the direction of blast wave propagation and imposing deformations across the first- and second-story LFRS springs. The first story LFRS springs have a rigid boundary (the ground) to react against; however, the second story LFRS force is pushing against the combined mass of the upper floors. The upper floors effectively act as a counterweight to achieve equilibrium after the sudden displacement of the first floor mass. This behavior is somewhat interrupted by the arrival of blast loads in the upper stories, however the imposition of this initial response has a significant impact upon the peak story drift demands, which occur as a result of the dynamic response of the building well after the blast loading has ceased.

Yield of each story's LFRS springs occurs around 0.125% drift. Fig. 9-41 indicates that all three stories exceed yield, however these peaks occur at different times, with the largest drift occurring in the top story. This is believed to be the result of a whiplash-type action, where the response of the lower floors drives LFRS demands towards the top story,

where there is no LFRS spring or floor mass above to help resist these demands. Additionally, LFRS frames typically get progressively weaker and more flexible moving up along the building height, making them particularly vulnerable to large drifts during this atypical action. Peak drifts for each story subjected to DBS1, 2 and 3 are shown in Table 5-10 with similar trends but diminishing magnitudes for these smaller scaled distance (Z) scenarios. While the observed building response is interesting to examine in detail, these peak story drifts are small relative to even frequent ground motion response results and generally consist of no more than two excursions which exceed yield, making them essentially meaningless when compared to any performance evaluation or loss estimation for seismic events, even in low-seismic hazard locations. However, this conclusion is predicated on the assumption that the façade system remains intact to prevent the blast wave from propagating into the building's interior, where the potential for damage and loss of human life or injury increases significantly. Failure of the façade system also exposes structural members to damage, which can lead to progressive collapse in extreme cases. Maintenance of the integrity of the façade system subjected to blast events is a primary objective of the MHFS design methodology, therefore the performance of this system designed for and subjected to these scenarios will be examined to ensure an adequate protective design is achieved through this process.

Peak MHFS connector crushing deformations for each panel on the blast-facing building side subjected to DBS1 are given in Table 9-24. As expected, the largest deformations occur in the first story interior panels, with symmetric peak responses relative to the charge's centered location along the building width. All connectors on the blast-facing building front exceeded yield, with the largest deformations essentially equal to the

target crushing deformation of four inches. The maximum panel moment divided by the design plastic moment capacity for each panel subjected to this blast scenario is given in Table 9-25. These results indicate that several panels (closest to the charge) reach their plastic moment capacity, indicating the proportional strength design of the panels and connectors functions as intended when subjected to a more realistic blast simulation than the idealized case discussed in Section 9.3. Maximum panel hinge rotations are given in Table 9-26. Note that even the largest panel hinge rotations are significantly less than the target maximum of 12 degrees. There are several potential reasons for this, including:

1. The design first-story impulse value for DBS1 is calculated considering the charge centered on a panel, however with an even number of panels—in this case, six—and a charge centered along the building's width, the charge is not centered on any one panel, and the actual impulse on the two center panels will be less than the design value due to increased distance from the charge location and increased angle of incidence.
2. The simulated DBS1 includes a negative loading phase, which is neglected when calculating design impulse values. This phenomenon occurs after the inward pressure wave and acts back towards the source of the air-blast. The negative loading phase has a much smaller peak force, but much longer duration than the positive phase loading. Inclusion of the negative phase reduces the effective net impulse imparted onto the panel, resulting in less demand on the MHFS.
3. The applied force time histories account for arrival time, meaning that points on panels, which are closer to the blast source, will begin to see loading before points, which are farther away. This so-called staggered arrival time can excite higher

modes, including both symmetric and anti-symmetric modes, which are neglected in design. Vibration in these modes allows more elastic potential energy to be stored via elastic deformations of the panel, leaving less total energy, which must be balanced through plastic deformations of the panel and connectors.

4. Flexibility of the building frame is also disregarded in design; however, this factor may “cushion” the panels to some extent as they absorb the air-blast energy, requiring less work from the MHFS than the rigid panel connector boundary assumed for design.

While the combined effect of these issues (and possibly others) clearly impacts the observed vs. design response, it should be noted that all of the assumptions made in design are conservative, and the performance of the MHFS subjected to DBS1 is believed to be adequate.

Peak connector crushing deformations and panel moment ratios for DBS2 are given in Table 9-27 and Table 9-28, respectively. In this scenario, all connectors reached yield but did not approach four inches. No panels reached their plastic moment capacity (i.e. all panels remained elastic). The performance objectives for DBS2—plastic connector response with elastic panels—were achieved for all panels. Connector crushing deformations and panel moment ratios for DBS3 are shown in Table 9-27 and Table 9-28, respectively. The performance objective for this scenario is to keep all MHFS components elastic, and this objective is achieved according to this analysis.

Table 9-1: HSS Radial Plastic Mechanism Strength FEA Results

HSS6, L=12 in Thickness (in)	Mechanism Strength (kip)		
	FEA	Design	% Dif.
0.125	5	4.03	19.5%
0.25	20.9	16.2	22.5%
0.5	88.3	64.4	27.1%

Table 9-2: HSS Radial Stiffness Calculation Comparison with FEA Results

HSS6, L=12 in Thickness (in)	Radial Stiffness (kip/in)		
	FEA	Design	% Dif.
0.125	19.6	15.5	20.9%
0.25	155	124	20.0%
0.5	1178	991	15.9%

Table 9-3: HSS Longitudinal Shear Mechanism Strength Calculation Comparison with FEA Results

HSS6 Thickness (in):	Longitudinal Shear Elastic Force Limit Prediction (kip)								
	0.125			0.25			0.5		
Length (in)	FEA	Design	% Dif.	FEA	Design	% Dif.	FEA	Design	% Dif.
3	1.8	0.829	53.94%	6.88	3.09	55.09%	22.7	10.9	51.98%
6	4.9	3.32	32.24%	21.3	12.4	41.78%	78	43.6	44.10%
9	9.8	7.46	23.88%	41.5	27.8	33.01%	153	98	35.95%
12	15.4	13.3	13.64%	68.8	49.5	28.05%	250	174	30.40%
16	26	23.6	9.23%	115	87.9	23.57%	397	310	21.91%

Note: FEA values obtained using intersection of pre- and post-yield force-deformation tangents. Design values intended to preclude onset of nonlinear response and thus are conservatively small relative to observed mechanism strengths.

Table 9-4: HSS Longitudinal Shear FEA Stiffness

HSS6 Length (in)	Longitudinal Shear Stiffness (kip/in)		
	Thickness (in)		
	0.125	0.25	0.5
3	8.39	57.1	294
6	39.2	270	1410
9	111	736	3503
12	241	1498	6368
16	524	2951	10873

Table 9-5: HSS Rolling Mechanism Strength Calculation Comparison with FEA Results

HSS6		Rolling Plastic Mechanism Strength (kip)								
Thickness (in):		0.125			0.25			0.5		
Length (in)	FEA	Design	% Dif.	FEA	Design	% Dif.	FEA	Design	% Dif.	
3	0.491	0.503	-2.44%	2.04	2.01	1.47%	8.25	8.05	2.42%	
6	1.03	1.01	1.94%	4.11	4.03	1.95%	16.3	16.1	1.23%	
9	1.55	1.51	2.58%	6.06	6.04	0.330%	24.6	24.2	1.63%	
12	2.07	2.01	2.90%	8.10	8.05	0.617%	32.9	32.2	2.13%	
16	2.68	2.68	0.00%	11.3	11.1	1.94%	44.0	42.9	2.50%	

Table 9-6: HSS Rolling Stiffness Calculation Comparison with FEA Results

HSS6		Rolling Stiffness (kip/in)								
Thickness (in):		0.125			0.25			0.5		
Length (in)	FEA	Design	% Dif.	FEA	Design	% Dif.	FEA	Design	% Dif.	
3	0.800	0.734	8.25%	6.32	5.87	7.12%	49.5	47.0	5.05%	
6	1.62	1.47	9.26%	12.9	11.7	9.30%	102	93.9	7.94%	
9	2.44	2.20	9.84%	19.4	17.6	9.28%	154	141	8.44%	
12	3.26	2.94	9.82%	26.0	23.5	9.62%	205	188	8.29%	
16	4.36	3.91	10.3%	34.7	31.3	9.80%	275	250	9.09%	

Table 9-7: Prototype MHFS Design with Reinforced Concrete Panels

Reinforced Concrete Panel						
<u>Edge Panels</u>						
Story	L _{MDC-V} (in)	L _{MDC-L} (in)	L _{MDC-B} (in)	B _{UFP} (in)	M _p (kip-in)	Factor
3	15	18.25	28	56	5049	4.40
2	14.5	17.25	26	56	4840	4.22
1	14.25	46.25	54.5	56	7823	6.81
<u>Interior Panels</u>						
Story	L _{MDC-V} (in)	L _{MDC-L} (in)	L _{MDC-B} (in)	B _{UFP} (in)	M _p (kip-in)	Factor
3	13.5	15.5	22.25	56	4448	3.87
2	13	15.25	21	56	4317	3.76
1	12.75	49.25	54.5	56	7823	6.81

Notes: All designs use HSS6x0.25 for MDCs, $d_{UFP}=6"$, $t_{UFP}=1/4"$, $l_{free}=4"$
 All panels 13'x30' surface area (nominal), $t=6"$
 Factor increase in M_p is relative to typical as-built details

Table 9-8: Prototype Braced Frame Seismic Analysis Model Dynamic Properties

Braced Frame	No Façade	Mode		
		1	2	3
	Period (s)	0.380	0.151	0.088
Shape Φ_{ij}	Floor 1	0.132	0.333	0.410
	Floor 2	0.282	0.313	-0.345
	Floor 3	0.447	-0.295	0.097

Braced Frame	With Façade	Mode		
		1	2	3
	Period (s)	0.339	0.137	0.086
Shape Φ_{ij}	Floor 1	0.163	0.306	0.411
	Floor 2	0.303	0.296	-0.327
	Floor 3	0.424	-0.337	0.078

Table 9-9: Prototype Moment Frame Seismic Analysis Model Dynamic Properties

Moment Frame	No Façade	Mode		
		1	2	3
	Period (s)	1.105	0.334	0.168
Shape Φ_{ij}	Floor 1	0.126	0.355	0.393
	Floor 2	0.289	0.292	-0.357
	Floor 3	0.444	-0.291	0.121

Moment Frame	With Façade	Mode		
		1	2	3
	Period (s)	0.696	0.228	0.152
Shape Φ_{ij}	Floor 1	0.208	0.276	0.418
	Floor 2	0.336	0.261	-0.338
	Floor 3	0.376	-0.394	0.069

Table 9-10: Peak Drift Response of Prototype Braced Frame Building without MHFS

Peak Inter-Story Drift (%)													
Frequent Earthquakes (50% Probability of Exceedance in 50 years)											Statistics		
Story	LA41	LA43	LA45	LA47	LA49	LA51	LA53	LA55	LA57	LA59	Mean	StdDev	Median
3	0.81	0.13	0.26	0.64	0.32	1.99	0.81	0.51	0.29	1.04	0.68	0.54	0.58
2	0.38	0.11	0.23	0.34	0.30	0.34	0.30	0.35	0.24	0.45	0.30	0.10	0.32
1	0.88	0.10	0.23	0.42	0.31	0.40	0.32	0.33	0.22	2.65	0.59	0.75	0.32
Maximum	0.88	0.13	0.26	0.64	0.32	1.99	0.81	0.51	0.29	2.65	0.68	0.75	0.58
Peak Inter-Story Drift (%)													
DBE (10% Probability of Exceedance in 50 years)											Statistics		
Story	LA1	LA3	LA5	LA7	LA9	LA11	LA13	LA15	LA17	LA19	Mean	StdDev	Median
3	0.51	0.59	0.27	0.28	0.47	0.88	1.10	0.84	0.37	1.47	0.68	0.39	0.55
2	0.34	0.34	0.23	0.26	0.32	0.30	0.43	0.43	0.30	0.56	0.35	0.10	0.33
1	0.89	0.43	0.21	0.26	0.60	0.30	0.62	1.53	0.30	1.42	0.66	0.48	0.52
Maximum	0.89	0.59	0.27	0.28	0.60	0.88	1.10	1.53	0.37	1.47	0.68	0.48	0.55
Peak Inter-Story Drift (%)													
MCE (2% Probability of Exceedance in 50 years)											Statistics		
Story	LA21	LA23	LA25	LA27	LA29	LA31	LA33	LA35	LA37	LA39	Mean	StdDev	Median
3	0.84	0.45	0.87	0.77	0.79	0.69	2.05	1.11	0.53	0.79	0.89	0.45	0.79
2	0.71	0.33	0.53	0.41	0.35	0.45	0.42	0.58	0.42	0.37	0.46	0.12	0.42
1	11.35	0.46	5.79	2.33	0.68	3.91	0.92	12.00	1.89	0.71	4.00	4.38	2.11
Maximum	11.35	0.46	5.79	2.33	0.79	3.91	2.05	12.00	1.89	0.79	4.00	4.38	2.11

Table 9-11: Peak Drift Response of Prototype Braced Frame Building with MHFS

Peak Inter-Story Drift (%)													
Frequent Earthquakes (50% Probability of Exceedance in 50 years)											Statistics		
Story	LA41	LA43	LA45	LA47	LA49	LA51	LA53	LA55	LA57	LA59	Mean	StdDev	Median
3	0.39	0.07	0.13	0.26	0.19	0.43	0.30	0.28	0.20	0.40	0.26	0.12	0.27
2	0.32	0.07	0.14	0.25	0.19	0.33	0.29	0.28	0.18	0.38	0.24	0.09	0.27
1	1.15	0.09	0.16	0.30	0.20	1.00	0.39	0.28	0.18	2.47	0.62	0.74	0.29
Maximum	1.15	0.09	0.16	0.30	0.20	1.00	0.39	0.28	0.20	2.47	0.62	0.74	0.29

Peak Inter-Story Drift (%)													
DBE (10% Probability of Exceedance in 50 years)											Statistics		
Story	LA1	LA3	LA5	LA7	LA9	LA11	LA13	LA15	LA17	LA19	Mean	StdDev	Median
3	0.29	0.28	0.15	0.21	0.27	0.43	0.42	0.33	0.30	0.41	0.31	0.09	0.29
2	0.27	0.28	0.16	0.21	0.27	0.34	0.35	0.34	0.28	0.34	0.28	0.06	0.28
1	0.42	0.45	0.19	0.23	0.43	0.51	1.66	0.98	0.41	1.94	0.72	0.61	0.44
Maximum	0.42	0.45	0.19	0.23	0.43	0.51	1.66	0.98	0.41	1.94	0.72	0.61	0.44

Peak Inter-Story Drift (%)													
MCE (2% Probability of Exceedance in 50 years)											Statistics		
Story	LA21	LA23	LA25	LA27	LA29	LA31	LA33	LA35	LA37	LA39	Mean	StdDev	Median
3	0.35	0.29	0.50	0.35	0.36	0.46	0.45	0.34	0.30	0.39	0.38	0.07	0.36
2	0.40	0.29	0.43	0.34	0.29	0.42	0.37	0.35	0.29	0.32	0.35	0.05	0.35
1	10.06	0.54	4.19	1.03	0.89	3.32	1.76	7.28	0.90	1.02	3.10	3.23	1.40
Maximum	10.06	0.54	4.19	1.03	0.89	3.32	1.76	7.28	0.90	1.02	3.10	3.23	1.40

Table 9-12: Drift Ratios for Prototype Braced Frame Building with and without MHFS

Ratio of Peak Inter-Story Drifts of Prototype Braced Frame Building with MHFS to without MHFS													
Frequent Earthquakes (50% Probability of Exceedance in 50 years)											Statistics		
Story	LA41	LA43	LA45	LA47	LA49	LA51	LA53	LA55	LA57	LA59	Mean	StdDev	Median
3	0.48	0.51	0.51	0.41	0.60	0.22	0.37	0.54	0.67	0.39	0.47	0.13	0.50
2	0.84	0.68	0.61	0.75	0.62	0.96	0.95	0.80	0.76	0.83	0.78	0.12	0.78
1	1.31	0.90	0.68	0.72	0.64	2.49	1.23	0.87	0.84	0.93	1.06	0.55	0.88
Maximum	1.31	0.90	0.68	0.75	0.64	2.49	1.23	0.87	0.84	0.93	1.06	0.55	0.88
Ratio of Peak Inter-Story Drifts of Prototype Braced Frame Building with MHFS to without MHFS													
DBE (10% Probability of Exceedance in 50 years)											Statistics		
Story	LA1	LA3	LA5	LA7	LA9	LA11	LA13	LA15	LA17	LA19	Mean	StdDev	Median
3	0.57	0.47	0.56	0.75	0.58	0.49	0.38	0.40	0.82	0.28	0.53	0.16	0.52
2	0.79	0.82	0.73	0.80	0.83	1.12	0.81	0.79	0.93	0.60	0.82	0.13	0.80
1	0.47	1.04	0.90	0.87	0.71	1.70	2.70	0.64	1.34	1.36	1.17	0.65	0.97
Maximum	0.79	1.04	0.90	0.87	0.83	1.70	2.70	0.64	1.34	1.36	1.17	0.65	0.97
Ratio of Peak Inter-Story Drifts of Prototype Braced Frame Building with MHFS to without MHFS													
MCE (2% Probability of Exceedance in 50 years)											Statistics		
Story	LA21	LA23	LA25	LA27	LA29	LA31	LA33	LA35	LA37	LA39	Mean	StdDev	Median
3	0.41	0.64	0.57	0.45	0.46	0.66	0.22	0.31	0.57	0.49	0.48	0.14	0.47
2	0.56	0.88	0.81	0.84	0.83	0.92	0.89	0.61	0.69	0.87	0.79	0.12	0.83
1	0.89	1.17	0.72	0.44	1.31	0.85	1.91	0.61	0.48	1.45	0.98	0.47	0.87
Maximum	0.89	1.17	0.81	0.84	1.31	0.92	1.91	0.61	0.69	1.45	0.98	0.47	0.87

Note: Values greater than 1 (greyed boxes) indicate peak drift is increased with MHFS included.

Table 9-13: Peak Drift Response of Prototype Moment Frame Building without MHFS

Peak Inter-Story Drift (%)													
Frequent Earthquakes (50% Probability of Exceedance in 50 years)											Statistics		
Story	LA41	LA43	LA45	LA47	LA49	LA51	LA53	LA55	LA57	LA59	Mean	StdDev	Median
3	2.57	0.76	1.29	1.10	1.52	2.12	1.79	1.75	1.00	4.32	1.82	1.03	1.63
2	2.33	0.88	1.36	0.89	1.36	1.30	1.40	1.54	0.91	3.49	1.55	0.80	1.36
1	3.32	0.74	1.23	0.75	1.34	1.37	1.22	1.34	0.73	2.68	1.47	0.86	1.29
Maximum	3.32	0.88	1.36	1.10	1.52	2.12	1.79	1.75	1.00	4.32	1.82	1.03	1.63

Peak Inter-Story Drift (%)													
DBE (10% Probability of Exceedance in 50 years)											Statistics		
Story	LA1	LA3	LA5	LA7	LA9	LA11	LA13	LA15	LA17	LA19	Mean	StdDev	Median
3	1.78	2.00	1.50	1.96	3.42	3.07	2.23	2.99	2.00	2.18	2.31	0.63	2.09
2	2.07	2.15	1.48	2.25	3.49	3.45	2.35	3.45	1.96	1.44	2.41	0.78	2.20
1	2.21	2.65	1.68	2.12	3.47	3.69	3.02	3.77	1.96	1.71	2.63	0.81	2.43
Maximum	2.21	2.65	1.68	2.25	3.49	3.69	3.02	3.77	2.00	2.18	2.63	0.81	2.43

Peak Inter-Story Drift (%)													
MCE (2% Probability of Exceedance in 50 years)											Statistics		
Story	LA21	LA23	LA25	LA27	LA29	LA31	LA33	LA35	LA37	LA39	Mean	StdDev	Median
3	5.40	1.89	4.75	6.22	2.14	4.01	2.95	8.68	7.71	3.87	4.76	2.27	4.38
2	5.02	1.91	4.90	6.57	2.04	3.58	2.80	8.83	7.84	3.79	4.73	2.38	4.34
1	3.83	2.09	5.06	6.48	2.18	3.78	3.23	9.70	7.55	3.57	4.75	2.46	3.80
Maximum	5.40	2.09	5.06	6.57	2.18	4.01	3.23	9.70	7.84	3.87	4.76	2.46	4.38

Table 9-14: Peak Drift Response of Prototype Moment Frame Building with MHFS

Peak Inter-Story Drift (%)													
Frequent Earthquakes (50% Probability of Exceedance in 50 years)											Statistics		
Story	LA41	LA43	LA45	LA47	LA49	LA51	LA53	LA55	LA57	LA59	Mean	StdDev	Median
3	0.70	0.27	0.29	0.40	0.52	0.60	0.54	0.56	0.35	0.74	0.50	0.16	0.53
2	1.33	0.47	0.53	0.67	0.75	0.85	0.81	0.81	0.50	1.56	0.83	0.36	0.78
1	2.48	0.64	0.70	0.79	1.20	1.18	1.24	1.47	0.71	5.17	1.56	1.38	1.19
Maximum	2.48	0.64	0.70	0.79	1.20	1.18	1.24	1.47	0.71	5.17	1.56	1.38	1.19

Peak Inter-Story Drift (%)													
DBE (10% Probability of Exceedance in 50 years)											Statistics		
Story	LA1	LA3	LA5	LA7	LA9	LA11	LA13	LA15	LA17	LA19	Mean	StdDev	Median
3	0.58	0.52	0.47	0.50	0.63	0.66	1.06	0.71	0.65	0.89	0.67	0.18	0.64
2	1.10	0.96	0.78	0.93	1.21	1.20	1.67	1.34	1.25	1.08	1.15	0.25	1.15
1	2.11	1.73	1.42	1.80	2.72	2.25	4.03	3.39	3.39	1.79	2.46	0.88	2.18
Maximum	2.11	1.73	1.42	1.80	2.72	2.25	4.03	3.39	3.39	1.79	2.46	0.88	2.18

Peak Inter-Story Drift (%)													
MCE (2% Probability of Exceedance in 50 years)											Statistics		
Story	LA21	LA23	LA25	LA27	LA29	LA31	LA33	LA35	LA37	LA39	Mean	StdDev	Median
3	0.86	0.58	0.92	0.90	0.86	0.96	1.00	0.68	0.71	0.58	0.80	0.15	0.86
2	1.87	1.28	1.90	1.56	1.17	1.78	1.35	1.52	1.78	0.94	1.52	0.33	1.54
1	7.97	3.16	8.33	7.27	2.42	6.43	5.46	7.39	9.36	1.81	5.96	2.65	6.85
Maximum	7.97	3.16	8.33	7.27	2.42	6.43	5.46	7.39	9.36	1.81	5.96	2.65	6.85

Table 9-15: Drift Ratios for Prototype Moment Frame Building with and without MHFS

Ratio of Peak Inter-Story Drifts of Prototype Moment Frame Building with MHFS to without MHFS													
Frequent Earthquakes (50% Probability of Exceedance in 50 years)											Statistics		
Story	LA41	LA43	LA45	LA47	LA49	LA51	LA53	LA55	LA57	LA59	Mean	StdDev	Median
3	0.27	0.36	0.23	0.37	0.34	0.28	0.30	0.32	0.35	0.17	0.30	0.06	0.31
2	0.57	0.53	0.39	0.74	0.55	0.66	0.57	0.52	0.55	0.45	0.55	0.10	0.55
1	0.75	0.88	0.57	1.06	0.89	0.86	1.02	1.10	0.97	1.93	1.00	0.36	0.93
Maximum	0.75	0.88	0.57	1.06	0.89	0.86	1.02	1.10	0.97	1.93	1.00	0.36	0.93

Ratio of Peak Inter-Story Drifts of Prototype Moment Frame Building with MHFS to without MHFS													
DBE (10% Probability of Exceedance in 50 years)											Statistics		
Story	LA1	LA3	LA5	LA7	LA9	LA11	LA13	LA15	LA17	LA19	Mean	StdDev	Median
3	0.33	0.26	0.31	0.26	0.18	0.22	0.47	0.24	0.33	0.41	0.30	0.09	0.28
2	0.53	0.45	0.53	0.41	0.35	0.35	0.71	0.39	0.64	0.75	0.51	0.15	0.49
1	0.96	0.65	0.85	0.85	0.78	0.61	1.33	0.90	1.72	1.05	0.97	0.33	0.87
Maximum	0.96	0.65	0.85	0.85	0.78	0.61	1.33	0.90	1.72	1.05	0.97	0.33	0.87

Ratio of Peak Inter-Story Drifts of Prototype Moment Frame Building with MHFS to without MHFS													
MCE (2% Probability of Exceedance in 50 years)											Statistics		
Story	LA21	LA23	LA25	LA27	LA29	LA31	LA33	LA35	LA37	LA39	Mean	StdDev	Median
3	0.16	0.30	0.19	0.15	0.40	0.24	0.34	0.08	0.09	0.15	0.21	0.11	0.18
2	0.37	0.67	0.39	0.24	0.57	0.50	0.48	0.17	0.23	0.25	0.39	0.17	0.38
1	2.08	1.51	1.64	1.12	1.11	1.70	1.69	0.76	1.24	0.51	1.34	0.48	1.38
Maximum	2.08	1.51	1.64	1.12	1.11	1.70	1.69	0.76	1.24	0.51	1.34	0.48	1.38

Note: Values greater than 1 (greyed boxes) indicate peak drift is increased with MHFS included.

Table 9-16: Peak MDC-V Demand-to-Capacity Ratio (D/C) of Prototype Braced Frame Building

Maximum Peak MDC-V Longitudinal Shearing Demand-to-Capacity Ratio													
Frequent Earthquakes (50% Probability of Exceedance in 50 years)											Statistics		
Panels	LA41	LA43	LA45	LA47	LA49	LA51	LA53	LA55	LA57	LA59	Mean	StdDev	Median
Edge	0.71	0.31	0.35	0.42	0.36	0.68	0.46	0.39	0.36	0.81	0.48	0.18	0.40
Interior	0.74	0.39	0.43	0.52	0.44	0.75	0.58	0.48	0.45	0.81	0.56	0.15	0.50
Maximum	0.74	0.39	0.43	0.52	0.44	0.75	0.58	0.48	0.45	0.81	0.56	0.18	0.50
Maximum Peak MDC-V Longitudinal Shearing Demand-to-Capacity Ratio													
DBE (10% Probability of Exceedance in 50 years)											Statistics		
Panels	LA1	LA3	LA5	LA7	LA9	LA11	LA13	LA15	LA17	LA19	Mean	StdDev	Median
Edge	0.46	0.49	0.35	0.38	0.46	0.53	0.59	0.46	0.48	0.65	0.49	0.09	0.47
Interior	0.58	0.60	0.44	0.48	0.58	0.66	0.69	0.57	0.59	0.73	0.59	0.09	0.59
Maximum	0.58	0.60	0.44	0.48	0.58	0.66	0.69	0.57	0.59	0.73	0.59	0.09	0.59
Maximum Peak MDC-V Longitudinal Shearing Demand-to-Capacity Ratio													
MCE (2% Probability of Exceedance in 50 years)											Statistics		
Panels	LA21	LA23	LA25	LA27	LA29	LA31	LA33	LA35	LA37	LA39	Mean	StdDev	Median
Edge	1.17	0.51	0.60	0.68	0.71	0.76	0.79	0.75	0.72	0.53	0.72	0.19	0.72
Interior	0.83	0.62	0.75	0.76	0.76	0.78	0.84	0.81	0.77	0.66	0.76	0.07	0.77
Maximum	1.17	0.62	0.75	0.76	0.76	0.78	0.84	0.81	0.77	0.66	0.76	0.19	0.77

Note: Vertical panel inertia not included in analyses (design value is approx. D/C = 0.2).

Table 9-17: Peak MDC-V D/C of Prototype Moment Frame Building

Maximum Peak MDC-V Longitudinal Shearing Demand-to-Capacity Ratio													
Frequent Earthquakes (50% Probability of Exceedance in 50 years)													
Panels	LA41	LA43	LA45	LA47	LA49	LA51	LA53	LA55	LA57	LA59	Mean	StdDev	Median
Edge	0.85	0.67	0.70	0.68	0.74	0.70	0.79	0.77	0.66	0.84	0.74	0.07	0.72
Interior	0.91	0.77	0.79	0.80	0.80	0.80	0.84	0.83	0.75	0.87	0.82	0.05	0.80
Maximum	0.91	0.77	0.79	0.80	0.80	0.80	0.84	0.83	0.75	0.87	0.82	0.07	0.80
Maximum Peak MDC-V Longitudinal Shearing Demand-to-Capacity Ratio													
DBE (10% Probability of Exceedance in 50 years)													
Panels	LA1	LA3	LA5	LA7	LA9	LA11	LA13	LA15	LA17	LA19	Mean	StdDev	Median
Edge	0.80	0.78	0.77	0.78	0.81	0.81	0.75	0.68	0.74	0.78	0.77	0.04	0.78
Interior	0.87	0.80	0.82	0.81	0.83	0.81	0.81	0.77	0.77	0.93	0.82	0.05	0.81
Maximum	0.87	0.80	0.82	0.81	0.83	0.81	0.81	0.77	0.77	0.93	0.82	0.05	0.81
Maximum Peak MDC-V Longitudinal Shearing Demand-to-Capacity Ratio													
MCE (2% Probability of Exceedance in 50 years)													
Panels	LA21	LA23	LA25	LA27	LA29	LA31	LA33	LA35	LA37	LA39	Mean	StdDev	Median
Edge	1.07	0.80	0.77	0.79	0.79	0.91	0.82	0.87	1.13	0.76	0.87	0.13	0.81
Interior	0.91	0.84	0.82	0.85	0.85	0.88	0.88	0.84	0.85	0.81	0.85	0.03	0.85
Maximum	1.07	0.84	0.82	0.85	0.85	0.91	0.88	0.87	1.13	0.81	0.87	0.13	0.85

Note: Vertical panel inertia not included in analyses (design value is approx. D/C = 0.2).

Table 9-18: Peak MDC-L D/C of Prototype Braced Frame Building Subjected to MCE Suite

Maximum Peak MDC-L Longitudinal Shearing Demand-to-Capacity Ratio													
Frequent Earthquakes (50% Probability of Exceedance in 50 years)													
Panels	LA41	LA43	LA45	LA47	LA49	LA51	LA53	LA55	LA57	LA59	Mean	StdDev	Median
Edge	0.31	0.05	0.08	0.15	0.13	0.27	0.29	0.23	0.13	0.25	0.19	0.09	0.19
Interior	0.37	0.07	0.11	0.21	0.16	0.34	0.39	0.31	0.17	0.33	0.25	0.11	0.26
Maximum	0.37	0.07	0.11	0.21	0.16	0.34	0.39	0.31	0.17	0.33	0.25	0.11	0.26
Maximum Peak MDC-L Longitudinal Shearing Demand-to-Capacity Ratio													
DBE (10% Probability of Exceedance in 50 years)													
Panels	LA1	LA3	LA5	LA7	LA9	LA11	LA13	LA15	LA17	LA19	Mean	StdDev	Median
Edge	0.17	0.19	0.10	0.13	0.16	0.26	0.21	0.20	0.17	0.29	0.19	0.06	0.18
Interior	0.23	0.25	0.13	0.17	0.22	0.34	0.26	0.27	0.23	0.38	0.25	0.07	0.24
Maximum	0.23	0.25	0.13	0.17	0.22	0.34	0.26	0.27	0.23	0.38	0.25	0.07	0.24
Maximum Peak MDC-L Longitudinal Shearing Demand-to-Capacity Ratio													
MCE (2% Probability of Exceedance in 50 years)													
Panels	LA21	LA23	LA25	LA27	LA29	LA31	LA33	LA35	LA37	LA39	Mean	StdDev	Median
Edge	0.22	0.16	0.27	0.21	0.23	0.33	0.30	0.18	0.22	0.29	0.24	0.05	0.23
Interior	0.28	0.23	0.37	0.32	0.32	0.49	0.36	0.26	0.29	0.33	0.33	0.07	0.32
Maximum	0.28	0.23	0.37	0.32	0.32	0.49	0.36	0.26	0.29	0.33	0.33	0.07	0.32

Table 9-19: Peak MDC-L D/C of Prototype Moment Frame Building Subjected to MCE Suite

Maximum Peak MDC-L Longitudinal Shearing Demand-to-Capacity Ratio													
Frequent Earthquakes (50% Probability of Exceedance in 50 years)											Statistics		
Panels	LA41	LA43	LA45	LA47	LA49	LA51	LA53	LA55	LA57	LA59	Mean	StdDev	Median
Edge	0.69	0.33	0.37	0.45	0.56	0.48	0.61	0.55	0.33	0.64	0.50	0.13	0.51
Interior	0.87	0.41	0.44	0.53	0.59	0.61	0.62	0.69	0.42	0.77	0.59	0.15	0.60
Maximum	0.87	0.41	0.44	0.53	0.59	0.61	0.62	0.69	0.42	0.77	0.59	0.15	0.60
Maximum Peak MDC-L Longitudinal Shearing Demand-to-Capacity Ratio													
DBE (10% Probability of Exceedance in 50 years)											Statistics		
Panels	LA1	LA3	LA5	LA7	LA9	LA11	LA13	LA15	LA17	LA19	Mean	StdDev	Median
Edge	0.65	0.67	0.58	0.66	0.66	0.63	0.67	0.58	0.59	0.54	0.62	0.05	0.64
Interior	0.61	0.62	0.61	0.60	0.65	0.77	0.85	0.73	0.67	0.71	0.68	0.08	0.66
Maximum	0.65	0.67	0.61	0.66	0.66	0.77	0.85	0.73	0.67	0.71	0.68	0.08	0.66
Maximum Peak MDC-L Longitudinal Shearing Demand-to-Capacity Ratio													
MCE (2% Probability of Exceedance in 50 years)											Statistics		
Panels	LA21	LA23	LA25	LA27	LA29	LA31	LA33	LA35	LA37	LA39	Mean	StdDev	Median
Edge	0.74	0.62	0.57	0.62	0.65	0.81	0.80	0.73	0.70	0.59	0.68	0.09	0.68
Interior	0.78	0.61	0.70	0.75	0.79	0.84	0.77	0.75	0.61	0.59	0.72	0.09	0.75
Maximum	0.78	0.62	0.70	0.75	0.79	0.84	0.80	0.75	0.70	0.59	0.72	0.09	0.75

Table 9-20: Peak UFP Deformation Ratio of Prototype Braced Frame Building Subjected to FrE Suite

Ratio of Peak UFP Rolling Deformation to Peak Inter-Story Drift													
Frequent Earthquakes (50% Probability of Exceedance in 50 years)											Statistics		
Story	LA41	LA43	LA45	LA47	LA49	LA51	LA53	LA55	LA57	LA59	Mean	StdDev	Median
3	1.01	1.02	1.02	1.02	1.02	1.00	1.02	1.02	1.02	1.00	1.01	0.01	1.02
2	1.00	1.00	1.00	0.99	0.99	1.00	0.99	1.01	0.99	0.98	1.00	0.01	0.99
1	0.99	0.99	0.99	0.99	0.99	0.99	0.99	0.99	0.99	0.99	0.99	0.00	0.99
Maximum	1.01	1.02	1.02	1.02	1.02	1.00	1.02	1.02	1.02	1.00	1.01	0.01	1.02

Table 9-21: Peak UFP Deformation Ratio of Prototype Moment Frame Building Subjected to MCE Suite

Story	Ratio of Peak UFP Rolling Deformation to Peak Inter-Story Drift MCE (2% Probability of Exceedance in 50 years)										Statistics		
	LA21	LA23	LA25	LA27	LA29	LA31	LA33	LA35	LA37	LA39	Mean	StdDev	Median
3	0.99	0.99	0.99	0.99	0.99	0.99	0.99	0.98	0.98	0.99	0.99	0.00	0.99
2	0.99	0.99	0.99	0.99	0.98	0.99	0.99	0.99	0.99	0.98	0.99	0.00	0.99
1	1.00	1.00	1.00	1.00	0.99	1.00	1.00	1.00	1.00	0.99	1.00	0.00	1.00
Maximum	1.00	1.00	1.00	1.00	0.99	1.00	1.00	1.00	1.00	0.99	1.00	0.00	1.00

Table 9-22: 3D Light-Mass Prototype Braced Frame Building Model Dynamic Properties

Braced Frame Bldg. Mode:	Translational Modes			Uniform Torsion	Panel Flexure	
	1	2	3			
Period (s):	0.290	0.120	0.073	0.182	0.100	
Shape Φ_{ij}	Floor 3	0.795	-0.588	0.152	4.55E-04	0
	Floor 2	0.532	0.554	-0.640	3.30E-04	0
	Floor 1	0.292	0.590	0.753	1.87E-04	0

Table 9-23: Maximum Inter-Story Drifts for Prototype Building Subjected to Design

Blast Scenario (DBS) Events			
W (lbsTNT):	500	300	100
R (ft)	30	100	200
Story	Maximum Inter-Story Drift (%)		
3	0.24	0.16	0.07
2	0.13	0.10	0.02
1	0.16	0.07	0.03
Note:	Air-blast analyses performed on 3-story steel braced frame office building designed for Boston, MA hazards with floor mass equivalent to uniform 60psf load per floor (light mass).		

Table 9-24: Maximum MHFS Connector Crushing Deformations during DBS1

Simulation						
Maximum MDC Deformation (in)						
DBS1	Panel (left-to-right)					
Story	1	2	3	4	5	6
3	0.57	0.91	1.82	1.82	0.91	0.57
2	0.64	1.04	3.31	3.31	1.04	0.64
1	0.35	1.01	3.90	3.90	1.01	0.35
Note:	All connectors exceeded yield def.					

Table 9-25: Maximum MHFS Panel Bending Moment Ratios during DBS1 Simulation

Maximum Panel Moment / M_p						
DBS1	Panel (left-to-right)					
Story	1	2	3	4	5	6
3	0.84	0.94	0.99	0.99	0.94	0.84
2	0.87	0.96	1.04	1.04	0.96	0.87
1	0.78	0.93	1.02	1.02	0.93	0.78

Table 9-26: Maximum MHFS Panel Hinge Rotation during DBS1 Simulation

Maximum Panel Hinge Rotation (deg.)						
DBS1	Panel (left-to-right)					
Story	1	2	3	4	5	6
3	1.72	2.18	2.21	2.21	2.18	1.72
2	1.73	2.16	2.29	2.29	2.16	1.73
1	2.51	3.57	3.79	3.79	3.57	2.51

Table 9-27: Maximum MHFS Connector Crushing Deformations during DBS2

Simulation						
Maximum MDC Deformation (in)						
DBS2	Panel (left-to-right)					
Story	1	2	3	4	5	6
3	0.27	0.62	0.75	0.75	0.62	0.27
2	0.32	0.66	0.64	0.64	0.66	0.32
1	0.17	0.26	0.39	0.39	0.26	0.17

Note: All connectors exceeded yield def.

Table 9-28: Maximum MHFS Panel Bending Moment Ratios during DBS2 Simulation

Maximum Panel Moment / M_p						
DBS2	Panel (left-to-right)					
Story	1	2	3	4	5	6
3	0.67	0.88	0.90	0.90	0.88	0.67
2	0.68	0.91	0.92	0.92	0.91	0.68
1	0.62	0.69	0.72	0.72	0.69	0.62

Table 9-29: Maximum MHFS Connector Crushing Deformations during DBS3

Simulation						
Maximum MDC Deformation (in)						
DBS3	Panel (left-to-right)					
Story	1	2	3	4	5	6
3	0.08	0.10	0.10	0.10	0.10	0.08
2	0.08	0.09	0.10	0.10	0.09	0.08
1	0.06	0.07	0.07	0.07	0.07	0.06

Note: All connectors remained elastic.

Table 9-30: Maximum MHFS Panel Bending Moment Ratios during DBS3 Simulation

Maximum Panel Moment / M_p						
DBS3	Panel (left-to-right)					
Story	1	2	3	4	5	6
3	0.26	0.33	0.35	0.35	0.33	0.26
2	0.25	0.33	0.35	0.35	0.33	0.25
1	0.21	0.22	0.22	0.22	0.22	0.21

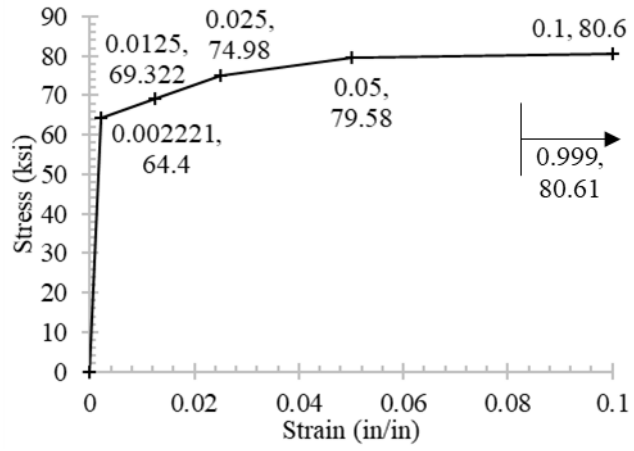


Fig. 9-1: ASTM A500 Gr. B Steel Material Stress-Strain Model for Round HSS Tubes

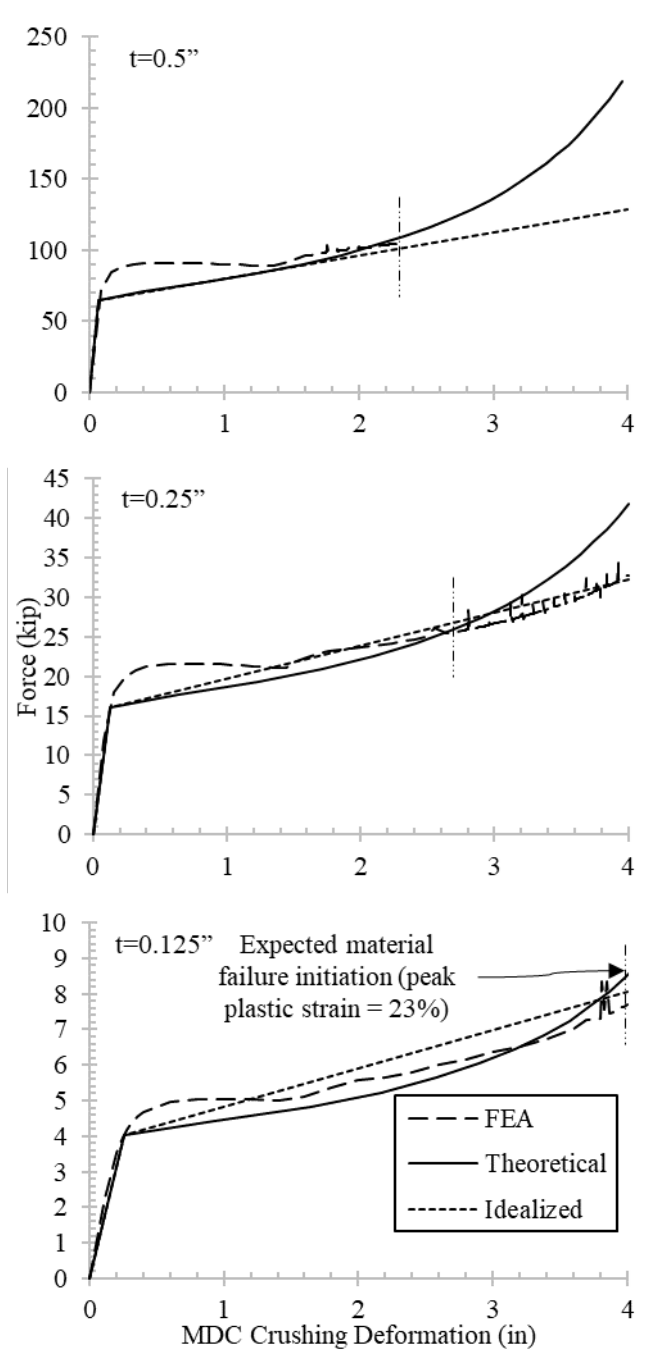


Fig. 9-2: MDC with 12-inch HSS6 Tube Radial Crushing Force-Deformation Behavior

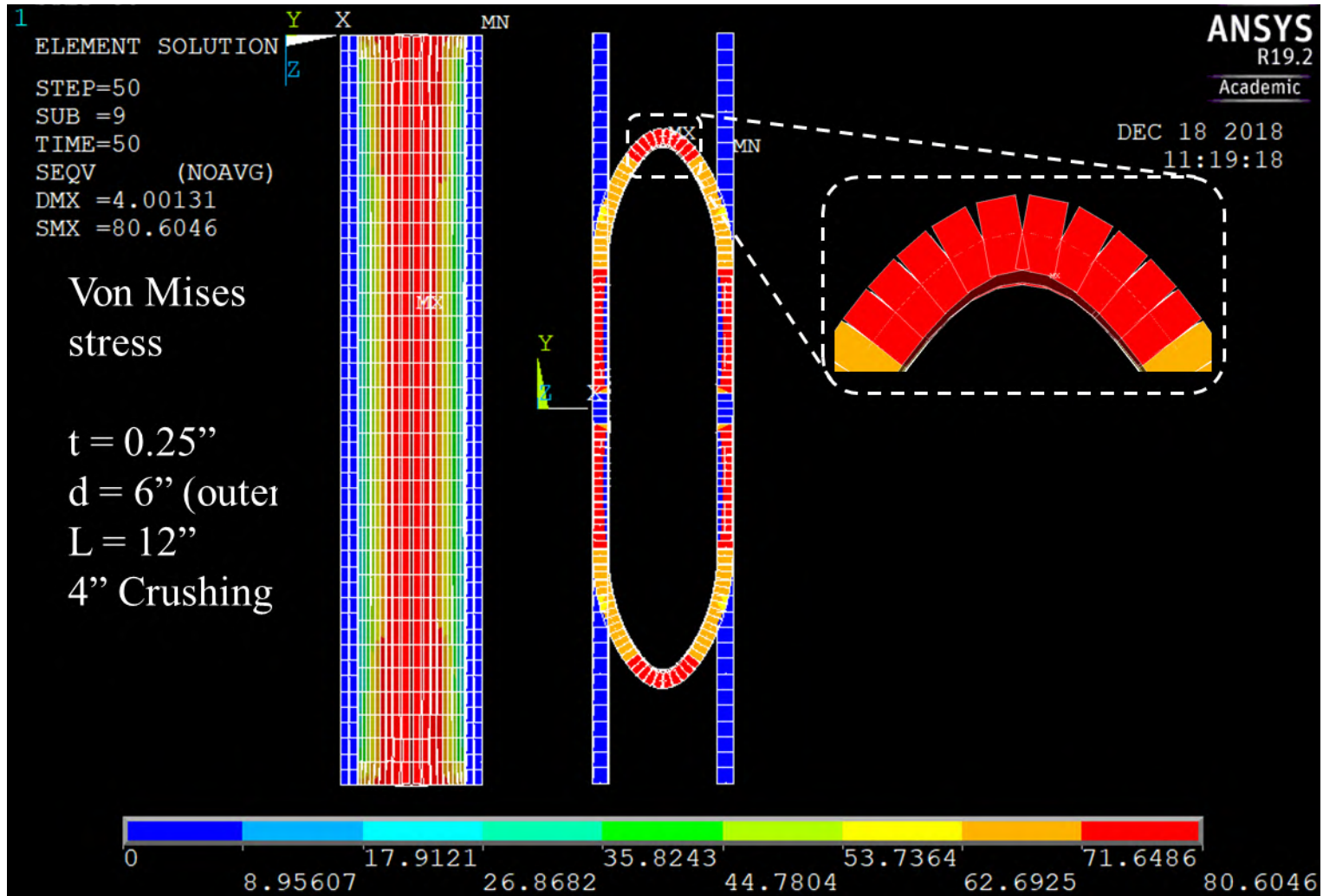


Fig. 9-3: Von Mises Stress Contours for Radially Crushed HSS Tube

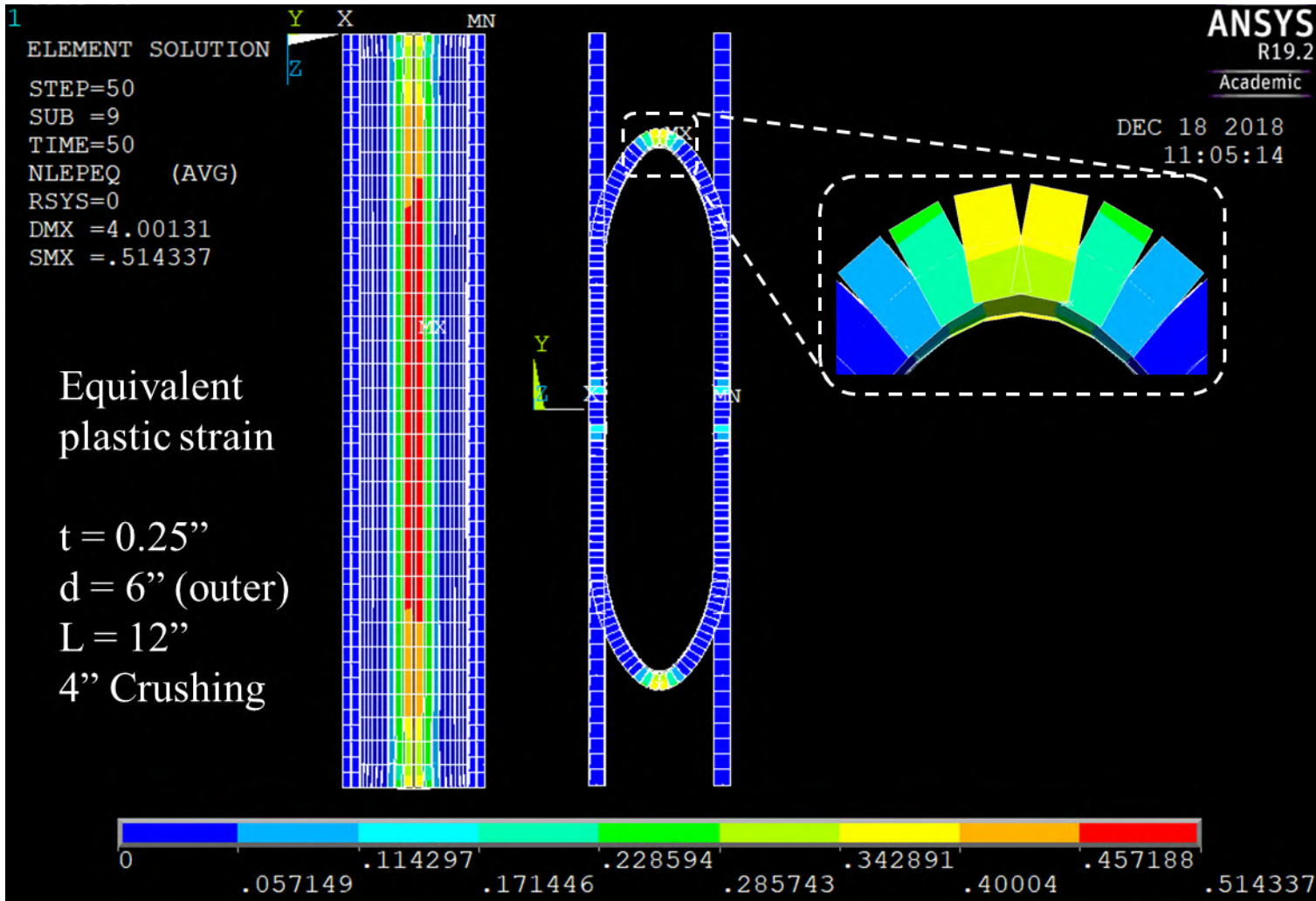


Fig. 9-4: Equivalent Plastic Strain Contours for Radially Crushed HSS Tube

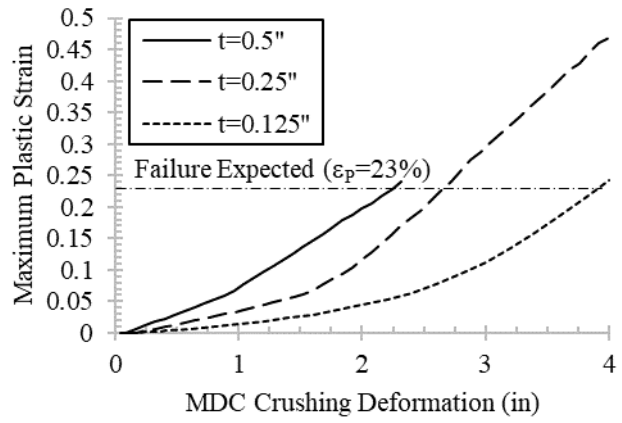


Fig. 9-5: MDC with 12-inch HSS6 Tube Radial Crushing FEA Maximum Plastic Strain

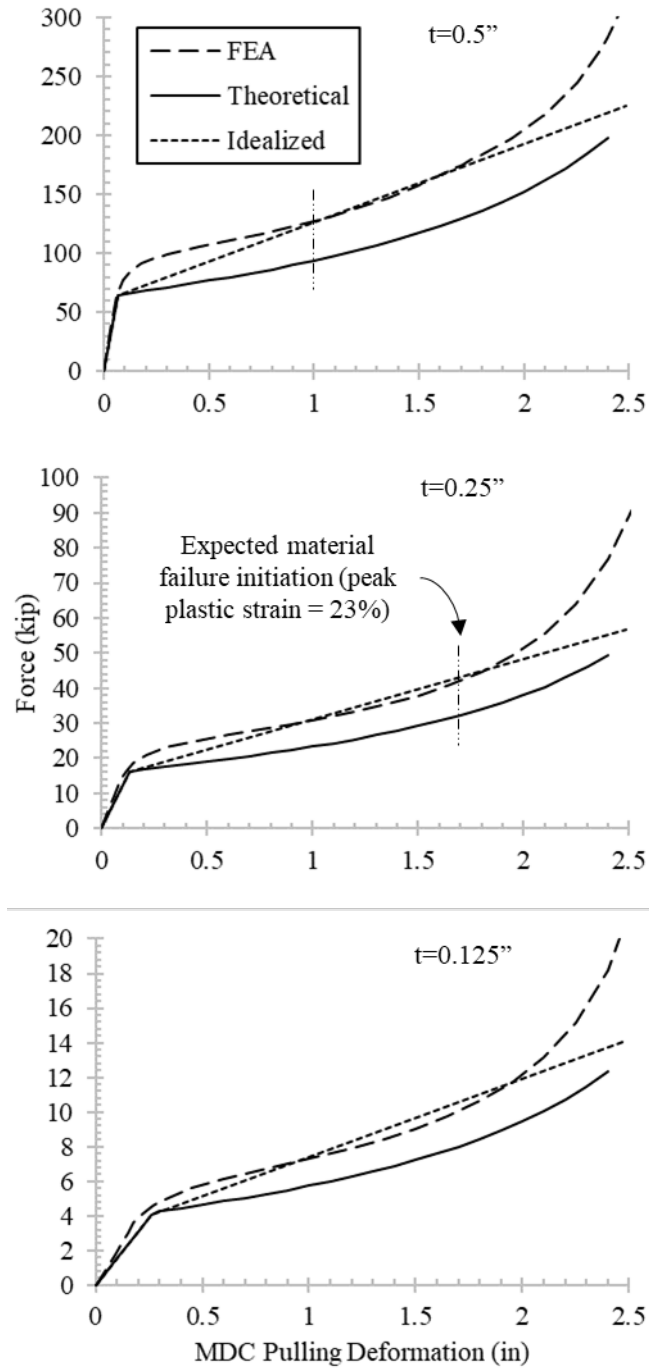


Fig. 9-6: MDC with 12-inch HSS6 Tube Radial Pulling Force-Deformation Behavior

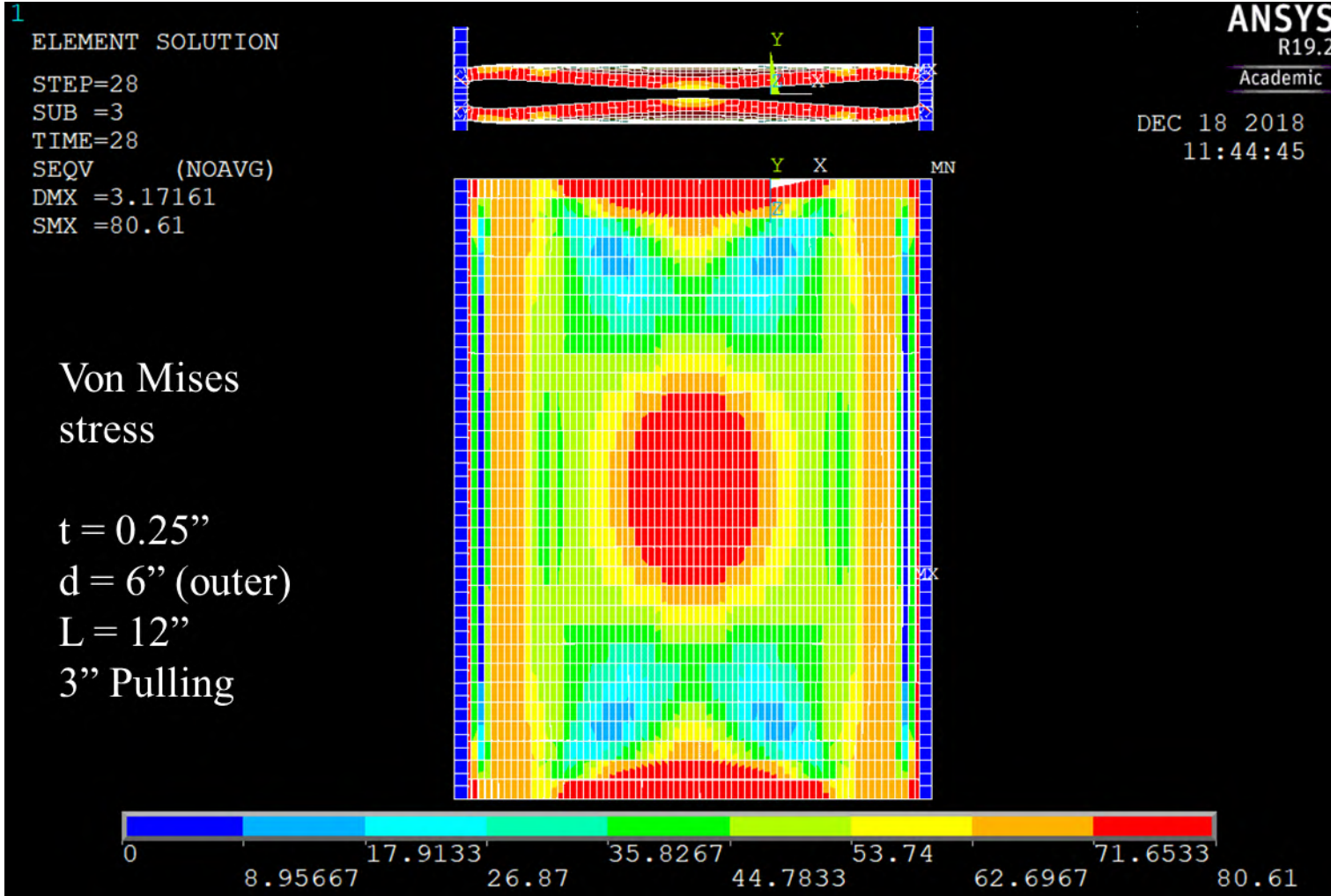


Fig. 9-7: Von Mises Stress Contours for Radially Pulled HSS Tube

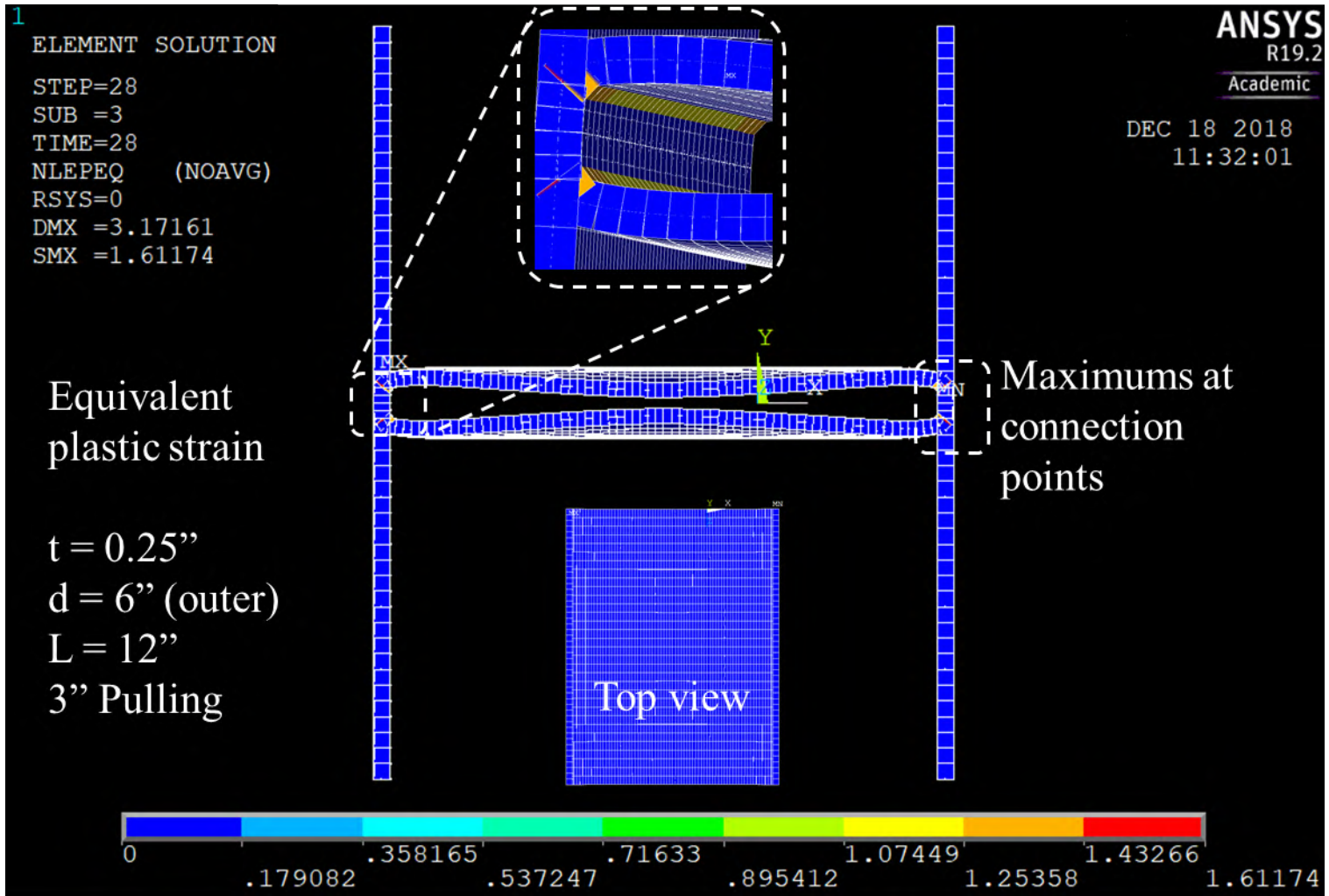


Fig. 9-8: Equivalent Plastic Strain Contours for Radially Pulled HSS Tube

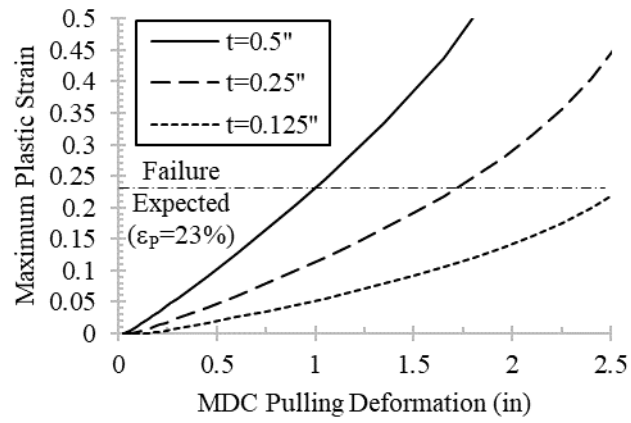


Fig. 9-9: MDC with 12-inch HSS6 Tube Radial Pulling FEA Maximum Plastic Strain

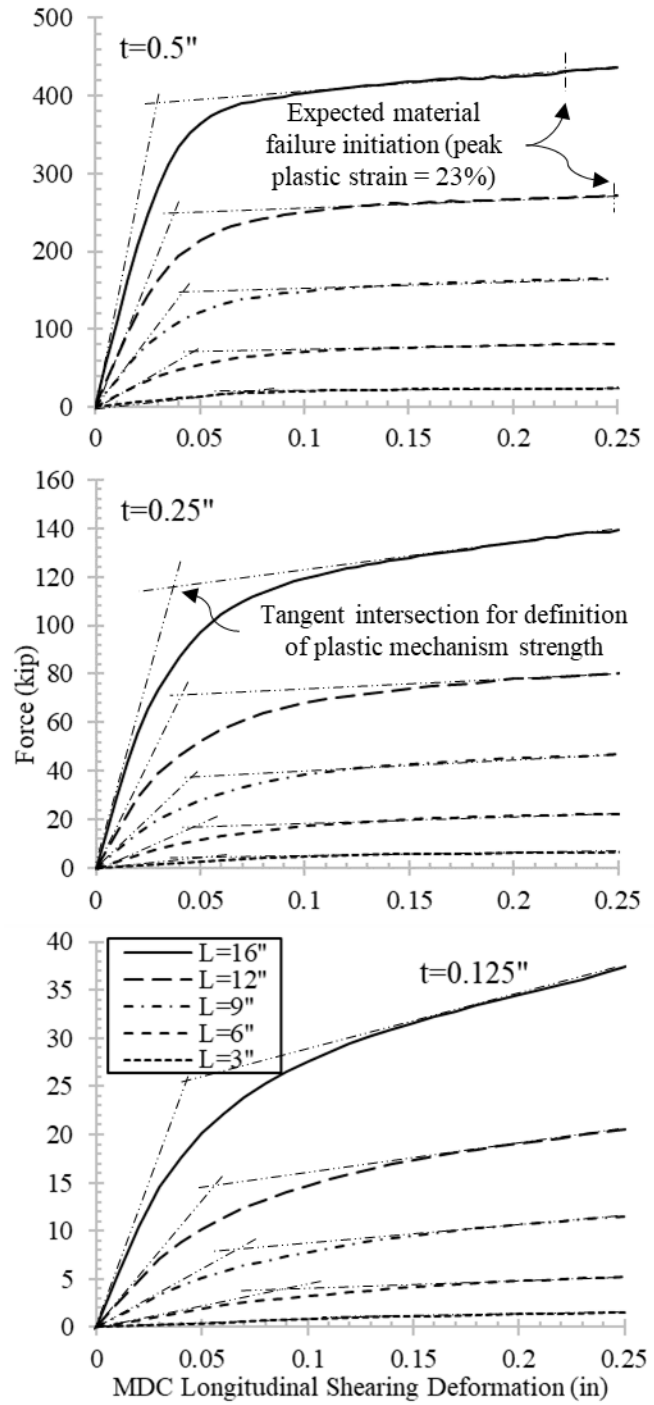


Fig. 9-10: MDC with 12-inch HSS6 Tube Longitudinal Shearing Force-Deformation Behavior

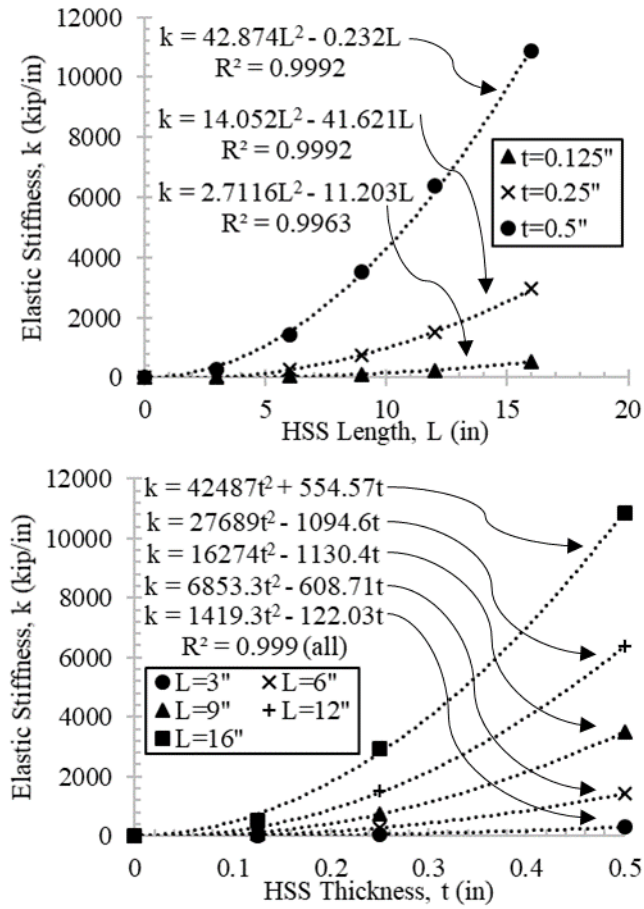


Fig. 9-11: HSS Tube Longitudinal Shearing Elastic Stiffness

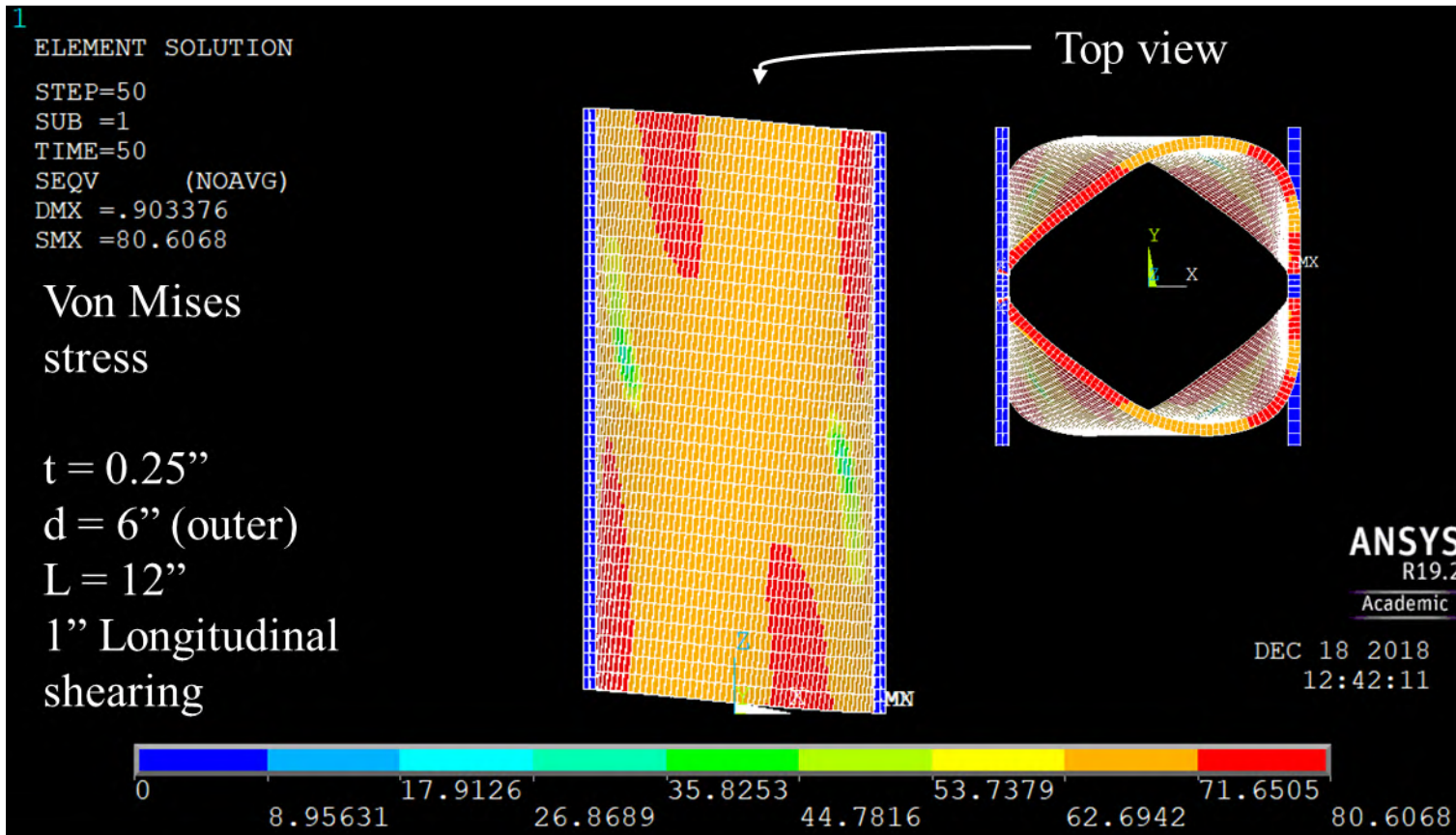


Fig. 9-12: Von Mises Stress Contours for Longitudinally Sheared HSS Tube

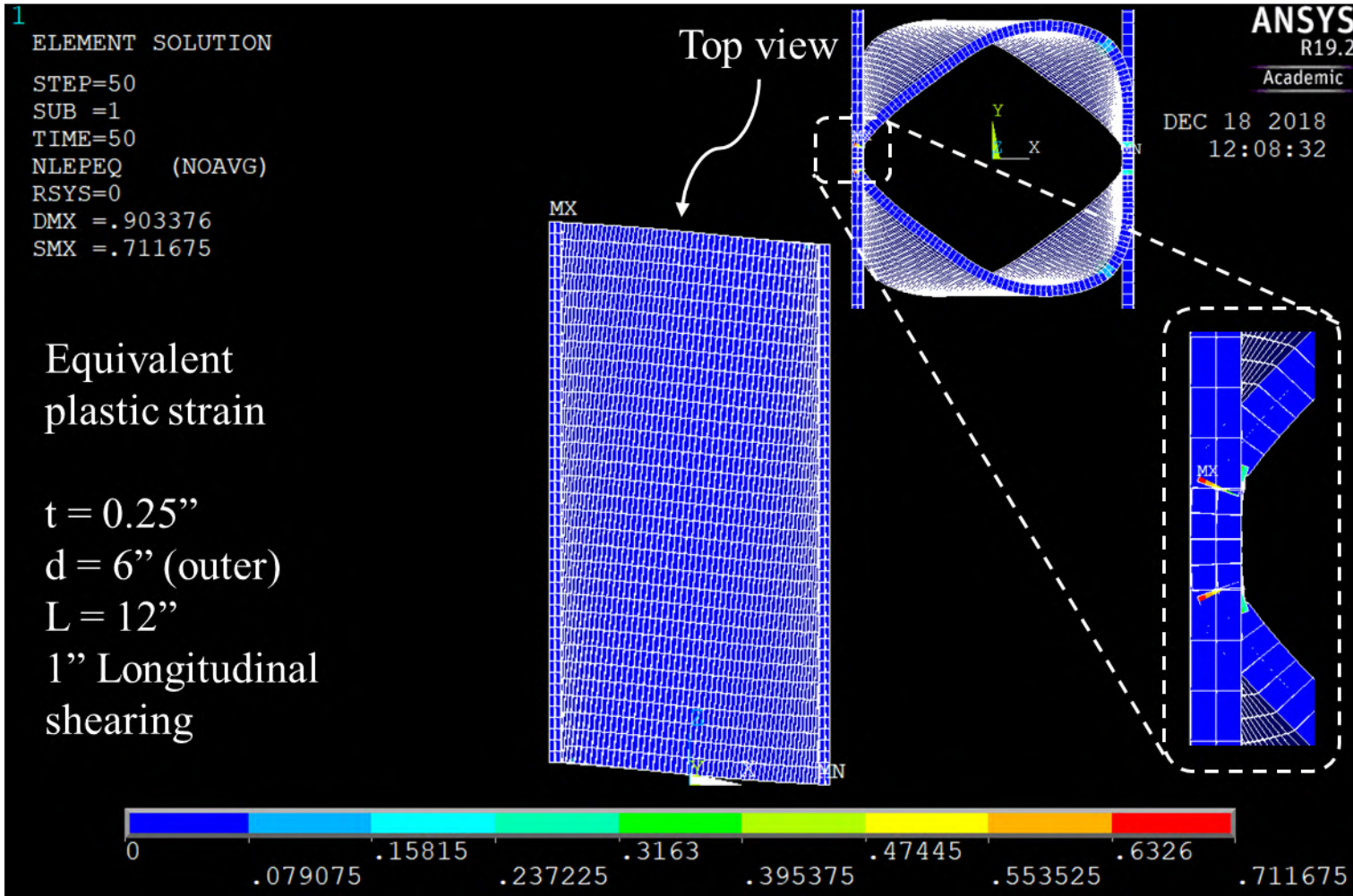


Fig. 9-13: Equivalent Plastic Strain Contours for Longitudinally Sheared HSS Tube

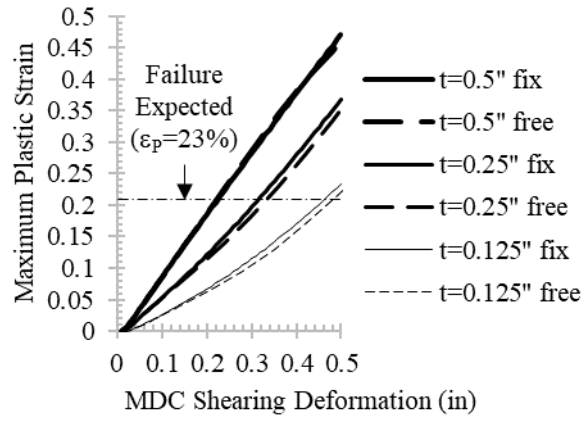


Fig. 9-14: MDC with 12-inch HSS6 Tube Longitudinal Shearing FEA Maximum Plastic Strain

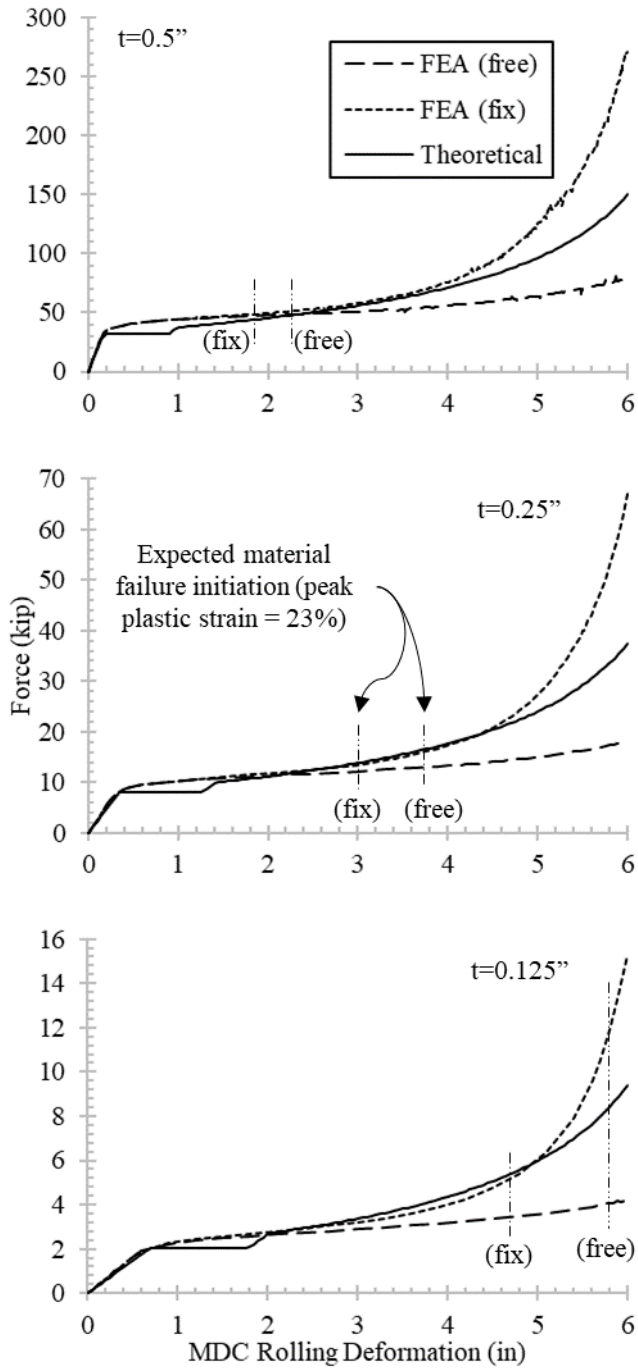


Fig. 9-15: MDC with 12-inch HSS6 Tube Rolling Force-Deformation Behavior

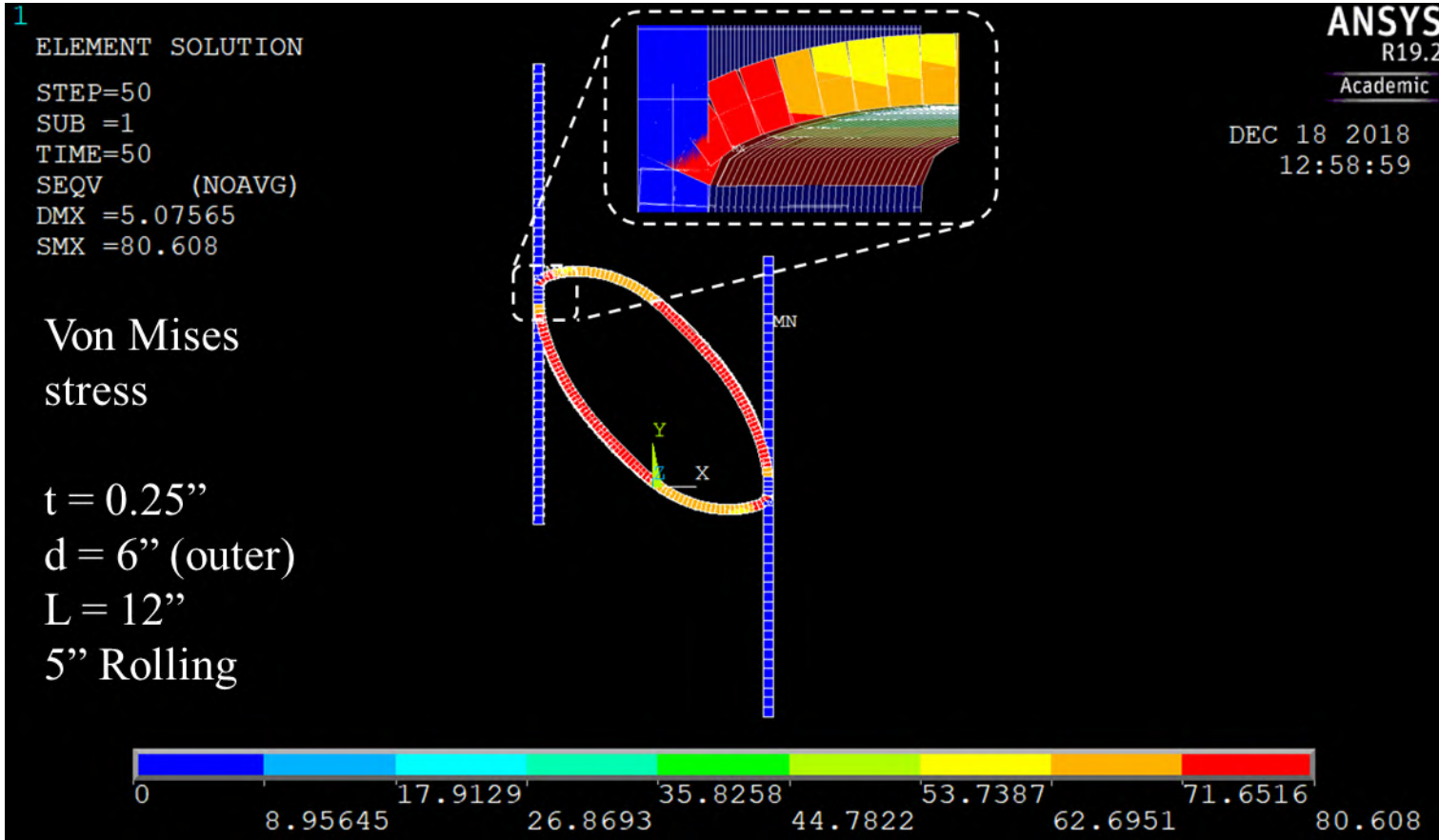


Fig. 9-16: Von Mises Stress Contours for Rolling HSS Tube

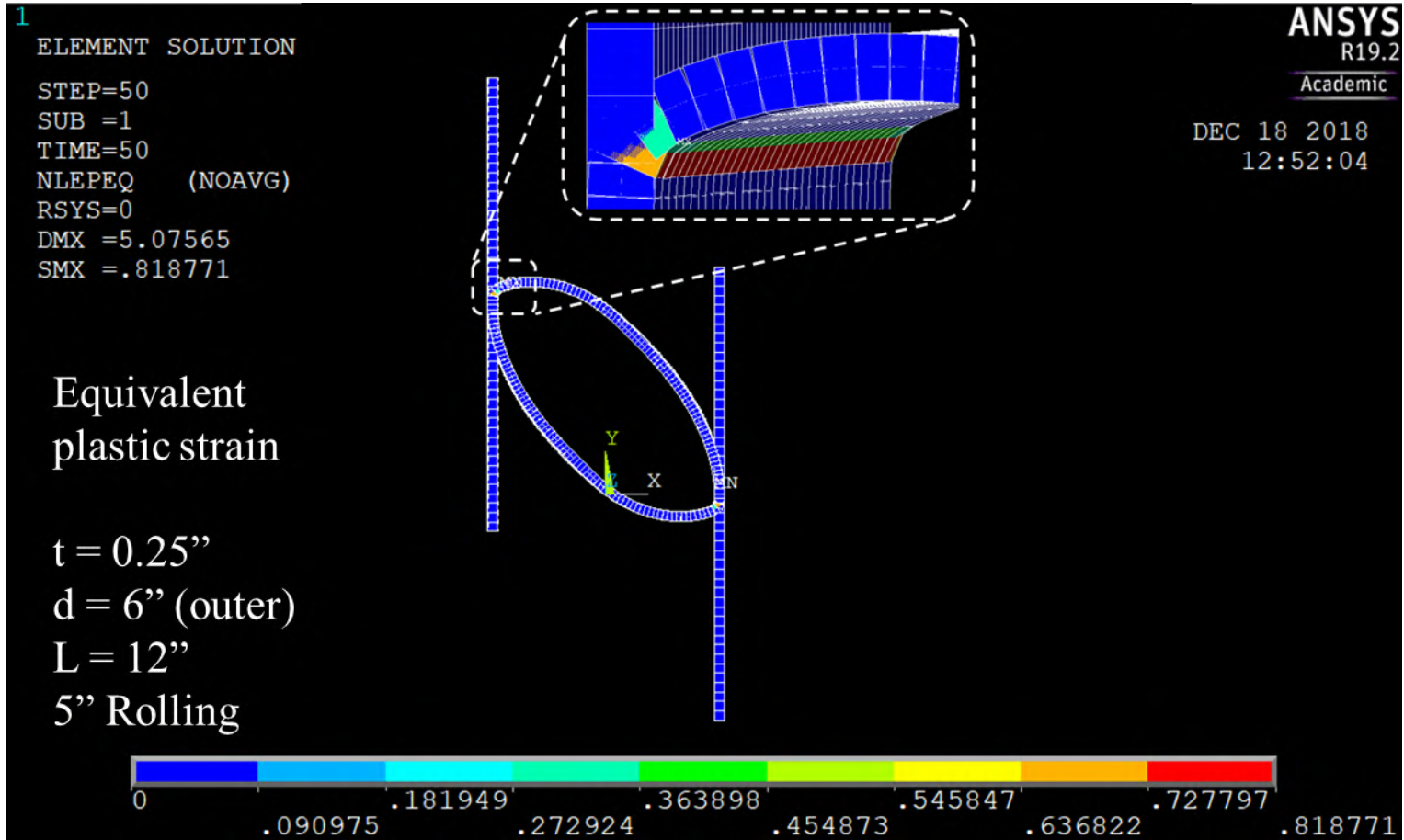


Fig. 9-17: Equivalent Plastic Strain Contours for Rolling HSS Tube

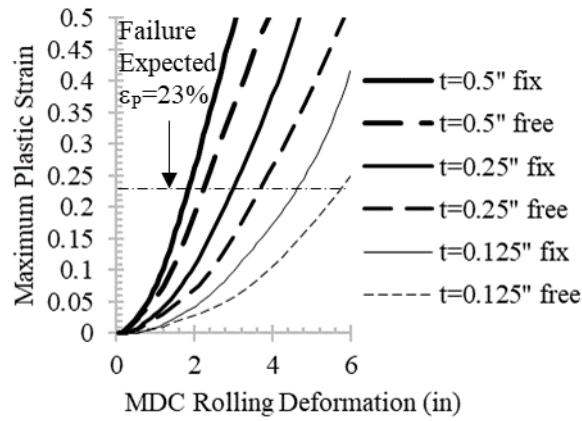


Fig. 9-18: MDC with 12-inch HSS6 Tube Rolling FEA Maximum Plastic Strain

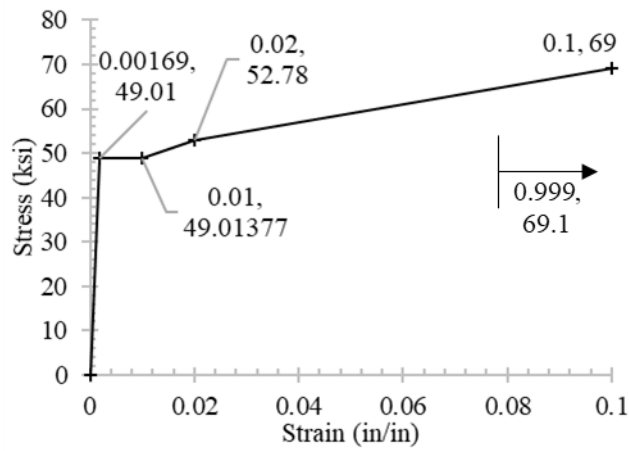


Fig. 9-19: ASTM A36 Steel Material Stress-Strain Model for Flat Plates

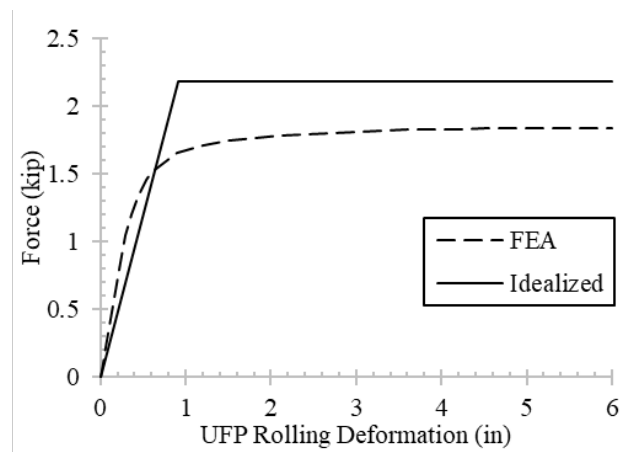


Fig. 9-20: UFP with d=6", b=4", t=0.25", and l_{free}=4" Rolling Force-Deformation Behavior

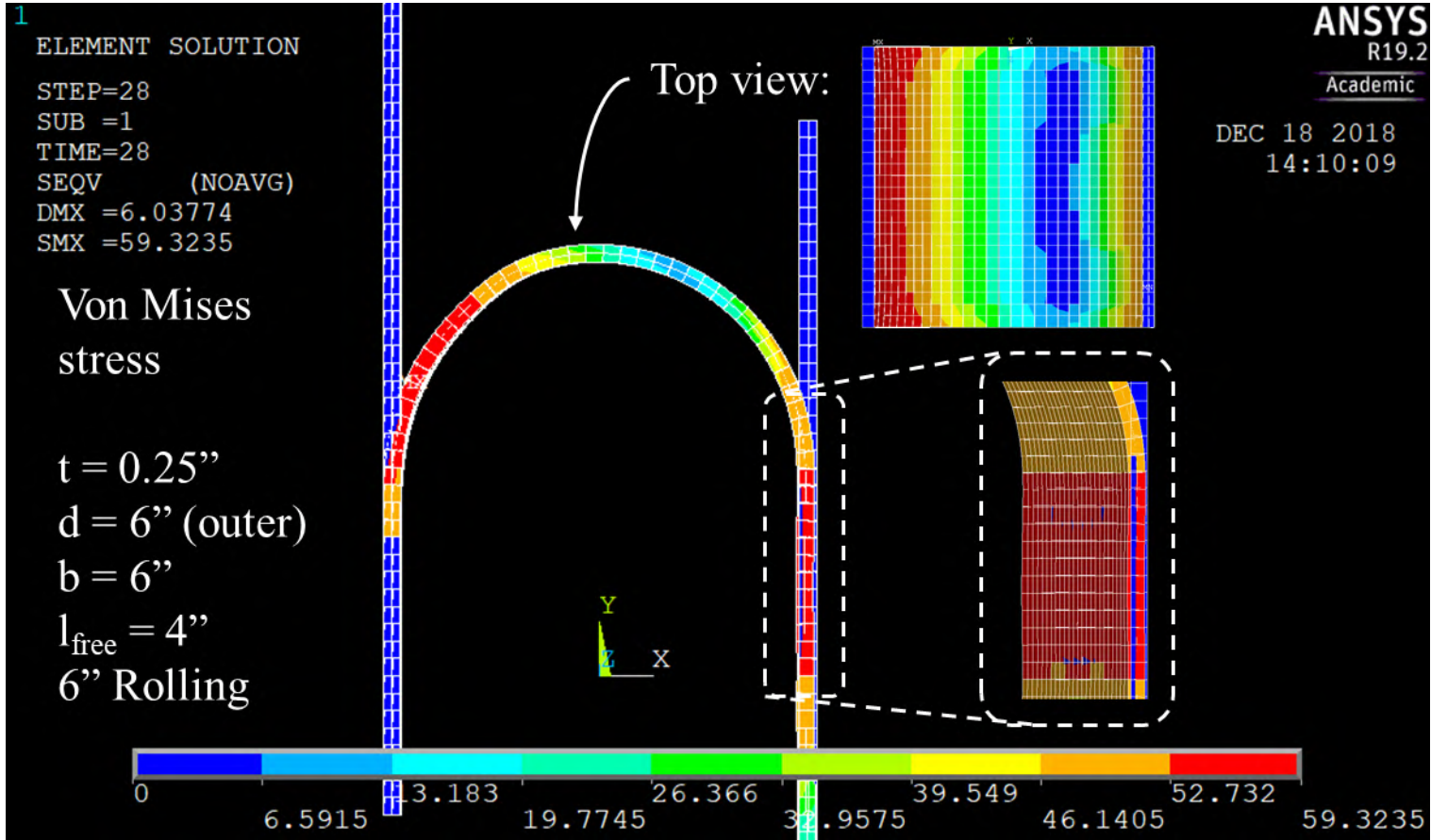


Fig. 9-21: Von Mises Stress Contours for Rolling UFPs

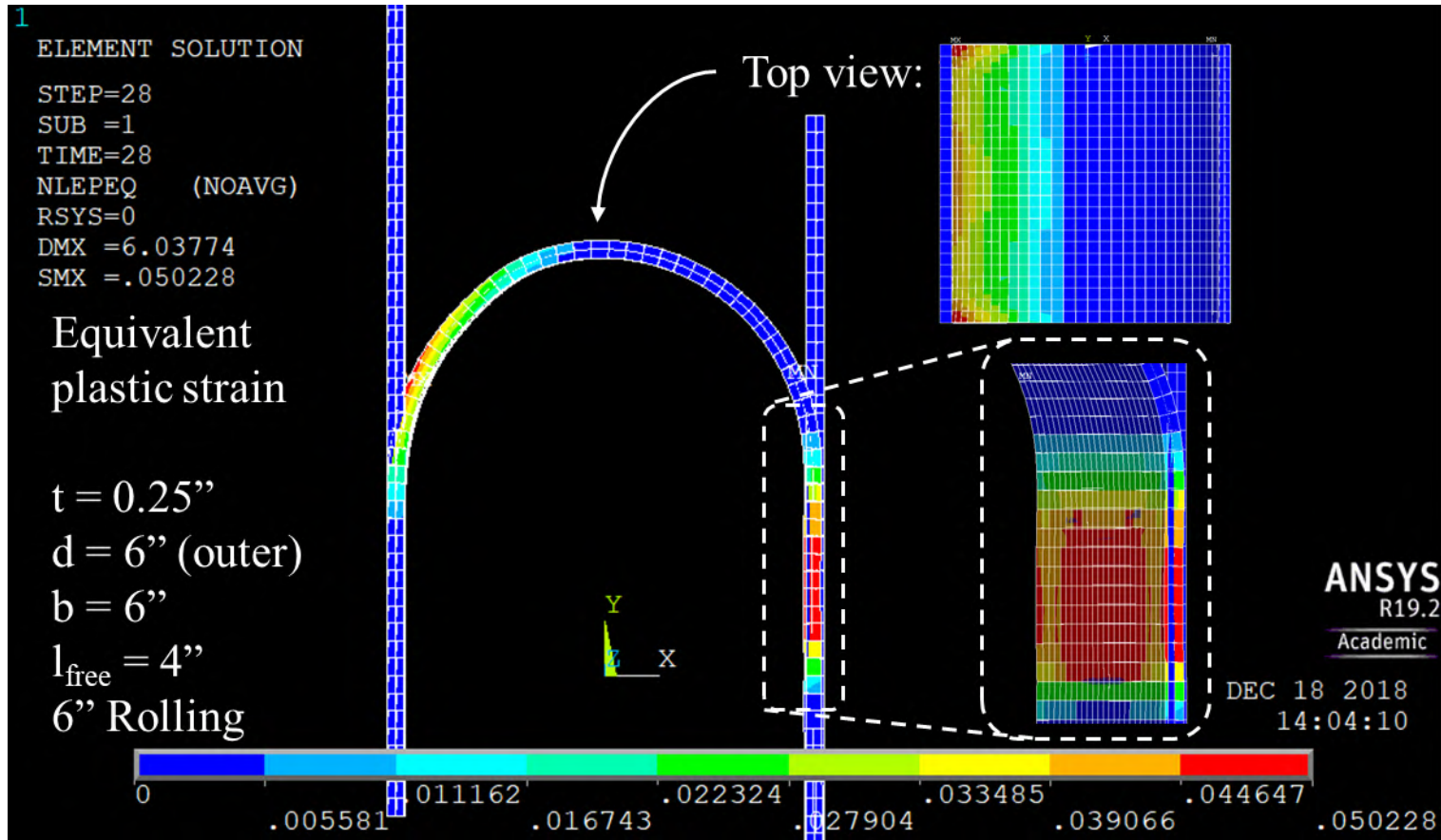


Fig. 9-22: Equivalent Plastic Strain Contours for Rolling UFP

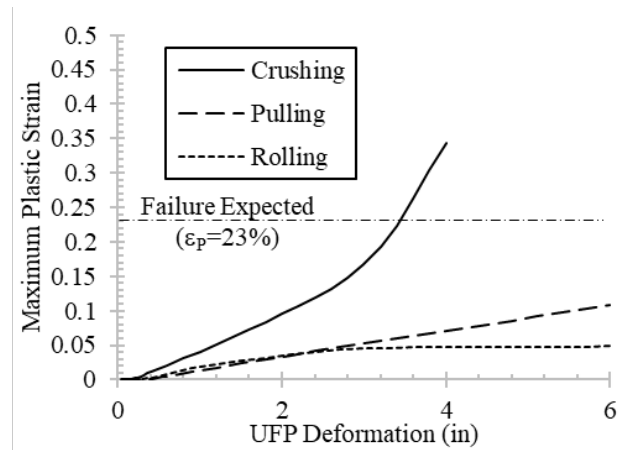


Fig. 9-23: UFP with $d=6''$, $b=4''$, $t=0.25''$, and $l_{free}=4''$ Maximum Plastic Strain

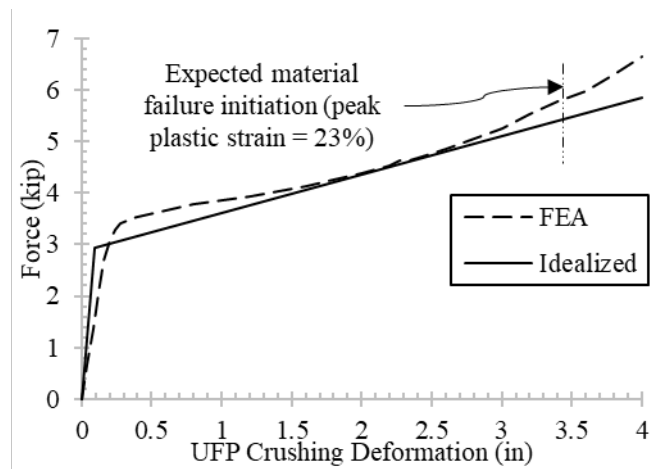


Fig. 9-24: UFP with $d=6''$, $b=4''$, $t=0.25''$, and $l_{free}=4''$ Radial Crushing Force-Deformation Behavior

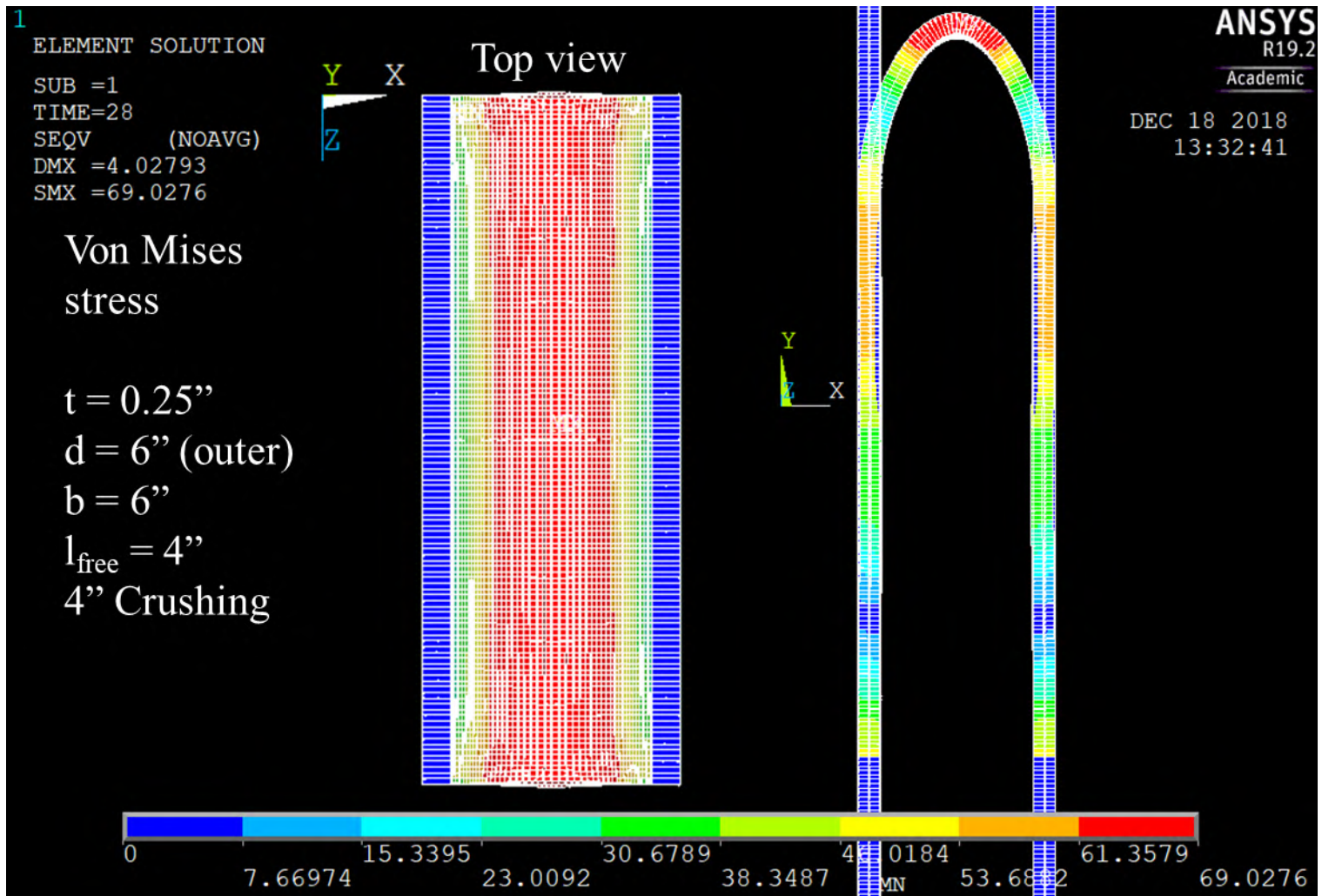


Fig. 9-25: Von Mises Stress Contours for Radially Crushed UFPs

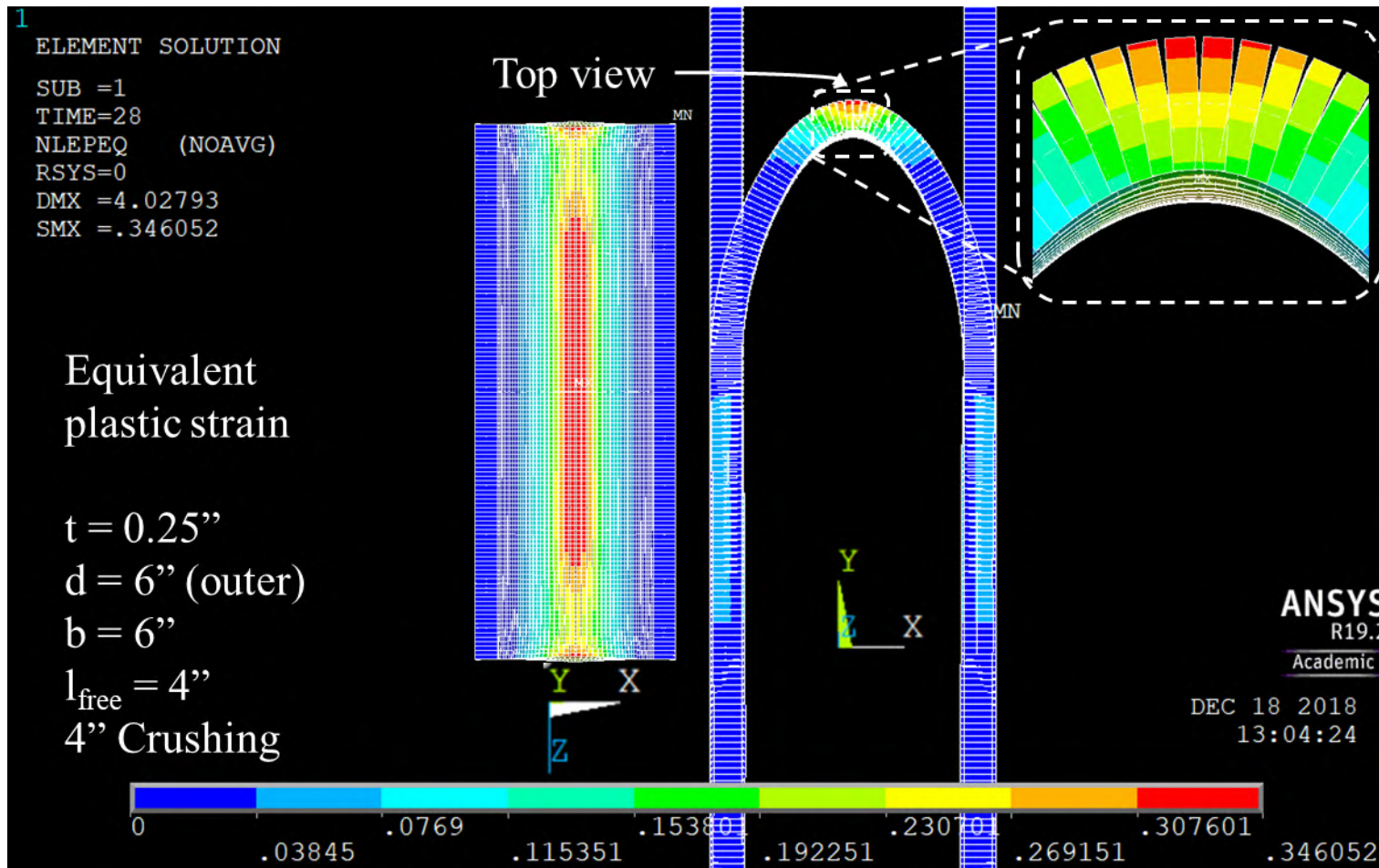


Fig. 9-26: Equivalent Plastic Strain Contours for Radially Crushed UFP

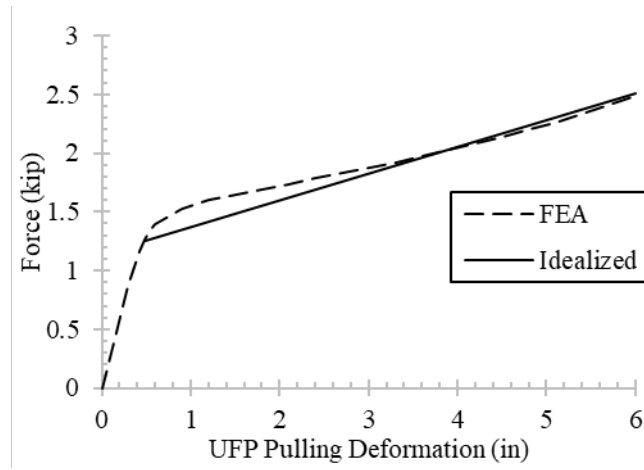


Fig. 9-27: UFP with $d=6''$, $b=4''$, $t=0.25''$, and $l_{free}=4''$ Radial Pulling Force-Deformation Behavior

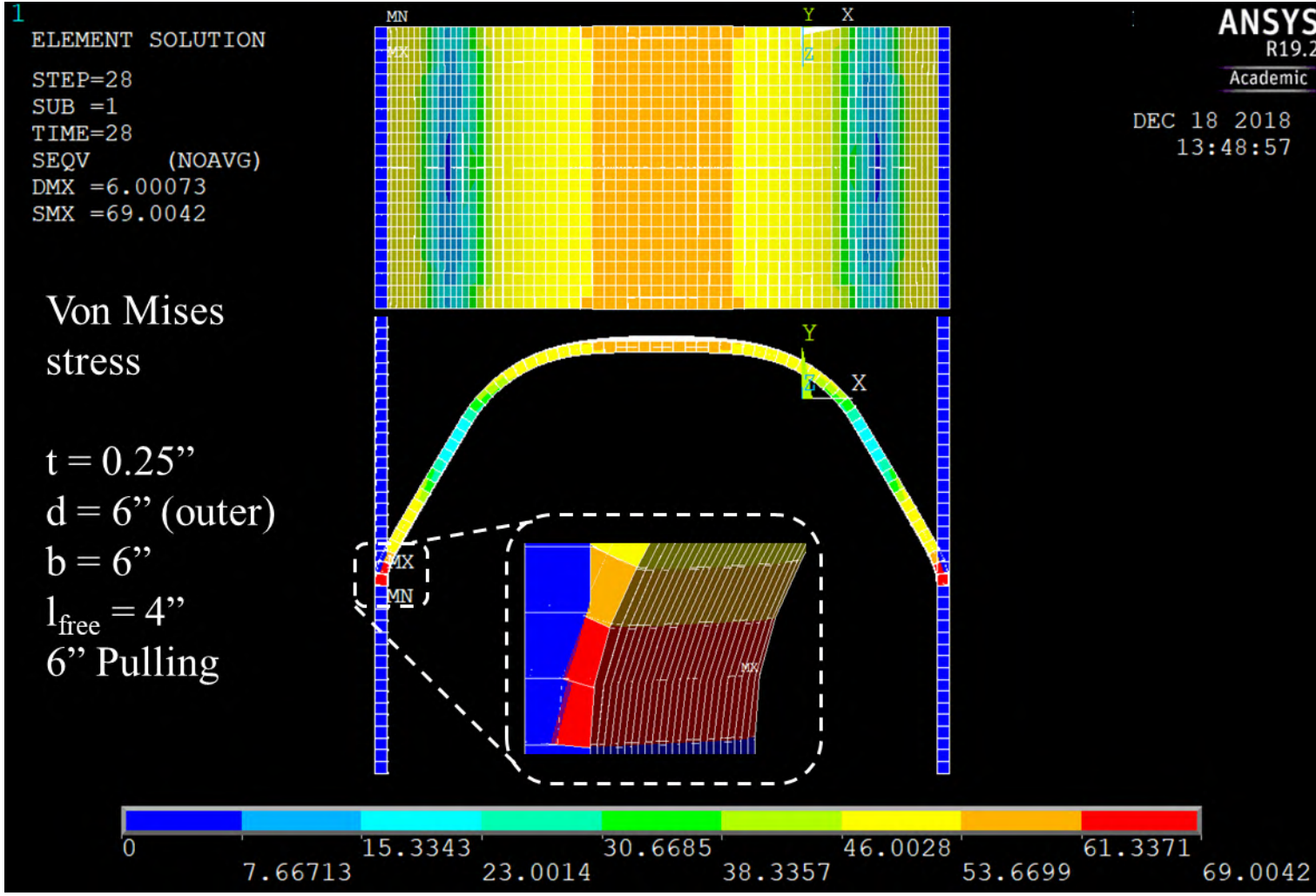


Fig. 9-28: Von Mises Stress Contours for Radially Pulled UFPs

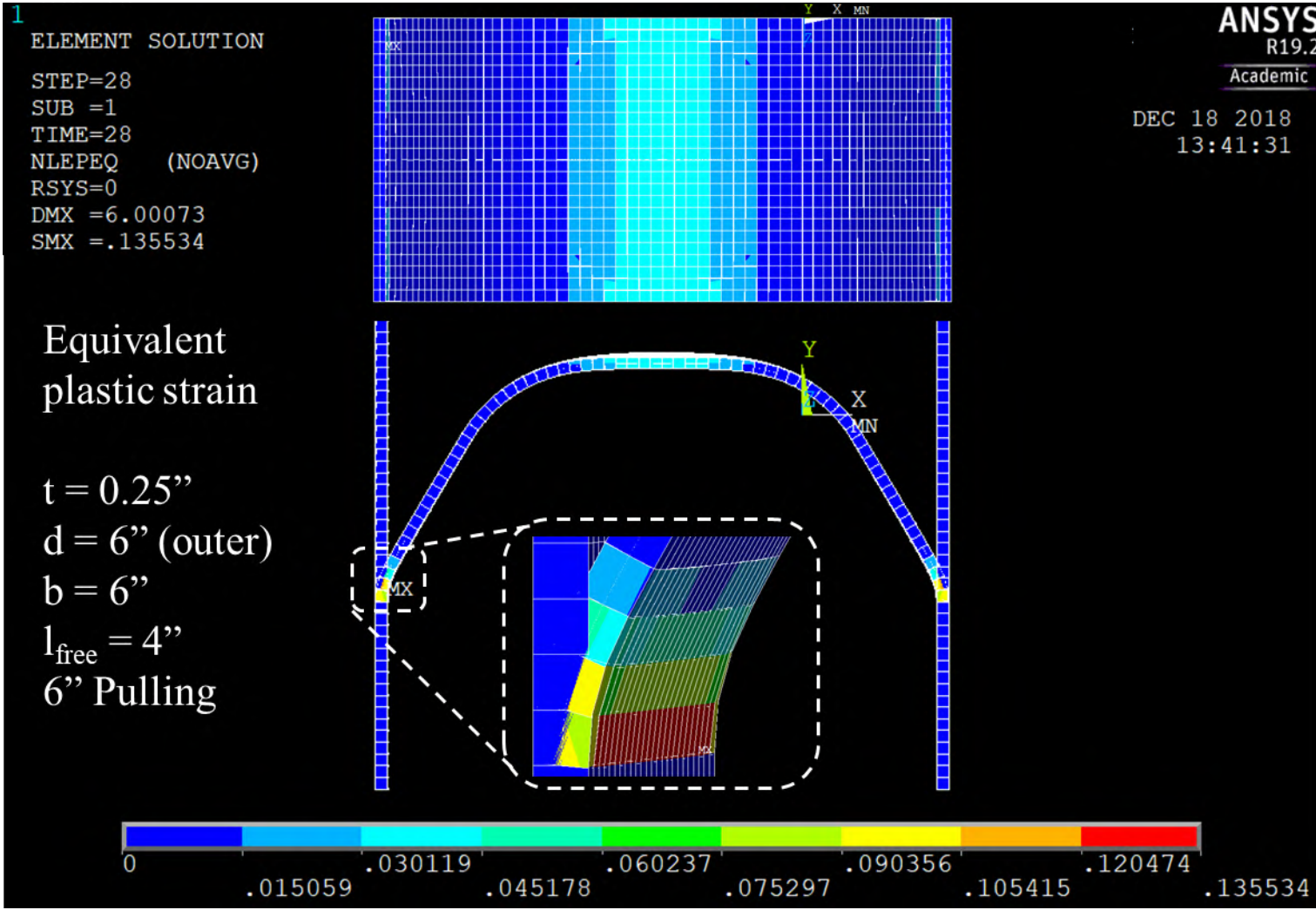


Fig. 9-29: Equivalent Plastic Strain Contours for Radially Pulled UFP

Façade panel discretized into 1-foot segments along height with total panel mass split evenly into nodal masses at each segment end. Identical point loads applied at each nodal panel mass location to approximate a uniformly distributed load.

Each panel segment consists of a nonlinear (force-based) beam-column with three integration points and a discretized fiber cross section as shown to the right.

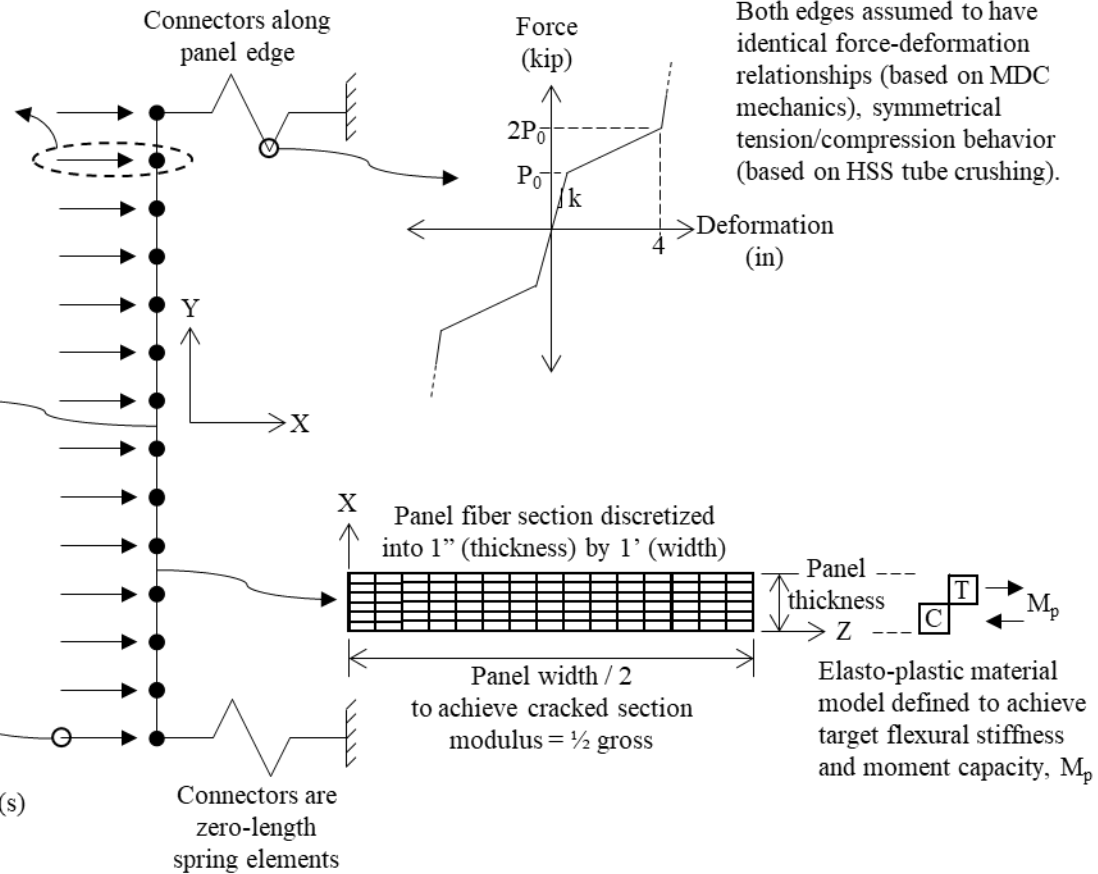
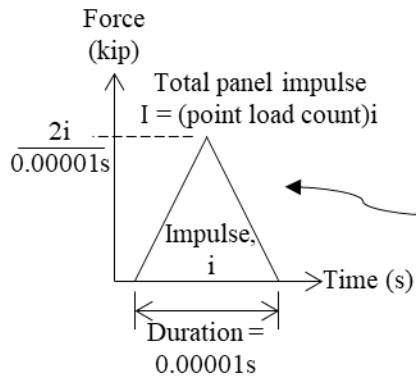


Fig. 9-30: MHFS Finite Element Analysis Model

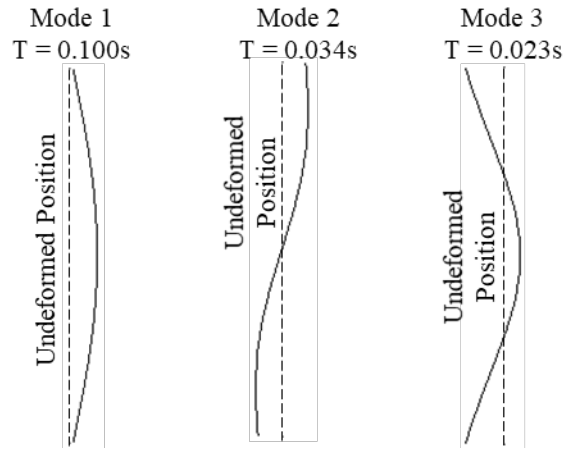


Fig. 9-31: MHFS Finite Element Analysis Model Modal Periods and Shapes

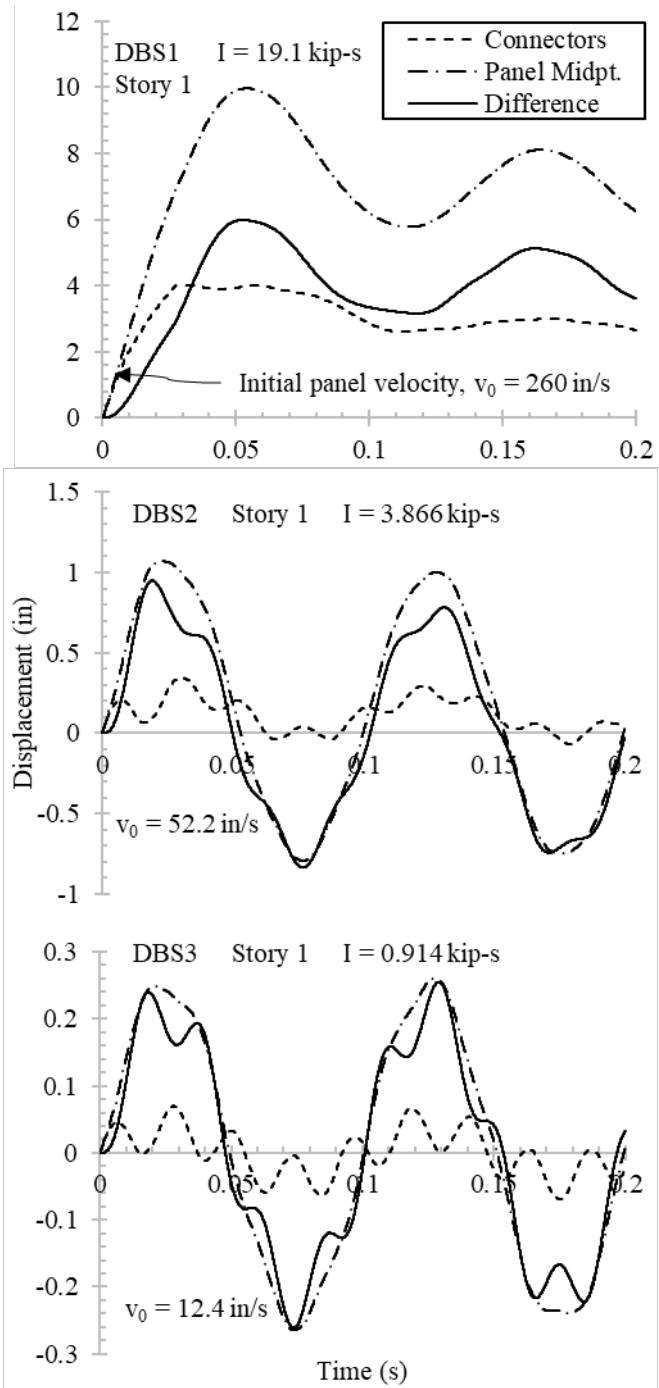
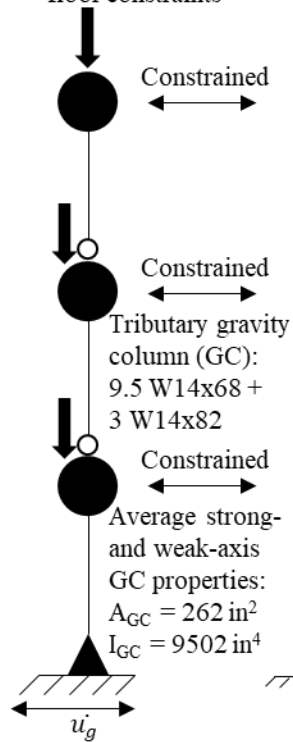


Fig. 9-32: MHFS Air-Blast Response Time Histories

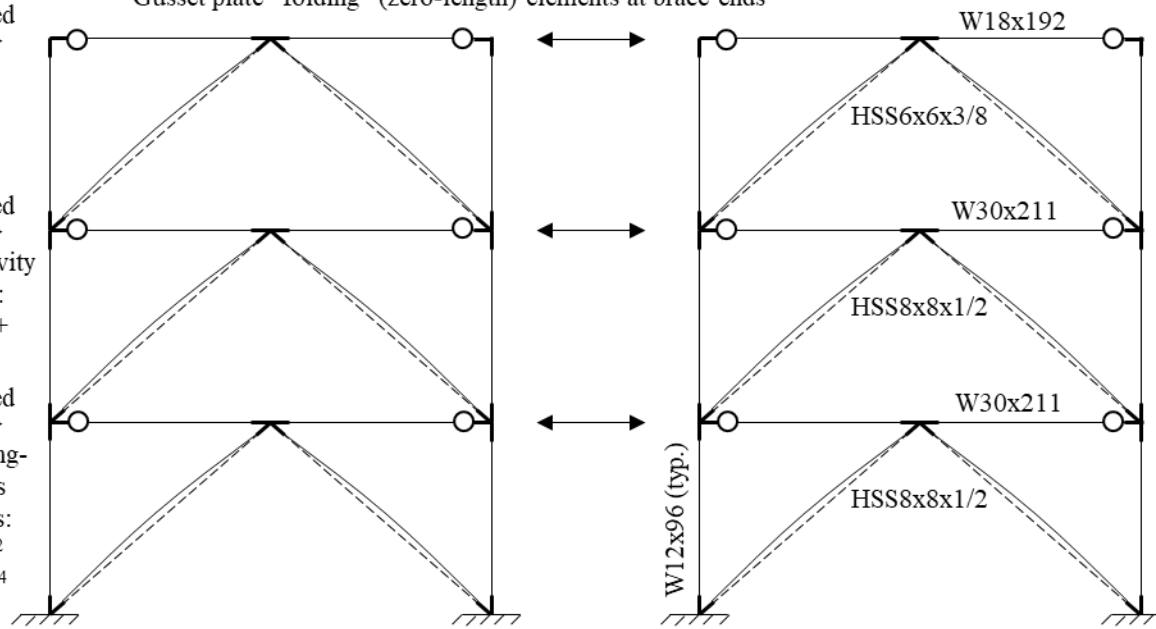
Gravity Column

- Concentrated floor mass
- Vertical P-Δ loads
- Master nodes for lateral floor constraints



Braced Frames

- Two identical frames with floors constrained laterally to gravity column master nodes
- Include rigid zones at beam/column/brace joints based on real frame design gusset plate dimensions
- Nonlinear fiber beam, column, and brace sections over clear spans
- Each brace discretized into 15 elements with initial out-of-straightness to capture buckling response
- Braces include low-cycle fatigue material failure at the section fiber level
- Gusset plate “folding” (zero-length) elements at brace ends

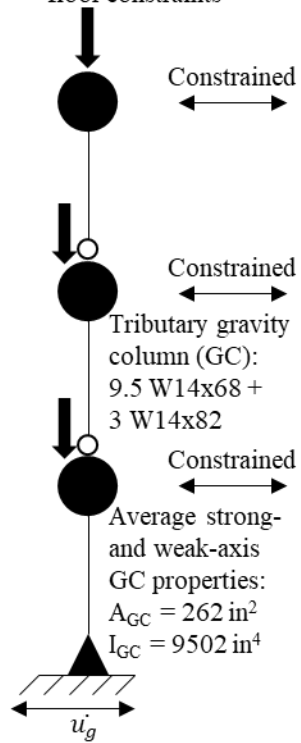


Applied ground acceleration (uniform, unidirectional)

Fig. 9-33: Braced Frame Building Model

Gravity Column

- Concentrated floor mass
- Vertical P-Δ loads
- Master nodes for lateral floor constraints



Moment Frame

- Two identical frames with floors constrained laterally to gravity column master nodes
- Include rigid panel zones at beam/column joints based on member dimensions
- Elastic sections over clear spans with nonlinear rotational springs at member ends

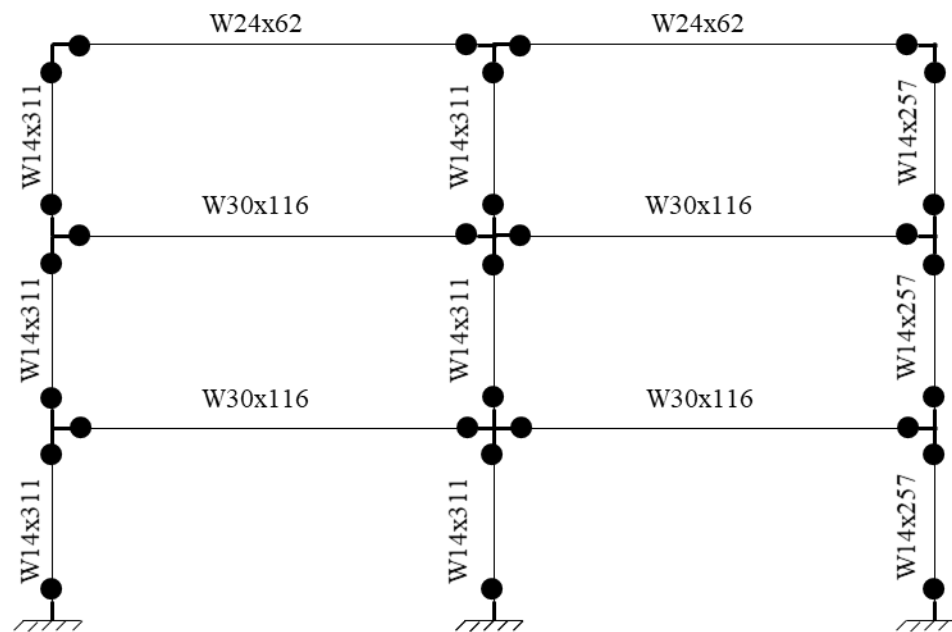


Fig. 9-34: Moment Frame Building Model

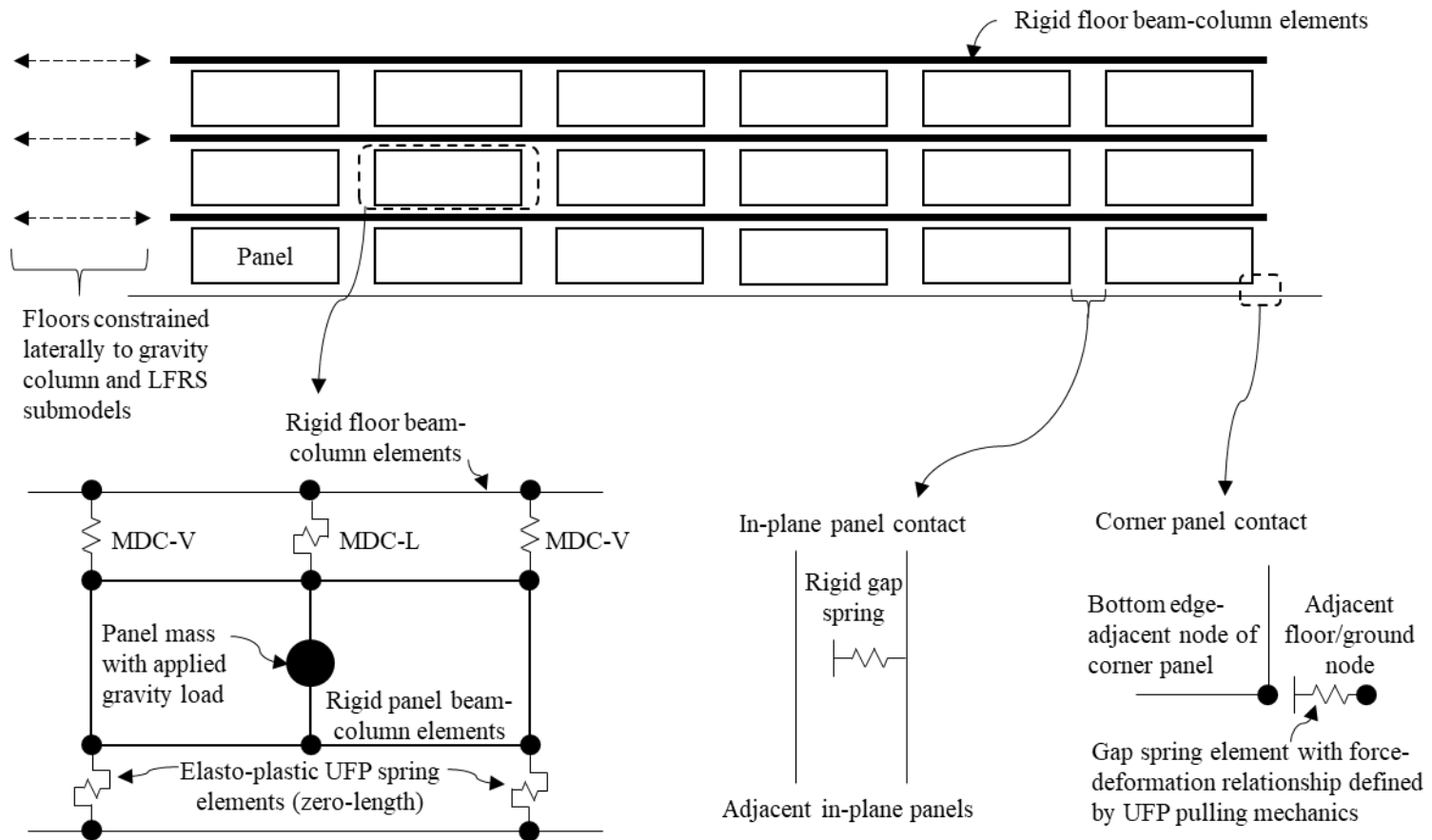


Fig. 9-35: MHFS Seismic Response Interaction Model

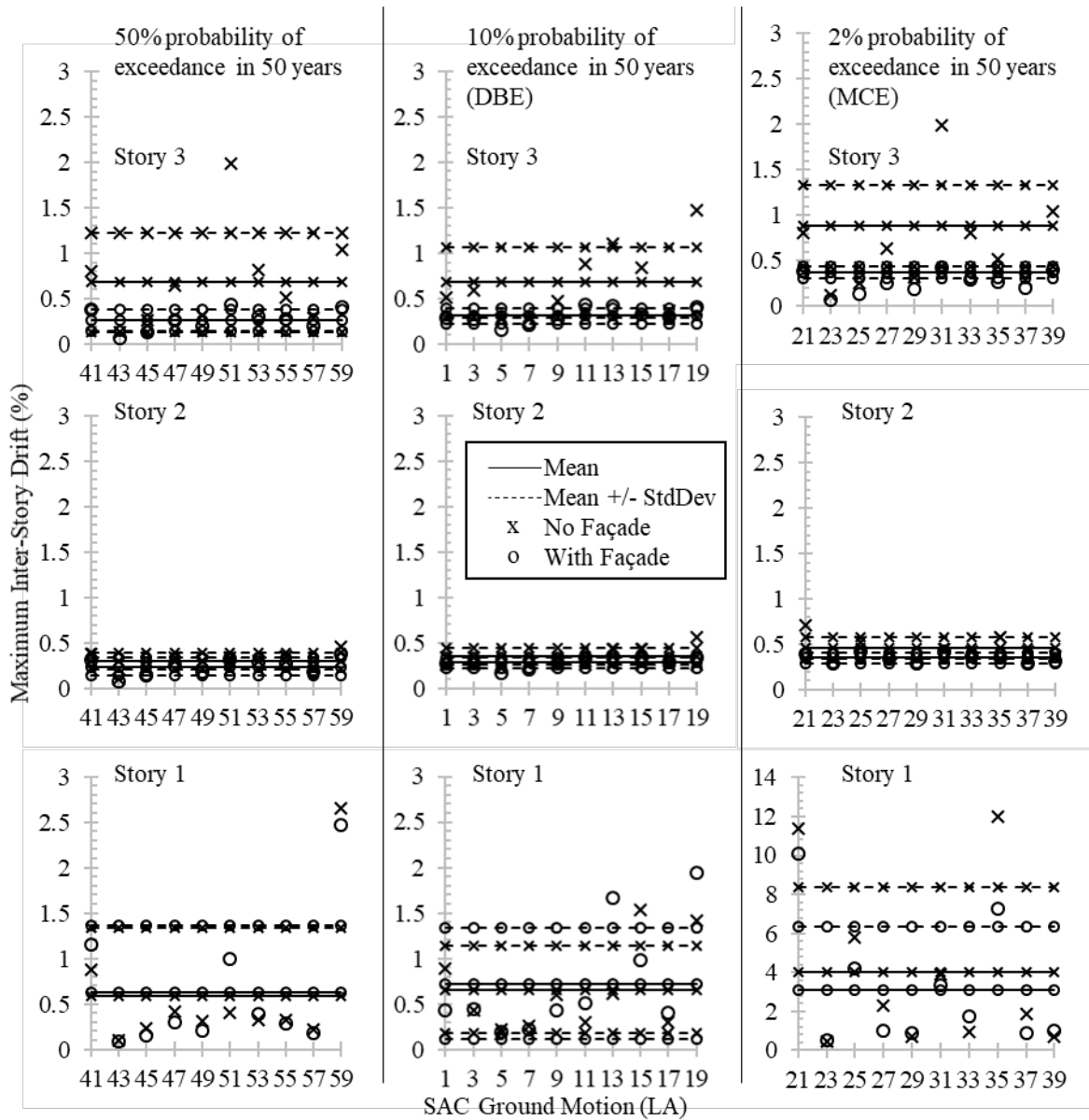


Fig. 9-36: Braced Frame Building with and without MHFS Seismic Inter-Story Drift

Results

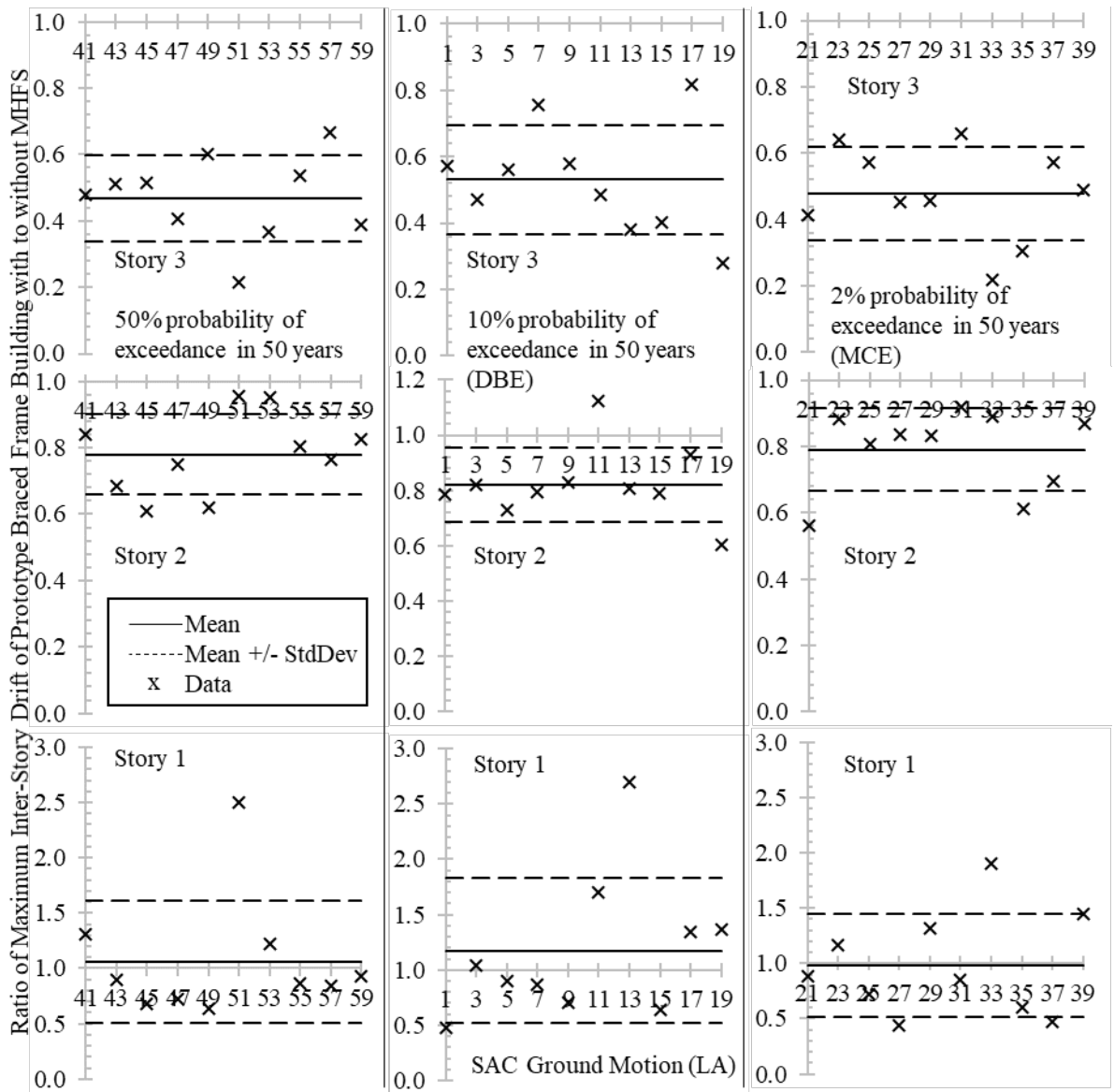


Fig. 9-37: Drift Ratios for Prototype Braced Frame Building with and without MHFS

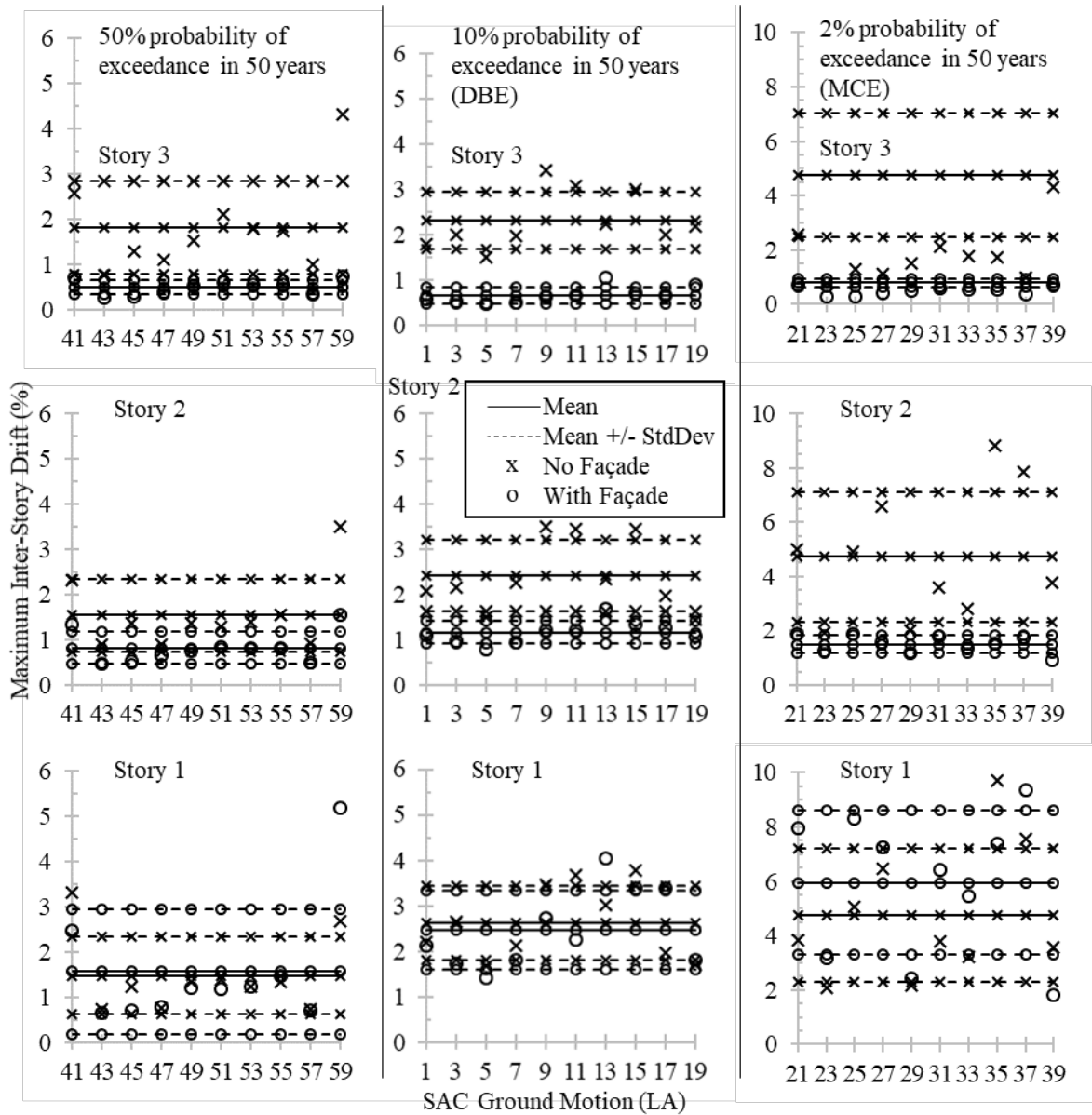


Fig. 9-38: Moment Frame Building with and without MHFS Seismic Inter-Story Drift Results

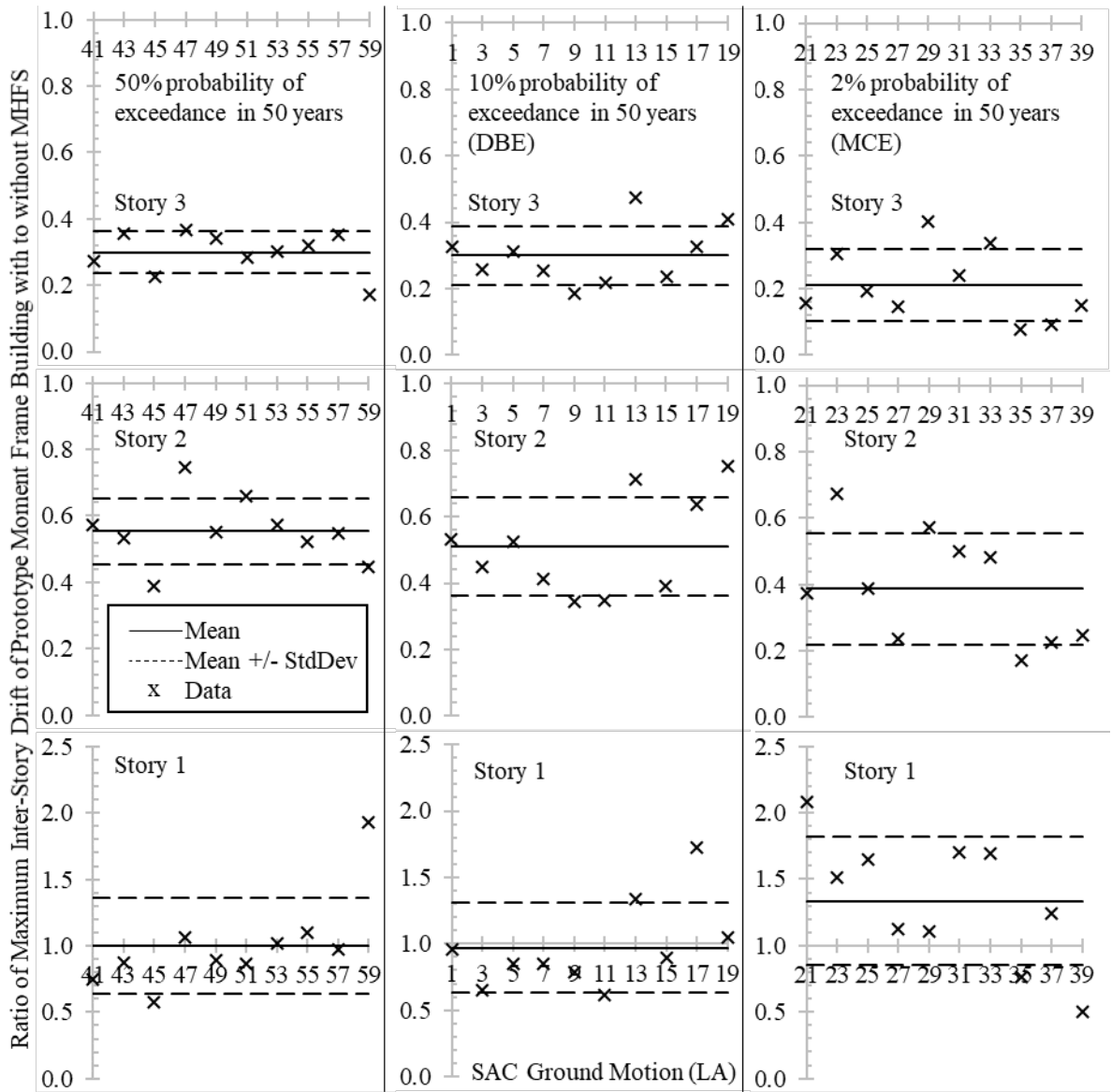


Fig. 9-39: Drift Ratios for Prototype Moment Frame Building with and without MHFS

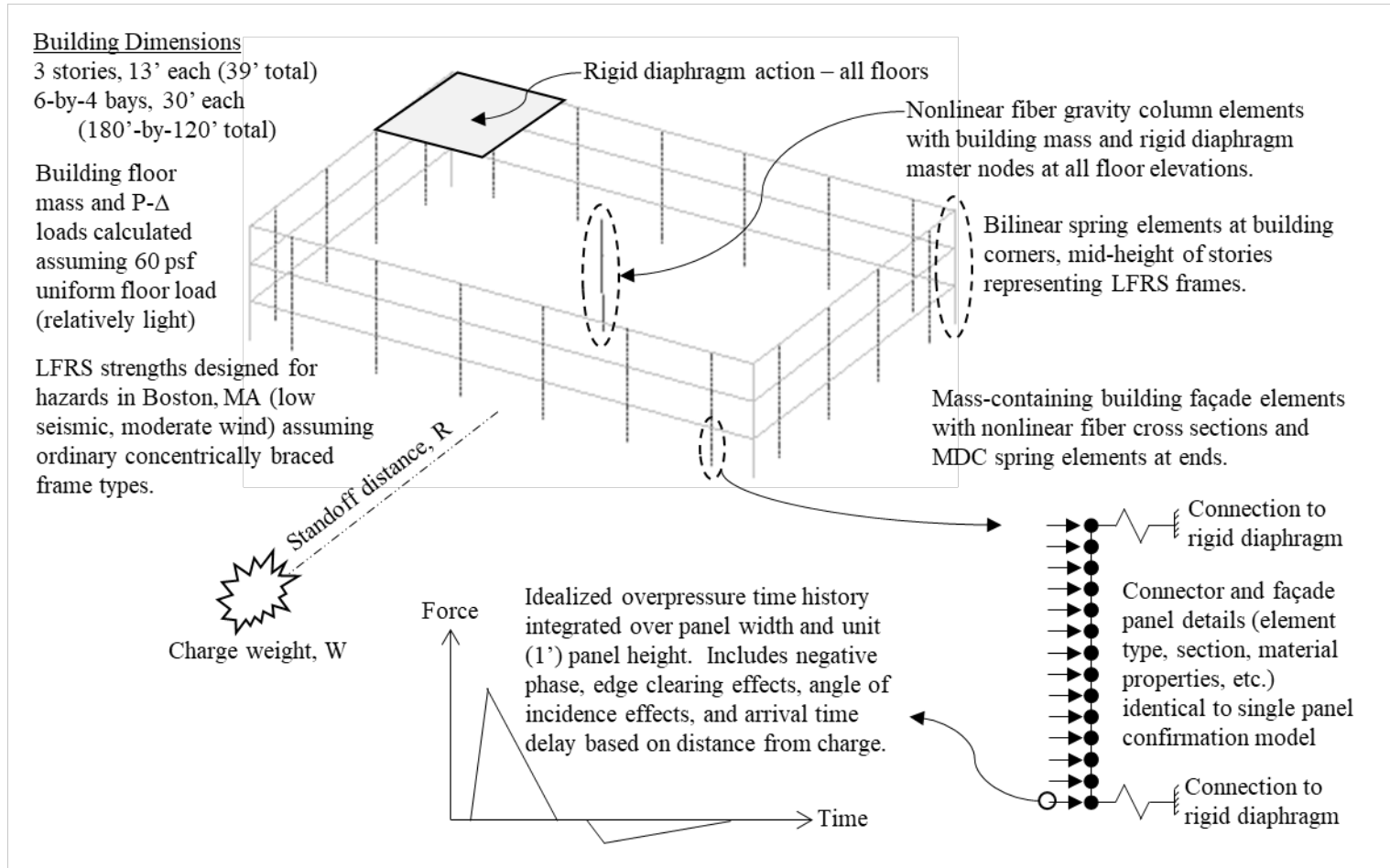


Fig. 9-40: 3D Braced Frame Building with MHFS Model for Air-Blast Response

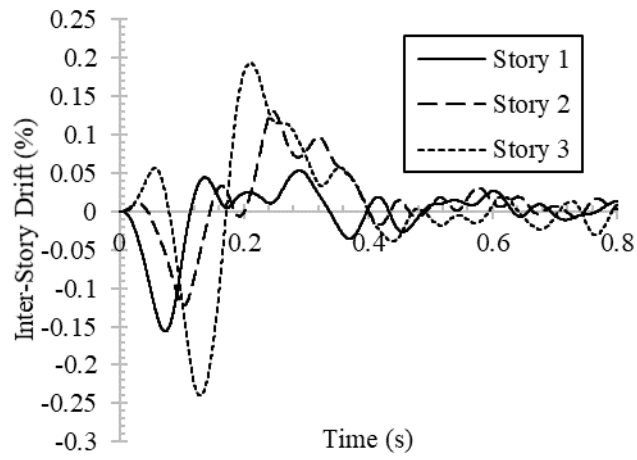


Fig. 9-41: 3D Braced Frame Building with MHFS Design Blast Scenario 1 (DBS1)

Response Time History

10. Summary, Conclusions, and Recommendations for Future Work

10.1. Summary and Conclusions

- Force-deformation behaviors of multi-hazard ductile connectors (MDCs) were developed for each component degrees-of-freedom using principles of elastic and plastic mechanics (including large-deformation geometry effects) to support utilization of these versatile components for improved façade system performance considering both service-level and extreme loading events. Established mechanics for U-shaped flexural plate (UFP) connectors were adopted and expanded upon in this research. While the behaviors of both MDCs and UFPs were primarily developed for their inclusion in the proposed multi-hazard façade system (MHFS), they offer several unique features, which may be advantageous in other structural or mechanical applications, particularly those with multi-degree-of-freedom design considerations and performance objectives.
- A step-by-step design procedure for the MHFS was developed and demonstrated through prototype design examples for various common façade panel types (primarily focused on reinforced concrete panels). This procedure includes traditional façade design considerations—including design-basis wind pressure, seismic inertia and drift effects, and allotments for thermal/moisture expansion/contraction and installation tolerances/adjustments—in addition to the accommodation of contact between adjacent panels at building corners during seismic drift (an issue for traditional façade systems known to cause detachment of panels during seismic events) and the option of including protective design measures for extreme hazards such as tornado effects, air-blast

(explosion) effects, and debris impact. HSS6 sections (HSS6x0.25 in particular) were found to be effective for the primary ductile element of the MDCs. The necessary out-of-plane (OP) flexural capacity of the façade panel is determined as a function of hardened ductile connector strength to promote a desirable sequence of damage and ensure the defined performance objectives are met.

- Quasi-static experimental tests were performed to verify the behavior of four design-critical MDC behaviors, including: radial crushing, radial pulling, longitudinal shearing, and rolling of the HSS tube. The radial crushing test included application of the tributary façade panel weight while imposing a large inward OP deformation and rotation to simulate demands during a design-basis air-blast event. Successful completion of this testing protocol confirmed the MDCs' capacity to provide the desired performance during extreme OP loading while maintaining support of the panel. Radial pulling and longitudinal shearing test specimens reached their target deformation and force capacities, respectively, and generally confirmed the theoretical and analytical models of these behaviors. The rolling test(s) showed that the MDCs were not capable of achieving the target deformation for accommodating in-plane seismic drifts across a façade panel—prompting the adoption of UFPs into the MHFS design methodology—however these tests were valuable for confirming theoretical and analytical models of this behavior.
- Potential ramifications for design of a building's primary lateral force resisting system (LFRS) for extreme hazardous loads which are incident upon its proportionally-hardened façade system (e.g. air-blast, debris impact, etc.) were investigated, however no justification was found for any consideration of such issues during design;

adherence to modern LFRS design practices—particularly those developed for seismic hazards—generally ensures adequate building performance with the inclusion of the MHFS. This supports a “decoupled” approach to design of the LFRS and MHFS, however some analysis and potential design iteration of the LFRS may be necessary based on seismic performance considering the inclusion of the MHFS (discussed in the final bullet point below).

- Finite element analysis (FEA) models of the MDCs (and, eventually, UFPs) were developed in ANSYS Mechanical ADPL to verify theoretical expressions and experimental testing results. These models utilized shell elements (ANSYS SHELL181) and material stress-strain models including kinematic and isotropic hardening based on tension coupon test data. A mesh refinement convergence study was conducted to ensure accuracy of the results. Comparison with experimental test results were generally favorable for all specimens. Some differences were observed between FEA, experimental, and theoretical mechanics developed in this research, primarily due to simplifying assumptions made for design in the theoretical expressions (e.g. neglect of HSS tube outer vs. centerline diameter, effects of restraint due to welded regions, etc.). All differences between FEA and theoretical behaviors were conservative for the purposes of design.
- MHFS behavior and façade-building frame interactions were examined using a set of FEA models developed in OpenSees. A single MHFS panel model was subjected to a set of (idealized) air-blast impulsive loadings, and the response of the system assumed for design was found to be accurate, if somewhat conservative. A full 3D prototype building model with MHFS was subjected to simulated blast loading. These analyses

indicated the prototype MHFS design achieved the performance objectives with some conservatism possibly due (at least in part) to idealizations of the design-basis air-blast loads made for simplicity in design (e.g. neglect of negative phase loading, higher mode participation, staggered arrival times, etc.). These analyses also showed limited yielding of the LFRS—despite the light floor mass and relatively weak prototype LFRS design (i.e. essentially a worst-case scenario for blast performance)—indicating that overall damage to the building is likely much less than expected during a moderate-intensity seismic event provided the integrity of the façade system is maintained to prevent infiltration of the air-blast pressure wave and debris (intended performance of MHFS). The proposed MHFS design methodology is believed to provide a resilient building envelope for any credible hazard based on these results.

- Additional OpenSees models were constructed to examine the effects of MHFS inclusion on seismic building performance for both braced and moment frame LFRS prototype buildings subjected to frequent, design-basis, and maximum-considered earthquake ground motion suites. The added stiffness of the MHFS in-parallel with the LFRS decreased modal periods in the prototype building models, with a greater effect observed for the moment frame building due to its lower stiffness relative to the braced frame LFRS. Peak drifts decreased in the upper (non-ground-level) building stories in nearly all cases, while first-story peak drifts—which were often the maximum of all peak story drifts—tended to increase somewhat. This effect is likely due to the shift in modal periods exposing the structure to different ground motion frequency content (often with higher energy), as well as the added inter-story shear strength due to MHFS changing the overall distribution of inter-story shear strength over the building height.

Based on these results, it is not yet known if the overall impact of the MHFS on seismic building performance is net-beneficial or detrimental, however these observations suggest analysis of façade-frame interaction during seismic events is likely necessary in any potential application of the proposed MHFS.

10.2. Recommendations for Future Work

During the course of this research, the following issues, which warrant additional investigation to improve or expand upon the findings presented in this report, were identified:

- A probabilistic seismic performance evaluation of prototype buildings with and without MHFS is needed to assess the effects of the MHFS considering this hazard, as the peak drift results alone are somewhat ambiguous. In a similar vein, some quantification of the change to the rate of functional recovery afforded by the inclusion of replaceable MHFS connectors relative to repair of traditional façade systems would help with cost-benefit analysis of the proposed design approach. Arup’s Resilience-based Earthquake Design Initiative (REDi) Rating System, and/or the FEMA P-58 Performance Assessment Calculation Tool (PACT) are potentially suitable for this work.
- Façade systems, which use cold-formed steel stud backing walls — including brick veneer, and exterior insulation and finish systems (EIFS)—pose challenges, which were not considered in this formulation of the proposed MHFS, which focused primarily on reinforced concrete panel types. Stud wall-backed systems involve different load paths and means of accommodating in-plane deformations, which would likely require a completely different connection scheme to those, discussed in this

- study. The MDCs and/or UFPs may still be useful in developing a MHFS using these panel types, however additional work is needed to determine an appropriate approach.
- Additional experimental testing could be performed to verify some of the system-level behaviors which were only confirmed analytically in this study, including:
 - Air-blast testing on a full-scale MHFS design
 - Seismic deformation compatibility testing for various façade system types, including panel(s) and connectors attached to spandrel beams, which can be displacement-controlled in both the lateral in- and out-of-plane directions.
 - Preliminary efforts to propose a simplified approach to design for debris impact panel loading attempted to simplify the dynamic system similar to the design approach taken for air-blast impulsive demands. This proved inadequate as analyses revealed more complex behavior of the system subject to impact loading. The proposed MHFS is still effective for mitigating damage due to impact loading; however, neither an idealized, closed-form impact design equation, nor any parametric impact design aids were produced in this research. Therefore, some trial-and-error with FEA modeling may be necessary to achieve a desired impact missile performance objective as a final step in the MHFS design methodology. Parameters believed to control the behaviors could likely be studied to improve this approach; these parameters include (but may not be limited to):
 - Panel and impact missile dimensions (ratio of impacted and total areas)
 - Impact location
 - Panel and missile masses (or the ratio thereof)
 - Missile impact velocity

- Deformation and/or energy dissipating capacity of a potentially deformable missile (e.g. vehicle)
- The MHFS may provide supplemental resistance against progressive collapse of perimeter frames by utilizing the strength and stiffness of the vertically-oriented MDC-Vs to transfer vertical forces through the façade system and away from the potential collapse zone in a column loss scenario. Although this mechanism is not explicitly designed for and should not be solely relied upon, it may provide an unintended benefit which a preliminary analysis indicates could increase the collapse capacity by as much as 20%. A somewhat atypical panel placement—where panels are centered laterally on frame columns rather than over the clear spans—is required to reap this benefit, and reinforced concrete façade panels are likely the only type capable of transferring the required shear forces.
- Traditional design for air-blast effects—particularly for deliberate, targeted explosive attacks—relies upon determining a design-basis scenario through a qualitative threat assessment procedure (per the U.S. Department of Defense procedures). The probability of the design-basis (or any) event occurring cannot be known as the occurrence of such an event is dependent on human action; this marks a fundamental difference between traditional hazards (e.g. seismic or extreme wind) resulting from naturally-occurring phenomena which can be modeled probabilistically. However, assuming a credible threat exists, probabilistic models can be assigned to the design-critical parameters—namely, charge weight and target standoff distance—to determine relative probabilities to various blast scenarios. These probabilities, coupled with a façade panel air-blast design impulse data set, can be used to inform design-basis

demands for blast loading based on, say, the panel impulse with 5% probability of exceedance, similar to how design-basis seismic and wind events are chosen. This approach would allow for characterization of blast hazards via a more quantitative paradigm. Preliminary work suggests that such a model would have the added benefit of producing design-basis demands for buildings adjacent to targeted buildings, which might be subjected to collateral damage despite not being explicitly targeted for attack. Such values can be used to determine appropriate proportional hardening of buildings near potential targets to improve public safety and reduce potential losses resulting from an explosive attack.

11. References

- ACI. (2011). *Building Code Requirements for Structural Concrete (ACI 318M-11) and Commentary*. Farmington Hills, MI: American Concrete Institute.
- AISC. (2010a). *Seismic Provisions for Structural Steel Buildings*. Chicago, IL: American Institute of Steel Construction.
- AISC. (2010b). *Specification for Structural Steel Buildings*. Chicago, IL: American Institute of Steel Construction.
- AISC. (2011). “Steel Construction Manual Thirteenth Edition.” American Institute of Steel Construction, Chicago, IL.
- Alavi Nia, A., & Parsapour, M. (2014). “Comparative analysis of energy absorption capacity of simple and multi-cell thin-walled tubes with triangular, square, hexagonal and octagonal sections.” *Thin-Walled Structures*, 74, 155–165.
- Alghamdi, A. (2001). “Collapsible impact energy absorbers: An overview.” *Thin-Walled Structures*, 39(2), 189–213.
- American Society for Testing and Materials. (2012). “A370-12: Standard Test Methods and Definitions for Mechanical Testing of Steel Products.” American Society for Testing and Materials, West Conshohocken, PA.
- ANSYS Inc. (2016). “Mechanical APDL Documentation.” ANSYS, Inc., Canonsburg, PA.
- Appelbaum, A. (2013). *Structural Assessment of Multiple Story Steel Buildings Subjected to Blast Loads*. Master’s thesis: OhioLINK ETD.
- ASCE (2013). *Minimum Design Loads for Buildings and Other Structures*. Reston, VA: American Society of Civil Engineers.

- Baird, A. C. (2014). Seismic Performance of Precast Concrete Cladding Systems. PhD. Dissertation: University of Canterbury, Christchurch, New Zealand.
- Chopra, A. K. (2011). *Dynamics of structures: Theory and applications to earthquake engineering*. 4th Edition. Upper Saddle River, N.J.: Pearson/Prentice Hall.
- Eyvazian, A., K. Habibi, M., Hamouda, A. M., & Hedayati, R. (2014). “Axial Crushing Behavior and Energy Absorption Efficiency of Corrugated Tubes.” *Materials & Design*, 54, 1028-1038.
- Fadden, M. F. (2013). “Cyclic Bending Behavior of Hollow Structural Sections and their Application in Seismic Moment Frame Systems.” University of Michigan, Ann Arbor, MI.
- Federal Emergency Management Agency (FEMA). (2000). State of the Art Report on Systems Performance of Steel Moment Frames Subject to Earthquake Ground Shaking. FEMA-355C. FEMA, Washington, DC.
- FEMA. (2003). “FEMA 427: Primer for Design of Commercial Buildings to Mitigate Terrorist Attacks.” Federal Emergency Management Agency, Washington, DC.
- FEMA, ATC. (2012). Seismic Performance Assessment of Buildings. FEMA P-58-1. Applied Technology Council, Redwood City, CA.
- Hanssen, A. G., Langseth, M., & Hopperstad, O. S. (2000). “Static and Dynamic Crushing of Circular Aluminium Extrusions with Aluminium Foam Filler.” *International Journal of Impact Engineering*, 24(5), 475–507.
- Hutchinson, T., Pantoli, E., McMullin, K., Hildebrand, M., Underwood, G. (2014). “Seismic Drift Compatibility of Architectural Precast Concrete Panels and

- Connections: A Design Guide for Engineers.” University of California, San Diego. Department of Structural Engineering, Report No. SSRP-14/16.
- Idriss, J., Fritz, J., Schmidt, J. (2016). “Dynamic Analysis of Insulated Metal Panels for Blast Effects.” *Structures Magazine*, Feb. 2016, 12-15.
- Kim, H. S. (2002). “New Extruded Multi-Cell Aluminum Profile for Maximum Crash Energy Absorption and Weight Efficiency.” *Thin-Walled Structures*, 40(4), 311–327.
- Lavarnway, D. (2013). Evaluating the use of Ductile Envelope Connectors for Improved Blast Protection of Structures. Master’s thesis: OhioLINK ETD.
- Mamalis, A. G., Johnson, W., & Viegelaahn, G. L. (1984). “The Crumpling of Steel Thin-Walled Tubes and Frusta Under Axial Compression at Elevated Strain-Rates: Some Experimental Results.” *International Journal of Mechanical Sciences*, 26(11–12), 537– 547.
- Mamalis, A. G., Manolakos, D. E., Saigal, S., Viegelaahn, G., & Johnson, W. (1986). “Extensible Plastic Collapse of Thin-Wall Frusta as Energy Absorbers.” *International Journal of Mechanical Sciences*, 28(4), 219–229.
- McKenna, F., & Fenves, G. L. (2004). OpenSees command language manual, version 1.5.2. *Pacific Earthquake Engineering Research Center*. (<http://opensees.berkeley.edu>).
- Naito, C., Dinan, R., and Bewick, B. (2011). “Use of Precast Concrete Walls for Blast Protection of Steel Stud Construction.” *Journal of Performance of Constructed Facilities*, 25(5); 454-463.

- National Institute of Standards and Technology (NIST). (2007). “Best Practices for Reducing the Potential for Progressive Collapse in Buildings”. U.S. Department of Commerce. *Report NISTIR 7396*.
- Parker, J. C. (2008). “Steel Design Guide: Facade Attachments to Steel Buildings.” American Institute of Steel Construction, Chicago, IL.
- Precast/Prestressed Concrete Institute (PCI). (2000). “Tolerance Manual for Precast and Prestressed Concrete Construction.” *Report MNL-135-00*.
- Reid, S.R., & Reddy, T.Y. (1978). Effect of strain hardening on the lateral compression of tubes between rigid plates. *International Journal of Solids and Structures*, 14(3), 213-225.
- Rendos, R. (2018). Experimental and Analytical Evaluation of Multi-Hazard Ductile Façade Connectors. Master’s thesis: OhioLINK ETD.
- Sabelli, R. (2001). Research on Improving the Design and Analysis of Earthquake-Resistant Steel-Braced Frames. *The 2000 National Earthquake Hazard Reduction Program (NEHRP) Professional Fellowship Report*. Oakland, CA: Earthquake Engineering Research Institute.
- Salehghaffari, S., Rais-Rohani, M., & Najafi, A. (2011). “Analysis and Optimization of Externally Stiffened Crush Tubes.” *Thin-Walled Structures*, 49(3), 397–408.
- Salim, H., Muller, P., Dinan, R. (2005). Response of conventional steel stud wall systems under static and dynamic pressure. *Journal of Performance of Constructed Facilities*, 19(4), 267-276.

- Slovenec, D. (2016). Seismic Evaluation, Rehabilitation, and Improved Design of Sub-Standard Steel Concentrically Braced Frame Buildings. Master's thesis: OhioLINK ETD.
- United States Department of Defense (DOD). (2008). "Unified Facilities Criteria, Structures to Resist the Effects of Accidental Explosion." *Report UFC 3-340-02*.
- United States Nuclear Regulatory Commission (USNRC). (2007). Design-Basis Tornado and Tornado Missiles for Nuclear Power Plants. USNRC Regulatory Guide 1.76, Revision 1.
- Young, W., & Budynas, R. (2002). *Roark's Formulas for Stress and Strain*. New York, NY: McGraw-Hill.
- Zhang, X., & Zhang, H. (2014). "Axial Crushing of Circular Multi-Cell Columns." *International Journal of Impact Engineering*, 65, 110–125.

Appendix A: MHFS Connector Thermal Fatigue Assessment

1. Introduction

The proposed multi-hazard façade system (MHFS) design methodology relies upon a combination of slotted or possibly oversized bolt holes to accommodate in-plane panel expansion and contraction due to changes in temperature and moisture content. While this approach is common in traditional façade system connection design, there is some question as to the long-term reliability of sliding bolts as corrosion or mechanical issues (e.g. bolts are displaced within the holes due to settlement/movement of building frame elements over time) can cause the connections to “lock up”. Large forces can develop rapidly in these locked connections due to the high in-plane stiffness of, say, a typical reinforced concrete façade panel, potentially resulting in premature failure of the connection(s).

The MHFS connectors—particularly the multi-hazard ductile connectors (MDCs)—differ from traditional façade connectors in that they include a ductile (rolling) in-plane deformation mode, allowing for a backup means of accommodating in-plane deformations in the event of connection lock-up. The preferred MHFS connector layout for a reinforced concrete panel type is shown in Fig. A-1 along with the fixity and resulting locations from which panel expansion and contraction are expected to occur. The MDC-Vs (effectively) fix the panel vertically along the top edge, while the lone MDC-L fixes the panel laterally along its centerline. In the event of connection lock-up, lateral panel expansion/contraction about this centerline imposes rolling deformations across the MDC-Vs, which are critical for supporting the panel’s weight. The MDC connection details include a somewhat atypical fillet weld detail which attaches the HSS tube to the plates on either side (building frame and panel); the boundary between HSS tube wall and the welds here is the expected failure location during tube rolling based on both experimental and

analytical observations. The fatigue life of this detail subjected to repeated temperature (and moisture) cycles is investigated in this section, along with the fatigue life of the same detail subjected to longitudinal shearing across the HSS tube.

2. Fatigue Evaluation

The fatigue life of the MDCs was evaluated using the following procedure:

1. Determine a prototype MHFS design
2. Obtain an appropriate set of temperature data
3. Convert temperature data to a deformation protocol at the connector(s) in question
4. Evaluate the maximum stress caused by each deformation excursion
5. Combine stresses from each cycle with the connection detail to estimate the number of cycles—and, thus, amount of time—before failure is expected (via Miner’s Rule).

2.1 Prototype MHFS Design and Estimated Maximum Stress

The chosen prototype MHFS design utilizes a reinforced concrete panel which is thirteen feet high by thirty feet wide. Concrete has a coefficient of thermal expansion of $6 \times 10^{-6}/^{\circ}\text{F}$, which can be multiplied by the change in temperature and length of the panel in the direction(s) of expansion or contraction to determine the expanded dimension(s). MDCs which use a 12-inch length of HSS6x0.25 section were chosen for simplicity and based on available finite element analysis (FEA) data however this section and length is similar to MDC designs obtained through the full MHFS design procedure. Critical MDC mechanical properties for both rolling and longitudinal shearing actions are summarized in Table A-1. The “stress rate” quantity shown in this table is simply the expected material yield stress ($R_y\sigma_y$) of 64.4 ksi divided by the yield deformation. This quantity is used to

estimate the maximum material stress during elastic deformations with the assumption of a linear variation of maximum stress up to 64.4 ksi at the yield (plastic mechanism formation) deformation. For the connector configuration shown in Fig. A-1, lateral deformations impose rolling deformations across the MDC-Vs which places transverse shearing stresses on the welds. Longitudinal shearing of the HSS tubes imposes longitudinal (and normal due to bending) stresses on the MDC welds. In either case, the maximum stress location is at the weld-to-tube wall interface based on FEA results.

2.2 Temperature Data and Deformation Protocol(s)

Temperature data was obtained from the U.S. National Oceanic and Atmospheric Administration (NOAA) National Data Buoy Center, Station LORO1 in Lorain Harbor, Ohio, which is located on the coast of Lake Erie, West of Cleveland. Northeast Ohio is an appropriate location for a temperature-based fatigue evaluation in the United States due to significant fluctuations in seasonal temperatures. This station continuously records weather data—including temperature—every ten minutes. Data from 2007-2017 was downloaded to utilize the most recent decade’s worth of data for this evaluation. This data is plotted in Fig. A-2. Plot (a) shows the daily maximum and minimum recorded data points for each day over the ten-year period, while plot (b) shows the maximum temperature fluctuation for each day.

The temperature data from 2007-2017 was combined into one “aggregate” year by taking the average (over ten years) maximum and minimum temperatures on each day (365) of the year. This procedure was performed to obtain a representative “typical” year of data with which to perform fatigue life estimation calculations. This aggregate year of data is shown in Fig. A-2 (a), with plot (b) showing the temperature fluctuation for each

day. The average fluctuation line uses the average daily maximum and minimum temperatures to calculate the daily fluctuation, while the other line—referred to herein as the “extreme” temperature fluctuation—uses the average maximum daily temperatures plus the standard deviation of maximum temperature for that day and the average minimum daily temperatures minus the standard deviation of minimum temperature for that day.

Each day was assumed to consist of one deformation cycle which starts with the panel at the previous day’s low temperature dimensions, increases to the daily maximum temperature dimensions, then decreases to the daily minimum dimensions; the maximum difference between these adjacent points is taken as the deformation amplitude for that day. Installation of the prototype panel was assumed to occur at the average overall temperature of the aggregate year (around 50 °F), at which time the panel is at its nominal dimensions of 13’x30’. With this starting point and the aggregate year temperature fluctuations, the vertical and lateral panel deformation per day were calculated as shown in Fig. A-3. The average and extreme temperature fluctuations (2 temperature data sets) were considered to evaluate the fatigue life of MDCs subjected to both the lateral and vertical deformation protocols (2 directions) considering all deformations accommodated via either rolling or longitudinal shearing of the HSS tubes (2 orientations; 8 total configurations).

2.3 Fatigue Life

Based on the deformation protocols shown in Fig. A-3, all potential rolling deformations are less than the expected yield deformation, which allows for the use of high-cycle fatigue evaluation methods. The longitudinal shear deformations are less than yield considering vertical panel expansion/contraction, however the lateral direction protocols would likely exceed yield in many cases. Evaluation of the fatigue life in this case would require some

combination of low- and high-cycle fatigue methods. For simplicity, longitudinal shearing deformations which exceed yield are treated as elastic (with linearly-varying stresses which exceed than their expected maximum); the MHFS connector layouts considered in this research do not include multiple MDCs oriented such that lateral panel expansion/contraction would require longitudinal shearing of the HSS tubes, and the consideration of their fatigue life subjected to this deformation protocol is included here simply for completeness. For all cases, Miner's Rule is applied with α coefficient of 3 (typical for structural steel and fillet welds). Threshold stresses—which set a lower limit for stress which contributes to fatigue damage of the material—are neglected in this evaluation due to the somewhat atypical weld detail employed in the MDC connection. A suitable prototype weld detail fatigue constant is not available in AISC 360-10 Appendix 3 for the MDC connection, however the rolling direction is believed to most closely match Case 5.1 with constant, C_f , equal to 120×10^8 . For longitudinal shearing, Case 4.1 is believed to be the closest match, with $C_f = 11 \times 10^8$. These constants are used with the estimated maximum stress for each daily cycle summed over the entire aggregate year to calculate the number of years it would take to induce fatigue failure in the connection.

Results of the fatigue evaluation for all combinations of aggregate year temperature data set, MDC orientation, and panel expansion/contraction direction are summarized in Table A-2. All C_f values in AISC 360-10 Appendix 3 are included in this table to consider the full range of potential constants and their resulting fatigue life estimations, with the assumed best estimate highlighted. Based on these results, the worst-case scenario for MDC rolling—considering the extreme temperature data set and smallest available C_f value—estimates a fatigue life of about 300 years, which far exceeds the expected

serviceable life for a practical MDC estimation. For a longitudinally-sheared MDC accommodating vertical expansion/contraction, the expected fatigue life ranges from 30 to 400 years. With an expected design life of, say, 50 years, this fatigue life is most likely adequate.

3. Conclusions and Recommendations for Future Work

A fatigue evaluation of MDCs installed on a reinforced concrete panel subjected to cyclic deformations due to temperature fluctuations was performed to evaluate the potential for premature failure of these critical connecting components in the proposed MHFS. Temperature data from 2007-2017 in Lorain, Ohio was used to create a representative year of daily temperature fluctuations, which in turn were used to create connector deformation protocols. Miner's Rule for high-cycle fatigue life evaluation was used to estimate the number of typical years of temperature effects the MDCs can withstand considering both the expected (average) and extreme (average plus/minus standard deviation) temperature data sets, and both potential in-plane MDC orientations. For the preferred MHFS connector layout, the MDC-Vs are expected to be capable of undergoing about 300 years of temperature effects, which far exceeds their expected design life. Additional work on this topic should add moisture effects, which also cause volumetric expansion/contraction in porous building materials. Brick veneer façade systems may also need to be evaluated depending on the proposed connector configuration.

Table A-1: Prototype MDC Design for Fatigue Evaluation

MDC Action:	<u>Rolling</u>	<u>Shearing</u>
Plastic Mechanism Strength (kip):	8.10	69.0
Elastic Stiffness (kip/in):	25.0	1500
Yield Deformation (in):	0.324	0.046
Stress Rate (kip/in/in):	199	1400

Notes: Based on 12-inch HSS6x0.25 MDC design.

Stress rate assumes linear variation from zero to 64.4 ksi at yield deformation.

Table A-2: MDC Fatigue Life Evaluation Considering Thermal Expansion and Contraction of Reinforced Concrete Façade Panel

Fatigue Life (years) Reinforced Concrete Panel 13'x30'		Lateral Expansion/Contraction Temperatures		Vertical Expansion/Contraction Temperatures	
MDC Action	C _f	Average	Extreme	Average	Extreme
Rolling	1.5E+12	15220000	1218900	187040000	14980000
	1.20E+10	121760	9751	1496320	119840
	6.10E+09	61895	4957	760629	60919
	4.40E+09	44645	3575	548651	43941
	2.20E+09	22323	1788	274325	21971
	1.10E+09	11161	894	137163	10985
	3.90E+08	3957	317	48630	3895
Shearing	1.5E+12	43578	3490	535560	42891
	1.20E+10	349	28	4284	343
	6.10E+09	177	14	2178	174
	4.40E+09	128	10	1571	126
	2.20E+09	64	5	785	63
	1.10E+09	32	3	393	31
3.90E+08	11	1	139	11	

Notes: Based on prototype MDC design using 12-inch HSS6x0.25 section.
 Temperatures taken from Lorain, OH from 2007-2017.
 Bold C_f values are believed to be the most appropriate based on connection details.
 Shaded boxes show best estimates of fatigue life for the proposed connector layout.
 Calculated using Miner's Rule ($\alpha = 3$), ignoring threshold stress.

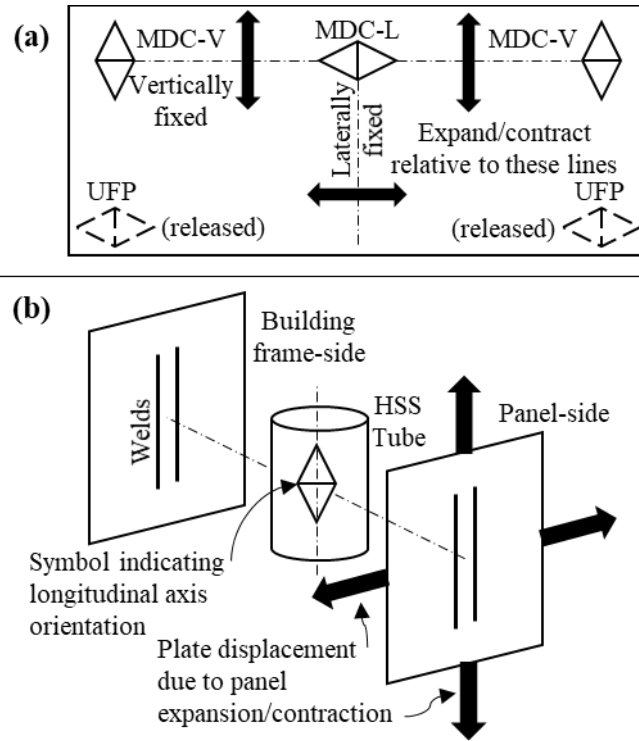


Fig. A-1: MHFS (a) Connector Layout and Expansion/Contraction Diagram and (b) MDC Orientation and Details

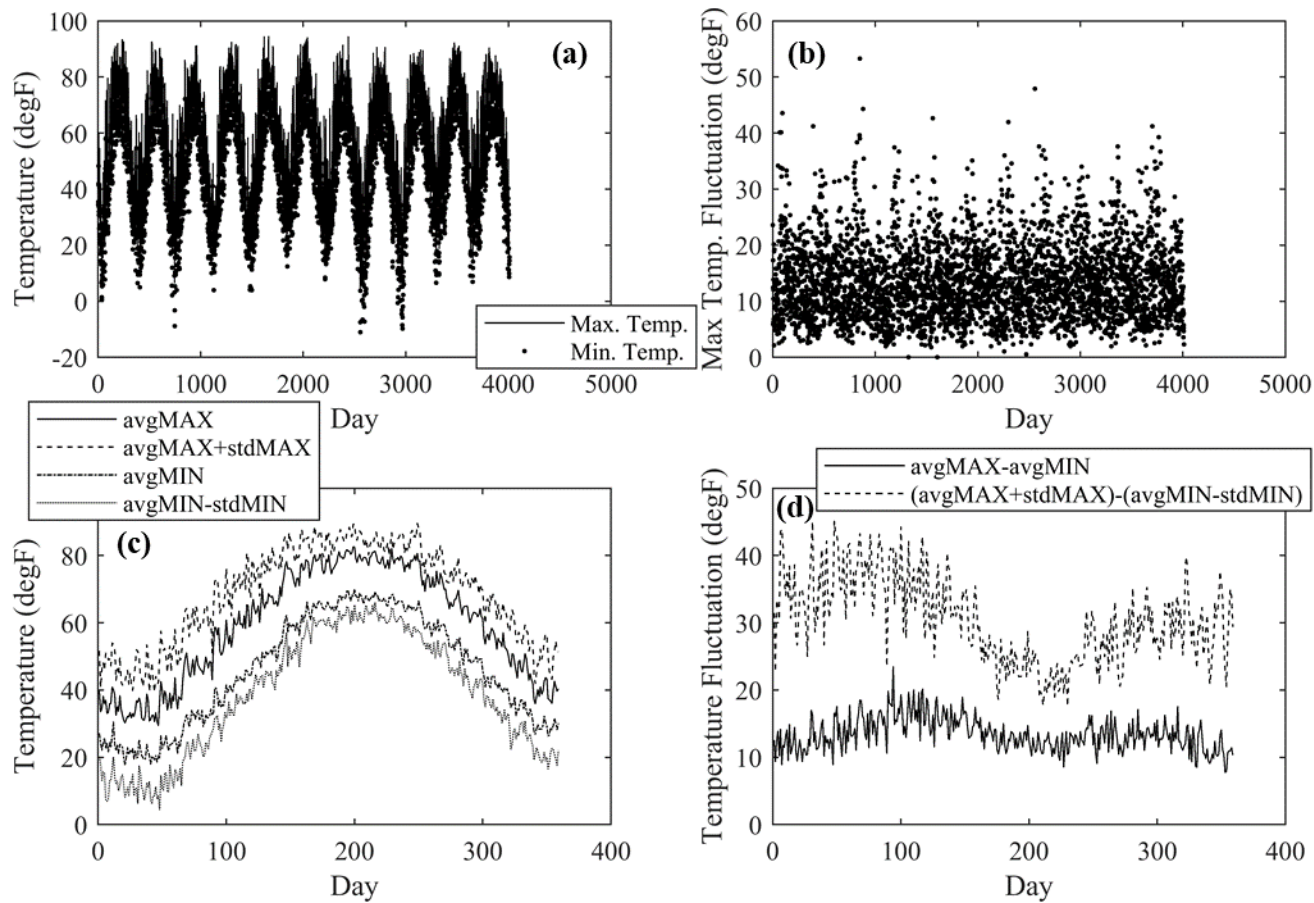


Fig. A-2: 2007-2017 Lorain, OH Temperature Data (a) Daily Maximum and Minimum and (b) Difference Between Extreme Temperatures; Aggregate Year (c) Daily Average Temperature Extremes, and (d) Daily Temperature Fluctuation

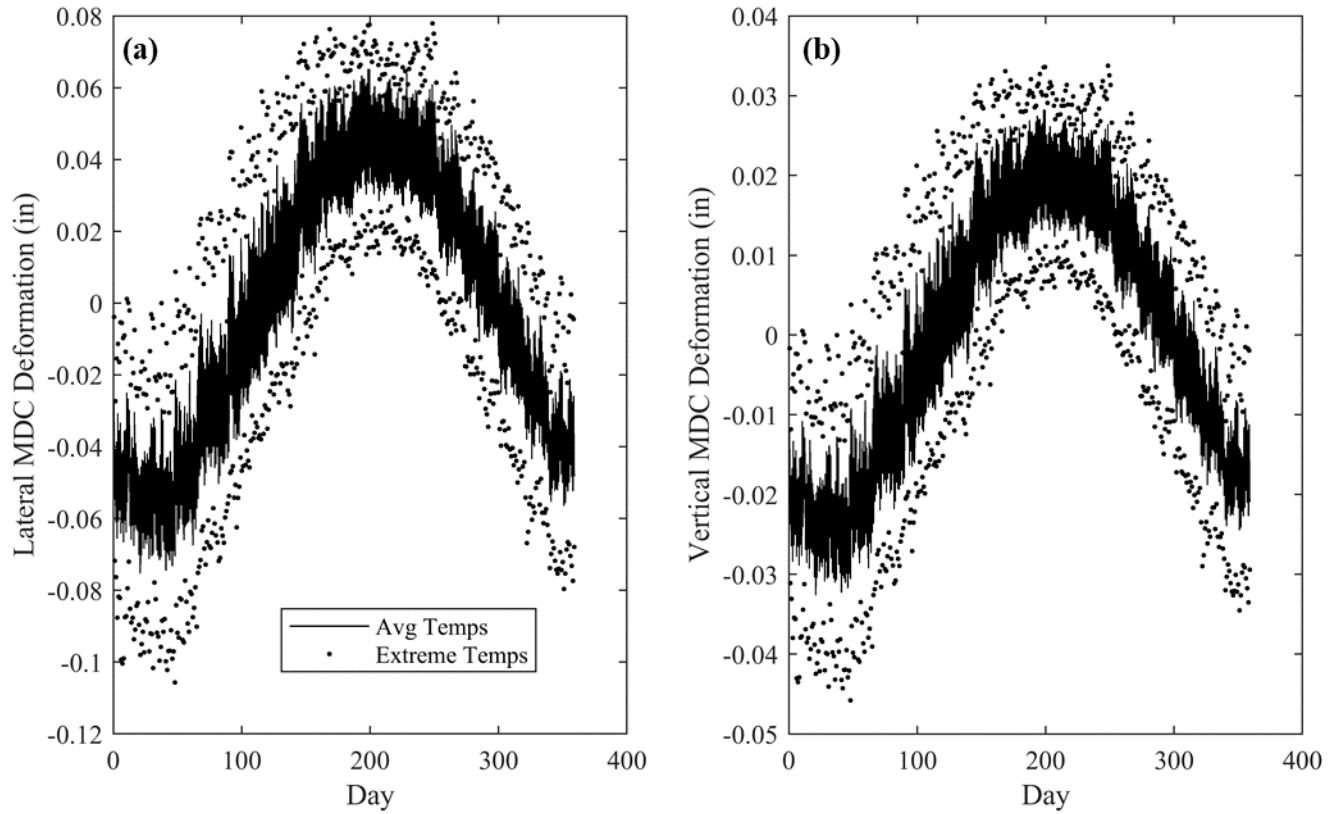
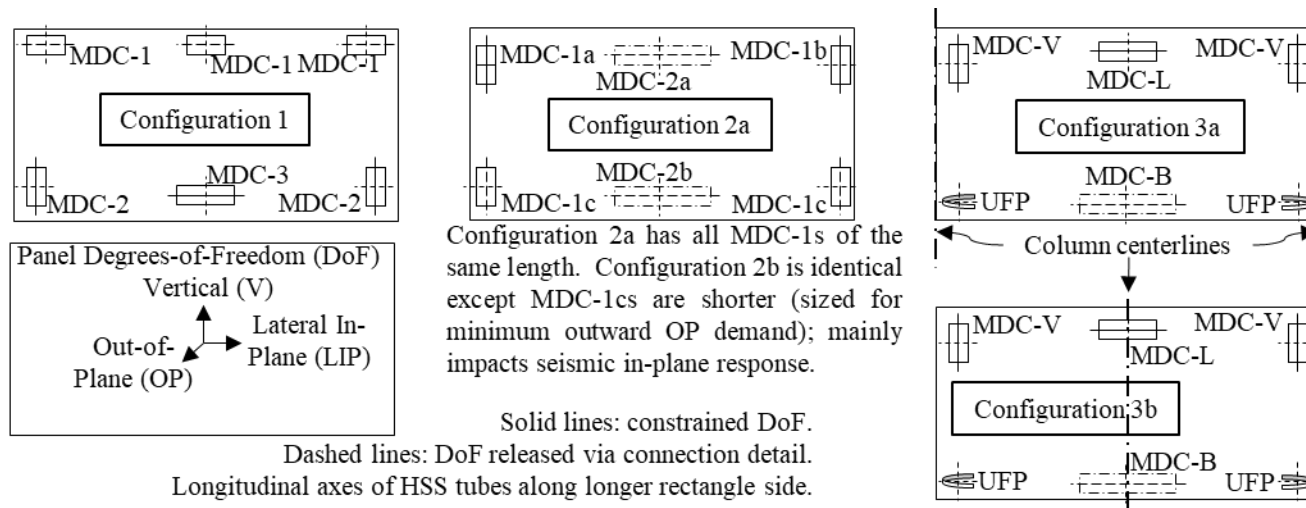


Fig. A-3: Annual MDC Deformation Protocols for (a) Lateral and (b) Vertical Directions for Reinforced Concrete Façade Panel (13'x30') Connectors based on Aggregate Year Daily Temperature Fluctuation Data

Appendix B: MHFS Alternative Connector Layouts



Configuration	Advantages	Disadvantages
1 ⁱ	Resists all minimum force demands in all degrees-of-freedom	Over-reliance on slotted bolt holes
	Accommodates corner panel contact during seismic drift	Over-constrained in-plane; adjustments difficult
	Includes performance-based, protective design for blast, impact, tornado, etc. events	Coupled minimum and extreme hazard designs
2 ⁱⁱ (a,b)	Shaded advantages above	Most complex corner panel contact accommodation mechanism
	Improved installation adjustability	Relies on HSS tube rolling for in-plane seismic drift accommodation
	Fewest bolt connections	HSS tubes lack adequate rolling deformation capacity
	Decoupled minimum force and protective designs	Potential amplification of in-plane drifts by façade system
3 ⁱⁱⁱ (a,b)	Corner panel contact uses HSS tube rolling (reduced force)	Reduced outward OP resistance due to de-coupled design
	Shaded advantages above	Multiple connector types (MDCs and UFPs) - complexity
	Corner panel contact uses UFP pulling (highly ductile)	Atypical "staggered" panel layout (centered on columns)
3b	Potential supplementation of progressive collapse mechanism	Reduced OP panel rotation capacity due to column location

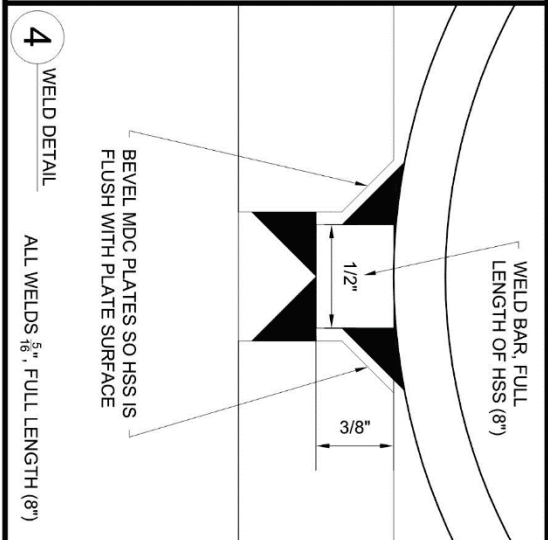
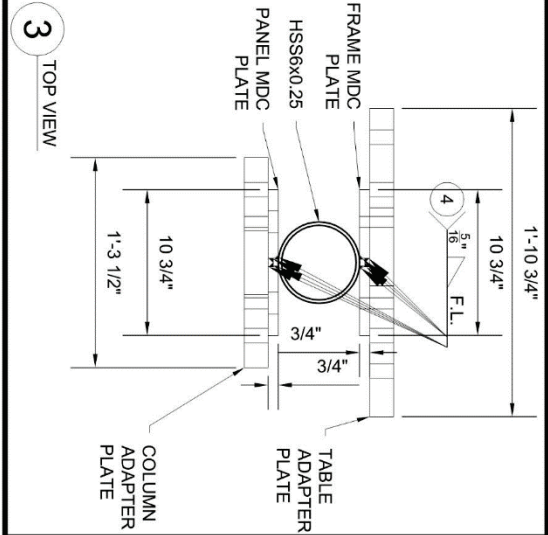
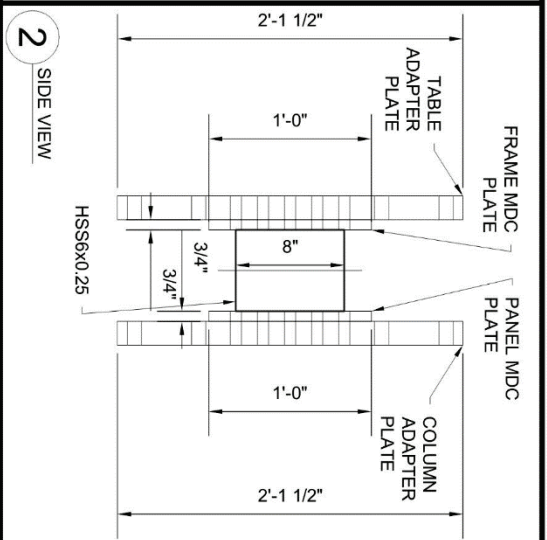
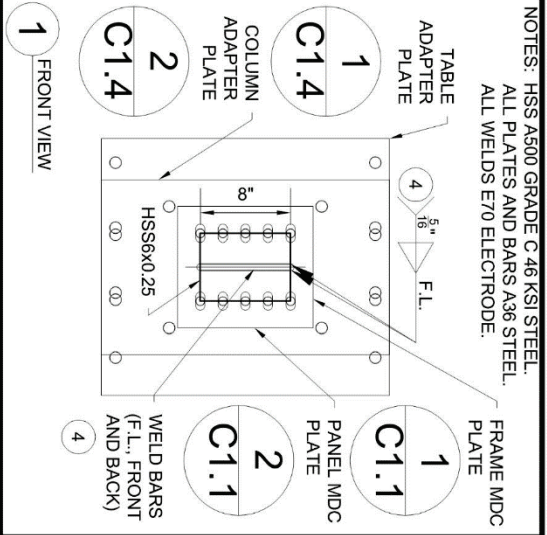
- Notes:
- i. Original connector layout; used during HSS crushing, pulling, and longitudinal shearing experimental tests.
 - ii. Second major iteration; used during HSS rolling experimental tests
 - iii. Current design iteration (focus of design methodology writing). Inclusion of UFPs resolved drift issues of configuration 2.

Configuration	Connector	Count	Location	Orientation ^a	Slots (short or long) / Oversize		In-Plane DOFs	
					Panel-Side	Frame-Side	Fixed	Released ^b
1	MDC-1	3	Top corners and center	LIP	V, short (ΔT) ^c	LIP, long (drift) ^d	-	V, LIP
	MDC-2	2	Bottom corners	V	-	LIP, short (ΔT)	V	LIP
	MDC-3	1	Bottom center	LIP	-	-	LIP	-
2	MDC-1a	1	Top corner	V	-	-	V, LIP	-
	MDC-1b	1	Top corner	V	-	LIP, short (ΔT)	V	LIP
	MDC-1c	1	Bottom corners	V	-	Oversize (ΔT)	-	V, LIP
	MDC-2a	1	Top center	LIP	-	No connection	-	All
	MDC-2b	1	Bottom center	LIP	-	No connection	-	All
3	MDC-V	2	Top corners	V	-	LIP, short (ΔT)	V	LIP
	MDC-L	1	Top center	LIP	-	V, short (ΔT)	LIP	V
	MDC-B	1	Bottom center	LIP	-	No connection	-	All
	UFP	2	Bottom corners	N/A	Slots (short) or oversize (ΔT)		-	V, LIP

- Notes:
- a. Principal panel degree-of-freedom (DOF) parallel to connector's HSS tube's longitudinal axis.
 - b. Released DOFs, other than connectors with no frame-side connection, rely on slotted/oversized bolt holes.
 - c. (ΔT) indicates slotted/oversized holes sized for maximum +/- thermal/moisture expansion/contraction effects, as well as tolerances for fabrication, installation, and potential on-site adjustment.
 - d. (drift) indicates slotted holes sized for maximum expected inter-story drift (+/-).

Appendix C: Experimental Specimens Fabrication Drawings

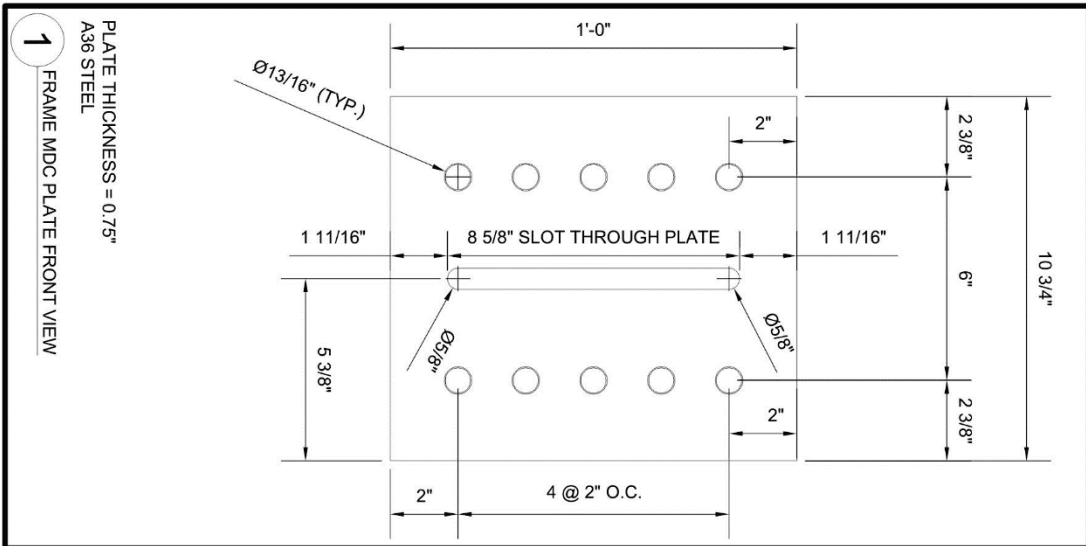
NOTES: HSS A500 GRADE C 46 KSI STEEL.
 ALL PLATES AND BARS A36 STEEL.
 ALL WELDS E70 ELECTRODE.



CASE WESTERN
 RESERVE UNIVERSITY
 CIVIL ENGINEERING DEPT.

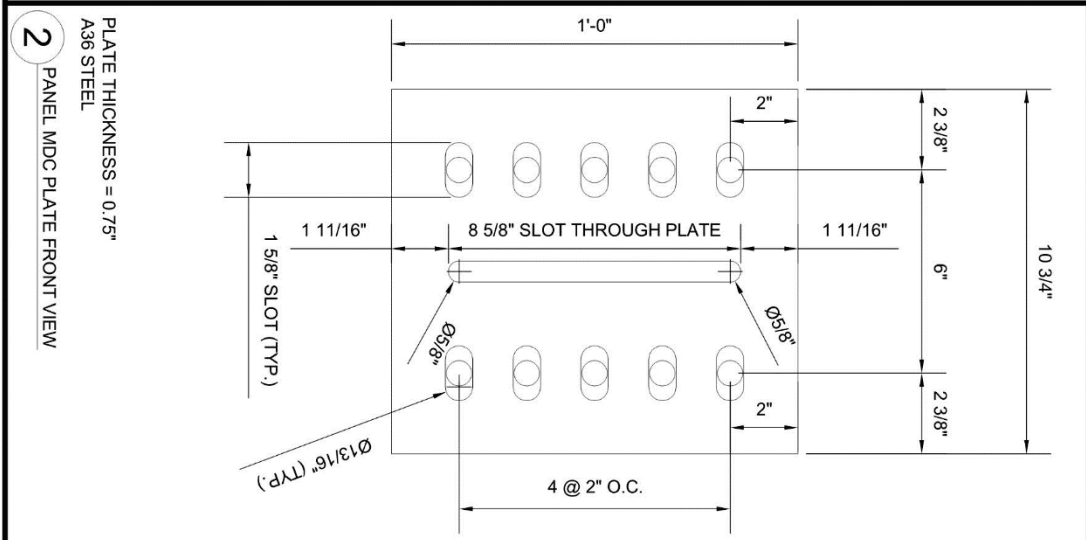
MULTI-HAZARD
 DUCTILE CONNECTOR
 EXPERIMENTAL DESIGNS

DRAWN BY: DES
 CHECKED BY:
 APPROVED BY:
 DATE: 05/16/2017
 SHEET: 1 OF 9
 SCALE: N/A
 SHEET TITLE:
C1.0
 MDC-2 ASSEMBLY



1 FRAME MDC PLATE FRONT VIEW

PLATE THICKNESS = 0.75"
A36 STEEL

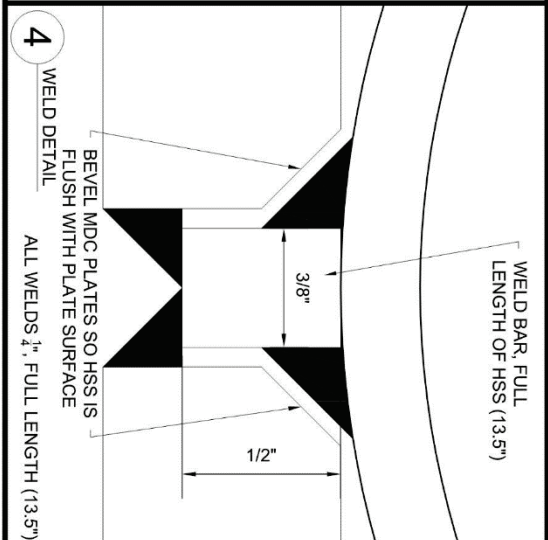
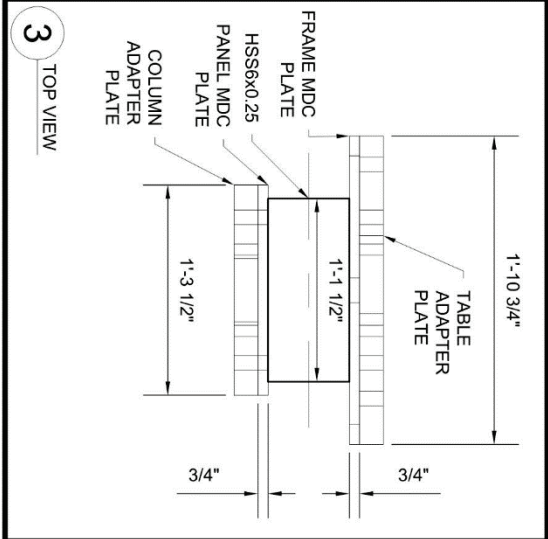
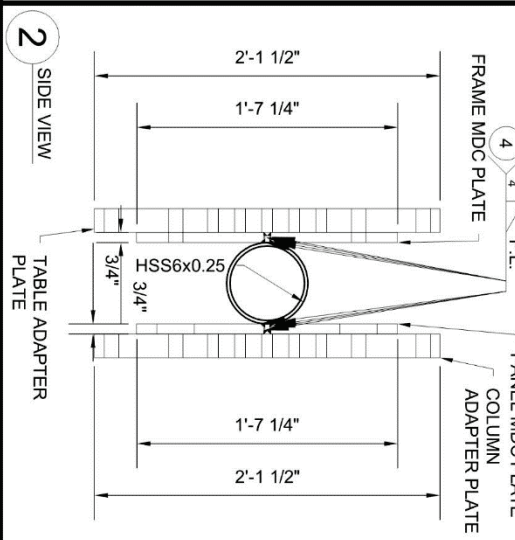
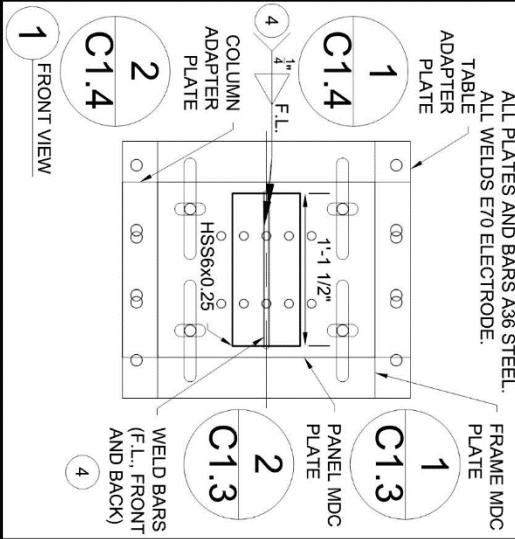


2 PANEL MDC PLATE FRONT VIEW

PLATE THICKNESS = 0.75"
A36 STEEL

<p>DRAWN BY: DES CHECKED BY: APPROVED BY: DATE: 05/16/2017 SHEET: 2 of 9 SCALE: N/A</p>	<p>MULTI-HAZARD DUCTILE CONNECTOR</p>	<p>CASE WESTERN RESERVE UNIVERSITY</p>
	<p>EXPERIMENTAL DESIGNS</p>	<p>CIVIL ENGINEERING DEPT.</p>
	<p>C1.1</p>	
	<p>SHEET TITLE: MDC-2 PLATES</p>	

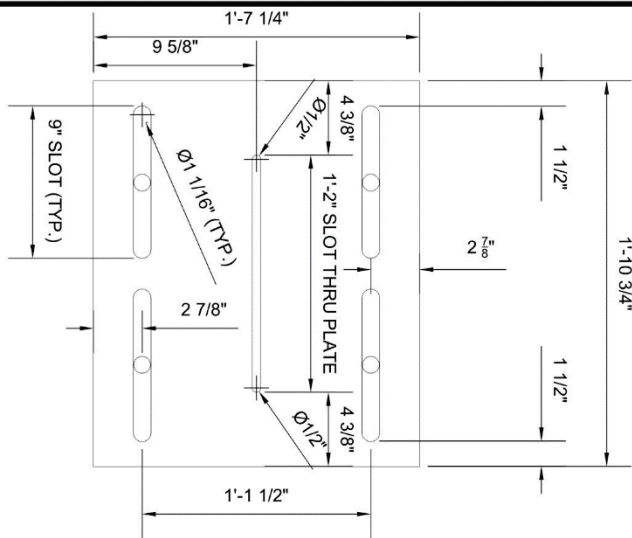
NOTES: HSS A500 GRADE C-46 KSI STEEL.
 ALL PLATES AND BARS A36 STEEL.
 ALL WELDS E70 ELECTRODE.



CASE WESTERN
 RESERVE UNIVERSITY
 CIVIL ENGINEERING DEPT.

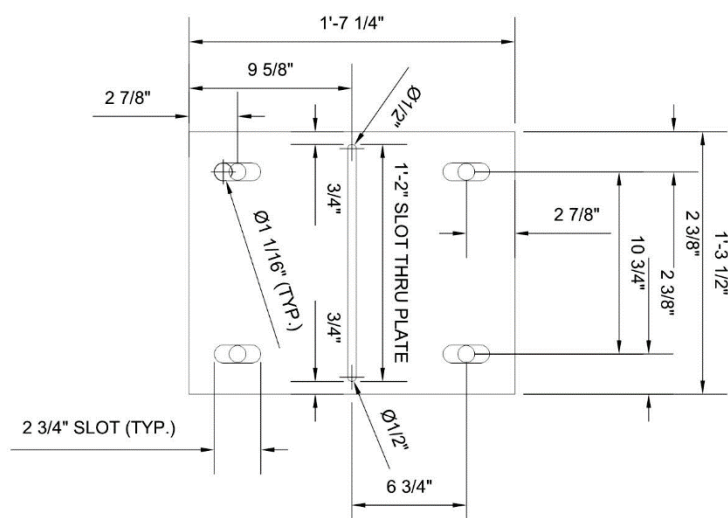
MULTI-HAZARD
 DUCTILE CONNECTOR
 EXPERIMENTAL DESIGNS

DRAWN BY: DES
 CHECKED BY:
 APPROVED BY:
 DATE: 05/16/2017
 SHEET: 3 of 9
 SCALE: N/A
 SHEET TITLE:
C1.2
 MDC-1 ASSEMBLY



1 FRAME MDC PLATE FRONT VIEW

PLATE THICKNESS = 0.75"
A36 STEEL



2 PANEL MDC PLATE FRONT VIEW

PLATE THICKNESS = 0.75"
A36 STEEL

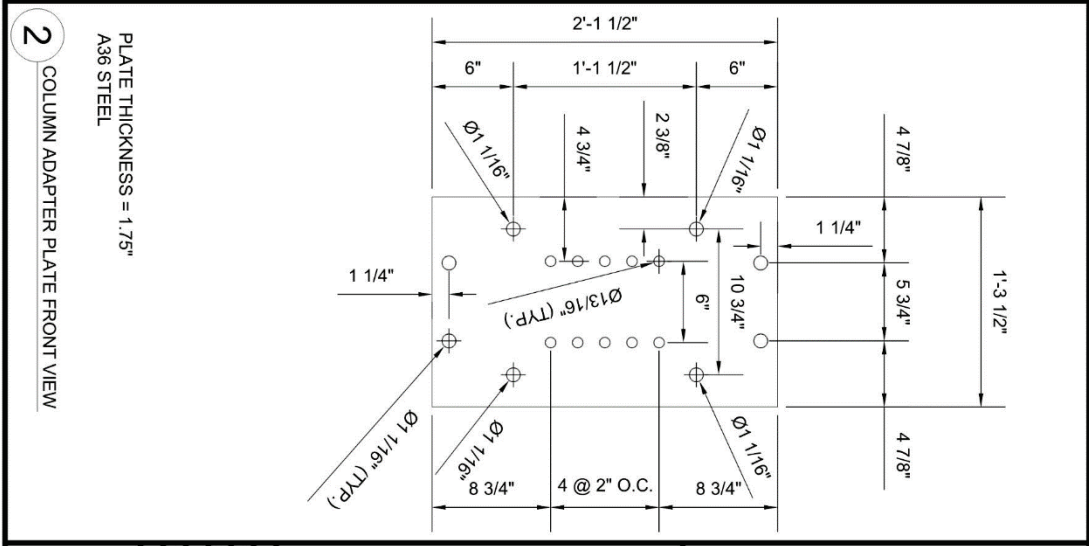
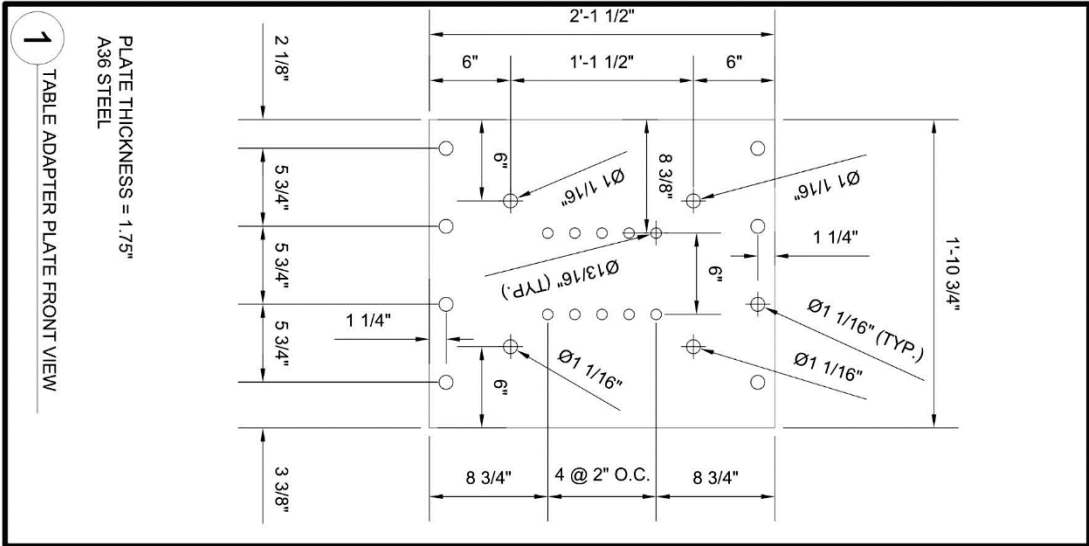
**MULTI-HAZARD
DUCTILE CONNECTOR**

EXPERIMENTAL DESIGNS

**CASE WESTERN
RESERVE UNIVERSITY**

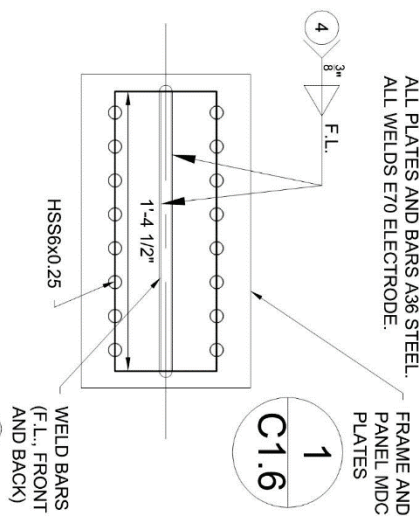
CIVIL ENGINEERING DEPT.

DRAWN BY: DES
CHECKED BY:
APPROVED BY:
DATE: 05/16/2017
SHEET: 4 of 9
SCALE: N/A
SHEET TITLE:
C1.3
MDC-1 PLATES

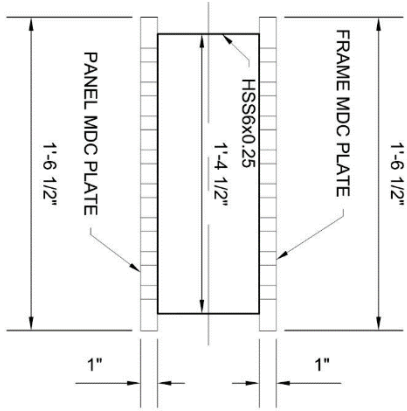


DRAWN BY: DES CHECKED BY: APPROVED BY: DATE: 05/16/2017 SHEET: 5 OF 9 SCALE: N/A	C1.4 SHEET TITLE: ADAPTER PLATES	MULTI-HAZARD DUCTILE CONNECTOR	CASE WESTERN RESERVE UNIVERSITY
		EXPERIMENTAL DESIGNS	CIVIL ENGINEERING DEPT.

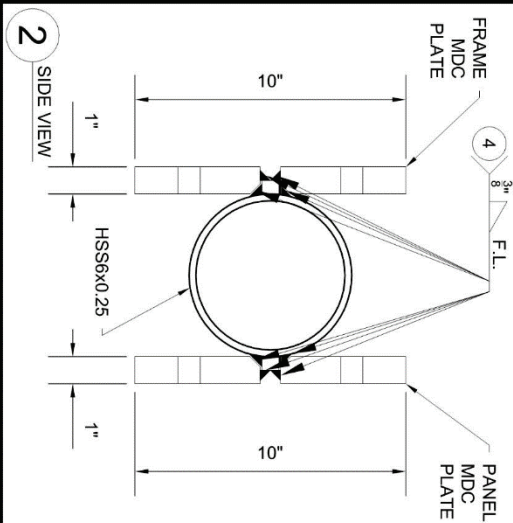
NOTES: HSS A500 GRADE C 46 KSI STEEL.
ALL PLATES AND BARS A36 STEEL.
ALL WELDS E70 ELECTRODE.



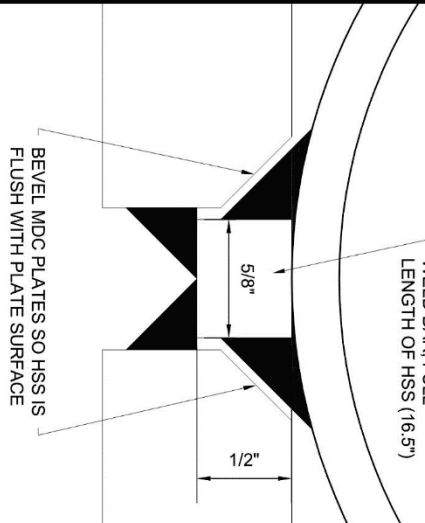
1 FRONT VIEW



3 TOP VIEW



2 SIDE VIEW

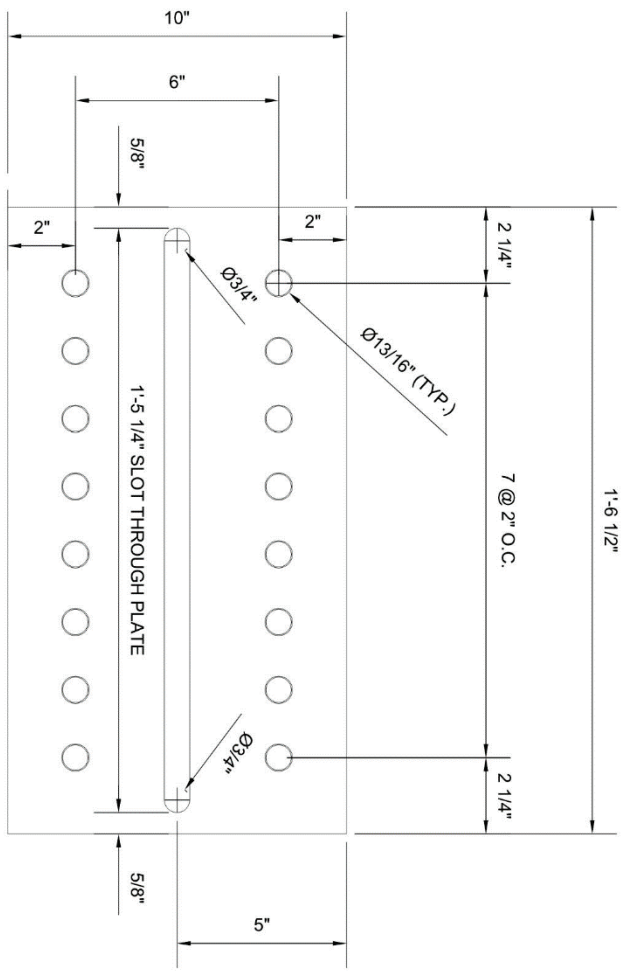


4 WELD DETAIL

CASE WESTERN
RESERVE UNIVERSITY
CIVIL ENGINEERING DEPT.

MULTI-HAZARD
DUCTILE CONNECTOR
EXPERIMENTAL DESIGNS

DRAWN BY: DES
CHECKED BY:
APPROVED BY:
DATE: 05/16/2017
SHEET: 6 OF 9
SCALE: N/A
SHEET TITLE:
C1.5
MDC-3 ASSEMBLY



1 FRAME AND PANEL MDC PLATE FRONT VIEW

PLATE THICKNESS = 1"
 A36 STEEL
 PANEL AND FRAME MDC PLATES ARE IDENTICAL.

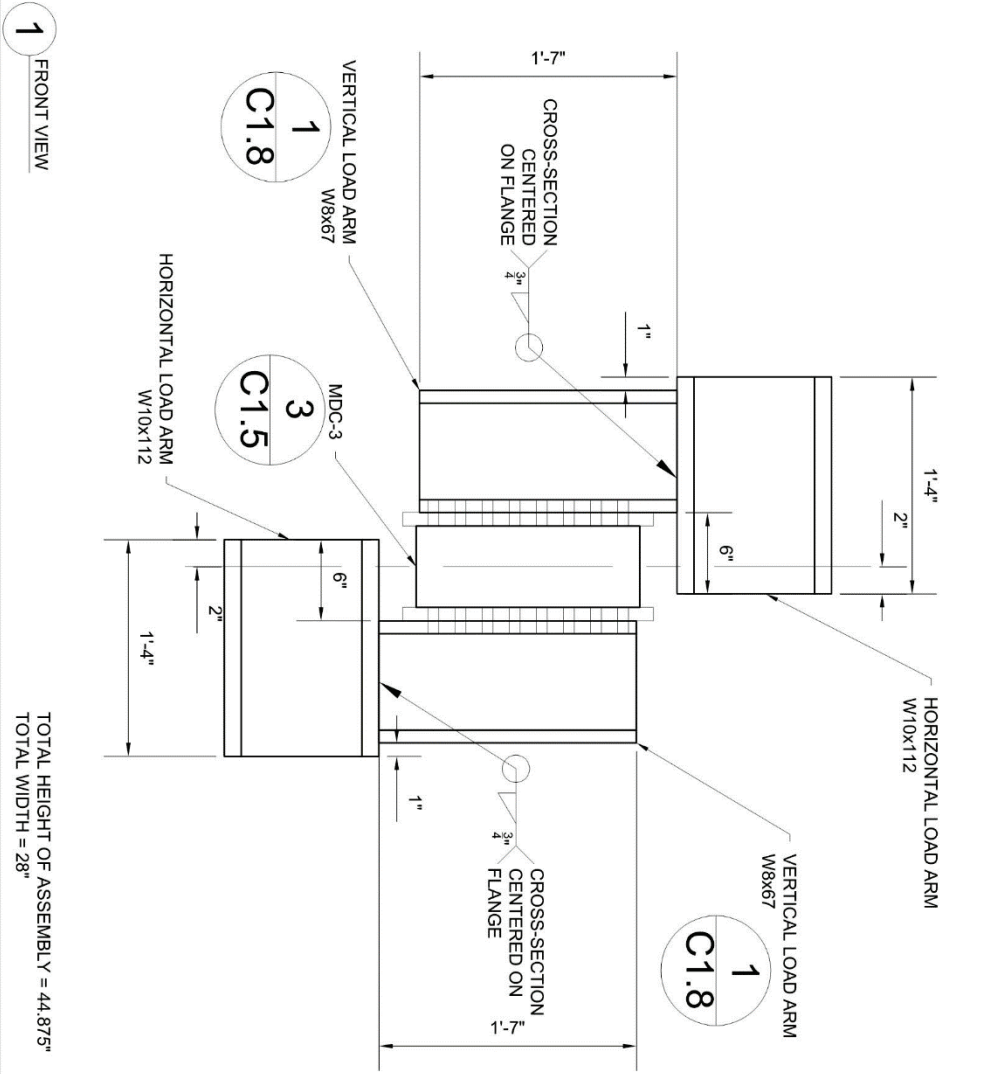
CASE WESTERN
 RESERVE UNIVERSITY
 CIVIL ENGINEERING DEPT.

MULTI-HAZARD
 DUCTILE CONNECTOR
 EXPERIMENTAL DESIGNS

DRAWN BY: DES
 CHECKED BY:
 APPROVED BY:
 DATE: 05/16/2017
 SHEET: 7 of 9
 SCALE: N/A

SHEET TITLE:
C1.6
 MDC-3 PLATES

NOTES: ALL W-SECTIONS A992 STEEL.
 ALL WELDS E70 ELECTRODE.
 HORIZONTAL AND VERTICAL LOAD ARM PAIRS ARE IDENTICAL (180° ROTATION)

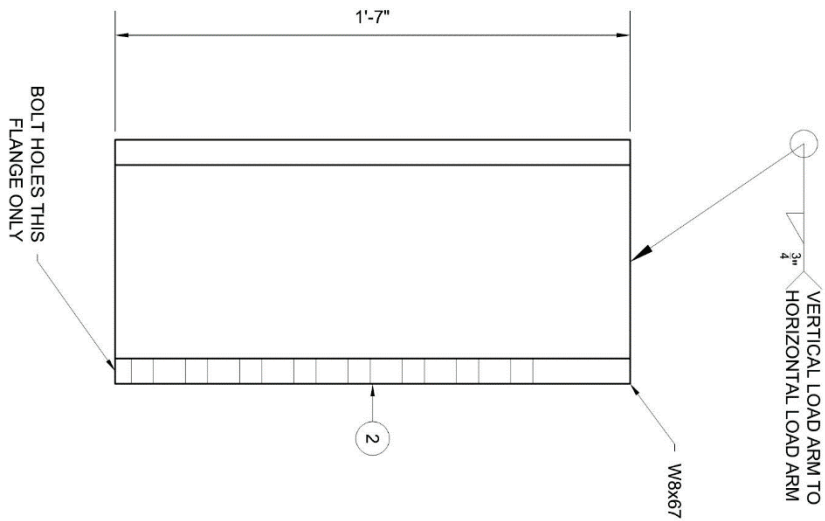


CASE WESTERN
 RESERVE UNIVERSITY
 CIVIL ENGINEERING DEPT.

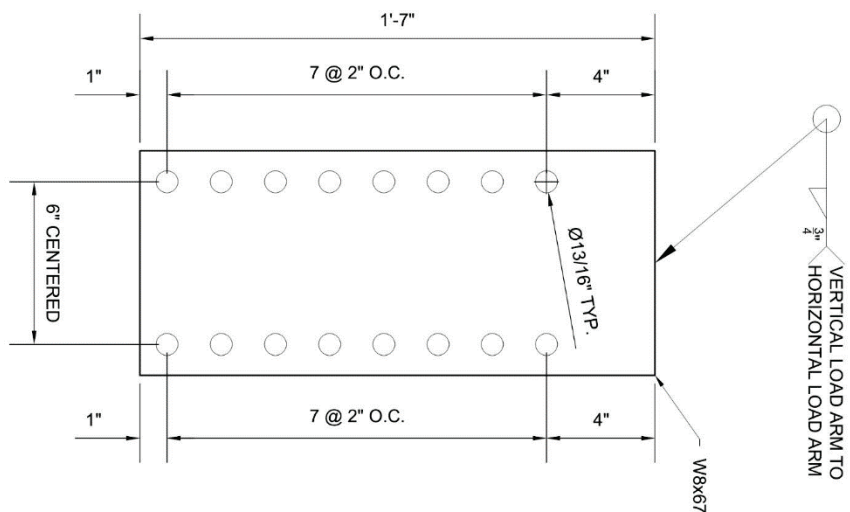
MULTI-HAZARD
 DUCTILE CONNECTOR
 EXPERIMENTAL DESIGNS

DRAWN BY: DES
 CHECKED BY:
 APPROVED BY:
 DATE: 05/16/2017
 SHEET: 8 OF 9
 SCALE: N/A
 SHEET TITLE:
C1.7
 MDC-3 TEST SETUP

NOTES: ALL W-SECTIONS A992 STEEL.
ALL WELDS E70 ELECTRODE.



1 FRONT VIEW



2 SIDE VIEW

MULTI-HAZARD
DUCTILE CONNECTOR
EXPERIMENTAL DESIGNS

CASE WESTERN
RESERVE UNIVERSITY
CIVIL ENGINEERING DEPT.

DRAWN BY: DES
CHECKED BY:
APPROVED BY:
DATE: 05/16/2017
SHEET: 9 of 9
SCALE: N/A

SHEET TITLE:
C1.8

VERTICAL LOAD ARM